Mechanisms and Machine Science 11

Yulin Wu · Shengcai Li
Shuhong Liu · Hua-Shu Dou
Zhongdong Qian

Vibration of Hydraulic Machinery

Springer

Mechanisms and Machine Science

Volume 11

Series Editor

Marco Ceccarelli

For further volumes:
http://www.springer.com/series/8779

Yulin Wu · Shengcai Li
Shuhong Liu · Hua-Shu Dou
Zhongdong Qian

Vibration of Hydraulic Machinery

Springer

Yulin Wu
Shuhong Liu
State Key Laboratory of Hydroscience and Engineering
Department of Thermal Engineering
Tsinghua University
Beijing
People's Republic of China

Shengcai Li
School of Engineering
University of Warwick
Coventry
UK

Hua-Shu Dou
Faculty of Mechanical Engineering and Automation
Zhejiang Sci-Tech University
Hangzhou
People's Republic of China

Zhongdong Qian
State Key Laboratory of Water Resources and Hydropower Engineering Science
Department of Hydraulic Engineering
School of Water Resources and Hydropower Engineering
Wuhan University
Wuhan
People's Republic of China

ISSN 2211-0984 ISSN 2211-0992 (electronic)
ISBN 978-94-007-6421-7 ISBN 978-94-007-6422-4 (eBook)
DOI 10.1007/978-94-007-6422-4
Springer Dordrecht Heidelberg New York London

Library of Congress Control Number: 2013932129

Printed on acid-free paper

Springer is part of Springer Science+Business Media (www.springer.com)

Foreword

It is a privilege to be asked to write a prefatory note for this monograph reflecting the latest advance in the field of vibration of hydraulic machinery. Working on this book with Prof. Yulin Wu, a good friend and colleague for decades, and his outstanding team members was an enjoyable experience.

A jointly authored book like this has a root back to the last century. It began in the early 1980s when for the first time I heard about Yulin, a fast-rising scholar from Prof. Zuyan Mei. Indeed in the late 1960s, with Prof. Mei and scholars from the Beijing Institute of Hydropower, a monograph *Transient Process of Hydraulic Turbine* (in Chinese) initiated by me was written but cancelled for publication in 1969. Nevertheless, it inspired the *Book Series on Hydraulic Machinery* in 1986. Yulin and Prof. Mei were actively participating in the writing of this book series meanwhile they extended their work into the new field of numerical simulations for turbines including pump-storage turbines. After Prof. Mei deceased in 2003, Prof. Wu continues leading and developing this team at Tsinghua, producing remarkable numerical works. The excellence of their work on vibration simulations made him an ideal candidate for writing a continuous volume of the title *Vibration and Oscillation of Hydraulic Machinery* published two decades ago, emphasizing on numerical predictions. Being thus invited, he discussed the scope and set up the framework with me in late 2003. Then he started preparing the manuscripts together with Prof. Shuhong Liu who joined later. During the summer of 2008, while Yulin and Shuhong visiting me at Warwick, the first draft manuscript was proposed by Yulin with my contributions mainly to Chaps. 1, 6 and 7. Later on Profs. Zhongdong Qian and Hua-Shu Dou, both former team members of Yulin at Tsinghua, joined in 2011 and 2012 respectively.

Now I am pleased to witness the completion of this book reflecting such a collective willingness and effort across decades.

Personally, I would like to thank all the supports received to my research programmes and involvement in this book. These are the UK ESRC/EPSRC grants, the 10-year support from the UK EPSRC WIMRC grants and the generous support from the UK Royal Academy of Engineering; and the Open Fund of Tsinghua University (State Key Laboratory of Hydroscience and Engineering) and the financial and technical support from the Three Gorges authority.

In particular, it is a great honour to receive the award of Chinese Global Recruit Programme of Peking University that enables me to work in Beijing closely with authors during the final stage of the book writing. The support from Prof. Cunbiao Lee of Peking University is thus highly appreciated.

20 October 2012

Shengcai Li
Zhong-guan Xin-yuan
Peking University

Preface

The present book *Vibration of Hydraulic Machinery* deals with the vibration problem which has significant influence on the safety and reliable operation of hydraulic machinery. It provides with the new achievements and the latest development in these areas in the community including those by the authors, even in the basic areas of this subject.

The prediction for vibration of hydraulic machinery is currently an important subject since vibration has a major effect on the performance of hydraulic machinery. In the last 10 years, progress has been achieved in theory, modeling, and mathematical analysis, as well as monitoring of vibration of hydraulic machinery. With hydraulic turbine capacities getting increasingly larger and pump speeds ever higher, there have been many research achievements in these areas published in symposiums, journals, and books.

This book covers the fundamentals of mechanical vibration and rotordynamics as well as their main numerical models and analysis methods for the vibration prediction. The mechanical and hydraulic excitations to the vibration are analyzed, and the pressure fluctuation induced by the unsteady turbulent flow is predicted in order to obtain the unsteady loads. This book also discusses the loads, constraint conditions, and the elastic and damping characters of the mechanical system, the structure dynamic analysis, the rotor dynamic analysis, and the instability of system of hydraulic machines, including the illustration of monitoring system for the instability, and the vibration in hydraulic units. Solutions of all the problems are necessary for vibration prediction of hydraulic machinery.

The authors of the present book are as follows: Chap. 1: Shengcai Li, Chap. 2: Shuhong Liu, Chap. 3: Zhongdong Qian, Chap. 4: Leqing Wang and Dazhuan Wu, Chap. 5: Shuhong Liu, Chap. 6: Shengcai Li, Chap. 7: Shengcai Li, Chap. 8: Dazhuan Wu and Yulin Wu, Chap. 9: Zhongdong Qian, Chap. 10: Hua-Shu Dou, and Chap. 11: Lei Jiao and Yulin Wu. Professor Hua-Shu Dou made final reviewing and compiling of the whole contents of the book.

The authors would like to thank the National Natural Science Foundation of China (NSFC) for main key project grants (contracts No. 59493700) on the key technology of hydraulic turbine generator unit of three gorges projects (1994–1999), and for key project grants (contracts No. 90410019, 2004–2007 and 10532010, 2006–2009), as well as other five projects, i. e., China Yangtze Three

Gorges Project Development Cooperation (CTGPC) for project grants (contracts No. CT-02-04-04 and CT-03-04-01); China Longtan Hydropower Development Company Ltd. for project grants (2001–2002); Harbin Institute of Large Electric Machinery & Hydraulic Turbine for project grants (contracts No. 2002158 and 2006429).

Many thanks to Fujian Electric Power Test & Research Institute, Beijing Huake Tongan Monitoring Technology Co. Ltd., Tianjin Tianfa Heavy Machinery & Hydro Power Equipment Manufacture Co. Ltd. for their supporting to the cooperative research on hydraulic machinery.

Sincere thanks to Hitachi Ltd including both Hitachi Industries Co. Ltd. and Hitachi Works, Mitsubishi Heavy Industries Co. Ltd., the Institute of Fluid Sciences of Tohoku University, and Kyushu Institute of Technology, for long time of cooperation.

The authors would highly appreciate the help of Profs. Naixiang Chen, Hongyuan Xu, Zhenwei Wang, Shuliang Cao, Yangjun Zhang, Jing Ren, Xianwu Luo, Baoshan Zhu (Tsinghua University), Profs. Jianzhong Xu (Academician), Jiezhi Wu, Cunbiao Lee, Qingdong Cai (Peking University), and Professors from China and other universities Sheng Zhou, Xingqi Luo, Shouqi Yuan, Zhenyue Ma, Fujun Wang, Guoyu Wang, Qingguang Chen, Lingjiu Zhou, Xuelin Tang, Jiandong Yang, Fengqin Han and Chao Yan. Drs. Jiang Dai, Zixiang Sun,Weizhang Wu, Jianming Yang, Wei Zhang, Zhaohui Xu, Liang Zhang, Yu Xu, Yuzhen Wu, Yong Li, Hongfen Tang, Shangfeng Wu, Penghui Xia, Xiaojing Wu, Jie Shao, Daqing Zhou, Wei Yang, Fan Yang, Guangjun Cao, Gang Chen, Zhaofeng Xu, Zhiping Li, and Jinwei Li have been long cooperated with the authors, their supports are gratefully acknowledged.

Special thanks to late Prof. Zuyan Mei and Prof. Ruchang Lin (Tsinghua University), Prof. Risaburo Oba (Tohoku University) for their guidance and advice, and to Profs. Teyu David Kao, Apostolos Goulas, D.-H. Hellmann, Michihiro Nishi, Hiroshi Tsukamoto, Yoshinobu Tsujimoto, Wei Shyy, Roger Leblanc, Michel Guilbaud, Kwang-Yong Kim, and Young-Ho Lee, and Drs. Peter Tillack, Berthold Matz, Baogang Wang, Tomoyoshi Okaomura, Takahide Nagahara, Kazuyoshi Miyagawa, Kazuo Niikura, and Joshiro Sato for long cooperation and assistance. We would also like to thank Ms. Angela Omalley and Prof. David Kao, as well as Mr. Tiejun Chen and Ms. Ling Shen for their devoted effort into the language revision and check of this book.

Finally, thanks to the UK EPSRC's Warwick-IMRC for their financial support (R.ESCM.9001 and R.ESCM9004) on turbine technology and cavitation.

Yulin Wu

Contents

Part III Hydrodynamic and Structural Analysis

Part I
Fundamental

Chapter 1
Introduction

In this book, a hydraulic machine is referred to a hydraulic turbine or a pump. Rotation of the turbine runner or the pump impeller is transmitted through a shaft supported on bearings to a generator or a motor that is connected with the electric grid. This whole assembly is called a hydraulic unit.

It is necessary to take vibration prediction into consideration since the vibration has a major influence on the performance of hydraulic machinery (Ohashi 1991). In this chapter, the main content of the vibration prediction of hydraulic machines will be briefly introduced. In the following chapters, detailed information will be given. First, the fundamentals on the prediction of mechanical vibration and rotordynamics will be briefly emphasized on their basic concepts, model, and essential equations in Chaps. 2 and 4. Chapter 3 introduces the main numerical methods used in structure and rotor dynamic analysis aspects, which are necessary for numerical simulation on the vibration prediction. Then mechanical excitations and hydraulic excitations as the source forces of forced vibration in hydraulic machinery will be analyzed in Chaps. 5 and 6 respectively. In Chap. 7, topics about pressure fluctuations induced by unsteady turbulent flow in turbine and pump will be presented in order to get the unsteady loads. Once information about the loads, the constrain conditions and the elastic and damping characters of the mechanical system is known, the structure and rotor dynamic analysis of hydraulic machines can be predicted as demonstrated in Chaps. 8 and 9 respectively. Chapter 10 focuses on the instability of hydraulic turbine system. Finally, Chap. 11 illustrates monitoring system of the instability and the vibration for hydraulic turbine units and pumps, including the sensor selection and system design. Some examples of large hydropower plants are also given in this chapter. This monitoring system is also used for checking the prediction results in hydraulic machinery.

Y. Wu et al., *Vibration of Hydraulic Machinery*,
Mechanisms and Machine Science 11, DOI: 10.1007/978-94-007-6422-4_1,

1.1 Hydraulic Machinery System

In this section, we introduce the concept of the mechanical systems of hydraulic turbines and pumps which is quite essential.

1.1.1 Hydraulic Turbine Structures

Most hydroelectric power comes from the potential energy of dammed water. The amount of energy stored in water depends on the volume and the difference in height between the source and the water's outflow. This height difference is called the head. The amount of potential energy in water is proportional to the head.

Hydroelectric plants with no reservoir capacity are called run-of-the-river plants, since it is not possible to store water.

With the increasing capacity and size of hydraulic turbines, vibration of the turbine structure and rotating system strongly influences the safety of the power house where turbines are installed. The dynamic analysis of the components, the rotor and its rotating system is therefore essential to design and operation.

The hydraulic turbine is a machine that converts the energy of an elevated water supply into the mechanical energy of a rotating shaft. All modern hydraulic turbines are fluid dynamic machinery of the jet and vane type that operates on the impulse or reaction principle and involves the conversion of pressure energy to kinetic energy. The shaft drives an electric generator, and the speed must be of an acceptable synchronous value. Efficiency of hydraulic turbine installations is always high, more than 85 % after allowances of hydraulic, shock, bearing, friction, generator, and mechanical losses. Material selection is not only a problem of machine design and stress loading from running speeds along with hydraulic surges, but also a matter of fabrication, maintenance, and resistance to erosion and corrosion, as well as cavitation pitting (Akahane and Suzuki 1996).

Storage hydro plants have employed various types of equipment to pump water to an elevated storage reservoir during off-peak periods and to generate power during on-peak periods when the water runs from the reservoir through hydraulic turbines. The principal equipment of the station is the pumping-generating unit. In most practices, the machinery is reversible and is used both for pumping and generating; it is designed to function as a motor and pump in one direction of rotation and as a turbine and generator in the opposite direction of rotation.

There are different types of turbines, such as, the Francis, Kaplan, bulb (or tubular) and impulse turbines, and their physical models need to be established for dynamic analysis of mechanical systems. There are three main categories of reaction hydraulic turbines: the Francis turbine (Fig. 1.1) and Kaplan turbine (Fig. 1.2), and bulb (or tubular) turbine.

In reaction turbines, pressure from working fluid changes as it flows through the turbine and thus the working fluid transfers energy to the turbine. A casement is needed to contain the water flow.

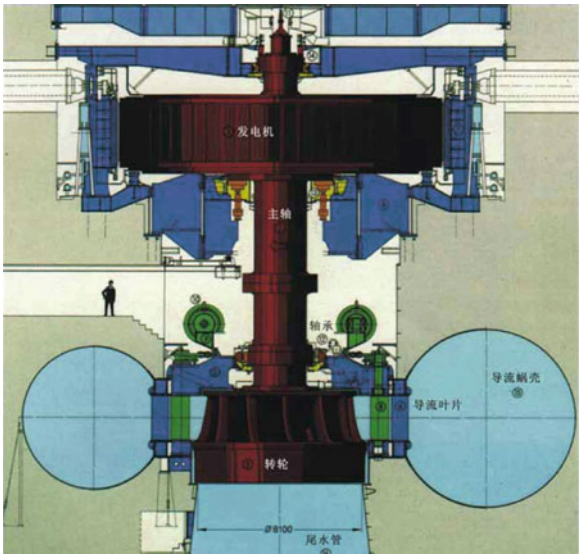

Fig. 1.1 Francis turbine (http://www.en.wikipedia.org/wiki/Kaplan_turbine)

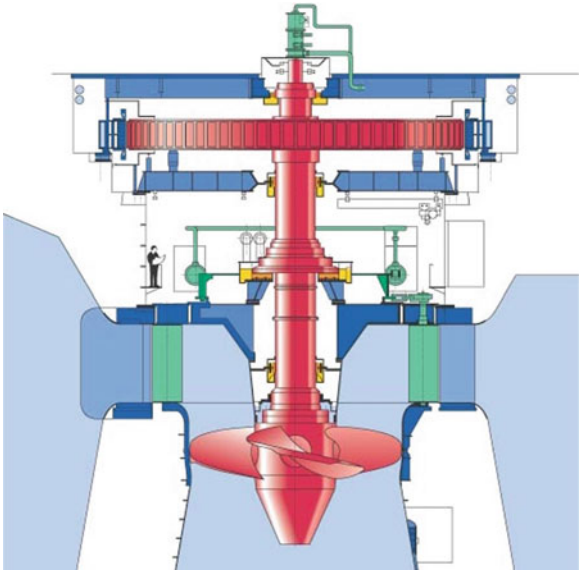

Fig. 1.2 Kaplan turbine (http://www.en.wikipedia.org/wiki/Kaplan_turbine)

The Francis turbine is located between the high pressure water source and the low pressure water exit, usually at the base of a dam. The inlet is spiral shaped. Guide vanes direct the water tangentially to the runner entrance. This radial flow acts on the runner vanes, propelling the runner to spin. The guide vanes (or wicket gate) may be adjustable to allow efficient turbine operation depending on the range of water-flow conditions (Fig. 1.3).

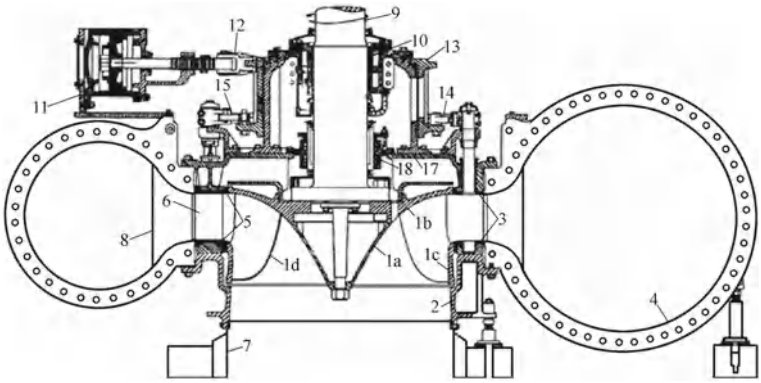

1	Turbine runner	8	Dischargering
1a	Runner cone	9	Turbine shaft
1b	Runner crown	10	Turbine guide bearing
1c	Runner band	11	GV servomotor
1d	Runner bucket	12	Servomotor rod
2	Wearing rings	13	GV opening ring
3	Facing plates	14	GV link
4	Spiral casing (SC)	15	GV arm
5	Stay vanes	16	Pacing box or stuffing box
6	Guide vanes (GV)	17	Head cover
7	Draft tube		

Fig. 1.3 Francis turbine structure components (from Wikipedia 2008a)

Large Francis turbines are individually designed for each site to optimize its operational efficiency, typically over 90 %. Francis type units cover a wide head range, from 20 to 700 m and their output varies from a few kilowatts to 1,000 megawatts. Apart from electrical production, they may also be used for pumped water storage.

The Kaplan turbine is another type of reaction turbine, i.e., pressure of working fluid changes as the fluid moves through the turbine losing energy. The inlet is a scroll-shaped tube that wraps around the turbine's wicket gate. Water is directed, through the spiral, on to the wicket gate, and then is turned from radial to axial direction before entering a propeller shaped runner. Different from the Francis turbine, the water is axially directed to the runner in the Kaplan turbine. The outlet is a specially shaped draft tube that helps decelerate the water and recover kinetic energy.

Variable Pitch angles of the wicket gate and turbine blades (often referred as "on cam" operation) allows efficient operation for a range of flow conditions. Kaplan turbine efficiencies are typically over 90 %, but may be lower in very low head applications. Kaplan turbines are widely used throughout the world for electrical power production. They cover the lowest head hydro-sites and are especially suitable for large flow rate conditions.

Propeller turbines have non-adjustable propeller vanes. They are used in situations where the range of water head is not large.

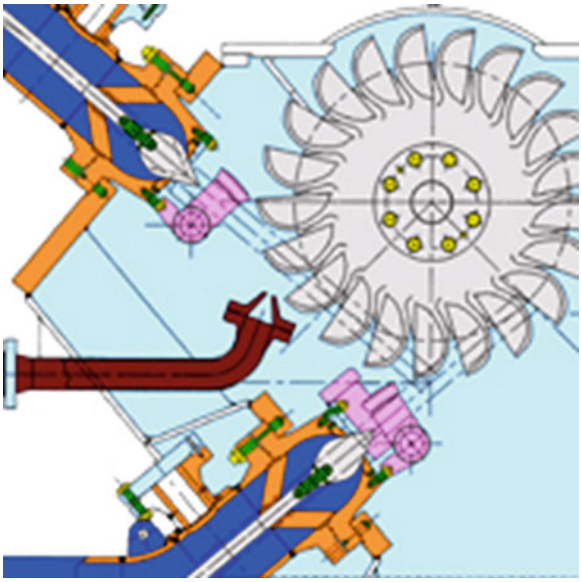

Fig. 1.4 Pelton turbine (http://www.en.wikipedia.org/wiki/Pelton_turbine)

Bulb or Tubular turbines are designed to allow the water flow directly into the draft tube. A large bulb is centered in the water pipe which holds the generator, wicket gate and runner. Tubular turbines are a fully axial design, whereas Kaplan turbines have a radial wicket gate.

The Pelton wheel is among the most efficient types of water turbines, and is an impulse machine which is designed to utilize the energy from a fluid jet (Fig. 1.4).

The water flows along the tangent to runner path. Nozzles direct forceful streams of water against a series of spoon-shaped buckets mounted around the edge of a wheel. As water flows into the bucket, the direction of the water velocity changes to follow the bucket contour. When the water-jet contacts the bucket, the decelerated water exerts pressure on the bucket as it flows out of the other side of the bucket at lower velocity. In the process, the water's momentum is transferred to the turbine. For maximum output and efficiency, the turbine system is designed so that the water-jet velocity is twice the velocity of the bucket. Often two buckets are mounted side-by-side, thus splitting the water jet in half. This balances the side-load forces on the wheel, and helps to ensure smooth, efficient momentum transfer from the fluid jet to the turbine wheel.

For detailed knowledge of fluid dynamics about these turbines, readers are referred to the volume titled 'Hydraulic Design of Hydraulic Machinery' (Krishna 1997).

1.1.2 Pump Mechanical Systems

A pump is a machine that draws fluid into itself through an entrance port and forces the fluid out through an exhaust port (see Figs. 1.5, 1.6, 1.7 and 1.8). A pump may

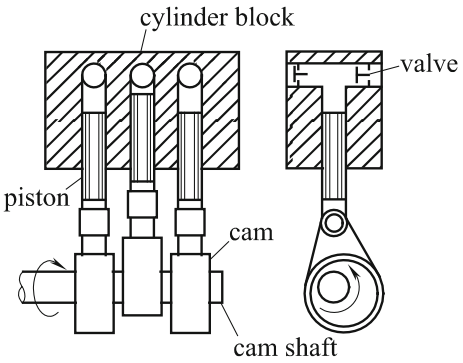

Fig. 1.5 Multi-cylinder reciprocating pump

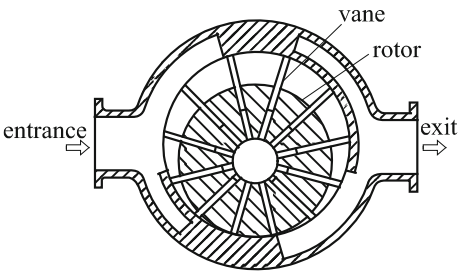

Fig. 1.6 Rotary pump (sliding type)

serve to move liquid, as in a cross-country pipeline; to lift liquid, from a well or to the top of a tall building; or to put fluid under pressure, as in a hydraulic brake.

A displacement pump is one that develops its action through the alternate filling and emptying of an enclosed volume. There are two basic types: reciprocating (Fig. 1.5) and rotary (Fig. 1.6).

Positive-displacement reciprocating pumps have cylinders and pistons with an inlet valve that opens the cylinder to the inlet pipe during suction stroke, and an outlet valve that opens to the discharge pipe during discharge stroke. Except for special designs with continuously variable strokes, reciprocating power pumps deliver an essentially constant capacity over their entire pressure range when driven at constant speed.

The purpose of a centrifugal pump is to move fluid by accelerating it radically outward. More fluid is transferred by centrifugal pumps than by all the other types combined (Fig. 1.7). As shown in Fig. 1.8, a centrifugal pump basically consists of one or more rotating impellers in a stationary casing which guides the fluid from one impeller to the next in the case of multistage pumps. Impellers may be single suction or double suction. Other essential parts of all centrifugal pumps are (1) wearing surfaces or rings, which make a close-clearance running joint between the impeller and the casing to minimize the backflow of fluid from the discharge to the suction; (2) the shaft, which supports and drives the impeller; and (3) the stuffing box or seal, which prevents leakage between shaft and casing.

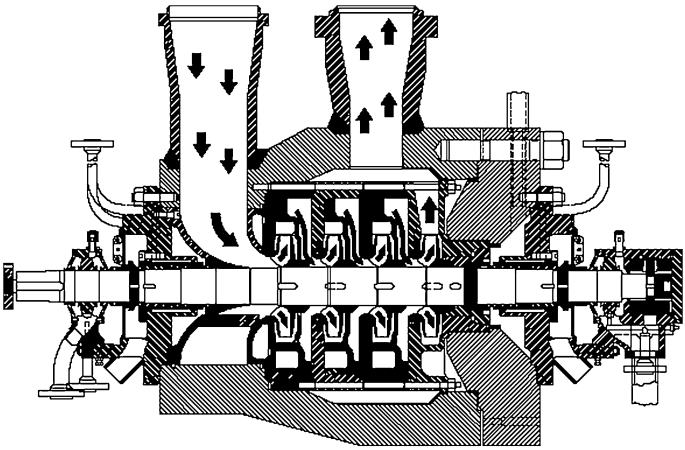

Fig. 1.7 Multi-stage centrifugal pump (http://www.architettisenzatetto.net/wp2/?cat=24)

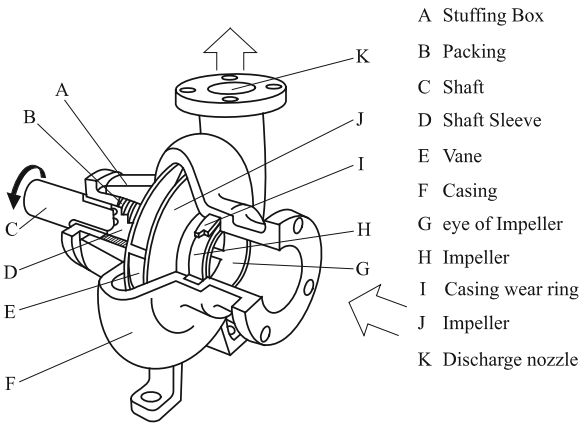

Fig. 1.8 Centrifugal pump assembly (http://www.pumpfundamentals.com/centrifugal_pump.htm)

1.2 Physical Model of Hydraulic Machinery as Mechanical System

Modern mechanical systems are often very complex and consist of many components interconnected by joints and force elements. These systems are referred to as multibody systems or continuous mass distributed systems. The dynamics of such systems are often governed by complicated relationships resulting from the relative motion and joint forces between components of the system. Figure 1.1 shows a Francis turbine generator unit, which can be considered as an example of a multibody system that consists of many components.

While most structures are stationary with respect to an inertial frame of reference, many machines contain rotating elements that may vibrate owing to their elasticity and inertia. Rotating bodies and structures are usually defined as rotors.

The dynamic analysis of vibration in hydraulic turbines has two aspects in engineering: (1) Dynamic analysis of the stationary structure's components (Structure dynamics analysis), which is performed for each component, such as a runner (even for a single runner-blade), a spiral casing and a draft tube, etc. The component is treated as a continuous mass object in the analysis. (2) Dynamic analysis of the rotating shaft system (shaft rotordynamics in hydraulic turbines), where the system is simplified as the lumped multibody system.

In each type of dynamic analysis, the following steps should be included:

(1) The first step is to establish the physical model of an analysis object.
(2) Secondly, it is important to determine which analytical approach should be used in the work. For example, in rotordynamics the Riccati transfer matrix (Garnett 1997), Newmark numerical integral method (Newmark 1959), or others should be adopted to calculate and analyze instantaneous non-linear response of the rotor system of hydroelectric units. In structure analysis, the finite element method (FEM) is usually applied to study the turbine components. The main analytical approaches from principle to their application in hydraulic machinery will be illustrated in following chapters, especially in Chaps. 8 and 9.
(3) The third step is to set up a grid system or other geometrical system of the analytical object. This process is determined according to the analytical approach and introduced in each calculation.
(4) The fourth step is to study the action forces and excitations which have impact on the analyzed objects, such as excitation induced by mechanical aspects, fluid flow (pressure distribution and pressure fluctuation) and by electric–magnetic effluences. Excitation will be covered in Chaps. 5, 6 and 7.
(5) The fifth step is to select the boundary and restrict conditions to each analytical object for numerical simulation.
(6) Afterwards, the numerical computation is carried out with different mathematical algorithms, and the computer resource and computation time is taken into consideration.
(7) The final step is to analyze the calculation results in order to apply them to an engineering design for enhance the performance of the machines.

The analytical procedure on pump dynamics is similar to that of turbines.

1.2.1 Physical Model of a Hydraulic Turbine Unit Shaft System

The hydraulic turbine unit is essential equipment to hydroelectric power generation, and shafts are an important component of these machines. Its dynamic characteristic is bound with the hydroelectric reliability, life-span, and economic

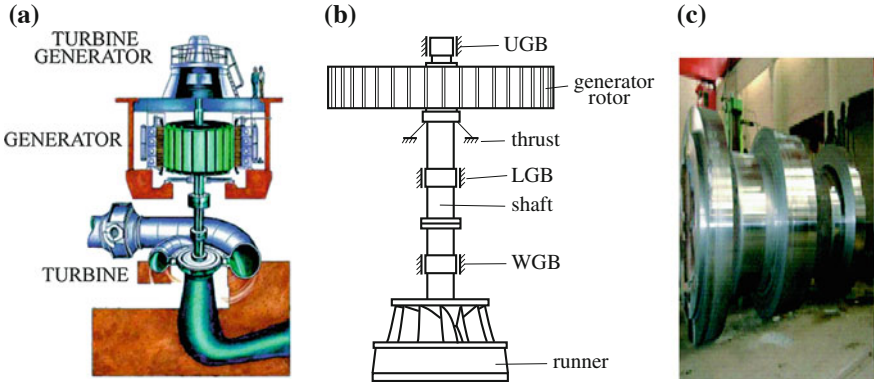

Fig. 1.9 Diagram of the umbrella-type shaft system of a Francis turbine unit. **a** Three dimensional diagram. **b** Meridional plane diagram. **c** Generator shaft

index of the entire machine. Therefore, it is necessary to analyze the large hydroelectric machines from this aspect.

The first step in rotor dynamic analysis of hydraulic turbines is to obtain the physical model from a real hydraulic turbine unit as shown in Fig. 1.9. The model is a simplified umbrella-type shaft system of a Francis turbine unit (http://www.rise.org.au/info/Tech/hydro/large.html).

The umbrella-type shaft system consists of a shaft, an upper guide bearing (UGB), a generator rotor, a thrust bearing, a low guide bearing (LGB), a coupling, a water guide bearing (WGB) and a runner (see Fig. 1.9b).

The shaft system of a real hydraulic turbine unit is a continuously distributed mass system with infinite degrees of freedom. Figure 1.10a and b show the mechanical models used for the analysis of shaft system. Figure 1.10a is a simplification of the shaft system that contains two-disc rotor system with

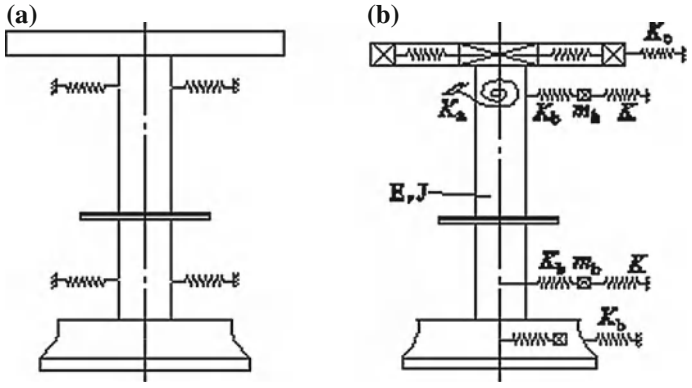

Fig. 1.10 Mechanics models of the shafts of the hydraulic turbine unit. **a** Simplified model. **b** Complex model

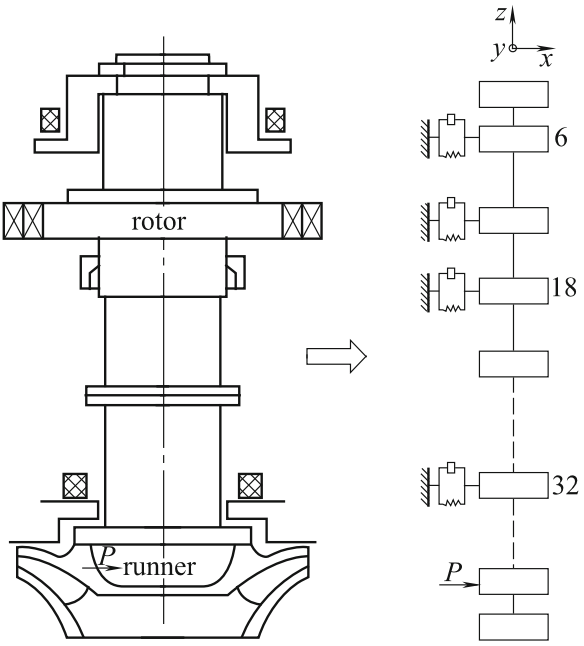

Fig. 1.11 Schematic drawing of a concentrated mass method in the shaft

multibearing supports; and Fig. 1.10b shows the rotor system with such effects, shear deformation, rotary inertia, gyroscopic moment, additional mass acting in the hydraulic turbine, and electromagnetic induction of instantaneous response in the rotor system. This model is necessitated because the diameter of the shaft is thick compared to its length (Fig. 1.9b). A non-linear oil film force on the bearing is identified and accounted by a factor in the calculation (Feng and Chu 2001).

Figure 1.11 shows a schematic drawing of the lumped mass method in a shaft using the Riccati transfer matrix method. In the model, the lumped parameters are set up from discrete treatment of the main assemblies contacting with the shaft (Feng and Chu 2001).

1.2.2 Physical Model of a Multi-Stage Pump Shaft System

A more effective approach to generate high pressure with a single centrifugal pump is to install multiple impellers on a common shaft within the same pump casing. Internal channels in the pump casing route the discharge of one impeller to the suction of another impeller. The illustration below shows a diagram of the impeller arrangement of a multistage pump. Water enters the pump from the top left and passes through each of the four impellers in a series, going from left to right. It goes from the volute surrounding the discharge of one impeller to the suction of the next impeller.

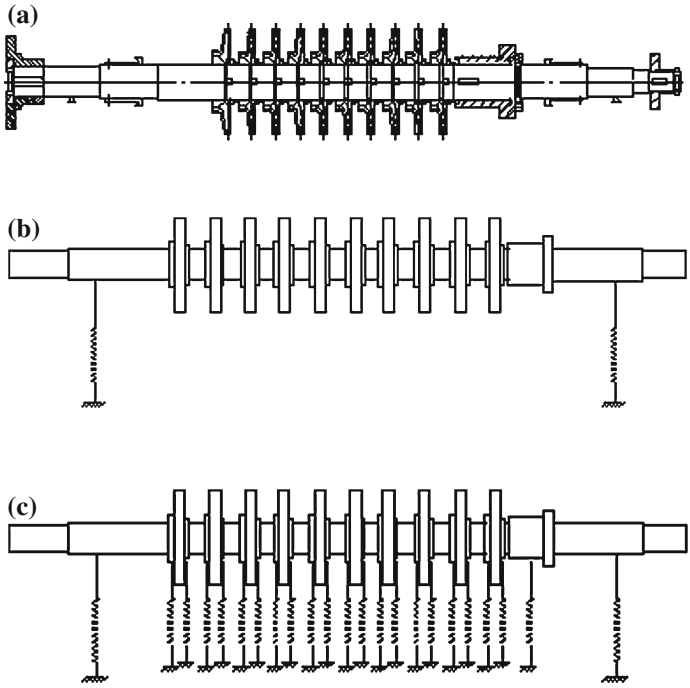

Fig. 1.12 **a** Model of multi-stage centrifugal pump. **b** Model of shaft operation in the air. **c** Model of shaft operation in the water

Now and then, centrifugal pumps are developed with larger capacity and higher head. The one shown in Fig. 1.12 has the head up to 3,000 m with power up to 3,000 KW, for the transportation of high pressure liquid in an industrial plant. For designing large rotating machinery, the values of critical speeds related to the desired operating range should be chosen carefully. For the rotor dynamic analysis of centrifugal pumps, the concepts of "dry" and "wet" critical speeds are introduced. The "dry" critical speed is one without consideration of the dynamic characteristics of seal as shown in Fig. 1.12b; The "wet" critical speed is when the pump is working in the power station with consideration of the dynamic characteristics of seal as shown in Fig. 1.12c (Chen et al. 2008).

1.2.3 Physical Model of Hydro-Turbine Structure Analysis

The physical model of hydro-turbine structure components for dynamic analysis is usually an exact geometric model of the components analyzed. For example, hydraulic excitation forces on Francis turbine runners (Fig. 1.13a and b) would increase due to higher heads and fluid velocities. A complete dynamic analysis of runner behavior is necessary for the prevention of vibration damage in a turbine.

Fig. 1.13 **a** Runner for three-gorges project. **b** Blade in machining of runner (http://www.xsrb.xsnet.cn/xsdaily/gb/content/2005-07/11/content_468089.htm, http://www.slsdge.com.cn)

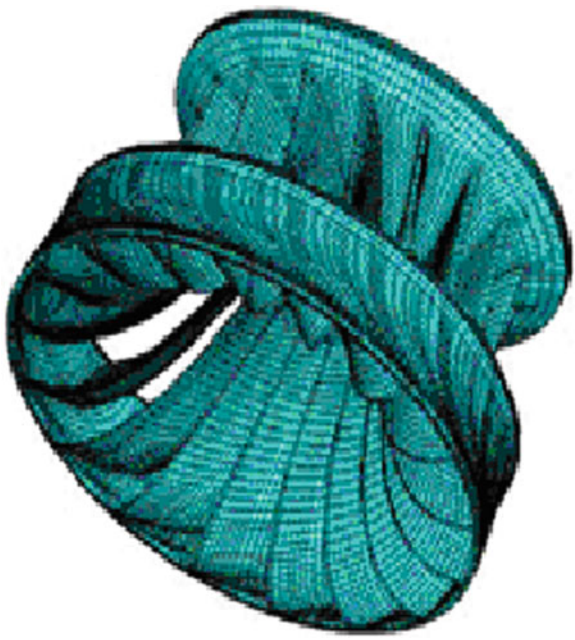

Fig. 1.14 Geometric model of a runner

Since runners are submerged in water inside the casing, the effects caused by the presence of this heavy fluid inside a rigid wall must be considered in dynamic analysis (From Wikipedia 2008b).

Owing to the cyclic symmetrical nature of the runner structure (total 17 blades), a blade covering an angle of 360/17 degrees can be used in simulation for dynamic analysis. Then the model is expanded to cover the whole runner (shown in Fig. 1.14) and the analysis on mechanical vibration is performed. The complete model will also be used in the water simulation, that is, the physical model of the runner is surrounded by a cylindrical fluid domain shown in Fig. 1.15 (Liang et al. 2006). The fluid mesh should be generated using extension from the structure mesh so the same set of nodes is shared between both domains on the interface.

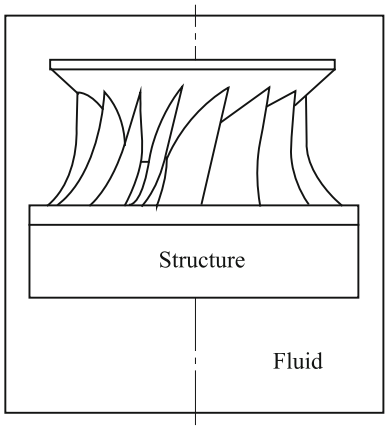

Fig. 1.15 Fluid domain around the runner (Liang et al. 2006)

Physical models of other components in a hydraulic turbine or pump are built in the same manner for dynamic analysis.

1.3 Mechanical Vibration of Hydraulic Machinery

The power density of hydraulic turbine is constantly increasing with new machines developed or existing ones upgraded. Consequently, hydraulic excitation forces acting upon runners rise. Moreover, hydroelectric power plants are subject to off-design operation in order to meet variable demand. In this context, Francis turbines operating at partial load may present instabilities in terms of pressure, discharge, rotational speed and torque. The operation under off-design conditions would result in greater forces combined with a reduced thickness/weight ratio in turbine structure, provoking even higher level of vibration. This dynamic excitation contributes to fatigue damage. A complete dynamic behavior analysis for the hydraulic turbine (or the high speed pump) is essential to prevent this type of damage (Egusquiza 2007).

1.3.1 Dynamic Analysis of Hydraulic Machinery

As mentioned above, since some working components are submerged in water inside the casing, the effects caused by the presence of this heavy fluid within the rigid wall must be considered. Therefore, analysis should focus on the fluid and wall effects on the modal behavior of hydraulic turbine or pump (BS ISO 10816-5 2001; Xiao et al. 2008).

Although both experimental and numerical modal analyses have been used to study the dynamic response of structures, most of them are limited to simple geometries. Furthermore, few works have been done with the consideration of the effects of surrounding fluid. For hydraulic turbines, it is very difficult (if not

impossible) to test the real operation conditions through experiments. From the viewpoint of numerical study, the main challenges lie in the complexity of the geometry, especially the mesh compatibility between the fluid and structure on the interfaces. In fact, the dynamic study of turbine components submerged in water is essential for developing better theoretical model.

1.3.2 Analysis of Vibration Generation of Hydraulic Turbines

The machine is a rotating structure supported by the fluid film of bearings. Consequently, the vibrations generated are determined by characteristics of excitation forces and the structural response. Perturbation forces responsible for vibration increase in a hydro turbine may be mechanical, hydraulic, or electrical (Swain 2008).

1. Mechanical excitations
a. Centrifugal forces due to imbalance of the rotating mass i.e., runner, shaft, and generator rotor.
b. Elastic force of the shaft due to incorrect shaft alignment.
c. Frictional forces.
d. Oil-film instability in bearing.
2. Hydraulic excitations
a. Flow through waterways: Nonuniform velocity distributions in various waterways of the turbine cause hydraulic unbalance.
b. Draft-tube flow instabilities: These occur in Francis turbines even during steady-state operation outside the optimum efficiency ranges.
c. Cavitation: This is caused by incorrect flow conditions around the runner or impeller blade profiles and occurs mostly within the higher load ranges.
d. Hydroelastic vibration: This is due to an incorrectly shaped discharge edge of hydraulic profiles (blades, wicket gates, and stay vanes etc.)
e. Self-excited vibration: This occurs in places where the movement of mechanical parts (seals and clearances, etc.) can influence the flow around or through them.
f. Pressure fluctuations in the penstock.
3. Electrical excitations
a. Magnetic forces between stator and rotor.
b. Forces due to non-uniform air gap between stator and rotor.
c. Forces created by the partial or total short-circuiting of the pole winding of rotor.

In most cases, the generated vibrations that do not affect the fluid excitations/forces are forced vibrations. In some circumstances the structural motion in turn can affect fluid forces that, in this case, depend on the structural displacement. This would happen when there is, in the absence of structural motion, some periodic excitation in the flow, and its resultant frequency coincides with a natural

frequency of the system. Then a resonance occurs, and if the response amplitude becomes sufficiently large, structural displacement will take control of the fluid excitation. Sometimes, the periodicity in flow is determined by the structural motion. This is the case of self-excited vibrations.

1.3.3 Structure Response of Hydraulic Turbines and Hydroelectric Units

The hydraulic forces generate vibrations on the runner and the shaft which are also transmitted to the bearings. For each type of hydraulic machine the main hydraulic forces have to be estimated and applied to a runner model to determine resultant vibrations and stresses.

Any uncertainty in the runner response depends not only on the mechanical structure but also on the added mass and damping generated by water, seals and on the mechanical constraints (shaft coupling). Simulation and experiment are needed for establishment of a consistent model. The evaluation of the rotor response is difficult in a power plant that is up and running. Therefore theoretical models may be applied to calculate the natural frequencies even though certain parameters required for an exact calculation are unavailable, such as the overall stiffness of the bearings and the excitation effect of oil film, etc.

Vibration analysis of hydroelectric units by nature is difficult because the complexity of the excitation forces that change with the operating conditions and the complexity of structural response are affected by fluid-structure interaction and rotor dynamics.

1.4 Structure Dynamics of Hydraulic Machinery

Structural dynamics is a subset of structural analysis that covers the behavior of structures subjected to dynamic loading. Any structure can be subjected to dynamic loading. Dynamic analysis could be used to find dynamic displacements, time history, and characteristics about vibration mode etc.

1.4.1 Basic Structure Dynamics

Apart from the vibratory motion studied in structural dynamics, structures are usually stationary with respect to an inertial frame of reference. A static load does not vary. A dynamic load is one that changes with time. If it changes slowly, the structure's response may be determined with static analysis, but if it varies quickly (relative to the structure's ability to respond), the response must be obtained with a dynamic analysis.

A dynamic load may have a more significant impact than a static load of the same magnitude due to the structure's inability to respond quickly enough to the loading (by deflecting). The impact of a dynamic load is given by the dynamic amplification factor (*DAF*):

$$DAF = u_{\max}/u_{static}$$

where u is the deflection of the structure against the load.

In the time history analysis, a full time history would exhibit the response of a structure over time during and after the application of a load. To find the full time history of a structure's response one must solve the structure's equation of motion.

A modal analysis calculates the frequency modes or natural frequencies of a given system. The natural frequency of a system depends only on the stiffness and the mass of the structure, but not on the load function.

It is useful to know the modal frequencies of a structure to ensure that any applied periodic loading frequency does not overlap thereby causing resonance that leads to large oscillations.

The modal analysis approach is:

a. Find the natural modes and natural frequencies.
b. Calculate the response of each mode.

1.4.2 Structure Dynamic Analysis of Hydraulic Turbine Components

In this section, the dynamic analysis for a turbine runner is used as an example for illustration purpose.

1.4.2.1 Simulation Model

For the dynamic analysis of a turbine runner, firstly the physical model and the mesh configuration of runner calculation must be set up. In order to determine the final mesh configuration, the influence of element shape and mesh density must be checked. Usually two types of elements, hexahedral and tetrahedral, can be considered.

The next step is to add the load on the calculated grid model. Loads acting on the runner model include the loads caused by restricting boundary, sustaining conditions, as well as the excitation loads, etc. According to their nature, the loads can be classified as freedom restricts, concentrated loads, surface loads, body loads, inertial loads, and coupling loads. As far as the solid–fluid coupling interaction is concerned, the water pressure acting on runner surfaces must be included in computation apart from the force of gravity and the centrifugal force.

Many researchers have recently engaged in improving calculation methods for the analysis of static and dynamic stresses caused by hydraulic forces in runner

blades. The static stresses in Francis turbine runners at various operating points may be computed using the sequential fluid–structure interaction (FSI) analysis method. The dynamic stress variations during load changing may be calculated with the sequential FSI analysis method as well (Xiao et al. 2008).

1.4.2.2 Static Stress Analysis

Once the simulation model of a runner is set for the finite element analysis (FEM), the static analysis should be carried out with FEM. There are two strategies for solving fluid–structure interaction. One is the fully coupled method, in which the fluid and structure are solved using the same code and same grid. However, this calculation is CPU-expensive, especially for large Francis turbine runners, owing to intensive iterations between the fluid and structure system. The other method is a sequentially coupled fluid-structure interaction that assumes the influence of the runner deformation in flow field is negligible in calculation. That is to say, there is no feedback of the runner blade motion on the flow.

The steady-state flow and static stresses are calculated for analyzing static stress characteristics of a Francis turbine runner. The results may indicate that the maximum stresses locate around the area between the blade leading edge and the runner band as well as around the trailing edge close to the runner crown. For certain operating points, especially near low heads and low loads, the pressure distribution on the runner blade has a considerable influence on the stress distribution.

1.4.2.3 Structure Modal Analysis

The objective of modal analysis in structural mechanics is to determine the natural mode shapes and frequencies of the structure during free vibration. The structure modal analysis of a hydraulic turbine can be conducted with FEM based on the free-vibration governing equations with or without damping effects of a component of the machine (Egusquiza 2007).

The FEM equations which arise from modal analysis are those seen in eigensystems. The physical interpretation of eigenvalues and eigenvectors obtained from solving this system is that they represent the frequencies and the corresponding mode shapes. Sometimes, the only desired modes are the lowest frequencies because they can be the most prominent modes at which the object would vibrate, dominating all other higher frequency modes.

1.4.2.4 Dynamic Stress Analysis

In order to conduct the dynamic stress analysis in a turbine runner, one should perform an unsteady turbulent flow simulation though the flow passage to predict the pressure fluctuation acting on the runner surfaces. The output data from the

unsteady flow computation should be saved at each time step. However, in order to reduce the computational complexity for a runner stress analysis, only the results for the last several rotations might be used.

The dynamic stresses for the runner of a Francis turbine can then be analyzed. Since stress concentrations often occur at the blade root, the fillet of a runner blade with a runner crown and a runner band should be modeled accurately. These sensitive areas should be accurately meshed to truly reveal those stress concentrations. Constraint for the stress calculation is the fixed joint between the runner crown and the main shaft. The loads on a runner consist of inertia force and surface forces. The inertia force includes the runner's own weight and rotational inertia force. The surface force is from water pressure and pressure pulsation on the fluid–solid interface.

This analysis should include the characteristics of the excitation forces and the runner response in order to avoid resonances.

The runner is a component of the whole rotor system that is composed of a runner, shaft and electrical generator. This system has its own natural lateral, axial, and torsional frequencies. An analysis of the system would involve rotor dynamics which is particularly important in machines that might experience critical (rotating) speed during the start up. However, hydraulic turbines have rather rigid shafts and the first natural frequency of the rotor would be far above their rotating frequency. In fact, the runner and the generator also have their own natural frequencies.

The runner is submerged in water and the effect of added mass on the runner response cannot be neglected. The quantification of this effect is one of the main problems concerning determination of the runner response. The added mass may only affect the rotor's lateral frequencies, because it increases the effective mass of the runner.

Recently, there are some studies on the modal analysis of hydraulic runners but with measurements conducted in air. A few publications provide some general data, but no publications provide detail information about the influence of the water on the modal characteristics of runners. Some studies have only performed numerical simulations without validations with experiments.

The added mass effects can also be modified through nearby structures. Although there is no structure close to blades in an actual turbine, the casing is close to the runner's band where the seals are equipped. That would modify the added mass effects on the runner vibration modes with deflection against the nearby structure. Therefore, the significance of this effect depends on the dimension of band and seal; that is, the longer the seals the more severe the effect. This effect was tested on a Francis runner of a low head (small pressure difference) and with small seals.

For all the reasons above, investigation of the added mass effects on a runner of Francis turbines is based on experimental modal analysis of a runner as a free body in air and in still water. Such conditions appear to be appropriate to approximately simulate the main mode-shapes of interest in an actual Francis turbine runner in operation. These modes correspond to those responsible for fatigue failure, and they are the modes with high deformation in the blades.

1.5 Rotordynamics of Hydraulic Machinery

Rotordynamics is a specialized branch of applied mechanics concerned with the behavior and diagnosis of rotating structures.

1.5.1 Basic Principles of Rotordynamics

At the most basic level, rotordynamics is concerned with one or more mechanical structures (rotors) supported by bearings and influenced by internal phenomena that rotate around a single axis. The supporting structure is called stator. As the speed of rotation increases, the amplitude of vibration often arrives at a maximum that is termed as critical speed. This amplitude is usually excited by an imbalance of the rotating structure. If the amplitude of vibration at these critical speeds is excessive, catastrophic failure would occur.

Rotordynamic studies are related to technological applications date back to the second half of the nineteenth century, when the increase of rotational speed made it necessary to add rotation into the analysis of their dynamic behavior top had been successfully dealt with by several mathematicians and experts in theoretical mechanics.

The first turbine rotor was very simple and could be studied with the help of simple models, the type now widely known as the Jeffcott rotor (Jeffcott 1919). Actually, the Jeffcott rotor can provide qualitative explanations for many important features of real-life rotors, the most important being self-centering in supercritical conditions. Yet it fails to explain other features such as the dependence of natural frequencies on the rotational speed. Above all, the simple Jeffcott rotor does not guarantee a precise quantitative analysis of the dynamic behavior of complex systems.

To cope with the increasing complexity of rotating systems, graphical computation schemes were devised (Nelson 2011). They can be found in books and papers from the first quarter of the last century and were the basic instrument for the dynamic analysis of turbine rotors. A large number of papers dealing with the flexural vibration of rotors, rotating shafts, and torsional vibration in reciprocating machinery appeared in the years after World War I. This trend lasted for many years, by the increase of the size of power-generating machinery.

The availability of electromechanical calculators made it possible to develop computational procedures, mainly based on the transfer matrices approach. In particular, Holzer's method (Holzer 1921) for the torsional vibration of shafts and the Myklestadt-Prohl method (Myklestad 1994) for computation of the critical speed of turbine rotor were, and still are, widely used. These methods were immediately automatized when digital computers became available.

The application of the finite element method (FEM) greatly influenced the research of rotordynamics. Strictly speaking, FEM codes with general purposes

cannot be used for rotordynamic analysis owing to the lack of consideration for gyroscopic effects. It is true that a gyroscopic matrix can be forced into the conventional formulation and several manufacturers have already used commercial FEM codes to perform rotordynamic analysis. However, purposely written, specialized FEM codes are still desired within the field of rotordynamics because of their capability.

Through FEM modeling, it is possible to study the dynamic behavior of machines containing high-speed rotors with greater detail consequently obtaining quantitative predictions with an unprecedented degree of accuracy. Correct quantitative prediction is of great importance, as the trend of technology development toward higher power density, lower weight, and faster machines tend to see a deterioration of problems linked with the dynamic behavior of rotating machinery.

Higher speed is often a desirable feature just like machine tools or production machines in which faster spinning directly relates to increasing productivity. In applications involving power generation or utilization, a faster machine can develop or convert more power out of the same torque. As torque is usually the critical factor in dimensioning machine elements, increasing speed requires a lighter power device. The use of materials capable of withstanding higher stress allows for a reduction of the mass and size of machinery, but stronger materials (e.g., high strength steels or light alloys) are mostly weak in stiffness. As a result these lighter machines are more compliant and more prone to vibration. Another trend of machine development is toward higher operating temperature, for increasing both the thermodynamic efficiency and power density. A higher power density implies that the same amount of heat is generated in a smaller space, with less material, and hence lower thermal capacity. Higher temperature leads to higher thermal stress, lower damping, and often lower stiffness, which makes strength and vibration problems more severe.

Rotordynamic analysis is not restricted to the design stage. It can function as a tool that is essential during testing and actual operation of machinery for gaining the insight of the machine status and performing preventive maintenance. The study of mechanical signature, i.e., the vibration spectrum, of a rotating machine enables identification of operating problems before they become dangerous or precipitate failure or damage to other parts of the machine. Any deviation of the signature from its usual pattern provides a symptom (easily interpreted in many cases) of a developing problem that allows corresponding countermeasures to be taken in time.

Interesting features of the rotor dynamic system of equations are the off-diagonal terms of stiffness, damping, and mass. These terms are named cross-coupled stiffness, cross-coupled damping, and cross-coupled mass. When positive cross-coupled stiffness exists, a reaction force caused by a deflection offsets the load with a counter deflection, as well as a reaction force in the direction of positive whirl. If this force is comparable with the available direct damping and stiffness, the rotor would be unstable. When a rotor is unstable, an immediate shutdown of the machine is expected to avoid catastrophic failure.

1.5.2 Rotordynamics Analysis of Hydro Turbine Units

For the analysis of rotor dynamic characteristics of the hydro turbine unit, with consideration of the lateral forces acting on turbine runner, many modeling methods have been developed. Also, many numerical integration methods (such as the Runge–Kutta method, the Newmark-β method (Newmark 1959), and the Wilson θ method (Wilson 1968), etc.) have been proposed. They are often needed in combination for the simulation of dynamic response of the shaft bearing system in a hydro turbine unit.

More and more field engineers and researchers emphasize the start-up and shutdown processes of hydro turbine units because faults frequently happen at these transient stages. At the same time, some nonlinear characteristics are exhibited in the vibration signals of the hydro turbine, such as nonlinear characteristics of the guide bearing, thrust bearing, and the magnetic forces. Studies on effects of these nonlinear characteristics on the vibration of the shaft will be very significant.

The method designated as the transient Riccati transfer matrix method (TRTMM) (Garnett 1997) should be utilized to compute the dynamic response of shaft system under random excitation, and this model considers all the nonlinear components.

For numerical analysis, the shaft system was simplified to an equivalent shaft system inclusive of several lumped masses and shaft spans. In the physical model used for computation, equivalent springs and dampers for the calculation of natural characteristics of the shaft replaced guide bearings. While analyzing the dynamic responses caused by external excitations, one should add reaction force of the bearing to the equivalent system.

For the concentrated mass method, the Riccati transfer matrix and the Newmark numerical integral method can be adopted to calculate and analyze instantaneous non-linear responses of the rotor system in hydraulic turbine units. The effects of shear deformation, rotary inertia and gyroscopic movement are taken into account. The effects of the added mass of water in the hydraulic turbine and the electromagnetic induction of instantaneous response of the rotor system under arbitrary forces are obtained.

The concept of a non-linear oil film force of the bearing is further identified, and its influencing factors are summed up. The effect of non-linear oil film force is considered during calculation. The resultant critical speeds and vibration modes of the shaft system can be obtained. The elasticity of the bearings, the unbalanced condition of the shaft and the magnetic pull of the generator would greatly influence the conclusions of rotor dynamic analysis.

Rotordynamics study should include the analyses on critical speed, whirl speed and stability, steady state synchronous response (unbalance, disk skew, and rotor bow), nonlinear transient behaviour with acceleration, blade loss, rotor drop, bird impact, rub, and balancing in mechanical rotating system.

1.6 Vibration of Pumps

Vibration of pumps needs to be studied since it has a major impact on the performance of the device. At least six components of pumps are seriously affected by vibration (MCNally 2009).

The lifespan of a mechanical seal is directly related to shaft movement. Vibration may induce carbon face chipping and seal face opening. Drive lugs would wear, and metal bellows seals would fatigue. On occasion, shaft movement can cause the rotating seal components to contact the inside of the stuffing box or some other stationary objects, giving rise to leakage on the seal faces which allows solid particles to be dragged in between the lapped faces. Vibration is also a major cause for loosing set-screws and slipping on the shaft that leads to the lapped seal faces to open.

Packing is sensitive to radial movement of the shaft. Once something goes wrong with it, one would not only experience excessive leakage, but also more abrasion on the sleeve and shaft.

Bearings are designed to handle both radial and axial loads. They are not designed in consideration of vibration which may cause a brinneling (denting) of the bearing races.

Critical dimensions and tolerances such as wear ring clearance and impeller setting would be affected by vibration. Internal clearance of a bearing is measured in order of one tenth centimeter.

Pump components may be damaged by vibration. Wear rings, bushings and impellers are all vulnerable to vibration.

Bearing seals are very sensitive to radial movement of the shaft. Shaft damage would increase the chance of over-early failing in seals. Labyrinth seals operate within a very limited tolerance. Thus, excessive displacement could damage these tolerances as well.

The vibration in pumps comes from a number of sources that include mechanical problems, hydraulic causes and others.

Currently the monitoring systems for pumps are not as good as those for large turbines. The vibration readings almost always indicate that the equipment has started to destroy itself. Most companies are now trying to collect enough data to more accurately predict the remaining life before total destruction.

The obvious solution to all of these is to adopt good maintenance practice that could eliminate most vibrations.

In reality, one cannot prevent all of the vibrations that induce problems on seal, packing, bearing, and critical clearance. The only solution is to live with it.

References

Akahane, K., & Suzuki, R. (1996). Recent analysis technologies for hydropower equipment. *FUJI Electric Journal*, *69*(9).

BS ISO 10816-5. (2001). *Mechanical vibration*: *Evaluation of machine vibration by measurements on non-rotating* parts—Part 5: Machine sets in hydraulic power generating and pumping plants.

Chen, C.X., Wu, D.Z., Tan, S.G., & Wang, L.Q. (2008). Computing critical speeds for multiple-stage centrifugal pumps with speed dependent support properties. *Fluid Machinery and Fluid Mechanics* (pp. 306–309). Berlin: Springer.

Egusquiza, E. (2007). Vibration behavior of hydraulic turbines, application to condition monitoring. *Proceedings of 2ND IAHR International Meeting of the WG on Cavitation and Dynamic Problems in Hydraulic Machinery and Systems*.

Feng, F. Z., & Chu, F. L. (2001). Dynamic analysis of a hydraulic turbine unit. *Mechanics of Structures and Machines, 29*(4), 505–531.

Garnett, C. H. (1997). The Riccati transfer matrix method. University of Virginia, 1975.

Holzer, (1921). Die Berechnung der Drehschwingugen, Springer-Verlag, Berlin.

Jeffcott, H. H. (1919). The lateral vibration loaded shafts in the neighborhood of a whirling speed.—the effect of want of balance. *Philosophical Magazine*. *6* 37

Krishna, H. R. (1997). *Hydraulic design of hydraulic machinery*, Book Series on Hydraulic Machinery. Avebury, London: Ashgate Publishing Ltd.

Liang, Q.W., Egusquiza, E., Escaler, X, & Avellan, F. (2006). Modal analysis on a Francis turbine runner considering the fluid added mass effect. *Proceedings of IAHR International Meeting of WG on Cavitation and Dynamic Problems in Hydraulic Machinery and Systems*.

MCNally. (2009). http://www.mcnallyinstitute.com/02-htm.

Ohashi, H. (1991). *Vibration and Oscillation of hydraulic machinery*, Book Series on Hydraulic Machinery. Avebury, London: Ashgate Publishing Ltd.

Swain, M. (2008).Vibrations in a Francis turbine: A case study. *Electrical India*, *48*(5).

Wikipedia, the free encyclopedia. (2008a). *Hydropower*. http://www.en.wikipedia.org/wiki/Hydropower.

Wikipedia, the free encyclopedia. (2008b). *Modal analysis*. http://www.en.wikipedia.org/wiki//wiki/Modal_analysis.

Wilson, E. L. (1968). A computer program for the dynamic stress analysis of underground structures. *SESM Report*, 68-1. University of California, Berkeley.

Xiao, R. F., Wang, Z. W., & Luo, Y. Y. (2008). Dynamic stresses in a Francis turbine runner based on fluid-structure interaction analysis. *Tsinghua Science and Technology, 13*(5), 587–592.

Chapter 2
Foundamental of Mechanical Vibration

The purpose of this chapter is to provide a theoretical background of vibration in mechanical systems. The theories and mathematical structures presented in this chapter are classical and based on the book by Krodkiewski (2008). In fact, vibration study is rooted in Newton's Law of Motion. The last four hundred years saw an increased interest in this subject as engineers began to reevaluate earlier formulations and designs in an effort to maximize stability of their particular creation.

2.1 Introduction

There are many situations where vibrations are permitted or even encouraged within the system. Some key terms are defined here, for they will be used often later:

Vibration is a reciprocating or periodic motion of an elastic body, rigid body, or virtually any medium forced from a state of equilibrium.

Oscillation is a repetitive variation of some measure about a centralized point in elapsed time. Vibration undergoes deformation, while an oscillating structure does not.

Structures ranges from small scale: beams and rods; to large scale: rotors and engine assemblies.

Systems are more general and abstract. It may be defined as a group of integrated parts which are behaving as a single entity, either man-made or naturally occurring. All structures are systems, not vice versa.

Environments are external to the system but have the ability to interact and even invoke the system's behavior.

Modeling is the overall goal of representing physical properties of mechanisms by means of mathematical formulations.

Inertia is defined as the property of a mass (or system) which acts to resist itself from a change in motion.

Stiffness describes the systems ability to store strain energy; typically represented by a spring and modeled by the properties of Hooke's Law.

Y. Wu et al., *Vibration of Hydraulic Machinery*,
Mechanisms and Machine Science 11, DOI: 10.1007/978-94-007-6422-4_2,

Damping describes the systems ability to dissipate energy.

Frequency of a vibrating body is the number of cycles of motion within a unit time.

Period of a wave is the time elapsed until the motion repeats itself. It is the reciprocal of the frequency.

Amplitude of a wave is the shortest distance between two particles along the wave which differ in phase by one cycle.

Mechanical Vibration is occasionally "desirable". But more often, it is undesirable because it wastes energy and creates unwanted sound or noise. For example, the vibration motions of a turbine, electric generator, or any mechanical device in operation are typically unwanted. Such vibrations can be brought along about by imbalances in the rotating parts or uneven friction. A careful design usually minimizes undesired vibrations.

It is standard to begin by establishing a behaviorally correct but simplified model from a relatively complex and seemingly disordered system. These simpler systems are called idealized systems. Only with a deeply sophisticated understanding of the actual system can one develop an idealized model for study. When working within an idealized system, insight into the limitations of the actual system is eventually realized; it is with this in mind that one always works from the ground up in all engineering and physical applications. Figure 2.1 shows a few examples of increasingly complex idealistic modular representations of an actual cantilever beam system; the below models are shown with one degree of freedom, four degrees of freedom or infinite degrees of freedom.

This chapter contains four parts:

(1) Mechanical vibration of one-degree-of-freedom (ODOF) linear system;
(2) Multi-degree-of-freedom (MDOF) models;
(3) Vibration of continuous systems;
(4) Approximation of the continuous systems by discrete models. The Rigid Element Method (REM) and the Final Element Method (FEM) are explained and utilized to produce the inertia and stiffness matrices.

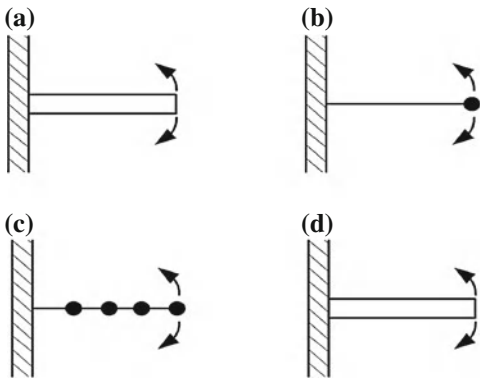

Fig. 2.1 The actual system and its idealized systems. **a** Actual system (cantilever beam). **b** One degree of freedom. **c** Four degrees of freedom. **d** Infinite degrees of freedom

2.2 Mechanical Vibration of One-Degree-of-Freedom Linear Systems

Modeling and analysis on mechanical vibration of ODOF linear system will be presented in this section. This part and following parts in this chapter reference the book by Krodkiewski (2008) as well as the following works: Burton (1994); Inman (2001); Thornton and Marion (2004).

2.2.1 Modeling of ODOF System

The mathematical description of mechanical vibration of ODOF linear system is considered.

2.2.1.1 Physical Model

As an example of vibration, let us consider the vertical motion of body 1 suspended on rod 2 shown in Fig. 2.2a. If the body is forced away from its equilibrium position and then released, each point of the body performs an independent oscillatory motion, like a body suspended at the end of a spring in Fig. 2.2b. Therefore, one generally has to introduce an infinite number of independent coordinates x_i to determine uniquely the body's motion.

The number of independent coordinates one has to use to determine the position of a mechanical system is called number of degrees of freedom.

It is assumed that rod 2 is without mass and body 1 is rigid, so only one coordinate is necessary to uniquely identify the whole system, the displacement

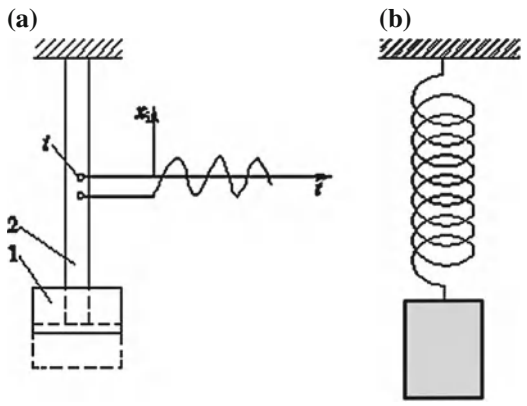

Fig. 2.2 Vertical motion of the body. **a** Physical model. **b** Body suspended at spring

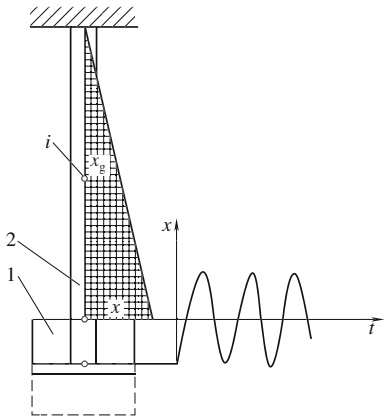

Fig. 2.3 One coordinate used in the system in Fig. 2.2

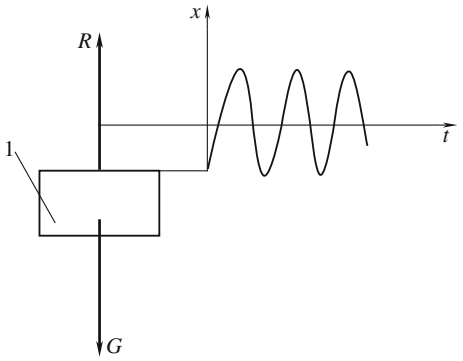

Fig. 2.4 Free body diagram of Fig. 2.2 system

x of the rigid body 1 (see Fig. 2.3). In order to get the equation of the vibration of body 1, one has to produce its free body diagram, which is shown in Fig. 2.4.

In Fig. 2.4, $\boldsymbol{G}$ ($\{\boldsymbol{G}\}$) represents the gravity force, whereas the force $\boldsymbol{R}$ ($\{\boldsymbol{R}\}$) represents so-called the restoring force. In a general case, the restoring force is a non-linear function of the displacement x and the velocity $\dot{x}$ of the body 1 ($R = R(x, \dot{x})$).

Confining the vibration within a small vicinity of the system equilibrium position, would allow the non-linear relationship to be linearized:

$$R = R(x, \dot{x}) \approx kx + c\dot{x} \tag{2.1}$$

where k is called stiffness and c is the coefficient of damping. Such cases are often referred to as linear vibration and the system is named linear system. The physical model that reflects all the above assumptions is labeled the ODOF linear system.

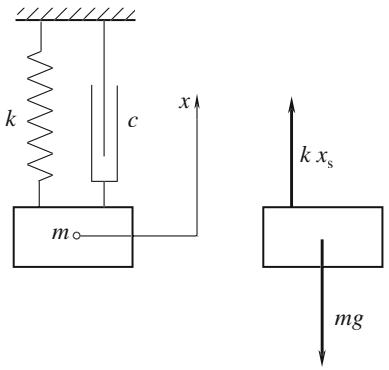

Fig. 2.5 Mathematical model for the ODOF system in Fig. 2.2

2.2.1.2 Mathematical Model

The mathematical model can be obtained through application of the laws of physics to the adopted physical model. In this section, the principle of setting up a mathematical model for the ODOF system is shown in Fig. 2.5.

Assume that the system is in an equilibrium status. The origin of absolute coordinates coincides with the centre of the body's gravity as the body stays at its equilibrium position shown in Fig. 2.5. The summation of all static force vectors (in the example considered gravity force mg and interaction force due to the static elongation of spring kx_s) is equal to zero. If the system is away from equilibrium position by a distance x, there is an increment in the interaction force between the spring and the block. This increment is called the restoring force, which can be represented in the equation of motion by term:

$$F_k = -kx. \tag{2.2}$$

The interaction force is called the damping force, which can be expressed in the equation of motion in the following way:

$$F_D = -c\dot{x}. \tag{2.3}$$

The assumption that the system is linear allows for the application of the superposition principle to integrate these forces into the external force $F_{ex}(t)$. Hence, the equation of motion of the block of mass m is

$$m\ddot{x} = -kx - c\dot{x} + F_{ex}(t). \tag{2.4}$$

Transformation of the above equation into the standard form yields

$$\ddot{x} + 2\varsigma\omega_n\dot{x} + \omega_n^2 x = f(t) \tag{2.5}$$

where

$$\omega_n = \sqrt{k/m},\ 2\varsigma\omega_n = c/m,\ f(t) = F_{ex}(t)/m \tag{2.6}$$

where, ω_n is called natural frequency of the undamped system; ς is the damping factor or damping ratio; $f(t)$ is the unit of external excitation. Equation (2.5) is known as the mathematical model of linear vibration for the ODOF system.

2.2.2 Analysis of ODOF System

Free vibration occurs when a mechanical system is set off by an initial input and then vibrates freely. The mechanical system will then vibrate at one or more of its "natural frequencies" and damp down to zero. In a general case, motion of a vibrating system is due to both the initial conditions and the exciting force. This motion is referred to as the forced vibration.

2.2.2.1 Free Vibration

According to the above definition, it is assumed that summation of all external forces $f(t)$ is equal to zero. Thus, the mathematical model analyzed in this section takes form:

$$\ddot{x} + 2\varsigma\omega_n\dot{x} + \omega_n^2 x = 0. \tag{2.7}$$

If the damping ratio ς is assumed to be zero, Eq. 2.7 governs the free motion of the undamped system.

$$\ddot{x} + \omega_n^2 x = 0 \tag{2.8}$$

(1) Free vibration of an undamped system. The general solution of homogeneous Eq. 2.8 is a linear combination of its two specific linearly independent solutions. These solutions can be obtained by means of the following procedure. The particular solution can be predicted in the form of Eq. 2.9:

$$x = \mathrm{e}^{\lambda t} \tag{2.9}$$

Introduction of solution 2.9 into Eq. 2.8 yields the characteristic equation:

$$\lambda^2 + \omega_n^2 = 0 \tag{2.10}$$

This characteristic equation has two roots:

$$\lambda_1 = +\mathrm{i}\omega_n, \quad \lambda_2 = -\mathrm{i}\omega_n. \tag{2.11}$$

Hence, in this case, the independent particular solutions are

$$x_1 = \sin\omega_n t \quad \text{and} \quad x_2 = \cos\omega_n t. \tag{2.12}$$

Their linear combination is the wanted general solution that approximates free vibration of the undamped system, i.e.,

$$x = C_s \sin \omega_n t + C_c \cos \omega_n t \tag{2.13}$$

where

$$C_s = x_0,\ C_c = v_0. \tag{2.14}$$

And x_0 is the position of the system at instant $t = 0$; v_0 is its initial velocity. The particular solution that represents the free vibration of the system is

$$x = \frac{v_0}{\omega_n} \sin \omega_n t + x_0 \cos \omega_n t = C \sin(\omega_n t + \alpha) \tag{2.15}$$

where

$$C = \sqrt{(x_0)^2 + \left(\frac{v_0}{\omega_n}\right)^2};\ \alpha = \arctan\left(\frac{v_0/\omega_n}{x_0}\right). \tag{2.16}$$

In this context, the period of undamped free vibrations is

$$T_n = 2\pi/\omega_n. \tag{2.17}$$

(2) Free vibration of a damped system. If the damping ratio is not equal to zero, the equation of the free motion is written as

$$\ddot{x} + 2\varsigma\omega_n \dot{x} + \omega_n^2 = 0. \tag{2.18}$$

The characteristic equation of free vibration in a damped system is

$$\lambda^2 + 2\varsigma\omega_n \lambda + \omega_n^2 = 0. \tag{2.19}$$

The characteristic equation has two roots:

$$\lambda_{1,2} = -\varsigma\omega_n \pm \omega_n \sqrt{\varsigma^2 - 1}. \tag{2.20}$$

The particular solution rests on a category of the above roots. Three cases are possible as discussed below.

(2–1) Underdamped vibration. If $\varsigma < 1$, the characteristic equation has two complex conjugated roots and it is often referred to as an underdamped vibration. The free motion solution of an underdamped vibration is in the form:

$$x = C\mathrm{e}^{-\varsigma\omega_n t} \sin(\omega_d t + \alpha) \tag{2.21}$$

where

$$C = \sqrt{(x_0)^2 + \left(\frac{v_0 + \varsigma\omega_n x_0}{\omega_d}\right)^2};\ \alpha = \arctan\left(\frac{x_0\omega_d}{v_0 + \varsigma\omega_n x_0}\right);\ \omega_d = \omega_n\sqrt{1 - \varsigma^2}. \tag{2.22}$$

In this case, the motion is not periodic but the time T_d between each second zero-point is constant and it is termed as a period of the dumped vibration, i.e.,

$$T_d = \frac{2\pi}{\omega_d}. \tag{2.23}$$

The natural logarithm ratio of two displacements $x(t)$ and $x(t + T_d)$ that are one period apart is called the logarithmic decrement of damping and will be denoted by δ. It will be shown that the logarithmic decrement is constant.

$$\delta = \ln \frac{x(t)}{x(t + T_d)} = \frac{2\pi\varsigma}{\sqrt{1 - \varsigma^2}}. \tag{2.24}$$

This formula is frequently used for the experimental determination of the damping ratio ς, i.e.,

$$\varsigma = \frac{\delta}{\sqrt{4\pi^2 - \delta^2}}. \tag{2.25}$$

The other parameter ω_n can be identified by measuring the period of the free motion T_d.

$$\omega_n = \frac{\omega_d}{\sqrt{1 - \varsigma^2}} = \frac{2\pi}{T_d\sqrt{1 - \varsigma^2}}. \tag{2.26}$$

(2–2) **C**ritically damped vibration. If $\varsigma = 1$, the characteristic equation has two real and equivalent roots, $\lambda_{1,2}$ and this case is often referred to as the critically damped vibration.

$$\lambda_{1,2} = -\varsigma\omega_n. \tag{2.27}$$

The expression for free motion of the critically damped vibration system is this form:

$$x = \mathrm{e}^{-\varsigma\omega_n t}(x_0 + t(v_0 + x_0\omega_n)). \tag{2.28}$$

(2–3) Overdamped vibration. If $\varsigma > 1$, the characteristic equation has two real roots and this case is often referred to as the overdamped vibration.

$$\lambda_{1,2} = \omega_n\left(-\varsigma \pm \sqrt{\varsigma^2 - 1}\right). \tag{2.29}$$

The solution of free motion of the overdamped vibration system is as follows:

$$x = \mathrm{e}^{-\varsigma\omega_n t}\left(C_s\mathrm{e}^{\omega_n\sqrt{(\varsigma^2-1)}\,t} + C_c\mathrm{e}^{-\omega_n\sqrt{(\varsigma^2-1)}\,t}\right). \tag{2.30}$$

The two constants C_s and C_c are expressed as follows:

$$C_s = \frac{+\frac{v_0}{\omega_n} + x_0\left(+\varsigma + \sqrt{\varsigma^2 - 1}\right)}{2\sqrt{\varsigma^2 - 1}}, C_c = \frac{-\frac{v_0}{\omega_n} + x_0\left(-\varsigma + \sqrt{\varsigma^2 - 1}\right)}{2\sqrt{\varsigma^2 - 1}}. \tag{2.31}$$

2.2.2.2 Forced Vibration

For the forced vibration, the mathematical model is a linear non-homogeneous differential equation of the second order:

$$\ddot{x} + 2\varsigma\omega_n\dot{x} + \omega_n^2 x = f(t) \tag{2.32}$$

where

$$\omega_n = \sqrt{\frac{k}{m}},\ 2\varsigma\omega_n = \frac{c}{m},\ f(t) = \frac{F_{ex}(t)}{m}. \tag{2.33}$$

The general solution of the homogeneous equation for underdamped vibration is

$$x_g = C\mathrm{e}^{-\varsigma\omega_n t}\sin(\omega_d t + \alpha) \tag{2.34}$$

where

$$C = \sqrt{(x_0)^2 + \left(\frac{v_0 + \varsigma\omega_n x_0}{\omega_d}\right)^2};\ \alpha = \arctan\left(\frac{x_0\omega_d}{v_0 + \varsigma\omega_n x_0}\right);\ \omega_d = \omega_n\sqrt{1-\varsigma^2}. \tag{2.35}$$

To get the particular solution of the non-homogeneous equation, the assumption is made that the excitation can be approximated by a harmonic function, as follows:

$$f(t) = q\sin\omega t \tag{2.36}$$

where q represents the amplitude of the unit excitation and ω is the excitation frequency. Introduction of Eq. (2.36) into Eq. (2.32) yields

$$\ddot{x} + 2\varsigma\omega_n\dot{x} + \omega_n^2 x = q\sin\omega t. \tag{2.37}$$

One can obtain a general solution to the equation of motion that describes forced vibration of a system in the following form:

$$x = C_0\mathrm{e}^{-\varsigma\omega_n t}\sin(\omega_d t + \alpha_0) + A\sin(\omega t + \varphi) \tag{2.38}$$

where

$$A = \frac{\left(q/\omega_n^2\right)}{\sqrt{\left(1-(\omega/\omega_n)^2\right)^2 + 4\varsigma^2(\omega/\omega_n)^2}},\ \varphi = -\arctan\frac{2\varsigma(\omega/\omega_n)}{1-(\omega/\omega_n)^2}. \tag{2.39}$$

Based on the initial conditions, one can get the following set of algebraic equations for determination of the parameters C_0 and α_0.

$$\begin{aligned} x_0 &= C_0 \sin \alpha_0 + A \sin \varphi \\ v_0 &= -C_0 \varsigma \omega_n \sin \alpha_0 + C_0 \omega_d \cos \alpha_0 + A\omega \sin \varphi. \end{aligned} \tag{2.40}$$

The solution (2.38) consists of two terms. The first term represents an vibration with a frequency equal to the natural frequency of the damped system ω_d. Motion represented by this term, because of the existing damping, decays to zero and determines time of the transient state of the forced vibrations. Therefore, after a short time, the transient state changes into a steady state designated by the second term in Eq. (2.38), i.e.,

$$x = A \sin(\omega t + \varphi). \tag{2.41}$$

This harmonic term has amplitude A determined by Eq. (2.39). It is called the amplitude of forced vibration. Motion approximated by Eq. (2.41) is usually known as the system of forced vibration.

2.3 Mechanical Vibration of Linear Systems with MDOF

Since massless or rigid elements do not exist in reality, infinite numbers of coordinates have to be introduced to determine the element position. But in many cases, the real elements can be represented by a limited number of rigid elements connected to each other with massless elements of elastic and damping properties. This process is called discretization by which one arrives at a MDOF system. In this section, it is supposed that forces produced by these massless elements (springs and dampers) are linear functions of displacements and velocities respectively.

2.3.1 Two-Degrees-of-Freedom Model

The mass-spring-damper model is called an ODOF model because the mass is only considered to be moving up and down. In a more complex system of suspension, the system should be discretized into masses that move in more than one direction, which adds degrees of freedom. A two-degree-of-freedom model (2DOF) shown in the Fig. 2.6 would help to illustrate the major concepts of MDOF.

Equations of motion of the 2DOF system are found to be

$$\begin{aligned} &m_1\ddot{x}_1 + (c_1 + c_2)\dot{x}_1 - c_2\dot{x}_2 + (k_1 + k_2)x_1 - k_2x_2 = f_1 \\ &m_2\ddot{x}_2 - c_2\dot{x}_1 + (c_2 + c_3)\dot{x}_2 - c_3\dot{x}_3 - k_2x_1 + (k_2 + k_3)x_2 - k_3x_3 = f_2. \end{aligned}$$

Because $-c_3\,\dot{x}_3 \_\, k_3\,x_3 = 0$ (see Krodkiewski 2008), these equations could be written in matrix format, i.e.,

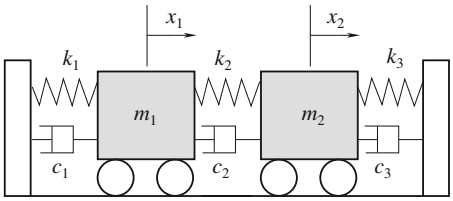

Fig. 2.6 Two degree of freedom model

$$\begin{bmatrix} m_1 & 0 \\ 0 & m_2 \end{bmatrix} \begin{Bmatrix} \ddot{x}_1 \\ \ddot{x}_2 \end{Bmatrix} + \begin{bmatrix} c_1 + c_2 & -c_2 \\ -c_2 & c_2 + c_3 \end{bmatrix} \begin{Bmatrix} \dot{x}_1 \\ \dot{x}_2 \end{Bmatrix} + \begin{bmatrix} k_1 + k_2 & -k_2 \\ -k_2 & k_2 + k_3 \end{bmatrix} \begin{Bmatrix} x_1 \\ x_2 \end{Bmatrix} = \begin{Bmatrix} f_1 \\ f_2 \end{Bmatrix}. \tag{2.42}$$

A more compact form of this matrix equation can be written as

$$[\boldsymbol{M}]\{\ddot{\boldsymbol{x}}\} + [\boldsymbol{C}]\{\dot{\boldsymbol{x}}\} + [\boldsymbol{K}]\{\boldsymbol{x}\} = \{\boldsymbol{f}\} \tag{2.43}$$

where $[\boldsymbol{M}]$, $[\boldsymbol{C}]$, and $[\boldsymbol{K}]$ are symmetric matrices of the mass, damping, and stiffness matrices. The matrices are $N \times N$ square matrices where N is the number of degrees of freedom of the system.

2.3.2 Free Vibration and Eigenvalues of the MDOF Model

In the following analysis, the case without damping and applied forces (i.e., free vibration) would be studied. The solution of a viscously damped system is somewhat more complicated.

$$[\boldsymbol{M}]\{\ddot{\boldsymbol{x}}\} + [\boldsymbol{K}]\{\dot{\boldsymbol{x}}\} = 0. \tag{2.44}$$

This differential equation can be solved by assuming the following type of solution:

$$\{\boldsymbol{x}\} = \{\boldsymbol{X}\}\mathrm{e}^{\mathrm{i}\omega t}. \tag{2.45}$$

The equation then becomes

$$\left[-\omega^2[\boldsymbol{M}] + [\boldsymbol{K}]\right]\{\boldsymbol{X}\}\mathrm{e}^{\mathrm{i}\omega t} = 0. \tag{2.46}$$

Since $\mathrm{e}^{\mathrm{i}\omega t}$ cannot equal zero, the equation reduces to

$$\left[-\omega^2[\boldsymbol{M}] + [\boldsymbol{K}]\right]\{\boldsymbol{X}\} = 0. \tag{2.47}$$

This is an eigenvalue problem in mathematics and can be put in the standard format by pre-multiplying the equation by $[\boldsymbol{M}]^{-1}$.

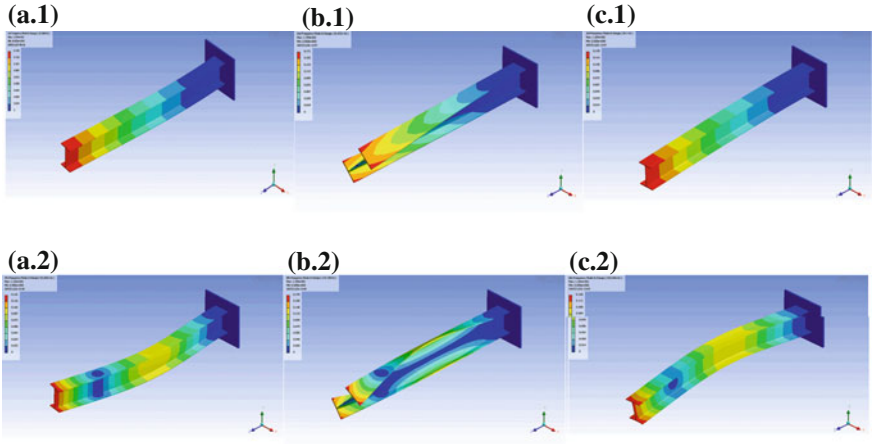

Fig. 2.7 Modes of a cantilevered I-beam. **a.1** 1st lateral bending **b.1** 1st torsional **c.1** 1st vertical bending **a.2** 2nd lateral bending **b.2** 2nd torsional **c.2** 2nd vertical bending (http://en.wikipedia.org/wiki/Vibration)

$$\left[[\boldsymbol{M}]^{-1}[\boldsymbol{K}] - \omega^2[\boldsymbol{M}]^{-1}[\boldsymbol{M}]\right]\{\boldsymbol{X}\} = 0,$$

and if $[\boldsymbol{M}]^{-1}[\boldsymbol{K}] = [\boldsymbol{A}]$ and $\lambda = \omega^2$, then

$$[[\boldsymbol{A}] - \lambda[\boldsymbol{I}]]\{\boldsymbol{X}\} = 0. \tag{2.48}$$

The solution results in N eigenvalues $(\omega_1^2, \omega_2^2, \omega_3^2, \ldots \omega_N^2)$, where N corresponds to the number of degrees of freedom. The eigenvalues provide the natural frequencies of the system. When these eigenvalues are substituted back into the original set of equations, values of $\{\boldsymbol{X}\}$ that correspond to each eigenvalue are called the eigenvectors. These eigenvectors reflect the mode shapes of the system.

Figure 2.7 shows the mode shapes of a cantilevered I-beam. A finite element model was used to generate the mass and stiffness matrices and solve the eigenvalue problem. Even this relatively simple model has a degree-of-freedom of over 100 and hence as many natural frequencies and mode shapes. Generally speaking, only the first few modes are important.

2.3.3 MDOF Problem Converted to a ODOF Problem

The eigenvectors have very important properties called orthogonality. These properties can be used to simplify the solution of multi-degree of freedom models. These properties are

$$[\boldsymbol{M}_r] = [\Psi]^{\mathrm{T}}[\boldsymbol{M}][\Psi] \tag{2.49}$$

$$[\boldsymbol{k}_r] = [\Psi]^{\mathrm{T}}[\boldsymbol{K}][\Psi] \tag{2.50}$$

where $[\boldsymbol{M}_r]$ and $[\boldsymbol{k}_r]$ are diagonal matrices that contain the modal mass and stiffness values for each mode. The solution is simplified with these properties through coordinate transformation, i.e.,

$$\{\boldsymbol{x}\} = [\Psi]\{\boldsymbol{q}\}. \tag{2.51}$$

When applied into the original free vibration equation, the equation is

$$[\boldsymbol{M}][\Psi]\{\ddot{\boldsymbol{q}}\} + [\boldsymbol{K}][\Psi]\{\boldsymbol{q}\} = 0. \tag{2.52}$$

One takes advantage of the orthogonality properties by multiplying this equation by $[\boldsymbol{\Psi}]^{\mathrm{T}}$ as

$$[\Psi]^{\mathrm{T}}[\boldsymbol{M}][\Psi]\{\ddot{\boldsymbol{q}}\} + [\Psi]^{\mathrm{T}}[\boldsymbol{K}][\Psi]\{\boldsymbol{q}\} = 0. \tag{2.53}$$

The orthogonality properties then simplify this equation to

$$[\boldsymbol{M}_r] + \{\ddot{\boldsymbol{q}}\} + [\boldsymbol{k}_r] + \{\boldsymbol{q}\} = 0. \tag{2.54}$$

This equation is the foundation of vibration analysis for MDOF systems. A similar result can be derived for damped systems. The key is that the modal and stiffness matrices are diagonal so that the equations could be "decoupled". In other words, the unwieldy MDOF problem is transformed into several ODOF problems that can be solved using the same methods outlined above.

The modal coordinates or modal participation factors q are the solving target instead of x. It may be clearer if one writes $\{\boldsymbol{x}\} = [\boldsymbol{\Psi}]\ \{\boldsymbol{q}\}$ as

$$\{\boldsymbol{x}\} = q_1\{\Psi\}_1 + q_2\{\Psi\}_2 + q_3\{\Psi\}_3 + \cdots + q_N\{\Psi\}_N. \tag{2.55}$$

As can be seen above, the vibration at each degree of freedom is just a linear sum of the mode shapes with the modal participation factor q.

2.3.4 Forced Vibrations-Transfer Functions

The response to external excitation $\{\boldsymbol{F}(t)\}$ of a MDOF system is obtained with the particular solution to the mathematical model expressed as

$$[\boldsymbol{M}]\{\ddot{\boldsymbol{x}}\} = -[\boldsymbol{K}]\{\boldsymbol{x}\} - [\boldsymbol{C}]\{\dot{\boldsymbol{x}}\} + \{\boldsymbol{F}(t)\}. \tag{2.56}$$

Let us assume that the excitation force $\{\boldsymbol{F}(t)\}$ is a sum of k addends. For further analysis, each of them has the following form:

$$F^k = F_0^k \cos\left(\omega t + \varphi_0^k\right) \tag{2.57}$$

To facilitate the process of looking for the particular solution of Eq. (2.56), the complex excitation force is introduced by adding to expression (2.57) the imaginary part:

$$f^k = F_0^k \cos\left(\omega t + \varphi_0^k\right) + \mathrm{i}F_0^k \sin\left(\omega t + \varphi_0^k\right). \tag{2.58}$$

The complex excitation may be written as follows:

$$f^k = f_0^k e^{\mathrm{i}\omega t}. \tag{2.59}$$

Here, f_0^k is a complex number that depends on the amplitude and phase of external excitation. Substitute Eq. (2.59) into Eq. (2.56) to yield

$$[\boldsymbol{M}]\{\ddot{\boldsymbol{x}}\} + [\boldsymbol{C}]\{\dot{\boldsymbol{x}}\} + [\boldsymbol{K}]\{\boldsymbol{x}\} = \{\boldsymbol{f}_0\}e^{\mathrm{i}\omega t}. \tag{2.60}$$

Now, the particular solution of Eq. (2.60) can be predicted in the complex form Eq. (2.61), i.e.,

$$\{\boldsymbol{x}^c\} = \{\boldsymbol{a}\}e^{\mathrm{i}\omega t}. \tag{2.61}$$

Substitution of Eq. (2.61) into Eq. (2.60) produces a set of the algebraic equations which are linear with respect to the unknown vector:

$$\left(-\omega^2[\boldsymbol{M}] + \mathrm{i}\omega[\boldsymbol{C}] + [\boldsymbol{K}]\right)\{\boldsymbol{a}\} = \{\boldsymbol{f}\}_0. \tag{2.62}$$

Its solution is

$$\{\boldsymbol{a}\} = \left(-\omega^2[\boldsymbol{M}] + \mathrm{i}\omega[\boldsymbol{C}] + [\boldsymbol{K}]\right)^{-1}\{\boldsymbol{f}\}_0. \tag{2.63}$$

According to Eq. (2.61), the response of the system $\{\boldsymbol{x}^c\}$ to complex force $\{\boldsymbol{f}\}$ is

$$\{\boldsymbol{x}^c\} = (\mathrm{Re}\{\boldsymbol{a}\} + \mathrm{iIm}\{\boldsymbol{a}\})(\cos\omega t + \mathrm{i}\sin\omega t). \tag{2.64}$$

Response of the system $\{\boldsymbol{x}\}$ to real excitation $\{\boldsymbol{F}\}$ is represented by the real part of the solution (2.64), i.e.,

$$\{\boldsymbol{x}\} = \mathrm{Re}\{\boldsymbol{a}\}\cos\omega t - \mathrm{Im}\{\boldsymbol{a}\}\cos\omega t. \tag{2.65}$$

According to Eq. (2.65), motion of the system along $\{\boldsymbol{x}^c\}$ is

$$x^k = x_0^k \cos\left(\omega t + \beta^k\right) \tag{2.66}$$

where

$$x_0^k = \sqrt{\mathrm{Re}(a^k)^2 + \mathrm{Im}(a^k)^2},\ \beta^k = \arctan\frac{\mathrm{Im}(a^k)}{\mathrm{Re}(a^k)}. \tag{2.67}$$

The amplitude of forced vibration x_0^k is equal to the absolute value of complex amplitude α^k and its phase β^k is equal to the phase between the complex amplitudes α^k and the vector $\mathrm{e}^{\mathrm{i}\omega t}$. The complex matrix

$$\left(-\omega^2[\boldsymbol{M}] + \mathrm{i}\omega[\boldsymbol{C}] + [\boldsymbol{K}]\right)^{-1} \tag{2.68}$$

is denoted by $[\boldsymbol{R}pq(\mathrm{i}\omega)]$ and is called the matrix of transfer functions.

Based on Eq. 2.63, it transfers the vector of complex excitation $\{\boldsymbol{f}_0\}e^{\mathrm{i}\omega t}$ into the vector of complex displacement $\{\boldsymbol{x}^{\mathrm{e}}\} = \{\boldsymbol{a}\}e^{\mathrm{i}\omega t}$.

$$\{\boldsymbol{x}^{c}\} = \left[\boldsymbol{R}_{pq}(\mathrm{i}\omega)\right]\{\boldsymbol{f}_0\}e^{\mathrm{i}\omega t}. \tag{2.69}$$

It is easy to notice that the element $R_{pq}(\mathrm{i}\omega)$ of the matrix of transfer functions represents complex displacement (amplitude and phase) of the system along the coordinates $\{\boldsymbol{x}_p\}$ in response to unit excitation $\{1e^{\mathrm{i}\omega t}\}$ along the coordinate $\{\boldsymbol{x}_q\}$.

2.4 Vibration of Continuous System

The logical extension of a discrete mass system is one with an infinite number of masses. At the end of the limit, it becomes a continuous system. This section is about the vibration associated with one-dimensional continuous systems such as shafts and beams. The natural frequencies and natural modes are used for exact solutions of free and forced vibrations.

2.4.1 Modeling of Continuous System

The mathematical description of mechanical vibration of shafts and beams is considered in this part.

2.4.1.1 Modeling of Shaft System

Shafts are elastic elements that are subjected to torques. Suppose that the torque $\tau(z,t)$ is distributed along the axis z and is a function of time t (see Fig. 2.8). The shaft has the shear modulus $G(z)$, the density $\rho(z)$, the cross-section area $A(z)$ and the second moment of area $J(z)$. Because of its moment $\tau(z,t)$, the shaft performs torsional vibrations and the instantaneous angular position of the cross-section at z is $\varphi(z,t)$. The angular position at the distance $z + \mathrm{d}z$ is expressed by the total differential $\partial\varphi(z,t)/\partial z\mathrm{d}z$. In consideration of the element $\mathrm{d}z$ in the shaft, its moment of inertia is

$$\mathrm{d}I = \int_A r^2\mathrm{d}A\rho(z)\mathrm{d}z = \rho(z)\mathrm{d}z\int_A r^2\mathrm{d}A = J(z)\rho(z)\mathrm{d}z. \tag{2.70}$$

Based on the generalized Newton's law, one can write the following equation:

$$J(z)\rho(z)\frac{\partial^2\varphi(z,t)}{\partial t^2} - \frac{\partial T(z,t)}{\partial z} = \tau(z,t). \tag{2.71}$$

Once the relationship between the torque on a section $T(z,t)$ and the angular deflection of $\varphi(z,t)$ is established, i.e.,

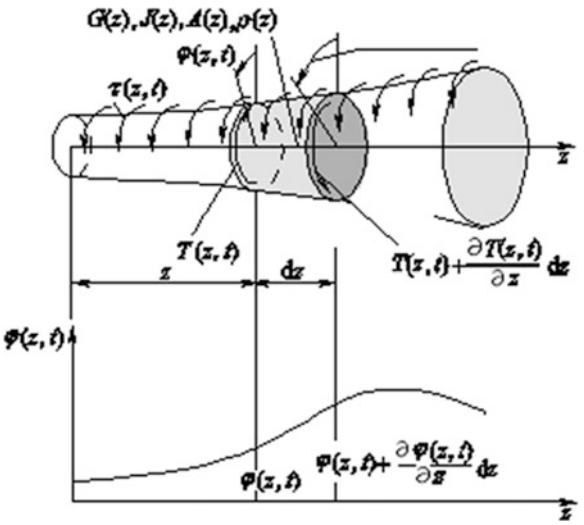

Fig. 2.8 Modeling of shaft (Krodkiewski 2008)

$$\frac{\partial \varphi(z,t)}{\partial z}\mathrm{d}z = \frac{T(z,t)}{J(z)G(z)}\mathrm{d}z. \tag{2.72}$$

And substituted into Eq. (2.71), one has

$$J(z)\rho(z)\frac{\partial^2 \varphi(z,t)}{\partial t^2} - \frac{\partial}{\partial z}\left[G(z)J(z)\frac{\partial \varphi(z,t)}{\partial z}\right] = \tau(z,t). \tag{2.73}$$

If $J(z)$, $\rho(z)$ and $G(z)$ are constant, the equation of motion takes form:

$$\frac{\partial^2 \varphi(z,t)}{\partial t^2} - \lambda^2 \frac{\partial^2 \varphi(z,t)}{\partial z^2} = q(z,t) \tag{2.74}$$

where

$$\lambda^2 = \frac{G}{\rho};\ q(z,t) = \frac{\tau(z,t)}{J\rho}. \tag{2.75}$$

2.4.1.2 Modeling of Beams

Beams are elastic elements that are subjected to lateral loads—forces or moments that have their vectors perpendicular to the centre line of a beam (Krodkiewski 2008). One considers a beam of the second moment of area J(z), cross-section A(z), density $\rho(z)$ and the Young's modulus $E(z)$. The beam performs vibrations in response to external distributed unit load $f(z,\ t)$. The instantaneous position of element dz is highlighted in Fig. 2.9.

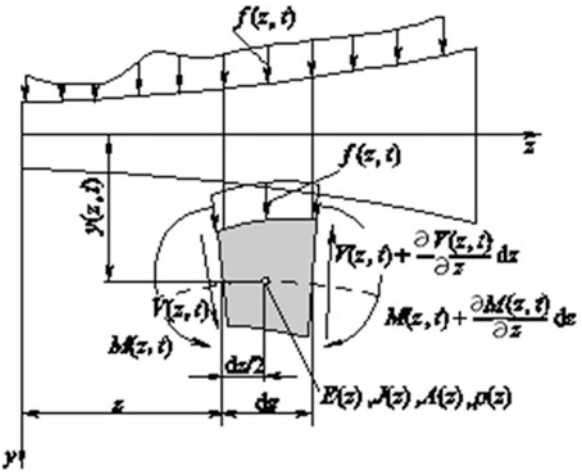

Fig. 2.9 Instantaneous position of the element dz (Krodkiewski 2008)

The beam's equation of motion in the z direction is

$$\mathrm{d}m\frac{\partial^2 y(z,t)}{\partial t^2}\mathrm{d}z = -\frac{\partial V(z,t)}{\partial z} + f(z,t)\mathrm{d}z. \tag{2.76}$$

If one neglects the inertia moment associated with rotation of the element dz, the terms of order higher than one with respect to dz, sums the moments about the point G to be equal to zero, yields the relationship between bending moment M and shearing force V, i.e.,

$$V(z,t) = \frac{\partial M(z,t)}{\partial z}. \tag{2.77}$$

Since mass of the element dz is

$$\mathrm{d}m = A(z)\rho(z)\mathrm{d}z. \tag{2.78}$$

Substituting into Eq. (2.76), one can get the beam's equation of motion, i.e.,

$$\frac{\partial^2 y(z,t)}{\partial t^2} + \lambda^2\frac{\partial^4 y(z,t)}{\partial t^4} = q(z,t) \tag{2.79}$$

where

$$\lambda^2 = \frac{EJ}{A\rho};\ q(z,t) = \frac{f(z,t)}{A\rho}. \tag{2.80}$$

2.4.2 Analysis of Continuous System

The solution of free vibration of shafts and beams is discussed in this part.

2.4.2.1 Free Vibration of Shafts

If parameters of the system considered are constant, the free vibration (natural vibration) of the shaft is governed by the homogeneous Eq. (2.81):

$$\frac{\partial^2 \varphi(z,t)}{\partial t^2} + \lambda^2 \frac{\partial^2 \varphi(z,t)}{\partial z^2} = 0 \tag{2.81}$$

where

$$\lambda^2 = G/\rho. \tag{2.82}$$

The goal is to get the particular solution of the above equation in a form that is the product of two functions. One of them is a function of position z and the other one is a function of time t.

$$\varphi(z,t) = \Phi(z) \sin \omega_n t. \tag{2.83}$$

Introduction of the predicted solution into (2.83) into Eq. (2.81) comes to the following ordinary differential equation:

$$-\omega_n^2 \Phi(z) - \lambda^2 \Phi^{II}(z) = 0 \tag{2.84}$$

or

$$\Phi^{II}(z) + \beta_n^2 \Phi(z) = 0 \tag{2.85}$$

where

$$\beta_n = \omega_n/\lambda. \tag{2.86}$$

The general solution of this equation is

$$\Phi_n(z) = S_n \sin \beta_n z + C_n \cos \beta_n z \tag{2.87}$$

where $\beta_n = \omega_n \sqrt{\rho/G}$.

The values for parameter β_n as well as the constants S_n and C_n should be chosen to fulfill boundary conditions. According to Eq. (2.87), the general solution of Eq. (2.81) may be adopted in the following form:

$$\varphi(z,t) = \sum_{n=1}^{\infty} \Psi_n(z) \left(S_n \sin \omega_n t + C_n \cos \omega_n t\right). \tag{2.88}$$

This solution has to meet the requirement of the initial conditions. The conditions determine the initial position $\Psi_0(z)$ and initial velocity $\Omega_0(z)$ of the system considered for the time t which equals to zero, i.e.,

$$\varphi(z,0) = \Psi_0(z) \quad \frac{\partial}{\partial t}\varphi(z,0) = \Omega_0(z). \tag{2.89}$$

Taking advantage of the orthogonality conditions, one derives the wanted constants S_n and C_n as

$$C_n = \frac{\int_0^l \Psi_0(z)\Psi_n(z)\mathrm{d}z}{\int_0^l \Psi_n^2(z)\mathrm{d}z},\ S_n = \frac{1}{\omega_n}\frac{\int_0^l \Omega_0(z)\Psi_n(z)\mathrm{d}z}{\int_0^l \Psi_n^2(z)\mathrm{d}z}. \tag{2.90}$$

2.4.2.2 Free Vibrations of Beams

For a uniform beam, the equation of motion (2.79) can be classified as a linear partial differential equation of two variables (z and t) with constant coefficients (λ^2). Its order with respect to time is 2, and 4 with respect to z. The general solution, a function of two variables, is the sum of the general solution of homogeneous equation and the particular solution of non-homogeneous equation. If external excitation $q(z, t) = 0$, Eq. (2.79) is one that describes free vibration of the beam with a non-zero initial condition. The free vibrations (natural vibrations) are governed by the homogeneous Eq. (2.79), i.e.,

$$\frac{\partial^2 y(z,t)}{\partial t^2} + \lambda^2 \frac{\partial^4 y(z,t)}{\partial z^4} = 0. \tag{2.91}$$

Similarly to the analysis of shafts, the solution of Eq. (2.91) is in the form of a product of two functions. One of them is a function of position z and the other is the function of time t, i.e.,

$$\mathrm{y}(z,t) = Y(z)\sin\omega_n t. \tag{2.92}$$

Substituting the predicted solution (2.92) into Eq. (2.91), one arrives at the following ordinary differential equation:

$$-\omega_n^2 Y(z) + \lambda^2 Y^{IV}(z) = 0 \tag{2.93}$$

$$Y^{IV}(z) - \beta_n^4 Y(z) = 0 \tag{2.94}$$

where

$$\beta_n^4 = \frac{\omega_n^2}{\lambda^2} = \frac{A\rho}{EJ}\omega_n^2. \tag{2.95}$$

The standard form of its particular solution is

$$\mathrm{y}(z) = \mathrm{e}^{rz}. \tag{2.96}$$

Introduction of this solution into the Eq. (2.94) yields the characteristic equation:

$$r^4 = \beta_n^4. \tag{2.97}$$

Its roots

$$r_1 = \beta_n,\ r_2 = -\beta_n,\ r_3 = \mathrm{i}\beta_n,\ r_4 = -\mathrm{i}\beta_n \tag{2.98}$$

determines the set of the linearly independent particular solution.

$$Y_1 = e^{\beta_n z},\ Y_2 = e^{-\beta_n z},\ Y_3 = e^{\mathrm{i}\beta_n z},\ Y_4 = e^{-\mathrm{i}\beta_n z}. \tag{2.99}$$

Alternatively, one can choose their combinations to be the set of the independent solutions, i.e.,

$$Y_1(z) = \left(e^{\beta_n z} - e^{-\beta_n z}\right)/2 = \sinh \beta_n z \tag{2.100}$$

$$Y_2(z) = \left(e^{\beta_n z} + e^{-\beta_n z}\right)/2 = \cosh \beta_n z \tag{2.101}$$

$$Y_3(z) = \left(e^{\mathrm{i}\beta_n z} - e^{-\mathrm{i}\beta_n z}\right)/2 = \sin \beta_n z \tag{2.102}$$

$$Y_4(z) = \left(e^{\mathrm{i}\beta_n z} + e^{-\mathrm{i}\beta_n z}\right)/2 = con\beta_n z. \tag{2.103}$$

The general solution for Eq. (2.93), as a linear combination of these particular solutions is

$$Y_n(z) = A_n \sinh\beta_n z + B_n \cosh\beta_n z + C_n \sin\beta_n z + D_n \cos\beta_n z. \tag{2.104}$$

Values for the parameter β_n as well as for the constants A_n, B_n, C_n and D_n should be chosen to fulfill boundary conditions. Since this equation is of the fourth order, one has to set four boundary conditions reflecting the conditions at both ends of the beam. They would involve the function $Y(z)$ and its first three derivatives with respect to z. Boundary conditions are applied to the beam for determination of the natural frequencies and the natural modes.

2.5 Conservative Discrete Vibrating Systems

The equations of motion for both ODOF and MDOF undamped vibrating systems are obtained through the dynamic equilibrium equations in Lagrange equations. The vibrating system is constrained to either an inertial reference frame or a moving one with respect to an inertial frame.

The dynamic equilibrium equations of a system comprised of a number of masses connected with each other to a supporting frame by linear springs can be written in the compact form:

$$[\boldsymbol{M}]\{\ddot{\boldsymbol{x}}\} + [\boldsymbol{K}]\{\boldsymbol{x}\} = \{\boldsymbol{f}(t)\} \tag{2.105}$$

where $[\boldsymbol{M}]$ is the mass matrix of the system. It is diagonal if all coordinates x_i are related to translational degrees of freedom in an inertial reference frame. $[\boldsymbol{K}]$ is the stiffness matrix, which generally is not a diagonal matrix. $\{\boldsymbol{x}\}$ is a vector of the

generalized coordinates. $\{\boldsymbol{f}(t)\}$ is a time-dependent vector containing forcing functions.

2.5.1 Lagrange Equations

The generalized coordinates in Eq. (2.105) are the coordinates x, y, and z at various point masses. The number of degrees-of-freedom of the system has been assumed to coincide with the number of coordinates of points P_i.

Under the condition that some constraints are located between the point masses, the number of degrees-of-freedom of the system is smaller than the number of coordinates, and the displacement vectors $\{\boldsymbol{r}_i\}$ can be expressed as functions of a number n of parameters x_i, i.e.,

$$\{\boldsymbol{r}_i\} = \{\boldsymbol{r}_i\}(x_1, x_2, ..., x_n). \tag{2.106}$$

Some of the x_i can be real displacements or rotations, but they can also bear a less direct meaning, as in the case where they are coefficients of a series expansion. Correspondingly, the generalized forces are real forces, moments, or just mathematical expressions linked with the forces and moments acting on the system in a less direct way.

To acquire the equations of motion, one can write the dynamic equilibrium equations for each of the masses m_i, i.e., impose that the sum of all forces acting on each mass is equal to zero. If the number of degrees-of-freedom is high or if some of the generalized coordinates are not easily linked with the displacements and rotations of masses, it is convenient to apply the methods of analytical mechanics, like the principle of virtual works, Hamilton's principle, or Lagrange equations, to get the equations of motion as follows:

$$\frac{\mathrm{d}}{\mathrm{d}t}\left(\frac{\partial \tilde{T}}{\partial \dot{x}_i}\right) - \frac{\partial \tilde{T}}{\partial x_i} + \frac{\partial \tilde{U}}{\partial x_i} = Q_i \tag{2.107}$$

where $\tilde{T}$ is the kinetic energy; $\tilde{U}$ is the potential energy and $\{\boldsymbol{Q}_i\}$ is ith generalized force. In the equation, the first two terms are functions of kinetic energy $\tilde{T}$, and the third term represents conservative forces obtainable from the potential energy $\tilde{U}$, and the right-hand side is a generic expression of forces that cannot be obtained from the potential energy. They can be derived from the virtual work δL performed by the forces acting on the system when the virtual displacement δx is given.

$$\{\boldsymbol{Q}_i\} = \frac{\partial \delta \tilde{L}}{\partial \delta x_i} \ . \tag{2.108}$$

In the case of linear systems, the potential energy is a quadratic form in the displacements and, apart from constant terms which do not affect the equation of motion, can be expressed as

$$\tilde{U} = \frac{1}{2}\{\boldsymbol{x}\}^T[\boldsymbol{K}]\{\boldsymbol{x}\} + \{\boldsymbol{x}\}^T\{\boldsymbol{f}_0\} \tag{2.109}$$

where $[\boldsymbol{K}]$ is a symmetric matrix.

Even in the case of nonlinear systems, the potential energy does not depend on the generalized velocities $\dot{x}_i$, and Eq. (2.107) may thus be written by the Lagrangian function $\left(\tilde{T} - \tilde{U}\right)$:

$$\frac{\mathrm{d}}{\mathrm{d}t}\left(\frac{\partial\left(\tilde{T} - \tilde{U}\right)}{\partial \dot{x}_i}\right) - \frac{\partial\left(\tilde{T} - \tilde{U}\right)}{\partial x_i} = \{\boldsymbol{Q}_i\}. \tag{2.110}$$

The kinetic energy is usually assumed to be a quadratic function of the generalized velocities:

$$\tilde{T} = \tilde{T}_0 + \tilde{T}_1 + \tilde{T}_2 \tag{2.111}$$

where $\tilde{T}_0$ does not depend on the generalized velocities, $\tilde{T}_1$ is linear, and $\tilde{T}_2$ is quadratic. In the case of linear systems, the kinetic energy must contain terms in which no power greater than two of the displacements and velocities is present. As a consequence, $\tilde{T}_2$ cannot contain the displacements, i.e.,

$$\tilde{T}_2 = \frac{1}{2}\sum_{i=1}^{n}\sum_{i=1}^{n} m_{ij}\dot{x}_i\dot{x}_j = \frac{1}{2}\{\dot{\boldsymbol{x}}\}^T[\boldsymbol{M}]\{\dot{\boldsymbol{x}}\} \tag{2.112}$$

where $[\boldsymbol{M}]$ is a symmetric matrix whose elements m_{ij} do not depend on either $\{\boldsymbol{x}\}$ or $\{\dot{\boldsymbol{x}}\}$. In this section, only the systems with constant parameters will be considered, hence $[\boldsymbol{M}]$ will be constant.

$\tilde{T}_1$ is linear in velocities and then can contain powers no greater than the first one in the generalized displacements:

$$\tilde{T}_1 = \frac{1}{2}\{\dot{\boldsymbol{x}}\}^T([\boldsymbol{M}_1]\{\dot{\boldsymbol{x}}\} + \{\boldsymbol{f}_1\}) \tag{2.113}$$

where matrix $[\boldsymbol{M}_1]$ and vector $\{\boldsymbol{f}_1\}$ do not contain the generalized coordinates, although $\{\boldsymbol{f}_1\}$ may be a function of time.

$\tilde{T}_0$ does not have the generalized velocities but only terms with order no higher than two in the displacements:

$$\tilde{T}_0 = \frac{1}{2}\{\boldsymbol{x}\}^T\left[\boldsymbol{M}_g\right]\{\boldsymbol{x}\} + \{\boldsymbol{x}\}^T\{\boldsymbol{f}_2\} + e \tag{2.114}$$

where matrix $[\boldsymbol{M}_g]$, vector $\{\boldsymbol{f}_2\}$, and the scalar e are constant. $\tilde{T}_0$ has a structure similar to that of the potential energy: The term $\tilde{U} - \tilde{T}_0$ is usually referred to as dynamic potential.

By performing the derivatives appearing in the Lagrange equations, one can obtain

$$\frac{\partial(\tilde{T}-\tilde{U})}{\partial \dot{x}_i} = [\boldsymbol{M}]\{\dot{\boldsymbol{x}}\} + \frac{1}{2}([\boldsymbol{M}_1]\{\boldsymbol{x}\} + \{\boldsymbol{f}_1\}) \tag{2.115}$$

$$\frac{\mathrm{d}}{\mathrm{d}t}\left[\frac{\partial(T-U)}{\partial \dot{x}_i}\right] = [\boldsymbol{M}]\{\ddot{\boldsymbol{x}}\} + \frac{1}{2}[\boldsymbol{M}_1]\{\dot{\boldsymbol{x}}\} + \{\dot{\boldsymbol{f}}_1\} \tag{2.116}$$

$$\frac{\partial(\tilde{T}-\tilde{U})}{\partial x_i} = \frac{1}{2}[\boldsymbol{M}_1]^T\{\dot{\boldsymbol{x}}\}^T + [\boldsymbol{M}_g]\{\boldsymbol{x}\} - [\boldsymbol{K}]\{\boldsymbol{x}\} + \{\boldsymbol{f}_2\} - \{\boldsymbol{f}_0\}. \tag{2.117}$$

The equation of motion can thus be written in the form:

$$\begin{aligned}[\boldsymbol{M}]\{\ddot{\boldsymbol{x}}\} + \frac{1}{2}([\boldsymbol{M}_1] - [\boldsymbol{M}_1]^T)\{\dot{\boldsymbol{x}}\} + ([\boldsymbol{K}] - [\boldsymbol{M}_g])\{\boldsymbol{x}\} \\ = -\{\dot{\boldsymbol{f}}_1\} + \{\boldsymbol{f}_2\} - \{\boldsymbol{f}_0\} + \{\boldsymbol{Q}\}.\end{aligned} \tag{2.118}$$

Matrix $[\boldsymbol{M}_1]$ is usually skew-symmetric. However, even if it is not so, it can be considered as the sum of a symmetric and a skew-symmetric part, i.e.,

$$[\boldsymbol{M}_1] = [\boldsymbol{M}_{1\mathrm{sy}}] + [\boldsymbol{M}_{1\mathrm{sk}}]. \tag{2.119}$$

When it is introduced into Eq. (2.118), only the skew-symmetric part of $[\boldsymbol{M}_1]$ appears in the equation of motion. Let $[\boldsymbol{M}_{1\mathrm{sk}}]$ be indicated as $[\boldsymbol{G}]$ and vectors $\{\boldsymbol{f}_0\}$, $\{\dot{\boldsymbol{f}}_1\}$ and $\{\boldsymbol{f}_2\}$ be included into the external forces vector $\{\boldsymbol{Q}\}$. The equation of motion then becomes

$$[\boldsymbol{M}]\{\ddot{\boldsymbol{x}}\} + [\boldsymbol{G}]\{\dot{\boldsymbol{x}}\} + ([\boldsymbol{K}] - [\boldsymbol{M}_g])\{\boldsymbol{x}\} = \{\boldsymbol{Q}\}. \tag{2.120}$$

The skew-symmetric matrix $[\boldsymbol{G}]$ is usually referred to as the gyroscopic matrix and the symmetric matrix $[\boldsymbol{M}_g]$ is usually called the geometric stiffness matrix.

A system in which $\tilde{T}_1$ vanishes is called a natural system and no gyroscopic matrix is present. In many cases, $\tilde{T}_0$ is also not present and the kinetic energy is expressed by Eq. (2.112); such is the case for an example of linear non-rotating structures. While in the case of linear systems, the Lagrangian is a quadratic form in the generalized coordinates and their derivatives, for general nonlinear systems it may have a different expression.

2.5.2 State Space

Any set of n numbers may be interpreted as a vector in an n-dimensional space. This space containing vector $\{\boldsymbol{x}\}$ is usually known as the configuration space, since any point in this space can be associated to a configuration of the system.

Positions and velocities, taken together, are thus the state variables of the system, even if this choice is not unique and other pairs of variables correlated with them can be used (e.g., positions and moments). A state vector

$$\{z\} = \{\dot{x} \quad x\}^{\mathrm{T}}$$

containing the displacements and velocities can thus be defined. It has $2n$ components and defines a point in a space with $2n$ dimensions, the state space, determined by a reference frame whose coordinates are the state variables of the system. In the case of systems with an ODOF, the state space has only two dimensions and is called the state plane. With reference to the state space, the equation of motion (2.120) of a linear system can be transformed into a set of $2n$ first-order linear differential equations, the state equations of the system, i.e.,

$$[\boldsymbol{M}]\{\dot{\boldsymbol{v}}\} + [\boldsymbol{G}]\{\boldsymbol{v}\} + \left([\boldsymbol{K}] - \left\{\boldsymbol{M}_g\right\}\right)\{\boldsymbol{x}\} = \{\boldsymbol{Q}\} \text{ and } \{\dot{\boldsymbol{x}}\} = \{\boldsymbol{v}\}. \tag{2.121}$$

The state equations are usually written in the form:

$$\{\dot{z}(t)\} = \left[\tilde{\boldsymbol{A}}\right]\{z(t)\} + \left[\tilde{\boldsymbol{B}}\right]\{\boldsymbol{u}(t)\} \tag{2.122}$$

where

$$\left[\tilde{\boldsymbol{A}}\right] = \begin{bmatrix} -\boldsymbol{M}^{-1}\boldsymbol{G} & -\boldsymbol{M}^{-1}\left(\boldsymbol{K} - \boldsymbol{M}_g\right) \\ \boldsymbol{I} & 0 \end{bmatrix}$$

is the dynamic matrix of the system. It is neither symmetrical nor positively defined. Vector $\{\boldsymbol{u}(t)\}$, whose size need not be equal to the number of degrees of freedom of the system, is the vector in which inputs affecting behavior of the system are listed. $[\tilde{\boldsymbol{B}}]$ is the input-gain matrix; if the number of inputs is r, it has $2n$ rows and r columns.If the inputs $\{\boldsymbol{u}(t)\}$ are linked with the generalized forces $\{\boldsymbol{Q}(t)\}$ acting on the various degrees of freedom by the relationship:

$$\{\boldsymbol{Q}(t)\} = [\boldsymbol{T}]\{\boldsymbol{u}(t)\} \tag{2.123}$$

then the expression of the input gain matrix is

$$\left[\tilde{\boldsymbol{B}}\right] = \left\{\boldsymbol{M}^{-1}\boldsymbol{T} \quad 0\right\}^{\mathrm{T}}. \tag{2.124}$$

If the output of the system consists of a linear combination of state variables, to which a linear combination of the inputs can be added, a second equation can be added to Eq. (2.122):

$$\{\boldsymbol{y}(t)\} = \left[\tilde{\boldsymbol{C}}\right]\{z(t)\} + \left[\tilde{\boldsymbol{D}}\right]\{\boldsymbol{u}(t)\} \tag{2.125}$$

where $\{\boldsymbol{y}(t)\}$ is the output vector, i.e., a vector in which the m outputs of the system are listed. $[\tilde{\boldsymbol{C}}]$ is a matrix with m rows and n columns, often named as the output gain matrix. If all generalized displacements are taken as outputs of the system, matrix $[\tilde{\boldsymbol{C}}]$ is simply $[\tilde{\boldsymbol{C}}] = [\boldsymbol{0}\ \boldsymbol{I}]$. $[\tilde{\boldsymbol{D}}]$ is a matrix with m rows and r columns, describing direct influence of the inputs on the outputs; it is therefore referred to as the direct-link matrix. The set of four matrices $[\tilde{\boldsymbol{A}}]$, $[\tilde{\boldsymbol{B}}]$, $[\tilde{\boldsymbol{C}}]$ and $[\tilde{\boldsymbol{D}}]$ is usually referred to as the quadruple of the dynamic system. In summary, equations that define the dynamic behavior of the system, from input to output, are

$$\begin{cases} \{\dot{z}(t)\} = \left[\tilde{A}\right]\{z(t)\} + \left[\tilde{B}\right]\{u(t)\} \\ \{y(t)\} = \left[\tilde{C}\right]\{z(t)\} + \left[\tilde{D}\right]\{u(t)\} \end{cases}. \tag{2.126}$$

A point in the state space which fulfills

$$\left[\tilde{A}\right]\{z(t)\} + \left[\tilde{B}\right]\{u(t)\} = 0$$

for any value of time is an equilibrium point. Since it is a static solution, it can be defined only if the input vector $\{u(t)\}$ is constant in time. All generalized velocities are identically equal to zero and thus the equilibrium point lies in the configuration space, thought as a subspace of the state space. Although a nonlinear system can contain a number of equilibrium points, a single equilibrium point exists if the system is linear. If $\{u(t)\}$ equals zero, the equilibrium point is the solution of the homogeneous algebraic equation:

$$\left[\tilde{A}\right]\{z(t)\} = 0$$

that is to say, the trivial solution $\{z(t)\} = 0$, except when the dynamic matrix is singular. In the case of nonlinear systems, equations of motion can often be linearized about any given equilibrium points. The motion of the linearized system about an equilibrium point is usually referred to as motion in the small.

Consider the system described in Eq. (2.120) and assume that matrices $[G]$ and $[M_g]$ are zero (the system is natural). Moreover, assume that matrix $[M]$ is diagonal.

The degrees of freedom can be subdivided into two sets: a vector $\{x_1\}$, to which a non-vanishing inertia is associated, and a vector $\{x_2\}$, containing all the other ones. All matrices and forces may be split:

$$[M] = \begin{bmatrix} M_{11} & M_{12} \\ M_{21} & M_{22} \end{bmatrix}, \; [K] = \begin{bmatrix} K_{11} & K_{12} \\ K_{21} & K_{22} \end{bmatrix}, \; \begin{Bmatrix} Q_1(t) \\ Q_2(t) \end{Bmatrix}.$$

The mass matrix $[M_{22}]$ vanishes and, since the mass matrix is diagonal, also $[M_{12}]$ and $[M_{21}]$ are cancelled.

The equations of motion can be written in the form:

$$\begin{cases} [M_{11}]\{\ddot{x}_1\} + [K_{11}]\{x_1\} + [K_{12}]\{x_2\} = \{Q_1(t)\} \\ [K_{21}]\{x_1\} + [K_{22}]\{x_2\} = \{Q_2(t)\} \end{cases} \tag{2.127}$$

The second set of equations can be readily solved in $\{x_2\}$:

$$\{x_2\} = -[K_{22}]^{-1}[K_{21}]\{x_1\} + [K_{22}]^{-1}\{Q_2(t)\}. \tag{2.128}$$

It is possible to find an equation of motion containing generalized coordinates $\{x_1\}$ and the mass matrix without singularity:

$$[M_{11}]\{\ddot{x}_1\} + \left([K_{11}] - [K_{22}]^{-1}[K_{21}]\right)\{x_1\} = \{Q_1(t)\} + [K_{22}]^{-1}\{Q_2(t)\} \tag{2.129}$$

References

Burton, T. D. (1994). *Introduction to dynamic systems analysis*. New York: McGraw-Hill.
Inman, D. J. (2001). *Engineering vibration*. New York: Prentice Hall.
Krodkiewski, J. M. (2008). *Mechanical vibration*. Melbourne: The University of Melbourne.
Thornton S.T., Marion J.B. (2004). *Classical dynamics of particles and systems*, 5th(edn.), CA: Brooks/Cole Thomson Learning.
Wikibooks (2008). Mechanical vibration. http://en.wikibooks.org/wiki/mechanical/vibration.
Wikipedia (2008). Resonance. http://encyclopedia.thefreedictionary.com/Re-sonance.
Wikipedia (2012). Vibration. http://en.wikipedia.org/wiki/Vibration.

Chapter 3
Numerical Model of Dynamics

A numerical model describes a scientific system in language of numbers. There are two kinds of models in mathematics: the lumped parameter model and the distributed parameter model. If the model is homogeneous, or represents a consistent state throughout the entire system, the parameters are distributed, and the model may be referred to as a continuum. If the model is heterogeneous, or represents a varying state throughout the system, then the parameters are lumped. Distributed parameters are typically represented with partial differential equations.

3.1 Discretization Techniques

A number of discretization techniques have been developed for solving the partial differential equations (PDEs) related to continuum models. They are particularly useful when shape and boundary conditions of the continuous system are complex. The aim is to replace the continuous model with a discrete one, i.e., to replace the continuous model made of PDEs with a model of ordinary differential equations (ODEs).

3.1.1 Introduction of Discretization Techniques

Over the last two centuries, many discretization techniques have been created. It is possible to group these techniques into four classes.

3.1.1.1 The Assumed Modes Method

Here, the deformed shape of the system is assumed to be a linear combination of n known functions of the space coordinates, defined in the whole space occupied by the body.

Y. Wu et al., *Vibration of Hydraulic Machinery*,
Mechanisms and Machine Science 11, DOI: 10.1007/978-94-007-6422-4_3,

3.1.1.2 The Lumped-Parameters Method

In this method, the mass of a deformed body is lumped into a certain number of stations in the body (sometimes a number of point masses). These lumped masses are then connected by massless fields that possess elastic and damping properties often assumed to be uniform in space. Because the degree of freedom of the lumped masses describes system motion, the model intuitively leads to a discrete system.

3.1.1.3 The Transfer Matrices

Instead of dealing with the system as a whole, the study can start at a certain place and proceed station by station using the so-called transfer matrices. The methods based on transfer matrices have been used recently because they can be implemented on very small computers. Yet their evident limitations lead many to use the FEM instead.

3.1.1.4 The Finite Element Method (FEM)

In the FEM, the body is divided into regions. The deformed shape of each finite element is assumed to be a linear combination of space coordinate functions through a certain number of parameters. Usually such functions of space coordinates (called shape functions) are quite simple. Then a set of differential equations of the same type can be written as those obtained for discrete systems.

3.1.2 The Assumed-Modes Methods

The displacement field $\{\boldsymbol{u}(x, y, z, t)\}$ of a general undamped continuous elastic body can be approximated by a linear combination of n arbitrarily assumed functions $\{\boldsymbol{q}_i(x, y, z)\}$, often referred to as assumed modes:

$$\{\boldsymbol{u}(x, y, z, t)\} = \sum_{i=1}^{n} a_i(t)\{\boldsymbol{q}_i(x, y, z)\}. \tag{3.1}$$

Equation (3.1) would yield exact results if the assumed functions $\{\boldsymbol{q}_i(x, y, z)\}$ were the system eigenfunctions with infinite numbers. In this case, functions $a_i(t)$—considered to be the generalized coordinates expressing deformation of the system—are the modal coordinates. Expressions of kinetic and potential energies of the system can be easily obtained from Eq. (3.1):

$$\tilde{T} = \frac{1}{2}\{\dot{\boldsymbol{a}}\}^T[\boldsymbol{M}]\{\dot{\boldsymbol{a}}\}, \quad \tilde{U} = \frac{1}{2}\{\boldsymbol{a}\}^T[\boldsymbol{K}]\{\boldsymbol{a}\} \tag{3.2}$$

where $\{\boldsymbol{a}\}$ is a vector containing the n generalized coordinates $a_i(t)$, $[\boldsymbol{M}]$ and $[\boldsymbol{K}]$ are square matrices of order n that depend on the inertial and elastic properties of the system, respectively, also on the assumed functions $\{\boldsymbol{q}_i(x, y, z)\}$.

In the same way, virtual work performed by a given force distribution $\{\boldsymbol{f}(x, y, z, t)\}$ for the virtual displacement is given by

$$\delta\{\boldsymbol{u}(x, y, z)\} = \sum_{i=1}^{n} \delta a_1 \{\boldsymbol{q}_i(x, y, z)\} \tag{3.3}$$

corresponding to a virtual change of the generalized coordinates δa_i is

$$\delta\tilde{L} = \sum_{i=1}^{n} \delta a_i \{\boldsymbol{f}(x, y, z, t)\} \cdot \{\boldsymbol{q}_i(x, y, z)\} \mathrm{d}V. \tag{3.4}$$

Equations expressing motion of the system can thus be computed through Lagrange equations, i.e.,

$$[\boldsymbol{M}]\{\ddot{\boldsymbol{a}}\} + [\boldsymbol{M}]\{\boldsymbol{a}\} = \{\boldsymbol{f}(t)\} \tag{3.5}$$

where the generalized forces f_i are

$$f_i = \int_V \{\boldsymbol{f}_i(x, y, z, t)\} \cdot \{\boldsymbol{q}_i(x, y, z, t)\} \mathrm{d}V.$$

3.1.3 Lumped-Parameters Methods

Lumped-parameters methods are based on the idea of discretizing continuous systems in their physical structure. The inertial properties are concentrated into a number of rigid bodies or point masses, located at chosen points that are called stations or nodes. They are connected by fields within which the elastic properties of the structure are ascribed and damping properties are also considered. External force distributions are substituted by concentrated forces acting at the stations. Generalized displacements at the nodes are generalized coordinates (Wikipedia 2008c).

Construction of the stiffness matrix is usually a difficulty in computation. Traditionally, a compliance matrix $[\boldsymbol{B}]$ is obtained through computation of the influence coefficients rather than the stiffness matrix $[\boldsymbol{K}]$. It must be noted that compliance matrix can be obtained only if the stiffness matrix is non-singular.

3.1.4 Transfer-Matrices Methods

The lumped-parameters methods involve a lot of computation, mainly in two phases: the construction of the stiffness matrix (or of the compliance matrix) and

the solution of the eigenproblem. To avoid such difficulties, a different approach, the transfer-matrices method was evolved (see Rodney 1982).

In physics and mathematics, the transfer-matrix method is a general technique for solving problems in statistical mechanics. The basic idea is to write the partition function in this form:

$$Z = \{\boldsymbol{V}_0\} \cdot \left(\prod_{k=1}^{N} [\boldsymbol{W}_k] \right) \cdot \{\boldsymbol{V}_{N+1}\}$$

where $\{\boldsymbol{V}_0\}$ and $\{\boldsymbol{V}_{N+1}\}$ are vectors of dimension p and the $p \times p$ matrices, $[\boldsymbol{W}_k]$ are the so-called transfer matrices.

Two applications of this approach are well known and were widely used, particularly when no automatic computing machines were in use: Holzer's method for torsional vibrations of shafts and Myklestadt's method for flexural vibrations of beam-like structures. Their main limitation lies in the very principle of the transfer-matrices method, which is only suitable for in-line systems, i.e., systems where every station is linked to only two other stations, a leading station and a following station (see Genta 2009).

The method is based on the definition of state vectors and transfer matrices. A state vector is one that contains the generalized displacements and forces related to the degrees of freedom that characterize the ends of each field, considered as isolated from the rest of the structure. Consequently, each field would have two state vectors, one at its left end and one at its right end. State vectors at the ends of a field are linked by the transfer matrix of the field:

$$\{\boldsymbol{S}_{\mathrm{R}i}\} = [\boldsymbol{T}_{fi}]\{\boldsymbol{S}_{\mathrm{L}i}\} \tag{3.6}$$

where subscript i refers to the ith field, and R and L designate the right and left ends respectively. $[\boldsymbol{T}_{fi}]$ is the transfer matrix of the ith field.

The left end of the ith field and the right end of the $(i-1)$th field are located at the ith station, and between them there is the ith lumped mass. The corresponding state vectors are not coincident because the mass exerts generalized inertia forces on the node. They are linked by the transfer matrix of the ith station:

$$\{\boldsymbol{S}_{\mathrm{L}i}\} = [\boldsymbol{T}_{ni}]\{\boldsymbol{S}_{\mathrm{R}(i-1)}\}. \tag{3.7}$$

The station transfer matrix contains inertia forces from lumped mass that, in harmonic free vibrations, are functions of the square of vibration frequency. The field is massless and the field transfer matrix is independent of the frequency.

If there is a linear elastic constraint at the ith node, its stiffness can be introduced into the expression of the station transfer matrix. In this way it is possible to apply the transfer-matrix method for systems where the constraints are exerted to nodes other than the first and last ones. Rigid constraints are represented by elastic constraints with very high stiffness.

State vector in the left of the first station $\{\boldsymbol{S}_0\}$ and that in the right of the last station $\{\boldsymbol{S}_n\}$ can be linked together by the equation:

$$\{\boldsymbol{S}_n\} = [\boldsymbol{T}_{n_n}]\left[\boldsymbol{T}_{f_{n-1}}\right][\boldsymbol{T}_{n_{n-1}}]\left[\boldsymbol{T}_{f_{n-2}}\right]\cdots[\boldsymbol{T}_{n_2}]\left[\boldsymbol{T}_{f_1}\right][\boldsymbol{T}_{n_1}]\{\boldsymbol{S}_0\} = [\boldsymbol{T}_G]\{\boldsymbol{S}_0\}. \tag{3.8}$$

The overall transfer matrix:

$$[\boldsymbol{T}_G] = \prod_{i=n}^{1}[\boldsymbol{T}_i] \tag{3.9}$$

is the product of all transfer matrices of all nodes and fields from the last to the first in correct order. Matrix products depend on the order in which they are performed, so the overall transfer matrix must be computed by following the aforementioned rule. The overall transfer matrix is a function of system vibration frequency ω or, better, of ω^2.

3.2 The Finite Element Method

The FEM is a numerical technique for finding approximate solutions of PDEs as well as of integral equations. The solution approach is based either on eliminating the differential equation completely (steady state problems), or rendering the PDE into an approximating system of ODEs.

3.2.1 Introduction of FEM

In general, the FEM is characterized by the following processes (see Funnell 2008; Grandin 1986; Wikipedia 2008a).

1. Choose a grid for the computational domain. In the preceding treatment, the grid consisted of triangles, but one can also use squares or curvilinear polygons.
2. Choose basis functions (shape functions). One can use piecewise linear basis functions, but it is also common to use piecewise polynomial basis functions.

A significant concern is the smoothness of the basis functions. For second order elliptic boundary value problems, piecewise polynomial basis function that are merely continuous would suffice. For higher order PDEs, one must use smoother basis functions.

3. Element analysis. The behavior of a particular element type is analyzed in terms of loads and responses at discrete nodes of the element. This analysis is often based on the Ritz-Rayleigh procedure that originated from the theorem of minimum potential energy in mechanics. That is, the function is the system solution when it minimizes the potential energy.

The Ritz-Rayleigh procedure restricts the search to a space of linear combinations of n independent admissible basis functions $w_i(\{\boldsymbol{x}\})$, $I = 1,2,\ldots n$. The w_i represent, for example, displacement fields for a mechanical problem, and are functions of the spatial coordinates $\{\boldsymbol{x}\}$. The linear combinations can be expressed as

$$w(\{\boldsymbol{x}\}) = \sum_{i=1}^{n} c_i w_i(\{\boldsymbol{x}\})$$

where the c_j are n constants defining $w(\{\boldsymbol{x}\})$.

Now that each basis function is admissible, every function in the space of linear combinations will also be admissible. The aim is to find the $w(\{\boldsymbol{x}\})$ which minimizes the energy functional $F(w)$. F is now a function of c_i. Since c_i is the determinant, one could take the partial derivative of F with respect to each c_i in turn and set it to zero.

The result would be a set of n algebraic equations in c_i:

$$\frac{\partial}{\partial c_i}\left(\sum_{j=1}^{n} c_j w_j\right) = 0, \;\; i = 1, 2, \cdots n.$$

Thus, the boundary-value problem for a single element has been reduced to the solution of n linear algebraic equations in n unknowns.

4. Assembly of system equation.

The behavior of each element has been described in terms of its edge behaviors and at certain discrete nodes along its edges.

Based on the assumption that the elements can only interact at these discrete nodes, the assembly of element matrices into a system matrix is an expression of the fact that a node shared by two elements must have the same displacement when considered as part of either element.

Once the element matrices have been calculated, they are all combined together into one large matrix representing the whole complex system.

Any extra forces applied to individual nodes can also be added into the right-hand side. The equation representing the entire boundary-value problem is then solved using one of a variety of techniques, such as Gauss-Jordan elimination.

3.2.2 FEM in Galerkin Discretization for Poisson Problem

The Galerkin discretization for the Poisson problem in FEM was introduced briefly by Scholz (2003).

3.2.2.1 Poisson Problem

The true solution u of the Poisson (boundary value) problem (P) is approximated by a numerical one in the solution domain $V \subset \mathbb{R}^{\not\vdash}$ with closed bounder Γ. The Dirichlet boundary conditions apply on $\Gamma_D \subset \Gamma$ and Neumann boundary conditions apply on $\Gamma_N := \Gamma \setminus \Gamma_D$. The problem is at $f \in L^2(V)$, $u_D \in H^1(V)$ and $g \in L^2(\Gamma_N)$, to search for the solution $u \in H^1(V)$, which satisfies the Poisson equation, i.e.,

$$-\Delta u = f \text{ in } V \tag{3.10}$$

with Dirichlet boundary conditions:

$$u = u_D \text{ in } \Gamma_D \tag{3.11}$$

and Neumann boundary conditions:

$$\frac{\partial u}{\partial n} = g \text{ in } \Gamma_N \tag{3.12}$$

where Δu is Laplace operator to variable u.

3.2.2.2 The Weak Formulation

The weak formulation of boundary value problem (P) is gained by multiplication of Eq. (3.10) with

$$w \in H_D^1(V) := \left\{ w \in H^1(V) | w = 0 \text{ on } \Gamma_D \right\}$$

and integration over V:

$$-\int_V \Delta u \cdot w \mathrm{d}V = \int_V f \cdot w \mathrm{d}V.$$

After integration by parts and substitution of the boundary conditions, the rearrangement leads to

$$\int_V \nabla u \cdot \nabla w \mathrm{d}V = \int_V f \cdot w \mathrm{d}V + \int_{\Gamma_N} g \cdot w \mathrm{d}\Gamma.$$

Then, it is incorporated with the Dirichlet boundary conditions:

$$\int_V \nabla u \cdot \nabla w \mathrm{d}V - \int_V {}_D \cdot \nabla w \mathrm{d}V = \int_V f \mathrm{d}V + \int_{\Gamma_N} g \cdot w \mathrm{d}\Gamma - \int_V \nabla u_D \cdot \nabla w \mathrm{d}V.$$

and substituted with the homogeneous solution $y \in H_D^1(V)$ which is given by $y = u - u_D$ and satisfies $y = 0$ on Γ_D. This gives the weak formulation of the Poisson problem which reads: Find $y \in H_D^1(V)$ such that

$$\int_V \nabla y \cdot \nabla w \mathrm{d}V = \int_V f \mathrm{d}V + \int_{\Gamma_N} g \cdot w \mathrm{d}\Gamma - \int_V \nabla u_D \cdot \nabla w \mathrm{d}V. \tag{3.13}$$

3.2.2.3 Galerkin Discretization

In order to solve the Poisson problem numerically, one has to discretize the weak formulation of the Poisson equation and restrict the solution space of the numerical solution U to a finite dimensional subspace S of $H^1(V)$. Accordingly, $U_D \in S_D := S \cap H^1_\Omega$ approximates u_D in Γ_D. The discretized problem P_S can then be written as: Find $Y \in S_D$ such that

$$\int_V \nabla Y \cdot \nabla W \mathrm{d}V = \int_V f \cdot W \mathrm{d}V + \int_{\Gamma_N} g \cdot W \mathrm{d}\Gamma - \int_V \nabla U_D \cdot \mathrm{d}V \tag{3.14}$$

with $W \in S_D$.

One sets (η_1, η_2, $\cdots$, η_N) as a basis of the N-dimensional space S and $S_D := S \cap H^1_\Omega$, a M-dimensional subspace, then the last equation is given by

$$\int_V \nabla Y \cdot \nabla \eta_j \mathrm{d}V = \int_V f \cdot \eta_j \mathrm{d}V + \int_{\Gamma_N} g \cdot \eta_j \mathrm{d}\Gamma - \int_V \nabla U_D \cdot \nabla \eta_j \mathrm{d}V (\eta_j \in S_D). \tag{3.15}$$

If one makes a series expansion of Y and U_D in terms of η_k:

$$Y = \sum_{k=1}^{M} x_k \eta_k (\eta_k \in S_D) \text{ and } U_D = \sum_{k=1}^{N} U_k \eta_k (\eta_k \in S), \tag{3.16}$$

then:

$$\int_V \nabla \sum_k x_k \eta_k \cdot \nabla \eta_j \mathrm{d}V = \int_V f \cdot \eta_j \mathrm{d}V + \int_{\Gamma_N} g \cdot \eta_j \mathrm{d}\Gamma - \int_V \nabla \sum_{k=1}^{N} U_k \eta_k \cdot \nabla \eta_j \mathrm{d}V$$

can be rewritten as

$$\sum_k x_k \int_V \nabla \eta_k \cdot \nabla \eta_j \mathrm{d}V = \int_V f \cdot \eta_j \mathrm{d}V + \int_{\Gamma_N} g \cdot \eta_j \mathrm{d}\Gamma - \sum_{k=1}^{N} U_k \int_V \nabla \eta_k \cdot \nabla \eta_j \mathrm{d}V. \tag{3.17}$$

and simplified to a system of linear equations:

$$[\boldsymbol{A}]\{\boldsymbol{X}\} = \{\boldsymbol{B}\} \tag{3.18}$$

where the "stiffness matrix" is given by

$$A_{jk} = \int_V \nabla \eta_k \cdot \nabla \eta_j \mathrm{d}V$$

and the "right hand side" by

$$B_j = \int_V f \cdot \eta_j \mathrm{d}V + \int_{\Gamma_N} g \cdot \eta_j \mathrm{d}\Gamma - \sum_{k=1}^{N} U_k \int_V \nabla \eta_k \cdot \nabla \eta_j \mathrm{d}V.$$

The stiffness matrix is sparse, symmetric, and positive. Thus, Eq. (3.17) has exactly one solution $\{\boldsymbol{X}\} \in \mathbb{R}^{\mathbb{M}}$, which gives the Galerkin solution:

$$U = U_D + Y = \sum_{j=1}^{N} U_j \eta_j + \sum_{k=1}^{M} x_k \eta_k \tag{3.19}$$

where η_j and η_k are shape functions of elements.

3.2.3 FEM for Structure Analysis

The FEM originated from the need to solve complex elasticity and structural analysis problems. Integrated FEM is commonly used in the design phase of a variety of mechanical structure.

3.2.3.1 Virtual Work Principle

Virtual work on a system results from either virtual forces acting through real displacement or real forces acting through virtual displacement. Here the term "displacement" may refer to a translation or a rotation, and the term "force" to a force or a moment. Virtual quantities are independent and arbitary variables. For example, when a rigid body that is in equilibrium is subject to virtual compatible displacements, the total virtual work of all external forces is zero (Reddy 2002; Wikipedia 2008b).

1. Principle of virtual work for applied forces in static equilibrium.

If a system of particles, i, is in static equilibrium. The total force on each particle is zero, i.e.,

$$\left\{\boldsymbol{F}_i^{(t)}\right\} = 0. \tag{3.20}$$

Summing up the work exerted by force on each particle that acts through an arbitrary virtual displacement $\{\delta \boldsymbol{u}_i\}$ leads to the virtual work equivalent to zero:

$$\delta \tilde{L} = \sum_i \left\{\boldsymbol{F}_i^{(t)}\right\}^T \{\delta \boldsymbol{u}_i\} = 0 \tag{3.21}$$

where the expression must hold for arbitrary displacements. Dividing the forces into applied forces, $\{\boldsymbol{F}_i\}$, and constraint forces, $\{\boldsymbol{C}_i\}$, yields

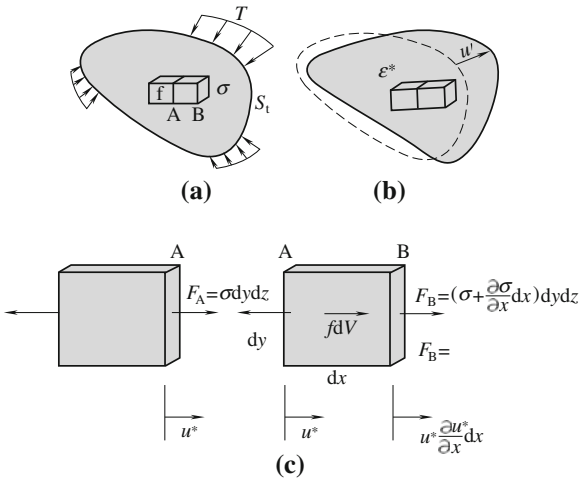

Fig. 3.1 Stress and strain states. **a** σ-State: External forces and stress in equilibrium. **b** ε−-State: Consistent deformations ε^* and displacements u^*. **c** Adjacent differential elements

$$\delta\tilde{L} = \sum_i \{\boldsymbol{F}_i\}^T \{\delta \boldsymbol{u}_i\} + \sum_i \{\boldsymbol{C}_i\}^T \{\delta \boldsymbol{u}_i\} = 0. \tag{3.22}$$

No work is done when virtual displacements are orthogonal to the direction of constraint force. Such displacements should be consistent with the constraints. And it leads to the principle of virtual work for applied forces, which states that forces applied to a static system do no virtual work:

$$\delta\tilde{L} = \sum_i \{\boldsymbol{F}_i\}^T \{\delta \boldsymbol{u}_i\} = 0. \tag{3.23}$$

Also, there is a corresponding principle for accelerating systems called D'Alembert's principle, which forms a theoretical basis for Lagrangian mechanics along with finite element analysis.

2. Virtual work principle for a deformable body.

It is assumed that a free body diagram of a deformable body is composed of an infinite number of differential cubes shown in Fig. 3.1. Two unrelated states for the body are defined as follows:

The $\{\boldsymbol{\sigma}\}$-State (Fig. 3.1a) shows external surface forces $\{\boldsymbol{T}\}$, body forces $\{\boldsymbol{f}\}$, and $\{\boldsymbol{\sigma}\}$ internal stresses in equilibrium. The $\{\boldsymbol{\varepsilon}\}$-State (Fig. 3.1b) shows continuous displacements $\{\boldsymbol{u}^*\}$ and consistent strains $\{\boldsymbol{\varepsilon}^*\}$. The superscript (*) emphasizes that the two states are unrelated. There is no need to specify whether any of the states are real or virtual.

Imagine that the forces and stresses in $\{\boldsymbol{\sigma}\}$-State undergo the displacements and deformations in $\{\boldsymbol{\varepsilon}\}$-State. Total virtual (imaginary) work is done by all forces acting on the faces of all cubes, for example, one dimension case is shown in Fig. 3.1c.

Then the equation of the total external virtual work done by $\{\boldsymbol{T}\}$ and $\{\boldsymbol{f}\}$ in whole deformable body can be written as

$$\int_{\Gamma} \{\boldsymbol{u}^*\}^T \{\boldsymbol{T}\} \mathrm{d}\Gamma + \int_V \{\boldsymbol{u}^*\}^T \{\boldsymbol{f}\} \mathrm{d}V = \int_V \{\boldsymbol{\varepsilon}^*\}^T \{\boldsymbol{\sigma}\} \mathrm{d}V. \tag{3.24}$$

The right-hand-side is often called the internal virtual work. The principle of virtual work states that external virtual work is equal to internal virtual work when equilibrated forces and stresses undergo unrelated but consistent displacements and strains. In order to impose equilibrium on real stresses and forces in practical applications, use consistent virtual displacements and strains in the virtual work equation. In cases of consistent displacements and strains, equilibrated virtual stresses and forces should be used.

These general scenarios give rise to two frequently stated variational principles. They are valid irrespective of material behavior.

3. Principle of virtual displacements.

In order to derive the principle of virtual displacements in variational notations for supported bodies, the following conditions should be specified: Virtual displacements and strains as variations for real displacements and strains use variational notation such as $\delta u \equiv u^*$ and $\delta\varepsilon \equiv \varepsilon^*$.

Virtual displacements are zero on the part of the surface that has prescribed displacements, and thus work done by the reactions is zero. The only remaining external surface forces on the part Γ can do work. The virtual work equation then becomes the principle of virtual displacements:

$$\int_{\Gamma} \{\delta\boldsymbol{u}\}^T \{\boldsymbol{T}\} \mathrm{d}\Gamma + \int_V \{\delta\boldsymbol{u}\}^T \{\boldsymbol{f}\} \mathrm{d}V = \int_V \{\delta\boldsymbol{\varepsilon}\}^T \{\boldsymbol{\sigma}\} \mathrm{d}V. \tag{3.25}$$

This relation is equivalent to a set of equilibrium equations for a differential element in the deformable body as well as of stress boundary conditions on the part Γ of the surface. Conversely, Eq. (3.25) can be reached, albeit in a non-trivial manner, by starting with the differential equilibrium equations and stress boundary conditions on Γ, proceeding in the manner similar to (a) and (b).

Since virtual displacements are automatically compatible when expressed in terms of continuous, single-valued functions, only the need for consistency between strains and displacements has to be stated.

4. Principle of virtual forces.

Virtual forces and stresses as variations of the real forces and stresses are specified. Virtual forces are zero on part Γ of the surface that has prescribed forces, and only surface (reaction) forces on Γ_u (where displacements are prescribed) would do work. The virtual work equation becomes the principle of virtual forces, i.e.,

$$\int_{\Gamma_u} \{\boldsymbol{u}\}^T \{\delta\boldsymbol{T}\} \mathrm{d}\Gamma + \int_V \{\boldsymbol{u}\}^T \{\delta\boldsymbol{f}\} \mathrm{d}V = \int_V \{\boldsymbol{\varepsilon}\}^T \{\delta\boldsymbol{\sigma}\} \mathrm{d}V. \tag{3.26}$$

This relation is equivalent to a set of strain-compatibility equations and to displacement boundary conditions on the part S_u. It is also named as the principle of complementary virtual work.

3.2.3.2 Element Analysis

The displacement is written as a vector in three-dimensional space (sometimes of higher order, if rotations are considered). Expression of the point displacement inside each element is (see Genta 2009)

$$\{\boldsymbol{u}(x,y,z,t)\} = [\boldsymbol{N}(x,y,z)]\{\boldsymbol{q}(t)\}, \tag{3.27}$$

where $\{\boldsymbol{q}(t)\}$ is a vector indicating n generalized coordinates of the element and $[\boldsymbol{N}]$ is the matrix containing the shape functions. Numbers of rows in $[\boldsymbol{N}]$ and in $\{\boldsymbol{u}(x, y, z, t)\}$ are equivalent, and number of columns in $[\boldsymbol{N}]$ equals the number n of degrees of freedom.

The strains can be expressed as functions of derivatives of displacements with respect to space coordinates:

$$\{\boldsymbol{\varepsilon}(x,y,z,t)\} = [\boldsymbol{B}(x,y,z)]\{\boldsymbol{q}(t)\} \tag{3.28}$$

where $\{\boldsymbol{\varepsilon}(x, y, z, t)\}$ is a column matrix in which elements of the strain tensor are listed and $[\boldsymbol{B}(x, y, z)]$ is a matrix containing appropriate derivatives of the shape functions. $[\boldsymbol{B}(x, y, z)]$ has the same number of rows as that of components in strain vector and the same number of columns as that of the element's degrees of freedom.

If the element is free from initial stresses and strains and the behavior of the material are linear, the stresses are obtained from the strains as

$$\{\boldsymbol{\sigma}(x,y,z,t)\} = [\boldsymbol{E}]\{\boldsymbol{\varepsilon}(x,y,z,t)\} = [\boldsymbol{E}(x,y,z)][\boldsymbol{B}(x,y,z)]\{\boldsymbol{q}(t)\} \tag{3.29}$$

where $[\boldsymbol{E}]$ is the stiffness matrix of material. It is a symmetric square matrix, and theoretically its elements can be functions of the space coordinates but they are usually constant within the element. Potential energy of the element can be expressed as

$$\tilde{U} = \frac{1}{2}\int_V \{\boldsymbol{\varepsilon}\}^T\{\boldsymbol{\sigma}\}\mathrm{d}V = \frac{1}{2}\{\boldsymbol{q}\}^T\left(\int_V \{\boldsymbol{B}\}^T[\boldsymbol{E}]\{\boldsymbol{B}\}\mathrm{d}V\right)\{\boldsymbol{q}\}. \tag{3.30}$$

The integral in Eq. (3.30) is the stiffness matrix of the element, i.e.,

$$[\boldsymbol{K}] = \int_V \{\boldsymbol{B}\}^T[\boldsymbol{E}]\{\boldsymbol{B}\}\mathrm{d}V. \tag{3.31}$$

Because shape functions are not affected by time, the generalized velocities can be expressed as

$$\{\dot{\boldsymbol{u}}(x,y,z,t)\} = [\boldsymbol{N}(x,y,z)]\{\dot{\boldsymbol{q}}(t)\}. \tag{3.32}$$

In the case where all generalized coordinates are related to displacements, kinetic energy and mass matrix of the element have the form as

$$\tilde{T} = \frac{1}{2}\int_V \rho\{\dot{\boldsymbol{u}}\}^T\{\dot{\boldsymbol{u}}\}\mathrm{d}V = \frac{1}{2}\{\dot{\boldsymbol{q}}\}^T\left(\int_V \rho[\boldsymbol{N}]^T[\boldsymbol{N}]\mathrm{d}V\right)\{\dot{\boldsymbol{q}}\} \tag{3.33}$$

and $[\boldsymbol{M}] = \int_V \rho[\boldsymbol{N}]^T[\boldsymbol{N}]\mathrm{d}V$.

If a force distribution $\{\boldsymbol{f}(x, y, z, t)\}$ acts on the body, the virtual work is linked with the virtual displacement by

$$\{\delta\boldsymbol{u}(x,y,z,t)\} = [\boldsymbol{N}(x,y,z)]\{\delta\boldsymbol{q}(t)\}$$

and the nodal force vector can be expressed in the form:

$$\delta\tilde{L} = \int_V \{\delta\boldsymbol{u}\}^T\{\boldsymbol{f}(x,y,z,t)\}\mathrm{d}V = \int_V \{\delta\boldsymbol{q}\}^T[\boldsymbol{N}]^T\{\boldsymbol{f}(x,y,z,t)\}\mathrm{d}V$$

$$\{\boldsymbol{f}(x,y,z,t)\} = \int_V [\boldsymbol{N}]^T\{\boldsymbol{f}(x,y,z,t)\}\mathrm{d}V \tag{3.34}$$

The equation of motion of the element is then the usual one for discrete undamped systems:

$$[\boldsymbol{M}]\{\ddot{\boldsymbol{q}}\} + [\boldsymbol{K}]\{\boldsymbol{q}\} = \{\boldsymbol{f}(x,y,z,t)\}. \tag{3.35}$$

3.2.3.3 Assembling the Structure

The element equations of motion are written with reference to a local or element reference frame. To describe behavior of the structure as a whole, one should define the global or structural reference frame.

With reference to orientation of the global frame, the orientation of any local frame in space can be expressed by a suitable rotation matrix, i.e.,

$$[\boldsymbol{R}] = \begin{bmatrix} l_x & m_x & n_x \\ l_y & m_y & n_y \\ l_z & m_z & n_z \end{bmatrix} \tag{3.36}$$

where l_i, m_i and n_i are direction cosines of the axes of the former in global frame. $\{\boldsymbol{q}_{il}\}$ and $\{\boldsymbol{q}_i g\}$ of displacement vector $\{\boldsymbol{q}_i\}$ of the ith node in local and global reference frames are linked by common coordinate transformation:

$$\{\boldsymbol{q}_{il}\} = [\boldsymbol{R}]\{\boldsymbol{q}_{ig}\}. \tag{3.37}$$

The generalized coordinates in the displacement vector of the element can be transformed from a local reference frame to a global one wherein an expanded

rotation matrix $[\boldsymbol{R}]$ is used to deal with all the relevant generalized coordinates. It is essentially made up by some matrices of the type as in Eq. (3.36) suitably assembled together to form $[\boldsymbol{R}']$, the assembled rotating matrix.

The force vectors also can be rotated if multiplied with $[\boldsymbol{R}]$, and the element equation of motion can thus be written with reference to the global frame and pre-multiplied by the inverse of matrix $[\boldsymbol{R}']$:

$$[\boldsymbol{R}']^{-1}[\boldsymbol{M}][\boldsymbol{R}']\{\ddot{\boldsymbol{q}}_g\} + [\boldsymbol{R}']^{-1}[\boldsymbol{K}][\boldsymbol{R}']\{\boldsymbol{q}_g\} = \{\boldsymbol{f}_g\}. \tag{3.38}$$

Given that the inverse of a rotation matrix is coincident with its transpose, expressions of mass and stiffness matrices of the element rotated from local to global frame are

$$[\boldsymbol{M}_g] = [\boldsymbol{R}']^T[\boldsymbol{M}][\boldsymbol{R}'] \tag{3.39}$$

and

$$[\boldsymbol{K}_g] = [\boldsymbol{R}']^T[\boldsymbol{K}][\boldsymbol{R}']. \tag{3.40}$$

Likewise, the nodal load vector can be rotated according to the obvious relationship:

$$\{\boldsymbol{f}_g\} = [\boldsymbol{R}']^T\{\boldsymbol{f}_l\}. \tag{3.41}$$

Once the mass and the stiffness matrices of the various elements are computed with reference to the global frame, matrices of the whole structure may be found. The n generalized coordinates of structure can be ordered in a single vector $\{\boldsymbol{q}_g\}$.

Matrices of the various elements can be rewritten in matrices of order $n \times n$, containing all elements equal to zero except those in rows and columns corresponding to generalized coordinates of the relevant element.

Because kinetic and potential energies of the structure can be obtained simply by adding energies of the various elements, one has

$$\begin{aligned} \tilde{T} &= \frac{1}{2}\sum_{\forall_i} \{\dot{\boldsymbol{q}}_g\}^T[\boldsymbol{M}_i]\{\dot{\boldsymbol{q}}_g\} = \frac{1}{2}\{\dot{\boldsymbol{q}}_g\}^T[\boldsymbol{M}]\{\dot{\boldsymbol{q}}_g\} \\ \tilde{U} &= \frac{1}{2}\sum_{\forall_i} \{\boldsymbol{q}_g\}^T[\boldsymbol{K}_i]\{\boldsymbol{q}_g\} = \frac{1}{2}\{\boldsymbol{q}_g\}^T[\boldsymbol{K}]\{\boldsymbol{q}_g\} \end{aligned}. \tag{3.42}$$

Matrices $[\boldsymbol{M}]$ and $[\boldsymbol{K}]$ are mass and stiffness matrices of the whole structure including all the mass and stiffness matrices of the elements. In practice, matrices of all elements with size $n \times n$ are just added into the global mass and stiffness matrices in the correct place.

In a similar way the nodal force vector can be easily assembled:

$$\{\boldsymbol{f}\} = \sum_{\forall_i} \{\boldsymbol{f}_i\}. \tag{3.43}$$

3.2.3.4 Constraining the Structure

One of the advantages in the FEM is easy definition of constraints. If the ith degree of freedom is rigidly constrained, the corresponding generalized displacement vanishes and, as a consequence, the ith column of stiffness and mass matrices can be neglected.

To avoid restructuring the whole model and all the matrices, rigid constraints can be transformed into very stiff elastic constraints. If the ith degree of freedom is constrained through a linear spring with stiffness k_i, potential energy of the structure corresponds to potential energy of the spring:

$$\tilde{U} = \frac{1}{2} k_i q_i^2. \tag{3.44}$$

It is sufficient to add the stiffness k_i to the element in the ith row and ith column of the global stiffness matrix, considering the constraint. In fact, an elastic constraint with rather high stiffness is added instead of canceling a degree of freedom in the case of rigid constraints, thanks to its simplicity. An additional advantage is that the constraint reaction can be obtained simply through multiplying the large generalized stiffness k_i by the small generalized displacement q_i.

3.3 Solution for Fluid–Structure Interaction

Fluid structure interaction (FSI) occurs when a fluid interacts with a solid structure, exerting pressure that may cause deformation to the structure and alter the fluid flow itself (see Tezduyar et al. 2006).

3.3.1 Governing Equations

Governing equations of the FSI solution include the equations both on fluid mechanics and structure mechanics (see Wall et al. 2006).

3.3.1.1 Fluid Mechanics

Let $\Omega_t \subset IR^{nsd}$ be the spatial domain with boundary Γ_t at time $t \in (0,\ T)$. The subscript t indicates time-dependence of the domain. The Navier–Stokes equations of incompressible flows are written on Ω_t and $\forall_t \in (0,\ bT)$ as

$$\rho\left(\frac{\partial\{\boldsymbol{v}\}}{\partial t} + \{\boldsymbol{v}\}\cdot\nabla\{\boldsymbol{v}\} - \{\boldsymbol{f}\}\right) - \nabla\cdot[\boldsymbol{\sigma}] = 0 \tag{3.45}$$

$$\nabla \cdot \{\boldsymbol{v}\} = 0 \tag{3.46}$$

where ρ, $\{\boldsymbol{v}\}$ and $\{\boldsymbol{f}\}$ are the density, velocity and the external force, respectively. The stress tensor σ is defined as

$$[\boldsymbol{\sigma}(p, \boldsymbol{v})] = -p[\boldsymbol{I}] + 2\mu[\boldsymbol{\varepsilon}(\boldsymbol{v})],$$

with $[\boldsymbol{\varepsilon}(\boldsymbol{v})] = \left[(\nabla\{\boldsymbol{v}\}) + (\nabla\{\boldsymbol{v}\})^T\right]/2$.

Here p is the pressure, $[\boldsymbol{I}]$ is the identity tensor, $\mu = \rho\, v$ is the viscosity, μ is the dynamic viscosity, and $[\boldsymbol{\varepsilon}(\boldsymbol{v})]$ is the strain-rate tensor. The essential and natural boundary conditions for Eq. (3.45) are represented as $\{\boldsymbol{v}\} = \{\boldsymbol{g}\}$ on $(\Gamma_t)_{\mathrm{g}}$ and $\{\boldsymbol{n}\}$ $[\boldsymbol{\sigma}] = \{\boldsymbol{h}\}$ on $(\Gamma_t)_{\mathrm{h}}$, where $(\Gamma_t)_{\mathrm{g}}$ and $(\Gamma_t)_h$ are complementary subsets of boundary Γ_t, $\{\boldsymbol{n}\}$ is the unit normal vector, and $\{\boldsymbol{g}\}$ and $\{\boldsymbol{h}\}$ are given functions. A divergence-free velocity field $\{\boldsymbol{v}_0(\boldsymbol{x})\}$ is specified as the initial condition.

3.3.1.2 Structural Mechanics

Let $\Omega_{st} \subset IR^{nxd}$ be spatial domain with boundary Γ_t^s, where $n^{xd} = 2$ for membranes and $n^{xd} = 1$ for cables. Parts of Γ_t^s corresponding to the essential and natural boundary conditions are represented by $(\Gamma_t^s)g$ and $(\Gamma_t^s)_h$. The superscript "s" indicates the structure. The equations of motion are written as

$$\rho^S\left(\{\ddot{\boldsymbol{u}}\} + \eta\{\dot{\boldsymbol{u}}\} - \left\{\boldsymbol{f}^S\right\}\right) - \nabla \cdot \left[\boldsymbol{\sigma}^S\right] = 0 \tag{3.47}$$

where ρ^s, $\{\boldsymbol{u}\}$, $\{\boldsymbol{f}^S\}$ and $[\boldsymbol{\sigma}^S]$ are the material density, structural displacement, external force, and the Cauchy stress tensor respectively. Here η is the mass-proportional damping coefficient. The damping provides additional stability and can be used where time-accuracy is not required, such as in determining deformed shape of the structure for specified fluid mechanics forces imposed on it. The stresses are expressed in terms of the second Piola–Kirchoff stress tensor $[\boldsymbol{S}]$, which is related to the Cauchy stress tensor through a kinematic transformation. With the assumption of large displacements and rotations, small strains, and no material damping, the membranes and cables are treated as Hookean materials with linear elastic properties. Membranes are viewed with plane stress, and $[\boldsymbol{S}]$ becomes

$$S^{ij} = \left[\bar{\lambda}_m + G^{ij}G^{kl} + \mu_m\left(G^{il}G^{jk} + G^{ik}G^{jl}\right)\right]E_{kl} \tag{3.48}$$

for the case of isotropic plane stress. Here E_{kl} are components of the Cauchy–Green strain tensor, G^{ij} are components of the contravariant metric tensor in original configuration, and λ_m and μ_m are Lam'e constants. For cables, on the assumption of uniaxial tension, $[\boldsymbol{S}]$ becomes $S^{11} = E_c G^{11} G^{11} E_{11}$, where E_c is Young's modulus for the cable. To account for stiffness-proportional material damping, Hookean stress–strain relationships defined by Eq. (3.48) and its version for cables are modified, and E_{kl} is replaced by $\hat{E}_{kl}$, where $\hat{E}_{kl} = E_{kl} + \zeta\dot{E}_{kl}$. Here ζ is the stiffness-proportional damping coefficient and $\dot{E}_{kl}$ is the time derivative of E_{kl}.

3.3.2 Fluid–Solid Coupling Mechanism

Fluid–Structure Interaction occurs in a physics simulation when the flow invokes deformation of a solid structure. This deformation of a solid structure, in turn, changes the boundary condition of the fluid problem. The coupled fluid–solid problems, characterized by interaction of fluid forces and structural deformations are commonly seen in many industrial and scientific applications. Hence, algorithmic realization of the coupling mechanisms is crucial in numerical simulation of such problems (Löhner et al. 2006; Schäfer et al. 2006).

3.3.2.1 Coupling Schemes

Two approaches for coupling between Computational Soil Dynamics (CSD) and Computational Fluid Dynamics (CFD) have been pursued: strong (or tight) coupling and loose (or weak) coupling.

1. The strong coupling

The strong coupling technique solves discrete systems of coupled, nonlinear equations resulting from the CFD, CSD and interface conditions in a single step. In an extreme example of tight coupling approach, even discretization on the surfaces was set to be the same. At each time step, the resulting matrix system is of the form (see Löhner et al. 2006):

$$\begin{bmatrix} \boldsymbol{K}_{ss} & \boldsymbol{K}_{sf} \\ \boldsymbol{K}_{fs} & \boldsymbol{K}_{ff} \end{bmatrix} \begin{Bmatrix} \Delta \boldsymbol{u}_s \\ \Delta \boldsymbol{u}_f \end{Bmatrix} = \begin{Bmatrix} \boldsymbol{r}_s \\ \boldsymbol{r}_f \end{Bmatrix} \tag{3.49}$$

where the subscripts *s, f* stand for structure and fluid fields, $\{\boldsymbol{u}\}$ are the unknown vectors, $\{\boldsymbol{r}\}$ the right-hand sides (vectors of sum of internal and external forces/fluxes). Diagonal sub-matrices are usually obtained for each sub-discipline, whereas the off-diagonal sub-matrices represent the coupling between disciplines. The predictor–corrector scheme is also known as a Jacobi iteration. If one considers the linearized implicit scheme for a complete fluid–structure system, a Jacobi iteration can be written as

$$[\boldsymbol{K}_{ss}]\{\Delta \boldsymbol{u}_s^i\} = \{\boldsymbol{r}_s\} - [\boldsymbol{K}_{sf}]\left\{\Delta \boldsymbol{u}_f^{i-1}\right\} \tag{3.50a}$$

$$[\boldsymbol{K}_{ff}]\left\{\Delta \boldsymbol{u}_f^i\right\} = \{\boldsymbol{r}_f\} - [\boldsymbol{K}_{fs}]\{\Delta \boldsymbol{u}_s^{i-1}\}. \tag{3.50b}$$

The steps taken in each iteration may also be summarized as follows:

Obtain loads from fluid and apply to structure $[K_{sf}]\{\Delta \boldsymbol{u}_s^{i-1}\}$;
Obtain new displacements $\{\Delta \boldsymbol{u}_s^i\}$;
Obtain mesh velocities for fluid boundary from the structure

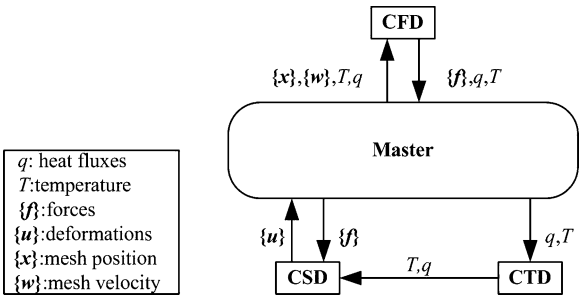

Fig. 3.2 Loose coupling for fluid/structure simulations (Löhner et al. 2006)

$[K_{fs}]\{\Delta \boldsymbol{u}_s^{i\,-\,1}\}$;
Obtain new flow variables $\{\Delta \boldsymbol{u}_s^i\}$.

The illustration is only precise for explicit time stepping schemes since the mesh motion of the flow solver and the displacement field of the structure are linked beyond the nearest neighbors in $[K_{sf}]$, $[K_{fs}]$.

2. The loose coupling

The loose coupling technique solves the complete FSI system with an iterative strategy of repeated a "CFD solution followed by a CSD solution" until convergence is achieved (see Fig. 3.2). In this case, coupling matrices in Eqs. (3.50a and 3.50b) contain only the direct load and displacement transfer terms (Löhner et al. 2006).

3. Combination scheme of weak and strong couplings

An implicit partitioned solution approach tries to combine the advantages of weakly and strongly coupled schemes in a complementary way (Schäfer et al. 2006).

A schematic view of the iteration process in the implicit partitioned approach is shown in Fig. 3.3, which is performed for each time step. After initializations the flow field is determined in actual flow geometry, friction and pressure forces on the interacting walls are computed. The under the action of the forces, the structural solver calculates the deformations with which fluid mesh is modified before the flow solver is started again. For mesh deformation, algebraic and elliptic approaches are employed.

3.3.2.2 Coupling of Implicit Time-Marching codes

The loose coupling of explicit CFD and CSD codes are used extensively. For some problems, explicit time-marching is required to capture all the transient phenomena. On the other hand, if the relevant physical phenomena are not linked to the system's highest eigenmodes, explicit time-marching can be a prohibitively expensive proposition. For problems such as a method including low frequency

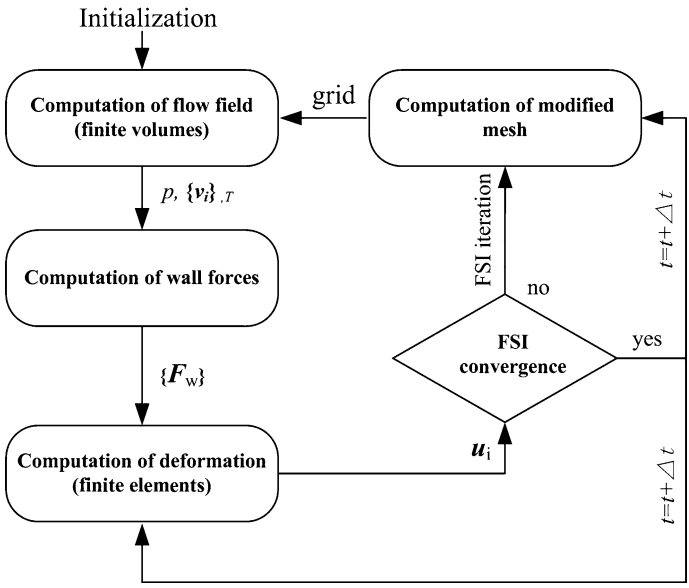

Fig. 3.3 Flow chart of coupled solution procedure (Schäfer et al. 2006)

aeroelasticity, and subsonic parachute unfolding, implicit time-marching is required. The question falls onto whether the loose coupling approach can be extended to solve multidisciplinary problems with codes that employ implicit time-marching schemes (see Löhner et al. 2006).

1. An under-relaxed predictor–corrector scheme.

An under-relaxed predictor–corrector scheme could offer a good compromise between simplicity and stability. By denoting i the iteration step, α the under-relaxation factor, $\{\boldsymbol{x}_s\}$ the position of the surface of the structure wetted by the fluid, $\{\boldsymbol{\sigma}_f\}$ the stresses exerted by the fluid on the structure, $\{\boldsymbol{f}(\boldsymbol{\sigma}_f)\}$ the surface deformation due to fluid loads, and $\{\boldsymbol{g}(\boldsymbol{x}_s)\}$ the change of fluid stresses due to surface deformation, the predictor–corrector scheme for each time step takes the following form.

If not converged, update the structure with fluid load:

$$\{\boldsymbol{x}_s^i\} = (1-\alpha)\{\boldsymbol{x}_s^{i-1}\} + \alpha\left\{\boldsymbol{f}\left(\boldsymbol{\sigma}_f^i\right)\right\}.$$

And to update the fluid with structure position/velocity:

$$\left\{\boldsymbol{\sigma}_f^i\right\} = (1-\alpha)\left\{\boldsymbol{\sigma}_f^{i-1}\right\} + \alpha\left\{\boldsymbol{g}\left(\boldsymbol{x}_s^i\right)\right\}.$$

Typical under-relaxation factors are in the range of $0.5 \leq \alpha \leq 0.9$.

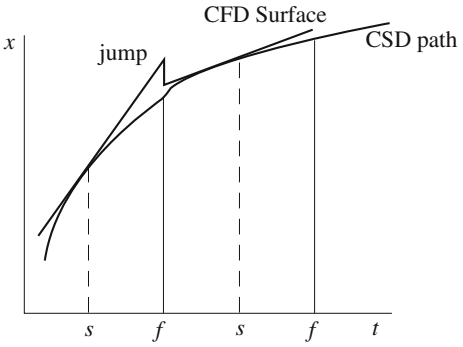

Fig. 3.4 Loose coupling: surface matching (Löhner et al. 2006)

2. Calculation of displacements.

A loose coupling between CFD and CSD codes implies that ending times of respective codes can be different.

The fluid surface (boundary) is imposed by a CSD surface, which is moving according to fluid forces. If time of CFD code t_f at the end of a time step lies beyond time of CSD code t_s, the CSD surface is extrapolated. This can be done in a variety of ways but the assumed position of the CSD surface and the one calculated by CSD code in the next time step will not coincide.

As a result, correction will be required at the beginning of the next CFD time step. An exaggerated situation is sketched in Fig. 3.4. Notice that the jump exists in surface positions at the beginning of the next CFD time step. An alternative is to ignore the new surface velocities at the end of one CSD time step, and to compute velocities directly from positions.

Surface velocity of a CFD domain is then continued from the previous position in such a way that the CSD surface seen by CFD code is in coincidence with the CSD surface position by CSD code at $t = t_s$.

Though simple as it is, the method is unstable if the ending time of fluid is larger than that of the structure by half the time step taken. This behavior is shown in Fig. 3.5. For optimal stability, the ending time of fluid should be limited within a small scope beyond the ending time of the structure, i.e.,

$$t_{\mathrm{s}} = t_f + \varepsilon.$$

3.4 Large Deformation Fluid–Structure Interaction

When the effects of fluid-structure interaction are essential, it comes along with large structural deformations. So it is of great relevance of being able to adequately deal with this case.

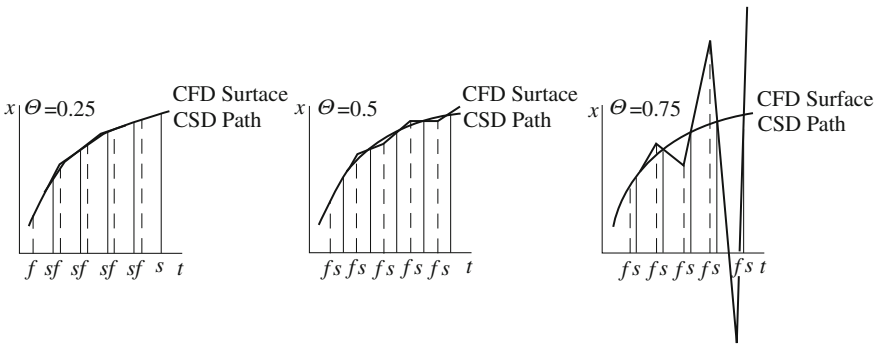

Fig. 3.5 Loose coupling: Mesh velocity instability (Löhner et al. 2006)

3.4.1 General Fluid Structure Interaction Problem

A general fluid structure interaction problem consists of a description of the fluid and solid fields, appropriate fluid structure conditions at the conjoined interface, and conditions for the remaining boundaries. Here, discussion is confined to incompressible flows, which is a reasonable choice for many engineering applications.

In the following sections, fields and interface conditions are introduced. Furthermore, a brief sketch of the solution procedure for each field is presented (Wallh et al. 2006).

3.4.1.1 Fluid

Without consideration of a specific reference system, the conservation of momentum is stated as

$$\rho^{\mathrm{f}} \frac{\mathrm{D}\{\boldsymbol{v}\}}{\mathrm{D}t} - \nabla \cdot [\boldsymbol{\sigma}] = \rho^{\mathrm{f}} \{\boldsymbol{b}\}. \tag{3.51}$$

Here, the material time derivative of the velocity vector $\{\boldsymbol{v}\}$ multiplied by the fluid density ρ^{f} is balanced by the gradient of the Cauchy stress tensor $[\boldsymbol{\sigma}]$ and the external, velocity independent volumetric forces $\{\boldsymbol{b}\}$. Mass conservation for an incompressible fluid is stated as

$$\nabla \cdot \{\boldsymbol{v}\} = 0. \tag{3.52}$$

The Newtonian material law defines internal stress tensor $[\boldsymbol{\sigma}]$ as

$$[\boldsymbol{\sigma}] = -p[\boldsymbol{I}] + 2\mu[\boldsymbol{\varepsilon}(\{\boldsymbol{v}\})] \tag{3.53}$$

with strain rate tensor $[\boldsymbol{\varepsilon}]$ as

$$[\boldsymbol{\varepsilon}(\boldsymbol{v})] = \nabla\{\boldsymbol{v}\} + (\nabla\{\boldsymbol{v}\})^T \tag{3.54}$$

where p is the pressure and μ dynamic viscosity.

A material time derivative depends on the choice of the reference system. There are basically three alternative reference systems: the Eulerian, the Lagrangian and the Arbitrary Lagrangian–Eulerian formulation. Traditionally, for flows without moving boundaries, the Eulerian system is used where the momentum equation reads as

$$\frac{\partial\{\boldsymbol{v}\}}{\partial t} - \nabla\cdot(\{\boldsymbol{v}\}\otimes\{\boldsymbol{v}\}) + \nabla p - 2\frac{\mu}{\rho}\nabla\cdot[\boldsymbol{\varepsilon}] = \{\boldsymbol{b}\} \text{ in } \Omega^{\mathrm{f}}\times(0,T). \tag{3.55}$$

Fluid structure interaction problems require consideration of moving boundaries for fluid domain. The most commonly used description, namely the ALE description, will be discussed in Sect. 3.4.3.

If the moving boundary is described on a fixed grid, the Eulerian description from Eq. (3.55) can be used, albeit additional effort goes to depicting the interface on the fixed grid. Finally, even Lagrangian flow descriptions are applied, e.g. to depict the flow of fluid particles, which allows one to track the interface in a simple way.

3.4.1.2 Structure

The structure is described with a Lagrangian description where the material derivative becomes a partial derivative with respect to time, i.e.,

$$\rho^{\mathrm{s}}\frac{\partial^2\{\boldsymbol{u}\}}{\partial t^2} = \nabla\cdot[\boldsymbol{\sigma}] + \rho^{\mathrm{s}}\{\boldsymbol{f}\} \tag{3.56}$$

with displacement $\{\boldsymbol{u}\}$ defined as the difference of the current position $\{\boldsymbol{x}\}$ and initial position $\{\boldsymbol{X}\}$.

In a large deformation case, the constitutive equation is commonly described according to the stress-strain relation based on the Green-Lagrangian strain tensor $[\boldsymbol{E}]$ and the two Piola-Kirchhoff stress tensor $[\boldsymbol{S}(\boldsymbol{E})]$ as a function of $[\boldsymbol{E}]$. The two Piola-Kirchhoff stressors can be obtained from the Cauchy stress $[\boldsymbol{\sigma}]$ as

$$[\boldsymbol{S}] = J[\boldsymbol{F}]^{-1}[\boldsymbol{\sigma}][\boldsymbol{F}]^{-T} \tag{3.57}$$

and the Green-Lagrangian strain tensor $[\boldsymbol{E}]$ as

$$[\boldsymbol{E}] = \frac{1}{2}\left([\boldsymbol{F}]^T[\boldsymbol{F}] - [\boldsymbol{I}]\right). \tag{3.58}$$

J denotes the determinant of the deformation gradient tensor $[\boldsymbol{F}]$, which itself is defined as

$$[\boldsymbol{F}] = \frac{\partial\{\boldsymbol{x}\}}{\partial\{\boldsymbol{X}\}}. \tag{3.59}$$

Different structural models, mainly 3D shells and solid-shell models are engaged along with sophisticated element technology.

3.4.1.3 Interface Conditions

The main conditions at the interface are dynamic- and kinematic coupling conditions. The force equilibrium requires

$$\left[\boldsymbol{\sigma}^{\mathrm{f}}\right] \cdot \{\boldsymbol{n}\} = \left[\boldsymbol{\sigma}^{S}\right] \cdot \{\boldsymbol{n}\} \, \forall(\{\boldsymbol{x}\}) \in \Gamma^{\mathrm{fsi}}. \tag{3.60}$$

For abbreviation, fluid surface forces at the interface are also referred to as $\{\boldsymbol{h}_{\Gamma}^{f}\} = \{\boldsymbol{\sigma}^{f}\} \cdot \{\boldsymbol{n}\}$. When viscous fluids are considered, 'no slip' boundary conditions have to be fulfilled, i.e.,

$$\{\boldsymbol{v}\} = \frac{\partial\{\boldsymbol{u}\}}{\partial t} \, \forall(\{\boldsymbol{x}\}) \in \Gamma^{\mathrm{fsi}}. \tag{3.61}$$

3.4.1.4 Partitioned Analysis

In general, one can describe the whole coupled system in a monolithic way and solve all fields together, or separate the fields and couple them in a partitioned analysis.

In the latter case either sequential (staggered) or iterative algorithms can be applied. The monolithic approach is straight forward and enables solving the resulting system of equations with a complete tangent stiffness matrix (if—in an ALE setting—fluid, structure and mesh degrees of freedom are included). Nevertheless, it does have several drawbacks such as loss of software modularity, limitations with respect to the application of different sophisticated solvers in different fields, and challenges with respect to problem size and conditioning of the overall system matrix. Consequently they are generally considered ill-suited for practical applications where not only specific solution approaches but also specific codes should be used in the single fields.

3.4.2 Coupling of Partitioned Fields

The algorithmic implementation of a coupled problem of fluid-structure interaction is based on a field-wise partitioned solution approach. This modular software concept allows for complex and specifically designed approaches for single fields of the structure, the fluid and, for the ALE approach, and the mesh.

A wet structural surface is the natural interface of a coupling surface Γ^{fsi}. For brevity, Γ^{fsi} will be simply termed as Γ. Complete kinematic and dynamic continuity at Γ would ensure conservation of mass, momentum, and energy at the interface. The forces generated from fluid pressure and viscous friction are exerted on structural interface as Neumann boundary conditions.

Structural displacement at Γ is transferred into velocities and used as a Dirichlet condition for fluid field to update the mesh position in the ALE approach. The fluid mesh velocity u_g is used to describe the fluid mesh movement, which will be discussed in next section.

The following developments are made via a partitioned ALE approach for FSI. However, since fundamental properties of the partitioned approach are independent of fluid or structural discretization and interface description, the results also serve as a foundation for partitioned fixed-grid schemes and can directly be applied in this case too.

3.4.3 ALE Based Formulation for Fluid Structure Interaction

ALE-based methods are frequently used for issues with moving surfaces (see Wall et al. 2006). The following discussion is important when dealing with large deformations of fluid boundary.

3.4.3.1 ALE and Geometric Conservation Revisited

The ALE equation of motion can be derived from a Eulerian formulation of the balance of linear momentum in Eq. (3.55) through the introduction of a deforming reference system $\{\boldsymbol{\chi}\}$ that follows the respective boundaries of motion and deforms, e.g. according to a mesh smoothing, in the remaining domain.

The reference system deformation is described with the unique mapping $\{\boldsymbol{x}\} = \{\boldsymbol{\varphi}(\{\boldsymbol{\chi}\}, t)\}$ depicted in Fig. 3.6. According to Reynolds transport theorem, Eq. (3.55) can be reformulated on moving grids as

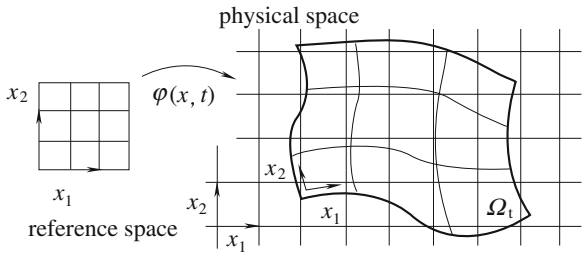

Fig. 3.6 Sketch of ALE system of reference

$$\left.\frac{\partial(\{\boldsymbol{v}\}J_t)}{\partial t}\right|_{\boldsymbol{\chi}} + \left\{\nabla\cdot(\{\boldsymbol{v}\}\otimes(\{\boldsymbol{v}\}-\{\boldsymbol{v}^g\})) - 2\frac{\mu}{\rho^f}\nabla\cdot[\boldsymbol{\varepsilon}(\{\boldsymbol{v}\})] + \nabla p\right\}J_t = \{\boldsymbol{b}\}J_t \tag{3.62}$$

where $J_t = \det(\partial\{\boldsymbol{x}\}/\partial\{\boldsymbol{\chi}\})$ designates the time-dependent Jacobian of the mapping, and $\{\boldsymbol{v}\mathrm{g}\} = \partial\{\boldsymbol{x}\}/\partial t|_{\boldsymbol{\chi}}$ represents velocity of the reference system to be identified with grid velocity after discretization. Together with Eqs. (3.55), (3.62) is in a divergent form and thus the point of departure for a finite volume discretization in space. However, in the weak form the first term in Eq. (3.62) yields an integral over a temporally changing domain and if improperly represented in a discrete scheme, stability problems may emerge.

Geometric conservation demands a correct expression of mass term in a deforming domain, that is, a temporally and spatially constant solution should be represented with the discrete scheme.

Thus geometric conservation in conjunction with a discretized Eq. (3.62) result in the need for temporal averaging of either geometries or fluxes within a time step. Variation of the temporal discretization scheme would lead to different versions of the geometric conservation law, i.e., Discrete Geometric Conservation Laws (DGCL), and thus averaging schemes to be employed. In a strong form the geometric conservation equation is given by

$$\frac{\partial J_t}{\partial t} = J_t\nabla\cdot\{\boldsymbol{v}^g\} \tag{3.63}$$

which bridges temporal change of the domain and the domain velocity. Equation (3.63) can be incorporated into Eq. (3.62):

$$\left.\frac{\partial\{\boldsymbol{v}\}}{\partial t}\right|_{\boldsymbol{\chi}} + (\{\boldsymbol{v}\}-\{\boldsymbol{v}^g\})\cdot\nabla\{\boldsymbol{v}\} - 2\frac{\mu}{\rho^f}\nabla\cdot[\boldsymbol{\varepsilon}(\{\boldsymbol{v}\})] + \nabla p = \{\boldsymbol{b}\} \tag{3.64}$$

yielding an ALE form of the momentum balance that eliminates integrals over temporally deforming domains.

Discretization of Eq. (3.64) in time and space is straightforward, while stability and accuracy properties of the discretization scheme can be directly transferred to deforming domain formulation.

3.4.3.2 Distorted Meshes

Severe deformations of the moving fluid mesh are originated from large deformations. Consequently, ALE methods are in need of formulations that yield reliable results on significantly distorted meshes to solve the above problem. Additionally, boundary adapted fluid meshes may result in highly stretched elements or complicated geometries, and it needs unfavorably shaped elements to be adequately represented. In the context of fluid structure interaction, accurate coupling information, even on distorted meshes, is of particular interest.

Numerical investigations show that stabilized ALE formulation can be designed so that the scheme is reliable and insensitive to mesh distortion.

3.4.3.3 ALE Mesh Motion Schemes

Even though ALE schemes are developed to reduce element distortion caused by pure Lagrangian formulations, a certain portion of distortion is unavoidable. Hence, the mesh motion scheme is a key issue for robust simulations of general complex systems.

A number of mesh motion techniques have been developed in an effort to equally distribute elemental distortion for the best remaining element quality. Most of these schemes are more or less based on a pseudo structural approach, given as

$$[\boldsymbol{K}^{\mathrm{g}}]\{\boldsymbol{r}\} = \{\boldsymbol{F}\} \tag{3.65}$$

where the 'mesh stiffness' matrix $[\boldsymbol{K}^{\mathrm{g}}]$ is designed for modes which could create element failure to be stiffened compared with other distortion modes. Nevertheless, the best mesh moving algorithm, to some extent, cannot avoid an unacceptable fluid mesh deformation and a partial or complete re-meshing of the fluid domain becomes necessary. Such scenarios include problems with topology changes, e.g. when a fluid penetrates an opening crack or when a valve closes, or simply when the structure moves too far in the domain or rotates. An interpolation between the old and new mesh in re-meshing always brings about errors, therefore a fixed-grid method might be an attractive alternative on condition that frequent re-meshing is needed.

References

Funnell, R. (2008). Finite element method. http://audilab.bmed.mcgill.ca/AudiLab/teach/fem/fem001.html.

Genta, G. (2009). *Vibration dynamics and control* (pp. 341–361, 363–400). Berlin: Springer.

Grandin, H. (1986). *Fundamentals of the finite element method*. New York: Macmillan.

Löhner, R., Cebral, G.R., & Yang, C. (2006). Extending the range and applicability of the loose coupling approach for FSI simulations. *Fluid-structure interaction, modeling, simulation, optimization* (pp. 82–100). Berlin: Springer.

Reddy, J. N. (2002). *Energy principles and variational methods in applied mechanics*. 2nd ed., New York: John Wiley.

Rodney, J. B. (1982). *Exactly solved models in statistical mechanics*. London: Academic Press.

Schäfer, M., Heck, M., & Yigit, S. (2006). An implicit partitioned method for the numerical simulation of fluid-structure interaction. *Fluid-structure interaction, modeling, simulation, optimization* (pp. 171–194). Berlin: Springer.

Scholz, W. (2003). Scalable parallel micromagnetic solvers for magnetic nanostructures. *Doctor dissertation,* Technical University of Vienna. http://www.cwscholz.net/projects/diss/html/node9.html.

Tezduyar, T.E., Sathe, S., Stein, K., & Aureli, L. (2006). Modeling of fluid-structure interactions with the space-time techniques. *Fluid-structure interaction, modeling, simulation, optimization* (pp. 50–81). Berlin: Springer.

Wall, W.A., Gerstenberger, A., & Gamnitzer, P. (2006). Large deformation fluid-structure interaction—Advances in ALE methods and new fixed grid approaches. *Fluid-structure interaction, modeling, simulation, optimization* (pp. 195–233). Berlin: Springer.

Wikipedia. (2008a). http://en.wikipedia.org/wiki/Finite_element_method.

Wikipedia. (2008b). http://en.wikipedia.org/wiki/Virtual_work.

Wikipedia. (2008c). http://en.wikipedia.org/wiki/Lumped_parameters.

Chapter 4
Elementary Concept of Rotordynamics

Rotordynamics is a branch of system dynamics dealing with mechanical devices in which at least one part, usually referred to as rotor, rotates with the angular momentum.

Rotors with bearings that constrain their rotating axis to a fixed position in space are usually referred to as fixed rotors whereas those without bearings are defined as free rotors. Spin speed in fixed rotors is usually considered as constant, whereas the speed of free rotors is governed by conservation of angular momentum. Parts of the machine that do not rotate are generally referred to as stators (Chen and Gunter 2005).

4.1 Jeffcott Rotor

The Jeffcott rotor (also known as the De Laval rotor in Europe) is a simplified lumped parameter model, consisting of a point mass located on a massless elastic and damped shaft. Several features of rotor vibration, such as the unbalance response, self-centering, and the roles of rotating and non-rotating damping can be studied based on this model (Childs 1993; Krämer 1993).

4.1.1 Introduction of Vibrations of Jeffcott Rotor

Features of Jeffcott rotor without viscous damping is explained in this section.

4.1.1.1 Rotordynamics with Constant Angular Velocity

Figure 4.1 shows a disc rotating at a constant angular velocity (spin speed), Ω, around the rotating disc axis. It is assumed that there is a simplified lumped mass at point P, with no gyroscope, no cross-coupling between x and y, as well as no damping.

Y. Wu et al., *Vibration of Hydraulic Machinery*,
Mechanisms and Machine Science 11, DOI: 10.1007/978-94-007-6422-4_4,

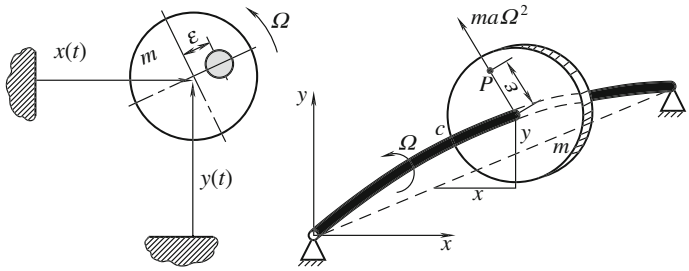

Fig. 4.1 External mass unbalance force, mass center different from rotating center

The system only has two degrees of freedom, that is, displacements along x and y ordinates. Equations of motion in x and y directions of point P with mass m and stiffness k is (see Bucher 2009)

$$\begin{cases} m\dfrac{\mathrm{d}^2x}{\mathrm{d}t^2} + kx = f_x(t) \\ m\dfrac{\mathrm{d}^2y}{\mathrm{d}t^2} + ky = f_y(t) \end{cases}. \tag{4.1}$$

All other forces except centrifugal force are neglected, Eq. (4.1) becomes

$$\begin{cases} \dfrac{\mathrm{d}^2}{\mathrm{d}t^2} m(x + \varepsilon\cos\Omega t) + kx = 0 \\ \dfrac{\mathrm{d}^2}{\mathrm{d}t^2} m(y + \varepsilon\sin\Omega t) + ky = 0 \end{cases} \tag{4.2}$$

where ε is eccentricity of P point. Rearranging Eq. (4.2) one gets

$$m\ddot{x} + kx = m\varepsilon\Omega^2\cos\Omega t \tag{4.3a}$$

$$m\ddot{y} + ky = m\varepsilon\Omega^2\sin\Omega t \tag{4.3b}$$

where $\ddot{x} = \frac{\mathrm{d}^2x}{\mathrm{d}t^2}$, and $\ddot{y} = \frac{\mathrm{d}^2y}{\mathrm{d}t^2}$.

In rotor dynamics it is sometimes convenient to use complex coordinates in the xy-plane. Define

$$z = x + \mathrm{i}y, \quad \mathrm{i} = \sqrt{-1}. \tag{4.4}$$

Add Eq. (4.3a) together with Eq. (4.3b) multiplied by i to Eq. (4.4), and one obtains

$$m\ddot{z} + kz = m\varepsilon\Omega^2\mathrm{e}^{\mathrm{i}\Omega t}. \tag{4.5}$$

4.1.1.2 Steady State Response of an Undamped Simple Rotor to Unbalance

A solution (a particular integral) for response of undamped simple rotor to the unbalance $m\varepsilon\Omega^2 e^{i\omega t}$ in Eq. (4.5) is assumed in the following form:

$$z(t) = z_0 \Omega^2 e^{i\Omega t}. \tag{4.6}$$

Substitute it into Eq. (4.5)

$$(-m\Omega^2 + k) z_0 e^{i\Omega t} = m\varepsilon\Omega^2 e^{i\Omega t}. \tag{4.7}$$

Relative amplitude of the steady-state response to unbalance $m\varepsilon\Omega^2 e^{i\Omega t}$ as a function of a rotating circular frequency, Ω and the unbalance are defined as

$$\frac{z_0}{\varepsilon} = \frac{m\Omega^2}{\left(-m\Omega^2 + k\right)}. \tag{4.8}$$

Define

$$\omega_n = \sqrt{k/m}. \tag{4.9}$$

Then one gets the expression of relative amplitude z_0/ε by Ω^2/ω_n^2 as follows:

$$\frac{z_0}{\varepsilon} = \frac{\Omega^2/\omega_n^2}{\left(1 - \Omega^2/\omega_n^2\right)} \tag{4.10}$$

where ω_n is actually the critical speed defined (see next section). The value of the amplitude z_0 is real and it rotates with velocity Ω in a xy-plane. The value of Ω, one that makes the denominator of the z_0 expression in Eq. (4.10) vanish, i.e., the amplitude reaches an infinite value, is coincident with the flexural critical speed of the rotor (see next section, Fig. 4.2a).

The amplitude of the point motion due to the presence of the unbalance response is indicated as a function of the speed in Fig. 4.2a. In subcritical range (Fig. 4.2b), the amplitude grows from zero to a value tending to infinity at critical speed (Fig. 4.2c), always remaining positive. In supercritical range (Fig. 4.2d), however, the value of the amplitude z_0 is negative, and its absolute value decreases monotonically with speed. As the speed tends to infinity, amplitude would approach $-\varepsilon$.

The solution sign determines the equilibrium configurations shown in Fig. 4.2b–c. In the supercritical field (Fig. 4.2d), when the speed tends to infinity, the amplitude z_0 tends to $-\varepsilon$. This phenomenon is usually referred to as self centering because the rotor rotates about its center of mass instead of its geometrical center.

When rotor behavior is controlled by its stiffness, rotation takes place about a point close to geometrical center. And when it is dominated by inertia it occurs about a point close to the mass center.

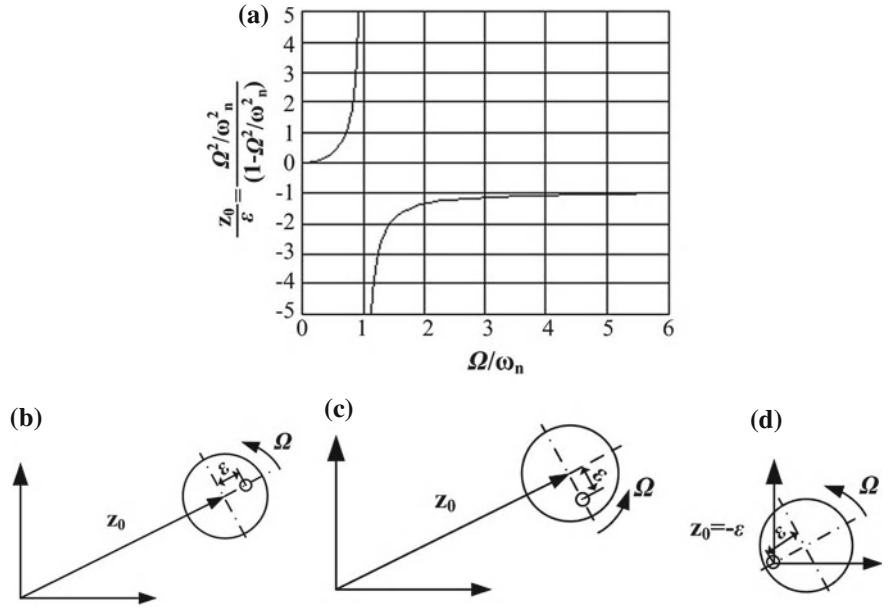

Fig. 4.2 Unbalance response of an undamped Jeffcott rotor. **a** Dimensionless amplitude variation with the dimensionless spin speed. **b** At the system in subcritical conditions $\Omega/\omega_n \ll 1$. **c** At the synchronous condition $\Omega/\omega_n = 1$. **d** At the system in supercritical conditions

The motion of point P can thus be expressed as superimposition of a free motion that can be circular, elliptical, or even rectilinear with frequency $\omega_n = \sqrt{k/m}$ and a circular motion with angular speed Ω.

4.1.1.3 Campbell Diagram

Rotors are subjected to forces that vary with time, and sometimes their variation with respect to time is harmonic. For instance, forces due to the unbalance of rotor itself are described as a vector rotating with the same angular speed, Ω, in the fixed reference frame. Otherwise, if this variation is periodical, it can always be represented as the sum of harmonic components.

As for excitation from unbalance, for example, the force frequency can be represented on ($\omega\Omega$)-plane by a straight line $\omega = \Omega$ in the Campbell diagram. In this case, the excitation is synchronous. The relationship linking the frequency of the forcing function to spin speed is often of simple proportionality and can be represented on the Campbell diagram by a straight line through the origin.

When one of the forcing functions has a frequency that coincides with one of the system's natural frequencies, the spin speeds are usually referred to as critical speeds. They can be identified on the Campbell diagram by intersecting the curves

related to natural frequencies with those related to forcing frequencies. A case in which natural frequencies are independent of speed and the forcing frequencies are proportional to Ω as reported in Fig. 4.3.

Not all intersections on the Campbell diagram indicate equally dangerous incidents. If the frequency of a forcing function coincides with the natural frequency of a mode that is completely uncoupled with it, no resonance actually occurs.

When a rotor operates at a critical speed, the vibration amplitude grows linearly and only the damping of the stator and supports can prevent failure of rotor. Actually, it is necessary to control the normal operating range either below or above critical speeds and sustained operation at critical speed should be avoided.

Speeds ranging from zero to the first critical speed are usually referred to as the subcritical range; above the first critical speed, the supercritical range starts.

If the Campbell diagram related to flexural vibrations is made by straight lines that are parallel to Ω-axis, i.e., if natural frequencies are independent of the speed, numerical values of the critical speeds coincide with those of the natural frequencies at standstill, as can be seen from Fig. 4.2.

A rotor operating at a critical speed is not subject to vibration but is a source of periodic excitation that can cause vibration, which can be very strong in nonrotating parts of the machine.

4.1.1.4 Free Whirling of the Simple Jeffcott Rotor

The Jeffcott rotor consists of a point mass m at point P attached to a massless shaft. The only force on mass m is one due to shaft elasticity. The stiffness where the elastic force is from can be considered as stiffness of the shaft, the supporting structure, or a combination of both. The two schemes sketched in Fig. 4.4, a flexible shaft on stiff supports and a stiff shaft on compliant supports, yield the same results as long as the system is undamped and axisymmetrical.

The mass m with two degrees of freedom is always confined within a xy-plane. This statement is justified by uncoupling axial and radial motions and relies on small-displacement assumptions resting on linear structural analysis.

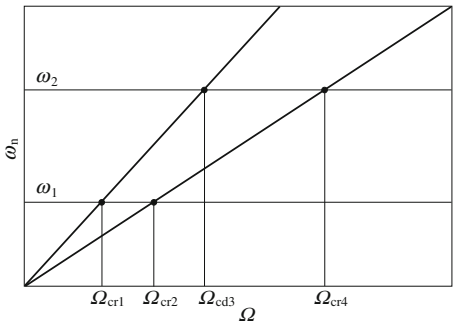

Fig. 4.3 Campbell diagram of simple Jeffcott rotor

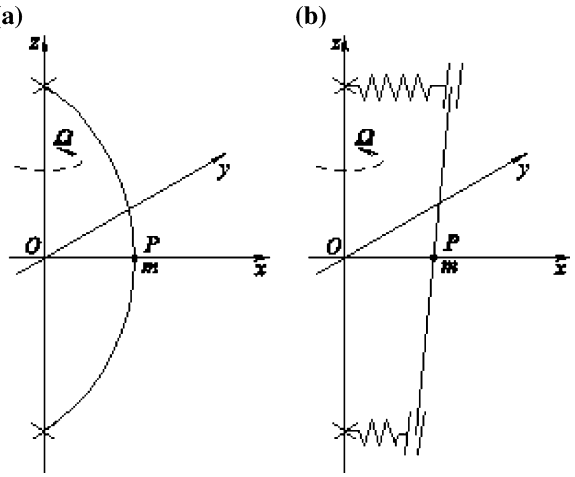

Fig. 4.4 Sketch of a Jeffcott rotor. The model is sketched in its deformed configuration at the time in which point P crosses the *xz*-plane. **a** Flexible shaft on stiff supports. **b** Stiff shaft on compliant supports (Bucher 2009)

The equations of motion of mass m are simply

$$\begin{cases} m\ddot{x}(t) + kx(t) = 0 \\ m\ddot{y}(t) + ky(t) = 0 \end{cases} \tag{4.11}$$

where x and y are the coordinates of point P at generic time t.

The equations of motion along each axis are in the same form as the equation of the free motion of a system with a single degree of freedom and their solution is a harmonic motion with frequency ω_n in Eq. (4.9).

The motion of point P can be viewed as a combination of two harmonic motions taking place along axes x and y with the same frequency ω_n, coinciding with the natural frequency of the nonrotating shaft. They can add to each other and give way to a trajectory of point P that can be circular, elliptical, or straight in any direction in a xy-plane depending on initial conditions.

The same result could be obtained with respect to complex coordinates in xy-plane:

$$m\ddot{z} + kz = 0. \tag{4.12}$$

The solution to this homogeneous differential equation is

$$z = z_0 e^{i\omega_n t}$$

where $z_0 = x_0 + iy_0$.

Introducing this solution into Eq. (4.12) yields a homogeneous algebraic equation that has solutions other than the trivial solution $z_0 = 0$ only if

$$\omega_n = \pm\sqrt{k/m}.$$

The general solution of Eq. (4.12) is thus

$$z = Z_1 e^{i\omega_n t} + Z_2 e^{-i\omega_n t}. \tag{4.13}$$

The physical meaning of Eq. (4.13) is obvious: z is a vector $\{z\}$ that rotates in a xy-plane with angular velocity $\Omega = \omega_n$. If the amplitude z_0 is real, point P crosses the x-axis at time $t = 0$. The motion expressed by Eq. (4.13) is the superimposition of a forward circular or direct motion (i.e., occurring in the same direction as the spin speed) and a backward circular motion.

They both occur at an angular velocity, often called whirl speed, equal to the natural frequency of a nonrotating system. In the following study, spin speed Ω will always be considered positive: A forward motion will then be characterized by a positive whirl speed ω_n, while a backward motion is characterized by a negative value of ω_n. The resulting superimposition of the two motions depends on the initial conditions, i.e., on values of complex constants Z_1 and Z_2. If, for example, Z_2 is equal to 0, circular forward whirling emerges, and if the two constants are equal, the harmonic vibration along the x-axis would take place.

The rotating vector $e^{i\omega nt}$ in the complex plane is used to express the motion in the form

$$x = x_0 e^{i\omega_n t},\ y = y_0 e^{i\omega_n t}$$

where only the real components of $x = x_0 e^{i\omega_n t}$ and $y = y_0 e^{i\omega_n t}$ have a physical meaning.

Natural frequency of the rotor is not determined by spin speed Ω: The Campbell diagram of a Jeffcott rotor is then made of straight lines, as shown in Fig. 4.3. The flexural critical speed

$$\Omega_{cr} = \sqrt{k/m} \tag{4.14}$$

is defined as the speed at which the natural frequency of the system is coincident with the rotational frequency and the natural frequency of the nonrotational system.

4.1.1.5 Reaction at Supports of the Simple Jeffcott Rotor

The reaction force from supports of the simple Jeffcott rotor can be obtained as

$$f_b = kz(t) = kz_0 \frac{\left(\Omega^2/\omega_n^2\right)\varepsilon}{\left(1 - \Omega^2/\omega_n^2\right)} e^{i\Omega t}. \tag{4.15}$$

4.1.1.6 Interaction Between Torsional Torque and Lateral Vibration

In Fig. 4.5, a disc rotates at its torsion around the central axis in the xy plan. The system now has three degrees of freedom, i.e., displacements along x and y ordinates, as well as the torsional angle θ. The radius vector and its derivatives with respect to the time of the lumped mass m are

$$\boldsymbol{r} = (x(t) + \varepsilon\cos\theta)\boldsymbol{e}_x + (\dot{y}(t) + \varepsilon\sin\theta)\boldsymbol{e}_y \tag{4.16}$$

$$\dot{\boldsymbol{r}} = \Big(\dot{x}(t) - \dot{\theta}\varepsilon\sin\theta\Big)\boldsymbol{e}_x + \Big(\dot{y}(t) + \dot{\theta}\varepsilon\cos\theta\Big)\boldsymbol{e}_y \tag{4.17}$$

$$\ddot{\boldsymbol{r}} = \Big(\ddot{x}(t) - \ddot{\theta}\varepsilon\sin\theta - \dot{\theta}^2\varepsilon\cos\theta\Big)\boldsymbol{e}_x + \Big(\ddot{y}(t) + \ddot{\theta}\varepsilon\cos\theta - \dot{\theta}^2\varepsilon\sin\theta\Big)\boldsymbol{e}_y \tag{4.18}$$

where $\boldsymbol{e}_x$ and $\boldsymbol{e}_y$ are the unit vectors along x and y axes.

Equations of motion along x, y and directions θ of the disc with mass m and stiffness k include linear motion along x and y, and angular motion on the x, y plan are written as

$$\ddot{x}(t) - \ddot{\theta}\varepsilon\sin\theta - \dot{\theta}^2\varepsilon\cos\theta + \omega_{nx}^2 x = 0 \tag{4.19}$$

$$\ddot{y}(t) + \ddot{\theta}\varepsilon\cos\theta - \dot{\theta}^2\varepsilon\sin\theta + \omega_{ny}^2 y = 0 \tag{4.20}$$

$$\ddot{\theta} + \frac{m\varepsilon}{J_p}\Big[\ddot{\theta}\varepsilon - \ddot{x}\sin\theta - \dot{\theta}\dot{x}\cos\theta + \ddot{y}\cos\theta - \dot{\theta}\dot{y}\sin\theta\Big] = T(t) \tag{4.21}$$

where $\omega_{nx}^2 = k_x/m$ and $\omega_{ny}^2 = k_y/m$; $T(t)$ is torsional torque around the disc center; Jp is the torsional moment of inertia of the disc.

Equations (4.19) and (4.20) of motion in terms of complex coordinate z are as follows

$$m\ddot{z} + kz = m\varepsilon\Big(\dot{\theta}^2 - \mathrm{i}\ddot{\theta}\Big)e^{\mathrm{i}\theta}. \tag{4.22}$$

Equation (4.21) is transformed to

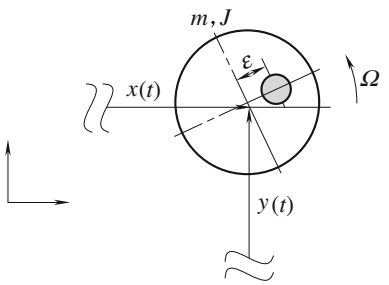

Fig. 4.5 Disc with torsion around the central axis in the x–y plan

$$\left(1+\frac{\varepsilon^2}{2R^2}\right)\ddot{\theta}+\frac{\varepsilon}{2R^2}\left[\ddot{y}\cos\theta-\ddot{x}\sin\theta-\dot{\theta}(\dot{x}\cos\theta+\dot{y}\sin\theta)\right]=T(t)$$

where $2R^2 = Jp/m$.

If $\dot{\theta} = \text{const} = \Omega$, one obtains Eqs. (4.3a, 4.3b). The torque to meet this demand of constant speed is

$$T(t) = -\varepsilon k(\dot{x}(t)\sin\Omega t - y(t)\cos\Omega t). \tag{4.23}$$

Otherwise Eqs. (4.19–4.21) are nonlinear coupled differential equations that should be treated with numerical integration or perturbations (i.e., multiple scales).

4.1.1.7 Instability Range

A rotating machine is stable if its rotor performs a pure rotational motion around an axis and the motion is not accompanied by other vibrations within admitted amplitude values. A stable rotating machine can withstand external perturbing forces, that is, any perturbation cannot drastically change its behavior.

In rotors, there is a source of energy that may cause an unbounded growth of free vibration amplitude. The frequencies in which this growth occurs are usually called instability ranges, and the speed at the beginning of these ranges is the threshold of instability.

It is easy to predict the onset of unstable working conditions in a linear system. Variation of amplitude vector of the vibration system with respect to time is expressed in the form:

$$\{\boldsymbol{u}\} = \{\boldsymbol{u}_0\}\mathrm{e}^{\mathrm{i}\omega t}. \tag{4.24}$$

Sign of decay rate, *i.e.*, of imaginary part of the complex frequency ω, implies a stability condition: If it is positive the amplitude decays exponentially in time indicating a stable condition; a negative imaginary part of the complex frequency indicates an unstable operation. The plot of decay rate as a function of spin speed must then be drawn with the Campbell diagram. At vanishing small speeds all decay rates are positive because there is no external source of energy that can excite vibration. With increasing speed, the decay rate of some modes would drop, showing a deterioration of stability.

4.1.2 Jeffcott Rotor with Viscous Damping

In this section, features of Jeffcott rotor with viscous damping is discussed.

4.1.2.1 Free Whirling

It is very important to distinguish between non-rotating and rotating damping in a damped rotor. Non-rotating damping is associated with stationary parts and has a stabilizing effect on the machine's whole operation range. Rotating damping is directly associated with the rotor and can reduce vibration amplitude in subcritical conditions, and destabilize effects in supercritical range (see Genta 2008).

The model of Fig. 4.4 can be extended to the damped system with the generalized forces due to damping added to right-hand side of Eq. (4.3). Use a viscous damping model and complex notation, and the force due to nonrotating damping is

$$\boldsymbol{F}_n = F_{nx} + \mathrm{i}F_{ny} = -c_n\dot{x} - \mathrm{i}c_n\dot{y} = -c_n\dot{z} \tag{4.25}$$

where c_n is the non-rotating damping coefficient.

A rotating reference frame $O\xi\eta z$ (Fig. 4.6) must be introduced for study of rotating damping. When rotational speed is constant, the angle between the two reference frames is simply $\theta = \Omega t$. A complex coordinate ς is defined in $\xi\eta$-plane as

$$\varsigma = \xi + \mathrm{i}\eta \;=\; z\mathrm{e}^{-\mathrm{i}\theta}. \tag{4.26}$$

Expressions of the force due to a rotating viscous damping coefficient, c_r, both in $\xi + i\eta = z$ frame and $Oxyz$ frame, are as follows:

$$\boldsymbol{F}_{r\xi\eta} = -c_r\dot{\varsigma} = -c_r\left(\dot{z} - \mathrm{i}\dot{\theta}z\right)\mathrm{e}^{-\mathrm{i}\theta} \tag{4.27}$$

$$\boldsymbol{F}_{rxy} = \boldsymbol{F}_{r\xi\eta}\mathrm{e}^{\mathrm{i}\theta} = -c_r\left(\dot{z} - \mathrm{i}\dot{\theta}z\right). \tag{4.28}$$

After the introduction of expressions (4.25) and (4.28) for the forces due to non-rotating and rotating damping to the right-hand side of the equation of motion (4.22), it follows that

$$m\ddot{z} + (c_r + c_n)\dot{z} + (k - \mathrm{i}c_r\dot{\theta})z = m\varepsilon(\dot{\theta}^2 - \mathrm{i}\ddot{\theta})e^{-\mathrm{i}\theta} \tag{4.29}$$

Here, rotating damping is assumed to be synchronous with the rotor. If whirl speed ω is constant, Eq. (4.29) is easily modified by neglecting the term in $\ddot{\theta}$.

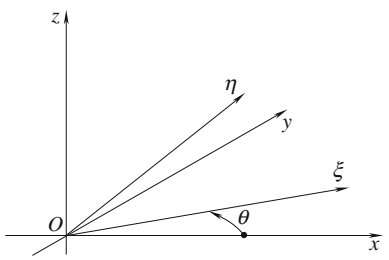

Fig. 4.6 Reference frames $Oxyz$ and $O\xi\eta z$ at time t

Introduce the solution $z = z_0 e^{i\omega t}$ with both the amplitude z_0 and the frequency ω in complex numbers into Eq. (4.22), and the following characteristic equation is obtained:

$$m\omega^2 + i(c_r + c_n)\omega + k - i\Omega c_r = 0. \tag{4.30}$$

The imaginary part is

$$c_n\omega + c_r(\omega - \Omega). \tag{4.31}$$

Non-rotating damping always produces stabilizing effects provided that c_n is positive.

Rotating damping multiplied by a term, $(\omega - \Omega)$, that may be either positive or negative, would result in the following three cases:

Subcritical operation ($\Omega < \omega$). The rotating damping term is positive and has a stabilizing effect.

Synchronous operation ($\Omega = \omega$). The rotating damping term vanishes and has no effect.

Supercritical operation ($\Omega > \omega$). The rotating damping term is negative and has a destabilizing effect.

This is also true for other forms of damping, such as hysteretic damping: All forms of rotating damping are stabilizing in subcritical operation and destabilizing above critical speed. The roots of this quadratic equation with complex coefficients are

$$\omega = \pm\frac{1}{\sqrt{2}}\sqrt{\Gamma + \sqrt{\Gamma^2 + \left(\frac{\Omega c_r}{m}\right)^2}} + i\left[\frac{c_r + c_n}{2m} \mp \frac{1}{\sqrt{2}}\sqrt{-\Gamma + \sqrt{\Gamma^2 + \left(\frac{\Omega c_r}{m}\right)^2}}\right] \tag{4.32}$$

where $\Gamma = k/m - (c_r + c_n)^2/(4\ m^2)$.

Without loss of generality, because it is sufficient to assume that at time $t = 0$ point C crosses x-axis, the amplitude z_0 is then real. Separating real part ω_R and imaginary part ω_I of the complex frequency ω, the time history can then be written as

$$\begin{cases} x = z_0 e^{-\omega_I t}\cos(\omega_R t) \\ y = z_0 e^{-\omega_I t}\sin(\omega_R t) \end{cases}. \tag{4.33}$$

The real part of ω indicates a true angular velocity: It is the angular velocity at which deflected shape rotates about undeformed configuration. The imaginary part is a decay rate: If it is positive the amplitude decays in time and point C tends to point O. The rotor shows a stable behavior as whirl motion tends to reduce its amplitude.

If ω_I is negative the amplitude grows exponentially in time. The motion is unstable, as any small perturbation can trigger this self-excited whirling.

4.1.2.2 Unbalance Response

If the rotor is not perfectly balanced, it is necessary to resort to the nonhomogeneous equation (4.29). If the angular acceleration is neglected, the complementary function and particular integral are, respectively,

$$z = Z_1 e^{i\omega_1 t} + Z_2 e^{i\omega_2 t}, \quad z = z_0 e^{i\Omega t} \tag{4.34}$$

The first allows description of rotor motion which is perfectly balanced, while the second yields response to static unbalance m. It is a synchronous whirling, i.e., a whirling with $\omega = \Omega$. Amplitude of the unbalance response is then obtained by introducing the particular integral into the equation of motion:

$$z_0\left(-m\Omega^2 + i\Omega c_n + k\right) = m\varepsilon\Omega^2. \tag{4.35}$$

As can be seen, rotating damping is not included in Eq. (4.35). Unbalance produces a synchronous excitation and the latter rotates in deflected configuration but is not subject to deformations that change in time.

4.1.3 Equations of Motion with a Precession Rotation

The basic phenomenon and equations of motion of Jeffcott rotor with a precession rotation are described below

4.1.3.1 Precession of Rotating Disc

In Fig. 4.7, the rotating disc is not at a midpoint on the shaft between two end supports, A and B bearings. After deformation of the shaft, the axis of the disc shaft has been inclined to form an angle θ between it and line AB of the two supporting points. The rotating angular speed of the disc is Ω, and its moment of inertia around the disc centre is Jp. The moment of momentum of the rotating disc around its mass centre O' is $\{\boldsymbol{H}\} = Jp\{\boldsymbol{\Omega}\}$, and the moment vector $\{\boldsymbol{H}\}$ direction has a same inclined angle θ with line AB. When the disc shaft vibrates freely, frequency of this free vibration is f. Then the plane containing disc centre O' and axis AB performs a precession rotation with angular speed $\{\boldsymbol{\omega}_n\}$. Owing to the precession, the direction of moment vector will change continuously, so there is a moment of inertia force as follows:

$$\left\{\boldsymbol{M}_g\right\} = -(\{\boldsymbol{\omega}_n\} \times \{\boldsymbol{H}\}) = J_p\{\Omega\} \times \{\boldsymbol{\omega}_n\}. \tag{4.36}$$

The direction of $\{\boldsymbol{Mg}\}$ is perpendicular to plane O'AB, and its magnitude is as

$$M_g = J_p \Omega \omega_n \sin\theta. \tag{4.37}$$

Fig. 4.7 Disc precession

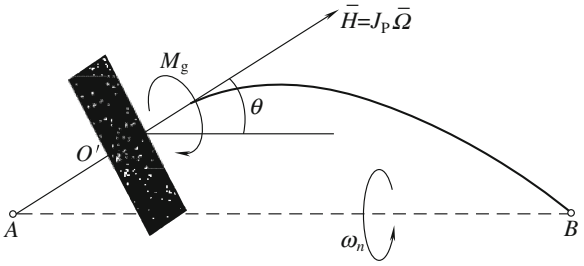

This is the gyroscope moment acting on the shaft from the disc. Because angle θ is small, it follows that

$$M_g = J_p \Omega \omega_n \theta \tag{4.38}$$

which is equivalent to the elastic moment. When it is in positive precession, then $0 < \theta < \pi/2$, and the moment will decrease. The shaft deformation means that it increases elastic stiffness of shaft. i.e., increases the shaft critical speed. Of course, when it is in negative precession, the shaft critical speed will drop.

4.1.3.2 Equation of Motion

The equation of motion, in generalized matrix form, for a rotor rotating at a constant spin speed Ω is

$$[\boldsymbol{M}]\{\ddot{\boldsymbol{u}}(t)\} + ([\boldsymbol{C}] + [\boldsymbol{G}])\{\dot{\boldsymbol{u}}(t)\} + ([\boldsymbol{K}] + [\boldsymbol{H}])\{\boldsymbol{u}(t)\} = \{\boldsymbol{f}(t)\} \tag{4.39}$$

where, $[\boldsymbol{M}]$ is the symmetric mass matrix; $[\boldsymbol{C}]$ is the symmetric damping matrix; $[\boldsymbol{G}]$ is the skew-symmetric gyroscopic matrix; $[\boldsymbol{H}]$ is the skew-symmetric circulatory matrix with rotating damping; $[\boldsymbol{K}]$ is the symmetric bearing or seal stiffness matrix; $\{\boldsymbol{u}(t)\}$ is the generalized coordinates of the rotor in inertial coordinates; and $\{\boldsymbol{f}(t)\}$ is a forcing.

Equation (4.36) can be written with real coordinates x and y

$$[\boldsymbol{M}]\{\ddot{\boldsymbol{u}}(t)\} + [\boldsymbol{C}]\{\dot{\boldsymbol{u}}(t)\} + ([\boldsymbol{K}] + [\boldsymbol{H}])\{\boldsymbol{u}(t)\} = \{\boldsymbol{f}(t)\} \tag{4.40}$$

where $[\boldsymbol{M}] = \begin{bmatrix} m & 0 \\ 0 & m \end{bmatrix}$; $[\boldsymbol{C}] = \begin{bmatrix} c_n + c_r & 0 \\ 0 & c_n + c_r \end{bmatrix}$ $[\boldsymbol{K}] = \begin{bmatrix} k & 0 \\ 0 & k \end{bmatrix}$; $[\boldsymbol{H}] = \begin{bmatrix} 0 & \Omega c_r \\ -\Omega c_r & 0 \end{bmatrix}$; $\{\boldsymbol{u}(t)\} = \begin{Bmatrix} x \\ y \end{Bmatrix}$; $\left\{ \{\boldsymbol{f}(t)\} = m\varepsilon \begin{Bmatrix} \dot{\theta}^2 \cos\theta + \ddot{\theta} \sin\theta \\ \dot{\theta}^2 \sin\theta - \ddot{\theta} \cos\theta \end{Bmatrix} \right\}$.

Skew-symmetric gyroscopic matrix $[\boldsymbol{G}]$ vanishes whereas skew-symmetric circulatory matrix is presented and contains rotating damping. The presence of a circulatory matrix is linked with destabilizing effects, like in the rotating damping.

4.2 Dynamics of Multi-Degrees-of-Freedom Rotors

Real rotors are much more complex than Jeffcott rotors and therefore more realistic models are needed. A rotor must be modeled as a rigid body at least with its moment of inertia, which can produce gyroscopic effects. If it is flexible, multi-degrees-of-freedom models should be used (see Genta 2005, 2008; Lalanne and Ferraris 1998).

4.2.1 Model with 4 Degrees of Freedom

If a rotor is modeled as a rigid body without coupling between axial, flexural, and torsional behaviors of inertia, the four-degrees-of-freedom model is needed.

4.2.1.1 Generalized Coordinates and Equations of Motion

In a Jeffcott model, the rotor is assumed to be a point mass with no moment of inertia. This assumption excludes consideration of rotor dynamic behavior. The simplest model to evaluate this behavior is shown in Fig. 4.8a or b: either a rigid body attached to a compliant massless shaft or a rigid rotor spinning on compliant bearings. A more complex system is plotted in Fig. 4.8c where bearings, a compliant massless shaft, and rigid rotor are combined.

This model is a rigid body with moments of inertia locating at point C. One of the principal axes of inertia lies along rotating z-axis. The body's principal moments of inertia will be referred to as polar moments of inertia J_p around the rotation axis and the transversal moment of inertia J_t around any axis in rotation plane.

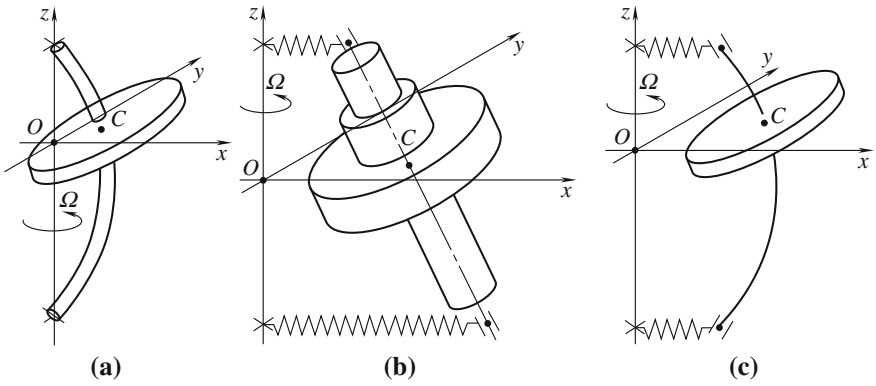

Fig. 4.8 Rotor models. **a** Rigid body on a massless compliant shaft. **b** Rigid rotor on compliant bearings. **c** Rotor in which both the bearings and the shaft are compliant

In Fig. 4.8a and c, the disc is rigid. If $Jp > J_t$, the rigid body is usually called a disc; one limiting case is that of an infinitely thin disc in which $Jp = 2J_t$. If $Jp = J_t$, the inertia ellipsoid degenerates into a sphere and the model is similar to Jeffcott rotor. If $Jp < 2J_t$, the rotor is usually named as a long rotor.

In fact, the system has six degrees of freedom. Uncoupling between axial, flexural, and torsional behaviors will be assumed to hold for elastic and inertial part of the model, so a model with four degrees of freedom is sufficient for the study of flexural behavior at a constant speed. The reference frames are shown in Fig. 4.9a (see Genta 2008).

(1) The inertial frame $OXYZ$ has its origin at point O and its Z-axis coincides with the rotation axis.
(2) The rotating frame $O\Xi HZ$ has its origin at point O and its Z-axis coincides with the rotation axis. Axes Ξ and H rotate on XY -plane with angular velocity Ω.
(3) Frame $CX'Y'Z'$ has its origin at C. Its axes remain parallel with those of frame $OXYZ$.
(4) Frame $Cxyz$ has its origin at C. Its z-axis coincides with the rotation axis of the body in a deformed position, and the x- and y-axes are defined according to rotations.
(5) Frame $CX'yz^*$ is formed after one rotates axes of $CX'Y'Z'$ frame about X'axis by an angle $\varphi_{X''}$ until Y'-axis enters the rotation plane of the rigid body in its deformed configuration. The two axes will be y- and z^*-axes.
(6) Frame $C\xi\eta z$ has its origin at C. It is obtained from frame $Cxyz$ if one rotates the x- and y-axes in a xy-plane by an angle equal to rotation angle θ of the rotor corresponding to spin speed.

As stated above, the rotor is assumed to be slightly unbalanced. Since the rotor position in $C\xi\eta z$ -frame is immaterial, the principal axis of inertia corresponding to the moment of inertia J_p will be considered parallel to the ξz-plane. Because static unbalance cannot lie in the same plane as coupled unbalance does, eccentricity

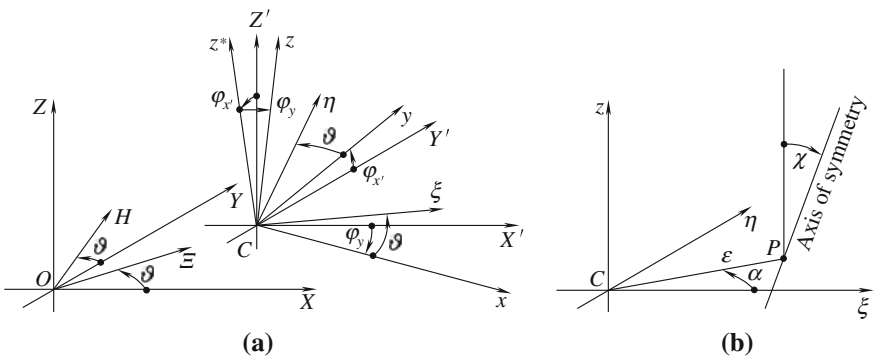

Fig. 4.9 Generalized coordinates. **a** Reference frames. **b** unbalance conditions in the $C\xi\eta z$ reference frame

must not be in the direction of ξ-axis, as in the case of the Jeffcott rotor. Conditions of unbalance are summarized in Fig. 4.9b, where static unbalance is shown to lead coupled unbalance by a phase angle α.

Take X-, Y -, and Z- as coordinates of point C and angles $\varphi_{X'}$, φ_y and θ as generalized coordinates of the rigid body. A small displacement assumption on coordinates X, Y, Z, $\varphi_{X'}$ and φ_y will greatly simplify the problem. Coordinate θ, on the contrary, cannot be considered small.

Before the computation of kinetic energy of the rigid body, velocity of its center of mass (point P) and its angular velocity expressed in principal system of inertia must be calculated.

In the following discussion, all terms containing product of eccentricity or angular error by a small quantity will be neglected to eliminate axial–flexural coupling. The translational kinetic energy is thus

$$\tilde{T}_t = \frac{1}{2} m \left\{ \dot{X}^2 + \dot{Y}^2 + \dot{Z}^2 + \varepsilon^2 \dot{\theta}^2 + \varepsilon \dot{\theta} \left[-\dot{X} \sin(\theta + \alpha) + \dot{Y} \cos(\theta + \alpha) \right] \right\}. \quad (4.41)$$

For computation of rotational kinetic energy, angular velocity must be expressed with reference to a frame coinciding with principal axes of the rotor. Three components of angular velocity can be viewed as vectors acting in different directions: $\dot{\varphi}_{x'}$ along X'-axis, $\dot{\varphi}_y$ along y-axis, and $\dot{\theta}$ along z-axis. Components of angular velocity along principal axes of inertia of the rotor $\{\Omega\}$ in form of relevant rotation vectors are

$$\{\Omega\} = \begin{Bmatrix} \dot{\varphi}_{X'} \cos\theta + \dot{\varphi}_y \sin\theta - \chi\dot{\theta} \\ -\dot{\varphi}_{X'} \sin\theta + \dot{\varphi}_y \cos\theta \\ \dot{\varphi}_{X'}(\chi \cos\theta + \varphi) + \dot{\varphi}_y \chi \sin\theta + \dot{\theta} \end{Bmatrix} \quad (4.42)$$

where χ is the angle between symmetrical axis of the disc and rotating axis of the system.

Since components of $\{\boldsymbol{\Omega}\}$ are referred to as the principal axes of inertia, after neglecting small terms, one could write rotational kinetic energy as

$$\begin{aligned} \tilde{T}_r = \frac{1}{2} \Big(& J_t \left(\dot{\varphi}_{X'}^2 + \dot{\varphi}_y^2 + \chi^2 \dot{\theta}^2 \right) + J_t \left(\dot{\theta}^2 + 2\dot{\theta} \dot{\varphi}_{X'} \varphi_y \right) \\ & + 2\dot{\theta}\chi \left(J_p - J_t \right) \left[\dot{\varphi}_{X'} \cos\theta + \dot{\varphi}_y \sin\theta \right] \Big). \end{aligned} \quad (4.43)$$

It is expedient to introduce into the Lagrange equations only the expression of kinetic energy and then to add elastic reaction of the shaft directly, as external generalized forces. Generalized forces Q_i related to translational degrees of freedom are simply the forces F_X, F_Y, and F_Z in the direction of inertial frame axes. The equations of motion can be obtained through the Lagrange equation:

$$\begin{cases} m\ddot{X} = m\varepsilon\left[\ddot{\theta}\sin(\theta+\alpha) + \dot{\theta}^2\cos(\theta+\alpha)\right] + F_X \\ m\ddot{Y} = m\varepsilon\left[-\ddot{\theta}\cos(\theta+\alpha) + \dot{\theta}^2\sin(\theta+\alpha)\right] + F_Y \\ m\ddot{Z} = F_Z. \end{cases} \tag{4.44}$$

The generalized forces to be introduced into the three equations of motion related to rotational degrees of freedom are not exactly moments about axes of the Cxyz frame because the first generalized coordinate for rotation is set on X' axis, so

$$Q_{\phi_{X'}} = M_x\cos\varphi_y + M_z\sin\varphi_y,\ Q_{\phi_y} = M_y,\ Q_\theta = M_z. \tag{4.45}$$

According to expressions (4.45) for generalized forces, with all the relevant derivatives and linearizing performed again, the following equations of motion for rotational degrees of freedom can be obtained:

$$\begin{cases} J_t\ddot{\varphi}_{X'} + J_p\dot{\theta}\dot{\varphi}_y = \chi\left(J_t - J_p\right)\left[\ddot{\theta}\cos\theta - \dot{\theta}^2\sin\theta\right] + M_x \\ J_t\ddot{\varphi}_y - J_p\dot{\theta}\dot{\varphi}_{X'} = \chi\left(J_t - J_p\right)\left[\ddot{\theta}\sin\theta + \dot{\theta}^2\cos\theta\right] + M_y \\ \left(J_p + J_t\chi^2 + m\varepsilon^2\right)\ddot{\theta} + m\varepsilon\left[\ddot{Y}\cos\theta - \ddot{X}\sin\theta\right] + \\ \chi\left(J_p - J_t\right)\left[\ddot{\varphi}_{X'}\cos\theta + \ddot{\varphi}_y\sin\theta\right] = M_z \end{cases} \tag{4.46}$$

4.2.1.2 Behavior of the System at a Constant Speed

If angular velocity of the rotor is constant, the last equation could also be uncoupled so flexural behavior can be studied separately. By stating that $\theta = \Omega t$, one could reduce the four relevant equations of motion to

$$\begin{cases} m\ddot{X} = m\varepsilon\Omega^2\cos(\Omega t+\alpha) + F_X \\ m\ddot{Y} = m\varepsilon\Omega^2\sin(\Omega t+\alpha) + F_Y \\ J_t\ddot{\varphi}_{X'} + J_p\Omega\dot{\varphi}_y = -\chi\Omega^2\left(J_t - J_p\right)\sin + M_x \\ J_t\ddot{\varphi}_y - J_p\Omega\dot{\varphi}_{X'} = \chi\Omega^2\left(J_t - J_p\right)\cos\Omega t + M_y. \end{cases} \tag{4.47}$$

The equations can be transformed into the following form:

$$\begin{aligned} m\ddot{X} + K_{11}X + K_{12}\varphi_y &= m\varepsilon\Omega^2\cos(\Omega t+\alpha) \\ m\ddot{Y} + + K_{11}Y - K_{12}\varphi_{X'} &= m\varepsilon\Omega^2\sin(\Omega t+\alpha) \end{aligned}$$

$$\begin{aligned} J_t\ddot{\varphi}_{X'} + J_p\Omega\dot{\varphi}_y - K_{12}Y + K_{22}\varphi_{X'} &= -\chi\Omega^2\left(J_t - J_p\right)\sin\Omega t \\ J_t\ddot{\varphi}_y - J_p\Omega\dot{\varphi}_{X'} + K_{12}Y + K_{22}\varphi_y &= \chi\Omega^2\left(J_t - J_p\right)\cos\Omega t \end{aligned}$$

by the usage of the following vectors transformation:

$$\begin{Bmatrix} F_X \\ M_y \end{Bmatrix} = -\begin{bmatrix} K_{11} & K_{12} \\ K_{12} & K_{22} \end{bmatrix} \begin{Bmatrix} X \\ \varphi_y \end{Bmatrix}, \begin{Bmatrix} F_Y \\ M_x \end{Bmatrix} = -\begin{bmatrix} K_{11} & -K_{12} \\ -K_{12} & K_{22} \end{bmatrix} \begin{Bmatrix} Y \\ \varphi_{X'} \end{Bmatrix}. \quad (4.48)$$

If $-\varphi_{X'}$ is used instead of $\varphi_{X'}$ as a generalized coordinate for rotations about the X-axis, it is possible to define a set of complex coordinates, i.e.,

$$\begin{cases} z = X + \mathrm{i}Y \\ \phi = \varphi_y - \mathrm{i}\varphi_{X'} \end{cases} \quad (4.49)$$

The equations of motion can be transformed to a compact form:

$$[\boldsymbol{M}]\{\ddot{\boldsymbol{q}}\} - \mathrm{i}\Omega[\boldsymbol{G}]\{\dot{\boldsymbol{q}}\} + [\boldsymbol{K}]\{\boldsymbol{q}\} = \Omega^2\{\boldsymbol{f}\}\mathrm{e}^{\mathrm{i}\Omega t} \quad (4.50)$$

where vectors of complex coordinates and of unbalances and the mass, gyroscopic, and stiffness matrices are

$$\{\boldsymbol{q}\} = \begin{Bmatrix} z \\ \phi \end{Bmatrix}, [\boldsymbol{M}] = \begin{bmatrix} m & 0 \\ 0 & J_t \end{bmatrix}, [\boldsymbol{G}] = \begin{bmatrix} 0 & 0 \\ 0 & J_p \end{bmatrix}, [\boldsymbol{K}] = \begin{bmatrix} K_{11} & K_{12} \\ K_{12} & K_{22} \end{bmatrix}, \{\boldsymbol{f}\} = \begin{Bmatrix} m\varepsilon\mathrm{e}^{\mathrm{i}\alpha} \\ \chi(J_t - J_p) \end{Bmatrix}.$$

All matrices are symmetric when a complex coordinate notation is used whereas the gyroscopic matrix is skew symmetric in real coordinates. If viscous or hysteretic damping models can be used, it is possible to distinguish between non-rotating and rotating damping and to separate the two damping matrices. In viscous damping, the equation of motion of the damped system is

$$\begin{aligned} [\boldsymbol{M}]\{\ddot{\boldsymbol{q}}\} + ([\boldsymbol{C}_n] + [\boldsymbol{C}_r] - \mathrm{i}\Omega[\boldsymbol{G}])\{\dot{\boldsymbol{q}}\} + \\ ([\boldsymbol{K}] - \mathrm{i}\Omega[\boldsymbol{C}_r])\{\boldsymbol{q}\} = \Omega^2\{\boldsymbol{f}\}\mathrm{e}^{\mathrm{i}\Omega t}. \end{aligned} \quad (4.51)$$

where the structure of matrices $[\boldsymbol{C}_n]$ and $[\boldsymbol{C}_r]$ is similar to that of the stiffness matrix.

4.2.1.3 Free Whirling of the Undamped System

Free whirling of the undamped system can be studied through the homogeneous equation associated with Eq. (4.50). Introduce a solution of the type:

$$z = z_0\mathrm{e}^{\mathrm{i}\omega t}, \quad \phi = \phi_0\mathrm{e}^{\mathrm{i}\omega t}$$

into the equation of motion, and one could get the following linear equations:

$$\begin{cases} z_0\left(-m\omega^2 + K_{11}\right) + \phi_0 K_{12} = 0 \\ z_0 K_{12} + \phi_0\left(-J_t\omega^2 + J_p\omega\Omega + K_{22}\right) = 0. \end{cases} \quad (4.52)$$

The characteristic equation allowing computation of the whirl frequency is

$$\omega^4 - \Omega\omega^3 \frac{J_p}{J_t} - \omega^2 \left(\frac{K_{11}}{m} - \frac{K_{22}}{J_t} \right) + \Omega\omega \frac{K_{11}}{m} \frac{J_p}{J_t} + \frac{K_{11}K_{22} - K_{12}^2}{mJ_t} = 0. \tag{4.53}$$

Equation (4.53) has four real roots among which two are positive. The system's Campbell diagram can be referred to Genta (2008): At each speed Ω, four whirl modes occurring at different frequencies are possible. Two of them are in forward direction and two are in backward direction.

Since all solutions of Eq. (4.53) are real, the corresponding eigenvectors q_i are also real.

Neglecting the negative solutions, one could define the following values of critical speed:

$$\Omega_{cr} = \frac{1}{\sqrt{2m}} \sqrt{K_{11} - \frac{K_{22}}{\delta} \pm \sqrt{\left(K_{11} + \frac{K_{22}}{\delta} \right)^2 - 4\frac{K_{12}^2}{\delta}}} \tag{4.54}$$

where

$$\delta = \left(J_p - J_t \right) / m. \tag{4.55}$$

If $J_p < J_r$ or $\delta < 0$, as happens in the case of long rotors, there are two real solutions and, as a consequence, two values for critical speed.

If, on the contrary, $J_p > J_r$ or $\delta > 0$, as happens in the case of discs, one of the solutions is imaginary and only one critical speed exists.

If $K_{12} = 0$, i.e., if translational and rotational degrees of freedom are uncoupled, the solution would be the same as in the case of Jeffcott rotors.

Values of critical speed are

$$\Omega_{crI} = \sqrt{K_{11}/m},\ \Omega_{crII} = \sqrt{-K_{22}/(m\delta)} = \sqrt{-K_{22}/\left(J_p - J_t \right)}. \tag{4.56}$$

The first one is real only if $\delta < 0$, i.e., $Jp < J_r$. Consider a rotor made up of a rigid gyroscopic body attached to a flexible uniform shaft running on rigid bearings. The stiffness matrix of the system is

$$[\boldsymbol{K}] = \frac{3EJl}{a(l-a)} \begin{bmatrix} \frac{l^2 - 3al + 3a^2}{a^2(l-a)^2} & \frac{2a-l}{a(l-a)} \\ \frac{2a-l}{a(l-a)} & 1 \end{bmatrix} \tag{4.57}$$

where a is the distance between the upper bearing and the disc mass centre in Fig. 4.8.

If $a/l = 0.5$, gyroscopic moment has no effect on the critical speed in a disc rotor but it would cause a second critical speed in the long rotors.

In all other cases, an increase in critical speed will take place in the disc-type rotor, sometimes explained by a stiffening of the system due to gyroscopic

moment. However, it is only a phenomenological explanation because there is no actual stiffening.

In the case of a long rotor, critical speed decreases and a second critical speed, usually quite higher than the first, is present.

4.2.1.4 Unbalance Response of the Undamped System

The unbalance response can be expressed in the form:

$$z = z_0 e^{i\Omega t},\ \phi = \phi_0 e^{i\Omega t}$$

where the amplitudes z_o and φ_o tend to be complex numbers because the phase angle α of static and couple unbalances is usually not equal to zero. Effects of the two types of unbalance can be studied separately with relevant solutions added to each other. In the case of a static unbalance with vanishing phase angle α, amplitude of the response is

$$z_0 = m\varepsilon\Omega^2\left(\left(J_p - J_t\right)\Omega^2 + K_{22}\right)/\Delta \tag{4.58}$$

$$\phi_0 = -m\varepsilon\Omega^2 K_{12}/\Delta \tag{4.59}$$

where

$$\Delta = -m\left(J_p - J_t\right)\Omega^4 + \left[K_{11}\left(J_p - J_t\right) + mK_{22}\right]\Omega^2 + K_{11}K_{22} - K_{12}^2.$$

In couple unbalance, the response is

$$\begin{cases} z_0 = \chi\Omega^2\left(J_p - J_t\right)K_{12}/\Delta \\ \phi_0 = \chi\Omega^2\left(J_p - J_t\right)\left(m\Omega^2 - K_{11}\right)/\Delta. \end{cases} \tag{4.60}$$

4.2.2 Rotors with Multi-Degree-of-Freedom

This section will focus on rotor model with multi-degrees of freedom of lateral displacements and rotations of its cross sections.

4.2.2.1 Lumped-Parameters Models

Among lumped-parameters methods, the transfer matrix approach, namely, the Myklestadt method was, and still is, widely used in rotor dynamics, mainly for critical speed prediction. As it can be easily obtained from the second Eq. (4.52), gyroscopic moment created by the *i*th rigid body located in the *i*th node can be

accounted for if $-J_t\omega^2 + Jp\omega\Omega$ is replaced by $-J_t\omega^2$. If the aim is to evaluate critical speeds only, it is possible to introduce $\omega = \Omega = \Omega_{cr}$ into node transfer matrix, which becomes

$$[\boldsymbol{T}_{in}] = \begin{bmatrix} 1 & 0 & 0 & 0 \\ 0 & 1 & 0 & 0 \\ -m_i\Omega_{cr}^2 + k_c & 0 & 1 & 0 \\ 0 & -\left(J_{ti} - J_{pi}\right)\Omega_{cr}^2 + \chi_c & 0 & 1 \end{bmatrix}. \tag{4.61}$$

The whole structure is modeled as a non-rotating system in the stiffness or compliance approach. If complex coordinates are applied, the relevant equations are either Eq. (4.50) or (4.51), depending on whether or not damping is neglected. The size of all matrices and vectors is equal to the number of complex degrees of freedom, which coincides with the number of degrees of freedom related to bending behavior in *xz*- and *yz*-planes. Mass, stiffness, and damping matrices, i.e., $[\boldsymbol{M}]$, $[\boldsymbol{K}]$, and $[\boldsymbol{C}]$ are those linked to the flexural behavior of the non-rotating system in the *xz* plane.

If complex coordinates are ordered as follows:

$$\{\boldsymbol{q}\} = \{\, z_1 \quad \phi_1 \quad z_2 \quad \phi_2 \quad \cdots\cdots \quad z_n \quad \phi_n \,\}^T \tag{4.62}$$

where matrices $[\boldsymbol{M}]$ and $[\boldsymbol{G}]$ and vector $\{\boldsymbol{f}\}$ of unbalances are, respectively,

$$[\boldsymbol{M}] = \mathrm{diag}[\, m_1 \quad J_{t1} \quad m_2 \quad J_{t2} \quad \cdots\cdots \quad m_n \quad J_{tn} \,] \tag{4.63a}$$

$$[\boldsymbol{G}] = \mathrm{diag}[\, 0 \quad J_{p1} \quad 0 \quad J_{p2} \quad \cdots\cdots \quad 0 \quad J_{pn} \,] \tag{4.63b}$$

$$\{\boldsymbol{f}\} = \left\{ \begin{matrix} m_1\varepsilon_1 e^{i\alpha 1}\left(J_{t1} - J_{p1}\right)\chi_1 e^{i\beta 1} & m_2\varepsilon_2 e^{i\alpha 2}\left(J_{t2} - J_{p2}\right)\chi_2 e^{i\beta 2} \rightarrow \\ & m_n\varepsilon_n e^{i\alpha n}\left(J_{tn} - J_{pn}\right)\chi_n e^{i\beta n} \end{matrix} \right\}^{\mathrm{T}}.$$

The phases α_i and β_i should reflect different orientations in the space of vectors expressing static and couple unbalances. The rotating damping matrix $[\boldsymbol{C}_r]$ can be built in the same way as general damping matrices.

4.2.2.2 Models with Consistent Inertial Properties

It is not difficult to add a rotation to kinetic energy of any element into the FEM. The mass matrix in this approach is coincident with that related to a non-rotating model. Also, stiffness and damping matrices are not affected by rotation apart from a possible geometrical effect due to the stiffening of the element that can be ascribed to centrifugal stressing. This effect, usually neglected in a formulation of beam elements that models rotating shafts, must be considered when one deals with beam elements aligned in a direction perpendicular to the rotational axis, such as turbine blades, propellers, and similar structural members. Centrifugal stiffening generally can be taken into account by adding a term of the type $\Omega^2[\boldsymbol{K}_\Omega]$ to the

stiffness matrix, where $[\boldsymbol{K}_\Omega]$ is a matrix of constants that can be computed at the element level and then assembled.

As in the case of an axi-symmetrical beam $Jz = 2Jy$, the gyroscopic contribution is twice the rotational one to the mass matrix. If there is damping in system, damping matrices of non-rotating and rotating elements can be assembled separately, yielding two matrices $[\boldsymbol{C}_n]$ and $[\boldsymbol{C}_r]$ to be introduced into the equations of motion. Then one can study the consistent unbalance vectors for a linear distribution of static and couple unbalance.

4.2.3 Dynamic Equation in Real Coordinates

Equation (4.51) can be written after separation of real part of each equation from imaginary part:

$$[\boldsymbol{M}]\{\ddot{\boldsymbol{u}}\} + ([\boldsymbol{C}] + \Omega[\boldsymbol{G}])\{\dot{\boldsymbol{u}}\} + ([\boldsymbol{K}] + \Omega[\boldsymbol{C}_r])\{\boldsymbol{u}\} = \Omega^2\{\boldsymbol{F}\} \tag{4.64}$$

where

$$\{\boldsymbol{u}\} = \left\{\mathrm{Re}\{\boldsymbol{q}\}^{\mathrm{T}}, \mathrm{Im}\{\boldsymbol{q}\}^{\mathrm{T}}\right\}^{\mathrm{T}}, \{\boldsymbol{F}\} = \left\{\mathrm{Re}\left\{\boldsymbol{f}e^{i\Omega t}\right\}^{\mathrm{T}}, \mathrm{Im}\left\{\boldsymbol{f}e^{i\Omega t}\right\}^{\mathrm{T}}\right\}^{\mathrm{T}},$$
$$[\boldsymbol{M}] = \begin{bmatrix} \boldsymbol{M} & 0 \\ 0 & \boldsymbol{M} \end{bmatrix}, [\boldsymbol{G}] = \begin{bmatrix} 0 & \boldsymbol{G} \\ -\boldsymbol{G} & 0 \end{bmatrix}, [\boldsymbol{C}] = \begin{bmatrix} \boldsymbol{C} & 0 \\ 0 & \boldsymbol{C} \end{bmatrix}, [\boldsymbol{K}] = \begin{bmatrix} \boldsymbol{K} & 0 \\ 0 & \boldsymbol{K} \end{bmatrix},$$
$$[\boldsymbol{C}_r] = \begin{bmatrix} 0 & \boldsymbol{C}_r \\ -\boldsymbol{C}_r & 0 \end{bmatrix}$$

and $[\boldsymbol{C}]$ is the total damping matrix, $[\boldsymbol{C}] = [\boldsymbol{C}_n] + [\boldsymbol{C}_r]$.

The real coordinates $\{\boldsymbol{u}\}$ differ from standard real coordinates used in study of non-rotating systems because sign of rotational degrees of freedom are related to rotation movement.

The damped system's equation of motion is thus

$$[\boldsymbol{M}]\{\ddot{\boldsymbol{u}}^*\} + ([\boldsymbol{C}] + \Omega[\boldsymbol{G}])\{\dot{\boldsymbol{u}}^*\} + ([\boldsymbol{K}] + \Omega[\boldsymbol{C}_r])\{\boldsymbol{u}^*\} = \Omega^2\{\boldsymbol{F}\} \tag{4.65}$$

where

$$\{\boldsymbol{u}\} = \left\{\mathrm{Re}\{\boldsymbol{q}\}^{\mathrm{T}}, \mathrm{Im}\{\boldsymbol{q}\}^{\mathrm{T}}\right\}^{\mathrm{T}}, \{\boldsymbol{F}\} = \begin{Bmatrix} f_x\cos(\Omega t) - f_y\sin(\Omega t) \\ f_x\sin(\Omega t) + f_y cos(\Omega t) \end{Bmatrix}$$
$$[\boldsymbol{M}] = \begin{bmatrix} \boldsymbol{M}_x & 0 \\ 0 & \boldsymbol{M}_y \end{bmatrix}, [\boldsymbol{G}] = \begin{bmatrix} 0 & \boldsymbol{G}_{xy} \\ -\boldsymbol{G}_{yx} & 0 \end{bmatrix}, [\boldsymbol{C}] = \begin{bmatrix} \boldsymbol{C}_x & 0 \\ 0 & \boldsymbol{C}_y \end{bmatrix},$$
$$[\boldsymbol{K}] = \begin{bmatrix} \boldsymbol{K}_x & 0 \\ 0 & \boldsymbol{K}_y \end{bmatrix}, [\boldsymbol{C}_r] = \begin{bmatrix} 0 & \boldsymbol{C}_{rxy} \\ -\boldsymbol{C}_{ryx} & 0 \end{bmatrix}.$$

where matrices with subscripts x and y are the same as complex coordinates, except for when the sign of elements with subscripts made up of two numbers

whose sum is odd. Matrices with subscripts xy and yx have signs that differ from those of the corresponding matrices in Eq. (4.65), so global gyroscopic and rotating damping matrices are skew-symmetrical. $\{\boldsymbol{u}^*\} = \{X, \varphi_{X'}, Y, \varphi_y\}^{\mathrm{T}}$ is the generalized coordinates [see Eq. (4.48)].

4.2.4 Dynamic Equation in Rotating Coordinates

A set of complex coordinates $\{\boldsymbol{r}\}$, related to coordinates $\{\boldsymbol{q}\}$, can be obtained through the relationship

$$\{\boldsymbol{r}\} = \{\boldsymbol{q}\}\mathrm{e}^{\mathrm{i}\Omega t} \tag{4.66}$$

and the equation of motion (4.51) transforms into the following equation in rotating coordinates:

$$\begin{aligned}&[\boldsymbol{M}]\{\ddot{\boldsymbol{r}}\} + ([\boldsymbol{C}_n] + [\boldsymbol{C}_r] + \mathrm{i}\Omega(2[\boldsymbol{M}] - [\boldsymbol{G}]))\{\dot{\boldsymbol{r}}\} + \\ &\left([\boldsymbol{K}] - \Omega^2([\boldsymbol{M}] - [\boldsymbol{G}]) + \mathrm{i}\Omega[\boldsymbol{C}_n]\right)\{\boldsymbol{r}\} = \Omega^2\{\boldsymbol{f}\}\end{aligned} . \tag{4.67}$$

In rotating coordinates, the relevant equation can be easily derived after separating the real and imaginary parts of Eq. (3.35). The gyroscopic, Coriolis, and non-rotating damping terms give way to skew-symmetrical matrices. Use of rotating coordinates, which is not very convenient in axi-symmetrical systems, becomes advisable when one is dealing with machines including an anisotropic rotor.

4.3 Anisotropic Rotordynamics

Rotors studied in previous sections are axisymmetrical. In this section the assumptions will be replaced by more general models in order that the effects of axial symmetry in the rotor could be studied (see Genta 2005).

4.3.1 Jeffcott Rotor on Anisotropic Supports

Consider the rotor in Fig. 4.4b and suppose that the stiffness of its supports is not isotropic on the xy-plane. All other assumptions of the linear rotor system remain the same. The motion on the xy-plane will be studied where the polar diagram of support-stiffness is an ellipse. Axes x and y are the principal axes of stiffness ellipse of supports elasticity. This elasticity along the x-direction is lower than that along y-direction. Elastic reaction of the shaft is

$$F_x = -k_x x\,,\; F_y = -k_y y. \tag{4.68}$$

Two different values of stiffness could be introduced into the equation of motion, and the latter transforms into

$$\begin{cases} m\ddot{x} + k_x x = m\varepsilon\left[\dot{\theta}^2\cos\theta + \ddot{\theta}^2\sin\theta\right] \\ m\ddot{y} + k_y y = m\varepsilon\left[\dot{\theta}^2\sin\theta - \ddot{\theta}^2\cos\theta\right] \end{cases}. \tag{4.69}$$

Consider that spin speed is constant, i.e., $\dot{\theta} = \Omega$, and $\ddot{\theta} = 0$. From the homogeneous equation, it is clear that there are two natural frequencies, the lower one is related to motion in the xz-plane and the other related to motion in the yz-plane:

$$\Omega_{n1} = \sqrt{k_x/m},\; \Omega_{n2} = \sqrt{k_y/m}. \tag{4.70}$$

Neither one is influenced by spin speed. At the first critical speed the motion reduces to a straight vibration along x-axis, and at the other critical speed a straight motion along y-axis.

Unbalance response can be obtained directly from Eq. (4.70) with $\ddot{\theta} = 0$. Response in each plane equals that of the Jeffcott rotor

$$x_0 = \frac{m\varepsilon\Omega^2}{k_x - m\Omega^2},\;\; y_0 = \frac{m\varepsilon\Omega^2}{k_y - m\Omega^2}. \tag{4.71}$$

The unbalance response can be subdivided into three speed ranges (Fig. 4.10).

Responses in the two planes are in same sign and are out of phase from each other by 90°, as shown in Eq. (4.70). Orbit grows mainly along x axis and exhibits the shape of an elongated ellipse. Approaching the first critical speed, axis of

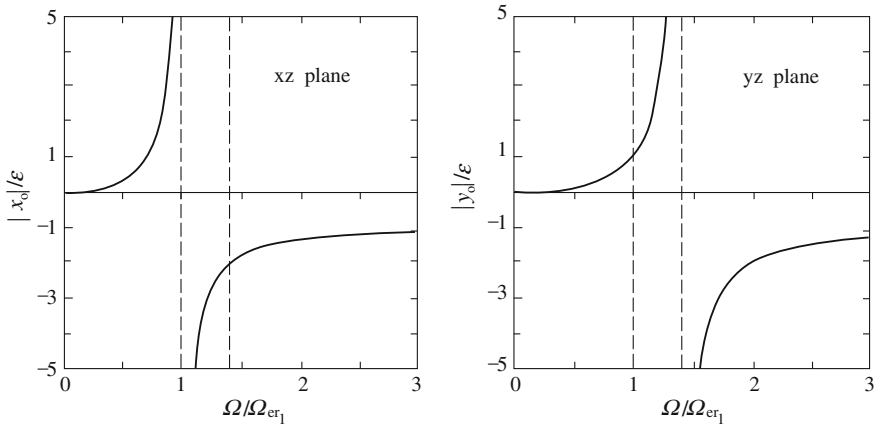

Fig. 4.10 Unbalance response of a Jeffcott rotor on anisotropic supports Amplitude of the motion along the x- and y-axes as a function of the speed

the orbit along the x-axis tends to infinity. One can get the same situation along the y-axis.

The mean and the deviatory stiffness are

$$k_m = 0.5\left(k_x + k_y\right), \quad k_d = 0.5\left(k_x - k_y\right). \tag{4.72}$$

Thus, the equation for unbalance response in terms of complex coordinates is

$$m\ddot{z} + k_m z + k_d \bar{z} = m\varepsilon\Omega^2 \mathrm{e}^{\mathrm{i}\Omega t} \tag{4.73}$$

where $\bar{z}$ is the conjugate of the complex number z. The solution of the homogeneous equation is in the form:

$$z = z_1 \mathrm{e}^{\mathrm{i}\omega t} + z_2 \mathrm{e}^{\mathrm{i}\bar{\omega} t}$$

which gives way to elliptical orbits. It can be introduced into the homogeneous equation of motion, yielding values of whirl frequencies. The unbalance response of Eq. (4.74) is obtained as follows:

$$z = \frac{m\varepsilon\Omega^2}{\left(k_x - m\Omega^2\right)\left(k_y - m\Omega^2\right)} \left[\left(k_m - m\Omega^2\right)\mathrm{e}^{\mathrm{i}\Omega t} - k_d \mathrm{e}^{-\mathrm{i}\Omega t}\right]. \tag{4.74}$$

The possibility of backward whirling to be excited by unbalance is, however, more obvious when complex coordinates are used. At the speed

$$\Omega_b = \sqrt{k_m/m}$$

the amplitude of the forward component vanishes, and the orbit is a circular backward whirl with amplitude

$$z_{0b} = \varepsilon k_d / k_m.$$

If the system is damped, the field in which backward whirling occurs is either reduced or cut out if damping is large enough. In the proximity of first critical speed, amplitude of elliptical orbits remains limited while the axis of the ellipse is not exactly aligned with one of the axes of support elasticity.

4.3.2 Anisotropic Jeffcott Rotor

Consider a Jeffcott rotor shown in Fig. 4.4a, whose stiffness is anisotropic. The polar diagram of stiffness is an ellipse lying along ξ and η-axes. An equation similar to Eq. (4.69) referred to $O\xi\eta z$ frame could be written as

$$F_\xi = -k_\xi \xi, \; F_\eta = -k_\eta \eta.$$

When dealing with rotating asymmetry, one could write the equation of motion with reference to the rotating $O\xi\eta z$-frame by introducing mean and deviatory stiffness and by neglecting damping, i.e.,

$$m\ddot{\varsigma} + 2im\Omega\dot{\varsigma} - m\Omega^2\varsigma + k_m\varsigma + k_d\bar{\varsigma} = m\varepsilon\Omega^2 e^{i\alpha} \tag{4.75}$$

where α is the angle between the ξ-axis and the direction of unbalance vector in the $\xi\eta$-plane. The unbalance response is easily obtained as a steady-state solution of the equation:

$$\xi = \frac{m\varepsilon\Omega^2 \cos\alpha}{k_\xi - m\Omega^2},\ \eta = \frac{m\varepsilon\Omega^2 \sin\alpha}{k_\eta - m\Omega^2}. \tag{4.76}$$

Critical speeds of the system are

$$\Omega_{cr1} = \sqrt{k_\xi/m},\ \Omega_{cr2} = \sqrt{k_\eta/m}. \tag{4.77}$$

A free whirling solution of the homogeneous equation (4.76) is

$$\xi = \xi_0 e^{i\omega' t},\ \eta = \eta_0 e^{i\omega' t}$$

where ω' is a complex whirl speed in $\xi\eta$-plane which does not coincide with the whirl speed ω in xy-plane. If stiffness ratio α^* is greater than unity (i.e., $k_\xi < k_\eta$), its first real dimensionless solutions can be expressed from the characteristic equation:

$$\omega'^{*2} = \Omega^{*2} + \frac{1+\alpha^*}{2} \pm \sqrt{\Omega^{*2}(1+\alpha^*) + \frac{(1+\alpha^*)^2}{4}} \tag{4.78}$$

where

$$\omega'^* = \frac{\omega'}{\Omega_{crI}},\ \omega^* = \frac{\omega}{\Omega_{crI}}\ \Omega^* = \frac{\Omega}{\Omega_{crI}}\ \alpha^* = \frac{k_\eta}{k_\xi}.$$

As α^* is assumed to be greater than unity, i.e.,

$$\Omega^* < 1;\ \alpha^* < \Omega^*,\ \text{i.e. } \Omega < \sqrt{k_\xi/m};\ \sqrt{k_\eta/m} < \Omega. \tag{4.79}$$

The characteristic equation owns four real roots—two positive and two negative. The system behavior is stable. If, however, value of spin speed Ω lies between two critical speeds of the system, shown in Eq. (4.80), two imaginary roots are found. Because the equation of motion has real coefficients, the solutions are conjugate numbers. Yet, if the real parts vanish, the solutions have opposite signs which leads to a negative imaginary solution that corresponds to an unstable behavior of the system and an amplitude that grows indefinitely with exponential law. The presence of an elastic anisotropy of the system's rotating parts gives rise to an instability range that spans from the lowest to the highest critical speed.

The Campbell diagram $\omega(\Omega)$ for a system with $\alpha^* = 2$ obtained from Eq. (4.79) is plotted in Fig. 4.11. All four quadrants of the $\omega\Omega$-plane have been reported, even if just two of them, i.e., the first and fourth render a complete picture of the situation.

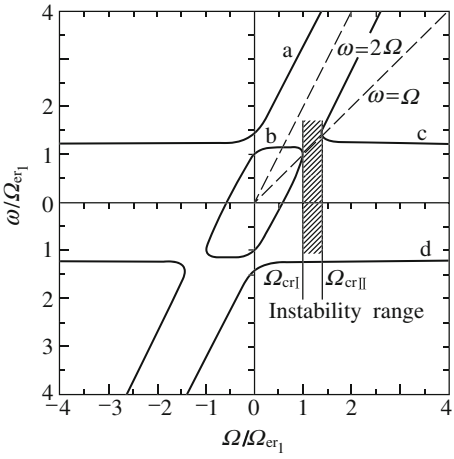

Fig. 4.11 Campbell diagram for an anisotropic Jeffcott rotor; ratio between the stiffness in the two planes

Rotating damping, which invokes instability of the system at high speed, also could cut the instability range between critical speeds. A similar effect is due to non-rotating damping, which is stabilizing at any speed. The higher the damping is, the smaller the instability range gets. The damped system's homogeneous equation of motion in the rotating frame is

$$\begin{bmatrix} m & 0 \\ 0 & m \end{bmatrix} \begin{Bmatrix} \ddot{\xi} \\ \ddot{\eta} \end{Bmatrix} + \begin{bmatrix} c_n + c_r & -2m\Omega \\ 2m\Omega & c_n + c_r \end{bmatrix} \begin{Bmatrix} \dot{\xi} \\ \dot{\eta} \end{Bmatrix} + \begin{bmatrix} k_\xi - m\Omega^2 & -\Omega c_n \\ \Omega c_n & k_\eta - m\Omega^2 \end{bmatrix} \begin{Bmatrix} \xi \\ \eta \end{Bmatrix} = 0. \tag{4.80}$$

The solution for free whirling could be introduced to get characteristic equation.

4.3.3 Secondary Critical Speeds Due to Rotor Weight

Speed will be referred to as secondary critical speed when the resonance frequency is between one of the system's natural frequencies and an exciting force that is different from the rotating force due to unbalance. When constant bending forces, such as inherent weight of a horizontal axis rotor, act on the rotor, the critical speed is not influenced. Whirling takes place about the deflected configuration of the rotor, yet, thanks to linearity, the two effects, namely, static bending and whirling do not interact. Rotor weight can cause the occurrence of secondary critical speeds, whose values are about half of those of primary critical speeds, or those located at intersections on the Campbell diagram of curves for free whirling with straight line $\omega = 2\Omega$. These secondary critical speeds are linked to deviations from a perfect axial symmetry of the rotor.

In a previously studied Jeffcott rotor, these secondary critical speeds are easily deduced from Fig. 4.11. The value of secondary critical speeds for the Jeffcott rotor in Fig. 4.11 can be computed as follows:

$$\Omega^* = \sqrt{k_\xi k_\eta / \left[2\left(k_\xi + k_\eta\right)\right]}. \tag{4.81}$$

If k_ξ and k_η tend to a single value $k \cdot \alpha^* \to 1$, the value of secondary critical speed becomes

$$\Omega_{crs} = \frac{1}{2}\sqrt{k/m} = \frac{1}{2}\Omega_{cr} \tag{4.82}$$

4.3.4 Equation of Motion for an Anisotropic System

In this section, equations of motion of systems with both anisotropic stator and rotor, with only anisotropic stator, as well as with only anisotropic rotor are discussed.

4.3.4.1 Equation of the System with Anisotropic Stator and Rotor

Consider a beam element of the type shown in Fig. 4.12, for which all the assumptions of uncoupling among flexural, torsional, and axial behavior would hold. If the principal axes of inertia and elasticity exist in *xz*- and *yz*-planes (hereafter designated by subscripts *x* and *y*), the mass and stiffness matrices for flexural behavior is written in the form:

$$[\boldsymbol{M}] = \begin{bmatrix} \boldsymbol{M}_x & 0 \\ 0 & \boldsymbol{M}_y \end{bmatrix}, \; [\boldsymbol{K}] = \begin{bmatrix} \boldsymbol{K}_x & 0 \\ 0 & \boldsymbol{K}_y \end{bmatrix} \tag{4.83}$$

where the matrices are related to the two bending planes. In the following analytical development, generalized coordinates for rotation in the *yz* -plane will be $-\varphi_x$ instead of φ_x so that matrices related to *xz* - and *yz* -planes are equal if an element is axisymmetrical.

When assembling the structure, one assumes that the global reference frame possesses the same *z*-axis as those of each element, but the *x*-axes of the elements are twisted by an angle α with respect to the global reference frame.

After introduction of mean and deviatory stiffness matrices of the elements, the stiffness matrix in the global reference frame is

$$\left[\boldsymbol{K}_g\right] = \begin{bmatrix} \boldsymbol{K}_m + \boldsymbol{K}_d \cos 2\alpha & \boldsymbol{K}_d \sin 2\alpha \\ \boldsymbol{K}_d \sin 2\alpha & \boldsymbol{K}_m - \boldsymbol{K}_d \cos 2\alpha \end{bmatrix} \tag{4.84}$$

where

$$[\boldsymbol{K}_m] = \left([\boldsymbol{K}_x] + [\boldsymbol{K}_y]\right)/2, \; [\boldsymbol{K}_d] = \left([\boldsymbol{K}_x] - [\boldsymbol{K}_y]\right)/2.$$

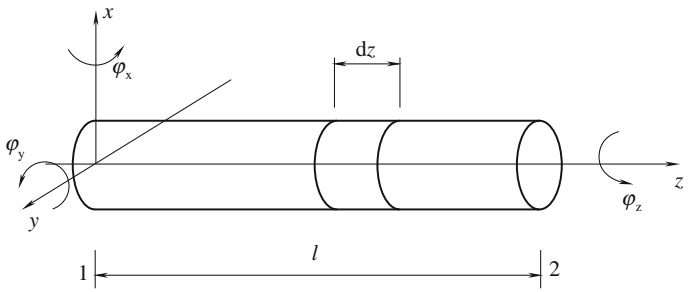

Fig. 4.12 Beam element: geometrical definitions and reference frame

If the element belongs to the rotor, angle α must be substituted by $\alpha + \theta$, or, and in the case of constant spin speed Ω, by $\alpha + \Omega t$. All the aforementioned considerations hold for mass and damping matrices and for elements other than beam elements. In general, rotating elements must be assembled separately from non-rotating elements.

Due to the presence of deviatory matrices, the structure of the assembled matrices is more complex than that of Eq. (4.84). For the assembled stiffness matrix it follows that

$$[\boldsymbol{K}] = \begin{bmatrix} \boldsymbol{K}_x & \boldsymbol{K}_{xy} \\ \boldsymbol{K}_{yx} & \boldsymbol{K}_y \end{bmatrix}. \tag{4.85}$$

Due to the coupling terms of the *xy* and *yx* subscripts, a definition of mean and deviatory matrices for the whole structure is needed, i.e.,

$$\begin{cases} [\boldsymbol{K}_m] = \dfrac{1}{2}\left([\boldsymbol{K}_x] + [\boldsymbol{K}_y]\right) + \mathrm{i}\dfrac{1}{2}\left([\boldsymbol{K}_{yx}] - [\boldsymbol{K}_{xy}]\right) \\ [\boldsymbol{K}_d] = \dfrac{1}{2}\left([\boldsymbol{K}_x] - [\boldsymbol{K}_y]\right) + \mathrm{i}\dfrac{1}{2}\left([\boldsymbol{K}_{yx}] + [\boldsymbol{K}_{xy}]\right) \end{cases}. \tag{4.86}$$

Except in the above-mentioned case of elements used for linearized modeling of hydrodynamic bearings, matrices with subscripts *xy* and *yx* are equivalent and the mean matrices are real, whereas deviatory matrices are complex. With the help of the complex coordinate approach and definitions of mean and deviatory matrices given by Eq. (4.87), one could write the equation of motion describing flexural behavior of a general system containing stationary elements and elements rotating at constant spin speed Ω as

$$\begin{aligned} &[\boldsymbol{M}_m]\{\ddot{\boldsymbol{q}}\} + ([\boldsymbol{C}_m] - \mathrm{i}\Omega[\boldsymbol{G}])\{\dot{\boldsymbol{q}}\} + ([\boldsymbol{K}_m] - \mathrm{i}\Omega[\boldsymbol{C}_{rm}])\{\boldsymbol{q}\} \\ &+[\boldsymbol{M}_{nd}]\{\ddot{\bar{\boldsymbol{q}}}\} + [\boldsymbol{M}_{rd}]\mathrm{e}^{2\mathrm{i}\Omega t}\{\ddot{\bar{\boldsymbol{q}}} + 2\mathrm{i}\Omega\dot{\bar{\boldsymbol{q}}}\} + [\boldsymbol{C}_{nd}]\{\dot{\bar{\boldsymbol{q}}}\} + [\boldsymbol{C}_{rd}]\{\mathrm{e}^{2\mathrm{i}\Omega t}\dot{\bar{\boldsymbol{q}}}\} \\ &+[\boldsymbol{K}_{nd}]\{\bar{\boldsymbol{q}}\} + ([\boldsymbol{K}_{rd}] - \mathrm{i}\Omega[\boldsymbol{C}_{rd}])\mathrm{e}^{2\mathrm{i}\Omega t}\{\bar{\boldsymbol{q}}\} = \{\boldsymbol{F}_n\} + \Omega^2\{\boldsymbol{F}_r\}\mathrm{e}^{\mathrm{i}\Omega t} \end{aligned} \tag{4.87}$$

.

Matrices and vectors with subscript r refer to rotating elements, and those with subscript n refer to stator ones. Mean matrices without r or n subscripts are related to the whole system. A non-rotating force vector is designated to static forces, while rotating vector forces that are stationary in a reference frame rotate at spin speed Ω.

If neither the stator nor the rotor is axisymmetrical, and the coefficients are periodic functions of time with period π/Ω, solution of the homogeneous equation associated with Eq. (4.88) is of the type:

$$\{\boldsymbol{q}\}=\{\boldsymbol{q}_{1j}(t)\}\mathrm{e}^{\mathrm{i}\omega t}+\{\boldsymbol{q}_{2j}(t)\}\mathrm{e}^{-\mathrm{i}\bar{\omega}t}.$$

The general solution is then a sum of the number of those terms, each with its value of ω, plus a solution of the complete equation. Unknown functions $\{\boldsymbol{q}_1(t)\}$ and $\{\boldsymbol{q}_2(t)\}$ can be expressed with trigonometric series:

$$\{\boldsymbol{q}\}=\sum_{j=-\infty}^{\infty}\{\boldsymbol{q}_{1j}(t)\}\mathrm{e}^{\mathrm{i}(\omega+2j\Omega)t}+\{\boldsymbol{q}_{2j}(t)\}\mathrm{e}^{-\mathrm{i}(\bar{\omega}+2j\Omega)t}. \tag{4.88}$$

Equation (4.90) is then introduced into the homogeneous equation associated with Eq. (4.88), and the following equation is obtained:

$$\begin{aligned}&\sum_{j=-\infty}^{\infty}[\boldsymbol{A}_j]\{\boldsymbol{q}_{1j}\}\mathrm{e}^{\mathrm{i}(\omega+2j\Omega)t}+[\bar{\boldsymbol{B}}_j]\{\boldsymbol{q}_{2j}\}\mathrm{e}^{-\mathrm{i}(\bar{\omega}+2j\Omega)t}+[\bar{\boldsymbol{C}}_j]\{\bar{\boldsymbol{q}}_{1j}\}\mathrm{e}^{-\mathrm{i}(\bar{\omega}+2j\Omega)t}+\\&[\boldsymbol{D}_j]\{\bar{\boldsymbol{q}}_{2j}\}\mathrm{e}^{\mathrm{i}(\omega+2j\Omega)t}+[\bar{\boldsymbol{E}}_j]\{\bar{\boldsymbol{q}}_{1j}\}\mathrm{e}^{-\mathrm{i}(\bar{\omega}+2(j-1)\Omega)t}+[\boldsymbol{F}_j]\{\bar{\boldsymbol{q}}_{2j}\}\mathrm{e}^{\mathrm{i}(\omega+2(j+1)\Omega)t}=0\end{aligned} \tag{4.89}$$

where

$$\begin{aligned}[\boldsymbol{A}_j]&=-(\omega+2j\Omega)^2[\boldsymbol{M}_m]+\Omega(\omega+2j\Omega)[\boldsymbol{G}]+\mathrm{i}(\omega+2j\Omega)[\boldsymbol{C}_m]+[\boldsymbol{K}_m]-\mathrm{i}\Omega[\boldsymbol{C}_{rm}]\\[\bar{\boldsymbol{C}}_j]&=-(\omega+2j\Omega)^2[\bar{\boldsymbol{M}}_{nd}]+\mathrm{i}(\omega+2j\Omega)[\bar{\boldsymbol{C}}_{nd}]+[\bar{\boldsymbol{K}}_{nd}]\\[\boldsymbol{D}_j]&=-(\omega+2j\Omega)^2[\boldsymbol{M}_{nd}]+\mathrm{i}(\omega+2j\Omega)[\boldsymbol{C}_{nd}]+[\boldsymbol{K}_{nd}]\\[\bar{\boldsymbol{E}}_j]&=-\left(\omega^2-2\omega\Omega(2j-1)-4j\Omega^2(j-1)\right)^2[\bar{\boldsymbol{M}}_{nd}]+\mathrm{i}(\omega+2j\Omega)[\bar{\boldsymbol{C}}_{rd}]+[\bar{\boldsymbol{K}}_{rd}]-\mathrm{i}\Omega[\bar{\boldsymbol{C}}_{rd}]\\[\boldsymbol{F}_j]&=-\left(\omega^2-2\omega\Omega(2j+1)-4j\Omega^2(j+1)\right)^2[\boldsymbol{M}_{nd}]+\mathrm{i}(\omega+2j\Omega)[\boldsymbol{C}_{rd}]+[\boldsymbol{K}_{rd}]+\mathrm{i}\Omega[\boldsymbol{C}_{rd}]\end{aligned}$$

4.3.4.2 Equations of a System with Anisotropic Stator

Consider a system described by Eq. (4.88), but with an isotropic rotor. The simplest system of this type is the Jeffcott rotor on anisotropic supports. With all deviatory matrices related to the rotor vanishing, Eq. (4.88) reduces to the following differential equation with constant coefficients in complex coordinates:

$$\begin{aligned}&[\boldsymbol{M}_m]\{\ddot{\boldsymbol{q}}\}+([\boldsymbol{C}_m]-\mathrm{i}\Omega[\boldsymbol{G}])\{\dot{\boldsymbol{q}}\}+([\boldsymbol{K}_m]-\mathrm{i}\Omega[\boldsymbol{C}_{rm}])\{\boldsymbol{q}\}\\&+[\boldsymbol{M}_{nd}]\{\ddot{\bar{\boldsymbol{q}}}\}+[\boldsymbol{C}_{nd}]\{\dot{\bar{\boldsymbol{q}}}\}+[\boldsymbol{K}_{nd}]\{\bar{\boldsymbol{q}}\}=\{\boldsymbol{F}_n\}+\Omega^2\{\boldsymbol{F}_r\}\mathrm{e}^{\mathrm{i}\Omega t}.\end{aligned} \tag{4.90}$$

The solution for static loading, $\{\boldsymbol{f}_n\}$, is similar to the corresponding solution for axisymmetrical systems, i.e., a solution vector $\{\boldsymbol{q}\} = \{\boldsymbol{q}_0\}$, leading to

$$([\boldsymbol{K}_m] - \mathrm{i}\Omega[\boldsymbol{C}_{rm}])\{\boldsymbol{q}_0\} + [\boldsymbol{K}_{nd}]\{\bar{\boldsymbol{q}}_0\} = \{\boldsymbol{f}_n\}. \tag{4.91}$$

The unbalance response is a synchronous elliptical whirling. The solution to the equation of motion can be expressed as

$$q = q_1 \mathrm{e}^{\mathrm{i}\Omega t} + q_2 \mathrm{e}^{-\mathrm{i}\Omega t}$$

i.e., as the sum of two circular whirling motions emerging at speed Ω in opposite directions. Both q_1 and q_2 are complex vectors, that physically correspond to elliptical orbits without axes x and y as symmetrical axes.

Orbits of the system are elliptical in free whirling. The relevant solution of the homogeneous equation of motion is in the form of $q = q_1 \mathrm{e}^{\mathrm{i}\Omega t} + q_2 \mathrm{e}^{\mathrm{i}\Omega t}$ which give rise to the following algebraic equation:

$$\left(-\omega^2 \begin{bmatrix} \boldsymbol{M}_m & \boldsymbol{M}_{nd} \\ \bar{\boldsymbol{M}}_{nd} & \boldsymbol{M}_m \end{bmatrix} + \omega\Omega \begin{bmatrix} \boldsymbol{G} & 0 \\ 0 & \boldsymbol{G} \end{bmatrix} + \mathrm{i}\omega \begin{bmatrix} \boldsymbol{C}_m & \boldsymbol{C}_{nd} \\ \bar{\boldsymbol{C}}_{nd} & \bar{\boldsymbol{C}}_m \end{bmatrix} + \begin{bmatrix} \boldsymbol{K}_m & \boldsymbol{K}_{nd} \\ \bar{\boldsymbol{K}}_{nd} & \bar{\boldsymbol{K}}_m \end{bmatrix} - \mathrm{i}\Omega \begin{bmatrix} \boldsymbol{C}_r & 0 \\ 0 & -\boldsymbol{C}_r \end{bmatrix}\right) \begin{Bmatrix} \boldsymbol{q}_1 \\ \bar{\boldsymbol{q}}_2 \end{Bmatrix} = 0. \tag{4.92}$$

Generally speaking, Eq. (4.93) yields a set of $2n$ equations.

4.3.4.3 Equations of a System with Anisotropic Rotor

Consider a system modeled in Eq. (4.88), only the stator is isotropic. The simplest system of this type is the anisotropic Jeffcott rotor. With all deviatory matrices related to the stator vanishing, Eq. (4.88) reduces to

$$\begin{aligned} &[\boldsymbol{M}_m]\{\ddot{\boldsymbol{q}}\} + ([\boldsymbol{C}_m] - \mathrm{i}\Omega[\boldsymbol{G}])\{\dot{\boldsymbol{q}}\} + ([\boldsymbol{K}_m] - \mathrm{i}\Omega[\boldsymbol{C}_{rm}])\{\boldsymbol{q}\} + \\ &[\boldsymbol{M}_{rd}]\mathrm{e}^{2\mathrm{i}\Omega t}\{\ddot{\bar{\boldsymbol{q}}} + 2\mathrm{i}\Omega\dot{\bar{\boldsymbol{q}}}\} + [\boldsymbol{C}_{rd}]\{\mathrm{e}^{2\mathrm{i}\Omega t}\dot{\bar{\boldsymbol{q}}}\} + ([\boldsymbol{K}_{rd}] - \mathrm{i}\Omega[\boldsymbol{C}_{rd}])\mathrm{e}^{2\mathrm{i}\Omega t}\{\bar{\boldsymbol{q}}\} \\ &= \{\boldsymbol{F}_n\} + \Omega^2\{\boldsymbol{F}_r\}\mathrm{e}^{\mathrm{i}\Omega t}. \end{aligned} \tag{4.93}$$

Equation (4.94) can be transformed into an equation with constant coefficients by resorting to rotating coordinates:

$$\begin{aligned} &[\boldsymbol{M}_m]\{\ddot{\boldsymbol{r}}\} + ([\boldsymbol{C}_m] + \mathrm{i}\Omega(2[\boldsymbol{M}_m] - [\boldsymbol{G}]))\{\dot{\boldsymbol{r}}\} \\ &\quad + \left(-\Omega^2([\boldsymbol{M}_m] - [\boldsymbol{G}]) + [\boldsymbol{K}_m] + \mathrm{i}\Omega[\boldsymbol{C}_n]\right)\{\boldsymbol{r}\} + [\boldsymbol{M}_{rd}]\{\ddot{\bar{\boldsymbol{r}}}\} \\ &\quad + [\boldsymbol{C}_{rd}]\{\dot{\bar{\boldsymbol{r}}}\} + \left(\Omega^2[\boldsymbol{M}_{rd}] + [\boldsymbol{K}_{rd}]\right)\{\bar{\boldsymbol{r}}\} = \{\boldsymbol{F}_n\}\mathrm{e}^{-\mathrm{i}\Omega t} + \Omega^2\{\boldsymbol{F}_r\}. \end{aligned} \tag{4.94}$$

The unbalance response solution can be written with reference to the fixed frame as

$$\{\boldsymbol{q}\} = \{\boldsymbol{r}_1\} + \{\boldsymbol{r}_2\}\mathrm{e}^{2\mathrm{i}\Omega t}.$$

The obvious meaning of $\{\boldsymbol{r}_1\}$ is mean-inflected shape, which is fixed in space, and $\{\boldsymbol{r}_2\}$ is a component of deflected shape, which rotates at a speed of 2Ω. Static loading then triggers the onset of vibrations, which take place on the stator with a frequency 2Ω and the rotor with a frequency Ω.

By equating the matrix of the coefficient to zero, one arrives at an exigent problem in Ω with secondary critical speeds due to a constant load distribution. The unbalance response solution, $\{\boldsymbol{q}\} = \{\boldsymbol{r}_0\}\mathrm{e}^{\mathrm{i}\Omega t}$, at a given unbalance distribution can be derived from the following equation of motion in fixed reference frame if $\{\boldsymbol{r}\}$ is constant, i.e., $\{\boldsymbol{r}\} = \{\boldsymbol{r}_0\}$:

$$\left(-\Omega^2([\boldsymbol{M}_m] - [\boldsymbol{G}]) + [\boldsymbol{K}_m] + i\Omega[\boldsymbol{C}_n]\right)\{\boldsymbol{r}_0\} + \left(\Omega^2[\boldsymbol{M}_{rd}] + [\boldsymbol{K}_{rd}]\right)\{\bar{\boldsymbol{r}}_0\} = \Omega^2\{\boldsymbol{f}_r\}. \tag{4.95}$$

The response to unbalance is a pure circular synchronous whirling, and rotating damping has no impact on system behavior since the rotor does not vibrate but merely rotates in deflected configuration.

The solution for an elliptical whirling with respect to the rotating frame $\xi\eta z$ is in the term:

$$\{\boldsymbol{r}\} = \{\boldsymbol{r}_1\}\mathrm{e}^{\mathrm{i}\omega' t} + \{\boldsymbol{r}_2\}\mathrm{e}^{\mathrm{i}\omega' t}$$

which is from the algebraic equation as follows:

$$\left(-\omega'^2\begin{bmatrix}\boldsymbol{M}_m & \boldsymbol{M}_d\\ \bar{\boldsymbol{M}}_d & \bar{\boldsymbol{M}}_m\end{bmatrix} + \omega'\Omega\begin{bmatrix}2\boldsymbol{M}_m + \boldsymbol{G} & 0\\ 0 & 2\boldsymbol{M}_m + \boldsymbol{G}\end{bmatrix} + \mathrm{i}\omega'\begin{bmatrix}\boldsymbol{C}_m + \boldsymbol{C}_{rm} & \boldsymbol{C}_{rd}\\ \bar{\boldsymbol{C}}_{rd} & \bar{\boldsymbol{C}}_n + \bar{\boldsymbol{C}}_{rm}\end{bmatrix}\right.$$
$$\left. + \mathrm{i}\Omega\begin{bmatrix}\boldsymbol{C}_n & 0\\ 0 & -\bar{\boldsymbol{C}}_n\end{bmatrix} + \begin{bmatrix}-\boldsymbol{M}_m + \boldsymbol{G} & \boldsymbol{M}_d\\ \bar{\boldsymbol{M}}_d & -\boldsymbol{M}_m + \boldsymbol{G}\end{bmatrix} + \begin{bmatrix}\boldsymbol{K}_m & \boldsymbol{K}_{nd}\\ \bar{\boldsymbol{K}}_{nd} & \bar{\boldsymbol{K}}_m\end{bmatrix}\right)\begin{Bmatrix}\boldsymbol{r}_1\\ \boldsymbol{r}_2\end{Bmatrix} = 0. \tag{4.96}$$

The same solution in fixed frame is

$$\{\boldsymbol{q}\} = \{\boldsymbol{r}_1\}\mathrm{e}^{\mathrm{i}\omega t} + \{\boldsymbol{r}_2\}\mathrm{e}^{\mathrm{i}(2\Omega - \bar{\omega})t}$$

The equation of motion could be written directly in terms of fixed coordinates, where whirl speed ω is present instead of ω'.

4.4 Nonlinear Rotordynamics

When rotors contain nonlinear elements or work outside their linearity range, typical nonlinear phenomena, may emerge, such as jump, or even deterministic chaos. Behavior of both lubricated journal bearings and rolling-element bearings is strongly nonlinear to affect the rotor. In the meantime, many other mechanisms may have similar effects, including nonlinear elasticity or dry friction (see Genta 2005; Yamamoto and Ishida 2001).

4.4.1 Equations of the Nonlinear Jeffcott Rotor

Consider a Jeffcott rotor with elastic and damping forces that are nonlinear functions of displacement and velocity, respectively. Axial symmetry of the system, decides elastic force in the same direction as displacement and damping force parallel to velocity. Using complex coordinate $z = x + \mathrm{i}y$, one can express elastic force and the forces due to non-rotating and rotating damping as

$$\boldsymbol{F}_e = -kz[1 + f(|z|)] \tag{4.97a}$$

$$\boldsymbol{F}_{dn} = -c_n\dot{z}[1 + \beta_n(|\dot{z}|)] \tag{4.97b}$$

$$\boldsymbol{F}_{dr} = -c_r(\dot{z} - \mathrm{i}\Omega z)[1 + \beta_r(|\dot{z} - \mathrm{i}\Omega z|)] \tag{4.97c}$$

Substituting expressions of nonlinear forces into the equation of the Jeffcott rotor written with constant spin speed, one has

$$\begin{aligned} &m\ddot{z} + (c_n + c_r)\dot{z} + (k - \mathrm{i}\Omega c_r)z + [c_n\beta_n(|\dot{z}|) + c_r\beta_r(|\dot{z} - \mathrm{i}\Omega z|)]\dot{z} + \\ &kf(|z|)z - \mathrm{i}\Omega c_r\beta_r(|\dot{z} - \mathrm{i}\Omega z|)z = m\varepsilon\Omega^2\mathrm{e}^{\mathrm{i}\Omega t} + \boldsymbol{F}_n. \end{aligned} \tag{4.98}$$

Equation (4.101) can be utilized to study the free behavior of the system (free circular whirling), the effect of a static load $\boldsymbol{F}_n$ or that of an eccentricity of mass m.

4.4.2 Unbalance Response

Consider an undamped system whose model can be obtained from Eq. (4.101) when all terms connected with damping, linear and nonlinear, as well as nonrotating forces are neglected. A possible solution for response to static unbalance m is

$$Z = Z_0\mathrm{e}^{\mathrm{i}\Omega t}.$$

This solution could be introduced into the equation of motion, and the following algebraic equation is readily obtained:

$$\left[k - m\Omega^2 + kf(|z_0|)\right]z_0 = m\varepsilon\Omega^2 \tag{4.99}$$

where $f(|z_0|) = \mu|z_0|^2$ and μ is the coefficient of the nonlinear term of stiffness.

The backbone of the response can be acquired on condition that the unbalance is vanishingly small, i.e., through the homogeneous equation associated with Eq. (4.102).

Since whirling is circular, the nonlinear element rotates, maintaining a given deformation. Algebraic equation of static unbalance is

$$\left[1 - \frac{m}{k}\Omega^2 + f(|z_0|) + \mathrm{i}\Omega\frac{c_n}{k} + \mathrm{i}\Omega\frac{c_n}{k}\beta_n|\Omega z_0|\right]z_0 = \frac{m}{k}\varepsilon\Omega^2. \tag{4.100}$$

The rotating damping does not have a great influence on synchronous whirling. One can separate the real and imaginary parts of Eq. (4.103), and amplitude and phase Φ of state unbalance vector response are thus

$$\begin{gathered}\left[\left[1-\frac{m}{k}\Omega^2+f(|z_0|)\right]^2+\left(\Omega\frac{c_n}{k}\right)^2(1+\beta_n|\Omega z_0|)^2\right]|z_0|^2=\left(\frac{m}{k}\varepsilon\right)^2\Omega^4 \\ \Phi=-\arctan\left[\Omega c_n\frac{1+\beta_n|\Omega z_0|}{k-m\Omega^2+kf(|z_0|)}\right]\end{gathered} \tag{4.101}$$

where Φ is the phase of the unbalance vector along ξ-axis.

If phase Φ is $-90°$, the equation of the limit envelope of the response becomes

$$z_0c_n(1+\beta_n|\Omega z_0|)=m\varepsilon\Omega. \tag{4.102}$$

The limit envelope of linear damping is just a straight line as

$$z_0c_n=m\varepsilon\Omega.$$

4.4.3 Free Circular Whirling

A possible solution of homogeneous equation associated with Eq. (4.101), i.e., of the model for a perfectly balanced Jeffcott rotor, is

$$z=z_0\mathrm{e}^{\mathrm{i}\omega t}.$$

Suppose the damping is linear, and one could introduce a solution for circular free whirling into the homogeneous equation of motion to get:

$$\left\{1-\frac{m}{k}\omega^2+f(|z_0|)+\mathrm{i}\left[\omega\Omega\frac{c_n}{k}+(\omega-\Omega)\frac{c_r}{k}\right]\right\}z_0=0. \tag{4.103}$$

The solution of ω is obtained as

$$\begin{cases}\omega_R^*=\pm\sqrt{\Gamma^*+\sqrt{\Gamma^*+\Omega^{*2}\varsigma_r^2}} \\ \omega_I^*=\varsigma_n+\varsigma_r\mp\sqrt{-\Gamma^*+\sqrt{\Gamma^*+\Omega^{*2}\varsigma_r^2}}\end{cases} \tag{4.104}$$

where dimensionless speeds Ω^* and ω^*, and damping ratios ζ_n and ζ_r are defined with reference to the linearized system, and

$$\Gamma^*=\frac{1+f(|z_0|)-(\varsigma_n+\varsigma_n)^2}{2}.$$

Equation (4.107) is close in form to the corresponding expression for the linear case, and the only difference is that in the current case whirl speed is a function of

motion amplitude. A three-dimensional plot where amplitude $|z_0|$ is a function of Ω and ωR can be drawn in Fig. 4.13. Ω, ωR-plane of the three-dimensional plot is the Campbell diagram of linearized system. The first Eq. (4.107) defines a surface depicting all the possible conditions of free whirling, and it can be considered as the backbone of the system at varying spin-speed Ω. Intersection of the surface with $|z_0|$, ωR-plane could shed light on the relationship linking the natural frequency with amplitude at a standstill: It is then the backbone of non-rotating system for a whirling mode in the xy-plane.

One of the mentioned plots has been reported in dimensionless form in Fig. 4.13, which is for a system with $\zeta_n = \zeta_r = 0.3$. The stability threshold of the linearized system is $\Omega^* = 2$.

Intersection of the surface with plane $\omega = \Omega$ gives the conditions for free synchronous whirling. It then coincides with the backbone of the unbalance response shown in Fig. 4.13. From the second Eq. (4.107) condition for stability is confined to

$$\Omega < \sqrt{1 + f(|z_0|)}\sqrt{k/m}(1 + c_n/c_r). \tag{4.105}$$

Threshold of stability depends on the amplitude, as shown in Fig. 4.13, where the unstable part of the surface is dashed. If spin speed Ω is lower than the instability threshold of the linearized system, the motion is always stable because amplitude of free whirling decays to zero.

4.4.4 Stability of the Equilibrium Position

Stability of the equilibrium position for an unbalance system response can be derived in the same way as with linear systems. Consider a damped nonlinear Jeffcott rotor without any non-rotating force, whose elastic and damping forces

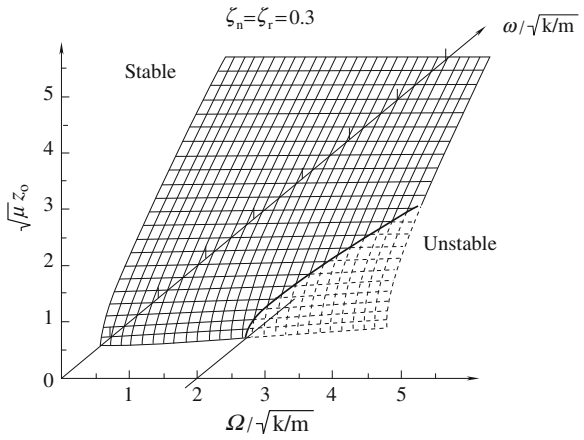

Fig. 4.13 3D plot for the study of the free whirling of the nonlinear Jeffcott rotor

have a cubic and linear characteristic, respectively, and neglect non-rotating forces. The equation of motion in rotating the $\xi\eta$ reference frame can be obtained:

$$\begin{aligned} m\ddot{\xi} + (c_n + c_r)\dot{\xi} - 2m\Omega\dot{\eta} + \left[k - m\Omega^2 + k\mu(\xi^2 + \eta^2)\right]\xi - c_n\Omega\eta &= m\varepsilon\Omega^2 \\ m\ddot{\eta} + (c_n + c_r)\dot{\eta} + 2m\Omega\dot{\xi} + \left[k - m\Omega^2 + k\mu(\xi^2 + \eta^2)\right]\eta + c_n\Omega\xi &= 0 \end{aligned} \tag{4.106}$$

The system behavior can be observed according to three dimensionless parameters: the damping ratios ζ_n and ζ_r and the nonlinear parameter 2μ. Equation (4.111) can also be used to study system motion under non-stationary conditions with reference to the rotating frame. The unbalance response can be immediately computed on the basis of a stationary solution in $\xi\eta$-plane. In a small proximity of equilibrium position, the equation of motion can be linearized, obtaining, in dimensionless terms,

$$\begin{aligned} &\begin{bmatrix} 1 & 0 \\ 0 & 1 \end{bmatrix} \begin{Bmatrix} \xi_1^{*\prime\prime} \\ \eta_1^{*\prime\prime} \end{Bmatrix} + \begin{bmatrix} 2(\zeta_n + \zeta_r) & -2\Omega^* \\ 2\Omega^* & 2(\zeta_n + \zeta_r) \end{bmatrix} \begin{Bmatrix} \xi_1^{*\prime} \\ \eta_1^{*\prime} \end{Bmatrix} + \\ &\begin{bmatrix} 1 - \Omega^{*2} + \mu^*\left(3\xi_0^{*2} + \eta_0^{*2}\right) & 2\left(-\Omega^*\zeta_n + \mu^*\xi_0^*\eta_0^*\right) \\ 2\left(\Omega^*\zeta_n + \mu^*\xi_0^*\eta_0^*\right) & 1 - \Omega^{*2} + \mu^*\left(3\xi_0^{*2} + \eta_0^{*2}\right) \end{bmatrix} \begin{Bmatrix} \xi_1^* \\ \eta_1^* \end{Bmatrix} = 0 \end{aligned} \tag{4.107}$$

where, apart from damping ratios and the usual dimensionless speed, other dimensionless quantities are defined as

$$\xi^* = \xi/\varepsilon,\ \eta^* = \eta/\varepsilon,\ \tau = t\sqrt{k/m},\ \mu^* = \mu\varepsilon^2$$

and prime denotes differentiation with respect to τ.

Stability of the motion in the vicinity of an equilibrium position can be assessed with the sign of decay rate of small vibrations. Because the solution of a simple fourth-degree algebraic equation is required, the study can be carried on in closed form.

A very general mathematical model of a nonlinear rotor can be established from Eq. (4.111) as long as a generic vector function $\{\boldsymbol{f}(\dot{\boldsymbol{q}}_i, \boldsymbol{q}_i, \theta, t)\}$ is added to include behavior of the nonlinear part of the system. Introducing the term $(\Omega^2 - ia)$ instead of Ω^2 to take into account angular accelerations:

$$\begin{aligned} &[\boldsymbol{M}_m]\{\ddot{\boldsymbol{q}}\} + ([\boldsymbol{C}_m] - \mathrm{i}\Omega[\boldsymbol{G}])\{\dot{\boldsymbol{q}}\} + ([\boldsymbol{K}_m] - \mathrm{i}\Omega[\boldsymbol{C}_{rm}])\{\boldsymbol{q}\} + [\boldsymbol{M}_{md}]\{\ddot{\bar{\boldsymbol{q}}}\} \\ &+ \quad [\boldsymbol{M}_{rd}]\mathrm{e}^{\mathrm{i}2\theta}\{\ddot{\bar{\boldsymbol{q}}}\} + [\boldsymbol{K}_{nd}]\{\bar{\boldsymbol{q}}\} + [\boldsymbol{C}_{nd}]\{\dot{\bar{\boldsymbol{q}}}\} + ([\boldsymbol{C}_{rd}] + \mathrm{i}2\Omega[\boldsymbol{M}_{rd}])\mathrm{e}^{\mathrm{i}2\theta}\{\dot{\bar{\boldsymbol{q}}}\} \\ &+ \quad ([\boldsymbol{K}_{rd}] + \mathrm{i}\Omega[\boldsymbol{C}_{rd}])\mathrm{e}^{\mathrm{i}2\theta}\{\bar{\boldsymbol{q}}\} + \{\boldsymbol{f}(\dot{\boldsymbol{q}}_i, \boldsymbol{q}_i, \theta, t)\} = \left(\Omega^2 - ia\right)\{\boldsymbol{f}_r\}\mathrm{e}^{\mathrm{i}\theta} + \{\boldsymbol{f}_n\}. \end{aligned} \tag{4.108}$$

Equation (4.113) can be gotten only with uncoupling among flexural, axial, and torsional behavior and neglecting centrifugal stiffening. The latter can be brought into scope simply via appropriate introduction of stiffness matrices proportional to Ω^2.

In general, it is reasonable to expect that time history of the accelerating system has a simpler expression in a rotating frame. As a result, one could apply rotating coordinates in Eq. (4.113), and it yields

$$\begin{aligned}
&[\boldsymbol{M}_m]\{\ddot{\boldsymbol{r}}\} + ([\boldsymbol{C}_m] + \ \mathrm{i}2\omega[\boldsymbol{M}_m] - \mathrm{i}\Omega[\boldsymbol{G}])\{\dot{\boldsymbol{r}}\} + ([\boldsymbol{K}_m] - \Omega^2[\boldsymbol{M}_m] + \\
&\Omega^2[\boldsymbol{G}] + \mathrm{i}a[\boldsymbol{M}_m] + \mathrm{i}\Omega[\boldsymbol{C}_{rm}])\{\boldsymbol{r}\} + ([\boldsymbol{C}_{rd}] + \mathrm{i}2\Omega[\boldsymbol{M}_{nd}])\mathrm{e}^{-\mathrm{i}2\theta}\{\dot{\bar{\boldsymbol{r}}}\} \\
&+ [\boldsymbol{M}_{nd}]\mathrm{e}^{-\mathrm{i}2\theta}\{\ddot{\bar{\boldsymbol{r}}}\} + \left([\boldsymbol{K}_{nd}] - \omega^2[\boldsymbol{M}_{nd}] - \mathrm{i}a[\boldsymbol{M}_{nd}] - \mathrm{i}\Omega[\boldsymbol{C}_{nd}]\right)\mathrm{e}^{-\mathrm{i}2\theta}\{\bar{\boldsymbol{r}}\} \qquad (4.109) \\
&+ [\boldsymbol{M}_{rd}]\{\ddot{\bar{\boldsymbol{r}}}\} + [\boldsymbol{C}_{rd}]\{\dot{\bar{\boldsymbol{r}}}\} + \left([\boldsymbol{K}_{rd}] + \Omega^2[\boldsymbol{M}_{rd}] - \mathrm{i}a[\boldsymbol{M}_{rd}]\right)\{\bar{\boldsymbol{r}}\} + \\
&\{\boldsymbol{f}'(\boldsymbol{r}_j, \dot{\boldsymbol{r}}_j, \theta, t)\}\mathrm{e}^{-\mathrm{i}\theta} = \left(\Omega^2 - ja\right)\{\boldsymbol{f}_r\} + \{\boldsymbol{f}_n\}\mathrm{e}^{-\mathrm{i}\theta}.
\end{aligned}$$

If angular acceleration is not small enough, Eq. (4.114) must be integrated numerically in time, and as a consequence there is no conceptual difficulty taking into account both nonlinearities and asymmetry.

References

Bucher, I. (2009). *Simple Jeffcott Rotor,* http://mechatronics.technion.ac.il/rotordynamics/pdf/Jeffcot.pdf.

Chen, W. J., & Gunter, E. J. (2005). *Introduction to dynamics of rotor-bearing systems*. Berlin: Springer.

Childs, D. (1993). *Turbomachinery Rotordynamics Phenomena, Modeling, and Analysis*. New York: Wiley.

Genta, G. (2005). *Dynamics of rotating systems*. Berlin: Springer.

Genta, G. (2008). *Vibration dynamics and control*. Berlin: Springer.

Krämer, E. (1993). *Dynamics of rotors and foundations*. New York: Springer.

Lalanne, M., & Ferraris, G. (1998). *Rotordynamics prediction in engineering* (2nd ed.). New York: Wiley.

Muszyńska, A. (2005). *Rotordynamics*. New York: CRC Press.

Nelson, F. (2007). Rotordynamics without equations, *International Journal of COMADEM* 10. ISSN 1363-7681.

Yamamoto, T., & Ishida, Y. (2001). *Linear and nonlinear rotordynamics*. New York: Wiley.

Part II
Excitation

Chapter 5
Mechanical and Magnetic Excitations in Hydraulic Machinery

Mechanical analysis of hydraulic machinery includes two fields, structural dynamics and rotor dynamics. Structural dynamics is a subset that covers areas of structural behavior subjected to dynamic loading. Rotordynamics is a specialized branch of applied mechanics concerned with the behavior and diagnosis of rotating structures (Ohashi 1991).

Generally, governing equations of a rotating mechanical system can be expressed as:

$$[\boldsymbol{M}]\{\ddot{\boldsymbol{u}}\} + ([\boldsymbol{C}] + \Omega[\boldsymbol{G}])\{\dot{\boldsymbol{u}}\} + ([\boldsymbol{K}] + \Omega[\boldsymbol{C}_r])\{\boldsymbol{u}\} = \Omega^2\{\boldsymbol{f}\} \tag{5.1}$$

where $[\boldsymbol{M}]$ is the mass matrix, $[\boldsymbol{C}]$ is the the damping matrix, $[\boldsymbol{G}]$ is the gyroscopic skew symmetric matrix, $[\boldsymbol{K}]$ is the stiffness matrix, $[\boldsymbol{C}_r]$ (or $[\boldsymbol{H}]/\Omega$) is the asymmetric part of rotating damping matrix, $\{\boldsymbol{u}\}$ is the displacement vector (including axial displacement as well) and $\{\boldsymbol{f}\}$ is the force of the unbalances—all expressed in real coordinates [see Eq. (4.64)].

If all matrices are expressed in complex coordinates, they are symmetric in a complex coordinate notation, whereas in real coordinates the gyroscopic matrix is a skew symmetric notation [see Eqs. (4.50), (4.51)].

Mechanical components of machine can produce excitation to vibration of both static structures and rotating structures, especially to the latter. The finite element method (FEM) is widely used in structural dynamic analysis, but in rotordynamic analysis, aside from the FEM, the Riccati transfer matrix method (RTMM) has been developed. There are three types of vibration in rotordynamics to be solved: flexural, torsional and axial. Considering the interaction between the first two types, the analysis model will be a nonlinear complex, as shown in Eq. (5.1). The alternating electro-magnetic force will act on the generator stator, which causes unbalance excitation on the torsional vibration of the shaft system during processes of unit start up, stop and load regulation.

Mechanical excitations inducing hydraulic machinery vibration are as follows (Swain 2008):

Y. Wu et al., *Vibration of Hydraulic Machinery*,
Mechanisms and Machine Science 11, DOI: 10.1007/978-94-007-6422-4_5,

1. Centrifugal forces due to imbalance of the rotating mass i.e., runner, shaft and generator rotor.
2. Elastic force of the shaft due to incorrect shaft alignment.
3. Frictional forces.
4. Oil-film instability in bearing.

Electrical excitations covered in this chapter are:

1. Magnetic forces between stator and rotor.
2. Forces due to non-uniform air gap between stator and rotor.
3. Forces created by partial or total short-circuiting of the pole winding of rotor.

Of course for different hydraulic machinery, mechanical excitation to vibration may include other factors.

5.1 Mechanical System of Hydraulic Machinery

In this section, the mechanical systems of hydraulic turbine generator units and pumps will be introduced, especially their shaft systems.

5.1.1 Mechanical System of Hydraulic Turbine Generator Unit

Figure 5.1 shows the structure of Francis turbine generator units, similar to other types. The main structural components to be examined include the runner, spiral casing, stay vanes and guide vanes, draft tube, shaft and flange connected to generator shaft (Wikipedia 2008).

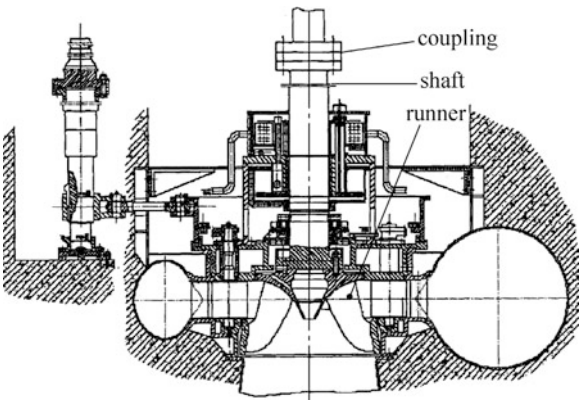

Fig. 5.1 Structure of the Francis turbine-generator units

5.1.1.1 The Turbine-Generator Shaft System

The main components of the turbine-generator shaft system consist of an upper guide bearing, generator rotor, thrust bearing, lower guide bearing, turbine guide bearing, and runner, etc. The left side of Fig. 5.2 illustrates the arrangement of a general hydraulic unit; it has an upper guide bearing (UGB) above the generator, a lower guide bearing (LGB) below the generator, a thrust bearing, and a turbine guide bearing (TGB) on the turbine head cover. The upper and lower guide bearings are center-pivoted with tilting-pads (they are journal bearings); and the turbine guide bearing is a circular bearing consisting of arcs. The thrust bearing is also a center-pivoted, tilting-pad bearing with several pads.

The shaft system has been simplified to resemble an equivalent shaft system for numerical analysis that contains several lumped masses with shaft spans shown on the right side of Fig. 5.2 in the transfer matrix method of a lumped-mass model (Feng and Chu 2001; Ma 2007).

In dynamic analysis, any structural system of hydraulic machinery must be simplified into a mechanical model. And different modeling would lead to distinct results in dynamical analysis. In RSMM, the runner can be modeled as a cylinder and the generator rotor as a rigid disc. Diverse models with dissimilar sustained conditions also exist in bearings.

In RTMM, as shown in Fig. 5.3, the disc rotor and a section of shaft can be jointed as a combined element of lumped mass and distributed shaft length. The coordinates and combined force acting on its end sections, shear Q and torque M are shown in Fig. 5.4 where moment of inertia must be considered.

5.1.1.2 Constrain Conditions of Supporting Points

For the shaft system, guide bearings and thrust bearings at supporting positions provide several constraint conditions to stabilize system rotation, as shown on the right side of Fig. 5.3. In numerical simulation, the following constraint conditions should be chosen (Wu 2002; Zhang 2006, 2008).

1. Complete rigid constraint. This type of constraint applies to sliding guide bearings as well as certain thrust bearings which are fixed on their brackets and

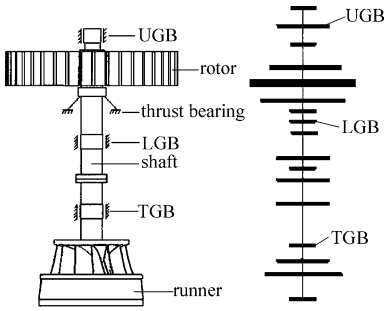

Fig. 5.2 Shaft system of turbine-generator units

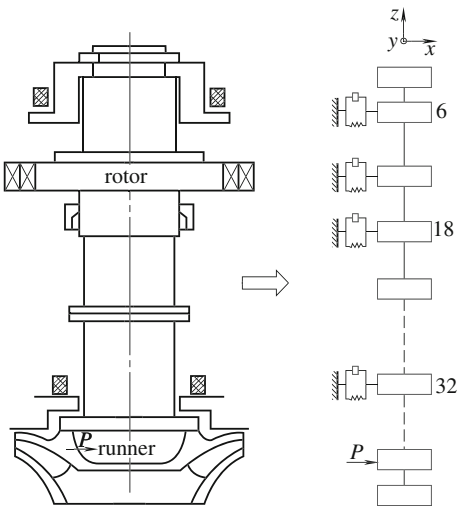

Fig. 5.3 Schematic drawing of the concentrated mass method of the shaft

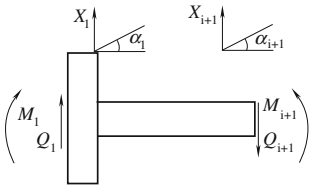

Fig. 5.4 Force analysis of combines

foundations with infinite stiffness. In those circumstances, only stiffness k and damping c of oil film in the bearings need to be considered as shown in Fig. 5.5 (see Kumar and Sankar 1986; Wu 2002).

2. Elastic constraint. If elastic constraint of brackets and foundations of bearings are considered, their stiffness k_b and damping c_b should be added as shown in Fig. 5.6.

The motion equation of lumped mass at the brackets of bearings is expressed as:

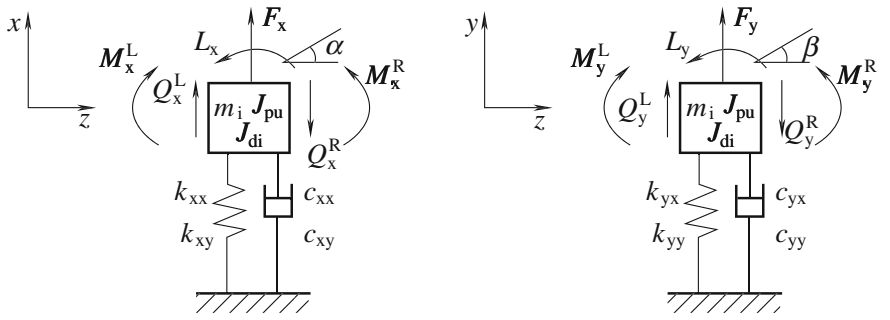

Fig. 5.5 Stiffness k and damping c of oil film at the bearings with rigid constraints

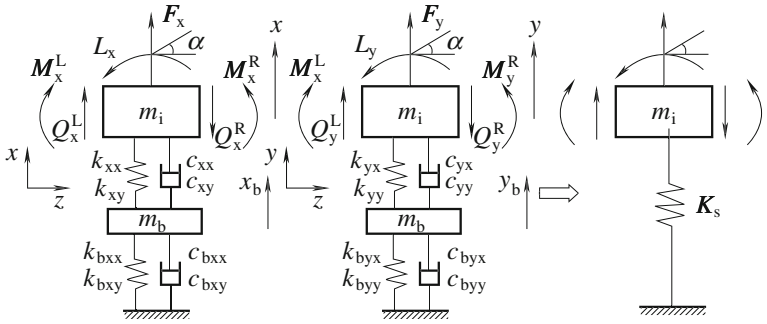

Fig. 5.6 Stiffness k and damping c of oil film at the bearings with *elastic brackets*

$$[\boldsymbol{M}_b]\{\ddot{\boldsymbol{u}}_b\} = -[\boldsymbol{K}_b]\{\boldsymbol{u}_b\} - [\boldsymbol{C}_b]\{\dot{\boldsymbol{u}}_b\} + [\boldsymbol{K}]\{\boldsymbol{u} - \boldsymbol{u}_b\} + [\boldsymbol{C}]\{\dot{\boldsymbol{u}} - \dot{\boldsymbol{u}}_b\} \tag{5.2}$$

where $[\boldsymbol{K}]$ is the stiffness matrix of oil film; $[\boldsymbol{C}]$ the damping matrix of oil film; and $[\boldsymbol{M}_b]$, $[\boldsymbol{K}_b]$, and $[\boldsymbol{C}_b]$ are the mass, stiffness, and damping matrices of the bearing brackets, respectively.

If $\{\boldsymbol{u}_b\}$ only describes displacement, then

$$[\boldsymbol{K}] = \begin{bmatrix} k_{xx} & k_{xy} \\ k_{yx} & k_{yy} \end{bmatrix},\ [\boldsymbol{C}] = \begin{bmatrix} c_{xx} & c_{xy} \\ c_{yx} & c_{yy} \end{bmatrix},\ [\boldsymbol{K}_b] = \begin{bmatrix} k_{bxx} & k_{bxy} \\ k_{byx} & k_{byy} \end{bmatrix},$$
$$[\boldsymbol{C}_b] = \begin{bmatrix} c_{bxx} & c_{bxy} \\ c_{byx} & c_{byy} \end{bmatrix},\ [\boldsymbol{M}_b] = \begin{bmatrix} m_b & 0 \\ 0 & m_b \end{bmatrix},\ \{\boldsymbol{u}\} = \begin{Bmatrix} x \\ y \end{Bmatrix} \text{ and } \{\boldsymbol{u}_b\} = \begin{Bmatrix} x_b \\ y_b \end{Bmatrix}.$$

In practical simulations, brackets of bearings are usually elastic, and damping of oil film may not be considered. The first order of critical speed is affected by bracket elasticity, especially by that of the upper guide bearing. Sometimes, both bracket elasticity and oil film damping may be included in the simulation. Damping effects mainly come from oil film, seal water, and water in the runner.

5.1.1.3 Torsional Vibration Model of a Turbine-Generator Unit

When torsion takes place in a unit's shaft system, an extra electro-magnetic force acts on the generator stator, one that is not generated by torsional interaction between the stator and its supports. The stator can be simplified as a rigid disc within the torsional model of the shaft system shown in Fig. 5.7, where J_1 and J_2 are the moment of inertia of the magnetic exciter (modern exciter is static type) and of the generator respectively; J_3 is the moment of inertia of the runner with water. M is the mass of yolks and the magnetic poles of the rotor. The rotor's supporting arms are modeled as beams without gravity. In fact, their gravity will be distributed to the rotor. The shaft's torsional angle and tangential displacement will be considered in simulation. Obviously, the rotor's momentum of inertia will greatly influence the torsional performance of the shaft system (see Jiang 2008).

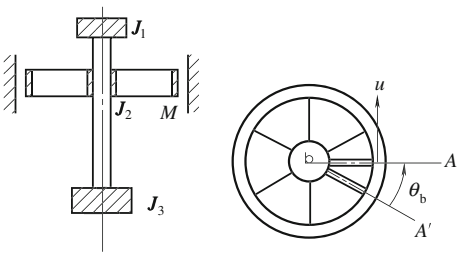

Fig. 5.7 Unit shaft and its torsional vibration system

5.1.1.4 FEM Model of the Shaft System of Turbine-Generator Units

Figure 5.8 shows the FEM model of the shaft system with three man components: shaft, rotor, and runner (Ma 2007).

Governing equations of a rotating mechanical system, Eq. (5.1) can be used to predict torsional, flexural, and axial vibrations interactively. In the non-rotating mode of a shaft system simulation, the Eigen frequency is determined by geometry, materials, and the constraints of the system which result in free vibration modes. Otherwise, the rotating mode will take into account centrifugal force and other unbalanced forces.

Similar simulations may also be carried out in static structures or individual components. In general, vibration modes would vary in the following sequence beginning from first order to high order, namely, from a simple mode to a complex one.

For the shaft system: torsional–swing–axial drawing–bending–radial drawing plus torsion.
For the rotor: torsional–swing–axial drawing–bending–radial drawing–torsion.
For the runner: torsional–swing–bending–twisting–drawing–swing torsion.
For the shaft itself: torsional(swing)–drawing–bidirectional bending–local bending–combined drawing.

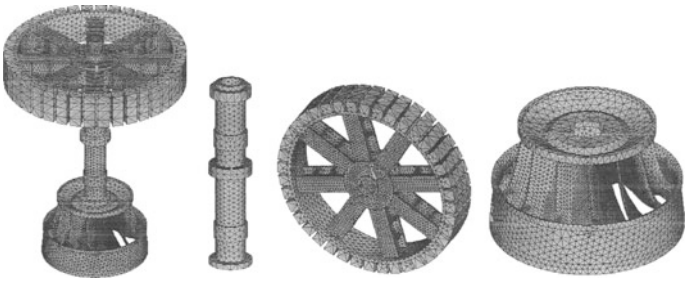

Fig. 5.8 FEA model of the shaft system

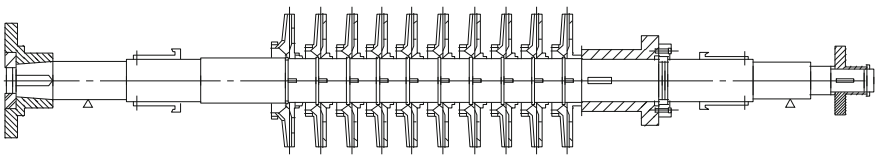

Fig. 5.9 Rotor system of multi-stage centrifugal pumpcentrifugal pump

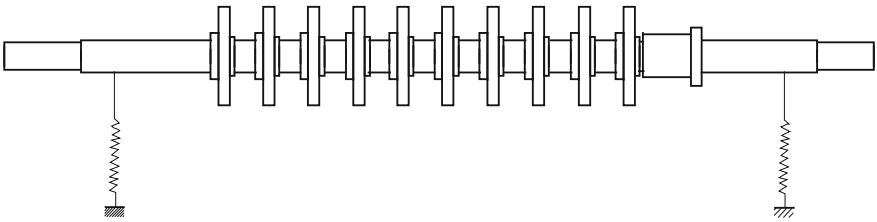

Fig. 5.10 Model of shaft operation in the air

5.1.2 Mechanical System of Pumps

The rotor system of an ultra-high-pressure multi-stage centrifugal pump works at high speeds with a long shaft and is featured in a complex structure shown in Fig. 5.9 (Chen et al. 2008).

The analysis of centrifugal pumps introduces the concept of "dry" and "wet" critical speeds. A "dry" critical speed does not take into consideration the effects of seal dynamic characteristics (Fig. 5.10), while a "wet" critical speed occurs when the pump is in a working station and dynamic characteristics of seal need to be considered (Fig. 5.11).

Table 5.1 lists calculation results of rotordynamics on two different rotor models. The first and second modes of free flexural vibration are in the "wet" model (Fig. 5.12).

5.2 Excitation Forces of Hydraulic Turbine Generator Unit

It is commonly known that large-scale and high-speed hydraulic machines can be exposed to severe vibration and excited mechanically, hydraulically, and electrically, particularly under transient operating conditions. To understand the dynamic response of the shaft system to radial forces, excitation forces should be determined first, including both amplitudes and frequencies. External excitation forces may be static, harmonic, or periodic; transient and stochastic; or any combination of these forces. Static forces that stem from hydraulic forces at the runner or from unbalanced magnetic forces at the generator, may result in static displacement of

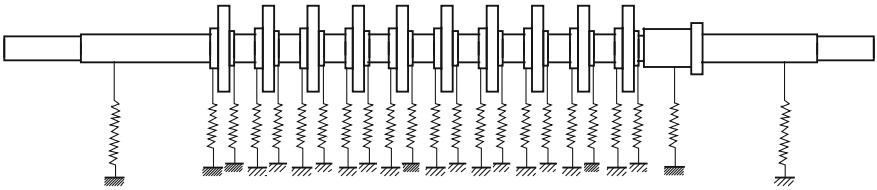

Fig. 5.11 Model of Shaft operation in the water

Table 5.1 The result of the calculation

Type of critical speed	First order bending (rpm)	Second order bending (rpm)
"dry" critical speed	3,158	9,731
"wet" critical speed	6,342	12,956

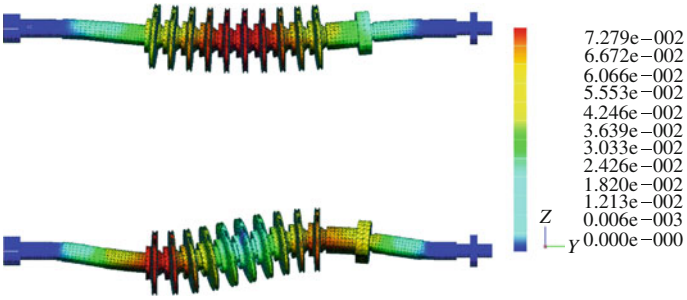

Fig. 5.12 First and second mode diagram

the shaft, that is, eccentricity. This eccentricity changes the bearing's dynamic characteristics. Additional static forces may occur with inaccurate alignment of the bearings. A magnetic pull within the generator is a radial force rotating at a frequency proportional to shaft deflection and comparable to the bearing's negative stiffness. Additional radial forces with rotational frequency may result from unbalanced mass, which mainly occurs at the generator and runner. Consideration of all aforementioned forces acting on a shaft system requires extensive calculation, and the results may be very complex (see Feng and Chu 2001; Wu 2002).

5.2.1 Unbalanced Mechanical Force

Typically, when the mass eccentric distance equals ε_0, inertial forces can be calculated as:

$$F_1 = m\varepsilon_0\Omega^2 \tag{5.3}$$

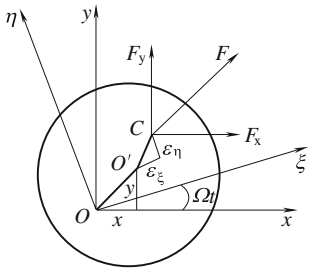

Fig. 5.13 Centrifugal force caused by eccentric error of rotor centre

where m is the unbalanced mass (kg), and Ω is the rotational speed (rad/s). Generally speaking, the unbalanced mechanical forces in large turbine-generator units appear mainly at the generator rotor and turbine runner.

The generator rotor can be simplified into a large thin disc with sizeable mass that produces a large unbalanced centrifugal load, shown in Fig. 5.13. The two components of centrifugal force are

$$\begin{cases} F_x = \mathrm{Re}\left[m\left(\varepsilon_\xi + \mathrm{i}\varepsilon_\eta\right)\Omega^2 \mathrm{e}^{\mathrm{i}\Omega t}\right] \\ F_y = ss\mathrm{Re}\left[m\left(\varepsilon_\eta - \mathrm{i}\varepsilon_\xi\right)\Omega^2 \mathrm{e}^{\mathrm{i}\Omega t}\right] \end{cases}$$

where $\varepsilon = \varepsilon_\xi + \mathrm{i}\varepsilon_\eta$ is the projection of an eccentric distance of the component in reference frame ($o\xi\eta$) rotating with the component.

For a node in the numerical grid system, displacement vector $\{\boldsymbol{u}\}$ and angular vector $\{\boldsymbol{\theta}\}$ at balanced conditions can be expressed as:

$$[\boldsymbol{M}]\{\ddot{\boldsymbol{u}}\} = [\boldsymbol{K}]\{\boldsymbol{u}\} + [\boldsymbol{C}]\{\dot{\boldsymbol{u}}\} + \{\boldsymbol{Q}\} + \{\boldsymbol{f}\} \tag{5.4}$$

$$[\boldsymbol{J}_d]\{\ddot{\boldsymbol{\theta}}\} = -\Omega[\boldsymbol{J}_p]\{\dot{\boldsymbol{\theta}}\} + \{\boldsymbol{M}_{xy}\} + \{\boldsymbol{l}\} \tag{5.5}$$

where

$$[\boldsymbol{M}] = \begin{bmatrix} m & 0 \\ 0 & m \end{bmatrix},\ [\boldsymbol{K}] = \begin{bmatrix} k_{xx} & k_{xy} \\ k_{yx} & k_{yy} \end{bmatrix},\ [C] = \begin{bmatrix} c_{xx} & c_{xy} \\ c_{yx} & c_{yy} \end{bmatrix},$$

$$\{\boldsymbol{M}_{xy}\} = \begin{Bmatrix} M_x^R - M_x^L \\ M_y^R - M_y^L \end{Bmatrix},\ \{\boldsymbol{M}_{xy}\} = \begin{Bmatrix} Q_x^R - Q_x^L \\ Q_y^R - Q_y^L \end{Bmatrix},\ [\boldsymbol{J}_d] = \begin{bmatrix} J_d & 0 \\ 0 & J_d \end{bmatrix},$$

$$[\boldsymbol{J}_p] = \begin{bmatrix} 0 & \boldsymbol{J}_p \\ -\boldsymbol{J}_p & 0 \end{bmatrix},\ \{\boldsymbol{u}\} = \begin{Bmatrix} x \\ y \end{Bmatrix},\ \{\boldsymbol{\theta}\} = \begin{Bmatrix} \alpha \\ \beta \end{Bmatrix},\ \{\boldsymbol{f}\} = \begin{Bmatrix} F_x \\ F_y \end{Bmatrix},\ \{\boldsymbol{l}\} = \begin{Bmatrix} L_x \\ L_y \end{Bmatrix}.$$

And Fig. 5.5 exhibits all physical parameters on both right and left sides of the node.

For a vertically mounted rotor system, a rotating component may rotate around its own axis or the geometrical axis of the bearings. The latter is called arching rotation. Possible reasons for this rotation may be the misalignment of bearing

centers or bending of the shaft. If the radius of the arch is r, unbalanced forces caused by the bending of shaft can be written as:

$$F_2 = mr\Omega^2. \tag{5.6}$$

5.2.2 Nonlinear and Unbalanced Magnetic Force of the Generator

Magnetic force of the generator is important for rotordynamic analysis of a hydraulic turbine generator. Its nonlinear and unbalanced magnetic force is analyzed in this section.

5.2.2.1 Unbalanced Magnetic Force Caused by Eccentricity

Because the generator rotor and the stator may not be circular, resultant eccentricity would lead to an unbalanced magnetic force. On the other hand, eccentricity of the rotor center to the stator center, or other unknown factors such as a short circuit in the pole winding or an unbalanced three-phase load, can also generate unbalanced magnetic forces. If the eccentricity is notated as y, and k_0 is the coefficient of unbalanced magnetic forces, one could define the unbalanced magnetic force with a linear approximate formula (see Feng and Chu 2001; Wu 2002; Zhang 2008):

$$F_3 = k_0 y. \tag{5.7}$$

The nonlinear formula for an unbalanced magnetic force is given as:

$$F_{mag} = \frac{\mu_0 \pi L F_0^2}{\lambda \ln^2\left(\frac{1/R_0+b}{1/R_1+a}\right)} \tag{5.8}$$

where $\lambda = \frac{1}{\varepsilon}\sqrt{\left(\left(R_1^2+R_0^2-\varepsilon^2\right)/2\right)^2 - R_1^2R_0^2}$, $a = \sqrt{1/R_1^2+1/\lambda^2}$, $b = \sqrt{1/R_0^2+1/\lambda^2}$, $F_0 = \left(R_1-R_0\right)/\mu_0 - \hat{B}$.

Parameter definitions are listed as follows: R_1 is the inner radius of the stator; R_0 is the outlet radius of the generator rotor; L is the axial length of the radial magnetic loop; $\hat{B}$ is the average magnetic flux density; ε is the eccentricity of rotor to stator determined by the shaft runoff at the generator rotor; μ_0 is the magnetic conductivity in the air space (W/A − m); $R_1 - R_0$ is radial clearance.

A similar expression for a nonlinear formula is:

$$F_{mag} = \frac{\mu_0 \pi L F_0^2}{\lambda \ln^2 E_0 \ln^2[(1/R_0+b)/(1/R_1+a)]} \tag{5.9}$$

where $E_0 = (1/R_0+b)/(1/R_1+a)$.

5.2.2.2 Potential Energy in the Air Gap of the Generator

Figure 5.14 indicates the air gap eccentric of generator, where O is the centre of stator circle, and O' is that of rotor circle. If the relative air gap is $\bar{\varepsilon} = \varepsilon/(k_\mu \delta_0)$; saturation is $k_\mu = 1 + \delta_{Fe}/(k_1\delta_0)$:k_1 is the mean gap coefficient; δ_{Fe} is the equivalent gap coefficient of ferromagnet; δ_0 is mean gap; F_{sm} is amplitude of stator magnetic potential; and F_{jm} amplitude of rotor magnetic potential; then potential energy in the air gap of generator is:

$$N_{12} = \frac{R_1 L}{2}\int_0^{2\pi} \Lambda_0 \sum_{n=0}^{\infty} \bar{\varepsilon}^n \cos^n(\alpha - \beta)\left[F_{sm}\cos\left(\Omega_f t - p\alpha\right)\right.$$
$$\left. + F_{jm}\cos\left(\Omega_f t - p\alpha + \theta + \varphi + \frac{\pi}{2}\right)\right]^2 \mathrm{d}\alpha$$

where $\Lambda_0 = \mu_0/(k_\mu\delta_0)$ is the mean magnetic conductance and μ_0 is the air magnetic conductance; the rotating speed of the generator is $\Omega_f = 2\pi f/p$; f is the electric net frequency; p is the pair number of generator poles; θ is the inner power angle of generator; and $\theta = -\varphi$; its inner power coefficient is as follows:

$$= \arctan\left[IX_q + U\sin\varphi/(IR_a + U\sin\varphi)\right]$$

where U is its voltage, I is the phase current of generator; X_q is the reactance of generator armature; and R_a is the resistance of generator armature. n is the order number of Taylor series, usually $n = 3$ is adopted.

And N_{12} can be simplified in the matrix form:

$$N_{12} = \frac{1}{2}\{\boldsymbol{u}_1\}^T[\boldsymbol{K}_{12}]\{\boldsymbol{u}_1\} + \{\boldsymbol{u}_1\}^T\{\bar{\boldsymbol{k}}\} \tag{5.10}$$

where $[\boldsymbol{K}_{12}]$ is the stiffness matrix of the air gap magnetic field, there are only limited non-zero elements; $\{\bar{\boldsymbol{k}}\}$ is the rotor vibration eccentric vector; and $\{\boldsymbol{u}_1\}$ is the general coordinate vector of the generator, which contains flexural displacement and torsional angle at the generator element nodes.

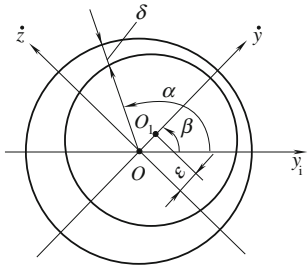

Fig. 5.14 Air gap eccentric of generator

5.2.2.3 Moment Equation of Hydro Generator

In the transient process, the torque equation of the hydro generator, Eq. (5.11), must be brought into the scope of the governing equation to predict the vibration, especially the vibration of the shaft system, i.e.,

$$m_g = m_e + m_D \tag{5.11}$$

where m_g is the generator load torque (whole damping torque); m_e is the electromagnetic torque of generator; and m_D is the magnetic torque of the damping winding in the generator.

Operation angle δ is expressed as difference between the torsion angle of shaft, θ, and its initial value, θ_0, so

$$\frac{\mathrm{d}\delta}{\mathrm{d}t} = \frac{\mathrm{d}\theta}{\mathrm{d}t} = \Omega. \tag{5.12}$$

And $m_e = P_e/\Omega$, then

$$P_e = \frac{E'V_t}{x'_d}\sin\delta + \left(\frac{1}{x_q} - \frac{1}{x'_d}\right)\frac{V_t^2}{2}\sin 2\delta \tag{5.13}$$

where E' is the transient electric potential of the generator; V_t is the voltage at the generator output's ends; x_q is the generator shaft reactance; and x'_d is the generator shaft reactance during the transient process. Consider the damping coefficient D, and the torque of the damping winding becomes

$$m_D = D\frac{\mathrm{d}\delta}{\mathrm{d}t} = D\Omega. \tag{5.14}$$

5.2.3 Unbalanced Radial Hydraulic Force Acting on the Turbine Runner

In general, unbalanced radial hydraulic force can be determined by means of a field test or a calculation with known flow coefficient and measured flux. Chapter 7 will focus on commutated force with the help of computational fluid dynamics (CFD).

5.3 Forces in Transient Oil Film of Bearings in Hydraulic Unit

In a hydraulic turbine generator unit, lateral fluid forces at the runner may be split into three parts: a constant component, a component with rotational frequency but with constant magnitude (hydraulic unbalance), and the remaining lateral force.

The first two can be calculated with design parameters of the turbine. The last one can be calculated through the following steps: Calculation of the frequency response function; assumptions regarding the spectrum of hydraulic lateral forces; determination of vibrations; and calculation of hydraulic lateral force.

Water in the runner also has an impact on the stiffness and damping of a solid runner, but it needs further study.

5.3.1 Transient Oil Film Forces and Parameters of Guide Bearings

The dynamic oil-film forces and its parameters of guide bearings in a hydraulic turbine generator unit are important for the unit rotordynamic analysis. Their expressions and data must be given in the first place.

5.3.1.1 Transient Oil Film Forces

Tilting-pad journal bearings can be modeled with the generalized Reynolds equation of lubrication (Feng and Chu 2001; Wu 2002):

$$\frac{\partial}{\partial x}\left(G_x\frac{h^3\partial p}{\mu\partial x}\right)+\frac{\partial}{\partial y}\left(G_y\frac{h^3\partial p}{\mu\partial y}\right)=6U\frac{\partial h}{\partial x}+6h\frac{\partial U}{\partial x}+12\frac{\partial h}{\partial t} \tag{5.15}$$

where G_y, G_x denote the turbulent factor of the oil that can be calculated in Eq. (5.16); μ represents dynamic viscosity of the lubricating oil; U indicates the linear velocity of a certain point on the surface of the journal; p represents pressure distribution of oil film; $\partial p/\partial x$ and $\partial p/\partial y$ represent the pressure gradients of the oil film along circumferential and axial directions of the rotor, respectively; $\partial h/\partial t$ is the velocity of the journal center relative to the bearing center; and h the thickness of oil film within oil wedge.

For pad a in Fig. 5.15, h can be defined as ha, solved with Eq. (5.17)

$$\begin{cases} G_x=\begin{cases}1 & R_h>977\\ 12\Big/\left[0.0687(U\rho/\mu)^{0.75}h^{0.75}\right] & R_h>977\end{cases}\\ G_y=\begin{cases}1 & R_h\le 977\\ 12\Big/\left[0.0392(U\rho/\mu)^{0.75}h^{0.75}\right] & R_h>2060\end{cases}\end{cases} \tag{5.16}$$

where $R_h=Uh\rho/\mu$ represents the Reynolds number of a certain point in the oil film; and

$$h_a\approx c-\varepsilon_{a0}\cos(\phi_{ka}-\varphi)+\varepsilon\cos(\varphi-\theta)+R\delta_a\sin(\phi_{ka}-\varphi). \tag{5.17}$$

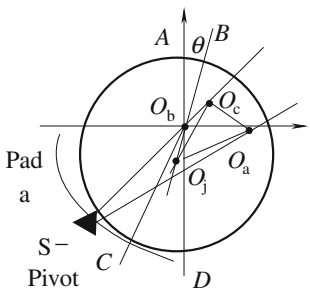

Fig. 5.15 Geometrical relationship between the journal and pad

In Eq. (5.17), $\delta_a = \angle O_a S Q'_a$, $\theta = \angle A O_b B$, and $\beta_a = \angle S O_b D$ specify the designed bearing clearance, the pad tilting angle, the angle of displacement, and the position angle of the pad pivot, respectively; other parameters can be found in Feng (2000).

Scaling Eq. (5.15) to dimensionless and expanding its right side, one could get a differential equation for a specific point in time. The right side of the equation is composed of the displacement and velocity of the journal center, pad tilting angle, and pad tilting velocity at that specific moment. The equation can be used for acquisition of pressure distribution over the surface of a bearing pad at that moment. Of course, there are some general assumptions for oil film in a journal bearing, listed as follows:

1. No outside field force acts on the lubricant.
2. Pressure distribution is constant throughout the thickness of oil film.
3. No slip is allowed at the lubricant boundaries.
4. The lubricant is Newtonian.

5.3.1.2 Parameters of a Multi-Tilting Pad Journal Bearing

The following stiffness and damping matrices are applied to express eight parameters of the multi-tilting pad journal bearings in UGB, LGB and WGB, just as in Eq. (5.2), which are

$$[\boldsymbol{K}] = \begin{bmatrix} k_{xx} & k_{xy} \\ k_{yx} & k_{yy} \end{bmatrix}, \ [\boldsymbol{K}_b] = \begin{bmatrix} k_{bxx} & k_{bxy} \\ k_{byx} & k_{byy} \end{bmatrix}, \ [\boldsymbol{C}_b] = \begin{bmatrix} c_{bxx} & c_{bxy} \\ c_{byx} & c_{byy} \end{bmatrix}$$

where $[\boldsymbol{K}]$, $[\boldsymbol{K}_b]$, and $[\boldsymbol{C}_b]$ are the mass, stiffness, and damping matrices of bearing bracket respectively.

Figure 5.16 shows a rigid model of guide bearing, where the bearing brackets and foundations are rigid with only stiffness and damping of oil film considered. In contrast, Fig. 5.17 shows an elastic model. And it is assumed that equivalent masses along the x- and y-directions of the bearing brackets are M_{bx} and M_{by}. The elastic model can reflect boundary characters at the bearing, especially where parameters vary with respect to time (Zhang 2006).

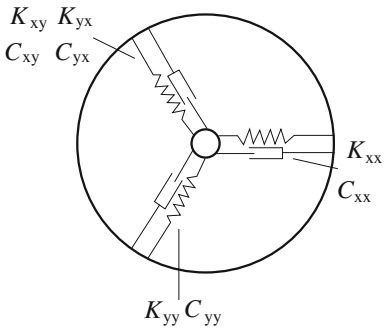

Fig. 5.16 Rigid model of guide bearing

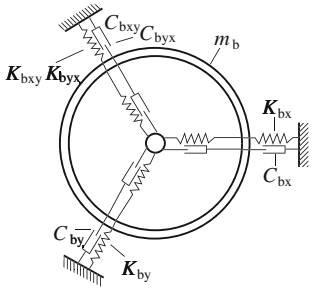

Fig. 5.17 Elastic model of guide bearing

Active forces R_x and R_y from oil film to shaft journal can be gained with solutions to the generalized Reynolds equation of lubrication (5.15). They are in the term of nonlinear function with respect to journal bearing displacements, x_j, y_j and their velocities, $\dot{x}_j$, $\dot{y}_j$, the bracket bearing displacements, x_f, y_f and their velocities, $\dot{x}_f$, $\dot{y}_f$, the pad swing angle, φ_{T1}, $\varphi_{T2}, \ldots$, and its velocity, $\dot{\varphi}_{T1}, \dot{\varphi}_{T2}, \ldots$, i.e.,

$$\begin{cases} R_x = R_x\left(x_j - x_f,\ \dot{x}_j - \dot{x}_f,\ y_j - y_f,\ \dot{y}_j - \dot{y}_f,\ \varphi_{T1},\ \varphi_{T2}, \ldots,\ \dot{\varphi}_{T1},\ \dot{\varphi}_{T2}, \ldots\right) \\ R_y = R_y\left(x_j - x_f,\ \dot{x}_j - \dot{x}_f,\ y_j - y_f,\ \dot{y}_j - \dot{y}_f,\ \varphi_{T1},\ \varphi_{T2}, \ldots,\ \dot{\varphi}_{T1},\ \dot{\varphi}_{T2}, \ldots\right) \end{cases}. \tag{5.18}$$

When the journal shaft whirls around the balance point with small angler displacement, Eq. (5.18) may evolve into a linear one:

$$\begin{cases} R_x = \left(x_j - x_f\right)\sum\limits_{i=1}^{NP} k_{xxi} + \left(y_j - y_f\right)\sum\limits_{i=1}^{NP} k_{xyi} + \left(\dot{x}_j - \dot{x}_f\right)\sum\limits_{i=1}^{NP} c_{xxi} + \\ \left(\dot{y}_j - \dot{y}_f\right)\sum\limits_{i=1}^{NP} c_{xyi} + \sum\limits_{i=1}^{NP}\left(-\beta_i c_{xxi} + \alpha_i c_{xyi}\right)\dot{\varphi}_{Ti} + \sum\limits_{i=1}^{NP}\left(-\beta_i k_{xxi} + \alpha_i k_{xyi}\right)\varphi_{Ti} \\ R_y = \left(x_j - x_f\right)\sum\limits_{i=1}^{NP} k_{yxi} + \left(y_j - y_f\right)\sum\limits_{i=1}^{NP} k_{yyi} + \left(\dot{x}_j - \dot{x}_f\right)\sum\limits_{i=1}^{NP} c_{yxi} + \\ \left(\dot{y}_j - \dot{y}_f\right)\sum\limits_{i=1}^{NP} c_{yyi} + \sum\limits_{i=1}^{NP}\left(-\beta_i c_{yxi} + \alpha_i c_{yyi}\right)\dot{\varphi}_{Ti} + \sum\limits_{i=1}^{NP}\left(-\beta_i k_{yxi} + \alpha_i k_{yyi}\right)\varphi_{Ti} \end{cases} \tag{5.19}$$

where k_{xxi}, k_{xyi}, k_{yxi}, k_{yyi} and c_{xxi}, c_{xyi}, c_{yxi}, c_{yyi} are stiffness and damping factors of the ith pad's fixed coordinates. $\alpha_i = R\sin\gamma_i$, $\beta_i = -R\cos\gamma_i$, γ_i is the position angle of the pad supporting point; and R is the inner radian of the pad. Usually, the stiffness and lamping factors are constants.

Nonlinear active forces can be expressed in the simplified form:

$$\begin{aligned} P_r &= \frac{6\mu R^3 L}{\delta^2}[(\Omega - 2\dot{\varphi})F_1(\hat{\varepsilon}) + 2\dot{\varepsilon}F_2(\hat{\varepsilon})] \\ P_\varphi &= \frac{6\mu R^3 L}{\delta^2}[(\Omega - 2\dot{\varphi})F_3(\hat{\varepsilon}) + 2\dot{\varepsilon}F_4(\hat{\varepsilon})] \end{aligned} \tag{5.20}$$

where $\hat{\varepsilon} = \varepsilon/\delta$ is the relative eccentricity; L is the length of bearing; δ is mean radius gap. And

$$F_1 = F_4 = \frac{2\hat{\varepsilon}^2}{(1-\hat{\varepsilon}^2)^{0.5}(2+\hat{\varepsilon}^2)},\ F_2 = F_3 = \frac{1}{(1-\hat{\varepsilon}^2)^{0.5}}\left(\frac{\pi}{2} - \frac{8}{\pi(2+\hat{\varepsilon}^2)}\right).$$

5.3.2 Transient Force of Oil Film and the Moment of Thrust Bearing

In a similar manner, dynamic equations of each pad in the pivot tilting-pad thrust bearing must be solved at each integration step. The generalized Reynolds equation for lubricant in thrust bearings takes the same form as that in guide bearings, but in cylindrical coordinates, i.e.,

$$\frac{\partial}{\partial r}\left(G_r\frac{h^3 r\partial p}{\mu\partial r}\right) + \frac{1}{r}\frac{\partial}{\partial\varphi}\left(G_\varphi\frac{h^3\partial p}{\mu\partial\varphi}\right) = 6r\Omega\frac{\partial h}{\partial\varphi} + 6r\frac{\partial h}{\partial t} \tag{5.21}$$

$$h = h_p + \gamma_j r\sin(\theta_p - \varphi) - \beta_j\left[r\cos(\theta_p - \varphi) - r_p\right] - \theta_{yj}r\cos\varphi - \theta_{xj}r\sin\varphi \tag{5.22}$$

where γ_j and β_j are tilting angles of the pad in circumferential and radial directions, respectively; θ_p and r_p are angular and radial coordinates of the pivot in the inertial coordinates, respectively; φ is the angular coordinate of any point on one pad; h_p is oil film thickness at the pad pivot; θ_{yj} and θ_{xj} are components of the tilting angle of the thrust block θy and θx projected on the pivot coordinate, respectively. The following relationship is also employed:

$$\theta_{yj} = \theta_x\sin\alpha_j + \theta_y\cos\alpha_j,\ \theta_{xj} = \theta_x\cos\alpha_j - \theta_y\sin\alpha_j \tag{5.23}$$

where α_j is the angle position of the line from pivot j to the bearing center in inertial coordinate. Hence, oil film thickness can be written as:

$$h = h_p + \gamma_j r\sin(\theta_p - \varphi) - \beta_j\left[r\cos(\theta_p - \varphi) - r_p\right] - \theta_x r\sin\alpha_j\cos\varphi. \quad (5.24)$$

Solving the above Reynolds equation, one would arrive at pressure distribution of the oil film in an oil wedge. Oil film force and oil moment can be integrated. Resultant forces and moments of the whole bearing can be calculated as:

$$\begin{aligned} W_z &= \sum_j \iint pr\mathrm{d}r\mathrm{d}\theta, \quad M_x = \sum_j \iint pr\big(r\cos\big(\theta_p - \phi\big) - r_p\big)\mathrm{d}r\mathrm{d}\theta, \\ M_y &= \sum_j \iint pr^2\sin\big(\theta_p - \phi\big)\mathrm{d}r\mathrm{d}\theta \end{aligned} \quad . \quad (5.25)$$

For a centrally pivoted pad, the balance equations are

$$J_{\beta j}\ddot{\beta}_j = M_{xj},\ J_{\gamma j}\ddot{\gamma}_j = M_{yj} \quad (5.26)$$

where $J_\beta j$ and $J_\gamma j$ are the pad's moments of inertia around the pivot in circumferential and axial directions, respectively. Thrust bearing holds the load of the unit weight and the water thrust acting on the runner, and then passes the forces to its bracket. Its lateral constraint is also important to rotordynamic computation, although the constraint is not as obvious as that of guide bearings. So thrust bearing may be regarded as an element with the combined actions both of torsional spring and torsional damper expressed in Cartesian coordinates as:

$$\begin{Bmatrix} F_x \\ F_y \end{Bmatrix} = \begin{bmatrix} 0 & K_{x\beta} \\ K_{y\alpha} & 0 \end{bmatrix} \begin{Bmatrix} \alpha \\ \beta \end{Bmatrix} \quad (5.27)$$

$$\begin{Bmatrix} L_x \\ L_y \end{Bmatrix} = \begin{bmatrix} K_{M\alpha} & 0 \\ 0 & K_{M\beta} \end{bmatrix} \begin{Bmatrix} \alpha \\ \beta \end{Bmatrix} + \begin{bmatrix} C_{M\alpha} & 0 \\ 0 & C_{M\beta} \end{bmatrix} \begin{Bmatrix} \dot{\alpha} \\ \dot{\beta} \end{Bmatrix} \quad (5.28)$$

where Ky_α, $K_{x\beta}$, $K_{M\alpha}$, $K_{M\beta}$, $C_{M\alpha}$, $C_{M\beta}$ are the stiffness and the damping of the oil film created by a thrust disc swing; α, β, $\dot{\alpha}$ and $\dot{\beta}$ are torsional angle displacements and velocities of a thrust disc on *xoz* and *yoz* planes respectively; and F_x, Fy, L_x, Ly are forces and moments of oil film on the same planes as foregoing.

5.4 Unbalanced Force and Dynamic Parameters of Water Seals

The gaps in the water seals of a turbine runner function as a prevention of water leakage from runner flow passage to its exterior. They are identified as the supporting points of water turbine shaft system. The unbalanced forces and the dynamic parameters of the seals play an important role for the rotordynamic analysis of the shaft system.

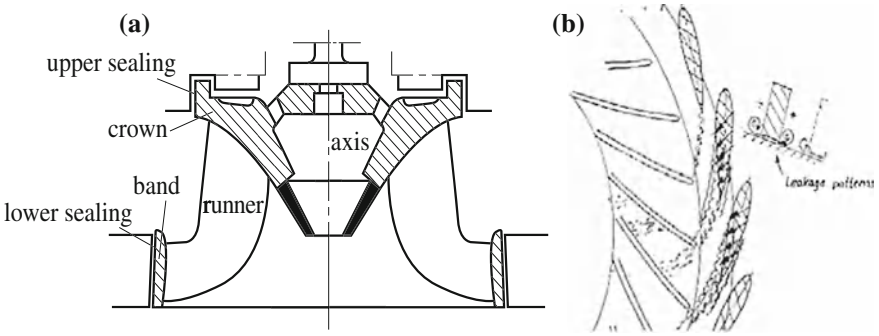

Fig. 5.18 Water seals in turbine runner. **a** Water seals. **b** Leakage patterns

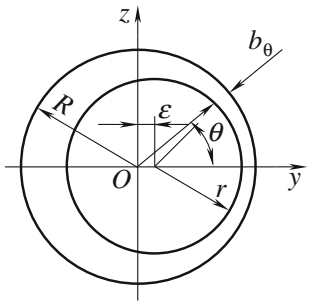

Fig. 5.19 Eccentric gap in water seal

5.4.1 Unbalanced Force of Water Seals

Figure 5.18a shows water seals on the outward surfaces of the crown and band of the turbine runner. Labyrinthine type seal are formed between those surfaces and the inner circular surfaces of stationery components, head cover in the upper seal and bottom ring of turbine in low seal (Fig. 5.18b). The gap in those seals will not be symmetrical when the turbine is running, which would result in an unbalanced force acting on the shaft system. An eccentric gap in the water seal shown in Fig. 5.19 will produce flow pressure fluctuation leading to the unbalance (Eide and Dahlhuang 2002; Liao and Li 2002).

Flow pressure drop, Δp, in the sealing consists of three parts: initial dynamic head of flow at the sealing flow inlet, $v_1^2/(2g)$; intake of local energy loss (head drop), $\varsigma v_1^2/(2g)$; and a friction head drop along the sealing flow passage, $\lambda l_s/(2b) \cdot v_1^2/(2g)$, i.e.,

$$\Delta p = \rho g\left(1 + \varsigma + \frac{\lambda l_s}{2b}\right)\frac{v_1^2}{2g} \tag{5.29}$$

where v_1 is the velocity at the sealing inlet; λ is the friction loss coefficient; ς is the local loss coefficient; l_s is the sealing passage length and b is the mean sealing gap width, which is expressed as:

$$b(\varepsilon, \theta) = b_0(1 - \delta \cos \theta)$$

where $\delta = \varepsilon / b$.

If it is assumed that the energy-loss distribution along the sealing flow passage is linear, then the pressure distribution along the sealing passage distance, x, can be written as:

$$p(x, \theta) = p_2 + (p_1 - p_2) \frac{\lambda x}{2b(\varepsilon, \theta)(1 + \varsigma) + \lambda l_s}$$

where p_1 and p_2 are the inlet and outlet pressures of the sealing passage, which can be determined by the inner pressure of the runner and the environmental pressure. Resultant unbalanced force stemming from unsymmetrical sealing can be obtained by integration within the sealing passage:

$$f(\delta) = \int_0^{l_s} \int_0^{2\pi} p(x, \theta) \cos \theta r \mathrm{d}\theta \mathrm{d}x$$

$$f(\delta) = \rho \lambda \mu \frac{r \pi \delta}{2b} l_s^2 \frac{v_1^2}{2} \tag{5.30}$$

where $\mu = (1 + \varsigma + \lambda l_s / 2b)^{-1}$, for simplification, $\mu = 0.25$. This prediction method of unbalanced forces from water seal is based on Hydraulics. Those forces can be evaluated by CFD simulation through the sealing and runner flow.

5.4.2 The Parameters of Water Seals in the Runner

The following stiffness and damping matrices are applied to describe dynamic parameters of the water seal in the runner which would contribute to the rotor-dynamic of the shaft and produce the unbalanced forces, F'_{sx} and F'_{sy} in a way as follows:

$$-\begin{Bmatrix} F'_{sx} \\ F'_{sy} \end{Bmatrix} = \begin{bmatrix} k_{xxs} & k_{xys} \\ k_{yxs} & k_{yys} \end{bmatrix} \begin{Bmatrix} x \\ y \end{Bmatrix} + \begin{bmatrix} c_{xxs} & c_{xys} \\ c_{yxs} & c_{yys} \end{bmatrix} \begin{Bmatrix} \dot{x} \\ \dot{y} \end{Bmatrix} + \begin{bmatrix} m_{xxs} & m_{xys} \\ m_{yxs} & m_{yys} \end{bmatrix} \begin{Bmatrix} \ddot{x} \\ \ddot{y} \end{Bmatrix} \tag{5.31}$$

where x, y, $\dot{x}$, $\dot{y}$, $\ddot{x}$, $\ddot{y}$ are the displacements, their velocity components, and their acceleration component along ordinates x and y respectively. And

$$[\boldsymbol{K}] = \begin{bmatrix} k_{xxs} & k_{xys} \\ k_{yxs} & k_{yys} \end{bmatrix} [\boldsymbol{C}] = \begin{bmatrix} c_{xxs} & c_{xys} \\ c_{yxs} & c_{yys} \end{bmatrix} [\boldsymbol{M}] = \begin{bmatrix} m_{xxs} & m_{xys} \\ m_{yxs} & m_{yys} \end{bmatrix}$$

are the mass, stiffness, and damping matrices of water seal in the runner respectively.

5.5 Excitation of Bearings and Seals of Multiple-Stage Pumps

The critical speeds of a rotor pump change with the bearing stiffness during operation. Centrifugal pumps of lower magnitude-critical speeds are more easily influenced by the bearing stiffness, whereas the higher ones are not. However, once the higher orders are impacted, they become more sensitive. In this section, the problems of modeling a steady rotor system with sliding bearings and a ring seal are introduced. We discuss this problem in light of the film force and of the slide bearings and the method of its application in modeling, as well as the method of simulating film stiffness.

5.5.1 Bearing Stiffness of Multi-Stage Centrifugal Pumps

Radial stiffness and damping of the film are important factors of the dynamic characteristics of rotor systems, whereas the impact of circumferential stiffness and damping are both small and generally not considered. In this dynamic model, incremental film force, together with the dynamic characteristic of film is calculated based on a static equilibrium position plus small disturbance of the film.

The main factors affecting rotor dynamic characteristics are the radial stiffness and damping of oil film.

Figure 5.20 shows the dynamic model. Given small disturbances in the static equilibrium position and calculating the increment of oil film force is calculated to determine dynamic characteristics of the oil film. Use the small disturbances Δx, Δy and the slow speed $\Delta\dot{x}$, $\Delta\dot{y}$, and suppose that force of oil film and disturbance changed with the linear relationship, one has the following equations (Ping et al. 2008; Hsu and Brennen 2002):

$$\begin{cases} F_x = F_{xo} + \dfrac{\partial F_x}{\partial x}|_0\Delta x + \dfrac{\partial F_x}{\partial y}|_0\Delta y + \dfrac{\partial F_x}{\partial x}|_0\Delta\dot{x} + \dfrac{\partial F_x}{\partial y}|_0\Delta\dot{y} \\ F_y = F_{yo} + \dfrac{\partial F_y}{\partial x}|_0\Delta x + \dfrac{\partial F_y}{\partial y}|_0\Delta y + \dfrac{\partial F_y}{\partial x}|_0\Delta\dot{x} + \dfrac{\partial F_y}{\partial y}|_0\Delta\dot{y} \end{cases} \tag{5.32}$$

In Eq. (5.32), F_x, F_y are components of oil film forces in the x, y-direction; F_{x0}, Fy_0 are components of oil film forces in the x, y-direction, when the journal is in static equilibrium position.

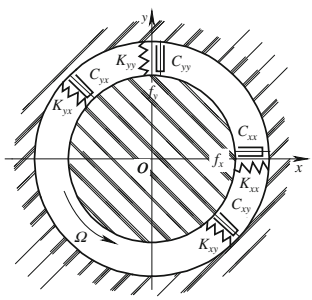

Fig. 5.20 Dynamic model of sliding bearing

Film stiffness would be defined as the increment of oil film force caused by displacement from the static equilibrium position, i.e.,

$$K_{xx} = \frac{\partial F_x}{\partial x}|_0,\ K_{xy} = \frac{\partial F_x}{\partial y}|_0,\ K_{yx} = \frac{\partial F_y}{\partial x}|_0,\ K_{yy} = \frac{\partial F_y}{\partial y}|_0. \tag{5.33}$$

Film damping is defined as the increment of oil film force caused by disturbance speeds, i.e.,

$$C_{xx} = \frac{\partial F_x}{\partial \dot{x}}|_0,\ C_{xy} = \frac{\partial F_x}{\partial \dot{y}}|_0,\ C_{yx} = \frac{\partial F_y}{\partial \dot{x}}|_0,\ C_{yy} = \frac{\partial F_y}{\partial \dot{y}}|_0. \tag{5.34}$$

So Eq. (5.32) could be transferred as

$$\begin{Bmatrix} \Delta F_x \\ \Delta F_y \end{Bmatrix} = [K]\begin{Bmatrix} \Delta x \\ \Delta y \end{Bmatrix} + [C]\begin{Bmatrix} \Delta \dot{x} \\ \Delta \dot{y} \end{Bmatrix} \tag{5.35}$$

where

$$\begin{Bmatrix} \Delta F_x \\ \Delta F_y \end{Bmatrix} = \begin{Bmatrix} F_x - F_{x0} \\ F_y - F_{y0} \end{Bmatrix},\ [K] = \begin{bmatrix} K_{xx} K_{xy} \\ K_{yx} K_{yy} \end{bmatrix} \text{ and } [C] = \begin{bmatrix} C_{xx} C_{xy} \\ C_{yx} C_{yy} \end{bmatrix}, \tag{5.36}$$

where $K_{xy,}$ K_{yx} and C_{xy}, Cyx are cross-stiffness and cross-damping coefficients, reflecting oil film force in two perpendicular directions to each other via coupling. Suppose the origin of coordinates xoy is the equilibrium position of bearing journal, x, y are displacement of journal, and fx, fy are dynamic force of the film.

$$\begin{Bmatrix} f_x \\ f_y \end{Bmatrix} = [K]\begin{Bmatrix} x \\ y \end{Bmatrix} + [C]\begin{Bmatrix} \dot{x} \\ \dot{y} \end{Bmatrix} \tag{5.37}$$

Equilibrium position of bearing journal ε_0, φ_0 is pictured in Fig. 5.21. The film thickness is h_0, the film pressure p_0. So the Reynolds equation is described as:

$$\frac{1}{R_2}\frac{\partial}{\partial \xi}\left(\frac{h_0^3}{12\mu}\frac{\partial p_0}{\partial \xi}\right) + \frac{\partial}{\partial z}\left(\frac{h_0^3}{12\mu}\frac{\partial p_0}{\partial z}\right) = \frac{1}{2}\Omega\frac{\partial h_0^3}{\partial \xi} \tag{5.38}$$

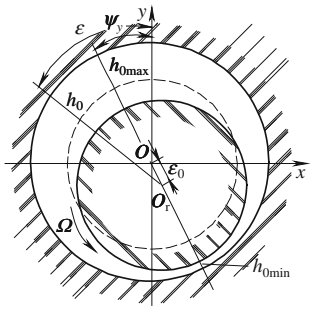

Fig. 5.21 Equilibrium position of bearing journal

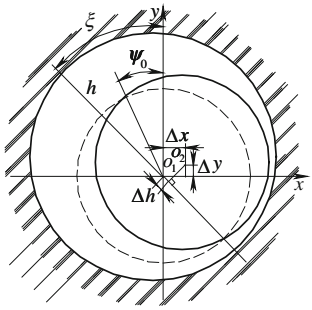

Fig. 5.22 Position of bearing journal after disturbed

where $h_0 = B[1 + \hat{\varepsilon}_0 \cos(\xi - \varphi_0)]$, $\hat{\varepsilon}_0 = \varepsilon_0/B$ is eccentricity; B is average radius clearance of bearing; μ is fluid viscosity. Give bearing journal a small disturbances$\Delta x, \Delta y$ and slow speed $\Delta\dot{x}$, $\Delta\dot{y}$ (Fig. 5.22):

$$h = h_0 + \Delta x \sin\xi - \Delta y \cos\xi \tag{5.39}$$

$$p = p_0 + \Delta p = p_0 + \frac{\partial p}{\partial x}|_0 \Delta x + \frac{\partial p}{\partial y}|_0 \Delta x + \frac{\partial p}{\partial \dot{x}}|_0 \Delta\dot{x} + \frac{\partial p}{\partial \dot{y}}|_0 \Delta\dot{y}. \tag{5.40}$$

The Reynolds equation of oil film is expressed in Eq. (5.41) when the position of shaft neck is random:

$$\frac{1}{R_2}\frac{\partial}{\partial\xi}\left(\frac{h_0^3}{12\mu}\frac{\partial p_0}{\partial\xi}\right) + \frac{\partial}{\partial z}\left(\frac{h_0^3}{12\mu}\frac{\partial p_0}{\partial z}\right) = \frac{1}{2}\Omega\frac{\partial h}{\partial\xi} + \frac{\partial h}{\partial t}. \tag{5.41}$$

From Eqs. (5.38–5.41), Eq. (5.42) could be elicited.

$$\frac{1}{R^2}\frac{\partial}{\partial\xi}\left(\frac{h_0^3}{12\mu}\frac{\partial p'}{\partial\xi}\right)+\frac{\partial}{\partial z}\left(\frac{h_0^3}{12\mu}\frac{\partial p'}{\partial z}\right)=\begin{cases}\frac{1}{2}\Omega\left(\cos\xi-3\frac{\sin\xi}{h_0}\frac{\partial h_0}{\partial\xi}\right)-\frac{h_0^3}{4\mu}\frac{1}{R}\frac{\partial p_0}{\partial\xi}\frac{\partial}{\partial\xi}\left(\frac{\sin\xi}{h_0}\right) & \left(p'=\frac{\partial p}{\partial x}\right)\\ \frac{1}{2}\Omega\left(\sin\xi-3\frac{\cos\xi}{h_0}\frac{\partial h_0}{\partial\xi}\right)-\frac{h_0^3}{4\mu}\frac{1}{R}\frac{\partial p_0}{\partial\xi}\frac{\partial}{\partial\xi}\left(\frac{\cos\xi}{h_0}\right) & \left(p'=\frac{\partial p}{\partial y}\right)\\ \sin\xi & \left(p'=\frac{\partial p}{\partial x}\right)\\ -\cos\xi & \left(p'=\frac{\partial p}{\partial y}\right)\end{cases} \tag{5.42}$$

By rewriting Eq. (5.42) in the form of differential equations and integrating them into the region of an entire film and shaft neck length within the numerical, one could get p'. Integrate again and then one could elicit dynamic coefficients of the oil film.

$$\begin{cases}\begin{Bmatrix}K_{xx}\\K_{yx}\end{Bmatrix}=-\int_{-\frac{L}{2}}^{\frac{L}{2}}\int_A\frac{\partial p}{\partial x}\begin{Bmatrix}\sin\xi\\-\cos\xi\end{Bmatrix}R\mathrm{d}\xi\mathrm{d}z\\ \begin{Bmatrix}K_{xy}\\K_{yy}\end{Bmatrix}=-\int_{-\frac{L}{2}}^{\frac{L}{2}}\int_A\frac{\partial p}{\partial y}\begin{Bmatrix}\sin\xi\\-\cos\xi\end{Bmatrix}R\mathrm{d}\xi\mathrm{d}z.\end{cases} \tag{5.43}$$

5.5.2 *Dynamic Model of a Ring Seal for a Multi-Stage Centrifugal Pump*

The equation for a seal fluid exciting force (see Fig. 5.23), stiffness, damping, and the following additional qualities are described in Eq. (5.44) (see Ping et al. 2008 and Blanco et al. 2006):

$$-\begin{Bmatrix}F_r\\F_\tau\end{Bmatrix}=\begin{bmatrix}k_{xx}&k_{xy}\\k_{yx}&k_{yy}\end{bmatrix}\begin{bmatrix}x(t)\\y(t)\end{bmatrix}+\begin{bmatrix}c_{xx}&c_{xy}\\c_{yx}&c_{yy}\end{bmatrix}\begin{bmatrix}\dot{x}(t)\\\dot{y}(t)\end{bmatrix}+\begin{bmatrix}m_{xx}&m_{xy}\\m_{yx}&m_{yy}\end{bmatrix}\begin{bmatrix}\ddot{x}(t)\\\ddot{y}(t)\end{bmatrix} \tag{5.44}$$

where $k_{xx}=k_{yy}=K$, $k_{yx}=k_{xy}=k$, $c_{xx}=c_{yy}=C$, and $c_{yx}=c_{xy}=c$, $m_{xx}=m_{yy}=M$, $m_{yx}=-m_{xy}=0$, and F_r is radial force, F_τ is circle force.

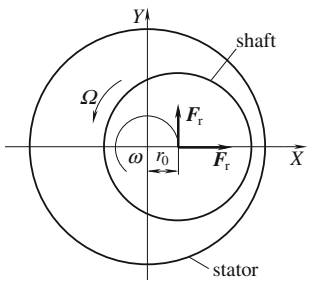

Fig. 5.23 Dynamic model of a *ring seal*

When the flow is steady, choose $t = 0$ for the ease of analysis in rotational coordinates. At this time,

$$X(0) = r_0,$$

So Eq. (5.44) could evolve into Eq. (5.45):

$$\begin{cases} \dfrac{F_r}{r_0} = K - c\Omega + M\Omega^2 \\ \dfrac{F_\tau}{r_0} = k - D\Omega \end{cases} \tag{5.45}$$

where D is radius of the shaft, and r_0 is amplitude of whirl. When F_r is more than 0, amplitude of whirl would increase. Because F_r is the factor that contributes to the whirl, and its direction is the same as that of the whirl, it would accelerate when the whirl exceeds 0 which soon lead to instability. According to Eq. (5.45), three different whirl frequencies are needed to calculate the dynamic coefficients of the ring seal, and that could result in three groups of equations.

References

Blanco, E., Parrondo, J. & Barrio, R. (2006). Fluid-dynamic radial forces at the blade-passing frequency in a centrifugal pump with different impeller diameters. *In: Proceeding of IAHR International Meeting of WG on Cavitation and Dynamic Problems in Hydraulic Machinery and Systems*, *Barcelona*.

Chen, C. X., Wu, D. Z., Tan, S. G. & Wang, L. Q. (2008). Computing critical speeds for multiple-stage centrifugal pumps with speed dependent support properties. *Fluid Machinery and Fluid Mechanics* (pp. 306–309). Hamburg: Springer.

Eide, S. & Dahlhuang, O. G. (2002). Analysis of the leakage flow and wear in guide vanes. In: *Proceedings of the XXI IAHR Symposium on Hydraulic Machinery and Systems*, *Lausanne.*

Feng, F. Z. (2000). Dynamic analysis and application of the rotor-bearing system of a large scale pumped storage power generator unit. *Ph.D dissertation*, Tsinghua University in China.

Feng, F. Z., & Chu, F. L. (2001). Dynamic analysis of a hydraulic turbine unit. *Mechanics of Structures and Machines, 29*, 505–531.

Hsu, Y., & Brennen, C. E. (2002). F1uid flow equations for rotordynamic flows in seals and leakage paths. *ASME Journal of Fluids Engineering, 124*, 176–181.

Jiang, Y. (2008). Research on torsion vibration water turbine generator unit. *Dissertation for Master degree*, Dalian University of Technology in China.

Kumar, A. S., & Sankar, T. S. (1986). A new transfer matrix method for response analysis of large dynamic systems. *Computers and Structures, 23*, 545–552.

Liao, W. L. & Li J. Z. (2002). Numerical simulation and experimental investigation on the flow in end clearance region of the guide vane of hydraulic turbine. In: *Proceedings of the XXI IAHR Symposium on Hydraulic Machinery and Systems*, *Lausanne.*

Ma, C. Z. (2007). The study of dynamic characteristics of shaft system of Francis turbine generator units. *Dissertation for Master degree*, Guangxi University in China.

Ohashi, H. (1991). *Vibration and oscillation of hydraulic machinery*. London: Avebury Teehnical Press.

Ping, S. L., Tan, S. G., Wu, D. Z. & Wang, L. Q. (2008). Analysis on modeling rotor system with sliding baring and ring seal by using FEM. *Fluid Machinery and Fluid Mechanics* (pp. 366–370). Hamburg: Springer.

Swain, M. (2008).Vibrations in a Francis turbine: A case Study, Electrical India 48(5).

Wikipedia. (2008). http://en.wikipedia.org/wiki/Francis_turbine.

Wu, Z. Y. (2002). Computer and analysis of linear characteristic of vibration of shafts of the hydro electric machines, *Dissertation for Master degree*, Xi'an University of Technology in China.

Zhang, L. (2006). The dynamics characteristic analysis for the shafts of large hydraulic generator unit, *Dissertation for Master degree*, Xi'an Univ. of Technology in China.

Zhang, W. (2008). Research on dynamics of shaft system of hydro-electric generating set. *Dissertation for Master degree*, Dalian University of Technology in China.

Chapter 6
Vibration Induced by Hydraulic Excitation

6.1 Introduction

Generally, hydraulic excitations that induce vibrations in hydraulic machinery can be categorized as follows:

(a) Flow through waterways: Non-uniform velocity distribution in various waterways of the turbine can cause hydraulic unbalance.
(b) Flow instabilities in turbine draft tube or pump sump and pump intake: These occur even during steady-state operation in machines working outside optimum efficiency range.
(c) Cavitation: This occurs mostly around the runner or impeller blades. For details, readers may refer to volume six on cavitation in this book series, Li (2001).
(d) Hydroelastic vibration: This is mainly caused by incorrectly shaped hydraulic profiles of discharge edge (such as on the blades, wicket gates, stay vanes etc.).
(e) Self-excited vibration: This occurs where the movements of mechanical parts (seals, clearances, etc.) interact with the flows around or within (Alford 1965).
(f) Pressure fluctuations in the penstock.

6.2 General Hydraulic Excitation in Hydraulic Turbines

Hydraulic excitations in hydraulic turbines include the unstable flows in runner, spiral case and guide vanes, the vortices in flow fields, the vortex rope in the draft tube, the transient flows in the penstock of power stations, and the self-excitation vibration in the hydraulic turbines.

Y. Wu et al., *Vibration of Hydraulic Machinery*,
Mechanisms and Machine Science 11, DOI: 10.1007/978-94-007-6422-4_6,

6.2.1 Forces and Frequencies of Hydraulic Excitation in Turbines

1. Vibration caused by unstable flows in runner, spiral case, and guide vanes.

In front of the runner, the asymmetrical flow, which results from an unevenly distributed flow of the spiral case or the opening of the guide vanes, will cause pressure pulsation in the runner with the following frequencies. (These pulsations with different frequencies may also present in the spiral case, guide vanes, or even draft tube).

(a) Runner blade rotating frequency: The unevenly distributed flow enters the blade; blade channels will generate vibrations at the blade passing frequency

$$f_b = \frac{nZ}{60}(\text{Hz}) \tag{6.1}$$

where n is the rotating speed of runner (rpm) and Z is the blade number.

(b) Guide vane passing frequency: Periodic variation of the inlet flow of the runner causes this frequency while passing the exits of the guide vanes

$$f_g = \frac{nZ_g}{60}(\text{Hz}) \tag{6.2}$$

where Z_g is guide vane number.

(c) Stay vane passing frequency: Periodic variation of the flow entering the runner causes this frequency while passing through the separating exits of stay vanes.

$$f_s = \frac{nZ_s}{60}(\text{Hz}) \tag{6.3}$$

where Z_s is stay vane number.

2. Pressure pulsations induced by vortices. The following vortices may contribute to a type of pulsation.

(a) The Karman vortex street from the trailing edge of runner blades or guide vanes. For turbines, the frequency of the Karman vortex street can be determined by an empirical formula as follows:

$$f_k = Sh\frac{W}{\delta_2 + \delta_v}(\text{Hz}). \tag{6.4a}$$

Here, Sh is the Strouhal number with values from 0.18 to 0.25 generally; W is the mean velocity at the separation point of the hydrofoil trailing edge; δ_v is a virtual boundary layer thickness to be added to the blade thickness, δ_2, which is obtained by experiments on runner blades with circular trailing edge:

$$\delta_v = 0.0294 \frac{x}{(Re_x)^{1/5}}. \tag{6.4b}$$

Here, x is the blade length and Re_x, is the Reynolds number based on the blade length. It is found that $Sh = 0.19$ is more appropriate if δ_v is added to the blade thickness. Other empirical formulas and information of the Karman vortex frequency will be introduced later.

(b) Vortices shedding from blades and vanes, as well as channel vortices. At part-load conditions, inlet flow enters the runner blade passage with large and positive attack angle, leading to flow separation on suction surfaces of the blades. The separation will develop into the downstream of the passage and finally form the channel vortex in the exit of runner. At overload conditions, similar separation will occur at the leading edge area of the runner blade. These vortices may induce pressure pulsation in the runner with a frequency several times the rotating frequency of the turbine.

3. Pressure pulsation generated by the vortex rope in the draft tube of Francis turbine.

The low frequency vortex rope emerges at part-load conditions of Francis turbine, and it causes low frequency pressure pulsation on the walls of draft tube, a swing power generation, as well as mechanical vibration and noise in the turbine unit.

In the case of part load, the circulation flow at the runner exit rotates in the same direction as that of the runner rotation. It forms a low pressure region in the central area of the runner's exit section, producing a back-flow in the axial direction. Any asymmetrical distribution of this back-flow would cause instability in the vortex rope to develop into a helical vortex in the draft tube. There are some models that can predict the frequency and amplitude of this pressure pulsation which will be discussed in next section. For engineering applications the frequency of this vortex-rope induced by pressure pulsation can be estimated using the following empirical formula:

$$f_v = \frac{n\mu}{60} (\text{Hz}) \tag{6.5}$$

where $\mu = 0.25 \sim 0.34$.

There is also another pulsation in the draft tube that exhibits a similar frequency as the rotation frequency of the runner.

4. Hydraulic vibration caused by transient flows in the penstock.

When the turbine's load suddenly changes, pressure surges may emerge in the penstock in the front of the turbine, leading to vibrations. These vibrations have the following frequencies:

$$f_{wh} = \frac{am}{2l}\,(\mathrm{Hz}). \tag{6.6}$$

Here, a is the sound speed in water; m is the number of resonance order ($m = 1, 2,\ldots,$ n); l is the length of the penstock.

5. Self-excitation vibration in hydraulic turbines.

The periodic motion of water and other fluids (such a lubricant oils) as well as other mechanical components may lead to the resonances of turbine structure. For example,

Oil film in the guide bearings may cause self-excitation vibration at the frequency:

$$f_{oil} = \frac{n}{120}\,(\mathrm{Hz}). \tag{6.7}$$

Here, n is the rotating speed of turbine; the number of the pads in guide bearings is assumed as 2.

The arcuate type of the gyroscopic rotation of shaft may occur when the turbine is working at overload condition. Arcuate gyroscopic rotation of the unit shaft will occur in the turbine, generating vibrations at frequencies equal to 2–4 times of the rotating frequency of the shaft.

Apart from the categories above, vibrations may stem from other sources such as the pressure fluctuations generated by the 'guide-plate' structure in the spiral case as shown in Fig. 6.1a. A typical case is the Three Gorges turbines in the left power house. Severe vibrations were generated by this structure and the structure itself

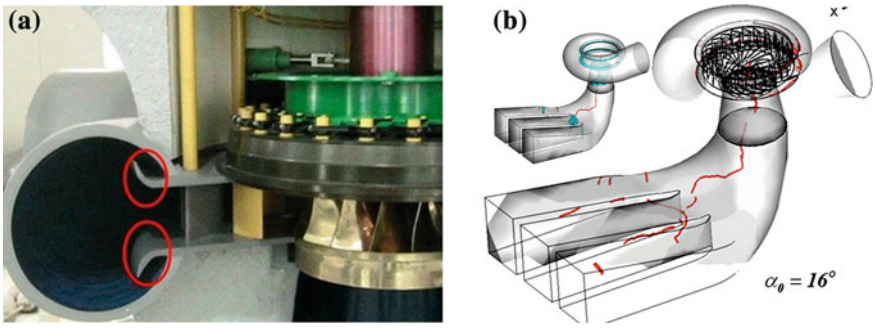

Fig. 6.1 **a** Guide plate (*circled*) in a model turbine (Li 2006). **b** Vortex cores in the entire flow passage of turbine at guide vane opening of 16° (Chen and Li 2011)

was also damaged (torn off) only after 10^3–10^4 h operation. All these guide plates are removed or modified for newer designs following the analysis (Li 2006).

This structure is responsible for a gust-like, extremely low-frequency fluctuation which is caused by an extremely long and complex vortex structure that starts at the guide-plate, moves through the entire turbine passage, and connects with the draft-tube vortices as shown by Fig. 6.1b. The frequency of this gust-like component is even lower than the dominant frequency of the machine without the guide-plate. It thus contributes to the triggering of the newly identified cavitation damage on the guide vane of the Three Gorges turbines by promoting the turbulent boundary-layer transition through the receptivity mechanism. For details, refer to recent studies (e.g. Li 2006, 2008; Chen and Li 2011).

6.2.2 Pressure Pulsations with Respect to Loads in Francis Turbines

Pressure pulsations are of great importance with regard to the reliable and smooth operation of Francis turbines for the whole guaranteed range. This range normally starts from at a very low part-load (in some cases no-load condition) and ends at far over the best efficiency point (BEP).

6.2.2.1 Operation Range and Pressure Pulsation

For a prototype Francis turbine, the range in the operation performance curve is divided into several zones according to flow features, as shown in Fig. 6.2a. These features are non-vortex rope, full load, part load, channel vortex, flow separation zone on the suction side of the blade's leading edge (i.e. high head case), flow separation zone on the pressure side of the blade's leading edge (i.e. very low head and large load case), and cavitation at the trailing edge of the blade (overload case). Figure 6.2b is another type of performance curve for a prototype Francis turbine proposed by Russian manufacturers. The abscissa is power ratio and the ordinate is head ratio. Figure 6.3 shows the shape of draft-tube cavity-vortex under different operation conditions.

Figure 6.2b shows four zones or regions:

Zone 1: The flow at the runner outlet has positive circulation. Vibration of the turbine is usually small, with a very low efficiency. However, Francis turbines are not recommended for operated at this zone except for spinning as a stand-by unit (i.e. no-load). The flow pattern is shown in Fig. 6.3a. There is a dead flow region in the draft tube.

Zone 2: The amplitude of pressure pulsation, especially in a draft tube, is high, with low frequency. This results from the helical vortex rope in the draft tube, as shown in Fig. 6.3b and c. The rotating frequency of this rope is 0.15–0.33 times the runner's rotating frequency. The turbine is usually not allowed to operate in this region for a long time if a reliable device for air admission to the draft tube is

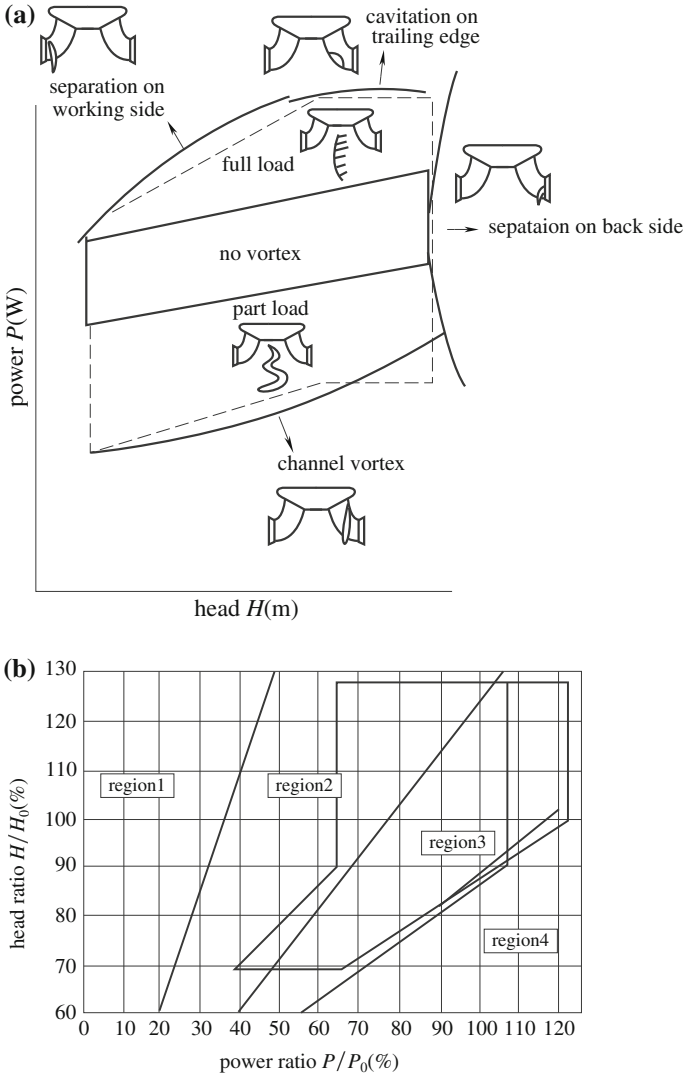

Fig. 6.2 **a** Operation zones in prototype characteristics' curves of Francis turbine Abscissa is water head (unit: m) and ordinate is power (unit: W) (Tao and Liu 2004). **b** Performance zones of prototype Francis turbine (From Leningrad Metallurgical Plant), (see Sotnikov and Pylev 2001)

available. If no air admission device is equipped, machines may be destroyed within a few years of operation.

Zone 3: Stable operation at high efficiency is achieved since no obvious vortex rope presents under the runner exit as shown in Fig. 6.3e.

Zone 4: Under the exit of runner there is a negative vortex rope (i.e. it rotates in the opposite direction of runner rotation). The pressure pulsation increases, and

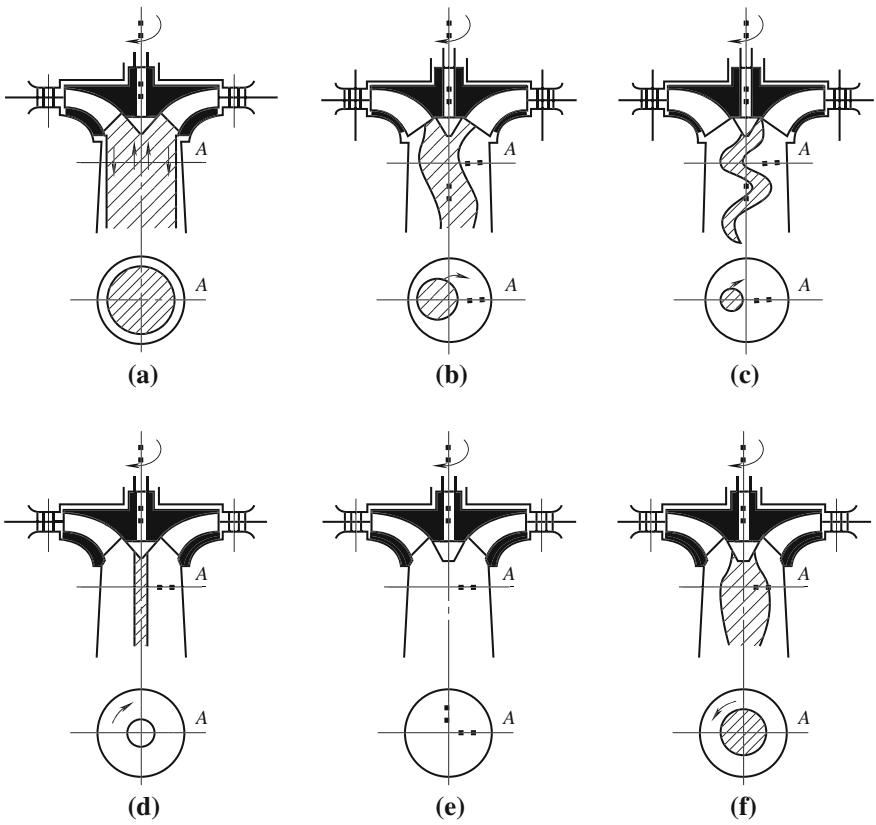

Fig. 6.3 Shape of draft tube cavity-vortices **a** dead flow case in the draft tube. **b** helical vortex rope in draft tube at very small flow case **c** helical vortex rope in draft tube at small flow rate **d** straight rope at higher part-load case **e** no votex rope at high efficiency case **f** onion shape rope at high flow rate case

severe cavitation occurs. This is the second vibration zone of the turbine runner. The vortex rope is shown in Fig. 6.3f as an onion-like shape.

Another operation zone named for higher part-load is possible where the vortex shape is similar to Fig. 6.3d. This zone usually appears on Francis turbines of high specific speed at the flow rate ranging from 75 to 90 % of the optimum. The pressure pulsation frequency is 1–5 times of the runner rotating frequency f_n.

6.2.2.2 Operation Range and Pressure Pulsation in Draft Tube

Figure 6.4 shows the operation ranges of Francis turbines with respect to the pressure pulsation in draft tube by Jacob and Prenat (1996). According to IEC60193, the stability of Francis turbine is strongly dependent upon the eigen

frequency, f_0, of the water in the draft tube. When the frequency of pressure pulsation is close to it, resonance would easily occur.

1. Classification of pressure pulsations against turbine operations.

The operating parameters describing the hydraulic performance are the unit energy coefficient, E_{nD}, and the unit flow-rate coefficient, Q_{nD}, with reference values at the best efficiency point,

$$E_{nD} = \frac{E}{n^2 D^2}, \quad Q_{nD} = \frac{Q}{nD^3}. \tag{6.8}$$

Here, E is the specific hydraulic energy, n is the rotating speed (rpm); D is the runner characteristic diameter; n_{QE} is the unit speed coefficient; and σ is the Tomas coefficient of cavitation with reference head, *NPSH*.

$$n_{QE} = \frac{Q_{nD}^{1/2}}{E_{nD}^{3/4}}, \quad \sigma = \frac{NPSE}{E}. \tag{6.9}$$

The graph on the left of Fig. 6.4 is the operation curve of a model turbine in which the abscissa is the flow rate coefficient, and the ordinate indicates energy coefficient. For a given rotating speed, the required efficiency contour and guide vane opening contour curves can be deduced from the model characteristics chart in this figure. Turbine characteristics are specified by the unit energy a and the unit flow rate b at BOP. But the rated turbine characters of a hydro power project is specified by unit energy c and unit flow rate at the rated point of the station, which are usually different from those at BOP.

The continuous operation range of the turbine is restricted by the following factors: the minimum of guide vane opening d, the maximum of guide vane opening e, the maximum and minimum unit energy coefficients f and g of the project and the maximum power of the generator used in the station.

The graph on the right of Fig. 6.4 shows variation of pressure pulsation amplitudes in the draft tube from minimum to maximum of guide vane openings under the rated energy unit c condition. In this figure, the dimensionless amplitude is the function of dimensionless flow rate and frequency (obtained via the Fourier transform). The turbine operation cases are ① very low flow rate, ② part load, ③ high part load, ④ high efficiency, and ⑤ full load.

2. Descriptions of pressure pulsation in a draft tube

(a) Helical vortex rope precession at part load. In Fig. 6.4, ② indicates the pressure pulsation zone with the precession of a helical vortex rope in draft tube. The vortex rope rotates around its center with angular speed Ω. The precession is a rotation movement of a rotating center of the vortex rope around another fixed axis (central axis of the conical part) with another angular speed ω. ω is called the precession angular speed as discussed in Chap. 4 . In the case of a part load, the combined effect of the conical diffuser and the elbow causes the

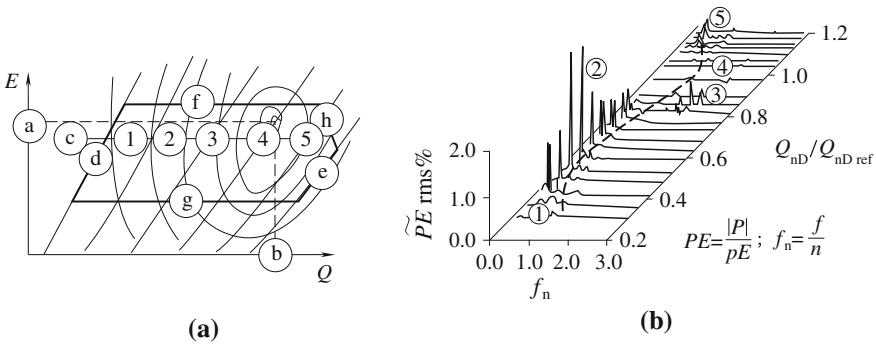

Fig. 6.4 Francis turbines operation range with a pressure pulsation water fall graph in draft tube (Jacob and Prenat 1996) **a** performance chat **b** waterfall of pressure fluctuation based on FFT

flow at the runner exit with a positive circulation to have a precession movement around the axis of the conical part of draft-tube. Furthermore, the Tomas cavitation number will be small enough to induce cavitation at the low pressure centre of the vortex rope, referred to as the cavity vortex precession.

The precession will produce an asymmetric rotating velocity field in the draft tube and pressure pulsation in the conical part. The pressure pulsation with the precession frequency will mainly occur in the elbow.

Although precession frequency varies greatly from turbine to turbine, the dimensionless precession frequency in most Francis turbines can be deduced through similarly laws. Z_t is the ratio of the precession frequency, f_p, to the rated frequency of turbine, f_n, is

$$Z_t = \frac{f_p}{f_n} \approx 0.26 \pm 20\ \%. \tag{6.10}$$

The precession frequency of some improved designs of hydraulic turbines has achieved that $f_p = 0.4\, f_n$.

The amplitude of pressure pulsation caused by the precession in part load is influenced by either the dynamic response of the prototype flow system or the testing conduit of the model turbine. If this dynamic response is very weak, the dimensionless pulsation amplitude at the ② position in Fig. 6.4, is approximately equal to

$$\tilde{P}_{Erms} \approx \frac{n_{QE}}{5} \pm 50\ \%. \tag{6.11}$$

Precession synchronic frequencies also appear in the spectrum, but contribute little to the pulsation amplitude. The multiple precession sometimes emerges in case ① with very low flow rate and induces small amplitude pulsation.

(b) The natural vibration of water flow in draft tube. Due to the rudimentary vortices and low pressure, cavitation bubbles accumulate in the middle of the runner's exit section. Elastic volume, V_{vap}, that enters the draft tube with the

fluid flow from runner will invoke vibration of the water body. In the draft tube system there exists the characteristic contents that are the water inertia I and the "cavitation compliance/stiffness (flexible capacitance)" (see notes) C. For such a vibrating system, its natural vibration frequency, f_0, is calculated as

$$f_0 = \frac{1}{2\pi\sqrt{IC}}, I = \int \frac{dL}{A}, C = -\frac{\partial V_{vap}}{\partial NPSE}. \tag{6.12}$$

Here, L is the length of the draft tube from its inlet to outlet, and A is the cross-section area of draft tube.

Notes: Apart from the passive model of "compliance", the cavitation cloud itself can also behave as a (pressure fluctuation) exciter with its own characteristic frequency and stimulate a particular low-frequency component in the whole turbine system through a double-oscillator mechanism. This is often referred to as cavitation resonance which was firstly identified in the Ventari flow by Li et al. (1983, 1986). For a systematic description of this phenomenon, see Li et al. (2008). Under Rudolf et al. (2006), this condition, the cavitation cloud is a complete oscillating system rather than a simply lumped-capacitive element in an oscillating system (e.g. the draft-tube). That is, apart from compliance, it possesses, at least, the inertia mass, elasticity, and viscous resistance. For some cases, these parameters have a rather discrete nature than lumped parameters, subject to the geometric shape and properties of the cloud.

The dashed line in Fig. 6.4 indicates the natural vibration frequency of the draft-tube system. When the cavity bubble approaches its maximum volume, the natural vibration frequency is close to the precession frequency of the vortex rope under part load conditions, causing a resonance in the draft tube and thus a strong pressure pulsation.

For a normally designed draft tube, it is assumed that $\sigma E_{nD} = 1$, where σ is the reference Tomas number and E_{nD} is the optimum unit energy coefficient. From these, the minimum natural vibration frequency $f_{0\min}$ of the draft tube at a part load case is close to the vortex precession frequency f_p, i.e.,

$$\sigma = \frac{1}{E_{nD}} \rightarrow f_{0\min} \approx f_p \pm 50\ \%. \tag{6.13}$$

As a first order approximation, the Tomas number and the unit energy coefficient have the following influences on the frequencies:

$$\begin{cases} \frac{\partial(f_0/f_n)}{\partial\sigma} \approx 20 - 35\sqrt{nQE} \pm 50\% \\ \frac{\partial(f_0/f_n)}{\partial\left(E_{nD}/E_{nDef}\right)} \approx 0.75 \pm 50\% \end{cases} \tag{6.14}$$

In full load cases, the natural vibration frequency in the draft tube has a large range of variation. Its partial derivatives with respect to Tomas number is almost

the same as in the part load case. So far, statistical data of these partial derivatives are still not available.

However, owing to various factors, such as the compressibility of water, geometric discrepancy between the prototype and the turbine model for which case the bubble cloud volume is small and the draft-tube is long (see notes), the prediction of the natural vibration frequency by using this lumped model will show a large warp. In the case of short draft tubes for part or full loads, the tested natural vibration frequency of the model turbine does not change greatly even with injected cavitation nucleus in an open type test.

Notes: That is, this model [often referred as "water plug" model, for a systematic review see Sect. 7.3.4. Draft Tube Free Vibration in Li (2001)] will deviate from the nature of the draft-tube that has rather discrete parameters.

(c) Instability in "higher part load" case. In Fig. 6.4, ③ indicates the pressure pulsation zone caused by higher part load instability in Francis turbine. This zone is located at a flow rate between 70–90 % of the optimum. This instability will lead to strong pressure pulsation in the draft tube and spiral case.

(d) Self excitation. In Fig. 6.4, ⑤ indicates the pressure pulsation zone at full load. In the cases of a full load and a very small flow rate, the partial derivatives of "cavitation compliance/stiffness (flexible capacitance)" with respect to relative flow rate and unit energy coefficient, have the same sign (positive or negative). The damping of natural vibration in the draft tube will be small and consequently it may transmit to the turbine conduit and cause resonance. This phenomenon will be covered in Sect. 6.3.

6.2.3 Higher Part Load Pressure Pulsation in Francis Model Turbine

The higher part load pressure pulsations exist for middle and high specific speed Francis turbine models within a relatively narrow part load zone near the optimum (shown in Fig. 6.5) where there is usually a cavitating vortex rope of small size at normal plant cavitation numbers. Therefore the amplitude of the vortex-rope basic (precession) frequency component is not as high as for the case of a typical part load. However, higher-frequency components with higher amplitudes will appear to increase the overall level of pressure pulsations. This phenomenon has also been observed in prototype turbines. However, this type of pressure pulsation has never caused any problems on prototype.

6.2.3.1 Model Test of Higher Part Load Pressure Pulsation

In order to understand the behavior of the vortex rope during higher part load operations, Koutnik et al. (2006) performed investigations on both model texts and theories in order to develop a correct model-to-prototype transposition analysis.

Pressure pulsations at higher part load can be categorized as forced vibrations, self-excited vibrations, or parametric vibrations.

In order to understand the nature of these pressure pulsations, Koutnik et al. (2006) tested the dependency of their amplitude and frequency on a model machine.

6.2.3.2 Elliptical Instability Model

An analytical approach is employed to study the influence of individual parameters on vortex rope behavior. For this purpose the Rayleigh-Plesset equation is derived for a cavitating cylindrical rope (see Rudolf et al. 2007):

$$-\tfrac{1}{2}\rho\dot{R}^2 - \rho \ln R\left(\ddot{R}R + \dot{R}^2\right) + \tfrac{\sigma}{R} - \left[p(z) + \tfrac{\sigma}{R_0}\right]\left(\tfrac{R_0}{R}\right)^{2k} + 2\eta_s \tfrac{\dot{R}}{R} + \eta_s \ln R \tfrac{\partial^2}{\partial z^2}\left(\dot{R}R\right) = -[p(z) + p_N(z,t)]. \tag{6.15}$$

Here, R is vortex rope radius; R_0 is initial vortex rope radius; $\dot{R}$ and $\ddot{R}$ are the first order and second order of derivatives respectively; z is the ordinates along the central axis of draft tube; k is the polytrophic coefficient; η_s is dynamic viscosity; σ is small unsteady change of pressure; $p_N(z, t)$ is pressure excitation.

In order to allow for a qualitative analysis of the vortex rope with, say elliptic cross-section, or for description of particle motion along an elliptical trajectory and precessional motion of elliptical rope, the Lagrange approach should be employed.

Thus the particle trajectory and pressure distribution must obey the following equation of motion:

$$\frac{\partial^2 x_i(a_j,t)}{\partial t^2}\frac{\partial x_i}{\partial u_j} + \frac{\partial p}{\partial u_j} = 0 \tag{6.16}$$

and continuity equation:

$$J(t) = J(0). \tag{6.17}$$

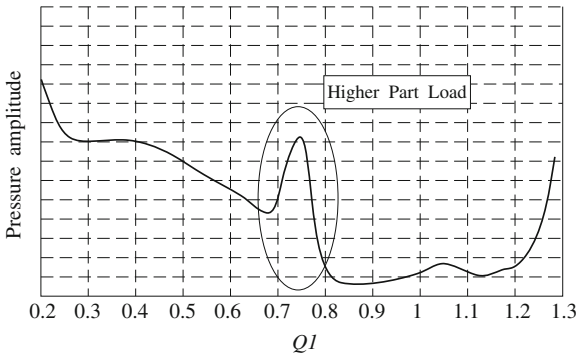

Fig. 6.5 Typical pressure trend in a model Francis turbine draft tube cone (Liu and Ji 2004)

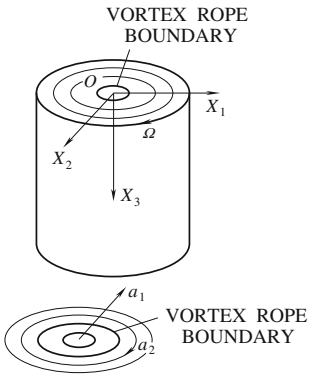

Fig. 6.6 Vortex rope with elliptical section (See Rudolf et al. 2006)

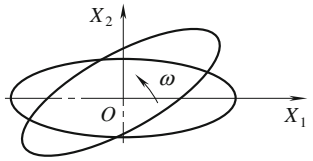

Fig. 6.7 Precession of vortex rope (See Rudolf et al. 2006)

Here, $x_i(aj, t)$ denotes particle trajectory; u_j is the curvilinear coordinate; p is pressure; $J(t)$is Jacobin in time t; and $J(0)$ is Jacobin initial condition at $t = 0$. Influence of viscosity is neglected for simplicity. Equations (6.16) and (6.17) must be supplemented by state equation of the gaseous phase and Laplace equation. The following conditions have been studied:

1. Cavitating vortex rope of elliptical cross-section in which liquid is rotating along the rope circumference, as shown in Fig. 6.6.
2. Cavitating vortex rope of elliptical cross-section with both rotational and precessional motions. There is a precessional motion of the cavitating vortex rope with an elliptical cross-section, as shown in Fig. 6.7.

Investigation of many Francis turbine models has indicated that during higher part load pressure vibrations, the cavitating vortex rope has an elliptical cross section and the rope ends up before draft tube elbow. When the elliptical form disappears, the high frequency components of the pressure pulsations disappear as well. The main peak in frequency spectra (of the higher part load) bears a synchronous character in the draft tube and the smaller peak on its right side has a dominating rotating component. The higher part load frequency is not a multiple of the vortex rope frequency.

Recently, with the development of Francis turbine design technology, optimization of circumferential velocity distribution on the exit section of turbine runner could minimize or even eliminate the high part load pressure pulsation. Figure 6.8 illuminates such a process. The variation of relative pressure pulsation amplitude against flow rate at different heads is shown, which is from the accepted model

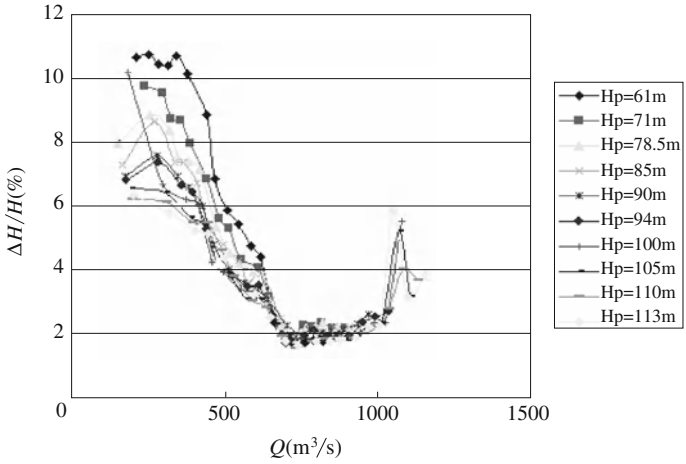

Fig. 6.8 Pressure pulsation amplitude distribution with the flow rate at different heads (Liu and Ji 2004)

test, measuring at a distance of $0.3D_1$ below the runner exit. This Francis turbine is now operating in the right hand power house of Three Gorges Project and a similar design has also been employed for other hydro power projects (Liu and Ji 2004).

6.2.4 Vibration Induced by Karman Vortex Shedding

The Karman vortex street is caused by unsteady separation of a fluid flow over bluff bodies. As shown in Fig. 6.9, a Karman vortex street develops under certain conditions in the wake of bluff cylindrical bodies. This periodic shedding of eddies first takes place alternatively from each side of the body though the oncoming flow is perfectly steady. A vortex street will only be observed over a given range of Reynolds numbers (*Re*), typically above a limit of $Re \approx 90$.

The range of *Re* values varies with size and shape of the eddies, as well as with the kinematic viscosity of fluid. Over a large *Re* range ($47 < Re < 10^7$ for circular cylinders) eddies shed continuously, forming rows of vortices in the wake.

When a single vortex is shed, an asymmetrical flow pattern forms around the body, changing the pressure distribution. This indicates that the alternate shedding

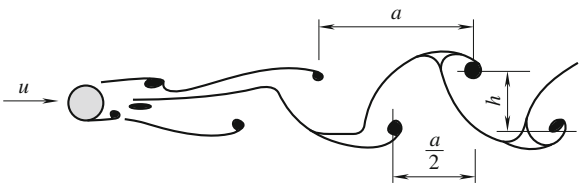

Fig. 6.9 Karman vortex street *V* stream speed; *a* spacing between vortices; *h* distance between two rows of vortices

of vortices can create periodic lateral (sideways) forces on the body, causing it to vibrate. If the vortex shedding frequency is close to the natural frequency of a body or structure, resonance could occur.

In hydraulic machinery, the Karman vortex street shedding can be found in the trailing edges of stay vanes, guide vanes and runner blades. This type of vibration induced in a turbine structure contributes to cracks or ruptures of blades.

6.2.4.1 Karman Vortex Street in the Wake from Stay Vane or Stationary Blade

In a long circular cylinder, the frequency of vortex shedding is given by the empirical formula (Torbjørn et al. 2001):

$$\frac{f_k d}{V} = 0.198\left(1 - \frac{19.7}{Re}\right) \tag{6.18}$$

where f_k is the vortex shedding frequency. This formula will generally hold for the range $250 < Re < 2 \times 10^5$. The dimensionless parameter $f_k d/V$ is known as the Strouhal number. V is the velocity of the main stream outside of the wake.

Heskestad and Olberts (1960) have done experiments on other geometries of outlet edge, leading to following formula:

$$f_k = 0.01StBV/(\delta_2 + \delta_v). \tag{6.19}$$

Here, B is a relative frequency that depends on the shapes of the trailing edge as shown in Table 6.1 (Heskestad and olberts 1960); St is the Strouhal number, $St = f_k\,(\delta_2 + \delta_v)/V$. Gongwer (1952) found $St = 0.19$ was more appropriate.

In reference to Fig. 6.9, the relative velocity v of the vortex row to the stream speed V is

$$v = V \cdot f_k a. \tag{6.20a}$$

Table 6.1 Relative frequency B for different geometries (Heskestad and olberts 1960)

Plate	Geometry	B	Plate	Geometry	B
1	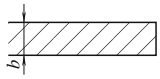	100	5	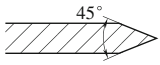	117
2	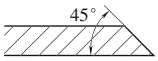	112	6	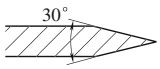	159
3	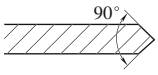	96	7	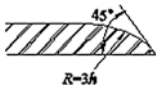	149
4	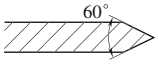	93			

Here a is the space between two successive vortices, and v can be based on potential flow as

$$v = \Gamma/(2a)\text{th}(h\pi/a). \tag{6.20b}$$

Here h is the distance between two rows of vortices and Γ is the velocity circulation (i.e., the vortex intensity of each vortex in the vortex row):

$$\Gamma = 2va/\text{th}(h\pi/a). \tag{6.21}$$

From experimental data, the following relations can be obtained:

$$h/a = 0.29 \tag{6.22}$$

$$h = k_2\delta_2 \tag{6.23}$$

$$\Gamma = k\delta_2 V. \tag{6.24}$$

Here δ_2 is the thickness trailing edge from which the double-vortices are generated, and k and k_2 are the coefficients determined by the shape of the trailing edge.

According to potential flow analysis, the force P acting on the stay vane or stationary blade of L length from the Karman vortex is (Wei 1989)

$$P = k\rho\delta_2 LV^2 \sin(2\pi f_k t). \tag{6.25}$$

6.2.4.2 Karman Vortex Street in the Wake from Rotating Blade

When water flows through the rotating runner blade under certain conditions, a Karman vortex street will also shed in the wake of the blade for both the Francis turbine blade and Kaplan the turbine blade, referring to Fig. 6.10a and b. The shedding frequency f_k is derived with a similar empirical formula as the stay vane:

$$f_k = k_1 W_2/\delta_2. \tag{6.26}$$

Here W_2 is the velocity in the main stream outside of the wake that increases from the crown to the band for Francis runner. This formula is generally true for

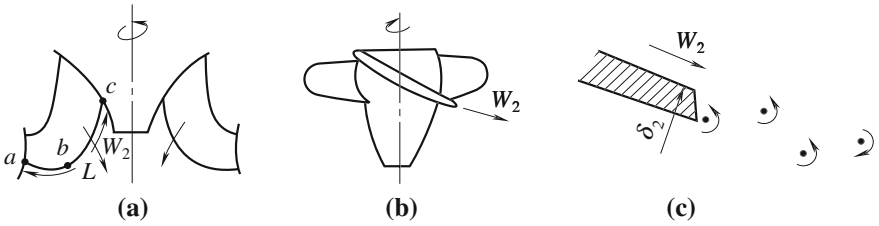

Fig. 6.10 Karman vortex street shedding from the blade of turbine. **a** Francis turbine blade. **b** Kaplan turbine blade. **c** vortex street behind the blade (Wei 1989)

the range $250 < Re < 2 \times 10^5$. The Reynolds and the Strouhal numbers are defined as follows:

$$Re = \rho W_2 \delta_2 / \mu \text{ and } St = f_k \delta_2 / W_2. \tag{6.27}$$

The value of W_2 increases from crown to band. Consequently, the values of f_k vary. Any values of such frequency f_k coincide with the eigenvalue of blade structure vibration, and the resonance of blade structure will follow. This is often referred as the excitation point. During resonance, the vortex shedding frequency near the excitation point may not initially equal the eigenvalue, but it will approach the value after resonance. The length of the trailing edge, within frequencies between 0.93 and 1.09 of the eigenvalue, is named as the synchronous length l as an estimation of the vortex force acting upon the blade.

The intensity of the Karman vortex behind the runner blade can be estimated in a similar way to Eq. (6.24) with the empirical coefficient,

$$\Gamma = 32.95 k_2 \delta_2 (0.29 W_2 - f_k k_2 \delta_2). \tag{6.28}$$

According to potential flow analysis, force P, acting upon the runner blade of length l by the Karman vortex is (Wei 1989)

$$P = k \rho \delta_2 l \overline{W_2^2} \sin(2\pi f_k t) \tag{6.29a}$$

$$k = 26.71 k_2 (0.29 - k_1 k_2). \tag{6.29b}$$

Here, $\overline{W_2^2}$ is the mean value of W_2^2 in the synchronous length l, and much smaller than the entire length L of trailing edge. For engineering calculations $l = 0.1L$, $k_1 = 0.19$, and $k_2 = 1$.

The vibration amplitude Y of the runner blade caused by force P can be estimated as

$$Y = K \rho \delta_2 / (C f_k) \left(1 - \cos\left(2\pi x_p / L\right)\right) (l/L) \overline{W_2^2}. \tag{6.30}$$

This is deduced from a model beam of length L at the blade's trailing edge under the load of vortex with damping. Here C is the damping factor; x_p is the coordinate of the acting force P along L ($x_p = 0.5L$ approximately); and $K(= 2k/(3\pi))$ is the factor of edge shape.

A calculation of the vibration amplitude excited by the vortex street on the blade trailing edge in a Francis turbine is illustrated in Fig. 6.11. The abscissa is the relative flow rate $\bar{Q} = Q/Q_r$(Q_r is rated), and the ordinate is the relative amplitude $\bar{A} = Y/Y_{max}$(Y_{ma} is Y at Q_r) of vibration. The excitation point is close to the crown (i.e. x_p equals zero approximately) at a very small flow rate. As flow rate grows, x_p moves towards the band to 0.5 (at $\bar{Q}_2$) or more, and the amplitude also increases. With an improved trailing edge, vibration from the vortex street is mitigated.

The optimized trailing edge with $l = 3\ \delta_2, r = 2\,\text{mm}, \alpha = 20^\text{o}$ and $R \approx 4\ \delta_2$ is shown in Fig. 6.12.

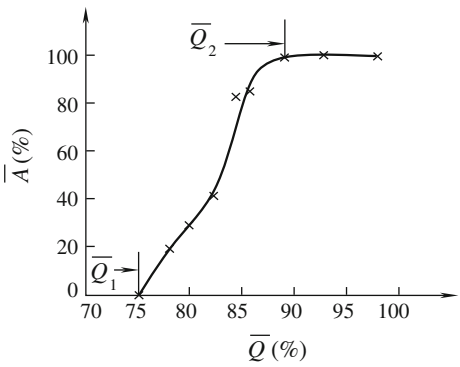

Fig. 6.11 The relative amplitude of vibration excited by the vortex street on blade trailing edge with relative flow rate (Wei 1989)

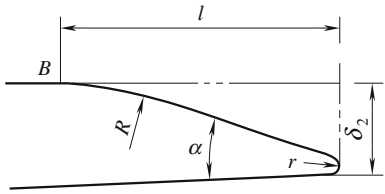

Fig. 6.12 Optimized blade trailing edge (Wei 1989)

6.2.4.3 Karman Vortex Street Through CFD Simulation

In 2006 Lockey and Keller published their results of an unsteady CFD simulation of a Karman vortex shedding at the stay vanes of a machine installed at a Canadian hydropower station (Lockey et al. 2006). Before applying CFD to this complex case Keller validated the CFD method for a NACA009 profile by comparing the CFD prediction with the measurements of the Hydro Dyna project (Ausoni et al. 2006). In a most recent study by Nennemann et al. (2007) they found that the shedding frequency shifts when the transition from a laminar to turbulent boundary layer is taken into account, leading to an improved accuracy of the prediction. Nennemann's finding was confirmed through varying the surface roughness on the blade inlet. The shape of the trailing edge strongly influences the intensity of the vortex shedding, and a major concern of the validation study is the effect of trailing edge geometry. The trailing edge geometry determines the interaction of the counter rotating vortices. A dovetail modification leads to a partial elimination of the vortices, because it forces them to move a way upstream into the dovetail centre.

6.3 Surge in Draft Tube in Francis Turbine

In Sect. 6.2, the operation range of Francis turbines relating to pressure pulsation in draft tube was discussed. In this section, their mechanics and similarities will be further analyzed.

6.3.1 Classifications of Draft Tube Surge

The occurrence of draft tube surge in Francis turbines was established in the early twentieth century. The first analytical study of this issue was conducted by Rheingans (1940). He found that the frequency of pressure pulsations and power swings could be determined by

$$f = f_n/3.6 \tag{6.31}$$

where f_n is the rotational frequency of the turbine runner and shaft.

Subsequent investigations (Deriaz 1960) using transparent draft tube models showed that the flow in surging regions contained a helical vortex that precessed about the axis of the draft tube at approximately the frequency given by Eq. (6.31). In a hydraulic turbine the vortex may be filled with water, air, or water vapor.

The undesirable effects of draft tube surge from the pressure field associated with precessing a helical vortex are well known. The fluctuating pressures provide an excitation that can interact with hydraulic, structural, mechanical, or electrical components of the turbine and power plant. Pressure pulsations within the draft tube tend to produce a fluctuating head on the turbine, which in turn gives rise to pulsations in discharge, torque, and output power.

6.3.1.1 Asynchronous Surging

Two types of pressure pulsations in draft tube surges are identified in literature. The first is an asynchronous pressure pulsation precession of the helical vortex about the axis of the draft tube. Purely asynchronous pulsation is a local effect of vortex motion which does not produce pulsations on the average pressure at a given cross section along draft tube axis. Despite of that, a purely asynchronous surge can cause excessive noise and vibrations.

6.3.1.2 Synchronous Surging

The second type of pulsation is synchronous pulsation where average pressure at a given cross section along draft tube axis varies with time. With the greatest potential for influence on the system's other parts, this type of pulsation also contributes to a change of net head across the runner that corresponds to changes of average pressure within the draft tube. This leads to discharge and power pulsations. Superposition of synchronous and asynchronous components is possible (Fanelli 1989).

Deriaz (1960) proposed that the interaction of a vortex with piers in the draft tube foot could induce a synchronous pressure pulsation.

Fanelli (1989) asserted that the interaction between the helical vortex and draft tube elbow produces synchronous pulsations. The cavitated vortex core was also

considered as a requirement for synchronous surging. Nishi et al. (1980) conducted a study in which the presence of a cavitated vortex core produced large synchronous pressure pulsations.

6.3.1.3 Air Admission

The first solution to reduce draft tube surges usually involves the admission of air into the draft tube. Air is commonly supplied just below the runner at the draft tube inlet. On some units, provisions are made to admit air through the runner head cover, the runner cone, or a snorkel attached to the runner cone. In some cases, air can naturally flow into the draft tube during operation at low tail water. However, at high tail water, or on units that are set quite low for cavitation protection, compressed air must be injected into the draft tube.

6.3.1.4 Structural Modifications

The structural modification most commonly seen is to straighten the flow in the draft tube that serves to break up the vortex. Typical devices include fins attached to the draft tube wall or concentric cylinders mounted in the draft tube. Fins are proven to be effective in many cases, but they introduce significant loss of efficiency and are vulnerable to cavitation erosion and structural vibrations. Concentric cylinders do not normally reduce efficiency significantly.

Problems of mounting cylinders in draft tube are significant, among which are cavitation erosion and vibration. One advantage of concentric cylinders is that the supporting struts can also function as locations for air injection. This may help reduce the surge further and prevent cavitation damage to the struts.

Another type of modification is an extension to the runner cone, sometimes called a snorkel. These devices may be attached to the runner, or fixed within the draft tube so they sit just beneath the runner cone. Some researchers suggest that these devices break up the surge by filling a portion of the reverse flow region. Air injection can also be combined with these structures.

6.3.1.5 Vortex Breakdown

The flow phenomenon associated with draft tube surging has been described in the literatures of fluid mechanics as vortex breakdown. The vortex breakdown has been found to coincide with a formation of a stalled or reversed flow region along the flow axis (Nishi et al. 1982). As the swirl of flow increases, the axial velocity is reduced at the tube's centerline and increased near the walls. At the critical swirl level, a sudden transition in the flow is observed. A region of stalled or reversed flow is developed in the flow center, and a helical vortex forms around the reversed flow.

If the swirl is clockwise when observed from upstream, the helical vortex takes the form of a left-handed screw. The precession of vortex is in the same direction as the swirl. The helical vortex can be visualized as a rolling, shear layer that forms at the boundary between the reverse flow region and the surrounding swirling flow. This generates a vortex rope that orients perpendicular to the swirling flow surrounding the reverse flow region (Nishi et al. 1982). Thus, as the swirl increases, pitch of the vortex can be expected to rise. The most common flow structure associated with the vortex breakdown is a single helical vortex.

6.3.2 Draft Tube Surge Mechanics

The precessing helical vortex rope in the draft tube causes a surge in part load and the over load cases.

6.3.2.1 Causation of Draft Tube Surge of Francis Turbine

In the Francis turbine, point 1 is directly upstream of the runner as the flow exits the guide vanes. Point 2 is on the downstream side of the runner as the flow enters the draft tube. For the angular momentum at point 2, $\tilde{\Omega}_2$ equals the difference between the angular momentum $\tilde{\Omega}_1$ at point 1 and the shaft toque, i.e.,

$$\tilde{\Omega}_2 = \tilde{\Omega}_1 - P/\Omega \tag{6.32a}$$

where P is the turbine output power and Ω is the angular velocity. Multiplying each term of the last equation by $D/(\rho Q^2)$ and rearranging them yields

$$\tilde{\Omega}_2 D/\left(\rho Q^2\right) = \tilde{\Omega}_1 D/\left(\rho Q^2\right) - PD/\left(\Omega \rho Q^2\right). \tag{6.32b}$$

The left side of Eq. (6.32b) is the parameter of draft tube swirl. The first term on the right is the swirl parameter for the flow leaving the guide vanes and entering the runner, with reference to the guide vane momentum parameter. The second term is the swirl extracted from the flow by turbine runner. The guide vane momentum is defined as

$$\tilde{\Omega}_1 = \rho Q^2 r \sin\alpha/\left(abZ_g\right). \tag{6.33}$$

Here, D_1 is the diameter of runner exit at the band (D is the runner diameter); b is the height of guide vanes; Z_g is the number of guide vanes; Q is the flow rate through the turbine; a is the opening of guide vanes; r is the radius of the central line of guide vanes; and α is the angle between the velocity vector and radius R, as is shown in Fig. 6.13.

The unit power, unit flow rate, and angular speed as well as unit speed of the turbine are as follows:

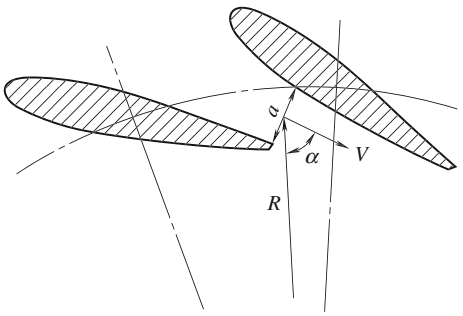

Fig. 6.13 Guide vane outlet flow

$$P_{11} = \frac{P}{D_1^2 H^{3/2}},\ Q_{11} = \frac{Q}{D_1^2 H^{1/2}},\ \Omega = \frac{\pi D_1 n}{60\sqrt{2gH}},\ n_{11} = \frac{nD_1}{H^{1/2}}.$$

The inlet angular parameter of draft tube yields

$$\frac{\tilde{\Omega}_2 D}{\rho Q^2} = \frac{Dr\sin\alpha}{abZ} - \frac{P_{11}D}{2\sqrt{2g\Omega Q_{11}^2 D_1^2}}. \tag{6.34}$$

The right side of Eq. (6.34) expresses the relative flow circulation into draft tube.

In the upcoming section, draft tube surge will be explained through vortex movement. Euler's equation for turbo machines and energy exchange has the following form in a hydraulic turbine:

$$\eta_h H = (U_1 V_1 \cos\alpha_1 - U_2 V_2 \cos\alpha_2)/g \tag{6.35}$$

where U_1, U_2 are the circumferential velocities at runner the inlet and outlet respectively; V_1, V_2 are the absolute velocities at inlet and outlet; α_1, α_2 are the angles between V_1, V_2 and U_1, U_2 at inlet and outlet respectively; H is the working head of turbine; and η_h is its hydraulic efficiency.

Figure 6.14 illustrates the velocity triangles at the runner blade inlet and outlet for the optimum operation case (a) with a subscript "o" and off-design case (b) respectively.

At the optimum operation, attack angle $\Delta\beta_1$ of the relative velocity W_{1o} at inlet is zero. And at outlet, absolute velocity V_{2o} flows out from runner along the axial direction, that is

$$\Delta\beta_1 = \beta_{1o} - \beta_{1A} = 0,\ \alpha_{2o} = \pi/2. \tag{6.36}$$

Here, β_{1o} is the relative angle at inlet for optimum case, and β_{1A} is the geometrical angle of blade at inlet. Incorporate Eq. (6.36) into Eq. (6.35) yields

$$\eta_{\max} H_0 = [U_{10}(U_{10} - W_{10}\cos(\pi - \beta_{1A}))]/g. \tag{6.37}$$

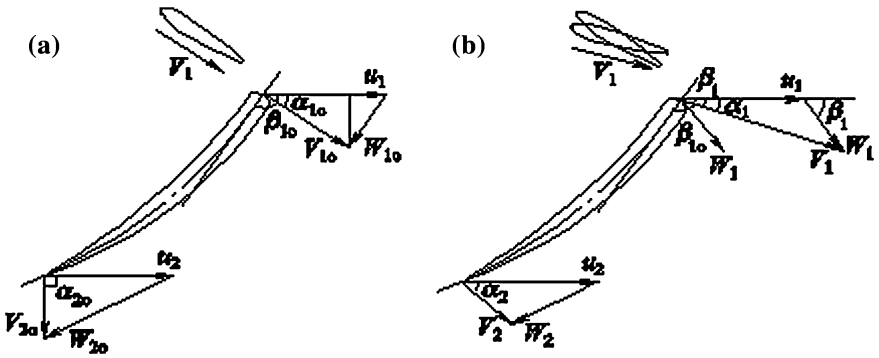

Fig. 6.14 Runner blade inlet and outlet velocity triangles, **a** at optimum operation case, **b** at off-design case

6.3.2.2 Helical Vortex Rope for Part Load Cases

For off-design operations with head $H > H_0$ or flow rate $Q < Q_0$ or in part load cases where the velocity triangles are shown in Fig. 6.14b, one may get an equation similar to Eq. (6.37):

$$\eta H = [U_1(U_1 + W_1 \cos \beta_1) - U_2 V_2 \cos \alpha_2]/g. \tag{6.38}$$

In this case, there is an attack angle $\Delta\beta_1 = \beta_1 - \beta_{1A} > 0$. At the runner exit, the absolute velocity V_2 has a positive circumferential component $V_2 \cos \alpha_2$ caused by a flow with a positive attack angle passing through the blade–blade channel to the exit. That means V_{u2} (=V_2 cos α_2) is in the same direction as U_2 (the runner rotation direction).

The existence of V_{u2} results in the formation of a helical vortex rope in the draft tube at part load. The precessional movement of helical vortex rope will induce pressure pulsation in the draft tube.

The design of modern Francis turbines shows that regulation of blade-angle distribution at the trailing edge α_2 and modification of V_{u2} distribution for different operation conditions will eliminate pressure pulsations in the flow passage.

Figure 6.15 shows the amplitude variation of pressure pulsation with the opening angle of the guide vane. The opening angle controls the flow rate in the turbine as well as the circumferential component of absolute velocity V_{u1} at the runner inlet.

As the flow rate of the turbine decreases, positive V_{u2} will increase; the positive vortex area in draft tube vortex rope will also grow, and the pressure at the center of helical vortex rope will lower.

This phenomenon will induce a forward axial velocity component near the side wall in the conical part of draft tube. A cavitating vortex rope will appear, and the inverse reverse axial velocity component will present in this centre of the cavitation vortex rope, leading to vortex instability in the draft tube as indicated in Figs. 6.3b, c and 6.16.

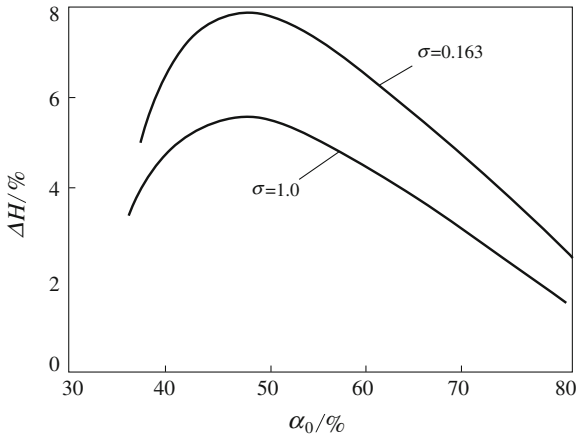

Fig. 6.15 Relations between pressure fluctuation and guide vane opening angle (Yu 2006)

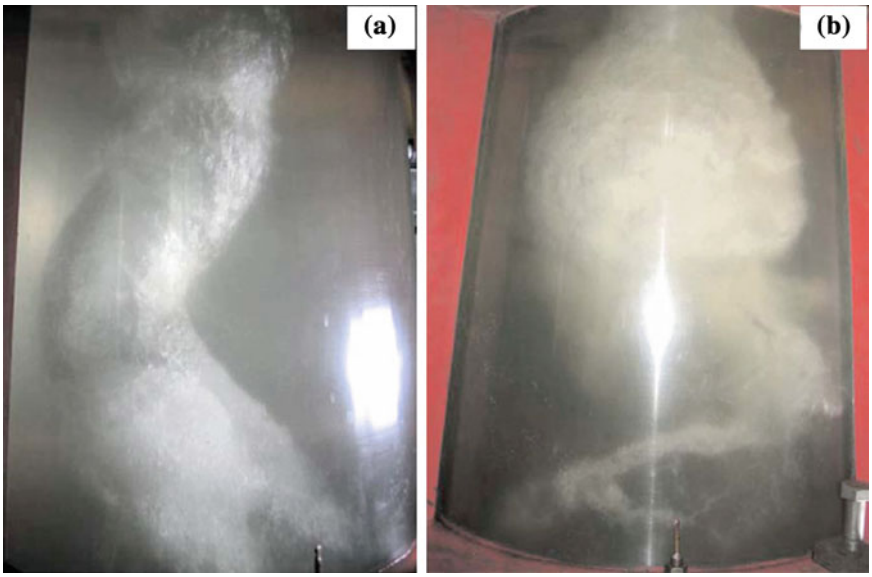

Fig. 6.16 Typical vortex ropes in the draft-tube cone of a Francis turbine model, (photos taken at Harbin Electric Machinery Co. by Q. D. Cai) **a** helical vortex rope and **b** bubble-type vortex rope

6.3.2.3 Helical Vortex Rope at Over Load Cases

Figure 6.17 shows velocity triangles at both the inlet and the outlet of runner for different opening angles. During the off-design operation with head $H < H_0$, or flow rate $Q > Q_0$, which is in over load cases, there is an attack angle, $\Delta\beta_1 = \beta_1 - \beta_{1A} < 0$. At the runner exit, the absolute velocity V_2 has a negative

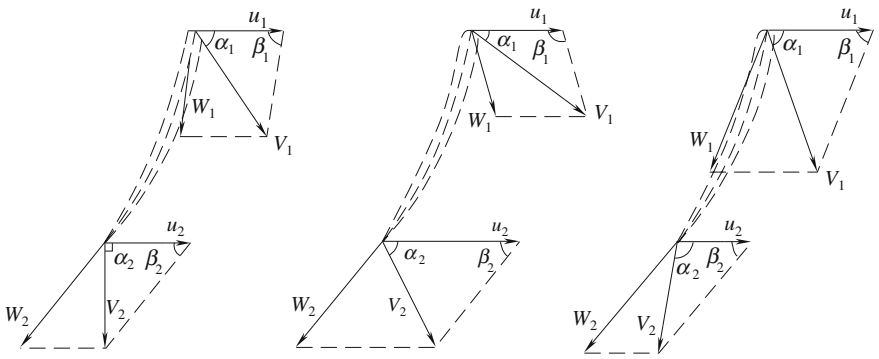

Fig. 6.17 Runner blade inlet, outlet flow velocity triangles. **a** optimum condition. **b** small guide vane angle. **c** big guide vane angle

circumferential component $V_2 \cos \alpha_2$ caused by the flow and a negative attack angle flowing through the blade–blade channel to the exit. That is, $V_{u2}(=V_2 \cos \alpha_2)$ is in the reverse direction as U_2 (the runner rotation direction). The existence of these negative V_{u2} results in an onion-shaped vortex rope in the draft tube for over load cases, as shown in Figs. 6.3f and 6.16b.

6.3.3 The Relation of V_{u2} with the Unit Speed and Unit Flow Rate

Since the circumferential component of absolute velocity at the runner exit has great influence over the vortex rope, the relation of V_{u2} with unit speed and unit flow rate will be discussed for different operation cases.

From the inlet and the out let velocity triangles in Fig. 6.14, one has

$$V_{u2} = U_2 - V_{m2}\text{ctan}\beta_2 \tag{6.39}$$

where

$$U_2 = 2\pi r_2 n/60; \text{ and } V_{m2} = Q/A_2. \tag{6.40}$$

Here, r_2 is the outlet radius of the runner; A_2 is the cross-section area of the runner exit. Substituting Eq. (6.39) into Eq. (6.40) yields

$$V_{u2} = \Omega r_2 - \frac{Q}{A_2 \tan\beta_2} = \left(\frac{\pi}{60}\right)\left(\frac{D_2}{D_1}\right)\sqrt{H}\left[n_{11} - \frac{240}{\pi^2}\left(\frac{D_1}{D_2}\right)^3 \frac{Q_{11}}{\tan\beta_2}\right]. \tag{6.41}$$

Let

$$k_1 = \left(\frac{\pi}{60}\right)\left(\frac{D_2}{D_1}\right) > 0 \text{ and } k_2 = \frac{240}{\pi^2}\left(\frac{D_1}{D_2}\right)^3 \frac{1}{\tan\beta_2} > 0,$$

then

$$V_{u2} = k_1\sqrt{H}(n_{11} - k_2 Q_{11}). \tag{6.42}$$

Partially differentiating the equation, one has

$$V_{u2} = \begin{cases} \dfrac{\partial V_{u2}}{\partial n_{11}} = k_1\sqrt{H} > 0 \\ \dfrac{\partial V_{u2}}{\partial Q_{11}} = k_1 k_2\sqrt{H} > 0. \end{cases} \tag{6.43}$$

The absolute value of V_{u2} is

$$|V_{u2}| = \begin{cases} k_1\sqrt{H}(n_{11} - k_2 Q_{11}) & (n_{11} > k_2 Q_{11}) \\ 0 & (n_{11} = k_2 Q_{11}) \\ k_1\sqrt{H}(k_2 Q_{11} - n_{11}) & (n_{11} < k_2 Q_{11}). \end{cases} \tag{6.44}$$

The linear equation $n_{11} = k_2 Q_{11}$ (the dashed line in Fig. 6.18) can divide the operation area of Francis turbine in the hill chart of $n_{11} \sim Q_{11}$ into three parts as shown in Figs. 6.2a and 6.18. Around the line, there are no circulations at the runner exit and in the vortex rope. The pressure pulsation is very weak.

On the left side of the line, i.e., $n_{11} > k_2 Q_{11}$, there is positive circulation at the runner exit which causes a positively rotating helical vortex rope with strong pressure pulsation at low frequency. On the right side of the line, i.e., $n_{11} < k_2 Q_{11}$, there is negative circulation at the runner exit which generates a negatively rotating vortex rope with rather strong pressure pulsation at low frequency.

Figure 6.15 also demonstrates that the cavitation number σ has an effect on the amplitude of pressure pulsation. When σ decreases to a critical value σ_p a large bubble will form in the center of the vortex rope, which causes the eccentric radius of vortex rope to become larger, aggravating the pressure pulsation. Under critical conditions, the amplitude will reach a value 2–3 times of its previous one. Afterwards, when σ further decreases, the amplitude will drop; although the bubble in the cavity continues to grow, the eccentric radius decreases. The large cavity volume with more air in vortex rope centre performs large damping and stiffness effects to stabilize pressure pulsation.

6.3.4 *Prediction of Pressure Pulsation Amplitude in Draft Tube*

The vortex rope frequency in the draft tube of the Francis turbine is predicted by a theoretical analysis and a method based on the eccentric vortex model in this section. This prediction can be given by the Computational Fluid Dynamics (CFD) method for computation of the three dimensional flow through the whole flow passage of the turbines.

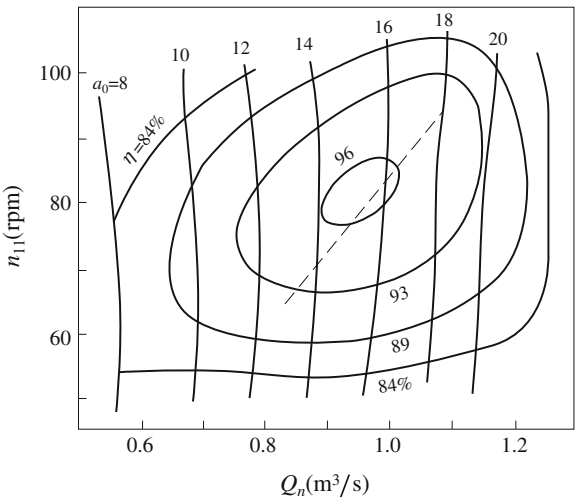

Fig. 6.18 Model Francis turbine runner characteristic *curves* (The *dashed line* shows the curve of $n_{11} = k_2 Q_{11}$) (Yu 2006)

6.3.4.1 Prediction of Circulation at Runner Exit

According to Eq. (6.41), the prediction equation of V_{u2} is

$$V_{u2} = \Omega r_2 (K - (Q/Q_o)\Omega_0/\Omega). \tag{6.45}$$

And the circulation at radius r is

$$\Gamma_r = 2\pi\Omega r^2 (K - (Q/Q_o)\Omega_0/\Omega). \tag{6.46}$$

Here, K is a factor($K > 1$)shown in Fig. 6.19; And K' is a factor of the ratio measured flow rate Q to the optimum Q_o.

After integrating the circulation in the range of $r_2 \le r \le R_2$ at the runner exit, where r_2 is the crown radius and R_2 is the band radius, the mean value of circulation at the runner exit is

$$\Gamma_2 = \frac{\pi^2 n}{30}\left(r_2^2 + R_2^2\right)\left(K - \frac{Q}{Q_o}\frac{\Omega_0}{\Omega}\right). \tag{6.47}$$

6.3.4.2 Prediction of Vortex Rope Frequency

1. Natural frequency of draft tube.

The natural frequency of the water body, f_0 in the draft tube is related to the vibration of cavity volume V_{vap} and caused by the water body in draft tube. If the eigen frequency of the cavity volume vibration equals or is close to the pressure pulsation frequency, resonance will occur.

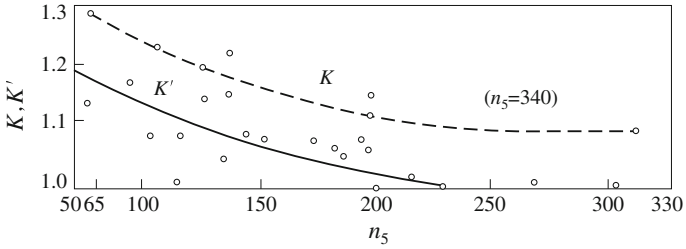

Fig. 6.19 Relation between K, K' and n_s (Yu 2006)

$$f_0 = \frac{1}{2\pi\sqrt{\left(-\frac{\mathrm{d}V_{vap}}{\mathrm{d}NPSH}\int\frac{\mathrm{d}L}{A}\right)}}. \tag{6.48}$$

Here, the term $-(\mathrm{d}V_{vap}/\mathrm{d}NPSH)$ is called the cavitation compliance of the draft tube; L is the length of draft tube measuring from its inlet to outlet; and A is the cross-section area of draft tube.

2. Calculation of pressure pulsation frequency.

The main pressure pulsation frequency in the draft tube equals the precessional frequency of the vortex rope, which is related to the inlet circulation at the draft tube entrance.

The forced eddy $V_u = \Omega r$ lies in the central core of the vortex rope and the free eddy $V_u r = \text{const}$ lies at outside of the core. Thus,

$$V_{u2} r_i = V_{uR} r_2 \tag{6.49}$$

where $V_{u2} r_i$ is the mean velocity moment at draft tube entrance, and $V_{u2} r_2$ is the velocity moment near the wall of draft tube entrance. The frequency of vortex rope is

$$f_{rope} = V_{uR}/\pi D_2 \tag{6.50}$$

where D_2 is the diameter of runner exit. Finally the dimensionless frequency is

$$f_{rope} = KSr_i^2 n_{11} - Tr_i^2 Q_{11}. \tag{6.51}$$

Here,

$$S = 4\sqrt{H}\Big/(60D_2 r_s); \text{and } T = 2\Omega_0\Big/\left(\pi Q_0 r_2^2\right)\cdot D_1^2\sqrt{H}.$$

The empirical formula of this frequency is listed in Sect. 6.2.

3. Amplitude and frequency of vortex-rope pressure-pulsation in the draft tube based on eccentric vortex model.

In reference to Fig. 6.20, the model of a draft-tube flow motion used to predict pressure pulsation caused by a helical vortex rope is sketched. O_1 is the rope center; r is the vortex rope radius; and e is the eccentric distance between O_1 and O_2 (the draft tube centre of inlet).

For two-dimensional potential flow, this eccentric vortex should be modeled as the vorticity with circulation Γ at point B and another vorticity with circulation $-\Gamma$ at point A.

The governing equation in terms of complex potential W as a function of the complex variable $Z = x + \mathrm{i}y$ is

$$\frac{\mathrm{d}W}{\mathrm{d}Z} = \frac{\mathrm{i}\Gamma}{2\pi(Z-c)} - \frac{\mathrm{i}\Gamma}{2\pi(Z+c)} \tag{6.52}$$

where $c = 1/(R-e) - 1/(R+e)$. The fluctuating pressure caused by the eccentric vortex on the plane can be deduced as

$$P_x = -c\rho\Gamma^2/(4\pi),\ P_y = 0.$$

The maximum amplitude of pressure pulsation can be estimated as

$$P = 2\pi\rho r^2 V_{ur}^2 e/\left(R^2 - e^2\right),\ A_{\max} = P_{\max}/(2\pi f\varsigma). \tag{6.53}$$

Here, f is the pulsation frequency; ς is the damping factor; V_{ur} is the circumferential velocity component at radius r.

The precession speed of the helical vortex rope can also be obtained as

$$\omega_{\mathrm{rope}} = V_B/\mathrm{BO}_1 = \Gamma_2\Big/\left[4\pi\left(\sqrt{R^2+L^2} - L\right)\right]$$

where V_B is the velocity at point B. The rope frequency can be estimated as

$$f_{rope} = \frac{\omega_{rope}}{2\pi} = \frac{\Gamma_2}{8\pi^2 R^2 L}\left(\sqrt{R^2+L^2} + L\right). \tag{6.54}$$

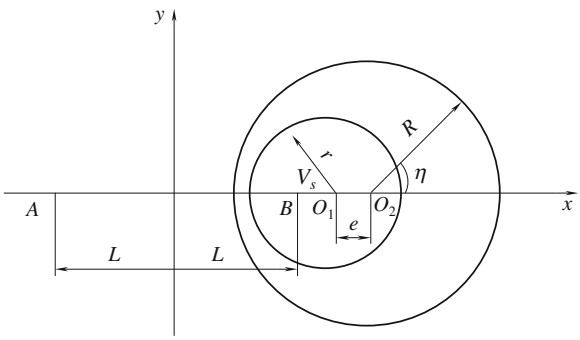

Fig. 6.20 Draft tube flow motion model (Yu 2006)

6.3.5 Characteristics of the Draft Tube Vortex Flow at Part Load in Francis Turbine

The two typical vortex ropes are shown in Fig. 6.16, i.e., the helical type occurring in part load operating conditions and the bubble-type in over load conditions (Wu et al. 2006). Susan-Resiga et al. (2004, 2006a, b) used an early theory of Benjamin (1962) on vortex breakdown to analyze their experimentally measured mean velocity profiles in the cone segment.

6.3.5.1 Formulation on Numerical Simulation

Since the upstream disturbances to flow in a draft-tube are on much smaller time scales (higher frequencies), one may ignore these upstream disturbances and investigate the simpler sole draft tube flow (SDTF) without any upstream components. This approach was introduced by Zhang et al. (2007, 2009). The computational domain is a draft-tube model connected to a "river" at the tube's exit. The cone inlet diameter D^*, water density ρ, and volume flux Q^* at full-load condition are used to nondimensionalize all quantities.

The quantities of mean flow are denoted with capital letters. Velocity scale ${V_0}^*$ and time scale ${T_0}^*$ are ${V_0}^* = 4Q^*/(\pi D^{*2})$ and ${T_0}^* = D^*/{V_0}^* = \pi D^{*3}/(4Q^*)$, respectively. The pressure is nondimensionalized by $\rho {V_0}^{*2}/2$, and the constant pressure at exit center of the "river" is chosen as reference pressure P^*_{ref}.

A linear static pressure distribution is assumed at the "river" exit, which is far bigger than the draft tube. The critical issue in formulating the SDTF computation lies in the inflow condition. The RANS simulation of WTF by Zhang et al. (2005) has shown that, with the exception of the near-wall shear layer, the average velocity profiles in the draft tube's cone center can be fitted with a Batchelor vortex. Therefore, in SDTF simulation it is natural to directly define the inflow condition with this vortex (see Zhang et al. 2009). In the cone segment, cylindrical coordinates ($r;\ \theta;\ z$) are used, in terms of velocity and vorticity components which are denoted by ($u;\ v;\ w$) and ($\omega_r;\ \omega_\theta;\ \omega_z$), respectively. Dimensional radial, azimuthal, and axial velocity components ($U^*;\ V^*;\ W^*$) of a Batchelor vortex are given by (Wu et al. 2005)

$$\begin{cases} U^*(r^*) = 0 \\ V^*(r^*) = \Omega_c^* R^* \big/ (r^*/R^*)\left[1 - e^{-(r^*/R^*)^2}\right] \\ W^*(r^*) = W_\infty^* + \left(W_c^* - W_\infty^*\right) e^{-(r^*/R^*)^2} \end{cases} \tag{6.55}$$

where W_∞^*, ${W_c}^*$, ${\Omega_c}^*$ and R^* are the free-stream axial velocity, the centre line axial velocity, the angular velocity at the axis, and the measure of the core size, respectively. Two Batchelor vortices have been chosen as inflow conditions, i.e. Case I and Case II, for simulations of a part load flow and an over-load flow.

6.3.5.2 Flow Characters and Instability in Conical Segment

1. Flow patterns for Cases I and II.

The SDTF simulation for Case I captures a strong helical vortex rope in the cone, shown in Fig. 6.21. This vortex rope pattern is of a strongly non-axisymmetrical shape described with the Δ-criterion as follows:

$$\Delta = (C_1/3)^3 + (C_2/2)^2 > 0 \tag{6.56}$$

where C_1 and C_2 are coefficients of the characteristic equation for eigenvalues of the velocity gradient tensor $[\nabla\{\boldsymbol{v}\}]$, i.e.,

$$\sigma^3 + C_1\sigma - C_2 = 0. \tag{6.57}$$

Associated with this helical vortex rope is a low-frequency and large-amplitude pressure fluctuation, as plotted in Fig. 6.22a for three check points marked in Fig. 6.21b. The corresponding frequency spectra are shown in Fig. 6.22b, from which it could be found that the dominant dimensionless frequency of the vortex rope is $St = f^* D^*/V_0^* = 0.279$, where f^* is the dimensional frequency.

Contrary to Case I, there is no helical vortex rope but simply a concentrated vortex in Case II, because streamlines in the tube shown in Fig. 6.23b are very smooth. The vortex is nearly steady.

The above results are in good qualitative agreement with those of RANS simulation for WTF, as well as with actual measurements (Zhang et al. 2005). For example, dominant frequency of the severe pressure fluctuations measured in

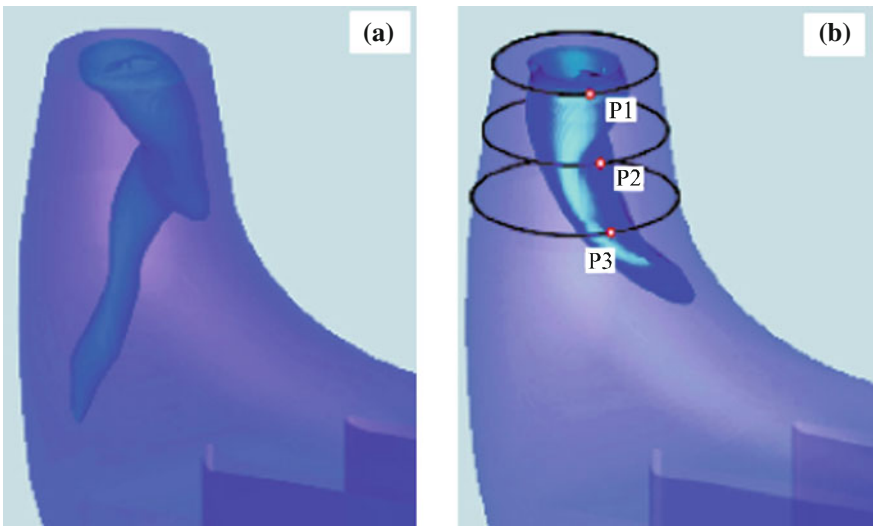

Fig. 6.21 Vortex rope in case I by using iso-surfaces of Δ ($\Delta/\Delta_{max} = 6 \times 10^6$, where Δ_{max} is the maximum of Δ in the draft tube): **a** $t = 11.52$; **b** $t = 13.39$ (Zhang et al. 2009)

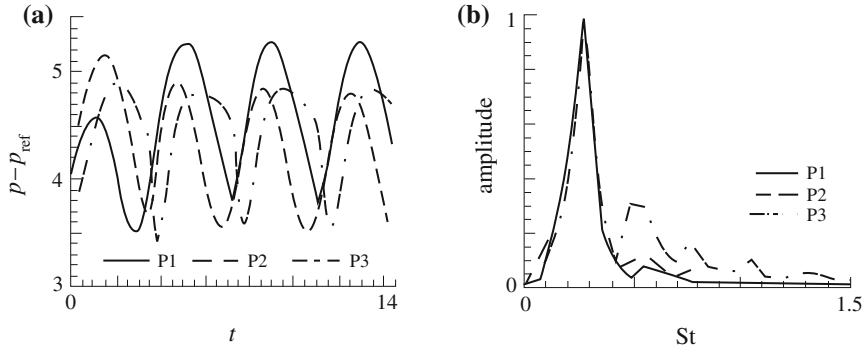

Fig. 6.22 **a** and **b** are the pressure fluctuations and their amplitude spectra at the points $P1 \sim P3$ (Fig. 6.21 **b**, respectively (Zhang et al. 2009)

prototype hydraulic turbines with $Q^* = 106$ kg/s and $D^* = 10$ m is about 0.31 Hz under two part-load conditions (Zhu 2006), and here result $St = 0.279$ implies $f^* = 0.355$ Hz.

2. Analysis of absolute/convective instability (AI/CI)

If the undisturbed basic flow of a swirling vortex is in the AI status, one of the azimuthal modes of eigen type ($n = 0; \pm 1; 2; 3; \ldots$) will develop into a dominating flow pattern. When mode $n = 0$ is dominant, the vortex will evolve to a bubble-type structure (Fig. 6.16b); whereas when mode $n = \pm 1$ or ± 2 dominates, there is a single or double helical vortex rope with severe pressure fluctuation.

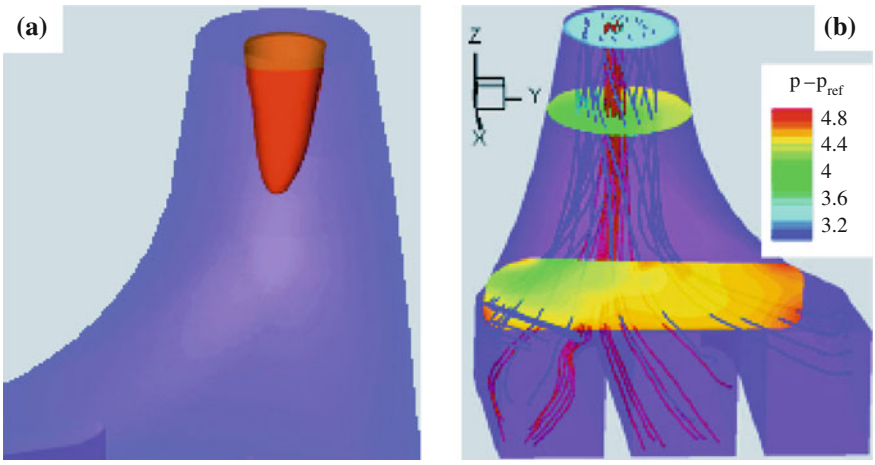

Fig. 6.23 **a** is a iso-surfaces of Δ ($\Delta/\Delta_{max} = 5 \times 10^7$), in case II at $t = 2{:}13$, **b** shows the corresponding instantaneous streamlines, where the *red* and *blue lines* initiate from the center jet and its surrounding, respectively (Zhang et al. 2009)

The AI/CI characters of the Batchelor vortex are defined as (Delbende et al. 1998)

$$\alpha = W_{\infty}^{*}/\Delta W^{*}, \quad q = \Omega_{c}^{*}R^{*}/\Delta W^{*}. \tag{6.58}$$

In Eq. (6.58), $\Delta W^{*} = W_{c}{}^{*} - W_{\infty}^{*}$ and vortex core size R^{*} are taken as a velocity scale and a length scale intrinsic to the vortex (different from our global scale R_0* and D*) respectively.

For the Batchelor vortex, the flow velocity components have the following distributions:

$$U(r) = 0,\ V(r) = q\left(1 - e^{-r^2}\right)\Big/ r,\ W(r) = a + e^{-r^2} \tag{6.59}$$

where $r = r^{*} = R^{*}$.

After the RANS flow fields in draft tube for Cases I and II are computed under their respective inflow conditions, the time average of solutions at many cross sections downstream of the runner is used to construct a steady and axisymmetric "basic flow". The "basic flow" velocity profiles are then fitted at different z-stations by the Batchelor vortex family, which yields a series of (a; q) pairs as functions of z that form a trajectory line on the (a; q) plane, seen in Fig. 6.24.

It is clear that, the approximate "basic flow" for Case I is in the AI zone from the beginning to the end of the cone downstream, so a helical vortex rope plotted in Fig. 6.21 emerges. But the "basic flow" for Case II is far from the AI zone, and as a result any local disturbance never pollutes the upstream flow. Therefore, Fig. 6.23 exhibits a nearly steady flow in the tube.

6.3.5.3 Elbow and Outlets Flow Analysis

The instantaneous streamlines in the draft tube for Case I at two different times are illustrated in Fig. 6.25. The red lines initiating from the forward flow ($W < 0$) of

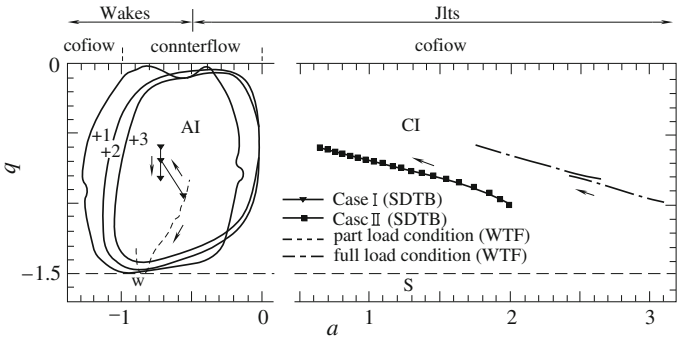

Fig. 6.24 AI/CI trajectory lines of the basic flow on the (a;q) plane for two cases, compared with the WTF simulation results. *Thin lines* are the AI/CI boundaries for azimuthal modes n = +1; +2; +3, and the *bold line* is the AI zone outermost boundary (Zhang et al. 2009)

cone segment are eventually discharged at the outlets. In contrast, the blue lines consist of two subsets: one with streamlines that pass through points lying in the vortex core of cone segment, spiraling around vortex rope, and then turning back to the inlet after some curved tours; and another subset with streamlines that come from downstream of the middle outlet due to the adverse pressure gradient there and eventually discharge from the left outlet.

The uneven partition of the mass flux among three outlets implies a side-by-side existence of the forward and reversed streams in the elbow segment. The former one forms a mass-flux channel of irregular shape, with higher flow speed and driven by a mean favorable axial pressure gradient which will be shown later.

At the upstream end of the elbow, this channel is obviously linked with the downward flow of the cone segment; at the downstream end with the left outlet. A complete channel exists from inlet to exit which carries almost the entire mass flux out of the draft tube. Flow in the lower portion of the tube is quasi-steady.

The vorticity line in draft tube is shown in Fig. 6.26 at $t = 11.52$ s. The pattern is very different from the streamline pattern because a vorticity line originally aligning to a streamline will turn away due to the stretching-tilting term $\{\boldsymbol{\omega}\} \cdot \nabla \boldsymbol{v}$ in the vorticity transport equation. Particularly, since the velocity-gradient field $[\nabla \boldsymbol{v}]$ in the elbow is very complex, so is the vorticity line tilting there. Interestingly, owing to influence of the sweeping vortex rope, vorticity lines have zigzags in the downstream part of the middle and left outlets, with their wavelength signifying the slowness of fluid motion—the shorter the slower. These vorticity lines then follow the square wall geometry of the outlets, indicating that they have entered the boundary layers.

The sectional ω_x contours in Fig. 6.26 are almost time independent in the right and middle outlets, and only a slow drift with time (figure not shown) in the left outlet. It validates that the flow in the outlets is quasi-steady. Most of vorticity lines either turn back to upstream or enter the cone boundary layer, leading to a

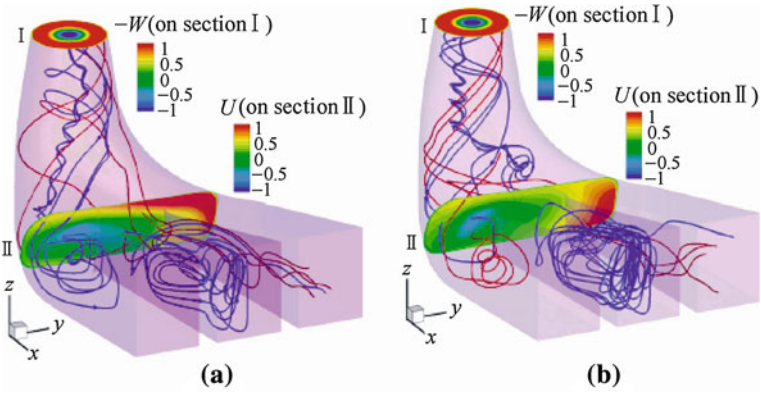

Fig. 6.25 Instantaneous streamlines in the draft tube for case I with the axial-velocity contours on two cross sections. *Red* and *blue lines* are the forward and reversed streams, respectively. **a** $t = 11{:}52$, **b** $t = 13{:}39$. (Zhang et al. 2009)

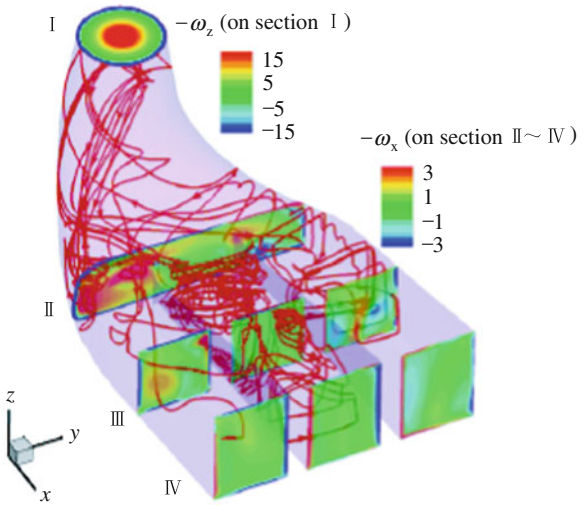

Fig. 6.26 Instantaneous vorticity lines in the case-I draft-tube flow (Zhang et al. 2009)

vorticity level in the outlet much lower than that in the cone. It should be pointed out that for Case I, pressure distribution at the three outlets' exits is nearly uniform.

6.3.6 Vortex Rope Control

For a Francis turbine, if vibration occurs in the middle range of the load, three mitigating methods can be employed in engineering practice.

1. Avoid loading the unit at levels where excessive vibration occurs. In this case, no corrective action is required. However, the flexibility of operation in an integrated grid system is limited.
2. Inject air below the runner. Air admission will suppress the upward surges in draft tube, reducing vibration (Biela and Beltran 1998; Pejovic 2002).
3. Modify the shape of the trailing edge of the runner blades. This is often the best method, yet it is more time-consuming. Furthermore, it has to be carried out by an expert hand otherwise it may aggravate the problem.

Other solutions for mitigating pressure pulsation are:

1. Draft-tube fins to induce swirl flow distortions and to modify pressure-source frequencies or amplitudes (Grein 1980; Biela and Beltran 1998);
2. A cylinder in the draft tube or extensions of runner cone to induce swirl flow distortions and to modify the pressure source frequencies or amplitudes (Biela and Beltran 1998);
3. Mechanical dampers that act as Frahm dampers to absorb resonance energy (Angelico et al. 1994);

4. Active control of the pressure fluctuations based on a complex control strategy, using a rotating valve or a mechanical piston to generate pressure fluctuations in draft tube with the same amplitude as the source but in opposite phase (Blommaert et al. 1999);
5. A controlled water jet injected into the center of the runner cone to modify swirl momentum ratio and eliminate pressure source.

Success of any of the above solutions is never ensured and often has detrimental effects on turbine efficiency. In addition, some are technically complex and thus difficult to set up. As for the full load surge, injection of air appears to be successful in some cases. Use of fins is also sometimes beneficial (Nicolet 2007).

6.3.6.1 Robustness of Draft-Tube Flow and Control Principles

In short, it can be concluded that even if the runner has been optimally designed to yield the highest efficiency in modern Francis turbines, under part load conditions the draft-tube flow with severe pressure fluctuations is a very robust existence. In the cone segment the robust helical vortex rope rules the flow and causes severe pressure fluctuation, but this strong disturbance is suppressed in the elbow and outlets by an even more robust coexistence of the quasi-steady, high-speed and mass-flux channel and the low-speed chaotic reversed flow.

From the overall assessment a few guiding principles for effective control of Case-I flow can be concluded:

1. The control should be imposed at the inlet of the draft tube (i.e. the outlet of the runner) rather than anywhere downstream of the cone segment.
2. The control should focus on dealing with the axial flow.
3. The control cannot be achieved with small-force disturbances; rather, a sufficiently strong interference by either solid or fluid means is necessary.

Following the principles above, two numerical tests have been conducted with different ideas.

6.3.6.2 Cross-Area Reduction

Adding a solid cylinder at the bottom of the runner center is a passive flow control of this kind because the cylinder displaces a portion of the reverse flow in the cone segment. This simple control method leads to a favorable effect though the cylinder size may be limited.

6.3.6.3 Water Injection at Inlet

It is possible to modify the axial flow at the draft-tube inlet. The currently used method is air admission at the inlet axis but its effect is too weak. An alternative is

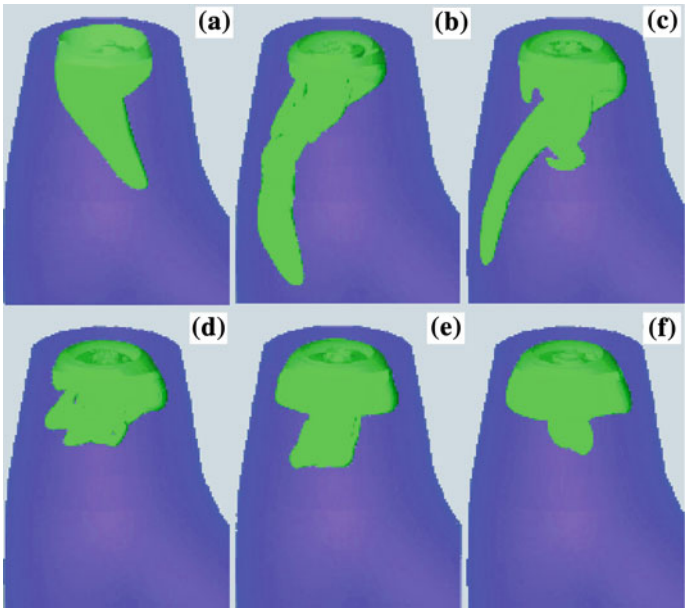

Fig. 6.27 Iso-surfaces of $\Delta(\Delta/\Delta_{max} = 6 \times 10^6)$ of controlled flow by jet injection. Starting from the onset of control, the dimensionless times in (**a**)–(**f**) are $t = 0$; 3.60; 5.04; 7.92; 12.25; 32.4, respectively (Zhang et al. 2009)

to replace the air admission by water injection. This kind of active control has been studied by Blommaert (2000) and Susan-Resiga et al. (2004).

According to Susan-Resiga et al. (2004), the axial jet can improve both the draft tube and the runner flow, so the overall efficiency losses due to jet operation are only of an order of 0.2 %.

In the following numerical experiment, a strong axial water jet is superposed to the uncontrolled axial velocity profile of Case I within a thin cylindrical region neighboring the axis. The total mass flux brought downward by the jet is less than 6 % of the total inlet flux. The azimuthal velocity profile remains unchanged.

Time sequence of the control effect on vortex rope from the jet injection is shown in Fig. 6.27 in terms of the Δ-criterion.

Shortly after the control, the jet causes the helical vortex rope to bifurcate into two branches, of which one is longer than the other (Fig. 6.27b). At the same time, the jet itself is entrained by the vortex rope to shift slightly away from the inlet axis. The shorter branch is then continuously split into several little ones, and the longer branch gradually shrinks (Fig. 6.27c and d). Finally, the helical vortex rope is converted into a "mushroom" (Fig. 6.27e and f). The vorticity is concentrated in a highly localized region near the cone-segment inlet. The almost axisymmetrical "mushroom" also indicates that the pressure fluctuation originally induced by the helical vortex rope should now be significantly alleviated.

6.3.6.4 Control of Swirling Flow in Turbine Discharge Cone by Water Jet

It was only recently that Zhang, et al. (2005) showed that the vortex rope is formed as a result of absolute instability of the swirling flow in the turbine's draft tube cone. Further, Susan-Resiga et al. (2006a) found that the flow becomes unstable as the turbine discharge decreases, and the eigen modes develop mostly near the symmetry axis. This prompts the idea of injecting a water jet from the runner crown downstream along the shaft in order to remove the main cause of the flow instability associated with severe flow deceleration in the axis. The water jet injection has proved successful in mitigating the vortex rope and the corresponding pressure fluctuation, Susan-Resiga et al. (2006a, b); Zhang et al. (2007). Susan-Resiga, et al. (2007) identified a flow feedback approach for the draft tube cone that allows the control jet to be supplied without any additional losses in the turbine. Moreover, as shown by Susan-Resiga and Muntean (2008), the hydraulic losses in the draft tube cone are reduced remarkably while the pressure recovery is increased.

It has been found that a jet injected axially at the conical diffuser inlet effectively suppresses the vortex breakdown. However, numerical experiments show that the required control jet discharge may reach 10 % of the incoming discharge.

Susan-Resiga et al. (2007) introduced a flow feedback, as shown in Fig. 6.28, where a fraction of the discharge was collected near the wall at the downstream end of the cone and re-directed toward the nozzle that issues the control jet.

Figure 6.28 shows a comparison between swirling flow in the conical diffuser with and without jet control. It is clear that the flow feedback mechanism generates a control jet that successfully eliminates the stagnant region, thus stabilizing the swirling flow.

From an engineering point of view, the diffuser must convert the dynamic pressure into static pressure with a minimal loss of total pressure. In practice, one measures the wall static pressure and uses it to evaluate the wall pressure recovery coefficient. However, a more rigorous hydrodynamic analysis should be employed to get the flow weighted averaged pressure, as follows:

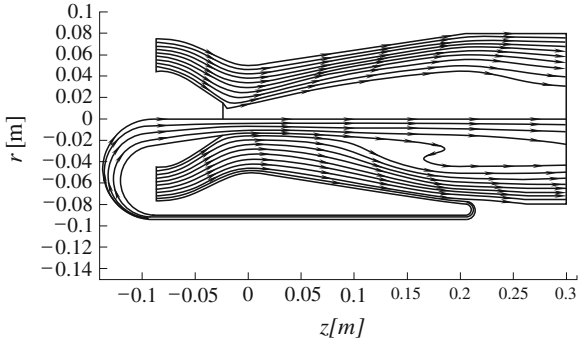

Fig. 6.28 Streamlines for the axisymmetric swirling flow without flow control (*upper half-plane*) and with flow feedback control (*lower half-plane*) (Susan-Resiga et al. 2007)

Table 6.2 Total pressure loss and static pressure recovery (Susan-Resiga et al. 2007)

$z =$	$\Delta\bar{p}_{\text{tot}} = \bar{p}_{\text{tot}}^{\text{throat}} - \bar{p}_{\text{tot}}(z)$		$\Delta\bar{p} = \bar{p}(z) - \bar{p}^{\text{throat}}$	
	$2R_{\text{throat}}$	$4R_{\text{throat}}$	$2R_{\text{throat}}$	$4R_{\text{throat}}$
No flow control	1,194 Pa	2,802 Pa	3,305 Pa	5,811 Pa
With flow feedback	360 Pa (−70 %)	1,038 Pa (−63 %)	7,278 Pa (+ 120 %)	8,286 Pa (+43 %)

$$\bar{p}(z) = \int_0^{R_{wall}} p(z,r)\, V_z(z,r)\, 2\pi r\, \mathrm{d}r \Big/ \int_0^{R_{wall}} V_z(z,r)\, 2\pi r\, \mathrm{d}r. \tag{6.60}$$

From experiments and numerical simulations, the average static pressure increases almost at a constant rate over the whole diffuser length of the draft tube, with a corresponding decrease in dynamic pressure by the flow feedback control (see Susan-Resiga and Muntean 2008). The total pressure monotonically decreases owing to the influence of viscous losses. On the other hand, the static pressure recovery is significantly improved thanks to a loss of total pressure when the jet control with flow feedback is employed. Moreover, with flow control, conversion of dynamic pressure into static pressure takes place practically on the upstream half of the conical diffuser in draft tube. Consequently, such flow control approaches allow the use of more compact turbine discharge cones.

Table 6.2 presents quantitatively the benefits of employing the above flow control approach.

It can be noticed that for the first half of the conical diffuser the losses are reduced by 70 % and the pressure recovery is increased by 120 %. For the whole diffuser length, there is still a 63 % reduction in the overall hydraulic loss, and the increase of the pressure recovery is 43 %. It can be concluded that the jet flow control approach allows for shorter, more compact, conical diffusers in hydraulic turbines while retaining good performances over an extended operating range. The jet discharge for the flow feedback is 3.26 L/s, representing 10.86 % from the inlet discharge.

6.4 Self Excited Vibration of Hydraulic Machinery

Normally, generated vibrations do not affect excitations or forces of flows that do not depend on structural motion. In this case, they are forced vibrations. However, in some cases, the structural motion can affect fluid forces subject to structural displacement. It may happen when periodic excitations take place in flow without structural motion and its frequency coincides with one of the natural frequencies of the system, followed by resonance. If the response amplitude becomes sufficiently large, the structural displacement will control the fluid excitation as shown in the case of a vortex shedding lock-in. On a few occasions, structural motion

determines the flow periodicity exhibited in the case of self-excited vibrations. In other situations, at least one of the oscillatory system parameters varies, usually periodically, with time to achieve parametric excitation.

When the output of a hydraulic machine exceeds a certain value, the arcuate gyroscopic vibration of its shaft system and other rotating components may occur. Seal rings of the runner will make arcuate gyroscopic rotations in the direction of the runner wheeling following an elliptical orbit. The frequency of arcuate gyroscopic vibrations equals 2–4 times of runner wheeling, f_n, which is approximately the self-free frequency of the arcuate gyration, called the self-excited vibration of hydraulic turbine. Self-excited vibration happens where the movement of mechanical parts (seals, clearances, etc.) influences the flow.

6.4.1 Mechanism of Self Excited Vibration in Hydraulic Turbine

Figure 6.29 shows the structure of a hydraulic turbine. On the back (upper) surface, there is a drainage chamber between the rotating back surface of runner crown and the stationary inner surface of head cover (outer cover). With high pressure, water leaks from the runner passage through the small gap between the runner brim and sealing labyrinth ring on head cover, and flows into the drainage chamber on the runner back surface (upper side). The leaking water then flows through another gap between the rotating shaft surface and the stationary inner surface of the head cover to the outside with atmospheric or lower pressure. The leakage excites vibration and its flow rate is proportional to the gap dimension around runner brim. In order to analyze the leakage flow, one could set up a simplified model composed of a shaft and runner such as the hydraulic turbine shown in Fig. 6.30.

Another pipe serves as drainage to leaking water in the chamber, but is not considered in this simple model.

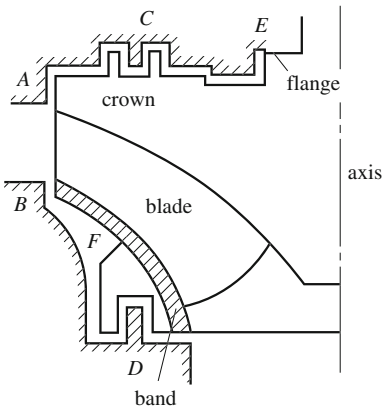

Fig. 6.29 Structure of Francis turbine (Wang 2005)

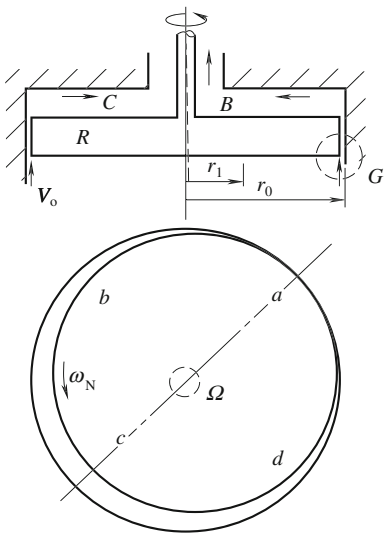

Fig. 6.30 Simplified model of turbine (Wang 2005)

In Fig. 6.30, the leakage flow rate is small near point a and large at point c. It is assumed that the shaft centre spins with an orbit in a dashed circle with angular velocity Ω which drives leaking water in the chamber to rotate along the runner's spinning direction. In chamber B there is a pressure gradient along the ac direction, that is, $p_a > p_c$. This pressure gradient induces a flow moment acting on the runner, and produces a whirling flow with the same rotating direction as the runner in the chamber.

Theoretically, there exist two kinds of arcuate gyroscopic whirls. One is in the same direction as the rotating runner; another in the opposite direction. The fluid-induced moments in both cases share the same mechanics but their magnitudes of induced moments on the runner are not equivalent owing to different flows in the chamber. And because the stability of the two kinds of arcuate gyroscopic whirls differs, they need to be analyzed.

In Fig. 6.31, $V_\varphi(r)$ is the circumferential component of the stead flow velocity in the chamber, $V'_r(r,\varphi)$ is its radius component. The difference of the momentum component along the bd direction between the inlet flow at the ring gape in the circle with radius r_0 and the outlet flow at the ring gape with radius r_1 is

$$\Delta = \int_0^{2\pi} \rho V'_r(r_0,\varphi) r_0 d\varphi \times H V_\varphi(r_0)\cos\varphi - \int_0^{2\pi} \rho V'_r(r_1,\varphi) r_1 d\varphi \times H V_\varphi(r_1)\cos\varphi. \tag{6.61}$$

Here, H is the chamber height, and φ is the argument at cylindrical coordinates.

When Δ is not equal to zero, the unbalance between the influent flow momentum to the chamber and the effluent one will appear which can cause an increase in the pressure gradient along line bd in Fig. 6.31 and a fluid dynamic moment on the runner. In the same direction, precession of the runner will be

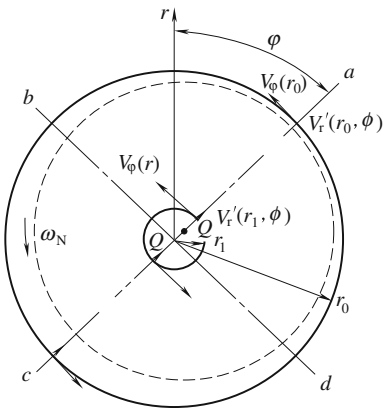

Fig. 6.31 Whirling of fluid flow in turbine (Wang 2005)

produced during the runner's operating rotation. The increased pressure gradient forms a further eccentric displacement of the shaft system. This increasing vibration is referred to as the self-excited vibration.

The sign of Δ is determined by relative value between the velocity components i.e. $V_\varphi(r)$ and $V'_r(r,\varphi)$. The flow velocity boundary condition at the circle with radius r_0 and velocity U is $V'_r(r_0, \varphi) = U\cos\varphi$, i.e.,

$$\begin{cases} \varphi = 0: \ V'_r(r_0,\varphi) = U, \ \varphi = \pi/2: \ V'_r(r_0,\varphi) = 0 \\ \varphi = \pi: \ V'_r(r_0,\varphi) = -U, \ \varphi = 3\pi/2: \ V'_r(r_0,\varphi) = 0. \end{cases}$$

The flow potential in the Chamber is

$$\phi = r\left[1 - (r_1/r)^2\right]\cos\varphi \Big/ \left[1 + (r_1/r_0)^2\right]. \tag{6.62}$$

The velocity component, namely $v'_r(r, \varphi)$, is

$$V'_r(r,\varphi) = \frac{\partial\phi}{\partial r} = \left[1 - (r_1/r)^2\right]U\cos\varphi \Big/ \left[1 + (r_1/r_0)^2\right]. \tag{6.63}$$

Substituting Eq. (6.63) into Eq. (6.61) and integrating yields

$$\begin{aligned} \Delta = &\int_0^{2\pi} \left\{ \left[1 - (r_1/r_0)^2\right]U\cos\varphi r_0 H V_\varphi(r_0)\cos\varphi \Big/ \left[1 + (r_1/r_0)^2\right] \right\} \mathrm{d}\varphi \\ &- \int_0^{2\pi} \left\{ \left[1 - (r_1/r_0)^2\right]U\cos\varphi r_0 H V_\varphi(r_1)\cos\varphi \Big/ \left[1 + (r_1/r_0)^2\right] \right\} \mathrm{d}\varphi \end{aligned}$$

Then

$$\Delta = UHr_0\pi\left\{V_\varphi(r_0) - V_\varphi(r_1)2(r_1/r_0)\Big/\left[1 + (r_1/r_0)^2\right]\right\}. \tag{6.64}$$

If the water flow in the chamber is free vortex, then

$$V_\varphi(r_0) = (r_1/r_0)V_\varphi(r_1).$$

Substituting above into Eq. (6.64) yields

$$\Delta = UHr_0\pi V_\varphi(r_1)\left\{1 - 2\Big/\left[1 + (r_1/r_0)^2\right]\right\}(r_1/r_0).$$

Since $1 + (r_1/r_0)^2 < 2$, one has

$$2\Big/\left[1 + (r_1/r_0)^2\right] > 1.$$

Under the condition of free vortex flow in the chamber, $\Delta < 0$, the pressure at point b is higher than that at point d, and the arcuate gyroscopic direction is opposite to the rotation of runner.

If water flow in the chamber is forced vortex by runner and shaft, then $V_\varphi(r_0) = (r_0/r_1)\ V_\varphi(r_1)$. Substituting it into Eq. (6.64) yields

$$\Delta = UHr_0\pi V_\varphi(r_1)\left\{1 - 2(r_1/r_0)^2\Big/\left[1 + (r_1/r_0)^2\right]\right\}(r_1/r_0).$$

Since $1 + (r_1/r_0)^2 < 2$, one has

$$1 - 2(r_1/r_0)^2\Big/\left[1 + (r_1/r_0)^2\right] > 0.$$

Under this condition of forced vortex flow in the chamber, $\Delta > 0$. The pressure at point b is lower than that at point d, and the arcuate gyroscopic direction is in the same direction as the rotation of runner.

6.4.2 *Flow Pattern in the Leakage Chamber of Hydraulic Turbine*

Flow in the chamber in the upper side of the runner crown is neither free vortex nor forced. Actually, it is a mixed type of both determined by dimensionless parameter β:

$$\beta = \xi r_0^2\omega_N/(2V_0h). \tag{6.65}$$

Here, h is the gap clearance between the runner crown and the inner surface of head cover as shown in Fig. 6.32; ξ is the friction coefficient; ω_N is the gyroscopic speed of water; and V_0 is the influent velocity at runner brim gap (Fig. 6.30).

When β is close to zero, water flow rate through the gap is quite large and the angular moment remains the same from the inlet to the outlet of chamber. In this scenario, water flow in the chamber is of the free vortex type. When β is infinite, water flow rate through the gap is very low, and the angular moment decreases

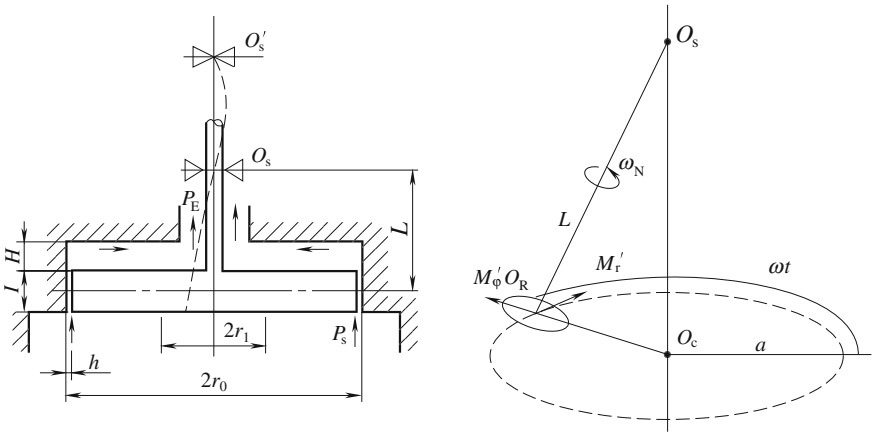

Fig. 6.32 The flow model in the chamber on the runner crown back surface (Wang 2005)

greatly from the inlet to the outlet. Water flow in the chamber is the forced vortex type.

Replacing β with α, one can rewrite V_φ expression as

$$V_\varphi(r) = V_\varphi(r_0)[(1-\alpha)(r_1/r_0) + \alpha(r_1/r_0)]\,(1 \geq \alpha \geq 0). \tag{6.66}$$

Here, $\alpha = 1$ or $\alpha = 0$ represent the free vortex or the forced vortex respectively. α is the same factor as β. If the dimension of the model is fixed, and r_0/h and the friction coefficient are same, then α is also the function of $r_0\omega_N/(2V_0)$.

6.4.3 The Excitation Force by the Sealing Chamber Flow

Referring to Fig. 6.32, the center of shaft O_c and the runner rotate in the dashed circle at angular speed Ω, and the disc makes the precession at angular speed ω_N. Pressure fluctuation in the chamber and in the gap of runner brim may be calculated based on the following assumptions:

1. The variation of pressure in the chamber is small;
2. The fluid is incompressible and inviscid;
3. The inlet pressure p_i and the outlet pressure p_e are constant;
4. Pulsations of flow rate and pressure at the gap exit are the same as those at the chamber entrance.

Then one can get the distribution of flow and pressure in the chamber. If there is only one fluid passage in the sealing chamber, pressure drop through the sealing is $p_i - p_e$. Here, p_i is the inlet pressure of the chamber; and p_e is the outlet pressure. This pressure drop includes three parts: initial velocity head, $V_0^2/2g$, local hydraulic loss head, $\varsigma V_0^2/2g$ and friction loss head $\lambda l/(2b)V_0^2/2g$, i.e.,

$$p_i - p_e = \rho \frac{1}{\mu^2} \frac{V_0^2}{2}. \tag{6.67}$$

Here, $\mu = 1/\sqrt{1 + \varsigma + \lambda l/(2b)}$; ς is the local friction loss head factor; λ is the friction loss factor; and l is the sealing length.

When the runner is eccentric, the gap, b between runner brim and inner surface of head cover is the function of the eccentric distance ε and the argument φ, i.e.,

$$b(\varphi, \delta) = b(1 - \delta \cos \varphi) \tag{6.68}$$

where $\delta = \varepsilon/h$.

Pressure drop at the gap inlet is $\rho(1 + \varsigma)V_0^2/2g$ and pressure drop of friction loss is $\rho\lambda l/(2b)V_0^2/2g$. They are all the function of argument φ. The sum of the pressure acting on runner is

$$F(\delta) = \int_0^l \mathrm{d}x \int_0^{2\pi} p(x, \varphi) \cos \varphi r \mathrm{d}\varphi. \tag{6.69}$$

The local hydraulic loss at the entrance of gap neglected, it becomes

$$F(\delta) = -(p_i - p_e) \frac{rl^2}{2b} \pi\lambda\mu^4\delta \tag{6.70}$$

where the minus sign indicates that the pressure difference direction is opposite the eccentric distance.

In practice, in order to reduce axial thrust on the shaft system of a hydraulic turbine, a pressure-equalizing rotating disc on the top of runner and pressure-equalizing holes in the runner crown may be designed. The pressure distribution in the sealing chamber will also be improved.

6.4.4 The Excited Force in a Labyrinth Clearance Seal

A labyrinth seal is a mechanical seal that fits around an axle to prevent the leakage of oil or other fluids.

A labyrinth seal is composed of many straight grooves that press tightly inside another axle or hole so the fluid has to pass through a long and difficult path to escape. Sometimes threads exist on the outer and the inner portions and these form a path to slow leakage. For labyrinth seals on a rotating shaft, there must exist a very small clearance between the tips of the labyrinth threads and the running surface.

Labyrinth seals on rotating shafts provide non-contact sealing action by controlling the passage of fluid by centrifugal motion through a variety of chambers, as well as the formation of controlled fluid vortices (Fig. 6.33).

At higher speeds, centrifugal motion forces the liquid towards the outside and therefore away from any passages. Similarly, if the labyrinth chambers are correctly

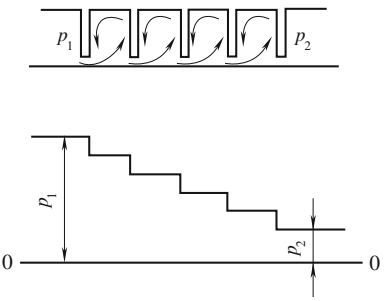

Fig. 6.33 Principle of a simple labyrinth seal (Wang 2005)

designed, any liquid that has escaped from the main chamber gets entrapped in a labyrinth chamber, where it is forced into a vortex-like motion. That prevents liquid from escaping, and also acts to repel any other fluids. Because these labyrinth seals are non-contact, they do not wear out. Referring to Fig. 6.33, the pressure will decrease from the inlet one, p_1, to the exit, p_2, step by step through every tooth.

6.4.4.1 Model of Excited Force in a Labyrinth Seal

Labyrinth seals are commonly employed in turbines in order to reduce runner brim leakage.

Varying from different seal design and boundary conditions, fluid within these seals induces damping or exciting forces on the rotor, thereby reducing or amplifying rotor vibrations.

Accurate models of labyrinth seals are needed for the prediction of leakage and rotordynamic characteristics during the design of a new turbine. Obviously leakage must be minimized for efficiency improvement. Leakage can be reliably predicted using 2D models. Bulk flow models can accomplish this task at a lower computational cost than grid-based Navier–Stokes solvers.

3D Navier–Stokes solvers are used widely nowadays because they are expected to produce more reliable results concerning rotordynamic characteristics of the seals than a bulk flow model. It is a well-known problem that seals induce fluid forces on the rotor, exciting rotor vibration and destabilizing the machine.

6.4.4.2 The Excited Force in a Labyrinth Seal

Under the assumption of a circular orbit for the rotor, this inherently unsteady problem is transformed into a steady one if the computational grid is placed on the stator-centric frame (which is a reference system rotating at an angular velocity, ω_n). The ratio of rotor whirl ω_n to rotor spin Ω is defined as processional frequency ratio $(PFR = \omega_n/\Omega)$.

An imbalance–induced vibration, with the same point on rotor surface always pointing outward, is termed as a synchronous whirl, and PFR is equal to unity.

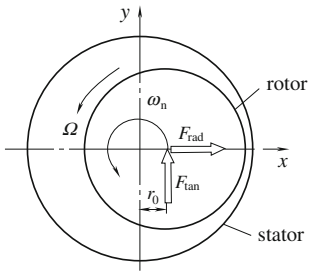

Fig. 6.34 Movement of the rotor (Wang 2005)

Stiffness and damping coefficients can be determined according to the following equation:

$$-\begin{Bmatrix} F_{\text{rad}}(t) \\ F_{\text{tan}}(t) \end{Bmatrix} = \begin{bmatrix} k_{xx} & k_{xy} \\ k_{yx} & k_{yy} \end{bmatrix} \begin{Bmatrix} x(t) \\ y(t) \end{Bmatrix} + \begin{bmatrix} c_{xx} & c_{xy} \\ c_{yx} & c_{yy} \end{bmatrix} \begin{Bmatrix} \dot{x}(t) \\ \dot{y}(t) \end{Bmatrix}. \tag{6.71}$$

Within the labyrinth seal, fluid forces acting upon the rotor result in an inhomogeneous pressure field caused by the movement of the rotor with respect to the stator. Fluid analysis and testing of the seal aim to determine the coefficients of rotordynamic force. These coefficients describe the stiffness and damping effects of the fluid resulting from the movements of the rotor centre with respect to the stator. Of course, in reality, this movement could be in various patterns. The rotor whirls around the stator centre, while spinning around its own centre, which is sketched in Fig. 6.34 (Wang 2005).

For movements of the rotor centre described above, $k_{xx} = k_{yy} = K$, $c_{xx} = c_{yy} = C$, $kxy = -kyx = k$, $cxy = -cyx = c$, $x(0) = r_0$, $y(0) = 0$, $\dot{x}(0) = 0$ and $\dot{y}(0) = r_0\omega_n$. Hence,

$$F_{rad}/\, r_0 = -K - c\omega_n \tag{6.72}$$

$$F_{\text{tan}}/\, r_0 = k - C\omega_n. \tag{6.73}$$

Here, K and C are commonly named as direct stiffness and direct damping coefficients, respectively; k and c are cross-coupled stiffness and damping coefficients. F_{rad} will push the rotor inward or outward, changing the radius of rotor's whirling motion, r_0. F_{tan} will influence the frequency of rotor center's whirling motion, ω_n. Once pressure within the seal has been calculated for a certain set of boundary conditions, these forces can be obtained from pressure integration over the rotor surface. Equations (6.72) and (6.73) then have two unknown coefficients. F_{rad} and F_{tan} must be determined for at least two different values of ω_n (otherwise constant boundary conditions). The equations can then be solved for the rotordynamic coefficients.

6.4.4.3 The Muszyńska/Bently Model of Excited Force in a Labyrinth Seal

The fluid force model developed by Bently and Muszyńska (1985) pertains to rotors at low and medium eccentricities. Among other contributions, this model has clarified understanding of self-excited rotor vibrations such as oil whirl and whip. An isotropic bearing is approximated by the Muszyńska/Bently model as follows (Muszyńska and Bently 1990):

$$-\{\boldsymbol{F}_f\} = [\boldsymbol{M}_f]\{\ddot{z} - \mathrm{i}2\lambda\Omega\dot{z} - \lambda^2\Omega^2 z\} + [\boldsymbol{C}]\{\dot{z}\} + [K - \mathrm{i}\lambda\Omega\boldsymbol{C}]\{z\}. \tag{6.74}$$

Here $\{\boldsymbol{F}_f\}$ denotes the fluid force vector; $[\boldsymbol{M}_f]$ the fluid inertia effect matrix; $[\boldsymbol{K}]$ and $[\boldsymbol{C}]$ are the fluid stiffness and damping matrices; Ω is shaft speed; and λ is the fluid circumferential average velocity ratio. The rotor lateral response is described with a vector of displacement (x and y are horizontal and vertical displacements, respectively; $z = x + \mathrm{i}y$ and $\mathrm{i} = \sqrt{-1}$). Equation (6.74) represents a fluid force rotating forward at average speed $\lambda\Omega$ with stiffness $[\boldsymbol{K}]$, damping $[\boldsymbol{C}]$ and fluid inertia effect $[\boldsymbol{M}_f]$. Unlike classical bearing coefficients, dynamic stiffness parameters such as previously mentioned $[\boldsymbol{K}]$, $[\boldsymbol{C}]$, λ (and reverse stiffness and damping, $[\boldsymbol{K}']$ and $[\boldsymbol{C}']$) are independent of the orientation of the x, y coordinate system. If the fluid inertia effect $[\boldsymbol{M}_f] = 0$ or is negligible, the first term in the right hand side can be cancelled.

In general, fluid bearings or seals attached to a rotor are anisotropic. Thus, a model that includes the effects of asymmetry suitable for analyzing a general anisotropic bearing or seal is desirable because the most accurate results could be obtained. A more generalized version of the Muszyńska/Bently model of Eq. (6.74) does contain such anisotropic effects.

While an isotropic bearing or seal leads to a circular orbit response for a symmetric rotor, an anisotropic bearing or seal results in an elliptical orbit response. As pointed out above, the latter causes a combination of both forward and reverse responses. To account for this effect, additional terms should be introduced into Eq. (6.74). If fluid inertia is neglected, the fluid force in an anisotropic bearing can be written as

$$\{\boldsymbol{F}_f\} = [\boldsymbol{C}]\{\dot{z}\} + [K - \mathrm{i}\lambda\Omega\boldsymbol{C}]\{z\} + [\boldsymbol{C}']\mathrm{e}^{\mathrm{i}\delta_C}\{\dot{\bar{z}}\} + [K']\mathrm{e}^{\mathrm{i}\delta_K}\{\bar{z}\}. \tag{6.75}$$

Here, $\bar{z} = x - \mathrm{i}y$ denotes the complex conjugate of $\mathbf{z}$, that is, if $\mathbf{z}$ rotates at forward frequency ω_n, for example, $\mathbf{z} = \mathbf{z}_0\mathrm{e}^{\mathrm{i}(\omega_n t + \alpha_0)}$, then $\bar{z}$ will rotate at reverse frequency, $-\omega_n, i.e., \mathbf{z} = \mathbf{z}_0\,\mathrm{e}^{-\mathrm{i}(\omega_n t + \alpha_0)}$. Reverse stiffness and damping K' and D' cause reverse component B. They are oriented at δ_C and δ_K, and vary with the orientation of x, y coordinate system. Major/minor stiffness and damping for this anisotropic bearing are relating to the anisotropic effect.

The major stiffness axis is oriented to the x-axis with a maximum value $[\boldsymbol{K} + \boldsymbol{K}']$ and the minor stiffness axis with a minimum value $[\boldsymbol{K} - \boldsymbol{K}']$. The major/minor axes for damping hold the same properties as those for stiffness. In general,

major/minor axes for the ellipse of a rotor's orbital response, stiffness, and damping, are neither co-linear nor perpendicular. At low speed, however, when damping effects are negligible, the major axis for the ellipse of rotor response is the same as- or co-linear to the minor axis for stiffness.

6.5 Rotor Stator Interaction

The unsteady flow produced by interaction between rotating and stationary blade rows Rotor Stator Interaction (RSI) in a turbomachine can generate, under certain conditions, several unwanted effects such as high pressure pulsations, noise, and structural vibrations. These effects are well-known as important sources of damage that affect not only runner blades and guide vanes but also the whole machine, leading to fatigue cracks in some cases. RSI in hydraulic machinery is generally classified as follows (Fig. 6.35).

Potential interactions: flow unsteadiness due to pressure waves which propagate both upstream and downstream.

Wake interactions: flow unsteadiness due to wakes from upstream blade rows convecting downstream.

For incompressible flow turbomachinery, there is another type of interaction:

Shock interactions: for transonic/supersonic flow unsteadiness due to shock waves striking the downstream blade row.

6.5.1 Mechanism of RSI in Turbomachinery

Interactions between impeller blades and guide vanes are one of the main causes of vibration in hydraulic machinery (Zobeiri et al. 2006). The phenomenology of rotor–stator interactions may be considered as a combination of inviscid flow, potential, and viscous flow, wake, interactions (Dring et al. 1982).

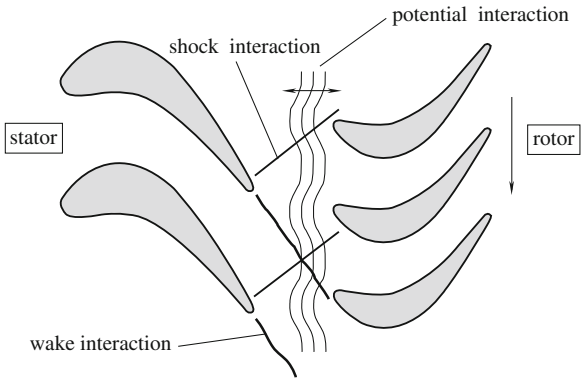

Fig. 6.35 Unsteadiness of rotor and stator interaction RSI (Adamczyk 2000)

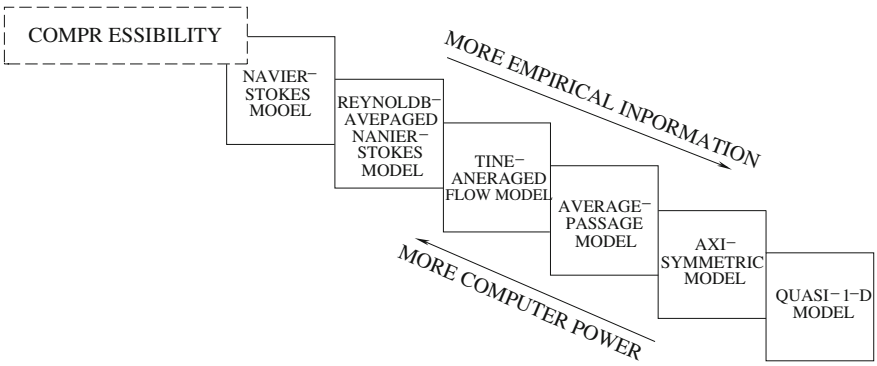

Fig. 6.36 Rotor-stator numerical model (Zobeiri et al. 2006)

6.5.1.1 Mechanism of RSI

With respect to the potential effect, flow in the distributor channels is periodically perturbed by rotating impeller blades, one of the main sources of pressure fluctuation extending backward up to the spiral casing. In such a case, Giesing (1968) developed an exact solution for unsteady potential flow. The key operating parameter for potential interaction is the clearance gap between the guide vanes under the impeller blade that controls the intensity of rotor–stator interactions. Therefore, the most important potential interaction will arise when the guide vanes are fully opened and one of the impeller blades is in the closest position to the trailing edge of a guide vane.

As for viscous effects, the hydrodynamic phenomena which play a major role in rotor–stator interactions are the non-uniformity of the velocity field in the spiral casing and the non-desirable flow angle in the distributor, the flow separations, and the wakes. The conceptual separation between potential and viscous effects has limitations that modern computational flow dynamics can overcome through unsteady RST simulations.

The different rotor-stator interaction models with the required computing power are shown in Fig. 6.36 (Adamczyk 2000) from the simplest up to the fully transient Navier–Stokes models. It can be seen that there are available computing resources enable us to resolve the 3D RANS equations with a transient rotor-stator model.

6.5.1.2 Rotor–Stator Behavior in a Hydraulic Turbine

In a stator frame, the non-uniform flow field caused by wake effect and blade loading at the guide vane outlet generates a periodic flow pattern. In a rotor frame, the pressure field attached to the rotating impeller blade also causes periodic flow field distortions. These stationary and rotating periodic flow components can be expressed in a Fourier series as

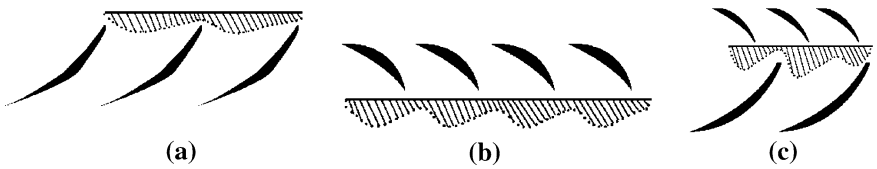

Fig. 6.37 Modulation process between impeller blade flow and guide vanes flow field: **a** Flow field distortion due to impeller pressure field, **b** Flow field distortion due to guide vane wakes, **c** Combination of both distortions (Zobeiri et al. 2006)

$$\begin{cases} p_s(\theta_s, t) = \sum_{n=1}^{\infty} B_n \cos(nz_g\theta_s + \varphi_n) \\ p_r(\theta_r, t) = \sum_{n=1}^{\infty} B_m \cos(nz\theta_r + \varphi_m). \end{cases} \tag{6.76}$$

Here, m, n are the harmonic orders; B_m, φ_m are the amplitude and the phase for the mth harmonic; θ_r, θ_s are the angle coordinates for the rotating and the stationary systems; z is the impeller blade number; and z_g is the guide vanes number.

The resultant pressure field, combining with both the guide vanes and impeller blade pressure fields is characterized by a strong modulation process illustrated in Fig. 6.37 (Nicolet et al. 2006).

Therefore this modulation can be treated as a product of both pressure fields given by Eq. (6.76). Since the impeller angle coordinate expression using the stationary reference frame is $\theta_r = \theta_s - \Omega t$, the modulation yields resultant pressure field:

$$p_{mn}(\theta_s, t) = \frac{A_{mn}}{2}\cos\left(mz\Omega t - k_1\theta_s + \varphi_n - \varphi_m\right) + \frac{A_{mn}}{2}\cos\left(mz\Omega t - k_2\theta_s - \varphi_n - \varphi_m\right). \tag{6.77}$$

The modulated pressure field results from the contribution of the high and the low order of diametrical pressure modes, k_1 and k_2:

$$k_1 = mz - nz_g \text{ and } k_2 = mz + nz_g. \tag{6.78}$$

The sign of the diametrical mode number indicates the direction of rotation. The positive implies a rotational mode in the same direction as the impeller.

6.5.1.3 Experimental Study on the Francis Pump Turbine

In order to understand the mechanism of RSI in hydraulic machinery, Zobeiri et al. (2006) introduced the experimental study of pressure measurement on a reduced scale model of a $\nu = 0.19$ specific speed pump-turbine with 20 stay vanes, 20 guide vanes and 9 impeller blades shown in Fig. 6.38. One operating point ($\varphi = 0.519$, $\psi = 5.254$, $Q = 1.43Q_{BEP}$) was investigated corresponding to the

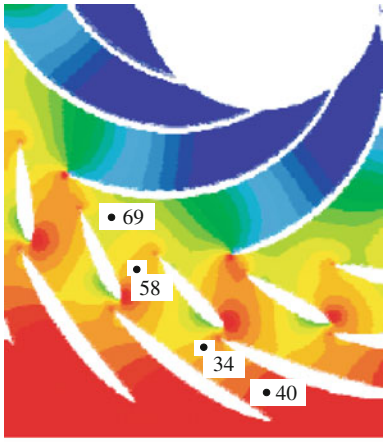

Fig. 6.38 Locations of the monitoring points in the distributor channel (Zobeiri et al. 2006)

maximum guide vane opening and the minimum clearance of the rotor–stator gap. The measurements of discharge, specific energy and efficiency are performed in compliance with the requirements of the IEC 60193 standards.

The wall pressure fluctuation measurements were performed on stationary parts of the pump-turbine model. Piezoresistive pressure sensors were mounted on the stay vane and guide vane channels, as shown in Fig. 6.38 (Zobeiri et al. 2006).

Pressure fluctuations for one impeller revolution were presented. The agreement between measured and computed values was very good. The most significant discrepancy of pressure amplitude arises in the guide vane channel, point 58, as seen in Fig. 6.39. The pressure coefficient fluctuation is defined as $c_p = 2(p - \bar{p})/(\rho U^2)$. Here, p is the pressure; $\bar{p}$ is the average pressure for one impeller revolution; and U is the impeller peripheral velocity.

The spectral analysis was carried out for the corresponding region, indicating that the difference stems from the pressure amplitude of the blade passing frequency component. For the point closest to the impeller, the maximum of pressure amplitude was observed for the same component, indicating strong influence of the potential effect in interactions between the guide vanes and the rotating impeller

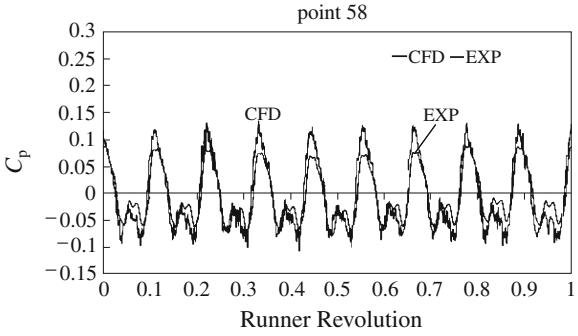

Fig. 6.39 Time history vibrations of pressure coefficient, comparison between numerical and experimental results at monitoring point 58 (Zobeiri et al. 2006)

blades. However, amplitude of this component decreases rapidly backward to the stay vane. The first harmonic corresponding to 2 times blade passing frequency spreads to the spiral case.

6.5.2 1D Modeling of RSI

Pump-turbine operating under steady state conditions is subject to pressure fluctuations that result from the interaction of rotating and stationary parts in the machine. This type of Rotor–Stator Interaction, RSI, is the consequence of interaction between rotating flow perturbations or so-called potential flow perturbations caused by the impeller blades and the flow perturbation caused by the guide vanes.

6.5.2.1 Combination of Unsteady Incompressible RANS Model and 1D Acoustic Model

The rotor–stator interaction generates pressure waves propagating throughout the entire hydraulic machine. As a result, the RSI phenomena may lead to two different kinds of pressure fluctuations in the machine (Ruchonnet et al. 2006):

Diametrical pressure mode rotating in the vaneless gap between the guide vane and the impeller blades has been described by Bolleter (1988) and Ohura et al. (1990). Propagation of standing waves in the spiral case has been described by Chen (1961) and Dörfler (1984).

The first phenomenon may cause resonance between the rotating diametrical pressure mode and the structure of the impeller or of the head cover. It may induce strong vibrations, noise, and fissures or ruin guide vanes bearings. The second phenomenon may cause resonance with the power house structure that generates unacceptable vibrations and noise. The standing wave phenomenon may also affect the penstock, which evidences the potential interaction of the hydraulic machine with the hydraulic circuit.

Some analytical models have been developed to predict the occurrence of the diametrical mode shape as well as the standing wave phenomena. The standing wave prediction is based on the traveling time of pressure waves propagating in a one-dimensional system that models the pump turbine according to its topology. Recently, Haban et al. (2002) developed more sophisticated one-dimensional models based on the matrix transfer method that showed capability for predicting spiral casing standing wave patterns.

The 3D simulation of unsteady flow in a vaneless centrifugal pump was performed by González et al. (2002). Their work shed light on the capability of CFD to accurately predict the unsteady convective field relating to the RSI phenomenon at the blade passing frequency which is dominantly close to the nominal operating point. However, some discrepancies appear for off-design operating conditions

where acoustic behavior becomes more effective due to a blade-tongue interaction. Such an incompressible code cannot account for the propagating part of the flow which may lead to a standing wave phenomenon.

Consequently, the separation of hydraulic and acoustic pressure fluctuations by means of the least-squares residual method has been developed. A model including both a jet-wake pattern of the convective flow and a blade tongue interaction has been set up (Ruchnnet et al. 2006).

It seems that the combination of an unsteady incompressible RANS model and a 1D acoustic model is a suitable approach for calculating amplitudes of pressure fluctuations resulting from RSI. This approach would leads to a RSI computing methodology for predicting pressure amplitudes where the unsteady incompressible RANS calculation accounts for the rotor–stator excitation mechanism, considering all the parameters (i.e. vaneless gap, impeller blade angle, guide vane opening, jet-wake effect, etc.).

The first step of this approach is to set up a hydroacoustic model of a pump turbine; to investigate RSI patterns; and to perform a sensitivity study of the model.

6.5.2.2 1D Acoustic Model

Neglecting convective terms $\partial C/\partial x$ and assuming plane pressure wave and uniform velocity field in a cross section, one could reduce the momentum and the continuity equations to a simple hyperbolic partial differential equations for a pipe of length dx, cross-section A, and wave speed a as shown by Fig. 6.40 (Ruchnnet et al. 2006):

$$\frac{\partial h}{\partial t} + \frac{a^2}{gA}\frac{\partial Q}{\partial x} = 0 \tag{6.79a}$$

$$\frac{\partial h}{\partial x} + \frac{1}{gA}\frac{\partial Q}{\partial t} + \frac{\lambda |Q|}{2gDA^2} = Q. \tag{6.79b}$$

Here, h and Q are the piezometric head and the flow rate with the mean velocity C expressed as

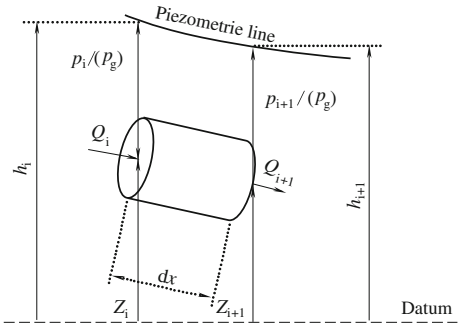

Fig. 6.40 Pipe with a length dx (Ruchnnet et al. 2006)

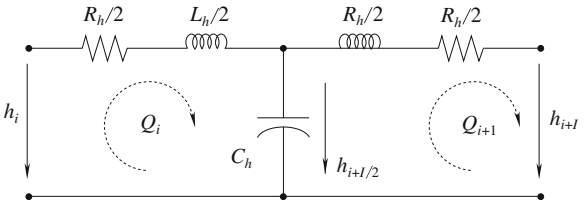

Fig. 6.41 Equivalent scheme of a pipe (Ruchnnet et al. 2006)

$$h = z + p/(\rho g)\, Q = CA. \tag{6.80}$$

The system of hyperbolic Eqs. (6.79a, 6.79b) is solved via the Finite Difference Method with a scheme of 1st order centered discretization in space and Lax for the discharge. This approach leads to a system of ordinary differential equations that can be represented as a T-shaped equivalent scheme as shown in Fig. 6.41.

The RLC parameters of this equivalent scheme are given by

$$R_h = \frac{\lambda |Q| \mathrm{d}x}{2gDA^2} \quad L_h = \frac{\mathrm{d}x}{gA} \quad C_h = \frac{gA\mathrm{d}x}{a^2}\,. \tag{6.81}$$

Here, λ is the friction coefficient; R_h is the hydraulic resistance; L_h is the hydraulic inductance; and C_h is the hydraulic capacitance. They indicate the losses, inertia, and storage effects.

The pipe model with a length L is made of a series of nb elements based on the equivalent scheme of Fig. 6.41.

The system of equations relating to this model is based on the Kirchoff laws. Time integration of the full system is achieved with a Runge–Kutta 4th order procedure.

6.5.2.3 Pump Turbine Hydroacoustic Model

The scale model of a Francis pump-turbine which has 20 guide vanes and 9 blades is presented in Fig. 6.42a. Its hydroacoustic model is made of a pipe network as shown by Fig. 6.42b.

The hydroacoustic model consists of 20 pipes for the guide vanes (pipes D1–D20), 9 pipes for the impeller (pipes R1–R9), and 19 pipes for the spiral casing (pipes B1–B19). The first part of the spiral casing between the turbine inlet and the guide vane No.1 is modeled as pipe B0. The diffuser is modeled as pipe A1. The energy transfer through the impeller is modeled as the pressure "source" VS1 whose head is a function of discharge, i.e. $H = H(Q)$, according to the slope of the pump turbine characteristics linearized around the operating point. The connection between the stationary and rotating parts is made up of 180 valves linking each guide vane to each impeller vane. The 180 valves are controlled by flow distribution between the stationary and rotating parts according to the impeller angular position $\theta(t)$. The valve head loss is calculated to ensure the idealized discharge evolution.

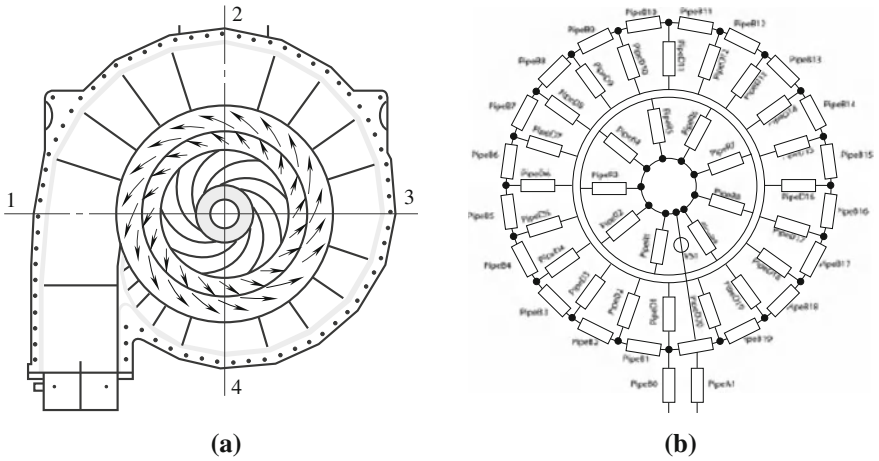

Fig. 6.42 Plan view of the pump turbine (**a**) and its hydroacoustic model (**b**) (Ruchnnet et al. 2006)

Based on the assumption of a constant impeller speed, discharge evolution between one guide vane and one impeller vane is a function of the connection area between them. During the rotation of impeller, four phases are identified:

Phase 1: the blade starts to pass in front of the first blade of the guide vane, and the discharge between guide vane and impeller vane increases linearly with an increase of the connection area until the impeller blade reaches the second blade of the guide vane;

Phase 2: the discharge between guide vane and impeller vane remains constant until the second impeller blade reaches the first blade of the guide vanes with the connection area being constant;

Phase 3: the discharge between guide vane and impeller vane decreases linearly with the reduction of connection area;

Phase 4: the discharge between guide vane and impeller vane is kept to zero as the connection area is zero until phase 1 appears again.

The discharge evolution described above acts like a sliding slot between the 20 guide vanes and one impeller vane. As a result, there are 9 slots for the full pump turbine, one for each impeller vane. Each slot angle is shifted by $2\pi/Zo$. The discharge law can be modified to take into account the thickness of guide vanes and impeller blades, e_o and e_b respectively. The thickness can be expressed as an equivalent angle measured in degrees at the vaneless gap radius. The thickness of the impeller blades is at first taken at an arbitrary angle equal to 4°, the real one being 3°. The consideration of blades thickness induces discontinuity in the overall discharge law, which means that point 3 of the discharge law of an impeller blade does not correspond to point 2 of the following impeller blade but is shifted by the value of e_b.

6.5.3 3D Modeling of RSI in Part Flow Passage

The rotor–stator interaction is the source of unsteady flows and dynamic force fluctuations. These are things to be considered for the improvement of turbine design and for the provision of higher efficiency at off-peak condition.

Through the 3D analysis of rotor-stator interactions, detailed information such as the potential interactions, wake interactions and other viscous interactions (e.g. blade tip vortices or Von Karman vortices) can be observed.

6.5.3.1 Introduction

In order to focus on the first two interactions and to seek a relationship among unsteady runner blade torque, guide vanes forces, and pressure fluctuations as functions of operating conditions, one needs to analyze these parameters at various locations in one passage of the rotor-stator. The simulations are carried out on a passage made of 4 guide vanes and one runner blade from total of 24 guide vanes and 6 runner blades. This type of passage modeling is common in numerical simulations of turbines since it reduces computing efforts compared to a full simulation. The system has an even pitch ratio, and therefore no other considerable benefits such as understandings of flow physics or the accuracy of the unsteady-flow prediction could be obtained by using a complete turbine simulation. A cut plane of the investigated propeller turbine is illustrated in Fig. 6.43 with a passage slice in the meridional plane marked in dashed line.

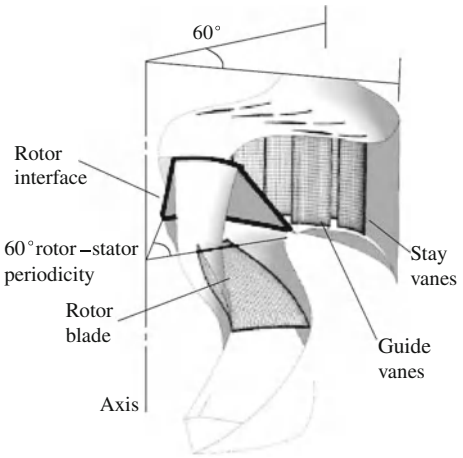

Fig. 6.43 Cut plane of the propeller turbine: 60° rotor/stator (Gagnon et al. 2008)

6.5.3.2 Mesh Connection, Moving Reference Frame, and Moving Mesh

Frozen rotor and Transient Rotor–Stator are the most appropriate methods within commercial codes. The former involves no physical displacement of the mating grid but only modification of equations in the moving reference frame. The basic conservation laws of mass and momentum are modified with additional source terms.

Transient Rotor–Stator accounts for physical grid displacement of the rotational domain. At each time step, the grid position is updated according to the rotation speed that has been specified in the pre-processing step; the flow field variables are solved in their respective domain.

Several interfaces are used to connect stationary and moving meshes for steady and unsteady calculations.

First, one estimates mesh performance and torque on the runner blade with a steady simulation averaging circumferential velocity at the interface (Stage simulation). Since the effect of circumferential velocity is filtered by the averaging operation, it is possible to use a partial stator passage with only one guide vane and one stay vane instead of four.

Other types of simulations are performed using a frozen rotor for steady calculations and a transient rotor–stator interface for unsteady calculations. Figure 6.43 shows interface definitions with 60° degrees rotor-stator passage. Figure 6.44 on the left shows the same interface with a stator pitch angle of 15° in theazimutal plane for stage calculation.

6.5.3.3 RSI Analysis

Unsteady RSI may be attributed to instantaneous pressure fluctuations. Wakes building along the boundary layer of stay vanes and guide vanes are the unsteady elements that need attention.

These flow phenomena are weaker in intensity, appearing as higher harmonics on the frequency spectrum. Results from the simulation of steady cases using a Frozen rotor interface are presented for wake interaction. Dissipation of the wake as well as its vorticity and the velocity profile has been investigated with the turbulent kinetic energy (Gagnon et al. 2008).

RSI in a 3D model of an axial turbine is analyzed by them. Potential and wake interactions are detected at multiple locations, and the interface influences on these interactions is observed.

Figure 6.44 shows a typical case of how velocity profiles in the rotor–stator passage gradually dissipate. For peak condition, the velocity gradients dissipate up to 99 % before reaching the blade.

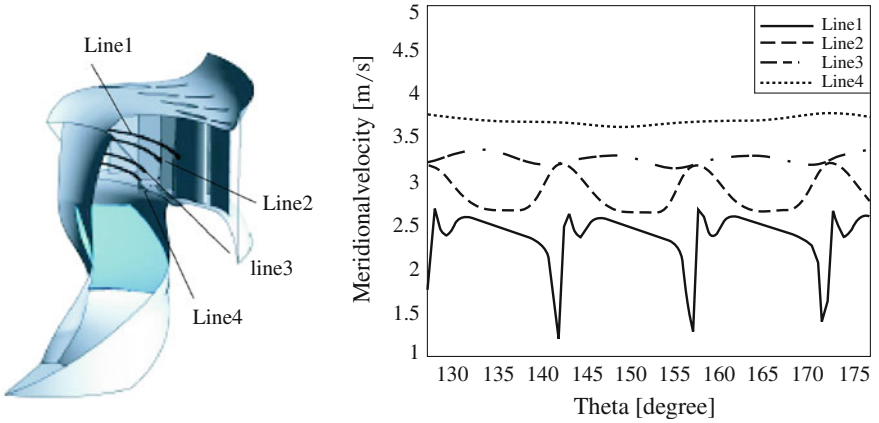

Fig. 6.44 Meridional velocity profiles along different streamwise stations in the rotor stator passage (Gagnon et al. 2008)

6.5.4 3D Modeling of RSI in Complete Flow Passage

It becomes necessary to simulate the unsteady flow in a complete turbine to investigate its rotor stator interaction if non-uniform inflow comes out of a spiral case and the pitching of guide vane and runner is not evenly distributed.

Typically a Francis turbine has 20–24 tandem cascade channels and 9–13 runner channels. For an accurate solution each channel has to be resolved with approximately 100,000 nodes. Therefore the unsteady simulation of an entire Francis turbine can only be carried out on high performance computers in parallel (Ruprecht et al. 1999, 2000). For example, Lipej et al. (2006) conducted a numerical analysis of rotor–stator interaction in an entire flow passage of a reversible pump-turbine. Roclawski and Hellmann (2006) conducted the rotor–stator-interaction of a radial centrifugal pump.

6.5.4.1 Basic Equations

For hydraulic turbomachinery, the Reynolds averaged Navier–Stokes equations for an incompressible flow are usually employed. Description of the flow in the Eulerian coordinates can be applied for unsteady boundary condition problems as well as for self excited unsteadiness. However, to depict problems with moving geometries in Eulerian coordinates is difficult. At the moving boundary a Lagrangian description can be used with great convenience since the fluid particles can be traced with this method. A combination of these two methods, an Arbitrary Lagrangian Eulerian (ALE) method can be utilized, which is suitable for problems with moving boundaries. In the ALE method the chosen reference coordinates can be arbitrary. In this referential coordinate system the material derivative can be described.

The moving velocity of the chosen reference system can be arbitrary. If it is equal to zero one gets the Eulerian description. On the other hand, if it is equal to the velocity of the fluid particle, the Lagrangian formulation is obtained. The convective term in the transport equations for scalar quantities changes in the same way as in the momentum equations. This applies likewise to the turbulence equations.

For industrial applications the k-ε turbulence, model is used mostly. This model, however, is not suitable for unsteady problems, since it does not distinguish between the resolved unsteady vortex structure and the averaged turbulence. Improved results can be obtained via multi-scale models which take into account different vortex scales. Other successful approaches such as filtering techniques can be applied too. In particular, for problems with self excited unsteadiness, the use of improved turbulence model is essential.

6.5.4.2 Recent Progress on CFD Simulation for Rotor–Stator Interaction

Due to their high blade loading, high rotating speed, thick guide vanes, and small gaps, the interaction between guide vanes and rotor blades in high head pump turbines is the main source of vibrations. There are also differences in mechanical conditions between the prototype and the model mounted on the test rig which makes measurements on prototype necessary as reported by Egusquiza et al. (2002). Thus, the objective of research should be reliable CFD prediction of the pressure vibrations originating from RSI combined with a numerical analysis of the mechanical properties of the prototype. Only then can the response of the structure to dynamic load be properly predicted.

A CFD method has been set up by Keller and Sallaberger (2006) for numerical simulation of the dynamic load on a pump turbine runner originating from the interaction of guide vanes and runner blades. The predicted excitation frequencies are the superposition of a constant part, three distinct frequencies, and the harmonics of runner-blade passing frequency.

With a time dependent CFD simulation of spiral casing, entire stator and entire rotor, it is possible to detect the node shapes of the exciting modes. This was demonstrated by comparing CFD prediction of the pressure vibrations for two different pump turbine runners. One has 7 blades and the other has 9 blades coupling to a 20 guide vanes stator (Keller and Sallaberger 2006).

According to Tanaka (1990) the RSI leads to pressure waves at rotating pressure modes depending on the number of stator channels (z_S) and the number of runner blades (z_R): $k = M\, z_R \pm N\, z_S$. While mode 0 represents a standing wave on a rotating runner system the other modes are rotating at speed n_M ($n_M = nZ_S/k$). Pressure modes with a negative node number k are counter rotating, and those with positive mode number are rotating with the runner. In Fig. 6.45, the CFD simulation reveals the exact pressure modes as expected. Thus, if the natural frequencies are known from structural analysis, the CFD simulation allows critical excitation modes to be identified and further analyzed with respect to their effect

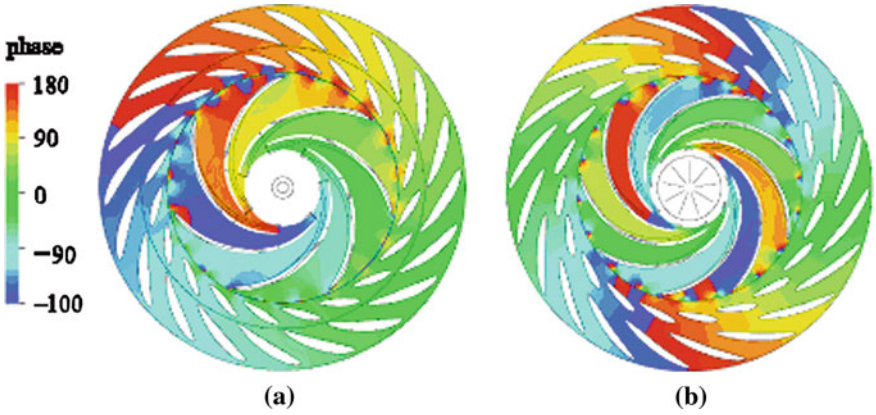

Fig. 6.45 Decomposition of the predicted pressure field shows the shape of the excitation mode (Keller and Sallaberger 2006). **a** Runner with 7 blades phase angle at 3rd harmonic. **b** Runner with 9 blades phase angle at 2nd harmonic

on the structure. Furthermore, CFD simulation accurately predicts the direction of the pressure wave propagation which is significant to the vibration behavior of the whole machine. For example, pressure waves propagating against the runner rotation into the spiral casing and further upstream can cause undesirable vibrations in the penstock (Keller and Sallaberger 2006).

A time dependent CFD simulation of the runner together with the stationary components illuminates the major mechanisms of RSI which take place at the basic frequency (pressure pulsations at rotational speed times the number of the blades) and its harmonics. Frequency, mode, and amplitude of the pressure vibration are found to be well represented in CFD when certain standards of grid density, discretisation scheme (2nd order accurate), time step, computational domain and boundary conditions are all fulfilled.

6.6 Vibration of Pumps Induced by Hydraulic Excitation

A current trend for developing machines with higher speed, high power density worsens the fluid/structure interaction problems. Without cavitation, even these interactions alone can lead to increased wear or at worst, structural failure.

6.6.1 Introduction

Three different categories of flow vibrations can be found, and there are a number of phenomena within each identified category. They are briefly listed here and some discussions are quoted from various sources.

6.6.1.1 Global Flow Vibrations

Examples of identified vibrations involving large scale vibrations of flow (Brennen 1994) are as follows:

1. Rotating stall or rotating cavitation occurs when a turbomachine is required operate at a high incidence angle close to the value where the blades may stall. Often, stalls will be first manifested on a small number of adjacent blades and this "stall cell" will propagate circumferentially at a fraction of the main impeller rotation speed. When the machine cavitates, similar phenomenon may appear, perhaps in some slightly altered form which will be referred to as "rotating stall with cavitation."
2. Surge is manifested in a turbomachine that is required to operate under highly loaded circumstances where the slope of the head rise/flow rate curve is positive. It affects the system instability and results in pressure and flow rate vibrations throughout the system. When cavitation is present the phenomenon is termed as "auto-vibration" and can occur even for the slope of the head rise/flow rate curve being negative.
3. Partial cavitation or supercavitation becomes unstable when the length of the cavity approaches that of the blade so that the cavity collapses in the region of the trailing edge. Such an occasion can lead to violent vibrations for which the cavity length oscillates dramatically.
4. Line resonance takes place when one of the blade passing frequencies in a turbomachine happens to coincide with one of the acoustic modes of the inlet or discharge line. The pressure vibrations associated with these resonances can often cause substantial damage.
5. It has been speculated that an axial balance resonance could occur for a turbomachine fitted with a balance piston (note: it is designed to equalize the axial forces acting on the impeller) if the resonant frequency of the balance piston coincides with the rotating speed or some blade passing frequency.
6. Cavitation noise can sometimes reach an amplitude value sufficient to generate resonance at the structural frequencies.

6.6.1.2 Local Flow Vibrations

Vibrations involving more localized flow vibrations are as follows:

1. Blade flutter. Similar to the case of airfoils, an individual blade may begin to flutter (or diverge) under particular flow conditions (e.g. incidence angle, velocity), or due to blade stiffness and its supports.
2. Blade excitation due to rotor-stator interaction. A row of stator blades operates just downstream of a row of impeller blades or vice versa. The wake from the upstream blades can induce a serious vibration for the downstream blades at a

blade passing frequency or some multiple values. Non-axisymmetry in the inlet, the volute, or the housing can also lead to excitation of impeller blades at the impeller rotation frequency.
3. Blade excitation due to vortex shedding or cavitation vibrations.

6.6.1.3 Radial Forces and Rotordynamic Forces

Global forces perpendicular to the rotational axis can generate several problems:

1. Radial forces are forces perpendicular to rotation axis caused by circumferential nonuniformities in inlet flow, casing, or volute. While these forces may be stationary in the frame of the pump housing, the loads acting upon the impeller may cause severe vibration.
2. Fluid-induced rotordynamic forces occur as the result of the rotation of the impeller-shaft system. These rotordynamic forces arise from seals, flow through the impeller, leakage flows, or flows in the bearings. Sometimes these forces reduce the critical speed of the shaft system, while unexpectedly limiting its operating range. A fluid-induced rotordynamic problem often occurs at subsynchronous frequency.

6.6.1.4 Frequencies of Vibration

For the diagnostics, it is often a good practice to examine the dominant frequencies and to investigate how they change with rotating speed.

Table 6.3 is a rough guide for those frequencies at which the above problems may occur. Some of the phenomena may scale with impeller rotating speed, Ω,

Table 6.3 Typical frequency ranges of pump vibration problems (Brennen 1994)

Vibration category	Frequency range
Surge	System dependent, 3–10 Hz in compressors
Auto-vibration	System dependent, 0.1–0.4Ω
Rotor rotating stall	0.5–0.7Ω
Vaneless diffuser stall	0.05–0.25Ω
Rotating cavitation	1.1–1.2Ω
Partial cavitation vibration	$<\Omega$
Excessive radial force	Some fraction of Ω
Rotordynamic vibration	Fraction of Ω when critical speed is approached.
Blade passing excitation	$Z_R\Omega/Z_{CF}$, $Z_R\Omega$, $mZ_R\Omega$ (in stator frame) $Z_S\Omega/Z_{CF}$, $Z_S\Omega$, $mZ_S\Omega$ (in rotor frame)
Blade flutter	Natural frequencies of blade in liquid
Vortex shedding	Frequency of vortex shedding
Cavitation noise	1−20 kHz

while others, such as surge, may vary somewhat with Ω but not linearly; still others, like cavitation noise, will be largely independent of Ω.

Among the frequencies listed in table 6.3, the blade passing frequencies need further clarification. The numbers of blades on an adjacent rotor and stator are denoted as Z_R and Z_S, respectively. In so far as a single stator blade is concerned, the fundamental blade passage frequency is $Z_R\Omega$ since the stator blade will experience the passage of Z_R rotor blades for each revolution of the rotor. Consequently, it will represent the fundamental frequency of blade passage excitation when the inlet or discharge lines or the static structure is concerned. Correspondingly, $Z_S\Omega$ is the fundamental frequency of blade passage excitation when it is linked with the rotor blades.

Though the phenomenon is periodic, it is not necessarily sinusoidal and thus the excitation will contain higher harmonics, $mZ_R\Omega$ and $m\ Z_S\Omega$ where m is an integer. But more importantly, when integers Z_R and Z_S have a common factor, say Z_{CF}, then, in the framework of the stator, a particular pattern of excitation is repeated at the subharmonic, $Z_R\Omega/Z_{CF}$, of the fundamental, $Z_R\Omega$. Likewise, in the rotor framework, the structure experiences subharmonic excitation at $Z_S\Omega/Z_{CF}$. These subharmonic frequencies be a problem more threatening than the fundamental blade passage frequencies for smaller dampings of fluid and structure.

6.6.2 Rotor–Stator Interaction

The two basic frequencies of RSI: excitation of the stator flow at $Z_R\Omega$ and excitation of the rotor flow at $Z_S\Omega$ have been thus designated. Apart from superharmonics $mZ_R\Omega$ and $mZ_S\Omega$ that are generated by nonlinearitis, subharmonics can also occur. They can cause major problems, since the fluid and structural damping is smaller for these lower frequencies. To avoid such subharmonics, turbomachines are usually designed with blade numbers Z_R and Z_S which have small common integer factors.

6.6.2.1 Flow Patterns of Rotor–Stator Interaction

Flow perturbations caused by blade passage excitation are illustrated by Miyagawa et al. (1992) in their observations of flows in high head pump turbines. Figure 6.46 shows two diametrically opposite perturbation cells propagating around at 9 times the impeller rotating speed.

6.6.2.2 RSI Forces

When one rotor (or stator) blade passes through the wake of an upstream stator (or rotor) blade, it will clearly experience a fluctuation of fluid forces that act upon it.

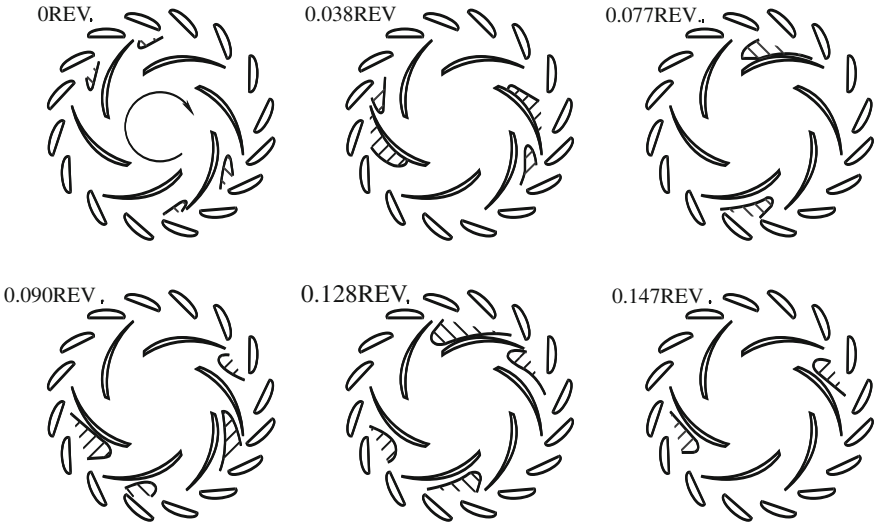

Fig. 6.46 Propagation of a low pressure region (hatched) at nine times the impeller rotational speed through a high head pump-turbine. The sketches show six instants in time equally spaced within one-sixth of a revolution (by Miyagawa et al. 1992)

In this section, the nature and magnitude of these RSI forces will be explored. Experience has shown that these unsteady forces are a strong function of the gap between locus of the trailing edge of the upstream blade and locus of the leading edge of the downstream blade. This distance will be termed "interblade spacing" and denoted by c_b.

Arndt et al. (1989, 1990) have made measurements of the unsteady pressures and forces that appear in a radial flow machine when an impeller blade passes a diffuser blade. Figure 6.47 presents instantaneous pressure distributions (ensemble-averaged over many revolutions) for two particular relative positions of the impeller and diffuser blades.

In the graph, the trailing edge of the impeller blade has just passed the leading edge of the diffuser blade, resulting in a large perturbation in pressure on the suction surface of the diffuser blade. Indeed, in this example, pressure over a small region has fallen below the impeller inlet pressure ($Cp < 0$). The lower graph is the pressure distribution at a later time when the impeller blade is about half-way to the next diffuser blade. Perturbation in the diffuser blade pressure distribution has largely dissipated. Closer examination of the data suggests that the perturbation takes the form of a wave of negative pressure traveling along the suction surface of the diffuser blade and attenuated as it propagates. That observation along with others suggest that the cause is a vortex shed from the leading edge of the diffuser blade by the passage of trailing edge of the impeller. The vortex is then convected along the suction surface of the diffuser blade.

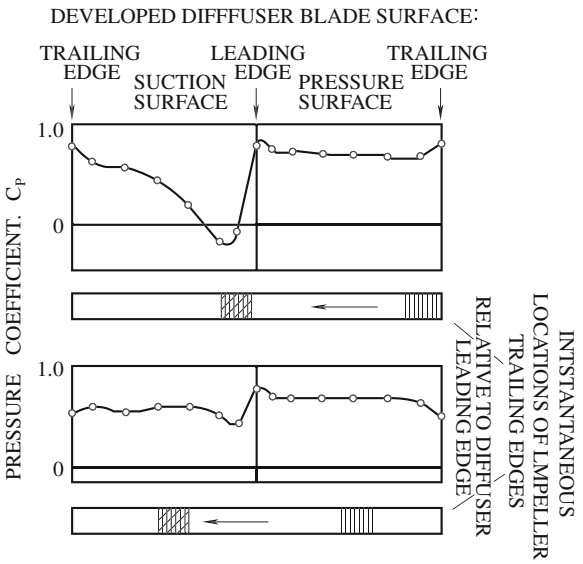

Fig. 6.47 Pressure distributions on a diffuser at two instants during the passage of an impeller blade. Data for an inter blade spacing of 1.5 % and $\varphi 2 = 0.12$ (Arndt et al. 1990)

6.6.2.3 Rotor-Volute Interaction in Centrifugal Pump

Conventional centrifugal pumps with vaneless volute casing usually present the fluid-dynamic interaction between the rotor and the stator associated with the blade passage frequency, which is responsible for a dynamic load on the machine and for noise generation (Brennen 1994). This excitation is originated from non-uniform profile of the flow exiting the impeller, with a jet-wake pattern behind the trailing edge of the blades, which, at the volute, is perceived as a flow with a fluctuating component. For a given pump, magnitude of the excitation is largely dependent on the point of operation, with increasing amplitudes when separating from the best efficiency flow-rate (Parrondo et al. 2002; Blanco et al. 2006). For different pumps, the excitation depends on the geometry of the region where distance between impeller and volute is small, including both tongue shape and, especially, the blade-to-tongue gap (Dong et al. 1997; Morgenroth and Weaver 1998).

González et al. (2006) observed that reducing the gap from 15.8 to 10 % of the impeller radius for a pump with a specific speed of 0.48 led to a 50 % increase in the maximum pressure amplitude at off design conditions. Eventually the amplitude of the vibration response of the pumps can exceed the maximum values allowed by specific regulations. Therefore, it is of use to predict in predicting the fluid-dynamic load on the machine at the design stage, especially for large units.

A study on fluctuations of the blade passing frequency has been presented by Blanco et al. (2006), in which they defined $f_{bp} = f_n \, Z_b$ with f_n being rotating frequency and Z_b blade number. The fluctuations induced in the flow field inside a conventional centrifugal pump with a single vaneless volute equipped with different external diameter impellers (190, 200, 210 and 215 mm) are investigated by experiments and numerical simulation.

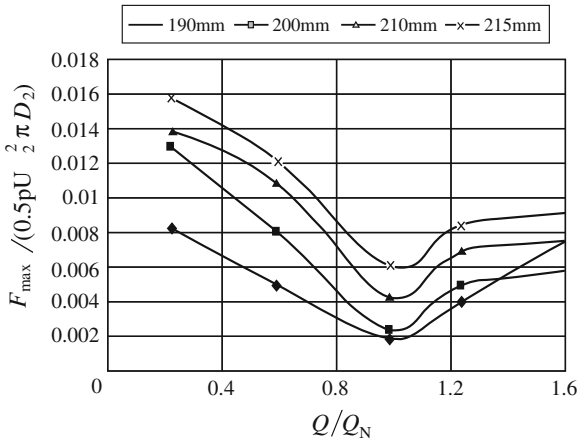

Fig. 6.48 Normalized amplitude of the maximum unsteady total force as a function of the relative flow-rate (Blanco et al. 2006)

The results, as shown in Fig. 6.48, indicate that unsteady phenomena at the blade-passage frequency clearly depend on the value of the impeller-tongue gap. Figure 6.48 exhibits the variation of the normalized amplitude of maximum unsteady total force, $F_{max}/(0.5\rho U_2 2\pi D_2)$, where D_2 and U_2 are the diameter and the rotating velocity at the impeller exit, with respect to the relative flow rate Q/Q_n (Q_n is flow rate at the rated point of pump). For most of the flow-rates and impellers, maximum value of this force increases when the impeller-tongue gap diminishes. For a given impeller, the maximum value of the force reaches its minimum at design flow-rate and increases for both low and high flow-rates. In fact, the force is particularly high at low flow rates.

A variation in this gap from 23.2 to 17 % (i.e. 190–200 mm impeller) produces an increment of about 15 % in the maximum amplitude of the pressure pulsations and 50 % in the unsteady total force. When this gap is further reduced from 23.2 to 11.4 % (i.e. 190–210 mm impeller), the increments of maximum amplitude and total force rise to 40 and 80 % respectively. Another reduction from 23.2 to 8.8 % (i.e. 190–215 mm impeller) brings an increment of 60 and 100 % respectively.

Figure 6.49 shows the normalized amplitude of the driving torque $M_A/(0.5\rho U_2^2 \pi D_2^2 b_2)$ at the blade passing frequency for each impeller, where b_2 is the impeller exit width.

The effects of the flow-rate and the impeller diameter on the driving torque fluctuations are very much the same as the blade-passing frequency forces. This indicates that the minimum torque fluctuations occur at design flow-rate with linear growth of the amplitude for either increasing or decreasing the flow rate from design flow-rate. Such growths become greater in the case of smaller blade-to-tongue gap. In the most critical case (215 mm impeller at 20 % of the nominal flow-rate) amplitude of the torque fluctuation represents about 4 % of the stationary driving torque.

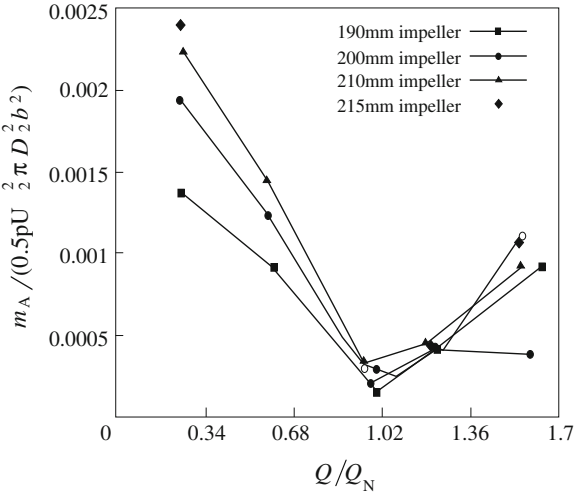

Fig. 6.49 Normalized amplitude of the fluctuation of the driving torque at the blade passing frequency, as a function of flow-rate (Blanco et al. 2006)

6.6.3 Steady Radial Forces

The flow through a pump can frequently be nonaxisymmetric and the resultant mean radial force can be significant. The nonaxisymmetries and hence the radial forces depend upon the geometry of the diffuser and/or volute as well as the flow coefficient. Measurements of radial forces have been made with a number of different impeller/diffuser/volute combinations. Stepanoff (1957) proposed an empirical formula for this nondimensional radial force:

$$|F_0| = (F_{0x}^2 + F_{0y}^2)^{1/2} = 0.229\,\psi\,\{1 - (Q/Q_D)^2\} \tag{6.82}$$

for centrifugal pumps with spiral volutes, and

$$|F_0| = 0.229\,\psi\,Q/Q_D \tag{6.83}$$

for collectors with uniform cross-sectional area. Here, ψ is the head coefficient. Both formulae yield radial forces that have the correct order of magnitude; however, measurements show that other geometric features of the impeller and its casing would also affect the forces.

Some typical nondimensional radial forces obtained experimentally by Chamieh et al. (1985) for an impeller and volute combination are shown in Fig. 6.50 with a range of speeds and flow coefficients. As anticipated in nondimensionalization, the radial forces increase scale with the square of impeller speed. It implies that, at least within the range of rotational speeds used for these experiments, the Reynolds number should be considered as the "design" objective in a way that the volute being well matched to the impeller appears to be satisfied at a flow coefficient, φ_2, of 0.092 where magnitude of the radial force appears to vanish. Other radial force data have also been presented (see Brennen 1994).

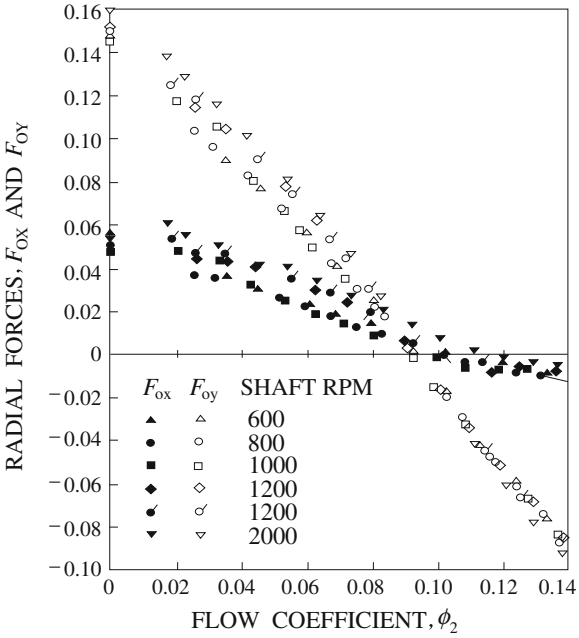

Fig. 6.50 Radial forces for centrifugal impeller and volute combination as a function of shaft speed and flow coefficient (Chamieh et al. 1985)

Further information on the variation of the radial forces in different types of pump is available. Figure 6.51 taken from KSB (1975) shows how F_0/ψ may vary with specific speed and flow rate in a class of volute pumps. Magnitudes of the forces shown in this figure are large.

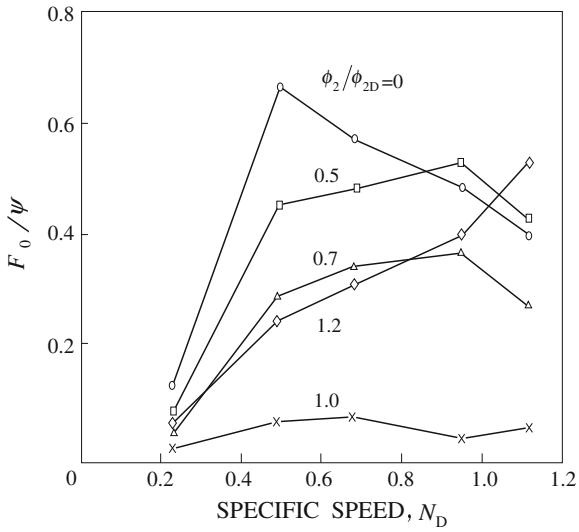

Fig. 6.51 Variation of radial force, F_0, divided by head coefficient, ψ, as a function of specific speed, N_D, and flow for volute casing pumps (adapted from KSB 1975)

The leakage flow from impeller discharge (between the impeller shroud and the pump casing) back to the pump inlet does make a significant contribution to radial force.

Measurements indicate that, in the absence of the rings, nonuniformity in impeller discharge pressure causes significant nonuniformity in the pressure of the leakage annulus which results in a remarkable contribution to the radial force. This is not the case once the rings are installed because the rings will effectively isolate the leakage annulus from the impeller discharge nonuniformity. However, a compensating mechanism exists that balances the total radial force in these two cases.

The increased leakage flow without the rings tends to relieve some of the pressure nonuniformity in the impeller discharge, thus reducing the contribution from the impeller discharge pressure distribution.

A number of other theoretical models are found in the literature. Most of them are based on modeling the impeller with a source/vortex in the volute. The results obtained from these potential flow models deviate too much from real flows to be of much applicability.

The principal focus of this section is on radial forces caused by circumferential nonuniformity in discharge conditions. It must be pointed out that nonuniformities in inlet flow due to, for example, bends in suction piping are also likely to generate radial forces. As yet, such forces have not been investigated. Moreover, it seems reasonable to suggest that inlet distortion forces are more important in axial inducers or pumps than in centrifugal pumps.

6.6.4 Rotating Stall

Rotating stall is a phenomenon which may occur in a cascade of blades when they are required to operate at a high angle of incidence close to the stall point. In a pump, that usually implies the flow rate is reduced to a point close to and below the maximum of the head characteristic.

Figure 6.52 shows the flow patterns in a centrifugal pump at different flow rates. When the flow rate is reduced, the meridian component of relative velocity w_m also decreases. With these reduced flow rates the angle of attack rises and the stagnation point is displaced to the pressure side of the blade. When the attack angle is oversized, flow on the suction side will detach and stall emerges (Fig. 6.52b). The static pressure inside the stall region is smaller than in the surrounding flow, therefore vortices can form with the same rotating direction as the impeller. In the outlet of the channel a second vortex can form with an opposite rotational direction (channel 2 in Fig. 6.52c). These vortices would increase in size until the whole channel is blocked. Then, the medium has to pass through the following channel (channel 3 in Fig. 6.52c) which leads once more to a displacement of the stagnation point, this time in channel 3, and a new stall cell will form in this channel. On the other hand, flow in channel 1 will reattach and thus flow conditions in this channel will be better once again. It is possible that more

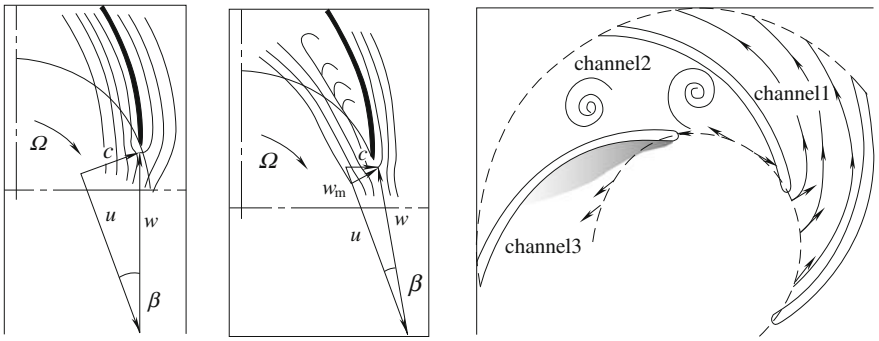

Fig. 6.52 Flow pattern in centrifugal pump at different flow rate (Emmons et al. 1959). **a** At design point, **b** Flow at partial flow rate, **c** Rotating stall of centrifugal pump

than one stall cell exists in the impeller. With this mechanism, stall cells can turn around the impeller, because this angular velocity of the cell stalling is lower than the impeller angular velocity. As a result the stall cell rotates in the impeller against the rotational direction of the impeller. This description of the rotating stall phenomenon was first published by Emmons et al. (1959).

Though rotating stall can occur in any turbomachine, it is most often observed and most widely studied in compressors with large numbers of blades.

Murai (1968) observed and investigated the phenomenon in a typical axial flow pump. The data on the rotating speed of the stall cell are reproduced in Fig. 6.53 where the onset of the rotating stall phenomenon occurs when the flow rate is reduced below the maximum of the head characteristic. It is also noticed that the velocities of the stall cell propagation have values typically between 0.45 and 0.6 of

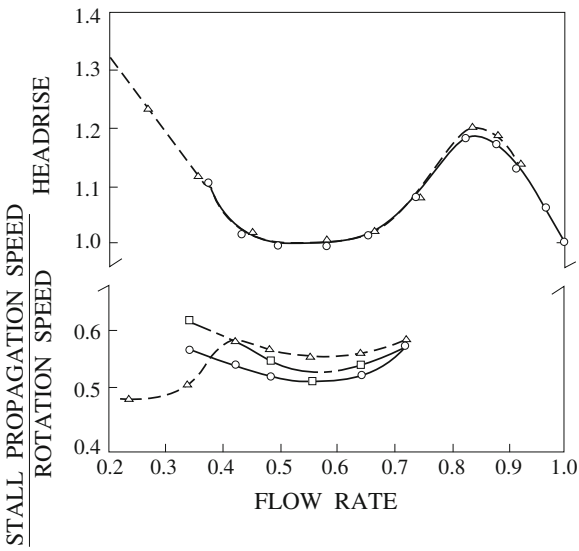

Fig. 6.53 Head characteristic for an 18-bladed axial flow pump along with the measurements of the propagation velocity of the rotating stall cell relative to the shaft speed. Adapted from Murai (1968). Data is shown for three different inlet pressures. Flow and head scales are dimensionless

the rotating speed. Rotating stall has not, however, been reported in pumps with small number of blades perhaps because the diffusion factor D_f will not approach 0.6 for typical axial pumps or inducers with small number of blades. D_f is defined as

$$D_f = 1 - \frac{w_2}{w_1} + \frac{v_{\theta 2} - v_{\theta 1}}{2sw_1}$$

where w is the relative velocity in the pump impeller; v is the absolute velocity; s is the solidity of the impeller blade cascade, and the subscripts θ is peripheral direction, 1 and 2 are the inlet and outlet of the impeller respectively.

Most of the stability theories are established on actuator disc models of the rotor in which the stall cell is assumed to be much longer than the distance between the blades. Such an assumption would not be appropriate in an axial flow pump with three or four blades.

Murai (1968) also examined the effect of limited cavitation on the rotating stall phenomenon and observed that the cavitation did cause some alteration in propagation speed as shown in Fig. 6.53. It is, however, important to have an insight view of this phenomenon (i.e. rotating cavitation) appearing at the points of the head-flow characteristics where the slop is negative and otherwise the operation would have been stable (i.e. without rotating stall) if there were no cavitation. For centrifugal pumps, there have been a number of studies showing rotating stall either in the impeller or in the diffuser/volute.

Perhaps the most detailed study is the work done by Yoshida et al. (1991) on a 7-bladed centrifugal impeller operating with a variety of diffusers, with and without vanes. Rotating stall with a single cell was observed in the impeller below certain critical flow coefficients, subject to the diffuser geometry. In the absence of a diffuser, cell speed was about 80–90 % of the impeller rotating speed. With diffuser vanes, this cell speed was reduced to the range 50–80 %. When impeller rotating stall was present, they also detected some propagating disturbances with 2, 3, and 4 cells rather than one. These were probably due to nonlinearities and an interaction with blade passage excitation. Rotating stall was also seen in the vaned diffuser at a speed less than 10 % of the impeller speed. It was most evident when the clearance between impeller and diffuser vanes was large. As this clearance decreased, the diffuser rotating stall tended to disappear.

The rotating stall may resonate with an acoustic mode of the inlet or discharge piping to produce a serious pulsation problem. Dussourd (1968) identified such a problem in a boiler feed system where the rotating stall frequency was in the range $0.15 \rightarrow 0.25\Omega$, much lower than usual.

Recently, many 3D turbulent simulations and velocity distribution measurements have been done by means of particle image velocimetry (PIV) to study the flow pattern in centrifugal pumps.

Krause et al. (2005) applied the time resolved PIV to the investigation of rotating stall in a radial pump, obtaining good results of velocity distribution in the impeller blade channels under both stationary and rotational stalls. For part-load

flow with standing stall, they found that the static pressure difference decreased slightly below $Q/Q_o = 0.6$ towards lower flow rates.

Due to the fact that in this part of characteristic curve a stall cell in two channels of the impeller appeared. The standing stall is subject to blade geometry which was not perfectly rotationally symmetric. The stall cells rotated in the impeller if the flow rate was reduced below 40 % of the design rate. In their study, a stall cycle within a channel was presented where the length of the cycle corresponded to nearly 7 rotations of the impeller.

For numerical simulation, Guleren and Pinarbasi (2004) conducted a simulation of stalled flow within a vaned centrifugal pump. Sano et al. (2002) treaded the flow instabilities in a vane diffuser of a centrifugal pump by CFD. A commercial code with the standard k-ε turbulence model was used for their work. It was found that the flow instabilities in the vane diffuser, i.e., rotating stall, alternate blade stall, and asymmetric stall, could be simulated. From the numerical and experimental results and discussions, the following conclusions can be drawn:

The flow instabilities in vane diffuser, such as the rotating stall, alternate blade stall, and asymmetric stall, occur in the range with negative slope of the diffuser pressure performance.

As clearance between the impeller and the diffuser increases, it is more susceptible to the occurrence of diffuser rotating stall owing to the decoupling of impeller/diffuser flow.

In cases of smaller clearance, the impeller/diffuser coupled rotating stall is observed at low flow rate. For wider clearance with smaller interaction between the impeller and diffuser, the impeller rotating stall appears independently from the diffuser rotating stall at low flow rate.

The switching between the reverse flow and jet flow in diffuser channel is observed under the rotating stall condition through CFD and experiments.

6.6.5 Cavitation Instabilities

Inducers or impellers of pumps that do not show any sign of rotating stall while operating under noncavitating conditions may exhibit a similar looks-like phenomenon known as “rotating cavitation” when they are required to operate at low cavitation numbers.

Rotating stall emerges at locations on the head-flow characteristics where the slope of this head/flow characteristic is usually positive and therefore it is unstable in a way that will be discussed in the next section. On the other hand, rotating cavitation is observed at locations where this slope is negative. Consequently, the dynamics of the cavitation are essential to rotating cavitation. Another difference between these two phenomena lies in their propagating speeds.

6.6.5.1 Rotating Cavitation

Extensive studies on the unsteadiness of cavitation (Brennen and Acosta 1976; Brennen 1982; Tsujimoto 2006) have been made in association with the POGO instability (Brennen 1994). From the viewpoint of the system including turbo-pump, the vibration is one-dimensional with disturbances in phase for all blades. The unsteady cavitation characteristics can be represented by a transfer matrix, which correlates to flow rate and pressure fluctuations at the pump inlet and discharge. Even without coupling with the structural mode, cavitating turbo-pump systems may suffer from one-dimensional system instability called cavitation surge. Apart from these system instabilities, modern turbo-pumps are also suffering from local two-dimensional instabilities such as rotating cavitation.

1. Rotating cavitation in 3-bladed inducers
   The characteristics of rotating cavitation in 3-bladed inducers at the design flow coefficient were presented by Tsujimoto (2006):

   (a) The rotating cavitation is observed at the design flow rate, which is quite different from rotating stall that occurs at partial flow rate.
   (b) The rotation coefficient C_s of the force vector is larger than 1, which means that the cavitating region rotates faster than the impeller. This is also different from rotating stall in which the stalled region rotates slower than the impeller.
   (c) As cavitation number σ decreases, radial force C_R suddenly increases at a certain cavitation number σ. There, the rotation coefficient is $C_s \approx 1.05 > 1$, and then it decreases to 1 with further decrease in σ.
   (d) In a certain range of cavitation number ($0.035 < \sigma < 0.050$) radial force rotates fixed to the rotor and sometimes wanders at random. This is called attached asymmetric cavitation.
   The radial force drops when the head starts to decrease steeply (this is called "head breakdown"). This drop in force indicates that the rotating cavitation occurs in a range just above the head breakdown cavitation number. The small head decrease under the occurrence of rotating cavitation and the attached asymmetric cavitation are the aftermath of those instabilities.

2. Rotating cavitation in 4-bladed inducers
   To study the cavitation instabilities in a 4-bladed inducer, Tsujimoto et al. (1997) conducted water and liquid hydrogen tests with the VULCAIN liquid hydrogen turbo-pump inducer. His team reported that no significant dependence on rotational speed was found in the tests. In Fig. 6.54, σ and σ_0 are the cavitation number and reference cavitation number; f and f_0 are the frequency of the pressure fluctuation and the rotational frequency of the impeller; and F_r and F_{r0} are the radial forces under cavitating and non-cavitating conditions.

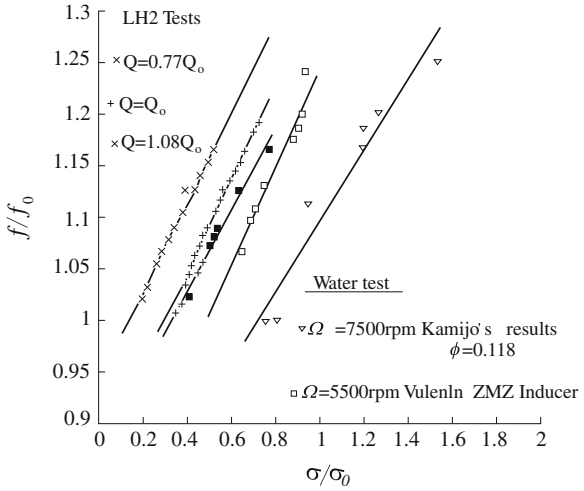

Fig. 6.54 Propagation velocity ratio f/f_0 via. cavitation number σ/σ_0 (Tsujimoto 2006)

(a) At a sufficiently large cavitation number with $\sigma/\sigma_0 = 1.477$, equal cavity appears on each blade and the frequency of the pressure fluctuation is the same as the blade passing frequency.
(b) At $\sigma/\sigma_0 = 1.055$, alternate blade cavitation appears with stable and balanced pattern, generating a pressure fluctuation of $f/f_0 = 2.0$.
(c) At $\sigma/\sigma_0 = 0.738$, rotating cavitation with unbalanced geometry emerges. The frequency of pressure fluctuation is slightly higher than the rotational frequency. Radial force is 3–5 times that under non-cavitating conditions.
(d) At $\sigma/\sigma_0 = 0.423$, one of the following two modes occurs. One is the unbalanced pattern of pressure fluctuation fixed to the impeller; the other is balanced equal cavitation of $f/f_0 = 1.0$.
(e) At $\sigma/\sigma_0 = 0.336$, stable and balanced flow with fully developed cavitation occurs at the beginning of the inducer head drop.

The frequency ratio f/f_0 of the rotating cavitation is summarized in Fig. 6.54. The range of frequency and its dependence on the cavitation number are the same in all cases. If the test results in water are compared between the three and the four bladed inducers, it can be discovered that the onset cavitation number shifts to lower values on four bladed inducer because of the alternate blade cavitation. In the LH2 test, the occurrence region alters to an even smaller cavitation number owing to the thermal effect.

6.6.5.2 One-Dimensional Stability Analysis

Cavitation instabilities in inducers can be categorized into two types, i.e. cavitation surge and rotating cavitation, although there are various higher order modes.

Cavitation surge is a system instability in which the flow rate of the hydraulic system fluctuates in-phase with cavity fluctuations on each blade. Rotating cavitation is a local cavitation instability in which the cavities propagate from blade to blade in the same way as a rotating stall. Typically, for rotating cavitation, the cavitating region rotates faster than the impeller whereas for rotating stall the stalled region rotates slower than the impeller.

Rotating cavitation, as well as cavitation surge, can be treated under the assumption that cavity volume V_c is a function of the cavitation number σ_1 and the local incidence angle to the blade α_1. The cavitation number is defined as $\sigma_1 = (p_1 - p_v)/(0.5\rho W_1^2)$, where p_1 is inlet pressure; p_v is vapor pressure; ρ is liquid density; and W_1 is inlet relative velocity. The cavity volume is normalized by the blade spacing

$$\alpha(\sigma_1, \alpha_1) = V_c/h^2. \tag{6.84}$$

The mass flow gain factor M and cavitation compliance K are defined as

$$M = \frac{\partial Q}{\partial \alpha_1} \text{ and } K = \frac{\partial \alpha}{\partial \sigma_1}. \tag{6.85}$$

Since the cavity volume will grow if the incidence angle is increased or the inlet pressure is decreased, both mass flow gain factor and cavitation compliance should have positive values. These parameters are introduced and evaluated from quasi-steady calculations of blade surface cavitation. Extensive experiments have been carried out and the results are reported.

One-dimensional linear stability analyses are possible for surge, rotating stall, cavitation surge, and rotating cavitation (Tsujimoto 2006). Consider a system composed of an inlet conduit, an impeller cascade with infinite number of blades, a downstream tank, and an exit valve as shown in Fig. 6.55.

The velocity triangle at the inlet of the impeller is plotted in Fig. 6.56. For one-dimensional instabilities of surge and cavitation surge, an axial velocity disturbance in a finite length upstream pipe is considered. For two-dimensional instabilities of rotating stall and rotating cavitation, a two-dimensional sinusoidal potential flow disturbance is assumed to be upstream of the impeller. In both cases pressure fluctuation at the inlet of the impeller can be correlated with the axial flow velocity disturbance via the momentum equation of the inlet flow.

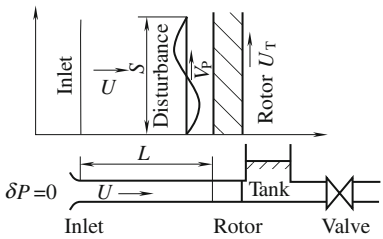

Fig. 6.55 Sketch of hydraulic system

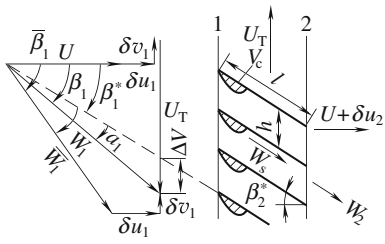

Fig. 6.56 Velocity triangle at the inlet

This is why one-dimensional stability analysis is also viable for two-dimensional instabilities such as rotating stall and rotating cavitation. The pressure increase in the impeller can be obtained if the flow in the impeller is perfectly guided by blades. To simulate surge and rotating stall, one could bring two types of losses into scope: an incidence loss proportional to the loss coefficient ς_S and square of the incidence velocity ΔV at the inlet, and a through flow loss proportional to the loss coefficient ς_Q and square of the relative flow velocity W_s through the impeller flow channel.

The effect of cavitation is taken into account in continuous relation to the impeller through the representation of the cavitation characteristics M and K. If one expresses axial velocity disturbance at the inlet and the outlet of the impeller by ∂u_1 and ∂u_2 and represents the cavity volume per blade by V_c, the continuity equation across the impeller can be written using V_c:

$$h(\partial u_2 - \partial u_1) = \frac{\partial}{\partial t}\partial V_c. \tag{6.86}$$

If the cavity volume is a function of cavitation number σ_1 and incidence angle α, the cavity volume fluctuation can be expressed as

$$\partial V_c = h^2(M\delta\alpha_1 - K\delta\sigma_1). \tag{6.87}$$

Here, the mass flow gain factor M and the cavitation compliance K are defined in Eq. (6.85). The effect of cavitation on pressure performance of the impeller is neglected since most of the cavitation instabilities occur in a range where the pressure performance is not affected by cavitation.

6.6.5.3 Surge, Rotating Stall, Cavitation Surge, and Rotating Cavitation

To obtain simple expressions of onset conditions and frequencies of surge, rotating stall, cavitation surge, and rotation cavitation, various assumptions (simplification) are made for each unstable occasion. For cavitation surge and rotating cavitation, it is assumed that the downstream flow rate fluctuation does not occur. This is a good approximation for typical inducers with a smaller blade angle. For surge, flow from the rotor is considered to be discharged to a surge tank followed by an exit valve. For rotating stall, one could assume that flow from the impeller is

Table 6.4 Onset condition and frequency of instabilities in turbo-pump (Tsujimoto 2006)

Instability	Onset condition	Frequency
Surge	$\frac{\partial \psi_{ts}}{\partial \phi} > \frac{1+(1/\cos\beta^*)(l/L)}{B^2\phi R}$	$n = \frac{1}{2\pi}\frac{1}{\sqrt{\rho C L}}\sqrt{\frac{1+(l/R)\left[L_u+(l/\cos^2\beta_2^*)\right]}{\left[1+(1/\cos\beta^*)l/s\right]}}$
Rotating stall	$\frac{\partial \psi_{ts}}{\partial \phi} > 0$	$\frac{V_P}{U_T} = 1 - \frac{2\varsigma_S[1-(\phi/\phi^*)]}{1+(2\pi/\cos\beta^*)l/s} < 1$
Cavitation surge	$M > 2(1+\sigma)\phi K$	$n = \frac{U_T}{2\pi}\frac{1}{\sin\beta_1}\frac{1}{\sqrt{2KLh}}$
Rotating cavitation	$M > 2(1+\sigma)\phi K$	$\frac{V_P}{U_T} > 1$, $\frac{V_P}{U_T} < 0$

discharged directly to a space of constant pressure. By writing down relations connecting the flow disturbances in upstream and downstream of the impeller, one obtains a set of linear equations in terms of fluctuation amplitudes. From the coefficient matrix of the linear equations, a polynomial characteristic equation is acquired in terms of a complex frequency whose real part represents the frequency and the imaginary part is the damping rate of possible instability mode.

The onset conditions and the frequencies obtained with characteristic equations are summarized in Table 6.4, where $\psi_{st} = (p_2 - p_{1t})/(\rho U_T^2)$ is the total static pressure coefficient from inlet to outlet of the impeller; $\phi = U/U_T$ is the flow coefficient, with mean axial velocity U and circumferential velocity U_T of the impeller; β^* is the mean blade angle measured from axial direction; l is the chord length of blades; L is the length of inlet conduit; R is the resistance of exit valve; $B = \sqrt{\rho C/L}U_T$ is called Greitzer's B factor with the compliance of a tank placed downstream of the impeller $C = V/(\rho a^2 f)$ for liquids or $C = A/(\rho g f)$ for gas; V is the volume of the tank; a is the speed of sound; f is the cross-sectional area of the inlet pipe; A is the free surface area of the surge tank; and g is the gravitational acceleration constant; L_u is an impeller loss coefficient; β_2^* is the blade outlet angle; s is the circumferential wavelength of the disturbance; $\bar{\beta}_1$ is the mean flow angle at the inlet; φ^* is the incidence free flow coefficient; Vp is the propagation velocities of rotating stall and rotating cavitation observed in a stationary frame; and n is the frequencies of surge and cavitation surge.

Results shown in Table 6.4 demonstrate the following characteristics:

1. Both surge and rotating stall occur at small flow rates with a positive slope of $\psi_{ts} - \varphi$ performance. Under this condition, the head produced by rotor will increase if the flow rate is increased, which accelerates the flow and results in a further increase in flow rate. The positive feedback is the source of surge and rotating stall.
2. Both cavitation surge and rotating cavitation occur when $M > 2(1+\sigma_1)\phi K$.
3. The frequency of surge is basically identical to $n = 1/(2\pi\sqrt{\rho C L})$, the natural frequency of a Helmholtz resonator composed of a tank with compliance C and an inlet pipe with the length L, and is not determined by impeller speed.

4. The frequency of cavitation surge is proportional to impeller speed U_T and inversely proportional to the square root of L and K. This shows that the cavitation surge is an vibration of upstream fluid associated with the compliance of cavitation in the impeller.
5. The propagation velocity ratio defined as V for rotating stall is less than 1, suggesting that the stalled region rotates slower than the impeller.
6. Two modes of rotating cavitation are predicted. One rotates faster than the impeller and this mode is generally observed in experiments (Tsujimoto et al. 1997). The other mode rotates slower than the impeller and is occasionally observed as a mode rotating in the opposite direction of the impeller, which will be discussed in the following section.

The criterion $M > 2(1 + \sigma_1)\phi K$ for the onset of cavitation surge and rotating cavitation illuminates the importance of positive mass flow gain factor which implies that the cavity volume decreases as the flow rate increases. The mechanism of instability can be explained as follows. When flow rate rises, the angle of attack to a rotor blade is decreased. If the value of the mass flow gain factor is positive, the cavity volume will also decrease according to the definition of mass flow gain factor. After that, the inflow to the rotor will grow to fill up the space occupied by the cavity volume decreased. Thus, the increase of flow rate results in further increase of flow rate. This mechanism of instability totally depends on the continuity relation and is not associated with impeller performance. Actually, both the rotating cavitation and cavitation surge happen at a higher inlet pressure where the performance degradation due to cavitation is insignificant.

On the contrary, positive cavitation compliance has an effect to suppress instabilities: When inlet flow rate goes up, inlet pressure will decrease due to the Bernoulli effects and the cavity volume will increase if $K > 0$, leading to the decrease of inlet flow rate. So, $K > 0$ provides negative feedback that stabilizes the system. The onset condition of cavitation surge and rotating cavitation does not depend on the steady $\psi_{ts} - \varphi$ performance and they may occur even at design flow rate. It makes the cavitation instabilities more serious than surge and rotating stall that occur at off design points. The mechanism of instabilities in turbo-machinery is summarized in Table 6.5.

In order to study the relation between rotating stall and rotating cavitation, a stability analysis is established on the assumption that the two-dimensional flow extends to upstream and downstream infinity. The flow downstream is composed of a potential flow disturbance and a vertical flow disturbance due to a vorticity shed from the impeller caused by unsteadiness of the flow. The mass continuity and pressure rise relations across the cascade result in a third order characteristic equation of the non-dimensional frequency k^* whose real part k_R^* gives the propagation velocity ratio Vp/U_r and the imaginary part gives the damping rate k_I^*:

$$\left(k^* - k_1^*\right)\left(k^* - k_2^*\right)\left(k^* - k_3^*\right) = 0 \tag{6.88}$$

Table 6.5 Mechanisms of instabilities in turbo-machinery (Tsujimoto 2006)

Performances	Mechanisms of instabilities
Flow rate is increased	Incidence angle is decreased
Loss is decreased	$M = \partial V_c/\partial\alpha > 0$
Pump head is increased	
Cavity volume is decreased (Continuity)	$\partial\psi/\partial\phi > 0$ (Performances)
Flow rate is increased further 	Upstream flow rate is increased Further to fill up the space Occupied by cavity
Surge and rotating stall	Cavitation surge and rotating surge
Occurs at partial flow	Occurs also for design point

The examination of these three roots of Eq. (6.88) has been done for an inducer tested by Kamijo et al. (Tsujimoto 2006).

6.6.5.4 2-D Flow Stability Analysis

The stability analysis of a two-dimensional cavitating flow using a closed model of blade surface cavitation is presented here.

A cascade shown in Fig. 6.57 is considered. For simplicity, it is assumed that the downstream conduit length is infinite and no velocity fluctuation is involved. The upstream conduit length is finite L in the x-direction and connected to a space with a constant (static total) pressure at the inlet AB.

Small disturbances with time dependence $e^{i\omega t}$ are assumed, where $\omega = \omega_R + i\omega_I$ is the complex frequency with ω_R being the frequency and ω_I being the damping rate.

The velocity disturbance is represented by a source distribution on the cavity region $q(s_1)$, vortex distributions $\gamma_1(s_1)$ and $\gamma_2(s_2)$ on the blades, and the free vortex distribution $\gamma_1(\xi)$ downstream of the blades shedding from the blades associated

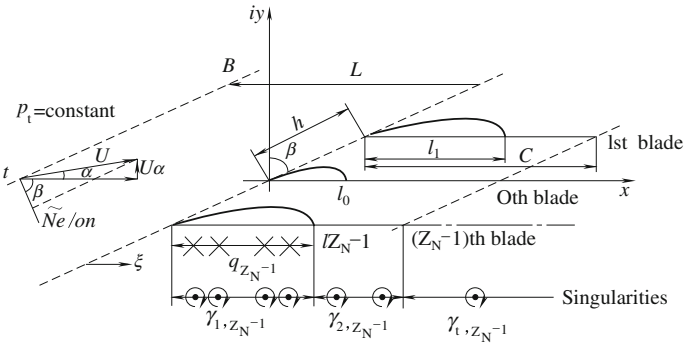

Fig. 6.57 2D stability analysis of cavitating flow through a cascade (Tsujimoto 2006)

with the blade circulation fluctuation. The strength of these singularities and the cavity length are divided into steady and unsteady components, and the velocity is expressed with steady uniform velocity (U, U_α), the steady disturbance (u_s, v_s), and the unsteady disturbance $(\tilde{u}, \tilde{v})$. It is also assumed that $\alpha \ll 1, |\tilde{u}|, |\tilde{v}| \ll |u_s|, |v_s| \ll U$ and the order small terms of higher are neglected.

The boundary conditions are:

1. The pressure on the cavity should be vapor pressure.
2. The normal velocity on the wetted blade surface should vanish.
3. The cavity should close at the (moving) cavity trailing edge (i.e. the closed cavity model).
4. The pressure difference across the blades should vanish at the blade trailing edge (Kutta's condition).
5. Total pressure along AB is assumed to be constant and the downstream velocity fluctuation to be zero.

After designating the strength of singularity distributions at discrete points on the coordinates fixed to fluctuating cavity is set as unknowns, they can be separated into steady and unsteady components. The use of the steady boundary conditions result in a set of non-homogeneous linear equations that show the steady cavity length l_s (normalized by blade spacing h) is a function of $\sigma/2\alpha$. On the other hand, the unsteady component of the boundary conditions would make a set of homogeneous linear equations. For non-trivial solutions, the determinant of the coefficient matrix should be zero. Since the coefficient matrix is a function of the steady cavity length and the complex frequency, the complex frequency $\omega = \omega_R + \mathrm{i}\omega_I$ can be determined from this relation as a function of the steady cavity length h_s/l, or equivalently of $\sigma/2\alpha$. The frequency ω_R and the damping rate ω_I, as well as possible modes of instability, depend only on the steady cavity length h_s/l, or equivalently on $\sigma/2\alpha$, for given geometry and flow conditions. Results of this stability analysis are referred to Tsujimoto (2006). The following remarks could be drawn:

One-dimensional stability analysis states that the onset condition of cavitation surge and rotating cavitation can be represented by $M > 2(1 + \sigma_1)\phi K$ and is independent of the pressure rise performance of the impeller. It implies that cavitation instabilities may occur at the design flow coefficient. The frequency of cavitation surge is proportional to rotational frequency of the rotor. Rotating cavitation has a mode that rotates faster than impeller rotation.

The two-dimensional cavitating flow analysis on a closed cavity model exhibits that cavitation instability depends on the steady cavity length, l_s/h or equivalently on $\sigma/2\alpha$. Various modes of cavitation instabilities start to form when the steady cavity length becomes larger than 65 % of the blade spacing, owing to the interaction of local flow near the cavity closure with the leading edge of the adjacent blade. Apart from alternate blade cavitation, cavitation surge, and rotating cavitation, and various higher order modes are predicted.

Although real inducer flows are far more complicated with three-dimensional cavities such as tip leakage and backflow cavitation, the two-dimensional flow stability analysis predicts cavitation instabilities surprisingly well if applied at the blade tip. However, in real engineering, the problem is to identify whether or not the predicted modes actually would occur for certain geometry. To fulfill this requirement, one needs to incorporate the effects of 3D cavitation in the stability analysis.

Another instability is rotating choke caused by the positive slope of the performance owing to the blockage effect of cavitation. It could be predicted with a waked cavity model, for details see (Tsujimoto 2006).

References

Adamczyk, J. J. (2000). Aerodynamic analysis of multistage turbomachinary flows in support of aerodynamic design. *Journal of Turbomachinary, 122*, 189–217.

Alford, J. S. (1965). Protecting turbomachinery from self-exited rotor whirl. *Journal of Engineering for Power, 10*, 333–344.

Angelico, F. M. G., Monaco, A. D., Fanelli, M., & Molinaro, P. A. (1994). Mechanical device for damping pressure vibrations in a hydroelectric power plant: A theoretical study through the transfer matrix method. *Proceedings of the 17th IAHR Symposium on Hydraulic Machinery and Systems*, pp. 1221–1232.

Arndt, N., Acosta, A. J., Brennen, C. E., & Caughey, T. K. (1989). Rotor stator interaction in a diffuser pump. *ASME Journal of Turbomachinery, 111*, 213–221.

Arndt, N., Acosta, A. J., Brennen, C. E., & Caughey, T. K. (1990). Experimental investigation of rotor-stator interaction in a centrifugal pump with several vaned diffusers. *ASME Journal of Turbomachinery, 112*, 98–108.

Ausoni, Ph., Farhat, M., Bouziat, Y. A., Kueny, J.L., & Avellan, F. (2006). Von Karman vortex shedding in the wake of 2 hydrofoil: Measurement and numerical simulation. *Proceedings of IAHR International Meeting of WG on Cavitation and Dynamic Problems in Hydraulic Machinery and Systems*, Barcelona, C 30.

Benjamin, T. J. (1962). Theory of the vortex breakdown phenomenon. *Journal of Fluid Mechanics, 14*, 593–629.

Bently, D.E., & Muszyńska, A. (1985). Perturbation study of a rotor/bearing system: Identification of the Oil Whirl and Whip Resonances. *Proceedings the 10th ASME Design Engineering Division Conference on Mechanical Vibration and Noise*, Cincinnati, 85-DET-142.

Biela, V., & Beltran, H. (1998). Draft tube fins. *Proceedings of the 19th IAHR Symposium on Hydraulic Machinery and Systems* (pp. 454–461), Singapore.

Blanco, E., Parrondo, J., & Barrio, R. (2006). Fluid-dynamic radial forces at the blade-passing reference in a centrifugal pump with different impeller diameters. *Proceedings IAHR International Meeting of WG on Cavitation and Dynamic Problems in Hydraulic Machinery and Systems*, Barcelona.

Blommaert, G. (2000). Etude du comportement dynamique des turbines Francis: controle actif de leur stabilit′e de fonctionnement. *E′cole polytechnique Fe′de′rale de Lausanne* (Paper No. 2222).

Blommaert, G., Pr′enat, J.-E., Avellan, F., & Boyer, A. (1999). Active control of Francis turbine operation stability. *Proceedings of the 3rd ASME/JSME Joint Fluids Engineering Conference*, San Francisco.

Bolleter, U. (1988). Blade passage tones of centrifugal pump. *Vibrations, 4*(3), 8–13.

Brennen, C. E. (1982). Bubbly flow model for the dynamic characteristics of cavitating pumps. *Journal of Fluid Mechanics, 89*, 223–240.

Brennen, C. E. (1994). *Hydrodynamics of pumps*. London: Oxford University Press.

Brennen, C. E., & Acosta, A. J. (1976). The dynamic transfer function for a cavitating inducer. *ASME Journal of Fluids Engineering, 98*, 182–191.

Chamieh, D. S., Acosta, A. J., Brennen, C. E., & Caughey, T. K. (1985). Experimental measurements of hydrodynamic radial forces and stiffness matrices for a centrifugal pump-impeller. *ASME Journal of Fluids Engineering, 107*, 307–315.

Chen, Y. N. (1961). Water pressure vibrations in the volute casings of storage pumps. Sulzer Technical Review, Research Number, pp. 21–34.

Chen, T. (2012). First step of verification of Li's hypothesis: Identification of a new vortex structure induced by Guide-Plate in three gorges turbines, PhD thesis, Warrick University, UK

Chen, T. & Li, S. C. (2011). Numerical investigation of guide-plate induced pressure fluctuations on the guide vanes of the Three Gorges turbine, ASME Journal of Fluids Engineering, 133(6)

Delbende, I., Chomaz, J. M., & Huerre, P. (1998). Absolute/convective instability in the Batchelor vortex: a numerical study of the linear impulse response. *Journal of Fluid Mechanics, 355*, 229–254.

Deriaz, P. (1960). A contribution to the understanding of flow in draft tubes of francis turbines. *IAHR Hydraulic Machinery and Equipment Symposium*, Nice, France, Sept. 1960

Dong, R., Chu, S., and Katz, J. (1997). Effect of modification to tongue and impeller geometry on unsteady flow, pressure fluctuations, and noise in a centrifugal pump. *Journal of Turbomachinery 119*: 506–515

Dörfler, P. (1984). On the phase role of phase resonance in vibrations caused by blade passage in radial hydraulic turbomachines, *Proceedings 12th IAHR Symposium* (pp. 227–241), Stirling.

Dring, R. P., Joslyn, H. D., Hardin, L. W., & Wagner, J. H. (1982). Turbine rotor-stator interactions. *Journal of Engineering for Power, 104*, 729–742.

Dussourd, J. L. (1968). An investigation of pulsations in the boiler feed system of a central power station. *ASME Journal of Basic Engineering, 90*, 607–619.

Egusquiza, E., Mateos, B., & Escaler, X. (2002). Analysis of runner stator interactions in operating pump-turbines. *Proceedings of the 21st IAHR Symposium on Hydraulic Machinery and Systems*, Lausanne.

Emmons, H. W., Kronauer, R. E., and Rockett, J. A. (1959). A survey of stall propagation—experiment and theory. Trans ASME, *Journal. Basic Engineering*, 1959, 81, 409–416.

Fanelli, M A. (1989). The vortex rope in the draft tube of Francis turbines operating at partial load. *Journal of Hydraulic Research,* 27(6):83–88.

Gagnon, J.-M., Ciocan, G.D. & Deschenese, C. (2008). Numerical and experimental investigation of rotor state interaction in an axial turbine: Numerical interface assessment. *Proceedings of ASME FEDSM 2008,* Jacksonville, FEDSM2008-55183.

Giesing, J. P. (1968). Nonlinear two-dimensional unsteady potential flow with life. *Journal of Aircraft, 5*(2), 135–143.

Gongwer, C.A. (1952). A Study of vanes singing in the water, Transaction of ASME, 74

González, J., Fernandez, J., Blanco, E., & Santolaria, C. (2002). Numerical simulation of the dynamic effects due to impeller-volute interaction in a centrifugal pump. *Transaction of ASME Journal of Fluids Engineering, 124*, 348–355.

González, J., Parrondo, J. L., Santolaria, C., & Blanco, E. (2006). Steady and unstead radial forces for a centrifugal pump with tongue gap variation. *ASME Journal of Fluids Engineering, 128*, 454–462.

Grein, H. (1980). Vibration phenomena in Francis turbines: Their causes and prevention. In *Proceedings of the 10th IAHR Symposium on Hydraulic Machinery and Systems* (pp. 527–539), Tokyo.

Guleren, K.M., & Pinarbasi, A. (2004). Numerical simulation of the stalled flow within a vaned centrifugal pump, Proc Instn Mech. Engrs, *Journal. Mechanical Engineering Science*, 218, Part C, 425–435, ISBN 09544062

Haban, V., Koutnik, J., & Pochyly, F.(2002). 1-D Mathematical model of high-frequency pressure vibrations induced by RSI including an influence of fluid second viscosity. *Proceedings 21st IAHR Symposium*, (pp. 735–740), Lausanne.

Heskestad, G., & Olberts, D. R. (1960). Influence of trailing-edge geometry on hydraulic turbine blade vibration resulting from vortex excitation. *Transactions of the ASME Journal of Engineering for Power, 82A*, 103–110.

Jacob, T., & Prenat, J.E. (1996). Francis turbine surge: Discussion and data base. *Proceedings* of *the 18th IAHR Symposium* (pp. 855–864) Valencia.

Keller, M., & Sallaberger, M. (2006). Modern hydraulic design of pump turbines. *Proceedings of the International Seminar on Hydropower Plants*, Vienna.

Koutnik, J., Krü1ge, K., Pochyly, F., Rudolf, P., & Haban, V. (2006). On cavitation vortex rope form stability during Francis turbine part load operation. *Proceedings IAHR International Meeting of WG on Cavitation and Dynamic Problems in Hydraulic Machinery and Systems*, Barcelona.

Krause, N., Zähringer, K. and Pap, E. (2005). Time-resolved particle imaging velocimetry for the investigation of rotating stall in a radial pump. *Exp Fluids*, *39*, 192–201

KSB (1975). Centrifugal pump lexicon, publisher: author, published by the (1975)

Li, S. C. (2001). *Cavitation of hydraulic machinery*. London: ICP. ISBN 1-86094-257-1.

Li, S. C. (2006, 27–29 October). Challenge to modern turbine technology: analysis of damage to guide vane surface of three Gorges turbine, invited plenary speech. *Proceeding 1st International Conference on Hydropower technology of Key equipment*, Beijing.

Li, S. C. (2008 October). A new cavitation (damage) identified from three Gorges turbines. *Proceedings IAHR 24th Symposium on hydraulic machinery of systems* (pp. 27–31), Brazil.

Li, S. C., Zhang, Y. J., & Hammitt, F. G. (1983), Investigation of low-frequency pressure fluctuation associated with Venturi flow, *Reprot No.UMICH O14571-64-I*. University of Michigan, Ann Arbor, USA.

Li, S. C., Zhang, Y. J., & Hammitt, F. G. (1986). Characteristics of cavitation bubble collapse pulses, associated pressure fluctuations and flow noise. *Journal of Hydraulic Research, 24*(2), 109–122.

Li, S. C., Zuo, Z. G., Liu, S. H., Wu, Y. L., & Li, S. (2008). Cavitation resonance. *ASME Journal of Fluids Engineering, 130*(3), 031302.

Lipej, A., Jošt, D., Mežnar, P., & Djelić, V. (2006). Numerical analysis of rotor-stator interaction in a eversible pump-turbine-pump mode. *Proceedings 23rd IAHR Symposium on Hydraulic Machinery and Systems*, Yokohama, No. F-239.

Liu, S. Z., & Ji, X. Y. (2004). 2004. *Hydraulic performance optimization of turbine in three gorges right bank hydropower station, large electric machine in China, 4*, 30–35.

Lockey, K. J., Keller, M., Sick, M., Staehle, M., & Gehrer, A. (2006). Flow induced vibrations at stay vanes: Experience at site and CFD simulation of von Karman vortex shedding. *Proceedings of Hydro 2006*, Porto Carras, pp. 25-28.

Miyagawa, K., Mutaguchi, K., Kanki, H., Iwasaki, Y., Sakamoto, A., Fujiki, S., Terasaki, A. & Furuya, S. (1992). An experimental investigation of fluid exciting force on a high head pump-turbine runner. *Proceedings 4th International Symposium on Transport Phenomena and Dynamics of Rotating Machinery*, B, pp. 133–142.

Morgenroth, M., & Weaver, D. S. (1998). Sound generation by a centrifugal pump at blade passing frequency. *ASME Journal of Turbomachinery, 120*, 736–743.

Murai, H. (1968). Observations of cavitation and flow patterns in an axial flow pump at low flow rates. *Memoirs of the Institute of High Speed Mechanics*, Tohoku University in Japan, 24, No. 246, pp. 315–333.

Muszyńska, A., & Bently, D.E. (1990). Frequency-swept rotating input perturbation techniques and identification of the fluid force models in rotor bearing/seal systems and fluid handling machine. *Journal of Sound and Vibration, 143*(1), 103–124.

Nennemann, B., Vu, T. C., Ausoni, Ph., Farhat, M. J. L., & Avellan, F. (2007). Unsteady CFD prediction of von Karman vortex shedding in hydraulic turbine stay vanes. *Proceedings of Hydro 2007*, Granada.

Nicolet, C., Ruchonnet, N., & Avellan, F. (2006). One-dimensional modeling of rotor-stator interaction in Francis pump-turbine. *Proceeding of ISROMAC-11, ASME: International Symposium on Transport Phenomena and Dynamics of Rotating Machinery*, Honolulu.

Nicolet, C. (2007). Hydroacoustic modelling and numerical simulation of unsteady operation of hydroelectric systems. PhD Thesis (EPFL n°3751, Lausanne, http://library.epfl.ch/theses/?nr=3751)

Nishi, M., Kubota, T., Matsunaga, S., & Senoo, Y. (1980). Study on swirl flow and surge in an elbow type draft tube. *Proceedings 10th Symposium IAHR Section for Hydraulic Machinery Equipment and Cavitation* (pp. 557–568), Tokyo.

Nishi, M., Matsunaga, S., Kubota, T. & Senoo, Y. (1982). Flow regimes in as elbow-type draft tube. *Proceedings of the 11th IAHR Symposium on Hydraulic Machinery and Systems* (pp. 1–13), Amsterdam, paper 38.

Ohura, Y., Fujii, M., Sugimoto, O., Tanaka, H. & Yamagata, I. (1990). Vibration of the powerhouse structure of pumped storage power plant. *Proceedings of 15th IAHR Symposium*, Belgrade, U2.

Parrondo, J. L., González, J., & Fernández, J. (2002). The effect of the operating point the pressure fluctuations at the blade passage frequency in the volute of a centrifugal pump. *ASME Journal of Fluids Engineering, 124*, 401–410.

Pejovic, S. (2002). Troubleshooting of turbine vortex core resonance and air introduction into the draft tube. *Proceedings of the 21st IAHR Symposium on Hydraulic Machinery and Systems* (pp. 511–516), Lausanne.

Rheingans, W. J. (1940) Power swings in hydroelectric power plants. Transactions of the ASME,Vol. 62, No.174, Apr.pp. 171-184.

Roclawski, H., & Hellmann, D.-H. (2006). Rotor-stator-interaction of a radial centrifugal pump stage with minimum stage diameter. *Proceedings of 4th WSEAS International Conference on Fluid Mechanics and Aerodynamics* (pp. 301–308), Elounda.

Ruchonnet, N., Nicolet, C., & Avellan, F. (2006). Hydroacoustic modeling of rotor stator interaction in francis pump-turbine. IAHR Int. Meeting of WG on Cavitation and Dynamic Problems in Hydraulic Machinery and Systems Barcelona, 28-30.

Ruchnnet, N., Nicolet, C., & Avellan, F. (2006, June 28–30). Hydroacoustic modeling of RSI in Francis pump-turbine. *Proceedings IAHR International Meeting of WG on Cavitation and Dynamic Problems in Hydraulic Machinery and Systems,* Barcelona.

Rudolf. P., Habán, V., Pochylý, F., Koutník, J., & Krüger, K. (2006). Model of pressure pulsations in hydraulic turbine draft tube based on linearized Rayleigh-Plesset equation. *Proceedings of IAHR International Meeting of WG on Cavitation and Dynamic Problems in Hydraulic Machinery and Systems*, Barcelona.

Rudolf, P., Haban, V., Pochyly, F., & Koutnik, J. (2007). Collapse of cylindrical cavitating region and conditions for existence of elliptical form of cavitating vortex rope. *Proceedings of 2nd IAHR International Meeting of the Workgroup on Cavitation and Dynamic Problems in Hydraulic Machinery and Systems*, Timisoara, Paper No. 16.

Ruprecht, A., Bauer, C., Gentner, C., & Lein, G. (1999). Parallel computation of stator-rotor interaction in an axial turbine. *ASME PVP Conference, CFD Symposium*, Boston.

Ruprecht, A., Heitele, M., & Helmrich, T. (2000). Numerical simulation of a complete Francis turbine including unsteady rotor/stator interactions. *Proceedings of 20th IAHR Symposium*, Charlotte, North Carolina.

Sano, T., Yoshida, Y., Tsujimoto, Y., Nakamura, Y. and Matsushima, T. (2002). Numerical study of rotating stall in a pump vaned diffuser. *Trans. ASME*, *124*, 363–370.

Sotnikov, A. A., & Pylev, I. M. (2001). Experience at Leningrad metallurgical plant with water turbines for use over wide ranges in head and load. *Power Technology and Engineering, 35*(2), 73–77.

Stepanoff, A. J. (1957). *Centrifugal and axial flow pumps*. New York: Wiley.

Susan-Resiga, R., & Muntean, S. (2008). *Decelerated swirling flow control in the discharge cone of Francis turbines. Fluid Machinery & Fluid Mechanics* (pp 89–96), Berlin: Springer.

Susan-Resiga, R., Ciocan, G. D., & Avellan, F. (2004). Swirling flow downstream a francis turbine runner, The 6th International Conference on Hydraulic Machinery and Hydrodynamics, Timisoara: Romania, October 21–22,

Susan-Resiga, R., Ciocan, G. D., Anton, I., & Avellan, F. (2006a). Analysis of the swirling flow downstream a Francis turbine runner. *Journal of Fluids Engineering, 128*, 177–189.

Susan-Resiga, R., Vu, T. C., Muntean, S., Ciocan, G. D., & Nennemann, B. (2006b, October). Jet control of the draft tube vortex rope in Francis turbines at partial discharge. *Proceedings of the 23rd IAHR Symposium on Hydraulic Machinery and Systems,* Yokohama, paper 192.

Susan-Resiga, R., Muntean, S., Bosioc, A., Stuparu, A., Milos, T., Baya, A., et al. (2007). Swirling flow apparatus and test rig for flow control in hydraulic turbines. *Scientific Bulletin of the Plitehnica University of Timisoara, Transactions on Mechanics, 52*(66), 203–216.

Tanaka, H. (1990). Vibration and dynamic stress of runners of very high head reversible pump-turbines. *Proceedings of 15th IAHR, Symposium*, Belgrade.

Tao, X. M., & Liu, G. L. (2004). Hydarulic satability problems of Francis turbine. *Large Hydraulic machinery in China, 4*, 40–45.

Torbjørn, K. Nielsen, T. K. & Antonsen, Ø. (2001). CFD simulation of von Karman vortex shedding. IAHR Work Group on The Behaviour of Hydraulic Machinery under Steady Oscillatory Conditions, Trondheim,Norway, June 26-28, 2001

Tsujimoto, Y. (2006). Cavitation instabilities in turbo-pump inducers for rocket engines. In *Proceedings of Cavitation: Turbo-machinery & Medical Applications*, Warwick University.

Tsujimoto, Y., Yoshida, Y., Maekawa, Y., Watanabe, S., & Hashimoto, T. (1997). Observations of oscillating cavitation of an inducer. *ASME Journal of Fluids Engineering, 119*, 775–781.

Wang, Q. L. (2005). *Vibration study on the main components of high head turbine*. Dissertation for the Degree of Engineering, Harbin Engineering University in China.

Wang, X. M., &, Nishi, M. (1996). Swirling flow with helical vortex core in draft tube predicted by a vortex method. *Proceedings of 18th IAHR Symposium on Hydraulic Machinery* (pp. 965–974), Kluwer Academic Publishers.

Wei, X. D. (1989). Blade vibration caused by Karman vortex shedding. *Journal of hydraulic Engineering in China, 1989*(4), 77–85.

Wu, J. Z., Xiong, A. K., & Yang, Y. T. (2005). Axial stretching and vortex definition. *Physics Fluids, 17*, 38–108.

Wu, J. Z., Ma, H. Y., & Zhou, M. D. (2006). *Vorticity and vortex dynamics*. Berlin: Springer.

Yoshida, Y., Murakami, Y., Tsurusaki, T., & Tsujimoto, Y. (1991). Rotating stalls in centrifugal impeller/vaned diffuser systems, *Proceedings of First ASME/JSME Joint Fluids Engineering Conference* FED-107, pp. 125–130.

Yu, Y. Q. (2006). Relation between the vortex and pressure fluctuation in draft tube of hydraulic turbine. M.S. Thesis of Engineering, *Xi'an University of Science and Technology in China.*

Zhang, R. K., Cai, Q. D., Wu, J. Z., Wu, Y. L., Liu, S. H., & Zhang, J. (2005). The physical origin of severe low-frequency pressure fluctuations in giant Francis turbines. *Modern Physics Letter, B19*(28–29), 99–102.

Zhang, R. K., Mao, F., Wu, J. Z., Chen, S. Y., Wu, Y. L. & Liu, S. H. (2007). Analysis and control of part-load unsteady flow in Francis turbine's draft tube. *Proceedings of ASME Turbo Expo 2007*, Montreal, Paper GT2007-27440.

Zhang, R. K., Mao, F., Wu, J. Z., Chen, S. Y., Wu, Y. L. & Liu, S. H. (2009). Characteristics and control of the draft-tube flow in part-load Francis turbine, *Journals of Fluids Engineering, 131*, 021101-1-13.

Zhu, Y. (2006). Stability study of giant Francis turbines, M.S. Thesis, *Tsinghua University in China.*

Zobeiri, A., Kueny, J. L., Farhat, M. & Avellan F. (2006). Pump-turbine rotor-stator interactions in generating mode: pressure fluctuation in distributor channel. *Proceedings of 23rd IAHR Symposium on Hydraulic Machinery and Systems*, Yokohama, Paper no. 235.

Part III
Hydrodynamic and Structural Analysis

Chapter 7
Prediction of Pressure Fluctuation by Turbulent Flow Analysis

Flows in pumps or hydraulic turbines are unsteady due to the system rotation, flow instabilities and mutual interactions between rotating and stationary parts. Flow instabilities are mostly viscous phenomena such as boundary layer transition and vortex shedding that produce small amplitude pressure fluctuations at relatively low frequencies. The flow caused unsteadiness is important because it leads to fluctuation of power output and affects efficiency. Interaction between runner blades and guide vanes produces pressure fluctuations of relatively high frequency and large amplitude. This phenomenon is more closely related to compressibility than viscosity. It is important because it may cause structural vibration and noise.

In the field of hydraulic machinery, Computational Fluid Dynamics (CFD) is widely used today in research and development as well as in daily design. Since many problems in turbomachinery arise from unsteady flows, unsteady flow analyzes play an essential role in gaining information about solutions to the problems.

Due to the interactions between stationary guide vanes and rotating runners, the flow in turbo-machines is unsteady and highly turbulent. Investigation of these phenomena requires transient simulations and special numerical treatments to the interface between the components. The flow modeling of the machine is complicated because of the fact that the stator and runner have different numbers of blades. This difference restricts the use of geometrical periodicity with simulations so as to the entire region of stator and runner has to be simulated. It requires such an enormous computational effort in terms of memory and CPU time that only modern high performance computers can do the job.

In this chapter, simulation of unsteady turbulent flows through the entire turbine or pump, that is, from the inlet of the machine to the outlet as a whole calculation domain, will be considered in prediction of the pressure fluctuations in hydraulic machinery.

Y. Wu et al., *Vibration of Hydraulic Machinery*,
Mechanisms and Machine Science 11, DOI: 10.1007/978-94-007-6422-4_7,

7.1 Principle of Prediction for Pressure Fluctuation

In hydraulic machinery, many problems arise from dynamical effects such as vibrations. Dynamic forces cannot be obtained from steady state analysis. Measuring dynamic forces requires complicated instruments and skills. Numerical simulation has thus become a desirable method. For this purpose an unsteady flow calculation including the stator-rotor interaction as mentioned before is essential. For demonstration, in this chapter, a turbine consisting of spiral case, stay vanes, guide vanes, runner, and draft tube will be considered.

7.1.1 The Multiple Reference Frame Model

In contrast of flows in a stationary (or inertial) reference frame, moving parts (such as rotating blades, impellers, and similar types of moving surfaces) in hydraulic machinery have made flow problems unsteady most of the time when viewed from a stationary frame. While a reference frame moving with the moving (rotating) part will make the flow around the moving part a steady problem.

However, the moving (non-inertial reference system) equations of motion need to be modified to incorporate the additional acceleration terms to the transformation from stationary to moving reference frame. By solving these equations in a steady-state manner, one can model the flow around the moving parts. For simple problems, it may be possible to refer the entire computational domain to a single moving reference frame, known as the single reference frame (SRF) approach.

For more complex geometries, one must split up the problem into multiple cells zones, with well-defined interfaces between the zones. The manner in which the interfaces are treated leads to two approximates, steady state modeling method-including the multiple reference frame (MRF) approach and the mixing plane approach, and the dynamic approach.

If unsteady interaction between stationary and moving parts is important, one can employ the Sliding Mesh approach to capture transient behavior of the flow.

7.1.1.1 Flow in a Rotating Reference Frame

One can run an unsteady simulation in a moving reference frame at constant rotational speed in hydraulic machinery. Consider a coordinate system (x, y, z) which is rotating steadily at angular velocity $\{\boldsymbol{\Omega}\}$ relative to a stationary (inertial) reference frame (x, y, z) illustrated in Fig. 7.1.

The axis of rotation is defined with a unit direction vector $\{\boldsymbol{a}\}$ such that $\{\boldsymbol{\Omega}\} = \Omega\{\boldsymbol{a}\}$. The computational domain is defined with respect to rotating frame such that the position of an arbitrary point in the domain is determined with a position vector $\{\boldsymbol{r}\}$ ($\overline{\boldsymbol{r}}$ in Fig. 7.1) from the origin of the rotating frame. The fluid

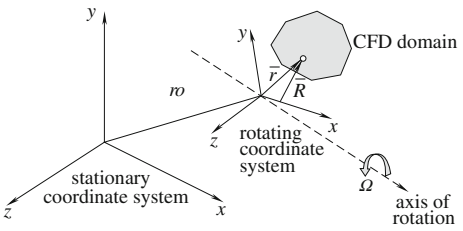

Fig. 7.1 Stationary and rotating reference frame

velocities can be transformed from stationary frame to rotating frame using the following relation:

$$\{\boldsymbol{v}_r\} = \{\boldsymbol{v}\} - \{\boldsymbol{u}_r\} \tag{7.1}$$

where $\{\boldsymbol{v}_r\}$ is the relative velocity, $\{\boldsymbol{v}\}$ is the absolute velocity, and $\{\boldsymbol{u}_r\}$ is the "whirl" velocity,

$$\{\boldsymbol{u}_r\} = \{\Omega\} \times \{\boldsymbol{r}\}. \tag{7.2}$$

For the relative velocity formulation, the governing equations of fluid flow in a steadily rotating frame can be written as follows:

1. Conservation of mass:

$$\frac{\partial \rho}{\partial t} + \nabla \cdot (\rho\{\boldsymbol{v}_r\}) = 0 \tag{7.3}$$

2. Conservation of momentum:

$$\begin{aligned} \frac{\partial \rho\{\boldsymbol{v}_r\}}{\partial t} &+ \nabla \cdot (\rho\{\boldsymbol{v}_r\}\{\boldsymbol{v}_r\}) + \rho(2\{\Omega\} \times \{\boldsymbol{v}_r\} + \{\Omega\} \times \{\Omega\} \times \{\boldsymbol{r}\}) \\ &= -\{\nabla p\} + \nabla \cdot [\boldsymbol{\tau}_r] + \{F\} \end{aligned} \tag{7.4}$$

3. Conservation of energy:

$$\frac{\partial \rho E_r}{\partial t} + \nabla \cdot (\rho\{\boldsymbol{v}_r\} H_r) = + \nabla \cdot \{k \nabla T + [\boldsymbol{\tau}_r] \cdot \{\boldsymbol{v}_r\}\} + S_h. \tag{7.5}$$

The momentum equation above contains two additional acceleration terms: the Coriolis acceleration $2\{\Omega\} \times \{\boldsymbol{v}_r\}$, and the centripetal acceleration $\{\Omega\} \times \{\Omega\} \times \{\boldsymbol{r}\}$. In addition, $[\boldsymbol{\tau}_r]$ is the viscous stress tensor in which relative velocity derivatives are used. $\{\boldsymbol{f}\}$ is body force. The energy equation is written in terms of the relative internal energy (E_r) and the relative total enthalpy (H_r), also known as the rothalpy; k is thermal conductivity; and S_h is thermal source term. These variables are defined as

$$E_r = h - \frac{p}{\rho} + \frac{1}{2}\left(v_r^2 - u_r^2\right) \tag{7.6}$$

$$H_r = E_r + p/\rho. \tag{7.7}$$

For the absolute velocity formulation, the governing equations of fluid flow in a steadily rotating frame can be written as

$$\frac{\partial \rho}{\partial t} + \nabla \cdot (\rho\{\boldsymbol{v}\}) = 0. \tag{7.8}$$

Conservation of momentum:

$$\frac{\partial \rho\{\boldsymbol{v}\}}{\partial t} + \nabla \cdot (\rho\{\boldsymbol{v}_r\}\{\boldsymbol{v}\}) + \rho(\{\Omega\} \times \{\boldsymbol{v}\}) = -\{\nabla p\} + \nabla \cdot [\boldsymbol{\tau}] + \{\boldsymbol{F}\}. \tag{7.9}$$

Conservation of energy:

$$\frac{\partial \rho E}{\partial t} + \nabla \cdot (\rho\{\boldsymbol{v}_r\}H_r + \rho\{\boldsymbol{u}_r\}) = +\nabla \cdot \{k\nabla T + [\boldsymbol{\tau}] \cdot \{\boldsymbol{v}\}\} + S_h. \tag{7.10}$$

7.1.1.2 Flow in Multiple Rotating Reference Frame

Both the MRF and mixing plane approaches are steady-state approximations but differ from each other primarily in their treatment of conditions at interfaces.

The MRF model is perhaps simpler for multiple zones. It is a steady-state approximation where individual cell zones move at different rotational and/or translational speeds. The flow in each moving cell zone is solved in the moving reference frame equations. If the zone is stationary, the stationary equations are used. At interfaces between cell zones, a local reference frame transformation is performed to enable flow variables in one zone to be used to calculate fluxes at the boundary of the adjacent zone.

It should be noted that the MRF approach does not account for relative motion of a moving zone with respect to adjacent zones and the grid remains fixed in computation. It is analogous to the way of freezing the motion of moving parts in a specific position and observing the instantaneous flow field with the rotor in that position. Hence, the MRF is often referred to as the "frozen rotor approach".

Though the MRF approach is clearly an approximation, it can provide a reasonable model of the flow for many applications. For example, it can be used for applications where rotor–stator interaction is relatively weak. In mixing tanks, for example, since the impeller-baffle interactions are relatively weak, large-scale transient effects are not present and the MRF model is applicable.

Another potential use of the MRF model is to compute a flow field which is subsequently used as an initial condition for a transient sliding mesh calculation. This can often eliminate the need for a startup calculation.

7.1.1.3 The MRF Interface Formulation

The MRF formulation applied to the interfaces is subject to the velocity formulation being used. The specific approaches will be discussed below for each case. The interface treatment applies to velocity and velocity gradients, since these vector quantities change in different reference frames. Scalar quantities, such as temperature, pressure, density, and turbulent kinetic energy *etc*., do not require any special treatment, and thus are adopted locally without any change.

1. Interface treatment of relative velocity:

In the MRF model, calculation domain is divided into subdomains, each of which may be rotating and/or translating in the inertial frame. The governing equations in each subdomain are written with respect to that subdomain's reference frame.

At the boundary between two subdomains, the diffusion and other terms in the governing equations in one subdomain require values for the velocities in the adjacent subdomain. The continuity of the absolute velocity is enforced, to provide correct neighbor values of velocity for the subdomain under consideration.

When the relative velocity formulation is used, velocities in each subdomain are computed according to the subdomain motion. Velocities and velocity gradients are converted from a moving reference frame to the absolute inertial frame using Eq. (7.11):

$$\{\boldsymbol{v}\} = \{\boldsymbol{v}_r\} + (\{\Omega\} \times \{\boldsymbol{r}\}) + \{\boldsymbol{v}_t\} \tag{7.11}$$

where $\{\boldsymbol{v}_t\}$ is a translational velocity of interface. The gradient of the absolute velocity vector is

$$\nabla\{\boldsymbol{v}\} = \nabla\{\boldsymbol{v}_r\} + \nabla(\{\Omega\} \times \{\boldsymbol{r}\}). \tag{7.12}$$

Scalar quantities such as density, static pressure, static temperature, and species mass fractions, *etc*., are simply obtained locally from adjacent cells.

2. Interface treatment: Absolute velocity formulation

When the absolute velocity formulation is applied, governing equations in each subdomain are written with respect to its reference frame, but the velocities are stored in the absolute frame. Therefore, no special transformation is needed at the interface between two subdomains. Again, scalar quantities are determined locally from adjacent cells.

7.1.2 The Mixing Plane Model

The mixing plane model provides an alternative to the multiple reference frame and the sliding mesh models for simulating flow through domains with one or more regions in relative motion. The MRF model is applicable when the flow at

boundary between adjacent zones move at different speeds is nearly uniform ("mixed out"). If it is not uniform, the MRF model may not be a physically meaningful solution. Instead, the sliding mesh model may be more appropriate, yet in many situations it is not practical to employ a sliding mesh. For example, in a multistage turbomachine, if the number of blades is different for each blade row, a large number of blade passages are required for maintenance of circumferential periodicity. Moreover, sliding mesh calculations are necessarily unsteady, and thus cost significantly more computation to achieve a final, time-periodic solution. For situations where the sliding mesh model is not feasible, the mixing plane model can be a cost-effective alternative.

For the mixing plane approach, each fluid zone is treated as a steady-state problem. Flow field data from adjacent zones are passed as boundary conditions that are spatially averaged or "mixed" at the mixing plane interface. This mixing removes any unsteadiness that would take place due to circumferential variations in the passage-to-passage flow field, thus yielding a steady-state result. Despite of these simplifications inherent in the mixing plane model, the resulting solutions can provide reasonable approximations of the time-averaged flow field.

Turbomachine stage consists of two flow domains: the rotor domain, which is rotating at a prescribed angular velocity, and the stator domain, which is stationary. In numerical simulation, each domain will be represented by a separate mesh. The flow information between these domains will be coupled at the mixing plane interface using the mixing plane model.

The essential idea behind the mixing plane concept is as follows: Each fluid zone is solved as a steady-state problem. At some prescribed iteration interval, flow data at the mixing plane interface are averaged in circumferential direction on both the stator outlet and the rotor inlet boundaries. By performing circumferential averages at specified radial or axial stations, one can define "profiles" of flow properties. These profiles, which will be functions of either axial or the radial coordinate, depending on the orientation of the mixing plane, are then used to update boundary conditions along the two zones of the mixing plane interface.

Passing profiles in the manner described above is based on the assumption that specific type of boundary conditions has been defined at the mixing plane interface. The coupling of an upstream outlet boundary zone with a downstream inlet boundary zone is called a "mixing plane pair".

The core of mixing plane algorithm can be described as follows:

1. Update the flow field solutions in the stator and rotor domains.
2. Average flow properties at the stator exit and rotor inlet boundaries to get profiles for use in updating boundary conditions.
3. Pass the profiles to the boundary condition inputs required for the stator exit and rotor inlet.
4. Repeat steps 1–3 until convergence.

The algorithm described above does not rigorously conserve mass flow across the mixing plane if it is represented by a pressure inlet and pressure outlet mixing

plane pair. If one uses a mass flow inlet and pressure outlet pair instead, mass conservation across the mixing plane would be fulfilled. The basic technique consists of computing mass flow rate across the upstream zone (pressure outlet) and adjusting the mass flux profile applied at the mass flow inlet so that the downstream mass flow matches the upstream mass flow. This adjustment is performed at every iteration to ensure rigorous conservation of mass flow throughout calculation.

Since mass flow is fixed in this case, there will be a jump in total pressure across the mixing plane. The magnitude of this jump is usually small compared with total pressure variations elsewhere in the flow field.

For applications such as torque converters, where sum of the torques acting on components should be zero, swirl conservation across the mixing plane is essential. Conservation of swirl is important because otherwise sources or sinks of tangential momentum will be present at the mixing plane interface.

Consider a control volume containing a stationary or rotating component. From the moment of momentum equation in fluid mechanics, it can be shown that for steady flow,

$$T = \iint_S r v_\theta \rho \{\boldsymbol{v}\} \cdot \{\boldsymbol{n}\} \mathrm{d}S \tag{7.13}$$

where T is torque of the fluid acting on the component, r is radial distance from the axis of rotation, v_θ is the absolute tangential velocity, v is the total absolute velocity, and S is the boundary surface. (The product rv_θ is referred to as swirl.)

For a circumferentially periodic domain with well-defined inlet and outlet boundaries, Eq. (7.13) becomes

$$T = \iint_{outlet} r v_\theta \rho \{\boldsymbol{v}\} \cdot \{\boldsymbol{n}\} \mathrm{d}S + \iint_{inlet} r v_\theta \rho \{\boldsymbol{v}\} \cdot \{\boldsymbol{n}\} \mathrm{d}S \tag{7.14}$$

where inlet and outlet denote the inlet and outlet boundary surfaces.

From Eq. (7.14), in the limit as the thickness shrinks to zero, the torque should vanish.

$$\iint_{outlet} r v_\theta \rho \{\boldsymbol{v}\} \cdot \{\boldsymbol{n}\} \mathrm{d}S = -\iint_{inlet} r v_\theta \rho \{\boldsymbol{v}\} \cdot \{\boldsymbol{n}\} \mathrm{d}S. \tag{7.15}$$

Equation (7.15) provides a rational method of determining the tangential velocity component, so that the swirl integral is satisfied. Interpolating the tangential (and radial) velocity component profiles at the mixing plane does not affect mass conservation because these velocity components are orthogonal to the face-normal velocity used in mass flux computation.

7.1.3 Unsteadiness of Flow Through Hydraulic Machines

The Reynolds-averaged Navier-Stokes equations (RANS) together with turbulence models are used to compute internal flows in hydraulic machines, which is a common practice for steady flow simulations. However, actual flows in hydraulic machinery are unsteady (Ruprecht et al. 1999, 2000). Two major groups of unsteady problems can be distinguished. The first group is flows with an externally forced unsteadiness caused by unsteady boundary conditions or by changing the geometry with time, for example, the rotor-stator interactions in hydraulic machines. The second group is flows with self excited unsteadiness, which are, say, turbulent motion, vortex shedding (Karman vortex street) or unsteady vortex behavior (*e.g.* vortex rope in a draft tube). Here the unsteadiness is obtained without any change in boundary conditions or of geometry. A combination of both groups could also exist (*e.g.* flow induced vibrations, change of geometry caused by vortex shedding) (Skotak 1999, Ruprecht 2002). For unsteady flows in hydraulic machinery, refer to Chap. 6.

7.1.3.1 Rotor–Stator Interaction Model in Hydraulic Machinery

The following example belongs to the first group where the unsteadiness is forced by moving geometries. In numerical simulation, there are several ways to model the interaction of stationary and rotating parts.

1. Simple 'top–down' computation,
2. Multiple reference frame computation, that is, the frozen rotor computation,
3. Mixing plane approach,
4. Transient computation.

The simplest way to compute the flow in a hydraulic machine is to solve each component in its own frame of reference and take the results of the upstream component as the inlet boundary condition of next component. However, there is no interaction between the components and the results depend on the selection of inlet boundary conditions greatly.

A simple method is a stage averaging method, where at the interface between stationary and rotating frames of reference the flow variables are averaged in the circumferential direction prior to their exchange. The advantage of this approach is that only one blade passage of the stator and rotor needs to be modeled regardless of the actual pitch, which leads to a huge reduction of memory demand, but neglects all transient interaction effects.

A more sophisticated method is the so-called MRF, that is, the frozen rotor approach. In contrast to the above stage averaging method, this method involves averaging the entire domains of the stator and rotor, but remaining in a fixed relative position ("frozen") throughout the simulation. The stator is calculated in stationary frame and the runner in rotating frame. At the interface the flow variables are

transformed into the corresponding frame of reference. As a result, the approach accounts partially for interactions across frame boundaries, yet transient effects remain unresolved. The main advantage of the frozen rotor method compared with a true transient simulation is the reduction of computing time.

7.1.3.2 Sliding Mesh Model and Dynamic Mesh Model

For sliding meshes, the relative motion of stationary and rotating components in a rotating machine give rise to unsteady interactions. In turbomachinery, these interactions are generally classified as follows: potential interactions, wake interactions, and shock interactions for transonic/supersonic flow.

The multiple reference frame (MRF) and mixing plane (MP) models are applied in steady state cases without consideration of unsteady interactions, whereas the sliding mesh model can explain unsteady interactions by considering the relative motion of stationary and rotating components, which is viable for unsteady flow computation in hydraulic machinery.

Another model for unsteady flow computation is the dynamic mesh model (moving mesh model). It is used when boundaries move rigidly or rotate with respect to each other, and when boundaries deform or deflect. Examples are: a piston moving with respect to a cylinder in positive displacement pumps, an angle moving guide vanes in hydraulic turbines around their pivots in prior ascertained regulation at their transient processes, and a turbine blade deforming owing to pressure pulsation in fluid and solid interactions of hydraulic turbine.

1. Sliding mesh model

When a time-accurate solution for rotor–stator interaction is required, the sliding mesh model must be used to compute the unsteady flow field because it is the most accurate method to simulate flows in multiple moving reference frames. Most of the time, the unsteady solution is time-periodic, that is, the unsteady solution repeats with a period related to the speeds of the moving domains.

In the sliding mesh technique two or more cell zones are used. Each cell zone is bounded by at least one “interface zone” where it meets the opposing cell zone. The interface zones of adjacent cell zones are associated with one another to form a “grid interface”. The two cell zones will move relative to each other along the grid interface. The grid interface must be positioned in a way that it has fluid cells on both sides. For example, the grid interface must lie in fluid region between rotor and stator; it cannot be on the edge of any part of the rotor or stator. During the calculation, the cell zones slide relative to one another along the grid interface in discrete steps. The sliding mesh model allows adjacent grids to slide relative to one another so that the grid faces do not need to be aligned on grid interface. This situation requires a computation of the flux across two non-conformal interface zones of each grid interface. To calculate the interface flux, the intersection between the interface zones should be determined at each new time step.

2. Dynamic mesh model

The dynamic mesh model can be employed to model flows where the domain shape changes with time due to motion on its boundaries. The dynamic mesh model can also be used in steady-state applications where it is beneficial to move the mesh in the steady state solver. The motion can be prescribed or unperceived where the subsequent motion is determined based on solution at the current time. To construct the dynamic mesh model, one needs to provide a starting volume mesh and description of the motion within any moving zones in the model using either boundary profiles or user-defined functions (UDFs).

For dynamic meshes, the integral form of the conservation equation for a general scalar, ϕ, on an arbitrary control volume, whose boundary is moving can be written as

$$\begin{aligned} &\frac{\mathrm{d}}{\mathrm{d}t}\iiint_V \rho\phi \mathrm{d}V + \iint_{\partial V} \rho\phi(\{\boldsymbol{v}\}-\{\boldsymbol{v}_g\})\cdot\{\boldsymbol{n}\}\mathrm{d}A \\ &= \iint_{\partial V} \Gamma\nabla\phi\cdot\{\boldsymbol{n}\}\mathrm{d}A + \iiint_V S_\phi \mathrm{d}V \end{aligned} \tag{7.16}$$

where ρ is the fluid density; $\{\boldsymbol{v}\}$ is the flow velocity vector; $\{\boldsymbol{v}_g\}$ is the grid velocity of the moving mesh; Γ is the diffusion coefficient; S_ϕ is the source term of ϕ. Here ∂V is used to represent the boundary of the control volume V.

The time derivative term in Eq. (7.16) can be written in a first order backward difference formula, as

$$\frac{\mathrm{d}}{\mathrm{d}t}\iiint_V \rho\phi \mathrm{d}V = \frac{(\rho\phi V)^{n+1}-(\rho\phi V)^n}{\Delta t} \tag{7.17}$$

where n and $n+1$ denote the respective quantity at the current and next time level. The $(n+1)$th time level volume V^{n+1} is computed from

$$V^{n+1} = V^n + \frac{\mathrm{d}V}{\mathrm{d}t}\Delta t \tag{7.18}$$

where $\mathrm{d}V/\mathrm{d}t$ is the volume time derivative of the control volume. In order to satisfy the grid conservation law, the volume time derivative of the control volume is computed from

$$\frac{\mathrm{d}V}{\mathrm{d}t} = \iint_{\partial V} \{\boldsymbol{v}_g\}\cdot\{\boldsymbol{n}\}\mathrm{d}A = \sum_j^{n_f} \{\boldsymbol{v}_{gj}\}\cdot\{\boldsymbol{n}_j\}A_j \tag{7.19}$$

where n_j is the number of faces on the control volume and A_j is the j face area. The dot product $\{\boldsymbol{v}_{gj}\}\cdot\{\boldsymbol{n}_j\}A_j$ on each control volume face is calculated from

$$\{\boldsymbol{v}_{gj}\}\cdot\{\boldsymbol{n}_j\}A_j = \frac{\partial V_j}{\Delta t} \tag{7.20}$$

where ∂V_j is the volume swept out by control volume face j over the time step Δt.

In the case of sliding mesh, the motion of moving zones is tracked relative to the stationary frame. Therefore, no moving reference frames are attached to computational domain, simplifying the flux transfers across the interfaces. In the sliding mesh formulation, the control volume remains constant, therefore from Eq. (7.18), $\mathrm{d}V/\mathrm{d}t = 0$ and $V^{n+1} = V^n$. Equation (7.17) can now be expressed as

$$\frac{\mathrm{d}}{\mathrm{d}t}\iiint_V \rho\phi \mathrm{d}V = \frac{\left[(\rho\phi)^{n+1} - (\rho\phi)^n\right]V}{\Delta t}. \tag{7.21}$$

7.2 Basic Equations of Unsteady Flow Through Hydraulic Machinery and Turbulence Models

The governing equations of unsteady flow, which are introduced in the present section, are the time-dependent Reynolds-averaged Navier–Stokes (RANS) equations for RANS simulation, and the Large-eddy equations through the filtering function treatment to the original Navier-Stokes (N-S) equations for the solutions of large-eddy simulation (LES). However, in order to close the both groups of equations of the turbulent flow, the turbulence models are necessary, for example, the eddy viscosity model (EVM), the non-linear eddy viscosity model (NLEVM) and the differential stress model (DSM) for closing RANS equations, and the sub-grid-scale model for LES.

7.2.1 Basic Turbulent Equations of Unsteady Flow

In fluid mechanics, the three basic equations describing water flows are the mass continuity equation, the momentum equations (N-S equations), and the energy equation. Since most of flows dealt with are turbulent, it is essential to model turbulent flows accurately based on the Navier-Stokes equations. The four major types of turbulence methodologies are Direct Numerical Simulation (DNS), Large Eddy Simulation (LES), Reynolds-Averaged N-S (RANS) Solution, and Detached Eddy Simulation (DES).

7.2.1.1 Reynolds Averaged Navier-Stokes Equations

The Reynolds-averaged N-S (RANS) equations are time-averaged equations of motion for fluid flow. They are primarily used for turbulent flows. These equations with approximations based on knowledge of the properties of flow turbulence are

able to give approximately averaged solutions to the N-S equations. For an incompressible flow of Newtonian fluid, these equations can be written as

$$\rho \frac{\partial \overline{v}_i}{\partial t} + \rho \bar{v}_j \frac{\partial \overline{v}_i}{\partial x_j} = \rho f_i - \frac{\partial \bar{p}}{\partial x_i} + \frac{\partial}{\partial x_j}\left(\mu \frac{\partial \overline{v}_i}{\partial x_j}\right) - \rho \frac{\partial}{\partial x_j}\left(\overline{v'_i v'_j}\right) \tag{7.22}$$

The left hand side represents the change in mean momentum of the fluid element due to unsteadiness with time in the mean flow and the convection by the mean flow. This change is balanced by mean body force, isotropic stress from mean pressure field, viscous stresses, and apparent stress $-\rho\overline{v'_i v'_j}$ due to the turbulent fluctuating velocity field, generally referred to as Reynolds stresses.

The mass conservation equations of this turbulent flow are

$$\frac{\partial \overline{v}_i}{\partial x_i} = 0, \text{ and } \frac{\partial v'_i}{\partial x_i} = 0 \tag{7.23}$$

7.2.1.2 Arbitrary Lagrangian-Eulerian Method (ALE)

Two different coordinate systems for the description of fluid motion are the Eulerian system describing fluid motion at fixed locations and the Lagrangian system following fluid particles. Accordingly, the Eulerian description views velocities and other properties of fluid as functions of both time and fixed space coordinates. The Lagrangian description considers the positions of fluid particles and their other properties to be functions of time and their permanent identifications, such as their initial positions or any set of material functions of fluid particles.

Analytically, both coordinate systems are capable of producing exact solutions of fluid flow, including discontinuous flow. They are regarded as equivalent to each other, except for the fact that the Lagrangian system gives more information such as each fluid particle's history.

From a numerical point of view, however, they are not equivalent. Computational cells in Eulerian coordinates are fixed in space while fluid particles move across cell interfaces in any direction. It is this convective flux that causes excessive numerical diffusion in numerical solutions. Another disadvantage of the Eulerian coordinates is that prior to flow computation a time-consuming grid generation is needed for boundary conditions on solid boundaries.

Computational cells in Lagrangian coordinates, on the other hand, are fluid particles. Consequently, there is no convective flux across cell interfaces and numerical diffusion is thus minimized. However, the fact that computational cells exactly follow fluid particles can result in severe grid deformation, causing inaccuracy and even breakdown of the computation. To prevent this from happening, the Arbitrary Lagrangian-Eulerian Technique (ALE) is introduced in the following unsteady flow simulation. Hui et al. (1999) extended the above idea to unsteady flow by introducing a new description of fluid motion in which the flow

variables are considered to be functions of time and of some permanent identifications of pseudo-particles which move with an arbitrary velocity.

1. Governing equation at ALE reference coordinates

At first, one defines the material coordinates (Lagrangian description coordinates) as X, the space coordinates (Eulerian description coordinates) as x, and the reference coordinates as χ, which denote coordinates of the grid system in computation. And velocity $\hat{v}$ is the velocity of reference coordinates χ relative to space coordinates x.

Secondly, three different reference coordinates can be selected as follows:

(a) The first one: To determine the velocity of reference coordinates, that is, the velocity of grid system $\hat{v}$ beforehand.
(b) The second one: To give the relation between velocity of fluid flow relative to grid system (reference system) W and fluid flow absolute velocities V at different moments. Then the grid velocity $\hat{v}$ will be obtained.
(c) The mixed method, in which one velocity component can be provided using the first method, and another component using the second one.

The mapped relationship of the three coordinates to corresponding functions can be expressed as

$$R_\chi \times [0,\infty] \to R_x,\ (\chi,t) \to \Phi(\chi,t) = x \tag{7.24}$$

$$R_\chi \times [0,\infty] \to R_X,\ (\chi,t) \to \Psi(\chi,t) = X \tag{7.25}$$

$$f(x,t) = f^*(\chi,t) = f^{**}(X,t) \tag{7.26}$$

where $f(x,t)$ is at Eulerian coordinates, $f^*(x,t)$ is at reference coordinates and $f^{**}(x,t)$ at Lagrangian ones.

And

$$f^* = f \cdot \Phi \; and \; f^{**} = f \cdot \Phi \cdot \Psi^{-1}. \tag{7.27}$$

The time partial differentials at three coordinates are defined as

$$f_t^M = \frac{\partial f}{\partial t},\ X = \text{cons};\ f_t^S = \frac{\partial f}{\partial t},\ x = \text{cons};\ f_t^R = \frac{\partial f}{\partial t},\ \chi = \text{cons} \tag{7.28}$$

where subscript t is the time differential, and superscripts M, S and R indicate three coordinates. The relationship between different time partial differentials can be obtained as

$$\left.\frac{\partial f^{**}}{\partial t}(X,t)\right|_X = \left.\frac{\partial f^*}{\partial t}(\chi,t)\right|_\chi + w_i \frac{\partial f^*}{\partial \chi_i}(\chi,t). \tag{7.29}$$

where $w_i = \left.\frac{\partial \chi_i}{\partial t}\right|_X$ and

$$\left.\frac{\partial {x_i}^{**}}{\partial t}(X,t)\right|_X = \left.\frac{\partial {x_i}^{*}}{\partial t}(\chi,t)\right|_\chi + w_j \frac{\partial {x_i}^{*}}{\partial \chi_j}(\chi,t). \tag{7.30}$$

Then, one defines the material velocity of flow v and the grid velocity $\hat{v}$ respectively as

$$v = \frac{\partial x}{\partial t}, \quad X = \text{cons that is}, v = \left.\frac{\partial {x_i}^{**}}{\partial t}(X,t)\right|_X$$
$$\hat{v} = \frac{\partial x}{\partial t}, \quad \chi = \text{cons that is}, \hat{v} = \left.\frac{\partial {x_i}^{*}}{\partial t}(\chi,t)\right|_\chi$$

And $v_i = \hat{v}_i + w_j \frac{\partial {x_i}^{*}}{\partial \chi_j}(\chi,t)$, $c_i = v_i - \hat{v}_i = w_j \frac{\partial {x_i}^{*}}{\partial \chi_j}(\chi,t)$

where $w_i = \left.\frac{\partial \chi_i}{\partial t}\right|_X$, where w_i is the relative velocity in reference system, and

$$c_i = w_j \frac{\partial x_i}{\partial \chi_j}(\chi,t) \tag{7.31}$$

where c_i is the convective velocity.

If $\chi = X$, then $\hat{v} = v$, reducing to a Lagrangian system; and if $\chi = x$, then $\hat{v} = 0$, reducing to an Enlerian system.

The relationship between of time partial differentials of any function f at three coordinates is

$$\left.\frac{\partial f^{**}}{\partial t}(X,t)\right|_X = \left.\frac{\partial f^{*}}{\partial t}(\chi,t)\right|_\chi + c_i \frac{\partial f^{*}}{\partial x_i}(x,t).$$

The continuity equation and momentum equations at the ALE coordinate system are as follows:

$$\left.\frac{\partial \hat{\rho}}{\partial t}\right|_\chi + \frac{\partial \hat{\rho} w_i}{\partial \chi_i} = 0 \quad in \quad R_\chi$$

$$\hat{\rho}\left.\frac{\partial v_i}{\partial t}\right|_\chi + \hat{\rho} w_j \frac{\partial v_i}{\partial \chi_j} = \frac{\partial \hat{T}_{ji}}{\partial \chi_j} + \hat{\rho} g_i \quad in \quad R_\chi \tag{7.32}$$

where

$$v_i = \hat{v}_i + w_j \frac{\partial {x_i}^{*}}{\partial \chi_j}(\chi,t) \tag{7.33}$$

$$c_i = v_i - \hat{v} = w_j \frac{\partial {x_i}^{*}}{\partial \chi_j}(\chi,t) \tag{7.34}$$

where $w_i = \frac{\partial \chi_i}{\partial t}\Big|_X$ is the flow relative velocity to the reference grid system and $c_i = w_j \frac{\partial x_i}{\partial \chi_j}(\chi, t)$. The Jacobin determinant is $\hat{J} = det\left[\frac{\partial x_i}{\partial \chi_j}\right]$, and $\hat{\rho}(\chi, t) = \hat{J}\rho(x, t)$, $\hat{T}_{ij} = \hat{J}\frac{\partial \chi_i}{\partial x_k}\sigma_{kj}$, here, superscript "$\wedge$" designates a variable at the AEL reference coordinates, is $\hat{\rho}(\chi, t)$ the system density, σ_{ij} is the Cauchy stress tensor at the Eulerian coordinate system; and $\hat{T}_{ij}$ is the first order of Piola-Kirchhoff stress tensor in the AEL reference coordinates.

2. Governing equation at quasi-Eulerian description coordinates

In the ALE reference coordinates, the first order of Piola-Kirchhoff stress tensor $\hat{T}_{ij}$ is asymmetrical, so the Quasi-Eulerian Description is developed to simplify Eq. (7.34). In the quasi-Eulerian description coordinates, only the time partial differential coefficient is expressed at the ALE reference coordinates, whereas other terms are indicated by the Eulerian method. The governing equations in this coordinate system are

$$\frac{\partial \rho}{\partial t}\Big|_\chi + c_i \frac{\partial \rho}{\partial x_i} + \rho \frac{\partial v_i}{\partial x_i} = 0 \ in \ R_\chi \tag{7.35a}$$

$$\frac{\partial \rho}{\partial t}\Big|_\chi + c_i \frac{\partial \rho}{\partial x_i} + \rho \frac{\partial v_i}{\partial x_i} = 0 \ in \ R_\chi \tag{7.35b}$$

3. Reynolds equation at ALE coordinates

The Reynolds averaged method is applied in Eq. (7.35), and the Reynolds equations of incompressible turbulent flow at the quasi-Eulerian description coordinates can be written as

$$\rho \frac{\partial \overline{v}_i}{\partial t}\Big|_\chi + \rho \frac{\partial \overline{c}_j \overline{v}_i}{\partial x_j} = \frac{\partial \overline{\sigma}_{ji}}{\partial x_j} + \rho \overline{g_i} - \rho \frac{\partial \overline{c'_j v'_i}}{\partial x_j} \ in \ R_\chi \tag{7.36}$$

And $c_i = v_i - \hat{v}_i$, $\overline{c}_i + c'_i = \overline{v}_i + v'_i - \hat{v}_i$

$$\rho \frac{\partial \overline{v}_i}{\partial t}\Big|_\chi + \rho \frac{\partial \overline{c}_j \overline{v}_i}{\partial x_j} = \frac{\partial \overline{\sigma}_{ji}}{\partial x_j} + \rho \overline{g_i} - \rho \frac{\partial \overline{v'_j v'_i}}{\partial x_j} \tag{7.37}$$

where Reynolds stresses $-\rho \frac{\partial \overline{v'_j v'_i}}{\partial x_j}$ will be closed by the turbulence model.

7.2.2 Turbulence Model for Unsteady Flow Simulation

The term $\left(-\rho \overline{v'_i v'_j}\right)$ on the right-hand side of Eq. (7.22) is called the Reynolds stress tensor. The tensor is symmetric, representing correlations between fluctuating

velocities. It is an additional unknown stress term due to turbulence (fluctuating velocities). One would need a model for $-\rho\overline{v_i' v_j'}$ to close the equation system in Eq. (7.22). Turbulence modeling is a key issue in most CFD simulations. Virtually all engineering applications are turbulent and hence require a turbulence model.

Complexity of different turbulence models may vary greatly depending on details to be observed and investigated. Complexity is due to the nature of Navier-Stokes equation (N-S equation) which is an inherently nonlinear, time-dependent, three-dimensional PDE.

Turbulence could be viewed as instability of laminar flow that occurs at high Reynolds numbers (*Re*). Such instabilities originate from interactions between non-linear inertial terms and viscous terms in N-S equations. These interactions are rotational, fully time-dependent, and fully three-dimensional. Rotational and three-dimensional interactions are mutually connected via vortex stretching which is not possible in two dimensional spaces. That is also the reason why no satisfactory two-dimensional approximations for turbulent phenomena are available.

Turbulence is viewed as a random process in time and therefore no deterministic approach is possible. Certain properties could be learned about turbulence through statistical methods. Though these introduce certain correlation functions among flow variables, it is impossible to determine the correlations in advance.

Another important feature of turbulent flow is that vortex structures move along them. Their lifetime is usually very long. Hence certain turbulent quantities cannot be specified as local. It also means that upstream history of the flow is also of great importance.

7.2.2.1 Turbulence Modeling

Nowadays turbulent flows may be computed via several different approaches. Either by solving the RANS equations with suitable models for turbulent quantities or by computing them directly, one can get results. The main approaches are summarized below.

1. Reynolds-averaged N–S (RANS) Models

Eddy viscosity models (EVM): Assume that the turbulent stress is proportional to the mean rate of strain. Furthermore, eddy viscosity is derived from turbulent transport equations (usually k + one other quantity).

Non-linear eddy viscosity models (NLEVM): Turbulent stress is modeled as a non-linear function of mean velocity gradients. Turbulent scales are determined through transport equations (usually k + one other quantity). The model mimics the response of turbulence to certain important types of strain.

1. Differential stress models (DSM): This category consists of Reynolds stress transport models (RSTM) or second-order closure models (SOC). Transport equations are solved for all turbulent stresses.

2. Large-eddy simulation (LES): One computes time-varying flow, but models sub-grid-scale motions.
3. Direct numerical simulation (DNS): No modeling is applied but one is required to resolve the smallest scales of the flow.

Extent of modeling for certain CFD approach is illustrated by Fig. 7.2. It is clear seen that models that compute fluctuation quantities such as approaches (2) and (3) resolve shorter length scales than those that solve RANS equations. As a result, they provide better results. However they demand much greater computer power than those applying RANS methods (Sodja 2007).

Classes of turbulence models from the view of methodology will be presented as follows:

1. Algebraic models
2. Eddy viscosity transport models, one and two-equation models
3. Non-linear eddy viscosity models and algebraic stress models
4. Reynolds stress transport models
5. Large eddy simulations
6. Detached eddy simulations and other hybrid models
7. Direct numerical simulations.

These are briefly depicted as follows.

7.2.2.2 Algebraic Turbulence Models

Algebraic turbulence models or zero-equation turbulence models are models that do not require the solution of any additional equations, and are calculated directly from the flow variables. As a consequence, zero equation models may not be able to properly account for historical effects on the turbulence such as convection and diffusion of turbulent energy. These models are often too simple in general situations, but can be quite useful for straightforward flow geometries or in start-up

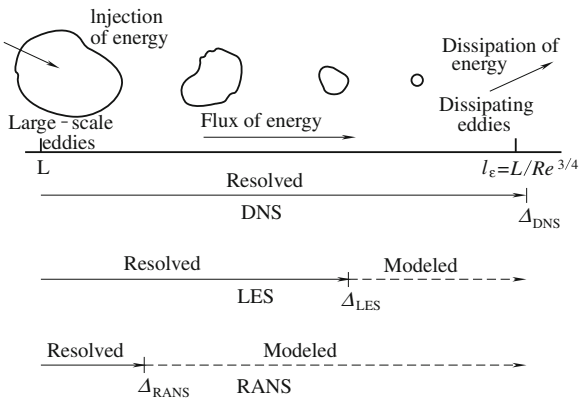

Fig. 7.2 Extent of modeling for certain types of turbulent models

situations (*e.g.* the initial phases of computation in which a more complicated model may have difficulties). The two most well-known zero equation models are the Baldwin-Lomax model and the Cebeci-Smith model. Other even simpler models, such as models with $\mu_t = f(y^+)$ (where μ_t is eddy viscosity, $y^+ = y_w v_* \rho/\mu$ and where y_w is the distance from the nearest calculation point to wall and $v_* = \sqrt{\tau_w/\rho}$ τ_w is the shear stress on wall), are sometimes used in particular situations (*e.g.* boundary layers or jets). The algebraic Johnson-King model (1985) is sometimes called a 1/2 equation model since it incorporates the solution of an ordinary differential equation.

7.2.2.3 One and Two-Equation Turbulence Models

One equation turbulence models solve one turbulent transport equation, usually the turbulent kinetic energy. The original one-equation model is Prandtl's one-equation model. Others commonly seen are the Baldwin-Barth model and Spalart-Allmaras model.

Two-equation turbulence models are also commonly used. Models like the *k*-epsilon model and the *k*-omega model have become industry standards for most types of engineering problems. Two-equation turbulence models are still an active area of research and newly refined two-equation models are still being developed.

According to definition, two-equation models include two extra transport equations to represent the turbulent properties of the flow. Thus, a two-equation model could account for historical effects like convection and diffusion of turbulent energy.

The turbulent kinetic energy, $k = \overline{v_i' v'}_i/2$ is one transported variable most often used. The second transported variable varies with the type of two-equation model. Common choices are the turbulent dissipation ε or the specific dissipation ω. The second variable can be considered as the variable that determines the scale of turbulence (length scale or time-scale), whereas the first variable k determines the energy in turbulence.

The basis for both two-equation models is the Boussinesq eddy viscosity assumption, which postulates that the Reynolds stress tensor, τ_{ij}, is proportional to the mean strain rate tensor, S_{ij}, and can be written in the following way:

$$\tau_{ij} = 2\mu_t \left(\frac{\partial \overline{v}_i}{\partial x_j} + \frac{\partial \overline{v}_j}{\partial x_i} \right) + \frac{2}{3} \rho k \delta_{ij}. \tag{7.38}$$

The last term is to ensure the definition of turbulent kinetic energy is obeyed: $k = \overline{v_i' v_i'}/2$. And

$$S_{ij} = \left(\frac{\partial \overline{v}_i}{\partial x_j} + \frac{\partial \overline{v}_j}{\partial x_i} \right).$$

There are varieties of two-equation turbulence models, such as Standard k-ε model, Realisable k-ε model, RNG k-ε model, k-ω models, Wilcox's k-ω model, Wilcox's modified k-ω model, and SST k-ω model. For unsteady turbulent flow calculations, RNG k-ε model and SST k-ω model are widely used.

7.2.3 Large Eddy Simulation and Detached Eddy Simulation

LES seeks to directly solve large spatial scales (like DNS) and model the smaller scales (k-epsilon). Its basic thought lies in two parts. First, the larger scales carry the majority of the energy, and hence are more important. Second, the smaller scales are found to be more universal, and hence are more easily modeled. The resulting methodology is a hybrid of these two, which involves filtering the N-S equations to separate scales from those solved directly.

Difficulties associated with the use of the standard LES models, particularly in near-wall regions, led to the development of hybrid models that combine the best aspects of RANS and LES methodologies in a single solution strategy. An example of a hybrid technique is the DES (Spalart et al. 1997).

7.2.3.1 Large Eddy Simulation

Mathematically, in LES, one may separate the velocity field into a resolved part and a subgrid part. The resolved part of the field represents the "large" eddies, while the subgrid part represents the "small scales" whose effect on the resolved field is included in a subgrid-scale model. Formally, filtering could be viewed as the convolution of a function with a filtering kernel, and

$$v_i = \overline{v}_i + v_i' \tag{7.39}$$

where $\overline{v}_i$ is the resolvable scale part and v_i' the subgrid-scale part. However, most practical (and commercial) implementations of LES use the grid itself as the filter (the box filter) and perform no explicit filtering. The filtered equations are developed from the incompressible N-S equations. The equations of motion for the resolved field are

$$\frac{\partial \overline{v}_i}{\partial t} + \bar{v}_j \frac{\partial \overline{v}_i}{\partial x_j} = \rho f_i - \frac{1}{\rho}\frac{\partial \bar{p}}{\partial x_i} + \frac{\partial}{\partial x_j}\left(\frac{\mu}{\rho}\frac{\partial \overline{v}_i}{\partial x_j}\right) + \frac{1}{\rho}\frac{\partial \tau_{ij}}{\partial x_j} \tag{7.40}$$

The last extra term arises from the non-linear advection terms, due to the fact that

$$\overline{v_j \frac{\partial v_i}{\partial x_j}} \neq \overline{v}_j \frac{\partial \overline{v}_i}{\partial x_j} \tag{7.41}$$

and hence

$$\tau_{ij} = \overline{v}_i \overline{v}_j - \overline{v_i v_j}. \tag{7.42}$$

Similar equations can be derived for the subgrid-scale field (*i.e.* the residual field). Subgrid-scale turbulence models usually employ the Boussinesq hypothesis and seek to calculate the SGS stress using

$$\tau_{ij} - \frac{1}{3}\tau_{kk}\delta_{ij} = -2\mu_t \bar{S}_{ij} \tag{7.43}$$

where $\bar{S}_{ij}$ is the rate-of-strain tensor for resolved scale, and μ_t is the subgrid-scale turbulent viscosity.

Subgrid-scale models are those such as the Smagorinsky model (Smagorinsky 1963), the Algebraic Dynamic model (Germano et al. 1991), the Dynamic Global-Coefficient model (You and Moin 2007), the, Localized Dynamic model (Kim and Menon 1995), the Wall-Adapting Local Eddy viscosity (WALE) model (Nicoud and Ducros 1999) and so on.

7.2.3.2 Detached Eddy Simulation

The DES (Spalart et al. 1997) model attempts to treat near-wall regions in a RANS-like manner, while treating the rest of the flow in a LES-like manner. The model was originally formulated with replacement of the distance function d in the Spalart-Allmaras (S-A) model with a modified distance function:

$$\tilde{d} = \min(d, C_{DES}\Delta) \tag{7.44}$$

where C_{DES} is a constant and Δ is the largest dimension of the grid cell in question. This modification of the S-A model, while very simple in nature, changes the interpretation of the model substantially. The modified distance function causes the model to behave as a RANS model in regions close to walls and in a Smagorinsky-like manner away from the walls. It is usually justified with arguments that the scale-dependence of the model is made local rather than global, and dimensional analysis backs up this claim.

The DES approach may be applied to any turbulence model that has an appropriately defined turbulence length scale (distance in the S-A model) and is a sufficiently localized model. The Baldwin-Barth model, very similar to the S-A model, is probably not suitable for DES. The standard version of this model contains several van Driest-type damping functions that make the distance function more global in nature. Menter's SST model is a good one and has been used by a number of researchers. Menter's SST model engages a turbulence length scale obtained from the model's equations and compares it with the grid length scale to switch between LES and RANS (Strelets 2001).

In practice, more programming with changes of the length scale is needed instead of calculation. Many implementations of the DES approach allow for regions to be

explicitly designated as RANS or LES regions, overruling the distance function calculation. Also, many implementations apply different differencing in RANS regions (*e.g.* upwinded differences) and LES regions (*e.g.* central differences).

7.3 Prediction for Pressure Pulsation in Kaplan Turbine by Turbulent Simulation of Unsteady Flow

Kaplan turbine is a great development in the early twentieth century. The pitch angle of Kaplan runner is adjustable; therefore the machine can handle a great variation of flow efficiently. Kaplan turbine has an efficiency of 90 % or even better but costs higher, which is primarily used in large power stations.

With the increase of turbine output and size, stability problems such as hydraulic vibration and runner blade cracks in large hydraulic turbines have become prominent. Vibrations, swings, and pressure fluctuations are three major parameters that characterize the stability of turbine units. Among them, pressure fluctuation is produced by unsteady flow field, which is the major hydraulic source leading to vibration and non-steady operation of the hydraulic turbine unit. It can cause turbine vibration, blade cracks, and even resonance of the powerhouse, directly threaten the safe operation of the whole power station. Therefore it is of great importance to investigate such pressure fluctuations.

Before a hydraulic power station is constructed, it is not possible to test the performance of a prototype hydraulic turbine. The only viable way is to conduct model tests and scale the results to predict the performance of the prototype. However, due to the lack of similar laws in scaling vibration and pressure fluctuations, prediction of turbine stability can only be done with computational simulations of fluid dynamics. Therefore the correctness and accuracy of a numerical simulation becomes extremely important.

At the end of the 1990s, pioneering calculations of fluid flow field in whole flow passages of hydraulic turbines were conducted on super computers. Nowadays the Computational Fluid Dynamics (CFD) method has been widely applied for the design of hydraulic turbines.

For Kaplan turbines, most researchers have conducted 3-D steady flow simulations to improve design or to study a particular flow phenomenon in the turbines. Nilsson and Davidson (2000, 2002) studied the internal flow inside the runner and flows through the gap between the runner and its chamber under four different operation conditions. Muntean et al. (2004) completed a flow analysis in the spiral case and distributor of a Kaplan turbine and obtained the information for a channel vortex at different operation conditions. Tomas et al. (2004) used the flow simulation to improve the hydraulic design of a Kaplan turbine. Lindsjö et al. (2004) calculated the movement of bubbles in a Kaplan runner. Gehrer et al. (2006) conducted Kaplan turbine runner optimizations using numerical flow simulations (CFD). Satisfactory prediction of pressure pulsation in the whole flow passage of a Kaplan turbine by

numerical approach is yet to be achieved. Liu et al. (2009) carried out prediction for flow fluctuation in a model Kaplan turbine by simulation of unsteady turbulent flow, Wu et al. (2012) did detailed numerical prediction and similarity study of pressure fluctuation in a prototype Kaplan turbine and the model turbine.

The following sections report computational work on three- dimensional unsteady turbulent flow in whole flow passage of a Kaplan turbine using the RNG k-ε turbulence model. The calculated results are compared to experimental results to verify the robustness of the numerical model.

7.3.1 Turbulence Model and Numerical Methods

The incompressible continuity equation and RANS equation are adopted to simulate the flow through the Kaplan turbine, and the RNG k-ε double equations turbulence model is selected to make the equations closed (Speziale and Thangam 1992).

The governing equations are discretized into algebra equations with the finite volume method in spatial domain at each time step. They are also discretized in temporal domain following a second-order implicit formula and integrated within one time step. The discretized equations reflect flow field parameters at each time step. The algebra equations obtained through discretization in spatial domain are solved with a sub-relaxation method.

Frequency analyzes of time-dependent results of unsteady flow are carried out with the Fast Fourier Transform (FFT) method. Figure 7.3 shows the calculated algorithm in present work which is based on the Fluent software.

Figure 7.4a and b show the flow passage and the runner. In the very beginning, one should study grid independence and calculation time independence where the optimum number of grids and optimum calculation time are obtained. The total grid element numbers in case I, II, and III are 1,933,265, 2,287,573 and 2,643,148, respectively. Finally, a mesh of 2,578,000 elements and 543,000 crunodes all over the flow passage are employed, which is dense enough to obtain detailed pressure data and velocity data required, referring to Fig. 7.4c.

The time step is 0.001 s. Rotation speed of the runner is 1,267.9 rpm, therefore the converged turbulent flow solution are obtained through rotating mesh in the runner region by 7.61° per time step. The converged solutions at all time thus form the unsteady solutions that are the pressure and velocity variations with time in the whole flow passage.

7.3.2 Prediction of Pressure Pulsation of a Model Kaplan Turbine

The numerical model is used to predict pressure pulsation of both a model turbine in this section and a prototype turbine in next section. The computational results of

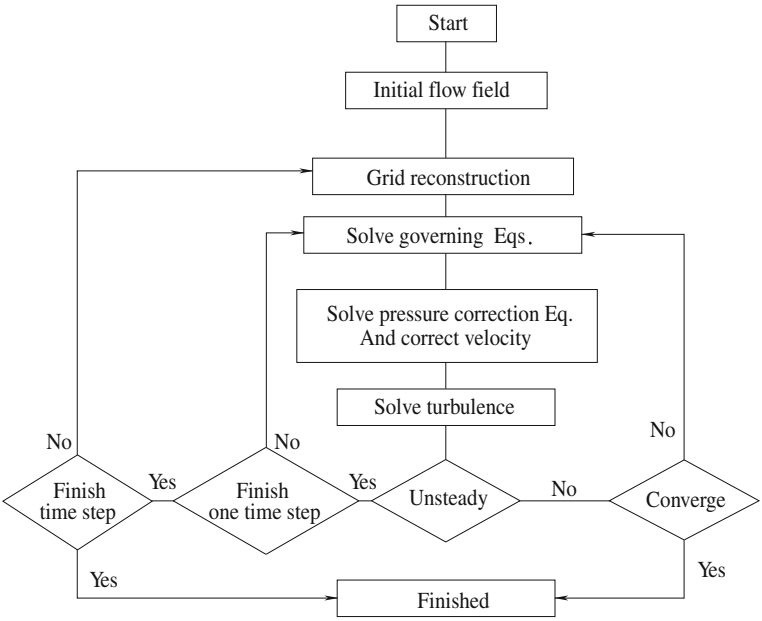

Fig. 7.3 Calculation algorithm

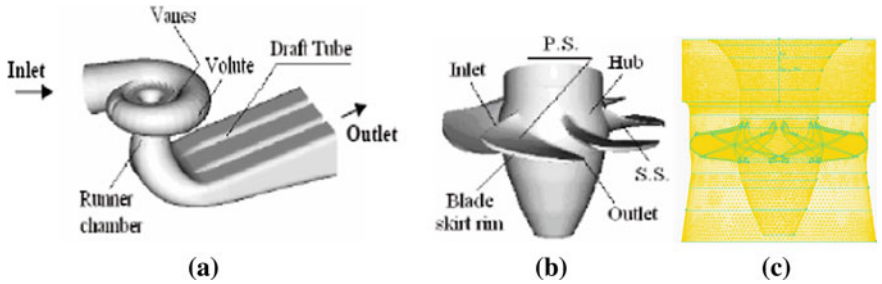

Fig. 7.4 Schematic diagram of the Kaplan turbine. **a** Whole flow passage of turbine. **b** Runner and blades. **c** Runner grid system

both the model turbine and the prototype are compared. The transmission characteristics of the pressure pulsation in the Kaplan turbine are also studied.

7.3.2.1 Measurement of Pressure Pulsation in a Model Turbine

Experiments are carried out on an experimental rig. Pressure transducers are located within the inner walls at $0.3D_1$ under the runner, the draft tube inlet at the point $(-X)$, which is located on the left side of the draft tube, and the outside of the draft tube elbow as is shown in Fig. 7.5.

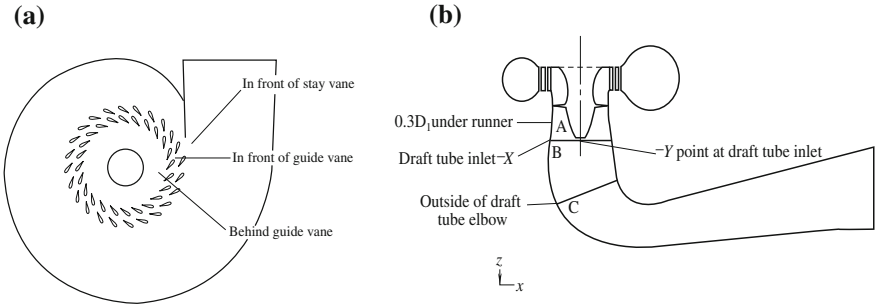

Fig. 7.5 Measuring and sampling points of pressures. **a** In front of the runner. **b** In draft tube

7.3.2.2 Computational Results of Pressure Pulsation for a Model Kaplan Turbine

For conditions listed in Table 7.1, unsteady turbulent flow calculations are carried out in a whole flow passage of the Kaplan turbine model.

Pressures at all measuring points indicated in Fig. 7.5 are recorded at each time step. The time domain graphs of the pressure are obtained. Fast Fourier Transforms is then utilized to transform the time domain data into the frequency domain graphs of pressure pulsation at all measuring points. The abscissa is energy of pressure pulsation in unit P_a^2/H_z, the ordinate is frequency of pressure pulsation in unit H_z.

Figures 7.6 and 7.7 show the results at $0.3D_1$ under the runner and the inlet of the draft tube $(-X)$ (Liu et al. 2008).

Table 7.2 lists the pressure pulsation frequency and corresponding amplitude at four measuring points.

The unit of amplitude is $\Delta H/H$, that is the ratio of pressure fluctuation amplitude ΔH in time domain to the turbine water head. In the table, the amplitude at time domain is defined as the maximum amplitude measured in the time domain graphs of the pressure variation with 97 % reliability.

The characteristics of pressure pulsation and its transmitting pattern of the model turbine are analyzed in Sect. 7.3.3.

7.3.3 Patterns of Pressure Pulsation Transmission

The rotating frequency of the runner is 21.13 Hz. From Table 7.2, it can be seen that the energy of the pressure pulsation peaks at several frequencies. The first peak appears at a low frequency of 0.15 times of the rotating frequency that is 3.2 Hz. The amplitude of pressure pulsation at this frequency is the highest sampled at the outside of the draft tube elbow and gradually decreases in upstream direction.

Table 7.1 Kaplan turbine pressure pulsation test operation condition parameters

Runner blade angle (°)	Guide vane opening A_0 (mm)	Unit speed n_{11} (r/min)	Unit flow Q_{11} (l/s)	Water head of prototype H_p (m)	Water head of model H (m)
15	20	118.6	805	52.2	14
Runner diameter of prototype D_{1p} (m)	Runner diameter of model D_1 (m)	Prototype speed n_p (r/min)	Model speed n (r/min)	Prototype flow rate Q_p (m^3/s)	Model flow rate Q (m^3/s)
8	0.35	107	1267.9	371.5	0.3688

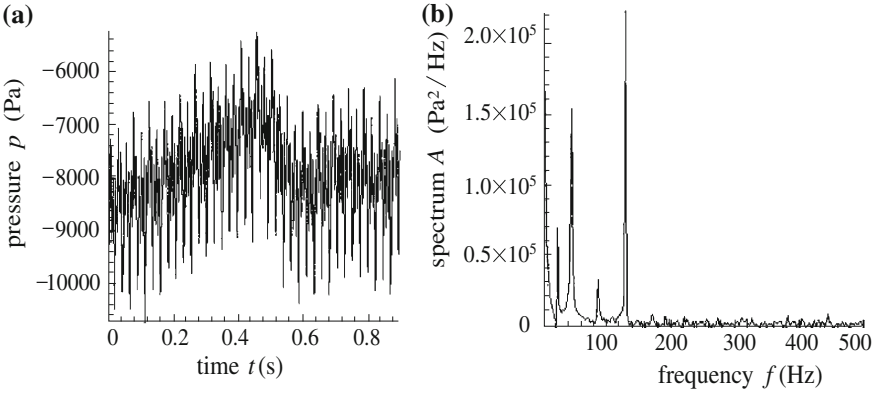

Fig. 7.6 Pressure fluctuation at $0.3D_1$ under model turbine runner. **a** Pressure variation with time. **b** Pressure fluctuation spectrum

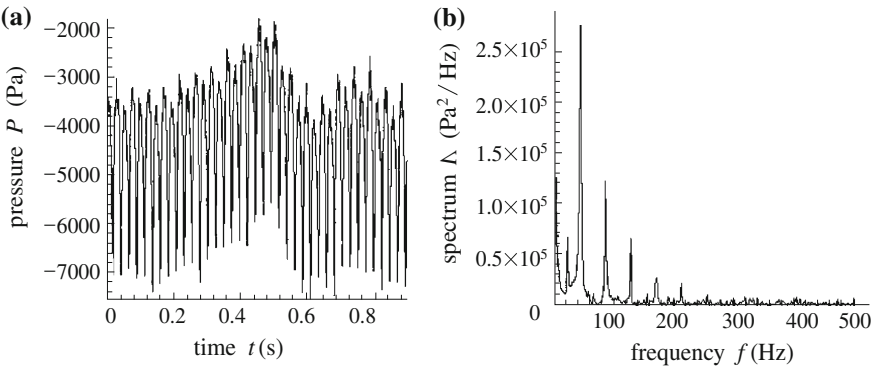

Fig. 7.7 Pressure fluctuations at inlet ($-X$) of draft tube of model turbine. **a** Pressure variation with time. **b** Pressure fluctuation spectrum

The second peak emerges at 21.3 Hz, which is approximately the rotating frequency. The amplitude of pressure pulsation at this frequency is the highest at the inlet of the draft tube and decreases in both upstream and downstream directions.

The third peak is at 42.3 Hz, which is approximately twice the rotating frequency. The amplitude of pressure pulsation at this frequency is the highest at the inlet of the draft tube and decreases in both upstream and downstream directions.

The fourth peak appears at 84.2 Hz, which is approximately four times the rotating frequency. The amplitude of pressure pulsation at this frequency is the highest at the inlet of the draft tube and decreases in both upstream and downstream directions.

The fifth peak appears at 125.8 Hz, which is approximately six times of the rotating frequency. The amplitude of pressure pulsation at this frequency is the highest at $0.3D_1$ under the runner and decreases in the downstream direction.

At all the measuring points, there are other peaks at frequencies 10.2, 104.1, 148.3 Hz, and *etc*. They correspond to 0.4, 5, and 7 times of the rotating frequency. However, their amplitudes are not significantly larger than the average.

For pressure transmission patterns, calculation results are in good agreement with experimental results. However, some high energy pressure pulsation frequencies at the measuring points are different from the experimental results.

7.3.4 Pressure Pulsation Prediction of a Kaplan Turbine Prototype

The good agreement of the pressure pulsation prediction for the model Kaplan turbine with the experimental study verifies the validity of the numerical method employed. Therefore, the numerical method is thus used for the prediction of pressure pulsation of the prototype turbine, which has the following primary parameters:

Weighted average head of power station $H = 52.2$ m;
Diameter of runner $D_1 = 8$ m;
Design output $P = 200$ MW;
Suction head of power station $H_s = +3.5$ m.

7.3.4.1 Computational Pressure Pulsation of a Prototype Kaplan Turbine

The results of 3D unsteady computation for the whole flow passage of the prototype Kaplan turbine are achieved with the pressure pulsation data FFT transformed. Theses pressure pulsations in both time domain and frequency domain are at locations of $0.3D_1$ under the runner, the inlet of the draft tube ($-X$), and the

Table 7.2 Comparison of calculation results and experimental results of pressure fluctuation frequency and corresponding relative amplitude ($\Delta H/H$) at all measuring stations of the Kaplan turbine model (Liu et al. 2008)

Pressure pulsation		Low frequency	1 × rotate frequency	2 × rotate frequency	4 × rotate frequency	6 × rotate frequency	Amplitude
Frequency (Hz)	Calculation	$f = 3.48$	$f = 23.4$	$f = 45.3$	$f = 86.0$	$f = 128.8$	
	Experimental	$f = 3.2$	$f = 21.3$	$f = 42.3$	$f = 84.2$	$f = 125.8$	
Frequency/rotation frequency	Calculation	0.165	1.107	2.144	4.07	6.096	
	Experimental	0.151	1.0004	2.002	3.965	5.954	
$\Delta H/H$ (%) at $0.3D_1$ under runner	Calculation	0.473	0.916	1.88	1.23	3.8	4.41
	Experimental	1.4	1.5	3	1.5	4.1	4.63
$\Delta H/H$ (%) at $-X$ of draft tube inlet	Calculation	0.516	0.9	2.53	2.34	2.11	4.03
	Experimental	2	1.6	2.4	3.6	2.02	5.14
$\Delta H/H$ (%) at $-Y$ of draft tube inlet	Calculation	0.49	0.963	2.496	2.26	2.11	4.01
	Experimental	1.6	1.6	2.5	3.5	2.0	5.1
$\Delta H/H$(%) at outside of elbow	Calculation	0.55	0.45	0.94	0.57	0.33	1.1
	Experimental	3.0	0.5	1.3	0.5	0.2	3.18

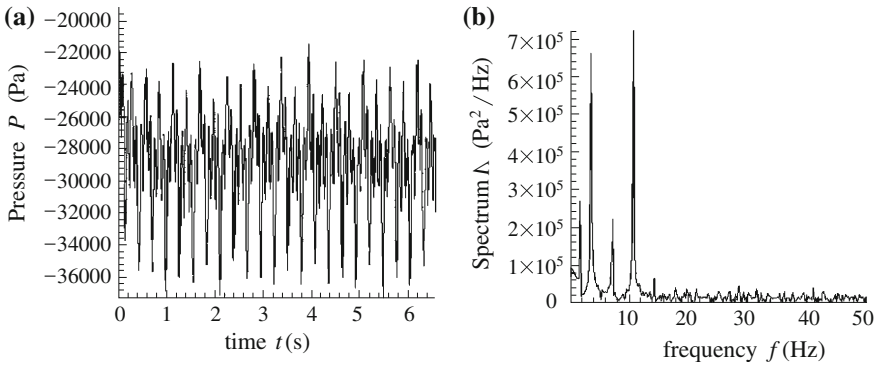

Fig. 7.8 Calculated pressure pulsation at $0.3D_1$ under runner of prototype turbine. **a** Pressure pulsation waveform. **b** Pressure pulsation frequency spectrum

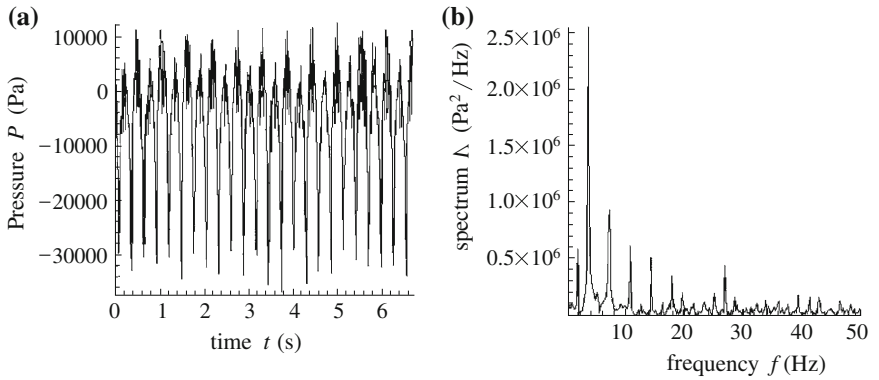

Fig. 7.9 Calculated pressure pulsation at the inlet of draft tube $-X$ of prototype turbine. **a** Pressure pulsation waveform. **b** Pressure pulsation frequency spectrum

outside of the draft tube elbow. Figures 7.8 and 7.9 show the calculated pressure pulsations at $0.3D_1$ under the runner and inlet of the draft tube $-X$.

7.3.4.2 Comparison of the Numerically Predicted Pressure Pulsation of the Model Turbine and the Prototype Turbine

Table 7.3 lists the numerical prediction of pressure pulsations at three measuring points for both model and prototype turbines. The similarities between the model and prototype turbines can be drawn as follows.

1. A low frequency pressure pulsation of 0.15–0.3 times of rotating frequency exists in the draft tubes. At the same time, pressure pulsations at frequencies of 1, 2, 4, and 6 times of the rotating frequency are also present in the draft tube.

Table 7.3 Comparison of computational of pressure pulsation frequencies and relative amplitudes ($\Delta H/H$) of model and prototype turbines

Pressure pulsation frequency		Low	1 × rotate	2 × rotate	4 × rotate	6 × rotate	Amplitude
Frequency (Hz)	Model	3.48	23.4	45.3	86.0	128.8	
	Prototype	0.547	1.94	3.73	7.41	10.89	
Frequency/rotate frequency	Model	0.165	1.107	2.144	4.07	6.096	
	Prototype	0.306	1.088	2.092	4.156	6.108	
$\Delta H/H(\%)$ at $0.3D_1$ under runner	Model	0.473	0.916	1.88	1.23	3.8	4.41
	Prototype	0.117	0.4797	0.971	0.796	1.732	2.66
$\Delta H/H(\%)$ at $-X$ of draft tube inlet	Model	0.516	0.9	2.53	2.34	2.11	4.03
	Prototype	0.616	1.24	4.78	4.32	4.23	8.04
$\Delta H/H(\%)$ at elbow outside	Model	0.55	0.45	0.94	0.57	0.33	1.1
	Prototype	0.276	0.395	0.64	0.43	0.49	0.99

2. The relative strength order for harmonics of the pressure pulsations for each measuring point is the same between model and prototype. For example, the pressure pulsation amplitude of six times the rotating frequency at $0.3D_1$ under the runner is the highest; the pressure pulsation amplitude of two times the rotating frequency at the inlet of the draft tube is the highest.
3. For all components of pressure pulsation, their source and transmission patterns are the same. For example, the pressure pulsation amplitude of two times of rotating frequency at the inlet of the draft tube is the highest and gradually decreases in both upstream and downstream directions.

7.4 Simulation of Unsteady Flow Through Francis Turbine by DES

In this section, the DES approach is applied to simulate the unsteady turbulent flow in a whole passage of a model Francis turbine. The internal flow, vortex motion and pressure fluctuation inside the turbine can be studied from the calculated results, which are compared with the experiment data. It can be seen that this method can describe the complex flow of the turbine well with a relatively low mesh density.

7.4.1 Introduction

The flows in hydraulic turbines are unsteady and complex 3D turbulent. They are characterized by vortices of length scales in a wide range, high shear and reversal flows, cavitating flows *etc*. The adverse pressure gradients at the exit of runner and the entrance of the draft tube lead to boundary detachment, secondary flows and formation of vortex rope, which all impact the hydraulic efficiency and cause

instabilities (*e.g.* pressure fluctuation and structure vibration). They may also contribute to runner blade cracks, structural vibrations, cavitation, and serious accidents.

The Francis turbine is designed for the designed operating condition such that the inlet flow is symmetrical with no striking and the outlet flow is perpendicular. However under off-design conditions, flows deviate from the design status, causing separate flows, inverse flows, vortex rope, and other unsteady phenomena. On part load operating conditions, there are vortices and swirling flows in the runner blade channels and the draft tube.

Generally, the vortices in hydraulic turbines can be divided into three categories: vortex rope in draft tube, Karman vortex, and blade passage vortex. The Karman vortex is caused by circuitous flow around runner blades. The blade passage vortex comes from separate flow of blade outlet edge, and the vortex rope is attributed to swirling flow and vortices from runner, which is most harmful to machine causing pressure fluctuations.

7.4.2 Numerical Simulation

In this calculation, to simulate the complex swirling flow in the whole passage of the Francis turbine (Fig. 7.10), the DES approach is applied in solving three-dimensional N-S equations. The finite volume method is used to convert the governing equations into algebraic equations for numerical simulation. The momentum and continuity equations are solved sequentially by the SIMPLEC algorithm (Wu et al. 2006).

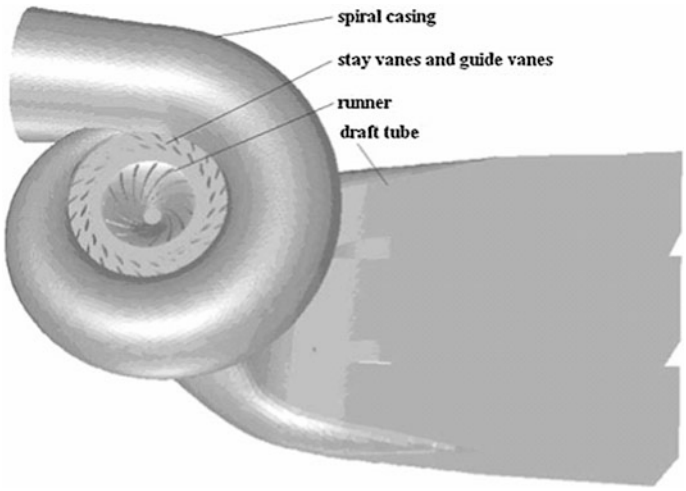

Fig. 7.10 The whole passage of three-gorge turbine

Table 7.4 Mesh scales and numbers (Wu et al. 2006)

Part	Casing	Guide blade	Runner	Draft
Size	10 mm	12 mm	5 mm	10 mm
Number	164088	139158	598391	694605

7.4.2.1 Numerical Method

In the unsteady turbulent simulation, the fully implicit scheme is utilized for temporal discretization because it is unconditionally stable with respect to time step size. The central-differenced method with second-order accuracy is employed for diffusion term; and for convection term, the second order upwind scheme is used. The SIMPLEC method is used for introducing pressure into the continuity equation. The mesh number of each part is shown in Table7.4 along with their mesh scales and numbers. The hexahedron mesh is used on the model because the number of this kind of mesh is lower than a tetrahedron with the same scale.

7.4.2.2 Boundary Conditions

For the inlet and outlet of the computational domain, the pressure conditions are given because they can reflect the actual flow state in the turbine. According to experimental data, the downstream level is assumed to be 1 m above the top of the draft tube outlet. The water head for the experiment is 20 m. Thus the pressure at the inlet can be calculated once the dimensions of the passage are known. For a more accurate simulation, the pressure distribution of the outlet is given, which can be calculated once the downstream level has been decided. The rotating speed is 87.4 rad/s. The time step is chosen as one hundredth of the rotating period, which is 7.19×10^{-4}s, where Ω is the angular speed of the runner (Wu et al. 2002).

The total and static pressure of the inlet and static pressure of the outlet are given as boundary conditions. The unit rotating speed and flow rate are all set the same those in experiments, as referring to Table 7.5.

7.4.3 Simulation Results

The results of this simulation show that this method can be effective to simulate the complex flow, which is full of large-scale vortices and separated flows. The energy characteristics such as hydraulic efficiency and the dominant frequency of

Table 7.5 Hydro condition for simulation

Guide opening (mm)	Unit rotating speed (rpm)	Unit Flow rate (m^3/s)
10	70	0.46

Table 7.6 External characteristics obtained from simulation and experiment (Wu et al. 2006)

	Guide opening (mm)	Flow rate (kg/s)	Water head (m)	Hydro efficiency (%)
Simulation	10	281.8	19.1	85.6
Experiment	10	288.8	20	86.2
Error (%)		2.5	4.7	0.9

pressure fluctuation inside the draft tube are compared with experiment results. Notice that the difference of simulation and experiment is small.

7.4.3.1 External Characteristic Results

The internal unsteady flow of the whole passage in a Francis turbine model is simulated using DES. The results such as flow rate and hydraulic efficiency are shown in Table 7.6. The results of the model tests are listed for comparison.

The difference between simulation and experiments is very small within 5.0 %, which indicates the simulation results are acceptable.

7.4.3.2 Results for Pressure Fluctuation

For the model test, pressure fluctuations are measured at 4 points inside the turbine model, as shown in Fig. 7.11. One is located between guide vane and runner while the others are inside the draft tube. For the simulation, the pressure fluctuations are sampled at the same points.

The comparison is shown in Table 7.7. The relative maximum fluctuation range are defined as

$$\bar{A} = \Delta H_{\max}/H_t \tag{7.45}$$

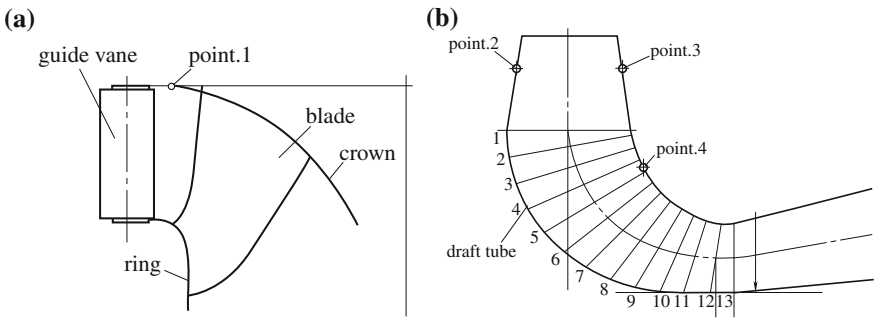

Fig. 7.11 Pressure fluctuation recording points inside hydro turbine. **a** *Point.1* between guide vane and runner. **b** *Point.2, point.3, point.4* inside draft tube

Table 7.7 Comparison between simulation and test

Point name	Relative pressure fluctuation (%)		Error (%)	Main frequency (Hz)	Error (%)
Point.1	Simulation	2.3	8.7	2.8	7.1
	Experiment	2.13		3.0	
Point.2	Simulation	5.1	10.5	3.1	10
	Experiment	5.75		3.4	
Point.3	Simulation	3.7	7.5	3.2	6.7
	Experiment	4.05		3.4	
Point.4	Simulation	4.2	10.6	2.85	5.0
	Experiment	4.69		3.0	

where ΔH_{max} is the maximum range of pressure fluctuation. H_t is the operating water head.

The comparison shows that the maximum error is about 10 %, and indicates that the DES simulation results are acceptable.

The difference between simulation and experiment might be caused by two factors. One is the mesh number of the turbine model not dense enough to simulate the complex 3D unsteady turbulent flow. The other might attribute to measuring errors during the model experiment.

7.4.3.3 Pressure Distribution in the Draft Tube

Pressure distribution on plane 1 and plane 2 inside draft tube are investigated. The 3D flow structure of the vortex rope inside the draft tube is also visualized by pressure isosurfaces. These instantaneous results are shown in Fig. 7.12.

From Fig. 7.12 it can be seen that the lowest pressure core (the blue part of these pictures) is rotating around the plane center, which reflects the vortex rope motion inside draft tube.

7.5 Simulation of Unsteady Flow Through Centrifugal Pumps

The same approach as demonstrated in Sect. 7.3 has been applied to the unsteady turbulent flow through the entire flow passage (that is, from inlet in front of an inducer to outlet of spiral diffuser) of a high speed centrifugal pump. Figure 7.13 shows the computational domain of inlet tube, inducer, guide vane support, centrifugal impeller, the vane diffuser and spiral casing diffuser (Xu 2004).

The specifications of the pump are:

1. 3 bladed inducer, diameter: 120 mm
2. Guide vane support: 8
3. 6 bladed impeller, diameter: 163 mm
4. 7 vaned diffuser

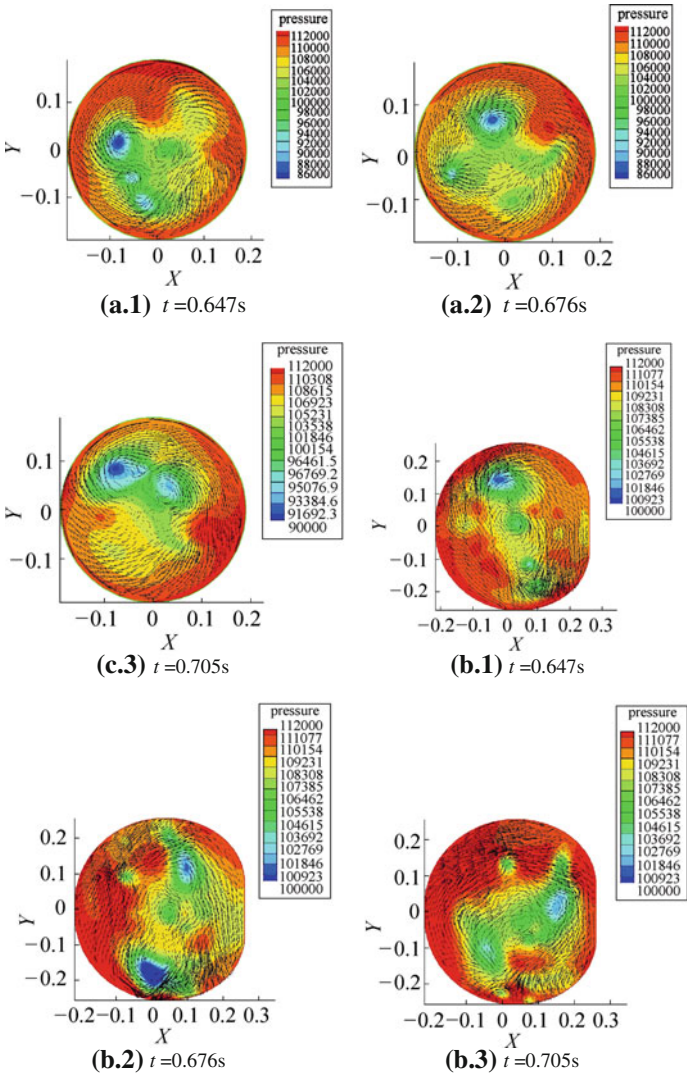

Fig. 7.12 Pressure and velocity vector on plane 1 (**a**) and plane 2 (**b**) (Unit: Pa). (Wu et al. 2006)

For the rotating inducer and impeller, there are four rotor-stator interfaces. They are in front of the inducer, between the inducer and guide vanes, between guide vanes and impeller, and between impeller and vane diffuser as shown in Fig. 7.13b.

In the unsteady flow simulation, the moving grid of impeller and inducer rotates 4° at every time step. The pressure variations at selected time intervals and at selected spatial points are usually recorded to reduce the size of data file.

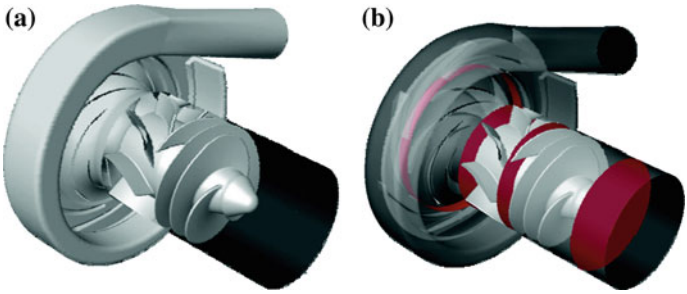

Fig. 7.13 Centrifugal pump. **a** Calculated domain. **b** Interfaces of centrifugal pump

Table 7.8 Amplitude of pressure fluctuation through inducer

Speed	Diameter	Amplitude/kPa								
($r \cdot min^{-1}$)	(mm)	inlet	50°	120°	140°	160°	180°	266°	318°	Outlet
9,000	46	20	95	47	58	63	63	142	162	110
11,000	46	30	110	–	–	–	–	–	–	259
13,000	24	124	100	220	239	236	220	324	288	220
13,000	46	124	100	253	268	264	260	384	267	120
13,000	56	98	416	279	297	320	317	423	296	148
20,000	46	128	450	382	41	433	405	897	879	259

7.5.1 Simulation of Stator–Rotor Interaction

In order to present the calculated results, one may plot the pressure fluctuations at sections with the wrap angles 50°, 120°, 140°, 160°, 180°, 266° and 318° (measured from the leading of inducer blade) and at diameters of 0.046, 0.024 or 0.056 m throughout the inducer. Table 7.8 shows the amplitudes of pressure fluctuations from inlet to outlet of the inducer under different rotating speeds. The fluctuation amplitude increases with the increase of rotating speed. Figure 7.14 shows the pressure spectrum at radius 0.056 m and at wrap angle 318°. The main frequency of the pressure fluctuation is 713 Hz and the second frequency is 1,331 Hz.

7.5.2 Simulation of Vortex Through Impellers

The normalized helicity method has been used to analyze the vortex motion through the inducer of pump for understanding the vortex character. The method was introduced by Levy et al. (1998) to find the central lines of vortex nuclei. The normalized helicity is defined as

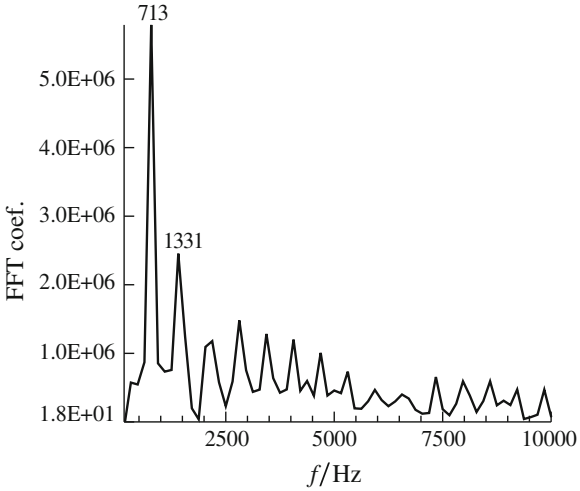

Fig. 7.14 Pressure spectrum at radius 0.056 m and at wrap angle 318° in inducer

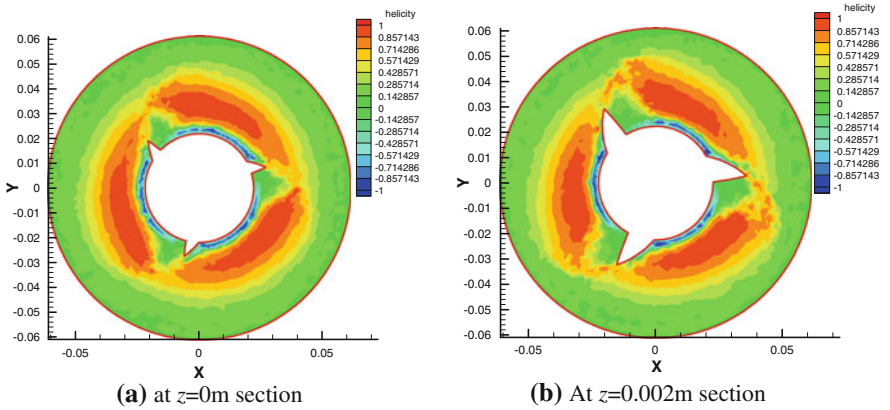

Fig. 7.15 Normalization helicity distribution at every section of inducer. **a** At $z = 0$ m section. **b** At $z = 0.002$ m section

$$H_n = \frac{\{\boldsymbol{V}\} \cdot \{\boldsymbol{\omega}\}}{|\{\boldsymbol{V}\}||\{\boldsymbol{\omega}\}|} \tag{7.45}$$

where $\{\boldsymbol{\omega}\}$ is the eddy of the flow and $\{\boldsymbol{V}\}$ is velocity in the flow. From Eq. (7.46) it is clear that $-1 \leq H_n \leq +1$.

Figure 7.15 indicates the normalization helicity distribution at each section from the leading edge of inducer to its outlet. In these contours, it is clear that in the front of the inducer there is a ring-type vortex rope which rotates with the flow.

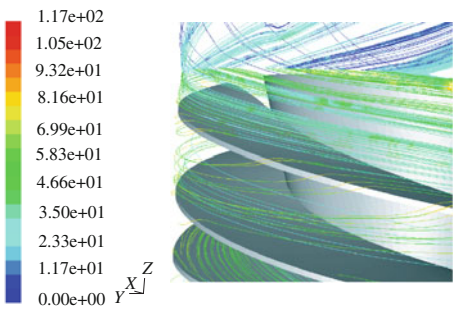

(speed unit: m/s)

Fig. 7.16 Particle trajectory in inducer (speed unit m/s)

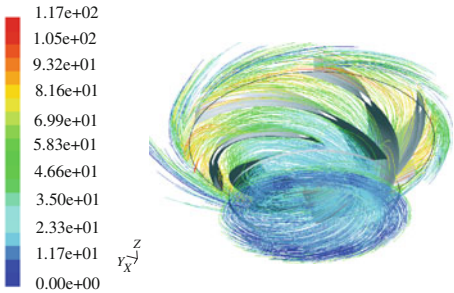

(speed unit: m/s)

Fig. 7.17 Particle trajectory in impeller (speed unit m/s)

7.5.3 Leakage Flow in Impeller

Figure 7.16 illustrates the particle trajectory in the inducer and Fig. 7.17 shows the particle trajectory in impeller under the operation condition of rotating speed 13,000 r/min.

The leakage flow can be clearly seen at the tip of the two rotational rotors, one being the axial inducer, and another being the semi-open type of centrifugal impeller.

References

Gehrer, A., Schmidl, R., & Sadnik, D. (2006). Kaplan turbine runner optimization by numerical flow simulation (CFD) and an evolutionary algorithm, *Proceedings of 23rd IAHR Symposium on Hydraulic Machinery and Systems*, Paper No. F125.

Germano, M., Piomelli, U., Moin, P., & Cabot, W. H. (1991). A dynamic sub-grid scale eddy viscosity model. *Physics of Fluids, A*(3), 1760–1765.

Hui, W. H., Li, P. Y., & Li, Z. W. (1999). A unified coordinate system for solving the two-dimensional Euler equations. *Journal of Computational Physics, 153*, 596–637.

Johnson, D. A., & King, L. S. (1985). A mathematically simple turbulence closure model for attached and separated turbulent boundary layers. *AIAA Journal, 23*, 1684–1692.

Kim, W., & Menon, S. (1995). A new dynamic one-equation subgrid-scale model for large eddy simulation, *Proceedings of the 33rd Aerospace Sciences Meeting and Exhibit*, Reno, NV

Levy, Y., Degani, D., & Seginer, A. (1998). Graphical visualization of vortical flow by means of helicity. *AIAA Journal, 28*, 1347–1352.

Lindsjö, H., Lörstad, D., & Fuchs, L. (2004). Modeling of the unsteady transport of bubbles past a Kaplan turbine model, *Proceedings of 22nd IAHR Symposium on Hydraulic Machinery and Systems*, Paper No. B3(1).

Liu, S. H., Shao, J., Wu, S. F., & Wu, Y. L. (2008). Numerical simulation of pressure fluctuation in Kaplan turbine. *Science in China Series E: Technological Sciences, 51*(8), 1137–1148.

Liu, S. H., Li, S. C., & Wu, Y. L. (2009), Pressure fluctuation prediction of a model Kaplan turbine by unsteady turbulent flow simulation, *ASME Journal of Fluids Engineering*, *131*(10), No. 101102.

Muntean, S., Balint, D., & Susan-Resiga, R. (2004). 3D Flow analysis in the spiral case and distributor of a Kaplan turbine, *Proceedings of 22nd IAHR Symposium on Hydraulic Machinery and Systems*, Paper No. A10-2.

Nicoud, F., & Ducros, F. (1999). Subgrid-scale modeling based on the square of the velocity gradient tensor. *Flow, Turbulence and Combustion, 62*, 183–200.

Nilsson, H., & Davidson, L. (2000). A Numerical comparison of operation in a Kaplan water turbine, focusing on tip clearance flow, *Proceeding of the 20th IAHR Symposium on Hydraulic Machinery and Systems,* Paper No. CFD-F12.

Nilsson, H., & Davidson, L. (2002). Validations and investigations of the computed flow in the GAMM Francis runner and the *Hölleforsen* Kaplan runner, *Proceedings of the 21st IAHR Symposium on Hydraulic Machinery and Systems*, Paper No. A-35.

Skotak, A. (1999). Draft tube swirl flow modeling, *Proceedings of the IAHR WG "The Behavior of Hydraulic Machinery under Steady Oscillatory Conditions*", Brno.

Smagorinsky, J. (1963). General circulation experiments with the primitive equations, the basic experiment. *Monthly Weather Review, 91*, 99–164.

Sodja, J. (2007). *Turbulence models in CFD*. Dissertation: University of Ljubljana.

Spalart, P. R., Jou, W.-H., Stretlets, M., & Allmaras, S. R. (1997). Comments on the feasibility of LES for wings and on the hybrid RANS/LES approach, advances in DNS/LES, *Proceedings of the First AFOSR International Conference on DNS/LES*.

Speziale, C. G., & Thangam, S. (1992). Analysis of a RNG based turbulence model for separated flows. *International Journal of Engineering Science, 30*, 1379–1388.

Strelets, M. (2001). Detached eddy simulation of massively separated flows, *AIAA* 2001–0879.

Tomas, L., Traversaz, M., & Sabourin, M. (2004). An approach for Kaplan turbine design, Hydraulic Machinery and Systems, *Proceedings of 22nd IAHR Symposium on Hydraulic Machinery and Systems*, paper No. A2-1.

Ruprecht, A., Bauer, C., Gentner, C., & Lein G. (1999). Parallel Computation of Stator-Rotor Interaction in an Axial Turbine, *Proceeding of ASME PVP Conference, CFD Symposium*, Boston.

Ruprecht, A., Heitele, M., & Helmrich, T. (2000). Numerical Simulation of a Complete Francis Turbine including unsteady rotor/stator interactions, *Proceedings of 20th IAHR Symposium*, paper No. CFD S03.

Ruprecht, A. (2002). Numerische strömungssimulation am beispiel hydraulischer strömungsmaschinen, *Habilitationsschrift*, Universität Stuttgart.

Wu, W.Z., Liu, S.H., Zhang L., Xu, D.H., & Wu, Y.L. (2002). Three-dimensional unsteady turbulent flow simulation through hydraulic machinery. *Proceedings of 4th International Conference on Pumps and Fans*, pp. 393–398.

Wu, X. J, Liu, S. H., & Wu, Y. L. (2006). Detached eddy simulation for model hydroturbine. *Proceedings of ASME Joint U.S.-European Fluids Engineering*. Miami, USA, FEDSM2006-98081.

Wu, Y. L., Liu, S. H., Dou, H.-S., Wu, S. F., & Chen, T. J. (2012). Numerical prediction and similarity study of pressure fluctuation in a prototype Kaplan turbine and the model turbine. *Computers and Fluids, 56*, 128–142.

Xu, Z. H. (2004). Turbulent flow analysis and its induced vibration in a high speed centrifugal pump, Ph. Doctor Dissertation, *Tsinghua University in China.*

You, D., & Moin, P. (2007). A dynamic global-coefficient subgrid-scale eddy-viscosity model for large-eddy simulation in complex geometries. *Physics of Fluids, 19*, 065110.

Chapter 8
Structural Dynamic Analysis in Hydraulic Machinery

The study of structural dynamics focuses on a structure's behaviour when it is subjected to dynamic loading. Dynamic analysis can be used to research dynamic displacements, time-history, and modal analysis. A static load is one that does not vary, whereas a dynamic load changes with time. If it changes slowly, the structure's response may be determined with static analysis. However, if it varies quickly, the response must be determined with dynamic analysis. Dynamic analysis for simple structures can be carried out manually, but for complex structures, FEM can be applied to calculate the mode shapes and frequencies (see Bathe and Wilson 1976).

8.1 Introduction to Structural Dynamic Analysis

A dynamic load can pose a significantly larger effect than a static load of the same magnitude because the structure is unable to respond the loading in deflecting (Clough and Penzien,1975). The increase in the effect of a dynamic load is given in the dynamic amplification factor (DAF) (Wikipedia 2012):

$$DAF = u_{\max}/u_{\text{static}}$$

where u is the deflection of the structure due to the load. The DAF for a given loading can be read from the graph, and the static deflection can be easily calculated for simple structures and the dynamic deflection found.

A full time-history implies the response of a structure over time, during and after the application of a load. To find the full time-history of a structure's response one must solve the structure's equation of motion. The Heaviside Step Function is a reasonable model to find the application of many real loads, such as the sudden addition of a piece of furniture, or the removal of a prop to a newly cast concrete floor. However, in reality loads are usually built up over a period of time instead of imposed instantaneously.

Any real structure will dissipate energy (mainly through friction). This can be modeled by means of modifying the DAF:

Y. Wu et al., *Vibration of Hydraulic Machinery*,
Mechanisms and Machine Science 11, DOI: 10.1007/978-94-007-6422-4_8,

$$DAF = 1 + e^{-c\pi}$$

where $c = (\text{Damping coefficient})/(\text{Critical Damping coefficient})$ is 2–10 % depending on the type of construction. Generally damping would be ignored for transient events (for example, an impulse load), but not for non-transient events.

A modal analysis calculates the frequency modes or natural frequencies of a given system, but not necessarily its full time-history response to a given input. The natural frequency of a system is dependent only on the stiffness of the structure and the mass which participates with the structure (including self-weight), and it is not dependent on the load function. It is useful to know the modal frequencies of a structure as it ensures that frequency of any applied periodic loading will not coincide with a modal frequency and hence eliminate resonance, one that leads to large vibrations. The method is:

(a) Find the natural modes (the shape adopted by a structure) and natural frequencies
(b) Calculate the response of each mode
(c) Superpose the response of each mode to find the full modal response to a given loading (optional).

It is possible to calculate the frequency of different mode shapes of the system manually with the energy method. Given the mode shape of a multiple degree of freedom system, one can find an "equivalent" mass, stiffness, and applied force for a single degree of freedom system. The basic mode shape of simple structure can be found through inspection, but this is not a conservative method. Rayleigh's principle states: The frequency ω of an arbitrary mode of vibration, calculated by the energy method, is always greater than or equal to the fundamental frequency ω_n.

For an assumed mode shape of a structural system with mass, M; stiffness, EI (Young's modulus, E, multiplied by the second moment of area, I); and applied force, $F(x)$, then

Equivalent mass, $M_{eq} = \int M\bar{u}^2 \mathrm{d}x$, Equivalent force, $M_{eq} = \int F\bar{u}\mathrm{d}x$, Equivalent stiffness, $k_{eq} = \int EI\left(\frac{\mathrm{d}^2\bar{u}}{\mathrm{d}x^2}\right)\mathrm{d}x$, then

$$\omega = \sqrt{k_{eq}/M_{eq}}.$$

The complete modal response to a given load $F(x, t)$ is $u(x, t) = \sum u_n(x, t)$. The summation can be carried out using one of three common methods:

1. Superpose complete time histories of each mode (time consuming, but exact);
2. Superpose the maximum amplitudes of each mode (quick but conservative);
3. Superpose the square root of the sum of squares (good estimate for well-separated frequencies, but unsafe for closely spaced frequencies).

To superpose the individual modal responses manually, one should calculate them with the energy method: $T = 2\pi\omega$.

Assume that the rise time t_r is known, and it is possible to read the *DAF* from a standard graph. The static displacement can be calculated with $u_{\text{static}} = F_{1,eq}/k_{1,eq}$. The dynamic displacement for the chosen mode and applied force can then be found from $u_{\max} = u_{\text{static}} DAF$.

For real systems there is often mass participating in the forcing function (such as the mass of the ground in an earthquake) and the mass participating in inertia effects (the mass of the structure itself, M_{eq}). The modal participation factor Γ is a comparison of these two masses:

$$\Gamma = \sum M_n \bar{u}_n \Big/ \sum M_n \bar{u}_n^2.$$

8.2 Principle of Dynamic Analysis of Hydraulic Machinery

Dynamic analysis of three dimensional structural systems is a direct extension of static analysis. The elastic stiffness matrices are the same for both dynamic and static analysis. It is only necessary to lump the mass of the structure at the joints. The addition of inertia forces and energy dissipation forces must satisfy dynamic equilibrium. In this section, the principals of dynamic analysis of hydraulic machinery comprise the following four parts: the dynamic equations of free vibration, the governing equations of the fluid–structure interaction (FSI) of hydraulic machinery in still fluid or in moving fluid, and the structure dynamic equations considering moving flow for FEM

8.2.1 Foundation of Free Vibration in Elastic Structures

The equation for free vibration in non-damping elastic structures is

$$[\boldsymbol{M}]\{\ddot{\boldsymbol{u}}\} + [\boldsymbol{K}]\{\boldsymbol{u}\} = 0 \tag{8.1}$$

where $[\boldsymbol{M}]$ is the structure's mass matrix; $[\boldsymbol{K}]$ is the structure's elastic matrix; and $\{\boldsymbol{u}\}$ is the structure's displacement vector.

For linear systems, the solution of this free vibration is a simple harmonic vibration, i.e.,

$$\{\boldsymbol{u}\} = \{\Phi\}_i \cos\ \omega_i t \tag{8.2}$$

where ω_i is ith order frequency; $\{\boldsymbol{\Phi}\}_i$ is the modal of the ith order frequency; and t is time. The equation then becomes

$$\left(-\omega_i^2[\boldsymbol{M}] + [\boldsymbol{K}]\right)\{\Phi\}_i = 0. \tag{8.3}$$

Since $\{\boldsymbol{\Phi}\}_i$ cannot equal zero, the equation reduces to the following term:

$$[\boldsymbol{K}] - \omega_i^2[\boldsymbol{M}] = 0. \tag{8.4}$$

Its solution will yield natural frequencies and vibration modals for a free vibration system.

8.2.2 Governing Equations of FSI in Still Fluid

8.2.2.1 Approaches of FSI

Fluid–structure interaction (FSI) is the interaction of some movable or deformable structure with an internal or surrounding fluid flow. Fluid–structure interactions can be stable or oscillatory. In oscillatory interactions, the strain induced in the solid structure forces it to move so that source of strain is reduced, and the structure returns to its former state only for the process to repeat (see Dubcová et al. 2008).

Fluid–structure interaction and multiphysics problems in general are often too complex to solve analytically, so they have to be analyzed by means of experiments or numerical simulation. Research in the fields of computational fluid dynamics and computational structural dynamics is still ongoing but the maturity of the research enables numerical simulation of fluid–structure interaction. Two main approaches exist for the simulation of fluid–structure interaction problems.

Monolithic approach: The equations governing the flow and the displacement of the structure are solved simultaneously. It is the fully coupled method, where the fluid and structure problem are solved within the same code and the same grids. This method is applied for strongly coupled problems, e.g., for modal analyses.

Partitioned approach: The equations governing the flow and the displacement of the structure are solved separately, with two distinct solvers.

The monolithic approach requires a code that is developed for this particular combination of physical problems whereas the partitioned approach preserves software modularity because an existing flow solver and structural solver are coupled. Moreover, the partitioned approach solves the flow equations and the structural equations with different, possibly more efficient techniques which are developed specifically for either flow equations or structural equations. On the other hand, a coupling algorithm is required in partitioned simulations.

8.2.2.2 Full Coupled Equation for FSI in Still Fluid

In structural dynamics, the dynamic equation of stricture is

$$[\boldsymbol{M}_s]\{\ddot{\boldsymbol{u}}\} + [C_s]\{\dot{\boldsymbol{u}}\} + [\boldsymbol{K}_s]\{\boldsymbol{u}\} = \{\boldsymbol{F}_s\} \tag{8.5}$$

where $[\boldsymbol{M}_s]$ is the structure mass matrix; $[\boldsymbol{C}_s]$ is the structure damping matrix; $[\boldsymbol{K}_s]$ is the structure stiffness matrix; $\{\boldsymbol{F}_s\}$ is the applied load vector on the structure, in this case, $\{\boldsymbol{F}_s\}$ pressure vector on the nodes; and $\{\boldsymbol{u}\}$ is the nodal displacement vector of the structure.

The governing equations for fluid dynamics are the Navier–Stokes (N–S) equations and the mass continuity equation. The simple form of FSI is still fluid and structure coupling. Therefore in that case the assumptions can be made as follows (Woyjak 1992).

The fluid is slightly compressible (density changes due to pressure variations); the fluid is non-viscous (no viscous dissipation); the flow is irrotational; and there is no mean fluid flow. Changes of mean density and pressure in different areas of the fluid domain remain small. The fluid governing equations may be changed to sound wave equation, i.e.,

$$\frac{1}{c^2}\frac{\partial^2 p}{\partial t^2} - \Delta p = 0 \tag{8.6}$$

where c is the wave speed in the fluid, $c = \sqrt{k/\rho_o}$; p is the fluid pressure induced from the sound wave and forces acted on fluid; Δ is the Laplace operator; k is the fluid volumetric modulus; and ρ_o is the mean fluid density.

The sound equation (8.6) and the dynamic equation of structure can describe the FSI in still fluid with fluid pressure on the structure wall and displacement of the wall:

$$\{\boldsymbol{n}\} \cdot \{\nabla p\} = -\rho_0 \{\boldsymbol{n}\} \cdot \{\ddot{\boldsymbol{u}}\} \tag{8.7}$$

where $\{\boldsymbol{n}\}$ is the unit normal vector on interface and $\{\nabla p\}$ is the pressure gradient (vector) along the normal vector.

Considering the interface effects, the Eq. (8.6) can be discritized as

$$[\boldsymbol{M}_f]\{\ddot{\boldsymbol{p}}\} + [\boldsymbol{C}_f]\{\dot{\boldsymbol{p}}\} + [\boldsymbol{K}_f]\{\boldsymbol{p}\} + [\boldsymbol{M}_{sf}]\{\ddot{\boldsymbol{u}}\} = 0 \tag{8.8}$$

where $[\boldsymbol{M}_f]$ is fluid equivalent "mass" matrix; $[\boldsymbol{C}_f]$ is the fluid equivalent "damping" matrix; $[\boldsymbol{K}_f]$ is the fluid equivalent "stiffness matrix"; $\{p\}$ is the fluid pressure "load", which makes structure displacements at the interface; $[\boldsymbol{M}_{sf} = \rho_f \boldsymbol{R}]$ is defined as equivalent coupling "mass" matrix acting to fluid; and $[\boldsymbol{R}]$ is the fluid "load" produced by structure displacement at the interface.

In order to account for the effect of pressure to structure on the interface, one would modify Eq. (8.5) as

$$[\boldsymbol{M}_s]\{\ddot{\boldsymbol{u}}\} + [\boldsymbol{C}_s]\{\dot{\boldsymbol{u}}\} + [\boldsymbol{K}_s]\{\boldsymbol{u}\} + [\boldsymbol{K}_{fs}]\{\boldsymbol{p}\} = \{\boldsymbol{F}_s\} \tag{8.9}$$

where $[\boldsymbol{K}_{fs} = -\boldsymbol{R}]$ is defined as equivalent coupling "stiffness" matrix, which changes due to pressure variations.

In the case of a monolithic approach, the equations governing the flow and the displacement of the structure are solved simultaneously, with a single solver. The structural dynamics equation is coupled with the equations of the fluid, which can be described as the following discretized equation:

$$\begin{bmatrix} [M_s] & 0 \\ [M_{sf}] & [M_f] \end{bmatrix} \begin{Bmatrix} \{\ddot{u}\} \\ \{\ddot{p}\} \end{Bmatrix} + \begin{bmatrix} [C_s] & 0 \\ 0 & [C_f] \end{bmatrix} \begin{Bmatrix} \{\dot{u}\} \\ \{\dot{p}\} \end{Bmatrix} + \begin{bmatrix} [K_s] & [K_{fs}] \\ 0 & [K_f] \end{bmatrix} \begin{Bmatrix} \{u\} \\ \{p\} \end{Bmatrix} = \begin{Bmatrix} \{F_s\} \\ 0 \end{Bmatrix}. \tag{8.10}$$

To simplify the expression, one might use the following equation:

$$\begin{bmatrix} \boldsymbol{M}_s & 0 \\ \boldsymbol{M}_{sf} & \boldsymbol{M}_f \end{bmatrix} \begin{Bmatrix} \ddot{\boldsymbol{u}} \\ \ddot{\boldsymbol{p}} \end{Bmatrix} + \begin{bmatrix} \boldsymbol{C}_s & 0 \\ 0 & \boldsymbol{C}_f \end{bmatrix} \begin{Bmatrix} \dot{\boldsymbol{u}} \\ \dot{\boldsymbol{p}} \end{Bmatrix} + \begin{bmatrix} \boldsymbol{K}_s & \boldsymbol{K}_{fs} \\ 0 & \boldsymbol{K}_f \end{bmatrix} \begin{Bmatrix} \boldsymbol{u} \\ \boldsymbol{p} \end{Bmatrix} = \begin{Bmatrix} \boldsymbol{F}_s \\ 0 \end{Bmatrix}. \tag{8.11}$$

8.2.3 FSI Governing Equations in Moving Fluid

In order to examine the dynamical behaviour of the long and thin structure of the blades of hydraulic machinery, the coupled simulations considering fluid flow and structural behaviour need to be performed. FSI governing equations in small or large deformations of the structure are presented in this section.

8.2.3.1 FSI Governing Equations in Small Deformation of Structure

There are two strategies for coupled solutions of dynamic fluid and structure interaction. One is the loosely coupled method (partitioned approach) with dynamic forces and structural displacement exchanged as boundary conditions for each other at every time step.

In the partitioned approach with small deformations in structure, it is assumed that blade vibrations in the hydraulic machinery cause unsteady effects that are significantly smaller than unsteady effects due to instability of the flow, sometimes even neglectable. That is to say, there is no feedback of blade motion on the flow.

The water is considered to be incompressible. A time-dependent Reynolds average Navier–Stokes (RANS) simulation is performed to calculate the flow field in hydraulic machinery. The continuity equation and the momentum equations for the fluid within still frame (spiral case, stay vanes, wicket gates, and the draft tube) are the Reynolds average Navier–Stokes equations of absolute velocity and the continuity equation.

In order to close those equations in turbulent flows, the turbulence model must be adopted.

For rotating components of hydraulic machinery, such as the runner and impeller, the continuity equation and the momentum equations for the flow expressed by relative velocity in the rotational frame must be used. Sometimes those equations in the frame may be written in absolute velocity, and turbulence models must be applied to close the governing equations. For the structure of hydraulic machinery in this approach, the transient dynamic equilibrium equation for the stresses in a linear structure is Eq. (8.5).

8.2.3.2 FSI Governing Equations in Large Deformation of Structure

In the case of a large displacement, the deformation of the fluid domain cannot be neglected and methods with moving meshes must be employed. The fluid and structure interaction represents in its generality a very complicated process.

Required considerations are the simulation of viscous flow, changes of the flow domain in time, nonlinear behavior of the elastic structure, and simultaneously solving the evolution systems for both the fluid flow and the oscillating structure.

Methods with moving meshes must be employed to investigate a vibrating structure with large displacements in which changes of the fluid domain cannot be neglected. An appropriate choice is to apply the Arbitrary Lagrangian–Eulerian (ALE) method.

Due to the mesh deformation, the velocity of the grid nodes $\{\boldsymbol{v}_G\}$ results in the Arbitrary-Langrange-Euler (ALE) formulation:

$$\frac{\partial v_i}{\partial x_i} = 0 \tag{8.12}$$

$$\frac{\partial v_i}{\partial t} + (v_j - v_{Gj})\frac{\partial v_i}{\partial x_j} = -\frac{1}{\rho}\frac{\partial p}{\partial x_i} + \frac{\partial v_i}{\partial x_j}\left[\frac{\mu}{\rho}\left(\frac{\partial v_i}{\partial x_j} + \frac{\partial v_j}{\partial x_i}\right) - \overline{v_i' v_j'}\right] + f_{Bi} \tag{8.13}$$

where v_Gj is the velocity component of grid nodes, and f_{Bi} is body force component.

For engineering problems the partitioned approach is usually employed. In order to account for the coupling and to avoid unstable simulations, some coupling schemes have been developed as shown in Fig. 8.1 (Lippold and Ogor 2007).

8.2.4 Structure Dynamic Equations Considering Moving Flow for FEM

When hydraulic machinery is in an operating condition, the centrifugal force of the runner/impeller rotation causes an initial stress field in the runner/impeller. The initial stress will change the natural frequencies of the runner and its blade. So it is necessary to solve the eigenvalues of runner or blade moving equations for its operation safety.

8.2.4.1 Dynamic Equations in Centrifugal Flow Field of a Runner

In moving flow conditions, especially in rotating runner/impeller, the structure will be affected by a centrifugal force besides the inertial force and damping force, as well as the pre-stress force. The structure dynamic equations considering moving flow in FEM are as follows:

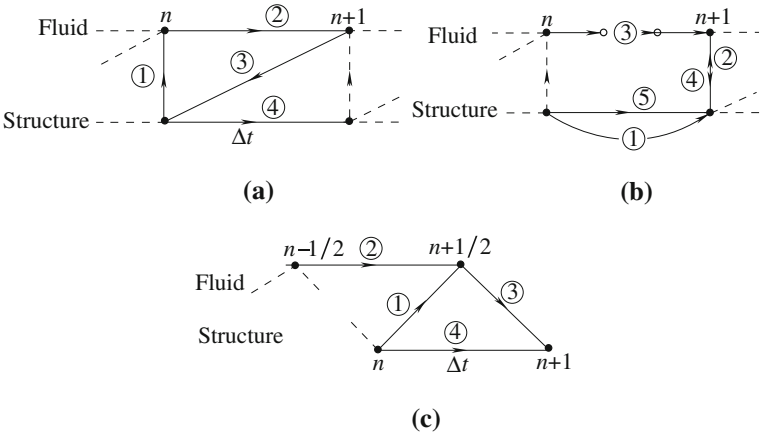

Fig. 8.1 Exchange schemes in partitioned approach (Lippold and Ogor 2007). **a** (*1*) deformations for time step *n*; (*2*) update grid and integrate fluid field to time step $n + 1$; (*3*) put fluid loads to structure; (*4*) advance structural solution to time step $n + 1$. **b** (*1*) predictor for structure to time step $n + 1$; (*2*) deformations for time step $n + 1$; (*3*) update grid and integrate fluid field to time step $n + 1$; (*4*) put fluid loads to structure to time step $n + 1$; (*5*) advance structural solution to time step $n + 1$. **c** (*1*) Deformed grid at time $n + 1/2$; (*2*) update grid and integrate fluid field to time step $n + 1/2$; (*3*) put fluid loads to structure; (*4*) advance structural solution to time step $n + 1$

$$[\boldsymbol{M}]\{\ddot{\boldsymbol{u}}\} + [\boldsymbol{C}]\{\dot{\boldsymbol{u}}\} + [\boldsymbol{M_G}]\{\dot{\boldsymbol{u}}\} + [\boldsymbol{K}]\{\boldsymbol{u}\} - [\boldsymbol{M_C}]\{\boldsymbol{u}\} = \{\boldsymbol{Q_c}\} + \{\boldsymbol{Q_p}\} - \{\boldsymbol{F_\sigma}\} + \{\boldsymbol{R}\} \tag{8.14}$$

where $[\boldsymbol{M}]$ is structure mass matrix; $[\boldsymbol{C}]$ is structure damping matrix; $[\boldsymbol{M_G}]$ is structure adding mass matrix caused by Coriolis force; $[\boldsymbol{K}]$ is structure stiffness matrix; $[\boldsymbol{M_c}]$ is the structure adding mass matrix caused by centrifugal force; $\{\boldsymbol{Q_c}\}$ is the centrifugal force vector before structure deformation; $\{\boldsymbol{Q_p}\}$ is the equivalent flow pressure loading vector; $\{\boldsymbol{F_\sigma}\}$ is the equivalent loading vector caused by initial stresses at nodes; $\{\boldsymbol{R}\}$ is the concentrated force vector at nodes; and $\{\boldsymbol{Q_c}\} + [\boldsymbol{M_c}]\{\boldsymbol{u}\}$ is the centrifugal force vector after structure deformation.

8.2.4.2 Static Equations in Centrifugal Flow Field of a Runner

When the runner is in a free vibration, initial stresses caused by external forces and other effects change Eq. (8.14) without damping to be simplified as

$$[\boldsymbol{M}]\{\ddot{\boldsymbol{u}}\} + [\boldsymbol{M_G}]\{\dot{\boldsymbol{u}}\} + [\boldsymbol{K}]\{\boldsymbol{u}\} - [\boldsymbol{M_C}]\{\boldsymbol{u}\} = \{\boldsymbol{Q_c}\}. \tag{8.15}$$

When the runner is at a standstill, i.e., $[\boldsymbol{M_G}] = [\boldsymbol{M_c}] = 0$, $\{\boldsymbol{Q_c}\} = 0$ the equation is transformed to the following equation in order to solve the static natural frequencies and modals (without consideration of FSI effects)

$$[\boldsymbol{M}]\{\ddot{\boldsymbol{u}}\} + [\boldsymbol{K}]\{\boldsymbol{u}\} = 0. \tag{8.16}$$

When the runner is rotating, the Coriolis force matrix $[\boldsymbol{M}_G]$ is proportional to a rotating speed of runner Ω. With a small Ω, it may be neglected and result in

$$[\boldsymbol{M}]\{\ddot{\boldsymbol{u}}\} + [\boldsymbol{K}]\{\boldsymbol{u}\} - [\boldsymbol{M}_C]\{\boldsymbol{u}\} = \{\boldsymbol{Q}_e\}. \tag{8.17}$$

Owing to the constant rotating speed, the centrifugal force would place the runner structure in a newly deformed equilibrium. Free vibration of the rotating structure with constant centrifugal force effects will have new characteristics apart from that in still condition.

8.2.4.3 Solution of Runner or Blade Vibration Eigenvalues in the Moving Flow Field

The solution of natural frequencies and modals of free vibration for a runner/impeller structure with a constant centrifugal force in moving flow condition may be carried out in the following procedure.

In the beginning it is necessary to solve the following static equation:

$$[\boldsymbol{K}]\{\boldsymbol{u}\} - [\boldsymbol{M}_C]\{\boldsymbol{u}\} = \{\boldsymbol{Q}_e\} \tag{8.18}$$

to get the new static balancing condition and the displacements due to the effects of centrifugal force.

Secondly, according to the solutions of $\{\boldsymbol{u}\}$ from the foregoing equation, one must modify the runner coordinates to form a new runner shape. Based on the new shape of the runner, the new stiffness matrix $[\boldsymbol{K}_t]$ should be assembled.

Then, one should solve the equation for the new free vibration dynamic, which includes the effect of the centrifugal force on the rotating state, to get the eigenvalues of the runner at new rotating balance:

$$[\boldsymbol{M}]\{\ddot{\boldsymbol{u}}\} + ([\boldsymbol{K}_t] - [\boldsymbol{M}_C])\{\boldsymbol{u}\} = 0. \tag{8.19}$$

This equation is used to calculate the runner's natural frequencies and modals with the effects of rotation and centrifugal force.

Equations (8.16) and (8.18) come down to solutions of eigenvalues for a dynamic system with n degrees of freedom which is expressed in the following equation:

$$[\boldsymbol{K}][\boldsymbol{\phi}] = [\boldsymbol{M}][\boldsymbol{\phi}][\Lambda] \tag{8.20}$$

where $[\boldsymbol{\phi}]$ is the matrix of the equation character vectors: $[\boldsymbol{\phi}] = [\{\boldsymbol{\phi}_1\}\{\boldsymbol{\phi}_2\}\cdots\{\boldsymbol{\phi}_n\}]$; $[\Lambda]$ is the character values diagonal matrix of the equation: $[\Lambda] = \mathrm{diag}[\omega j^2](i = 1, 2, \cdots n)$; and $[\boldsymbol{M}]$ is the structure mass matrix; and $[\boldsymbol{K}]$ is the structure (runner) stiffness matrix.

8.2.4.4 General Dynamic Equations with Moving Flow Load in FEM

Considering the added load of fluid flow only, the discretized dynamic equations of structure for moving flow in FEM are

$$[\boldsymbol{M}]\{\ddot{\boldsymbol{u}}\} + [\boldsymbol{C}]\{\dot{\boldsymbol{u}}\} + [\boldsymbol{K}]\{\boldsymbol{u}\} = \{\boldsymbol{F}(t)\} + \{\boldsymbol{R}_f(t)\} \tag{8.21}$$

where $\{\boldsymbol{F}(t)\}$ is the loading force at nodes; $\{\boldsymbol{R}_f(t)\}$ is the equivalent fluid loading force at nodes, which is the function of pressure. Then Eq. (8.24) can be transformed to

$$[\boldsymbol{M}]\{\ddot{\boldsymbol{u}}\} + [\boldsymbol{C}]\{\dot{\boldsymbol{u}}\} + [\boldsymbol{K}]\{\boldsymbol{u}\} = \{\boldsymbol{P}(p)\}. \tag{8.22}$$

8.3 Modal Analysis on Hydraulic Machinery

In order to take into account the added mass effect due to surrounding fluid, one has to treat the system as a fluid-structure interaction. In this case, the structural dynamics equation is coupled with equations of fluid, which can be described as the discretized Eq. (8.11) (Woyjak 1992).

8.3.1 Modal Analysis of a Model Turbine in Still Water by Monolithic Approach

Liang et al. (2006) conducted the modal analysis on a Francis turbine runner using the equation for consideration of fluid added to mass effect. Based on the cyclical symmetrical characteristic of the structure, one sector including one blade, covering an angle of 360/17 degrees was used to do the simulation. Then the results were expanded to the whole runner. Before definition of the final mesh configuration, the influence of the element shape and the mesh density was checked.

To complete the simulation model in water, the mesh of the runner was surrounded by a cylindrical fluid domain in order to consider the cyclic symmetric characteristic of the runner. The fluid mesh was extended from the structure mesh so that the same set of nodes was shared between both domains on the interface. The same type of hexahedral element was used to build up the fluid mesh, containing 29,460 nodes and 24,137 elements for each sector. The boundary conditions were carefully treated according to the experimental test (Liang et al. 2006).

The model runner had 17 blades and a diameter of 409 mm. The material used was a bronze alloy with density of 8,300 kg/m^3 and Young's Modulus of 110 Gpa.

The modal parameters of the runner, both in air and submerged in water, have been well determined by the experiments and the simulation. Given the cyclical symmetric characteristics of Francis turbine runners, the vibration modes can be

classified according to the numbers of nodal diameters (ND) appearing on the band part.

Under the condition ND = 0, the modes are singlet and natural frequencies are distinct. The modes with ND0 are doublet; they have a pair of mode shapes with the same natural frequency. The natural frequencies found for the same mode shapes are listed in Table 8.1.

The absolute maximum difference in natural frequency values between experiment and simulation is about 3.6 %. Moreover, the mode shapes also represent regular consistency between simulation and experiment.

Comparing the results in air and in water, one can observe a significant decrease in the natural frequencies. This reduction is due to the effect of the added mass induced by the surrounding water. The added mass effect can be quantified by the ratio, δ, of the frequency in water, f_w, to the frequency in air, f_a, for each mode shape:

$$\delta = f_w / f_a \tag{8.23}$$

which is listed in Table 8.1. Notice that the natural frequencies are brought down considerably by the presence of fluid, and the frequency ratio shows a significant variation from 0.61 to 0.90, depending on the corresponding mode shape.

The damping values obtained via experiment for the runner in air and submerged in water are listed in Table 8.2. The damping has low values in all the modes, which is typical behavior for a structure vibrating with small amplitudes and high frequencies in stagnant fluid in absence of wave radiation. With the presence of water, the damping increases and varies depending on the mode shapes, but not high enough to affect natural frequencies significantly.

The mode shapes of the band for the runner in air are shown in Figs. 8.2 and 8.3 from a bottom view. Similar mode shapes are obtained in water (Liang et al. 2006).

Table 8.1 Natural frequencies of the runner in air and in water (Hz) and frequency ratio

		0ND	1ND	2ND	3ND	4ND	5ND
Exp. air		417.50	616.75	373.50	487.50	573.75	649.75
Exp. water	f_w/Hz	370.50	481.50	279.50	331.25	359.00	400.00
	δ	0.89	0.78	0.75	0.68	0.63	0.62
Sim. air		425.87	635.53	370.80	485.61	568.18	635.46
Sim. water	f_w/Hz	383.28	498.90	280.17	335.49	362.34	387.89
	δ	0.90	0.79	0.76	0.69	0.64	0.61

Note Exp. = experiment, Sim. = simulation, 0ND: Torsion, 1ND: Torsion. Flexion

Table 8.2 Dampings obtained by experiment

	0ND (Torsion)	1ND (Flexion)	2ND	3ND	4ND	5ND
In air	0.0047	0.0033	0.0056	0.0068	0.0040	0.0039
In water	0.0068	0.0120	0.0070	0.0082	0.0070	0.0069

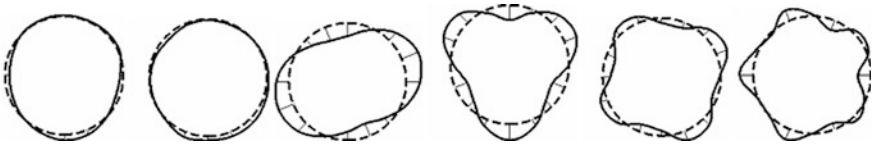

Fig. 8.2 *Mode shapes* obtained by test in air (ordered by ND from *left* to *right*)

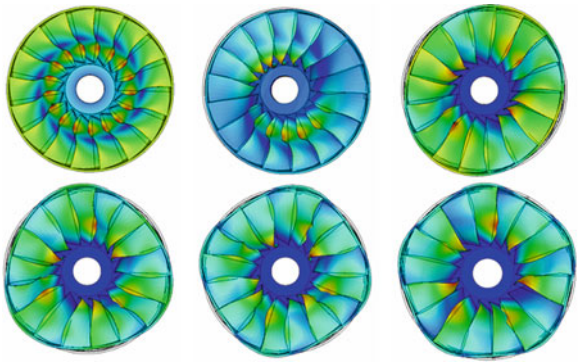

Fig. 8.3 *Mode shapes* obtained by simulation in air (ordered by ND from *left*)

8.3.2 Modal Analysis of a Turbine in Moving Water by Partitional Approach

Liu et al. (2008a) conducted the modal analysis of a prototypical water turbine in moving water by partitional approach. The physical model of runner blades for a Francis turbine in a power station was established, as is shown in Fig. 8.4, which is the geometric model of whole flowing passage. Basic parameters of the turbine are:

Design head: $H = 20$ m, design flow rate: $Q = 3.4$ m^3/s,
Rotational speed: $n = 428.5$ r/min, Number of stationary vanes: $Z_s = 8$,
Number of guide vanes: $Z_g = 16$, Height of guide vanes: $b_0 = 255$ mm,
Guide vane diameter: $D_0 = 986$ mm,
Diameter of runner: $D_1 = 840$ mm, Number of runner blades: $Z = 14$.

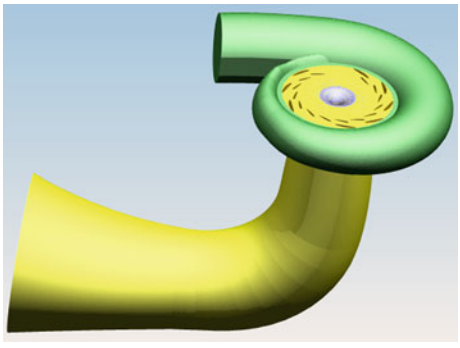

Fig. 8.4 3D model of all flowing parts of the turbine

Table 8.3 Runner natural frequency and frequency ratio at three flow rates

Order	Design flow rate		Small flow rate		Large flow rate		In air (Hz)
	In water (Hz)	Ratio δ	In water (Hz)	Ratio δ	In water (Hz)	Ratio δ	
1	1,756	0.800	1,441	0.656	1,590	0.724	2,195
2	1,758	0.801	1,442	0.656	1,592	0.724	2,197
3	1,759	0.798	1,443	0.654	1,593	0.722	2,204
4	1,759	0.798	1,444	0.655	1,593	0.723	2,204
5	1,761	0.796	1,445	0.653	1,595	0.721	2,210
6	1,762	0.793	1,446	0.651	1,596	0.719	2,221
7	1,763	0.776	1,447	0.638	1,597	0.704	2,269
8	1,764	0.773	1,448	0.635	1,598	0.701	2,280
9	1,765	0.771	1,449	0.634	1,599	0.699	2,287
10	1,765	0.771	1,449	0.633	1,599	0.698	2,288

In the work of Liu et al. (2008a), the partitional approach of FSI with consideration of large displacements of interfaces is adopted. The iterative computation method is applied to solve the coupling equations. This method is suitable for large scale problems and has relatively lower requirements for computer resources (see Sect. 8.4.2).

In the modal analysis, the runner blade in moving water is affected by centrifugal forces and dynamic pressure in a definite operation condition of runner, which is obtained through the steady flow simulation in the turbine. Then the static analysis of the runner baled is carried out to get the stiffness matrix under the centrifugal force and pressure, which will induce the initial stresses in the blade. Based on Eq. (8.23) the modal computation can be performed with consideration of the flow condition. This modal analysis is carried out in three different operation conditions:(1) design flow ($H = 20$ m, $Q = 3.40$ m^3/s), (2) small flow rate ($H = 20$ m, $Q = 2.38$ m^3/s), and (3) large flow ($H = 20$ m, $Q = 3.74$ m^3/s).

Table 8.3 shows the computational runner natural frequencies under three kinds of flow rate conditions and their frequency ratios with respect to frequency in air.

Table 8.3 indicates that the frequency ratio of the turbine is basically constant without significant variation at design flow rate. Values of the ratio become small under both off-design operation conditions. It can be understood that the calculated data of the frequency ratio by FSI with consideration of the flow conditions in Table 8.3 are larger than above tested data in still water.

8.4 Dynamic Analysis of Hydraulic Machinery

With increasing unit capacity and runner diameter, issues of unsteady flows in hydraulic turbines have attracted considerable attention. The energy transfer in a turbine is accompanied with pressure vibrations caused by vortexes, cavitations, and other complex flow phenomena in the flow path, which can give rise to

excessive blade vibration and lead to structural fatigue failures. Most research has focused on pressure fluctuations in flow path, such as those caused by RSI (rotor–stator interaction) effects, and the vortex rope in the draft tube. Recently a few researchers have measured dynamic stress in the blades. Comparison of unsteady flow calculation and the measured stress has implied that the dynamic stresses in blades are closely related to hydraulic instability.

8.4.1 Analysis of Dynamic Stresses in Kaplan Turbine Blades

In the work of Zhou and Wang (2007), the stresses in blades of a Kaplan turbine were analyzed using the partitional approach of FSI with small displacement. The prototype studied was a ZZA315-LJ-800 Kaplan turbine with a specific speed of 22.6, a runner diameter of 8 m, rated output of 204 MW, rated head of 47 m, and rated speed of 107 rpm. The stresses in blades were calculated under various operating conditions to analyze the relationship between the dynamic stresses and operating conditions. In the FSI, Zhou and Wang (2007) adopted the partitional approach, and assumed that blade vibrations causing unsteady effects are significantly smaller than unsteady effects due to instability of the flow, which sometimes are even negligible. That is to say, there is no feedback of blade motion on the flow.

The water was considered incompressible. A time-dependent Reynolds Average Navier–Stokes (RANS) simulation was performed to calculate the flow field in the Kaplan turbine path. The time-dependent RANS model was discretized via the control-volume technique through the SIMPLEC scheme with a second-order upwind scheme used for the convection terms and a central difference scheme for the diffusion terms in the momentum equations. The time step was 0.0056 s, which is 1/100 of the runner rotational period. This time step was validated as sufficient to capture some main pressure fluctuation frequencies such as rotational and blade passing frequency. The key problem was to transfer the pressure load p on the blades to the dynamic analysis code. To achieve this, grids on blade surfaces and the hub were identical for both fluid mesh and structure mesh. A small code was developed to generate an index for interface nodes in the two domains for the purpose of transferring data at each time. The advantage of this method is that pressure on the blades can be transferred precisely without any interpolation. The flow field simulation started first. For most cases, the frequencies and amplitudes of pressure vibrations on the monitoring nodes changed little after several rotational periods. Then the structure calculation was conducted and the calculation results were recorded for several periods.

During the calculations, two points on one blade pressure side ($p1$) and the suction side ($s1$) were selected as monitoring points (Fig. 8.5). Pressure fluctuations at the two points are shown in Fig. 8.6 for three typical conditions GK3, GK8 and GK10 (Table 8.4).

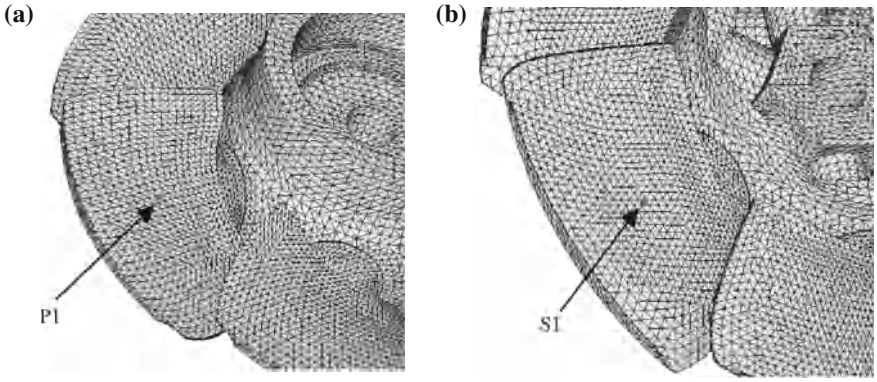

Fig. 8.5 Recording points on one blade. **a** Recording point *p1* on suction side. **b** Recording point *s1* on pressure side

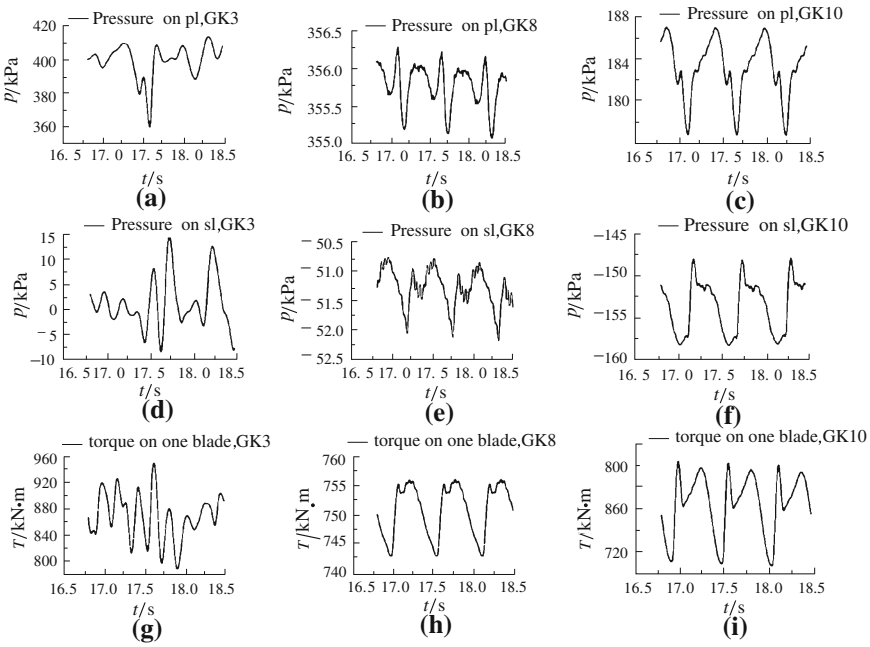

Fig. 8.6 Pressure fluctuations and torque on one blade for three operating conditions

Under conditions close to the optimum point and those with large blade angles and guide vane openings, pressure on the blade fluctuates with runner rotation frequency, f_n, as shown in Fig. 8.6b–f for cases GK8 and GK10. However, in cases with small blade angles and small guide vane openings, the blade pressure fluctuations are accompanied by increased turbulence and the fluctuations which does not exhibit any obvious periodic feature, as shown in Fig. 8.6a and d for condition GK3.

Table 8.4 Operation conditions of Kaplan turbine

Operation conditions	Working head H (m)	Power N (MW)	Guide vanes opening (%)	Blade angle (^{o})
GK3	61	100	36.21	5.57
GK8	53	150	59.03	11.72
CK10	43.8	235	94.6	25.82

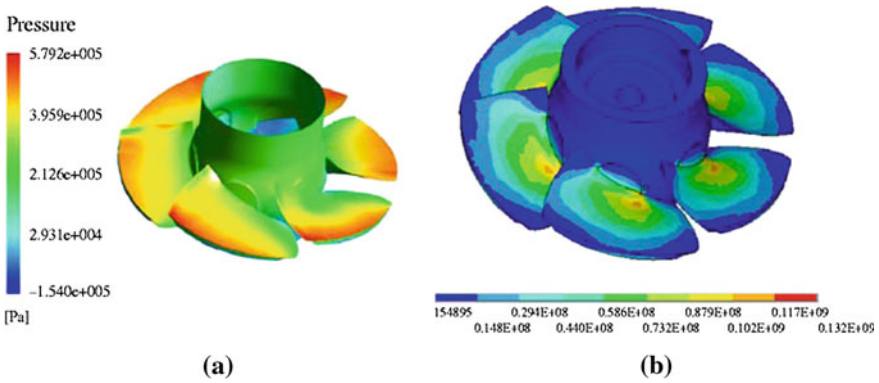

Fig. 8.7 Pressure distribution and stress distributions on blades at condition GK3. **a** Pressure distributions (Pa). **b** Stress distributions (Mpa)

Figure 8.6 also demonstrates that the mean value and amplitude of the torque fluctuations is small near the optimum point (GK8, Fig. 8.6h), larger in cases of large blade angles and large guide vane openings (GK10, Fig. 8.6i) and even larger in cases of small blade angles and small guide vane openings (GK3, Fig. 8.6g), verified from the power station's operating recordings. When the turbine is operated under approximately optimum condition (for example, GK8) the operating oil pressure inside the piston chamber is normal. But when it is operated under approximate the condition of GK3, the oil pressure inside the chamber is extremely high.

Typical pressure distribution and the von Mises static stress distributions in blades are plotted in Fig. 8.7 under condition GK3. The maximum stress is near the blade root in all cases which is consistent with general knowledge on static stress distributions in Kaplan turbine blades. The dynamic stresses at the node with maximum stress are rendered in Fig. 8.8 for the three typical conditions.

Figures 8.6 and 8.7 show that the dynamic stresses in blades are closely related to pressure fluctuations in the flow path. For most cases, main pressure fluctuation frequency and dynamic stress frequency is the runner rotation frequency f_r.

The same analysis was engaged in the computation of dynamic stresses for the Francis turbine blade (Xiao et al. 2008). It was found that under part load condition on several nodes in runner blade, the dynamic stresses are very high with amplitudes reaching 15 MPa, and dominant dynamic stress frequency with 0.77 f_r, where f_r is the rotating frequency of runner. The sum of the dominant frequency of

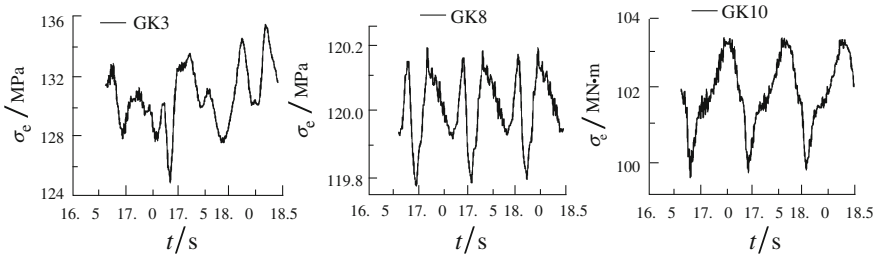

Fig. 8.8 Dynamic stress at the node with the maximum stress (cases *GK3*, *GK8*, *GK10*)

dynamic stresses and the dominant frequency of vortex rope in a draft tube is the source of excited force with a frequency of 0.3 f_r.

8.4.2 Analysis of Dynamic Stresses by Partitional Approach

Since it is almost impossible to carry out the prototype hydro-turbine experiment before the power plant is built, rational prediction of pressure fluctuations in the prototype turbine is very important in the design stage. Liu et al. (2008a) applied the modified RNG $k-\varepsilon$ turbulence model and the unsteady turbulent flow computation through the whole flow passage of a Kaplan turbine to simulate pressure fluctuation in a model turbine. The numerical results are in agreement with the experimental data. Afterwards, this numerical method was utilized to simulate the pressure fluctuation in a prototype Kaplan turbine with a head of 52.2 m and a runner diameter 8 m. The computation was carried out under the on-cam operation condition of blade angle 15° and guide vane opening 67 %.

Based on the pressure fluctuations forecast by an unsteady turbulent flow simulation with the blade displacement, and based on the dynamic stress computation by FEM in blades, the partitional approach was executed to renew the pressure fluctuation and the stress and strain data.

Figure 8.9 illustrates the FSI coupling scheme between CFD and CSM (computational solid mechanism), in which the CFD unsteady turbulent flow simulation through the whole flow passage of Francis turbine is carried out with the software Fluent. In CSM the software Abaqus is adopted for FEM computation in runner blades.

The pressure data of each time step obtained from the CFD computation are transmitted to the FSI coupling interfaces of blade surfaces using the technique of Mesh-based parallel Code Coupling Interface (Mpcci). The results of blade surface displacements by the CSM calculation are transmitted inversely to the blade grid system in each time step to form a new grid system with the dynamic mesh technique of the spring based smoothing (SBS). The forgoing procedure is included in only one time step iteration of the FSI coupling. The interaction between CFD, Mpcci, CSM, Mpcci, SBC and CFD would repeat to achieve the convergence of displacements of blade surfaces. This coupling was carried out

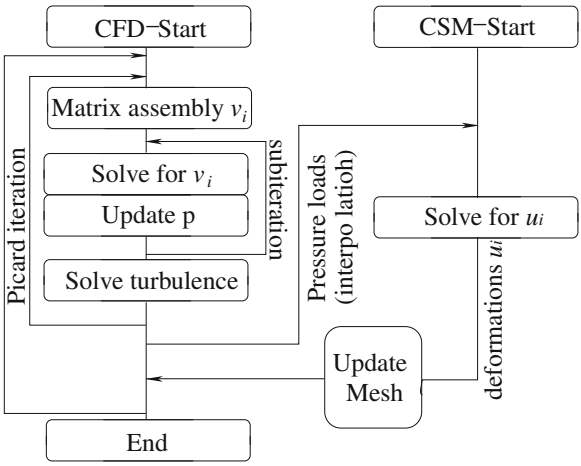

Fig. 8.9 FSI coupling scheme between CFD and CSM. (u_i displacement, v_i velocity, p pressure, see Lippold and Ogor 2007)

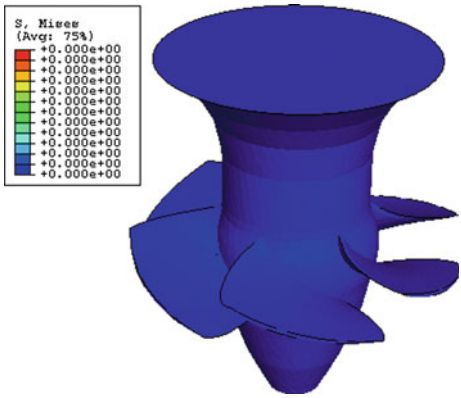

Fig. 8.10 Non-strain state of baled at $t = 0$ s

without any assumption of irrotational and non-viscous flow. The coupling results of the FSI are the dynamic strain and stress of the turbine blade and pressure pulsation in the turbine runner.

Figures 8.10, 8.11, 8.12, 8.13, 8.14, and 8.15 show stress distributions and displacements of runner and its blade at the initial moment $t = 0$ s and the moment $t = 3.0$ s during the computational process (Liu et al. 2008a).

From Fig. 8.10 to Fig. 8.12, it is indicated that the high stress area on the blades is at blade root and the joint between it and runner hub, as well as at its trailing edge. The maximum value of stress is 141.6 MP at $t = 3.0$ s moment. But the maximum value of stress is 222.1 MP during the whole computation process. From Fig. 8.13 to Fig. 8.15, it is implied that the z-direction or axial direction displacement has a large value at the outskirt of runner blades with a maximum of 4.865 mm at $t = 3.0$ s moment with read character in upper-direction and blue down-direction.

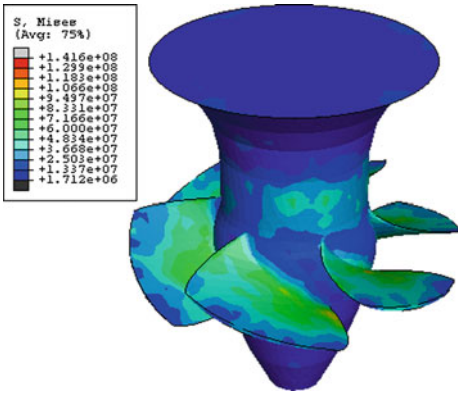

Fig. 8.11 Runner stain (Pa) at $t = 3.0$ s

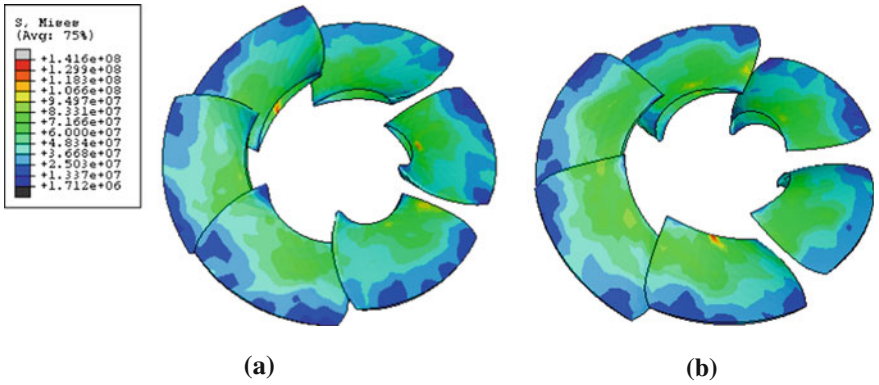

Fig. 8.12 Stress distribution on six runner blades (Pa) at $t = 3.0$ s. **a** Pressure side of blade. **b** Suction side of blade

Fig. 8.13 Non-strain state of baled at $t = 0$ s

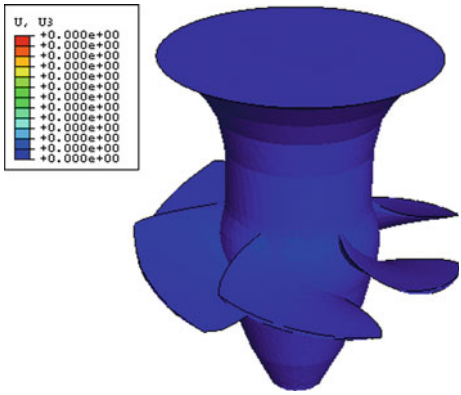

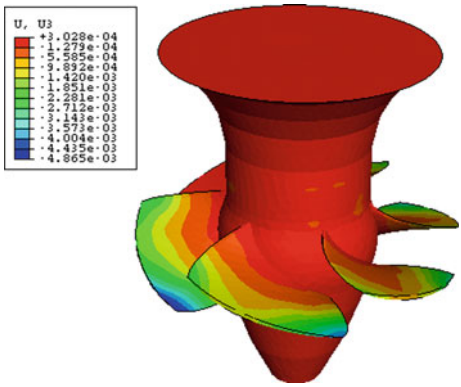

Fig. 8.14 z-displacement (m) at $t = 3.0$ s

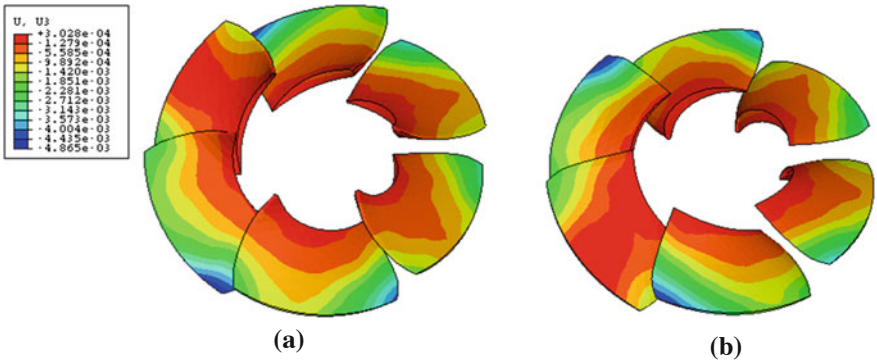

Fig. 8.15 The z-displacement (m) on six blade surfaces at $t = 3.0$ s. **a** Pressure side of blade. **b** Suction side of blade

The maximum value of z-displacement is 7.829 mm during the whole computation process. It is necessary to take into account the displacement in computational prediction of pressure pulsation in runner.

The similar computation was carried out for FSI simulation of a tidal current turbine by Lippold and Ogor (2007).

8.4.3 Analysis of Dynamic Stresses of a Pelton Turbine

The flow field in Pelton runners is more difficult to determine than that of Francis or Kaplan turbines because Pelton buckets are moving through the jets, filling and emptying continuously. With the progress in Pelton turbine CFD and fluid structure coupling (see Parkinson et al. 2007) more precise results have been achieved as Keck et al. (2009) summarized.

8.4.3.1 CFD Analysis of the Jet Bucket Interaction

The unsteady loading analysis of the bucket requires acquisition of the unsteady pressure loading in the rotating buckets. It is obtained in a flow simulation process (CFD) that has been analyzed and validated from various sets of unsteady pressure measurements located both at inner and outer surfaces of buckets obtained at model scale (see Parkinson et al. 2005a, b).

The action of the water jet in the Pelton bucket has three different phases in the interaction process: jet loading, maximum torque and water evacuation. The CFD simulation takes into account the entire bucket surface and its interaction with the jet. The CFD simulation provides sufficient data for a reliable structural analysis. During each time-step the pressure distribution on the Pelton bucket surface serves as input data for FEM Analysis which then reliably predicts deformation and stress. At maximum torque the hot spot of the stress is generally to be found in the root zone of the bucket (see Schmied et al. 2006).

8.4.3.2 Structural Analysis of the Pelton Bucket

A typical stress variation in the root consists of periodic stress related to the cyclic jet impact with some added stress component induced by the mechanical vibrations of the runner shown in Fig. 8.16a. As the bucket vibration takes place in response to the dynamic load, it is not possible to simulate the process with a quasi-static FEM analysis with fairly coarse time steps as used today (Fig. 8.16b).

CFD analysis of the jet flow in bucket delivers pressure distribution on the bucket surface for each time step with good accuracy thereby enabling FEM prediction of both deformation and stress.

Based on the excitation measurements on a number of individual buckets on one hand and an iterative solution of the transfer matrix on the other, it is possible

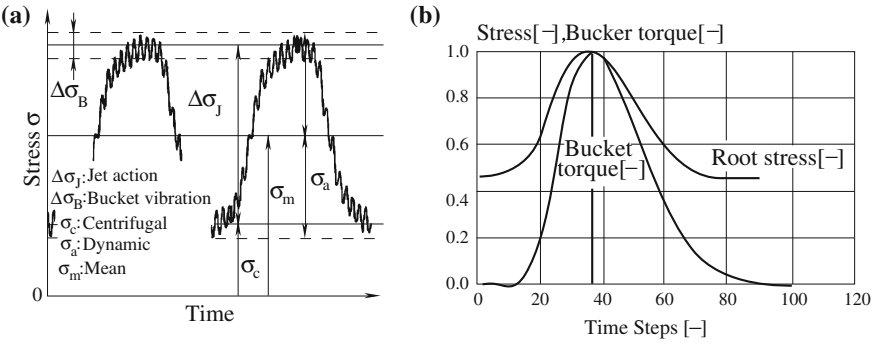

Fig. 8.16 Stress variation with time in the Pelton bucket (Keck et al. 2009). **a** Measurement. **b** CFD simulation and FEM analysis.

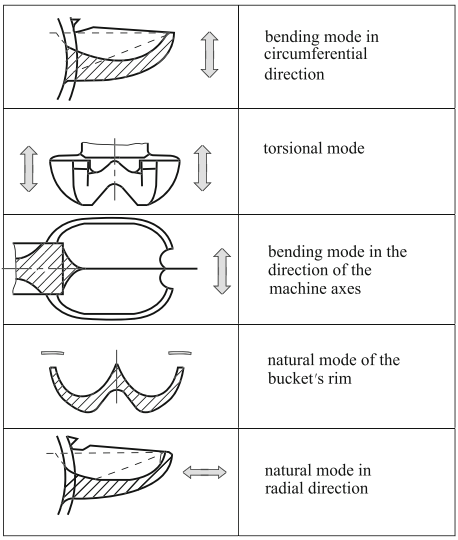

Fig. 8.17 Important natural modes of a Pelton runner (see Sick et al. 2009)

to determine the parameters of the Pelton runner as coupled multi-mass system and thereby to determine a detuning procedure if needed.

Some typical natural bucket modes are listed in Fig. 8.17. The relevant mode in operation is the bending mode in circumferential direction, which, in some cases, can be combined with a vibration of the buckets rim. (Keck et al. 2009; Sick et al. 2009).

8.5 Analysis of Response to Excited Force on Blades of Hydraulic Machinery

Both mean and dynamic loads on hydraulic machinery, especially on blades and vanes are well predicted with modern CFD methods and serve as reliable input for a structural analysis. Modern FEM has been proven to deliver realistic values of deformation and stress and thus can be relied on with respect to dynamic load. This procedure may be applied to the dynamic real time response in hydraulic machinery as discussed in last section. The following section will introduce the simple treatment of dynamic response if dynamic loading is analyzed in several harmonic components with the Fourier Transform (Wang 2003).

Dynamic analysis on the response of excited forces in hydraulic machinery and any structure may be carried out using several direct methods such as the direct numerical integration, which includes the Houbolt method, the Newmark method, and the Wilson-θ method, etc.

According to the direct integrate method, it is necessary to divide the time periodicity T of the structure vibration into n time intervals for a structure dynamic analysis.

The time increment for each interval is $\Delta t = T/n$. From the initial time $t = 0$ of the structure state, one should find the state vectors in the dynamic process of the structure vibration, such as displacement vector $\{\boldsymbol{u}\}$, velocity vector $\{\dot{\boldsymbol{u}}\}$, and acceleration vector $\{\ddot{\boldsymbol{u}}\}$ after each time interval, Δt, $2\Delta t$, $\cdots T$. In the end, the final state vector of the structure vibration is the solution for a structure dynamic response to the excitation of forces.

The general motion equation of a structure vibration is in the form:

$$[\boldsymbol{M}]\{\ddot{\boldsymbol{u}}\} + [\boldsymbol{C}]\{\dot{\boldsymbol{u}}\} + [\boldsymbol{K}]\{\boldsymbol{u}\} = \{\boldsymbol{f}(t)\} \tag{8.24}$$

where $[\boldsymbol{M}]$ is mass matrix of the structure system; $[\boldsymbol{C}]$ is its damping matrix; $[\boldsymbol{K}]$ is its stiffness matrix; and $\{\boldsymbol{f}(t)\}$ is its excitation force.

8.5.1 The Wilson-θ Method

One needs to consider the equations of structure vibration for simplicity.

$$\ddot{x} + 2\varsigma\omega\dot{x} + \omega^2 x = f$$

This is the equilibrium equation governing motion for the single-degree-freedom system with a vibration period T, dumping ς and applied load f.

When the equilibrium equation is written in time $t + \theta\Delta t$, it becomes

$$\begin{Bmatrix} \ddot{x}(t+\Delta t) \\ \dot{x}(t+\Delta t) \\ x(t+\Delta t) \end{Bmatrix} = [\boldsymbol{A}] \begin{Bmatrix} \ddot{x}(t) \\ \dot{x}(t) \\ x(t) \end{Bmatrix} + \{\boldsymbol{L}\} f(t+\theta\Delta t) \tag{8.25}$$

where

$$[\boldsymbol{A}] = \begin{bmatrix} 1 - \frac{1}{\theta} - \frac{\beta\theta^2}{3} - k\theta & \frac{1}{\Delta t}(-\beta\theta - 2k) & \frac{1}{\Delta t^2}(-\beta) \\ \Delta t\left(1 - \frac{1}{2\theta} - \frac{\beta\theta^2}{6} - \frac{k\theta}{2}\right) & 1 - \frac{\beta\theta}{2} - k & \frac{1}{\Delta t}\left(-\frac{\beta}{2}\right) \\ \Delta t^2\left(\frac{1}{2} - \frac{1}{6\theta} - \frac{\beta\theta^2}{18} - \frac{k\theta}{6}\right) & \Delta t\left(1 - \frac{\beta\theta}{6} - \frac{k}{3}\right) & 1 - \frac{\beta}{6} \end{bmatrix} \quad \{\boldsymbol{L}\} = \begin{Bmatrix} \frac{\beta}{\omega^2\Delta t^2} \\ \frac{\beta}{2\omega^2\Delta t} \\ \frac{\beta}{6\omega^2} \end{Bmatrix}$$

$$\beta = \left(\frac{\theta}{\omega^2\Delta t^2} + \frac{\varsigma\theta^2}{\omega\Delta t} + \frac{\theta^3}{6}\right)^{-1}, \; k = \frac{\varsigma\beta}{\omega\Delta t}.$$

In the widely used Wilson-θ method, the computational procedure is as follows:

1. It is assumed that at the time moment t, the state vectors of $\{\boldsymbol{u}\}$ and $\{\dot{\boldsymbol{u}}\}$ are known. Substituting them into Eq. (8.24), one obtains

$$\{\ddot{\boldsymbol{u}}(t)\} = [\boldsymbol{M}]^{-1}\{\boldsymbol{f}(t)\} - [\boldsymbol{M}]^{-1}[\boldsymbol{C}]\{\dot{\boldsymbol{u}}(t)\} - [\boldsymbol{M}]^{-1}[\boldsymbol{K}]\{\boldsymbol{u}(t)\}. \tag{8.26}$$

2. Transform Eq. (8.26) to get the vector $\{\boldsymbol{u}(t+\boldsymbol{\theta}\Delta\boldsymbol{t})\}$ at $t+\boldsymbol{\theta}\Delta\boldsymbol{t}$ moment:

$$\begin{aligned}\{\boldsymbol{u}(t+\boldsymbol{\theta}\Delta t)\} = &\left([\boldsymbol{K}] + \frac{3}{\boldsymbol{\theta}\Delta\boldsymbol{t}}[\boldsymbol{C}] + \frac{6}{(\boldsymbol{\theta}\Delta\boldsymbol{t})^2}[\boldsymbol{M}]\right)^{-1} \\ &\left\{[\boldsymbol{M}]\left(2\{\ddot{\boldsymbol{u}}(t)\} + \frac{6}{\boldsymbol{\theta}\Delta\boldsymbol{t}}\{\dot{\boldsymbol{u}}(t)\} + \frac{6}{(\boldsymbol{\theta}\Delta\boldsymbol{t})^2}\{\boldsymbol{u}(t)\}\right)\right. \\ &\left. + [\boldsymbol{C}]\left(\frac{\boldsymbol{\theta}\Delta\boldsymbol{t}}{2}\{\ddot{\boldsymbol{u}}(t)\} + 2\{\dot{\boldsymbol{u}}(t)\} + \frac{3}{\boldsymbol{\theta}\Delta\boldsymbol{t}}\{\boldsymbol{u}(t)\}\right) + \{\boldsymbol{f}(t+\boldsymbol{\theta}\Delta\boldsymbol{t})\}\right\}.\end{aligned} \tag{8.27}$$

3. Based on the Taylor's Series to get the expression of $\{\ddot{\boldsymbol{u}}(t+\boldsymbol{\theta}\Delta t)\}$:

$$\{\ddot{\boldsymbol{u}}(t+\boldsymbol{\theta}\Delta t)\} = \frac{6}{(\boldsymbol{\theta}\Delta t)^2}(\{\boldsymbol{u}(t+\boldsymbol{\theta}\Delta t)\} - \{\boldsymbol{u}(t)\}) - \frac{6}{\boldsymbol{\theta}\Delta t}\{\dot{\boldsymbol{u}}(t)\} - 2\{\ddot{\boldsymbol{u}}(t)\}. \tag{8.28}$$

4. Obtain $\{\ddot{\boldsymbol{u}}(t+\Delta t)\}$ with interaction factor $\boldsymbol{\theta}$

$$\{\ddot{\boldsymbol{u}}(t+\Delta t)\} = \left(1 - \frac{1}{\boldsymbol{\theta}}\right)\{\ddot{\boldsymbol{u}}(t)\} + \frac{1}{\boldsymbol{\theta}}\{\ddot{\boldsymbol{u}}(t+\boldsymbol{\theta}\Delta t)\}. \tag{8.29}$$

5. Make the first step of the direct interaction of Eq. (8.29)

$$\{\dot{\boldsymbol{u}}(t+\Delta t)\} = \{\dot{\boldsymbol{u}}(t)\} + \frac{\Delta t}{2}(\{\ddot{\boldsymbol{u}}(t)\} + \{\ddot{\boldsymbol{u}}(t+\boldsymbol{\theta}\Delta t)\}). \tag{8.30}$$

6. Finally solve the displacement vector at the next time step $\{\boldsymbol{u}(t+\Delta t)\}$ by second interaction

$$\{\boldsymbol{u}(t+\Delta t)\} = \{\boldsymbol{u}(t)\} + \Delta t\{\dot{\boldsymbol{u}}(t)\} + \frac{(\Delta t)^2}{6}(2\{\ddot{\boldsymbol{u}}(t)\} + \{\ddot{\boldsymbol{u}}(t+\boldsymbol{\theta}\Delta t)\}) \tag{8.31}$$

where upon the Wilson factor $\theta > 1.37$, the iterative solution is always stable whatever value is adopted for Δt. But if Δt is too large, accuracy of the solution will be unsatisfactory.

This method can be used for transient dynamic analysis of a structure on hydraulic machinery

8.5.2 Superposition Method of Vibration Mode

According to the superposition method, the vibration response displacement of a structure can be obtained if the preceding-order natural frequencies and their vibration modals are known, because the excitation force can be decomposed into its several low-order components with Fourier analysis. The dynamic responsive displacement of a structure is the superposition from the several preceding linear vibration models. The linear combination factors are the response factors of several modes of vibration, that is to say, the modal ordinates of the models.

8.5.2.1 Superposition Method Procedure

Main steps of the superposition method of vibration mode are as follows:

1. Solve the free vibration equation of a structure (blade) with n degrees of freedom through

$$[\boldsymbol{K}][\boldsymbol{\phi}] = [\boldsymbol{M}][\boldsymbol{\phi}][\Lambda] \tag{8.32}$$

where $[\boldsymbol{\phi}]$ is the matrix of the equation character vectors: $[\boldsymbol{\phi}] = [\{\boldsymbol{\phi}_1\}\{\boldsymbol{\phi}_2\}\{\boldsymbol{\phi}_3\}\cdots\{\boldsymbol{\phi}_n\}]$; $[\Lambda]$ is the character values diagonal matrix of the equation: $[\Lambda] = \mathrm{diag}\left[\omega_i^2\right](i = 1, 2, \cdots n)$; and $[\boldsymbol{M}]$ is the structure mass matrix; and $[\boldsymbol{K}]$ is the structure (blade) stiffness matrix.

Then one can get the preceding natural frequencies and vibration modals of the structure. For example, if the preceding p orders are needed, then one can obtain the equation character vectors: $[\boldsymbol{\phi}]=[\{\boldsymbol{\phi}_1\}\{\boldsymbol{\phi}_2\}\ \{\boldsymbol{\phi}_3\}\cdots\{\boldsymbol{\phi}_p\}]$; and the character values diagonal matrix of the equation: $[\Lambda] = \mathrm{diag}\ [\omega_i^2](p = 1,\ 2,\ \cdots n)$.

2. Based on the moving flow in the structure, the structure dynamic equation is

$$\begin{aligned}[\boldsymbol{M}]\{\ddot{\boldsymbol{u}}\} + [\boldsymbol{C}]\{\dot{\boldsymbol{u}}\} + [\boldsymbol{M}_G]\{\dot{\boldsymbol{u}}\} + [\boldsymbol{K}]\{\boldsymbol{u}\} \\ = \{\boldsymbol{Q}_c\} + \{\boldsymbol{Q}_p\} - \{\boldsymbol{F}_\sigma\} + \{\boldsymbol{R}\}\end{aligned} \tag{8.33}$$

One could perform the mode ordinate transform as follows to get the mass matrix in modal ordinates $[\bar{\boldsymbol{M}}]$, and etc.

$$\begin{aligned}&[\bar{\boldsymbol{M}}] = [\boldsymbol{\phi}]^T[\boldsymbol{M}][\boldsymbol{\phi}],\ [\bar{\boldsymbol{K}}] = [\boldsymbol{\phi}]^T[\boldsymbol{K}][\boldsymbol{\phi}],\ [\bar{\boldsymbol{C}}] = [\boldsymbol{\phi}]^T[\boldsymbol{C}][\boldsymbol{\phi}], \\ &\{\boldsymbol{u}(t)\} = [\boldsymbol{\phi}]^T\{\boldsymbol{Y}(t)\},\ \{\bar{\boldsymbol{F}}(t)\} = [\boldsymbol{\phi}]^T\{\boldsymbol{F}(t)\}.\end{aligned} \tag{8.34}$$

Then the following equation of structure vibration expressed in modal ordinates $\{\boldsymbol{Y}(t)\}$ can be obtained:

$$[\bar{\boldsymbol{M}}]\{\ddot{\boldsymbol{Y}}(t)\} + [\bar{\boldsymbol{C}}]\{\dot{\boldsymbol{Y}}(t)\} + [\bar{\boldsymbol{K}}]\{\boldsymbol{Y}(t)\} = \{\bar{\boldsymbol{F}}(t)\}. \tag{8.35}$$

Treatment of the mass matrix is based on regularizing transposition; the damping matrix is based on the assumption of the linear damping factor or on adopting the model damping, ς_i. The group of last differential equations can be decoupled from each other. The group of decoupling 2nd order differential equations can be gotten, one of which has the form

$$\ddot{Y}_i(t) + 2\varsigma_i\omega_i\dot{Y}_i(t) + \omega_i^2 Y_i(t) = \bar{F}_i(t) \quad (i = 1,\ 2,\ \cdots p). \tag{8.36}$$

3. Calculate the structure (blade) response displacement in the main modals' ordinates. On the assumption of small damping, the general solution of Eq. (8.36) with weak damping is

$$\begin{aligned} Y_i(t) \ &= \frac{1}{\omega_{di}}\int_0^t \bar{F}_i(\tau)\mathrm{e}^{-\varsigma_i\omega_i(t-\tau)}\sin\omega_{di}(t-\tau)\mathrm{d}\tau \\ &+ \mathrm{e}^{-\varsigma_i\omega_i t}\left(\frac{\dot{Y}_i(0) + \varsigma_i\omega_i Y_i(0)}{\omega_{di}}\sin\omega_{di}t + Y_i(0)\cos\omega_{di}t\right) \end{aligned} \tag{8.37}$$

where ω_{di} is the structure (blade) frequency of dynamic response ω_i after considering damping correction, $\omega_{di} = \omega_i(1\text{-}\varsigma_i^2)^{1/2}$. $Y_i(0)$ and $\dot{Y}_i(0)$ are the initial displacement and the initial velocity of structure respectively.

In a stable response condition, the solution of Eq. (8.37) is the stable solution in transformed main modal ordinates:

$$\{\boldsymbol{Y}(t)\} = \frac{\boldsymbol{\beta}_i\{\boldsymbol{\phi}_i\}^T}{K_{pi}}\sum_{K=1}^{\infty}[\{S_K\}\sin k\Omega t - \boldsymbol{\theta}_i] \tag{8.38}$$

where $\beta_i = 1\Big/\sqrt{\left(1-\lambda_{ik}^2\right)^2 + \left(2\varsigma_i\lambda_{ik}\right)^2}$, $\theta_i = \arctan\frac{2\varsigma_i\lambda_{ik}}{1-\lambda_{ik}^2}$, $\lambda_{ik} = \frac{k\Omega}{\omega_i}$ and Ω is rotating speed of runner.

4. Work out the response displacements in physical ordinates from those expressed in the model ordinates.

Because $\{\boldsymbol{u}(t)\} = [\boldsymbol{\phi}]^{\mathrm{T}}\{\boldsymbol{Y}(t)\}$, the response displacements in physical ordinates are as follows:

$$\{\boldsymbol{u}(t)\} = \sum_{i=1}^{p}\frac{\boldsymbol{\beta}_i\{\boldsymbol{\phi}_i\}\{\boldsymbol{\phi}_i\}^T}{K_{pi}}\sum_{k=1}^{\infty}(\{\boldsymbol{S}_k\}(k\Omega t - \Omega_i)). \tag{8.39}$$

When the S order free-vibration frequency ω_S falls in resonance with k order synchronic frequency, $\beta_S = 1/(2\varsigma_S)$, $\theta_S = 2\pi$, and then Eq. (8.39) will be simplified as

$$\{\boldsymbol{u}(t)\} \approx \{\boldsymbol{\phi}_S\} \frac{\{\boldsymbol{\phi}_S\}^T \{\boldsymbol{S}_k\}}{2\varsigma_k K_{pS}} \sin\left(k\Omega t - \frac{\pi}{2}\right). \tag{8.40}$$

That is to say, the response vibration displacement approaches the S order main model, while other models vanish. Also, it could be found that the larger the stiffness of main model is, the smaller the response displacement will be (that is, dynamic tress).

8.5.2.2 Calculation of Dynamic Stress in Blade

One of the main reasons for blade damage in hydraulic machinery is dynamic stress induced by excited force from the flow in runner under operation conditions. Based on the response displacements at one moment obtained in previous sections, the stress distribution on the blade can be obtained as follows:

$$\{\boldsymbol{\sigma}\}^e = [\boldsymbol{D}][\boldsymbol{B}]\{\boldsymbol{u}\}^e \tag{8.41}$$

where the stresses in element are given at each moment. Furthermore stresses on all nodes in the FEM physical model of structure can be obtained. The time-history of stresses on each node is the dynamic stress in the structure.

References

Bathe, K. J., & Wilson, E. L. (1976). *Numerical methods in finite element analysis*. Englewood Cliffs: Prentice-Hall.

Clough, R. W., & Penzien, J. (1975). Dynamics of structures, Mc-Graw Hill Inc: New York.

Dubcová, L., Feistauer, M., Horáček, J., & Sváček, P. (2008). Numerical simulation of interaction between turbulent flow and a vibrating airfoil. *Computing and Visualization in Science, 12*, 207–225.

Keck, H., Michler, W., Weiss, T., & Sick, M. (2009). Recent development in dynamic analysis of water turbine. *Proceedings of the Institution of Mechanical Engineers, Part A: Journal of Power and Energy, 223*, 415–427.

Liang, Q. W., Egusquiza, E., Escaler, X., & Avellan, F. (2006). *Modal analysis on a Francis turbine runner considering the fluid added mass effect: Proceedings of AHR International Meeting of WG on Cavitation and Dynamic Problems in Hydraulic Machinery and Systems*. Barcelona.

Lippold, F., & Ogor, I. B. (2007). Fluid-structure interaction: Simulation of a tidal current turbine. In *High Performance Computing on Vector Systems 2007*. In: S. Roller, P. Lammers, T. Furui, M. Galle, W. Bez (Eds.), (pp. 137–143) Berlin: Springer.

Liu, D. M., Liu, S. H., Wu, Y. L., & Liu X. B. (2008a). *Numerical simulation of hydraulic turbine based on fluid-structure coupling: Proceedings of the 4th International Symposium on Fluid Machinery and Fluid Engineering*. paper No. 4ISFMFE-Ch39.

Liu, S. H., Shao, J., Wu, S. F., & Wu, Y. L. (2008b). Numerical simulation of pressure fluctuation in Kaplan turbine. *Science in China Series E: Technological Science, 51*, 1137–1148.

Parkinson, E., Weiss, Th., Neury, C., Kuntz, M., & Braune, A. (2005a). *Computational analysis in Pelton hydraulic turbines: Proceedings of 22nd CAD FEM Users Meeting*. Dresden.

Parkinson, E., Neury, C., Garcin, G., Vullioud, G., & Weiss, Th. (2005b). *Unsteady analysis of a Pelton runner with flow and mechanical simulations: Proceedings of Hydro 2005*. Villach.

Parkinson, E., Angehrn, R., & Weiss, Th. (2007). Modern design engineering applied to Pelton runners. *Hydropower and Dams, 14*(4), 91.

Schmied, J., Weiss, T., & Angehrn, R. (2006). *Detuning of Pelton runners: Proceedings of 7th IFToMM-Conference on Rotor Dynamics*. Vienna.

Sick, M., Michler, W., Weiss, T., & Keck, H. (2009). Recent developments in the dynamic analysis of water turbines. *Proceedings of the Institution of Mechanical Engineers, Part A: Journal of Power and Energy, 223*, 415–427.

Wang, S. P. (2003). *Dynamic characteristic analysis and synthetical optimization of Francis turbine runner*. Dissertation for doctor degree, China Academy of Mechanical Science and Technology in China.

Wikipedia, (2012). http://en.wikipedia.org/wiki/Structural_dynamics

Woyjak, D. B. (1992). Acoustic and fluid structure interaction, a revision 5.0 tutorial.

Xiao, R. F., Wang, Z. W., & Luo, Y. Y. (2008). Dynamic Stresses in a Francis Turbine Runner Based on Fluid-Structure Interaction Analysis. *Tsinghua Science and Technology, 13*, 587–592.

Zhou, L. J., & Wang, Z. W. (2007). Analysis of dynamic stresses in Kaplan turbine blades. *Engineering Computations, 24*, 753–762.

Part IV
Rotordynamics

Chapter 9
Rotordynamic Simulation of Hydraulic Machinery

The shaft stability of generating and pumping units plays a crucial role on the units' operation: It directly affects the safe operation and also influences the life of units. In this chapter, the calculation and the analysis of rotordynamics in hydraulic machinery are introduced, including governing equations, the Riccati transfer matrix method, and the finite element method for rotordynamic analysis of hydraulic turbine units, the determination of pump rotordynamic parameters, and pump rotordynamic computation (Li and Wang 1996).

9.1 Basic Equations of Rotordynamics in Hydraulic Machinery

Rotordynamic analysis is important not only for understanding of the natural characteristics and dynamic response of a rotor-bearing system, but also for knowledge of the fault mechanism (Feng and Chu 2001). In this section, the governing equations of a rotating mechanical system, and the study subjects of rotordynamics in hydraulic machinery are introduced.

9.1.1 Governing Equations of a Rotating Mechanical System

Generally, the governing equations of a rotating mechanical system can be expressed in the inertial reference frame as

$$[\boldsymbol{M}]\{\ddot{\boldsymbol{u}}\} + ([\boldsymbol{C}] + \Omega[\boldsymbol{G}])\{\dot{\boldsymbol{u}}\} + ([\boldsymbol{K}] + \Omega[\boldsymbol{C}_r])\{\boldsymbol{u}\} = \Omega^2\{\boldsymbol{f}\} \tag{9.1}$$

where $[\boldsymbol{M}]$ is the mass matrix, $[\boldsymbol{C}]$ the damping matrix, $[\boldsymbol{G}]$ the gyroscopic skew symmetric matrix, $[\boldsymbol{K}]$ the stiffness matrix, $[\boldsymbol{C}_r]$ (or $[\boldsymbol{H}]/\Omega$) is the asymmetric part rotating damping matrix, $\{\boldsymbol{u}\}$ is the displacement vector (rotating can include axial

Y. Wu et al., *Vibration of Hydraulic Machinery*,
Mechanisms and Machine Science 11, DOI: 10.1007/978-94-007-6422-4_9,

displacement), and $\{\boldsymbol{f}\}$ is the unbalanced forces while all are in the real coordinates [see Eq. (4.65) or (4.32)].

If all matrices are expressed in complex coordinates, they are symmetric in the form of complex coordinate notation, while in real coordinates the gyroscopic matrix is skew symmetric [see Eqs. (4.50), (4.51)].

In a simple expression, Eq. (9.1) in inertial coordinates is as

$$[\boldsymbol{M}]\{\ddot{\boldsymbol{u}}\} + ([\boldsymbol{C}] + [\boldsymbol{G}])\{\dot{\boldsymbol{u}}\} + ([\boldsymbol{K}] + [\boldsymbol{H}])\{\boldsymbol{u}\} = \{\boldsymbol{f}\} \tag{9.2}$$

which is the equation of motion, in generalized matrix form, for an axially symmetric rotor rotating at a constant spin speed Ω, where: $[\boldsymbol{M}]$ is the symmetric mass matrix; $[\boldsymbol{C}]$ is the symmetric damping matrix; $[\boldsymbol{G}]$ is the skew-symmetric gyroscopic matrix; $[\boldsymbol{K}]$ is the symmetric bearing or seal stiffness matrix; $[\boldsymbol{H}]$ is the gyroscopic matrix of deflection for inclusion of e.g. centrifugal elements; $\{\boldsymbol{u}\}$ is the generalized coordinates of the rotor in inertial coordinates, and $\{\boldsymbol{f}\}$ is a forcing function.

The gyroscopic matrix $[\boldsymbol{G}]$ is proportional to spin speed Ω. The general solution to the above equation involves complex eigenvectors which are spin-speed dependent. Engineering specialists in this field resort to the Campbell Diagram to explore these solutions.

An interesting feature of the rotordynamic system of equations is the off-diagonal terms for stiffness, damping, and mass. These terms are called cross-coupled stiffness, cross-coupled damping, and cross-coupled mass. When there is a positive cross-coupled stiffness, a deflection will cause a reaction force opposite to the direction of deflection to counteract the load, and also a reaction force in the direction of positive whirl. If this force is large enough compared to the available direct damping and stiffness, the rotor will be unstable. When a rotor is unstable it will typically require immediate shutdown of the machine to avoid catastrophic failure.

If one uses the rotating frame of reference, the governing equations of a rotating mechanical system in a rotating frame is

$$[\boldsymbol{M}]\{\ddot{\boldsymbol{u}}_r\} + ([\boldsymbol{C}] + [\boldsymbol{G}_{Cor}])\{\dot{\boldsymbol{u}}_r\} + \left([\boldsymbol{K}] + [\boldsymbol{H}] - \left[\boldsymbol{K}_{spin}\right]\right)\{\boldsymbol{u}_r\} = \{\boldsymbol{f}\} \tag{9.3}$$

where $[\boldsymbol{K}_{spin}]$ is rotating effect stiffness matrix; $[\boldsymbol{G}_{Cor}]$ is Coriols effect matrix.

9.1.2 Problems of Rotordynamics in Hydraulic Machinery

The rotordynamics of hydraulic machines is more complicated due to a distinct number of operating features that are mostly load dependent; i.e., related to the power (pressure and flow conditions). The most important issues in a realistic analysis are as follows (Andrés 2006):

1. Hydraulic machines typically handle large-density liquids and the effects of interstage and wear seals on the rotor-bearing system dynamics is most significant. Liquid seals generate substantial direct stiffness and added mass

coefficients that can change the natural frequencies (critical speeds) of a hydraulic machine. Thus, there is a distinction between "dry" and "wet" critical speed.
2. Uneven static pressure distribution at the hydraulic machine discharge volute creates a side radial load. This load, which is of importance in single-tongue volute casing hydraulic machines, is greatly influenced by operation away from the hydraulic machine's Best Efficiency Point. The hydraulic load, whose magnitude and direction depends on operation away from BEP, makes the support bearings become more or less loaded, thus affecting rotordynamic behavior.
3. The rotating liquid flowing through the impeller/runner forms a condition of hydraulic imbalance due to inaccuracies in the manufactured impeller/runner surfaces. The hydraulic induced synchronous force is difficult to predict and even worse to measure in the field.
4. Dynamic forces and moments arise because of changes in pressure within the small clearance between hydraulic machine casing and its shroud. Lateral and angular shaft motions induce this type of impeller/runner shroud excitation force (and moment) which can affect the stability of high power density hydraulic machines, particularly in multiple-stage pumps which are quite flexible (low critical speeds).

9.1.3 Study on Rotordynamics in Hydraulic Machinery

The term "rotor dynamics" is used when the dynamics, i.e., time dependent forces and vibrations, of rotating machinery is studied or analyzed. "Dynamics" focuses on the natural frequencies of the system. In rotating machinery these natural frequencies stem from a gyroscopic effect, which in turn is a function of the driving frequency of the rotor. These natural frequencies give rise to high vibrations and thus have to be determined at the design stage to avoid dramatic consequences during operation. Several catastrophic events have been reported on rotating machinery (Cervantes et al. 2005).

Therefore, the main goal for rotor-dynamic analysis is to find the natural frequencies as functions of the rotating speed, as in the Campbell diagram. The complexity of industrial rotating machines requires several approximations in the mathematical modeling. The complexity level varies in different problems. However, the presence of non-linear phenomena adds to the complexity of such model.

Hence, rotor dynamic research in hydropower applications focuses on development of models and measuring techniques for creation of better tools for simulation and analysis. By increasing the predictability of the dynamics, one can develop the tools to reduce vibrations and increase reliability. The influence of new components can be analyzed before revisions are made, so early design changes can be suggested. Furthermore, stresses and load-analysis during different operating conditions can be performed to identify critical components and develop tools for lifetime evaluation.

In hydropower applications a rotor dynamic model should include electromagnetic forces from the generator, bearing models, and models for the turbine's interaction with the fluid. In the development of the models, it is essential to verify them against reliable measurements. Fundamental for a rotor model is that torsional and lateral natural frequencies can be measured at different driving frequencies and loadings.

In hydro power applications flow in the turbine, dynamics in bearings and electromagnetic load will all affect the eigen-frequencies of the rotor. Therefore the measurements and predictability is a key problem to be solved to develop good rotor models. Identification of the power transmission through the system will result in better load models.

For large machines, however, a more detailed analysis that can be used to predict the dynamic response of the rotor system under random hydraulic forces acting on the turbine runner is required. Some research work on natural vibration was carried out in lateral vibration analysis. In the 1970s, various methods for calculating vibrations and dynamic response (i.e., dynamic analysis of the rotor-bearing system) were proposed, but most of them could only deal with the periodic excitation force, not with the random excitation often observed in actual operation. Barp (Barp 1976) studied the complex problem of rotor vibration from the viewpoint of a design engineer with emphasis on the description of the general dynamic behavior. A method involving the stiffness matrix applicable to periodic or random external excitation force was proposed.

In the analysis of the rotor dynamic characteristics, with consideration of the lateral forces acting on the turbine runner, many modeling methods, such as the Prohl transfer matrix method, the Riccati transfer matrix method, the finite-element method, etc., have been developed. Also, many numerical integration methods, such as, the Runge–Kutta method, the Newmark-β method, the Wilson θ method, etc., have been proposed. These two kinds of methods can be integrated to simulate the dynamic response of the pump and turbine rotor-bearing system.

The start-up and shutdown processes of the water-turbine generator set and pump are highlighted by more and more field engineers and researchers due to the number of faults that often happen at these stages. At the same time, some nonlinear characteristics exhibit in the vibration signals of the hydro-turbine, such as nonlinear characteristics of the guide bearing, the thrust bearing, and the magnetic forces. Studies on the effects of these nonlinear characteristics on vibration of the shaft will prove to be very significant (Feng and Chu 2001).

9.2 The Riccati Transfer Matrix Method for Hydraulic Turbine Units

The hydraulic turbine unit is the essential equipment of the hydroelectric power generation, and shafts are an important part of large hydroelectric machines. Its dynamic characteristic is bound up with the hydroelectric reliability, life-span, and

economic index of the entire machines. Therefore, it is necessary to analyze the large hydroelectric machines with rotordynamics.

The dynamic response of the shaft system in hydraulic turbine units is the main subject of its rotordynamics. The main method to solve this subject includes the finite element method (FEM), the modal synthesis method (MSM), and the transfer matrix method. With rapid development of computer technology, application of FEM has been quickly adopted for its sententious and standard expression with high accuracy, despite a very large matrix.

Among three methods, the TMM can solve a series of small matrices with the help of simple software. In particular, it is suitable for a shaft system with chine character. It is combined with the direct integrate method to solve complicated shaft system.

9.2.1 Basic Equation of RTMM

In a lumped mass method, a mathematical model takes into account the system boundaries of machines affecting the shafts, such as the guide bearings, seal, electrical and hydraulic forces, the water in the runner etc., that may build up. Considering the different bracket constraint conditions of the shafts that are considered as rigidity or elasticity, one could compute the natural characteristic of the shafts by integrating with the highly stable Riccati Transfer Matrix Method (RTMM).

The Riccati transfer matrix and the Newmark β or the Wilson θ numerical integration methods could be adopted to calculate and analyze an instantaneous nonlinear response of the rotor system. The model of the rotor system should be found. Then the effect of shear deformation, rotary inertia, and gyroscopic moment could be considered, and the action of the water's additional mass in the hydraulic turbine and electromagnetic induction of instantaneous response of the rotor system under arbitrary forces could be obtained (see Chap. 5).

The TRTMM (transient Riccati transfer matrix method) is virtually a combination of the Riccati transfer matrix method (RTMM) and Wilson-θ method. In this section the basic equation of the TRTMM (Feng and Chu 2001) will be explained.

It is known that, in the Riccati transfer matrix method, elements in the state vector with values of zero are grouped as $\{\boldsymbol{f}\}$, and the other elements not equal to zero are grouped as $\{\boldsymbol{e}\}$. For the water-turbine unit studied, the first lumped mass at the top of the rotor and the last lumped mass of turbine runner at the bottom of the rotor can be viewed as free ends. This is to say that the force vectors of these two sections equal zero. Similarly, in the TRTMM, the following expressions can be employed:

$$\{\boldsymbol{f}\} = \{M_y, Q_x, M_x, Q_y\}^T \tag{9.4}$$

$$\{\boldsymbol{e}\} = \{\theta_y, \theta_x, y\}^T. \tag{9.5}$$

The Riccati transformation is

$$\{\boldsymbol{f}\}_i = [\boldsymbol{s}]_i\{\boldsymbol{e}\}_i + \{\boldsymbol{P}\}_i \tag{9.6}$$

where $[\boldsymbol{s}]_i$ and $\{\boldsymbol{P}\}_i$ represent the undetermined matrices. Combined with the transfer matrix between elements of the disk-shaft connected together, it can be shown that

$$\{\boldsymbol{f}/\boldsymbol{e}\}_{i+1} = \begin{bmatrix} [\boldsymbol{u}_{11}] & [\boldsymbol{u}_{12}] \\ [\boldsymbol{u}_{21}] & [\boldsymbol{u}_{22}] \end{bmatrix}_i \{\boldsymbol{f}/\boldsymbol{e}\}_i + \{\boldsymbol{F}_f/\boldsymbol{F}_e\}_i. \tag{9.7}$$

From Eqs. (9.6) and (9.7) the following expressions can be obtained:

$$[\boldsymbol{s}]_{i+1} = ([\boldsymbol{u}_{11}][\boldsymbol{s}] + [\boldsymbol{u}_{12}])_i([\boldsymbol{u}_{21}][\boldsymbol{s}] + [\boldsymbol{u}_{22}])_i^{-1} \tag{9.8}$$

$$\{\boldsymbol{P}\}_{i+1} = \left([\boldsymbol{u}_{11}]\{\boldsymbol{P}\} + \{\boldsymbol{F}_f\}\right)_i - [\boldsymbol{s}]_{i+1}([\boldsymbol{u}_{21}]\{\boldsymbol{P}\} + \{\boldsymbol{F}_e\})_i \tag{9.9}$$

where $[\boldsymbol{u}_{11}]$, $[\boldsymbol{u}_{12}]$, $[\boldsymbol{u}_{21}]$, $[\boldsymbol{u}_{22}]$, $\{\boldsymbol{F}_f\}$ and $\{\boldsymbol{F}_g\}$ are given as

$$[\boldsymbol{u}_{11}] = \begin{bmatrix} 1 & l & 0 & 0 \\ 0 & 1 & 0 & 0 \\ 0 & 0 & 1 & l \\ 0 & 0 & 0 & 1 \end{bmatrix}, [\boldsymbol{u}_{22}] = \begin{bmatrix} 1+\alpha_1 k_2 & -\alpha_2 k_1 & \alpha_1 k_3 & 0 \\ l+\alpha_2 k_2 & 1-\alpha_3 k_1 & \alpha_2 k_3 & 0 \\ -\alpha_1 k_3 & 0 & 1+\alpha_1 k_2 & -\alpha_2 k_1 \\ -\alpha_2 k_3 & 0 & 1+\alpha_2 k_2 & 1-\alpha_3 k_1 \end{bmatrix},$$

$$[\boldsymbol{u}_{12}] = \begin{bmatrix} k_2 & -lk_1 & k_3 & 0 \\ 0 & k_1 & 0 & 0 \\ -k_3 & 0 & k_2 & lk_1 \\ 0 & 0 & 0 & -k_1 \end{bmatrix}, [\boldsymbol{u}_{21}] = \begin{bmatrix} \alpha_1 & \alpha_2 & 0 & 0 \\ \alpha_2 & \alpha_3 & 0 & 0 \\ 0 & 0 & \alpha_1 & \alpha_2 \\ 0 & 0 & \alpha_2 & \alpha_3 \end{bmatrix},$$

$$\{\boldsymbol{F}_f\} = \begin{Bmatrix} A_1 + lB_1 \\ B_1 \\ A_2 + lB_2 \\ B_2 \end{Bmatrix}, \{\boldsymbol{F}_e\} = \begin{Bmatrix} \alpha_1 A_1 + \alpha_2 B_1 \\ \alpha_2 A_1 + \alpha_3 B_1 \\ \alpha_1 A_2 + \alpha_2 B_2 \\ \alpha_2 A_2 + \alpha_3 B_2 \end{Bmatrix}$$

where definitions of the parameters, such as k_1, k_2, k_3, A_1, A_2, B_1, B_2, α_1, α_2, α_3 can be found in Simon (1982).

From the above equations and expressions, elements of matrices $[s]_i$ and $\{P\}_i$ can be calculated, where $i = 1, 2, \ldots, N$. For the end node N, there exists such a relation:

$$\{\boldsymbol{f}\}_N = [\boldsymbol{s}]_N\{\boldsymbol{e}\}_N + \{\boldsymbol{P}\}_N. \tag{9.10}$$

Provided boundary conditions of the shaft where the force vector equals zero, Eq. (9.10) can give the displacement vector of the end node. Expanding Eq. (9.7) one would have

$$[\boldsymbol{e}]_{i+1} = [\boldsymbol{u}_{21}]_i\{\boldsymbol{f}\}_i + [\boldsymbol{u}_{22}]_i\{\boldsymbol{e}\}_i + \{\boldsymbol{F}_e\}_i \tag{9.11}$$

Substituting Eq. (9.6) into (9.11) yields

$$[\boldsymbol{e}]_{i+1} = \left([\boldsymbol{u}_{21}]_i + [\boldsymbol{u}_{22}]_i\right)\{\boldsymbol{e}\}_i + [\boldsymbol{u}_{21}]_i\{\boldsymbol{P}\}_i + \{\boldsymbol{F}_e\}_i \tag{9.12}$$

Thus,

$$[\boldsymbol{e}]_i = \left([\boldsymbol{u}_{21}]_i + [\boldsymbol{u}_{22}]_i\right)^{-1}\left(\{\boldsymbol{e}\}_{i+1} - [\boldsymbol{u}_{21}]_i\{\boldsymbol{P}\}_i + \{\boldsymbol{F}_e\}_i\right) \tag{9.13}$$

With the equations listed above, the displacement vector $\{e\}_i$ of each section can be obtained. Substituting $\{e\}_i$ into Eq. (9.6), the force vector of each section $\{f\}_i$ can also be obtained. So, the state vectors of all the sections can be determined. From the initial moment t_0, with the method mentioned above, the displacement of each node at the moment $t_0 + \theta\Delta t$ can be obtained. Then, according to Eq. (9.13), by means of the Wilson θ numerical integration method, it is easy to determine the displacement, velocity, and acceleration of each node at the moment of $t_0 + \Delta t$. Repeat the above procedure, and one can calculate the displacement, velocity, and acceleration of each node at the moment $t_0 + \Delta t$, $t_0 + 2\Delta t$, $t_0 + 3\Delta t$,…

$$\{\ddot{\boldsymbol{u}}\}_{t+\Delta t} = \frac{6}{\theta^3\Delta t^2}\left(\{\boldsymbol{u}\}_{t+\theta\Delta t} - \{\boldsymbol{u}\}_t\right) - \frac{6}{\theta^2\Delta t}\{\dot{\boldsymbol{u}}\}_t + \left(1 - \frac{3}{\theta}\right)\{\ddot{\boldsymbol{u}}\}_t \tag{9.14a}$$

$$\{\dot{\boldsymbol{u}}\}_{t+\Delta t} = \{\dot{\boldsymbol{u}}\}_t + \frac{\Delta t}{2}\left(\{\ddot{\boldsymbol{u}}\}_{t+\Delta t} + \{\ddot{\boldsymbol{u}}\}_t\right) \tag{9.14b}$$

$$\{\boldsymbol{u}\}_{t+\Delta t} = \{\boldsymbol{u}\}_t + \{\dot{\boldsymbol{u}}\}_t\Delta t + \frac{\Delta t^2}{6}\left(\{\ddot{\boldsymbol{u}}\}_{t+\Delta t} + 2\{\ddot{\boldsymbol{u}}\}_t\right). \tag{9.14c}$$

9.2.2 Transfer Matrices of Main Components of shaft System

In order to make the rotordynamic analysis by RTMM, the first step is to discretize the shaft system of a hydraulic turbine unit into several segments geometrically and to describe the transfer matrices for the segments.

9.2.2.1 Discretization of Shaft System

The number of degrees of freedom of each real element such as rotor or shaft is infinitive. But in RTMM analysis, with acceptable accuracy, the real elements can be represented by a limited number of rigid elements connected to each other by means of massless elements bearing elastic and damping properties. This process is called discretization and the final result of this process is named multi-degree-

of-freedom system. In rotating machines, the lumped mass and lumped equatorial moment of inertia are concentrated at several points selected on impeller, center of journal, coupling, shaft cross-section of sudden change, end cross-section of shaft etc., The hydraulic turbine unit generally has the constant section shaft. This discretization process will be easy (See Wu 2002, Zhang 2008).

1. Iso-area section shaft segment

Figure 9.1 shows a general lumped shaft element in RTMM. The whole shaft system is divided into N element. The element i, shown in Fig. 9.1, is an original iso-area section shaft segment to be modeled to a disc (or a section of shaft) with mass and without length (d) connected to two small shaft segments $i-1$ and i without mass. The lumped mass of the disc-section is $M^{(d)}$ with equatorial moment of inertia with respect to shaft section center $J_{pi}{}^{(d)}$ and axis moment of inertia with respect to shaft section diameter $J_{di}{}^{(d)}$ without length, two other shaft segments have the length of l_{i-1} and l_i, mass per unit length of μ_{i-1} and μ_i and moment of inertia, $j_{di-1}, j_{di}, j_{pi-1}$ and j_{pi}. All physical parameter is concentrated to the disc center (or shaft center), then the lumped mass of element i and moment of inertia are expressed as

$$M_i = M_i^{(d)} + 0.5(\mu l)_{i-1} + 0.5(\mu l)_i \tag{9.15a}$$

$$J_{di} = J_{di}^{(d)} + \left(0.5 j_d l - 0.083\,\mu l^3\right)_{i-1} + \left(0.5 j_d l - 0.083\,\mu l^3\right)_i \tag{9.15b}$$

$$J_{pi} = J_{pi}^{(d)} + 0.5\left(j_p l\right)_{i-1} + 0.5\left(j_p l\right)_i. \tag{9.15c}$$

2. Step shaft segment

Figure 9.2a shows a step shaft segment which consists of S sub-segments with different section areas. Each sub-segment has its mass per unit length μ_k, the equatorial moment of inertia with respect to shaft section center j_{pk}, the axis moment of inertia with respect to shaft section diameter j_{dk}, the length $l_k (k = 1, 2, \ldots, S)$, and the distance from the mass center of each sub segment to the left end $a_k (k = 1, 2, \ldots, S)$.

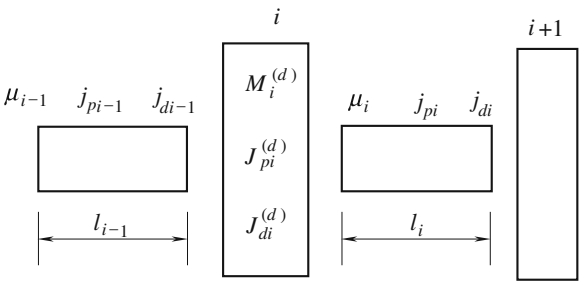

Fig. 9.1 Lumped shaft element in RTMM

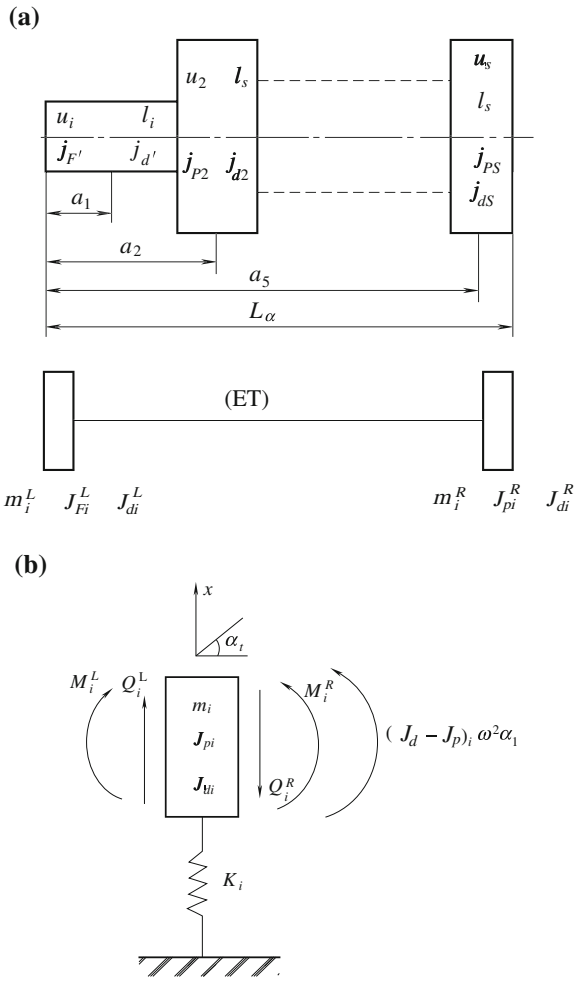

Fig. 9.2 Schematic of the stepped shaft segment. **a** shaft segment. **b** Rigid disc with elastic bracket constrain

If the whole length of the segment is L_i, as shown in Fig. 9.2b, the segment may be simplified into two rigid discs with concentrated masses and moments of inertia on right and left sides of the segment, connected to a shaft with iso-area section and without mass, like that in Fig. 9.1. Then the concentrated masses M^L and M^R are

$$M_i^R = \sum_{k=1}^{S} \frac{(\mu l a)_k}{L_i}, \odot M_i^L = \sum_{k=1}^{S} \frac{[\mu l (L_i - a)]_k}{L_i}. \tag{9.16}$$

And the concentrated moments of inertia at right and left sides of the segment are written as

$$\begin{cases} J_{p_i}^R = \sum_{k=1}^{S} \dfrac{a_k^2}{a_k^2 + (L_i - a_k)^2} j_{pi} l_k \\ J_{p_i}^L = \sum_{k=1}^{S} \dfrac{(L_i - a_k)}{a_k^2 + (L_i - a_k)^2} j_{pi} l_k \\ J_{p_i}^R = \sum_{k=1}^{S} \dfrac{a_k^2}{a_k^2 + (L_i - a_k)^2} \left\{ j_d l + \dfrac{\mu l^3}{12} - (L_i - a) \right\}_k \\ J_{p_i}^L = \sum_{k=1}^{S} \dfrac{(L_i - a_k)^2}{a_k^2 + (L_i - a_k)^2} \left\{ j_d l + \dfrac{\mu l^3}{12} - \mu l a (L_i - a) \right\}_k . \end{cases} \tag{9.17}$$

$$M_i = M_i^{(d)} + M_i^L + M_{i-1}^R \tag{9.18a}$$

$$J_{di} = J_{di}^{(d)} + J_{di}^L + J_{di-1}^R \tag{9.18b}$$

$$J_{pi} = J_{pi}^{(d)} + J_{pi}^L + J_{pi-1}^R \tag{9.18c}$$

Then the concentrated mass M_i and the moments of inertia J_{di} and J_{pi} of the whole segment can be calculated via Eq. (9.18).

One can get the equivalent bending stiffness of the segment:

$$(L/EJ)_i = \sum_{k=1}^{S} (l/EJ)_k$$

where $(EI)_k$ is the bending stiffness of each sub-segment.

9.2.2.2 Transfer Matrix of Typical Element of Shaft System

In RTMM, the shaft system is divided into components or assemblies of discs, shaft segments, and elastic bracket constraints.

The transfer matrices will be displayed below. For ith section of element the state variable vector $\{\boldsymbol{u}\}_i$ can be indicated as

$$\{\boldsymbol{u}\}_i = \{x, \alpha, M, Q\}_i^T \tag{9.19}$$

where x is displacement; α is torsion angle (angulations); M is bending moment; and Q is the shearing force.

The state vector at section $i + 1$, $\{\boldsymbol{u}\}_{i+1}$ may have a relation to the state vector $\{\boldsymbol{u}\}_i$:

$$\{\boldsymbol{u}\}_{i+1} = [\boldsymbol{T}]_i \{\boldsymbol{u}\}_i \tag{9.20}$$

where $[\boldsymbol{T}]_i$ is the transfer matrix at the ith section. It is $r \times r$ orders matrix if the state vector has r components.

1. The rigid disc element with elastic bracket constraints

Figure 9.2 illustrates a rigid disc element with an elastic bracket constraint of stiffness coefficient K_j Superscripts R and L denote the parameters of the right or left-side section, respectively.

If the disc makes the precessing rotation with angular speed ω, the inertia force and the inertia torque of the disc are $m_i\omega^2 x_i$ and $(J_p - J_d)_i\omega^2\alpha_i$ respectively. The stiffness coefficient K_j of the elastic bracket constrain can be calculated from the parallel arranged the elastic bracket stiffness K_b with mass m_b and oil film of bearing K:

$$K_j = \frac{K(K_b - m\omega^2)}{K + K_b - m\omega^2} \tag{9.21}$$

where ω is the processing speed of the rotor on the elastic bracket constraint.

Then the relation between two state vectors on the right and the left side sections is

$$\{\boldsymbol{u}\}_i^R = [\boldsymbol{D}]_i\{\boldsymbol{u}\}_i^L$$

The transfer matrix of the two vectors has the following form:

$$[\boldsymbol{D}]_i = \begin{bmatrix} 1 & 0 & 0 & 0 \\ 0 & 1 & 0 & 0 \\ 0 & (J_P - J_d)\omega^2 & 1 & 0 \\ m\omega^2 - K_j & 0 & 0 & 1 \end{bmatrix}_i \tag{9.22}$$

2. Shaft segment without mass

Figure 9.3 exhibits an element of the shaft segment without mass. For the assembly model, the element is massless based on the balancing conditions of force and condition of deformation in the element. The two state vectors have the following relation:

$$\{\boldsymbol{u}\}_{i+1} = [\boldsymbol{B}]_i\{\boldsymbol{u}\}_i$$

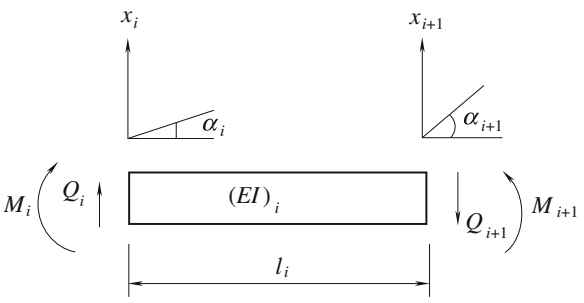

Fig. 9.3 Shaft segment without mass (Zhang 2008)

where the transfer matrix is

$$[\boldsymbol{B}]_i = \begin{bmatrix} 1 & l & \frac{l^2}{2EJ} & \frac{l^3}{6EJ}(1-\gamma) \\ 0 & 1 & \frac{l}{EJ} & \frac{l^2}{2EJ} \\ 0 & 0 & 1 & l \\ 0 & 0 & 0 & 1 \end{bmatrix} \tag{9.23}$$

where E is the Young's modulus; l is the length of the segment; J is the area moment of the segment section. γ is the effect coefficient considering the shear stress, which is

$$\gamma = 6EJ/\left(k_i G A l^2\right) \tag{9.24}$$

where k_i is section factor ($k_i = 0.886$ for solid circle shaft; $k_i = 0.667$ for hollow shaft with thin wall); G is shear modulus and A is section area.

3. Combination element of a disc and shaft segment

Figure 9.4 shows an element of the combined disc and shaft segment in a simplified shaft computational model. The matrices transfer expression and the transfer matrix can be expressed as

$$\{\boldsymbol{u}\}_{i+1} = [\boldsymbol{T}]_i \{\boldsymbol{u}\}_i$$

and

$$[T]_i = \begin{bmatrix} 1+\frac{l^3}{6EJ}(1-\gamma)\left(m\omega^2 - K_j\right) & l+\frac{l^2}{2EJ}\left(J_p - J_d\right)\omega^2 & \frac{l^2}{2EJ} & \frac{l^3}{6EJ}(1-\gamma) \\ \frac{l^2}{2EJ}(1-\gamma)\left(m\omega^2 - K_j\right) & 1+\frac{l}{2EJ}\left(J_p - J_d\right)\omega^2 & \frac{l}{EJ} & \frac{l^2}{2EJ} \\ l\left(m\omega^2 - K_j\right) & \left(J_p - J_d\right)\omega^2 & 1 & l \\ \left(m\omega^2 - K_j\right) & 0 & 0 & 1 \end{bmatrix}_i \tag{9.25}$$

where ω is the angular speed of the rotor precession. If there is not an elastic bracket constraint then K_j, γ, J_p and J_d equal zero.

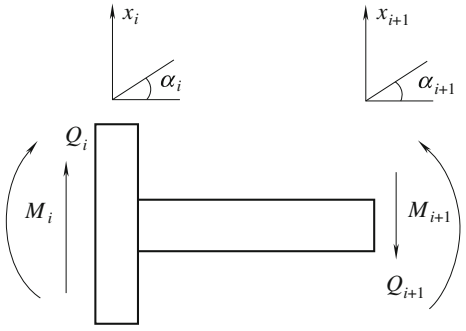

Fig. 9.4 Combination of elements of disc and shaft segment

9.2.3 Free-Vibration Analysis of a Hydraulic Turbine Unit

In order to calculate the natural characteristic of the shaft system, one should analyze its free vibration of a large hydraulic turbine unit through the RTMM (Zhang 2006).

After dividing the shaft system into 37 elements of lumped mass with 38 nodes, one establishes the assembly model of the HTGS shaft system displayed in Fig. 9.5, in which element 6 is the upper guide bearing (YGB), 13 is the generator rotor, 18 is the low guide bearing (LGB) and thrust, 32 is the guide bearing of the turbine (WGB), 36 is the water sealing (ES), 37 is the turbine runner, and 38 is the lowest node of the shaft system.

The maximum head of the turbine is 139.3 (m), the design head 117 m, the rotating speed 500 rpm.

The inner diameter of the magnetic core of generator stator is 2.56 m, its height is 1.60 m, the magnetic flux density of the core is 7,500 Gauss. Table 9.1 lists parameters of the elements of the shaft system.

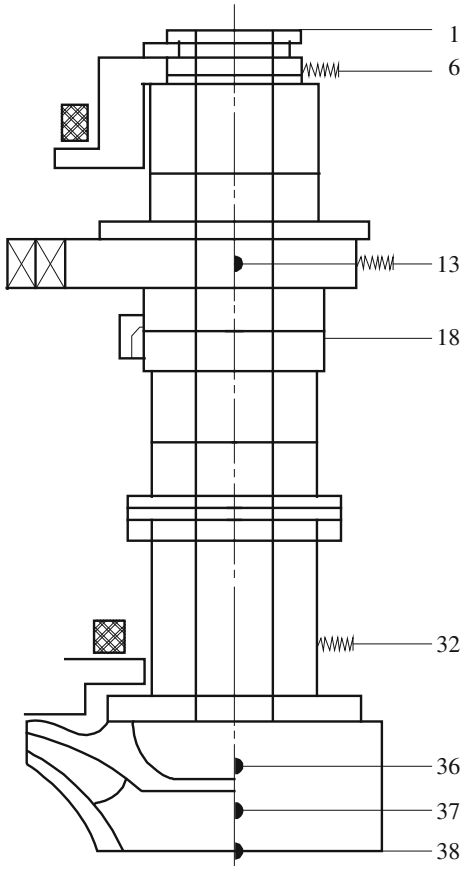

Fig. 9.5 Schematic drawing of structure and computation (Zhang 2006)

Table 9.1 Parameters of the elements of the shaft system (Zhang 2006)

Element	Stiffness (N/m)	Damping (Ns/m)
UGB	1.0×10^9	2.4×10^6
LGB	1.0×10^9	2.4×10^6
WGB	1.67×10^9	2.3×10^7
Bracket and base	3.0×10^9	2.0×10^7

9.2.3.1 Computation of Free Vibration with Elastic Bracket

Computation of free vibration of this shaft system with elastic brackets and base has been carried out based on the simulation model as schematically plotted in Fig. 9.5. The force analysis at node i is shown in Fig. 9.6. The motion equation of the equivalent mass of a bearing bracket, $[\boldsymbol{M}_b]$ is

$$[\boldsymbol{M}_b]\{\ddot{\boldsymbol{u}}_b\} = -[\boldsymbol{K}_b]\{\boldsymbol{u}_b\} - [\boldsymbol{C}_b]\{\dot{\boldsymbol{u}}_b\} + [\boldsymbol{K}](\{\boldsymbol{u}\} - \{\boldsymbol{u}_b\}) + [\boldsymbol{C}](\{\dot{\boldsymbol{u}}\} - \{\dot{\boldsymbol{u}}_b\}) \tag{9.26}$$

where the subscript b indicates the parameters of the bearing bracket with the bearing base shown in Fig. 9.6, and the parameters without subscript are those of bearing oil film.

Assume that

$$\{\boldsymbol{u}_b\} = \{\boldsymbol{u}_{b0}\}\mathrm{e}^{\omega t} = \{\boldsymbol{u}\} = \{\boldsymbol{u}_0\}\mathrm{e}^{\omega t}.$$

The oil film reaction force $\{\boldsymbol{R}\}$ is given by

$$\begin{aligned}\{\boldsymbol{R}\} = \begin{Bmatrix}\boldsymbol{R}_x \\ \boldsymbol{R}_x\end{Bmatrix} &= -([\boldsymbol{K}] + \omega[\boldsymbol{C}])([\boldsymbol{K}] + \omega[\boldsymbol{C}] + [\boldsymbol{K}_b] \\ &+ \omega[\boldsymbol{C}_b] + \omega^2[\boldsymbol{M}_b])^{-1}([\boldsymbol{K}_b] + \omega[\boldsymbol{C}_b] + \omega^2[\boldsymbol{M}_b])\{\boldsymbol{u}\}.\end{aligned} \tag{9.27}$$

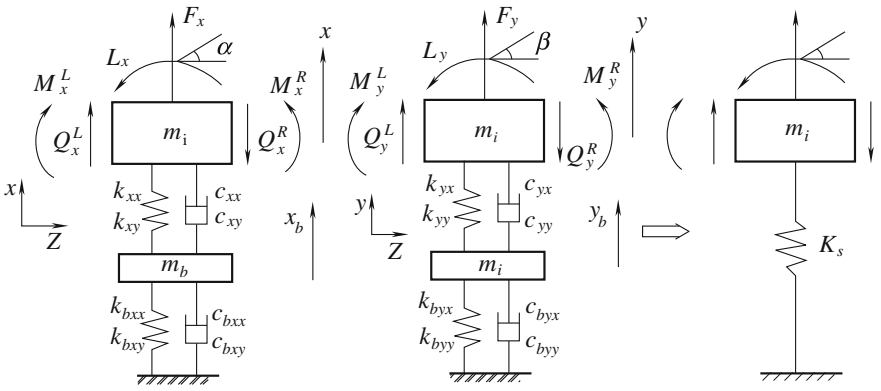

Fig. 9.6 Force analysis of bearing node (Zhang 2006)

The global stiffness matrix for bearing including the effects of stiffness and damping of bracket and base is obtained as

$$[\boldsymbol{K}_S] = \begin{bmatrix} k_{Sxx} & k_{Sxy} \\ k_{Syx} & k_{Syy} \end{bmatrix} = -([\boldsymbol{K}] + \omega[\boldsymbol{C}])([\boldsymbol{K}] + \omega[\boldsymbol{C}] + [\boldsymbol{K}_b] + \omega[\boldsymbol{C}_b] + \omega^2[\boldsymbol{M}_b])^{-1}([\boldsymbol{K}_b] + \omega[\boldsymbol{C}_b] + \omega^2[\boldsymbol{M}_b]). \tag{9.28}$$

For free vibration in the RTMM, Eq. (9.7) becomes

$$\{\boldsymbol{f}/\boldsymbol{e}\}_{i+1} = \begin{bmatrix} [\boldsymbol{u}_{11}] & [\boldsymbol{u}_{12}] \\ [\boldsymbol{u}_{21}] & [\boldsymbol{u}_{22}] \end{bmatrix}_i \{\boldsymbol{f}/\boldsymbol{e}\}_i \tag{9.29}$$

where in this dynamic problem,

$$[\boldsymbol{u}_{11}]_i = \begin{bmatrix} 1 & l & 0 & 0 \\ 0 & 1 & 0 & 0 \\ 0 & 0 & 1 & l \\ 0 & 0 & 0 & 1 \end{bmatrix}_i, \quad [\boldsymbol{u}_{12}]_i = \begin{bmatrix} \frac{l^2}{2EI} & \frac{l^3}{6EI}(1-\gamma) & 0 & 0 \\ \frac{l}{EI} & \frac{l^2}{2EI} & 0 & 0 \\ -k_3 & 0 & \frac{l^2}{2EI} & \frac{l^3}{6EI}(1-\gamma) \\ 0 & 0 & \frac{l}{EI} & \frac{l^2}{2EI} \end{bmatrix}_i,$$

$$[\boldsymbol{u}_{21}]_i = \begin{bmatrix} -l(M\omega^2 + k_{Sxx}) & J_d\omega^2 & -lk_{Sxy} & J_p\Omega\boldsymbol{\omega} \\ -(M\omega^2 + k_{Sxx}) & 0 & -k_{Sxy} & 0 \\ -lk_{Syx} & -J_p\Omega\boldsymbol{\omega} & -l\left(M\omega^2 + k_{Syy}\right) & J_d\omega^2 \\ -k_{Syx} & 0 & -\left(M\omega^2 + k_{Syy}\right) & 0 \end{bmatrix}_i,$$

$$[\boldsymbol{u}_{22}]_i = \begin{bmatrix} 1 - \frac{l^3(1-\gamma)}{6EI}(M\omega^2 + k_{sxx}) & l + \frac{l^2J_d\omega^2}{2EI} & \frac{l^3(1-\gamma)}{6EI}k_{sxy} & \frac{l^2J_p\omega\Omega}{2EI} \\ -\frac{l^2}{2EI}(M\omega^2 + k_{sxx}) & 1 + \frac{lJ_d\omega^2}{EI} & -\frac{l^2}{2EI}k_{sxy} & \frac{lJ_p\omega\Omega}{EI} \\ -\frac{l^3(1-\gamma)}{6EI}k_{syx} & -\frac{l^2J_p\omega\Omega}{2EI} & 1 - \frac{l^3(1-\gamma)}{6EI}\left(M\omega^2 + k_{syy}\right) & l + \frac{l^2J_d\omega^2}{2EI} \\ -\frac{l^2}{2EI}k_{syx} & -\frac{lJ_p\omega\Omega}{EI} & -\frac{l^2}{2EI}\left(M\omega^2 + k_{syy}\right) & 1 + \frac{lJ_d\omega^2}{EI} \end{bmatrix}_i.$$

Like Eq. (9.11), introducing the Reccaati transfer, then

$$\{\boldsymbol{f}\}_i = [\boldsymbol{s}]_i\{\boldsymbol{e}\}_i \tag{9.30}$$

Thus

$$[\boldsymbol{f}]_{i+1} = \left([\boldsymbol{u}_{11}][\boldsymbol{s}] + [\boldsymbol{u}_{12}]_i\right)_i\left([\boldsymbol{u}_{21}][\boldsymbol{s}] + [\boldsymbol{u}_{22}]_i\right)_i^{-1}\{\boldsymbol{e}\}_{i+1} \tag{9.31}$$

$$[\boldsymbol{e}]_i = ([\boldsymbol{u}_{21}][\boldsymbol{s}] + [\boldsymbol{u}_{22}])_i\{\boldsymbol{e}\}_{i+1} \tag{9.32}$$

From the above two equations, as shown in Eq. (9.8), one yields

$$[\boldsymbol{s}]_{i+1} = ([\boldsymbol{u}_{11}][\boldsymbol{s}] + [\boldsymbol{u}_{12}])_i([\boldsymbol{u}_{21}][\boldsymbol{s}] + [\boldsymbol{u}_{22}])_i^{-1}. \tag{9.33}$$

9.2.3.2 Solution of Free Vibration with an Elastic Bracket

1. Natural frequency. From boundary conditions at end nodes of the shaft system, the frequency equation becomes

$$|\boldsymbol{s}|_{\mathrm{N}+1} = \begin{vmatrix} s_{11} & s_{12} & s_{13} & s_{14} \\ s_{21} & s_{22} & s_{23} & s_{24} \\ s_{31} & s_{32} & s_{33} & s_{34} \\ s_{41} & s_{42} & s_{43} & s_{44} \end{vmatrix} = 0. \tag{9.34}$$

It is difficult to solve Eq. (9.34), and the best way to solve the no-singularity equation is the method of Newton–Raphson or Muller:

$$|\boldsymbol{s}|_{\mathrm{N}+1} \prod_{i=1}^{N} \left| \left([\boldsymbol{u}_{21}][\boldsymbol{s}] + [\boldsymbol{u}_{22}] \right)_i \right| = 0. \tag{9.35}$$

Solution of Eq. (9.26) represents the natural complex frequencies. Substituting the solution to Eqs. (9.31) and (9.32) yields the natural vibration modes in the complex, then transforms it to the real one:

$$x = \mathrm{Re}\left\{ \bar{\boldsymbol{X}} e^{j\Omega t} \right\} = \sqrt{X_C^2 + X_S^2} \cos(\Omega t + \boldsymbol{\theta}_x) \tag{9.36}$$

$$y = \mathrm{Re}\left\{ \bar{\boldsymbol{Y}} e^{j\Omega t} \right\} = \sqrt{Y_C^2 + Y_S^2} \cos\left(\Omega t + \boldsymbol{\theta}_y\right) \tag{9.37}$$

where $\theta_x = \arctan\,(X_S/X_C)$ and $\theta_y = \arctan\,(Y_S/Y_C)$; $\bar{X} = X_C + \mathrm{i}X_S$ and $\bar{Y} = Y_C + \mathrm{i}Y_S$ are complex displacements; x and y are real displacements.

2. Main modes. After solving for the natural frequency, substituting it into Eq. (9.30) ($i = \mathrm{N}$) yields

$$\begin{bmatrix} s_{11} & s_{12} \\ s_{21} & s_{22} \end{bmatrix}_{N+1} \begin{Bmatrix} X \\ A \end{Bmatrix}_{N+1} = 0. \tag{9.38}$$

The mode can thus be obtained from the solution and recursion formulae to get the modes.

9.2.3.3 Results of Free Vibration Computation of the Shaft System of a Francis Turbine Unit

The natural frequencies and their free vibration modes have been calculated for a shaft system of a Francis turbine unit shown in Fig. 9.5. The first and second

Table 9.2 Computational results of the critical speed (Zhang 2006)

Brackets constrains	1st order CRS	2nd order CRS
Rigid bearings	1,741.6	3,480.0
Elastic bearings (without damping)	1,112.8	1,635.4
Elastic bearings (with damping)	1,428.5	2,336.5

Table 9.3 Influence of the upper guide bearing stiffness to the critical speed (Zhang 2006)

Stiffness of UGB	0.5 GN/m	0.75 GN/m	1.0 GN/m	1.25 GN/m	1.5 GN/m
1st order CRS	1,379	1,575.4	1,741.6	1,885.2	2,010.6
2nd order CRS	3,420	3,449	3,480	3,515	3,553

critical rotating speeds (CRS) of the calculated results are listed in Table 9.2, in which the elastic brackets and elastic base of bearings has been considered in comparison to the results of the rigid bearings (see Chap. 5, Zhang 2006).

From the results in Table 9.2, notice that critical speeds of the shaft system are lower than the runway speed of the system, 973 rpm. The stiffness of the elasticity of the bearing bracket and its base has great influence on bringing down the critical speed. Table 9.3 shows that the stiffness of the upper guide bearing (UGB) has great impact on the first order critical speeds of the shaft system, but nearly no influence on the second order. The larger the stiffness, the higher the first order critical speed will be. Similar computation indicates that the turbine guide bearing (TGB) stiffness influences the second order critical speeds greatly, whereas its influence to the first order critical speed is less. The low guide bearing (LGB) stiffness has small influence to both the first and second order critical speeds.

Figure 9.7 demonstrates the first and second lateral vibration modes of the shafts. They are relative lateral displacements of each node of the system. The stiffness of bearings has a little influence of the modes.

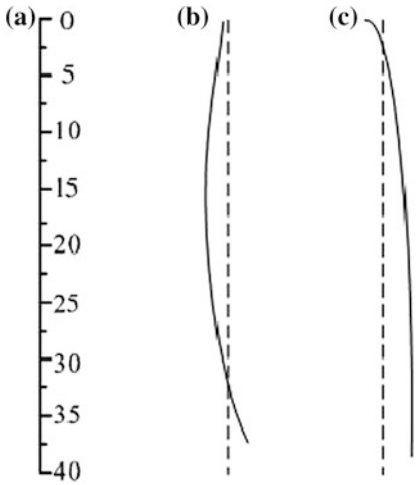

Fig. 9.7 Lateral vibration mode of the shaft. **a** Node number. **b** First order model. **c** Second order mode (Zhang 2006)

9.2.4 Transient Vibration Response of the Shaft System

The transient vibration response of the shaft system in a hydraulic turbine unit have been analyzed based on the RTMM with the Newmark β integration method. Equations in this computation are almost the same as those described in Sect. 9.2.2, except Eq. (9.14). For the Newmark β method, the following equation is adopted to get the displacement, velocity and acceleration at each time moment:

$$\{\ddot{\boldsymbol{u}}\}_{t+\Delta t} = \frac{1}{\beta \Delta t^2}\left(\{\boldsymbol{u}\}_{t+\Delta t} - \{\boldsymbol{u}\}_t\right) - \frac{6}{\beta \Delta t}\{\dot{\boldsymbol{u}}\}_t + \left(\frac{1}{2\beta} - 1\right)\{\ddot{\boldsymbol{u}}\}_t \tag{9.39a}$$

$$\{\dot{\boldsymbol{u}}\}_{t+\Delta t} = \{\dot{\boldsymbol{u}}\}_t + \frac{}{2}\left(\{\ddot{\boldsymbol{u}}\}_{t+\Delta t} + \{\ddot{\boldsymbol{u}}\}_t\right) \tag{9.39b}$$

$$\{\boldsymbol{u}\}_{t+\Delta t} = \{\boldsymbol{u}\}_t + \{\dot{\boldsymbol{u}}\}_t \Delta t + \frac{\Delta t^2}{6}\left(\{\ddot{\boldsymbol{u}}\}_{t+\Delta t} + 2\{\ddot{\boldsymbol{u}}\}_t\right) \tag{9.39c}$$

where β is the factor to consider deleting in the high order terms of the calculation.

Transient vibration responses of the shaft system of the same Francis turbine unit as in previous section were simulated in the following cases.

1. **Case 1** There is not an eccentric mass for every node of the system, but there is an initial displacement along x direction, 0.1 mm, and an initial velocity along y direction, 3.8 mm/s for all nodes at time moment $t = 0$. The calculation was carried out for two conditions considering the linear character and the nonlinear character of the oil film reaction force in the bearings (see Chap. 5).

Figure 9.8 shows the orbit of the runner node in case 1 with initial displacement and velocity as the dynamic response under conditions of linear oil film reaction force (a), and of nonlinear oil film reaction force (b). The difference between the two results is that under nonlinear condition the damping velocity of the forced vibration is greater than that under the linear condition.

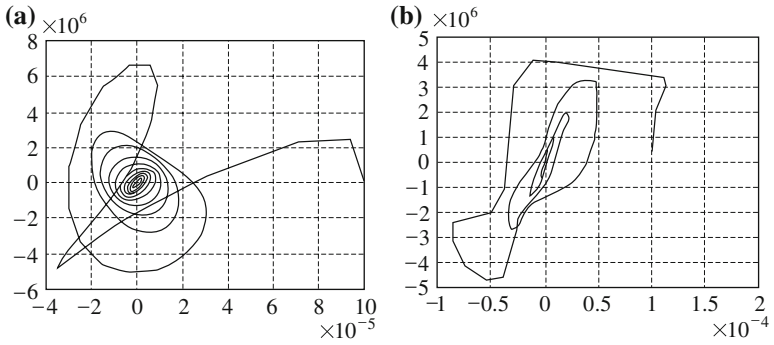

Fig. 9.8 Orbit of runner node at case 1 with initial displacement and velocity (Unit: m). **a** At linear oil film reaction force, **b** At nonlinear oil film reaction force (Zhang 2006)

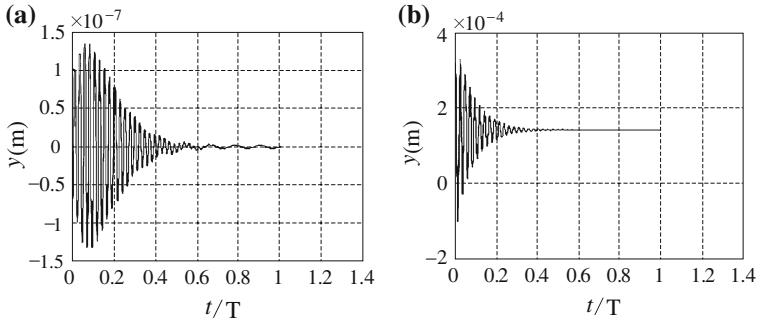

Fig. 9.9 Time history of runner displacement after a sudden force acts on the node. **a** Act of 650 N sudden force. **b** Act of 350 kN sudden force (Zhang 2006)

2. **Case 2** A sudden external force acts on the runner node at the time beginning. Figure 9.9 exhibits the time history of the runner node's displacement after the sudden force with 650 N (a) or 350kN (b). When the acting force is large, node displacement will reach to 3.2×10^{-4} mm).

Zhang (2006) conducted the transient response analysis for the shaft system of a hydraulic turbine unit. In computation, the concept of a non-linear oil film force of the bearing was indicated, and its influencing factor was summarized. The action of non-linear oil film force also was considered. Based on his computations, the following conclusions could be drawn: (1) The critical speed of the shafts is influenced by the elastic bearing; (2) Non-equilibrium magnetic pull reduces the first order critical speed, but has no effect on the second order critical speed; (3) When the rotor is in its initial position and initial speed, the shaft's nonlinear node conservation speed is larger than linear conservation speed; (4) Under an unbalanced condition, the nonlinear response will become much more complicated.

Feng and Chu (2001) applied the Riccati transfer matrix to calculate transient responses of a pump-turbine shaft system excited by different types of external forces. The natural vibration analysis revealed that the guide bearing stiffness coefficients have influence on the first three critical speeds. For large pump-turbine units, there exists a common characteristic in the first three vibration modes; that is, the maximum amplitude was at the generator rotor in the first vibration mode, while in the third vibration mode, the maximum amplitude was near the runner.

In the transient response calculation, a number of possible nonlinear factors in the unit were taken into account, such as nonlinearity of the journal guide bearing, the center-pivoted tilting-pad thrust bearing, and also a nonlinear magnetic force (see Chap. 5). The effect of hydraulic forces acting on the runner shows that the vibration amplitude and the time required for vibration at the three guide bearings to reach a steady state is different. When a lateral force, which consists of a constant lateral force and periodic forces with frequencies of 7 and 14-times the rotational frequency is suddenly exerted on the runner, the shaft would respond with the same frequencies, but with different amplitudes, especially different average amplitudes.

9.3 Rotordynamics Analysis in Hydraulic Turbine Units by FEM

It has been shown that hydraulic turbine units with vibration problems are directly connected to the rotordynamic properties of the unit. In order to deal with such vibration problems, one needs to perform the complete rotordynamic analysis of hydraulic turbine units at design stage or when problems occur during commissioning/operation. With modern rotordynamic software tools such as ANSYS, NASTRAN, ARMD (Advanced Rotating Machinery Dynamics), I-DEAS, TURBOROT, vibration behavior could be analyzed in detail. This calls for, not only the natural frequency analysis that has been the normal approach, but also response analysis for computation of the unbalanced response and prediction of the vibration levels with reasonable precision.

The most prevalent method used today for rotordynamics analysis is the FEM. The basic principles were introduced in Chaps. 5 and 8 for structure vibration. In this chapter, the content of specific research results will be introduced as follows:

1. To calculate the dynamic response of a turbine unit based on the FEM, one should establish the FEM model including the typical component model, which can reflect the actual structure of the unit.
2. To establish the FEM model, one ought to analyze the influence of dynamic characteristics on the shaft system by the gyroscopic effects, to select a reasonable guide bearing stiffness, and to consider the influence of magnetic pull on system imbalance.
3. The main task of the dynamic response analysis should be to find the most disadvantageous imbalance loads acting on the shaft, as well as their combination and phase's differences.

9.3.1 Computational Model of Shaft System of Hydraulic Turbine Unit

The FEM analysis for a hydraulic turbine unit includes its typical component models, which can reflect the actual structure of the unit.

9.3.1.1 Mechanical Model of Shaft System

Figure 9.10 depicts the mechanical model of a shaft system in a hydraulic turbine unit, which consists of a shaft and rotor of the excitation motor with mass M_1, a generator rotor with mass M_2, and a runner with mass M_3. The masses can be lumped to nodes in the components elements. All the components have the equatorial moments of inertia with respect to their circular section centers J_p and their axial moment J_d. The shaft is simulated by beam elements in FEM; rotors by disc elements; the runner by cylinder element or disc.

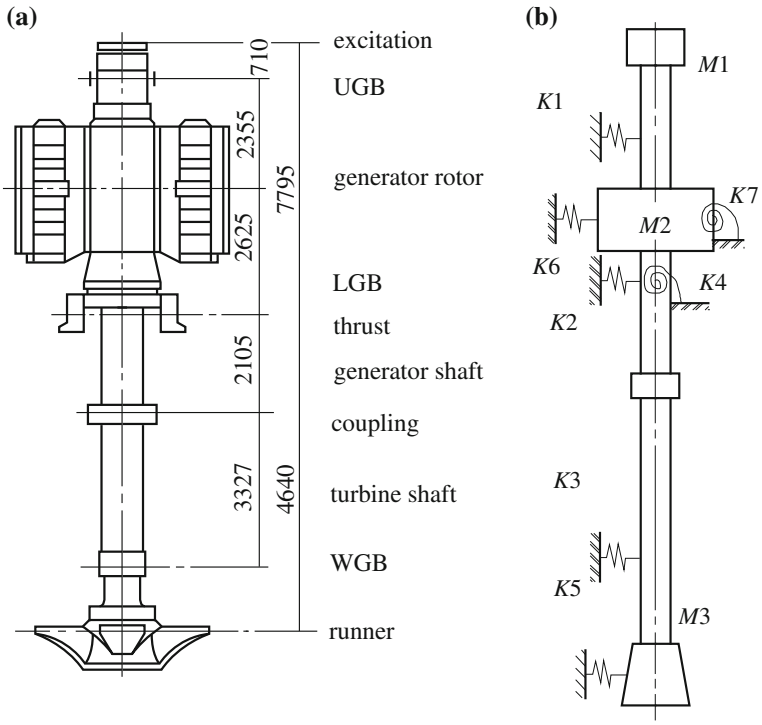

Fig. 9.10 Model of shaft system in a hydraulic turbine unit. **a** Structure. **b** Model (Zhang 2008)

In the model, the bearings are simulated by spring elements. K_1 is the stiffness of the upper guide bearing; K_2 is the stiffness of the low guide bearing; K_3 is the stiffness of the water guide bearing. The three kinds of stiffness include the oil film bearing stiffness and the stiffness of their bases and brackets which are installed in a series as shown in Fig. 9.6.

K_4 is the torsion stiffness of the thrust, whose action to the shaft system is equivalent to a torsion spring.

K_5 is the stiffness of runner that is formed by an imbalanced water reaction caused by asymmetric clearance between its outskirt and inner surfaces of head cover and bottom cover, respectively.

K_6 and K_7 are stiffness and torsion stiffness of the generator which represent the imbalanced reaction of an asymmetric magnetic pull caused by uneven clearance between rotor and stator.

9.3.1.2 Basic Equations of Shaft System Model in FEM

The General governing equations of a rotating mechanical system can be expressed in the inertial reference frame and in the rotating frame of reference as shown in Sect. 9.1: Eqs. (9.1)–(9.3).

1. Modal analysis in FEM

The goal of modal analysis in rotordynamics is to determine the natural mode shapes and frequencies of a rotor system during free vibration. It is common to use the FEM to perform this analysis, because like other calculations, the object being analyzed in the FEM can have an arbitrary shape and the results of the calculations are acceptable.

For the most basic problem involving a linear elastic material the matrix equations take the form of a dynamic three-dimensional spring mass system. The generalized equation of motion is given as

$$[\boldsymbol{M}]\{\ddot{\boldsymbol{u}}\} + [\boldsymbol{C}]\{\dot{\boldsymbol{u}}\} + [\boldsymbol{K}]\{\boldsymbol{u}\} = \{\boldsymbol{f}\} \tag{9.40}$$

where $[\boldsymbol{M}]$ is the mass matrix, $\{\ddot{\boldsymbol{u}}\}$ is the 2nd time derivative of the displacement $\{\boldsymbol{u}\}$ (i.e., the acceleration), $\{\dot{\boldsymbol{u}}\}$ the velocity, $[\boldsymbol{C}]$ is a damping matrix, $[\boldsymbol{K}]$ is the stiffness matrix, and $\{\boldsymbol{f}\}$ is the force vector

The only terms kept are the 1st and 3rd terms on the left hand side which give the following system:

$$[\boldsymbol{M}]\{\ddot{\boldsymbol{u}}\} + [\boldsymbol{K}]\{\boldsymbol{u}\} = 0. \tag{9.41}$$

This is the general form of the eigensystem encountered in structural engineering using the FEM. Furthermore, the harmonic motion is assumed for the system, so that $\{\dot{\boldsymbol{u}}\}$ is equal to $\lambda\{\boldsymbol{u}\}$, where λ is an eigenvalue, and the equation reduces to

$$[\boldsymbol{M}]\{\boldsymbol{u}\}\lambda + [\boldsymbol{K}]\{\boldsymbol{u}\} = 0. \tag{9.42}$$

In contrast, the equation for static problems is

$$[\boldsymbol{K}]\{\boldsymbol{u}\} = \{\boldsymbol{f}\} \tag{9.43}$$

which is expected when all terms having time derivatives are set to zero.

For the linear system, the solutions of Eq. (9.42) is expressed as

$$\{\boldsymbol{u}\}_i = \{\boldsymbol{\varphi}\}_i \cos(\omega_i t + \theta_i) \tag{9.44}$$

where $\{\boldsymbol{\varphi}\}_i$ is the ith order vibration mode vector; ω_i is the ith order free vibration frequency, θ_i is the ith order vibration phase angle. Introducing Eq. (9.43) into (9.41), one gets

$$\left([\boldsymbol{K}] - \omega^2[\boldsymbol{M}]\right)\{\boldsymbol{u}\} = 0. \tag{9.45}$$

In order to include the vibration amplitudes for each degree of freedom, the algebraic equations are given as

$$\left|[\boldsymbol{K}] - \omega^2[\boldsymbol{M}]\right| = 0. \tag{9.46}$$

The solutions of Eqs. (9.45) and (9.46) are the eigenvalues $\omega^2 = \lambda$ and their corresponding eigenvectors of the equations, which are dependent upon the mass matrix and stiffness matrix. For linear elastic problems, the stiffness and mass matrices and the system in general are positive definite. These are the easiest matrices to deal with because numerical methods commonly applied are guaranteed to converge to a solution. When all the qualities of the system are considered:

1. Only the smallest eigenvalues and eigenvectors of the lowest modes are desired.
2. The mass and stiffness matrices are sparse and highly banded.
3. The system is positive definite.

A typical prescription of the solution is to tridiagonalize the system using the Lanczos algorithm. Next, find the eigenvectors and eigenvalues of this tri-diagonal system. If inverse iteration is performed, the new eigenvalues will relate to the old by $\mu = 1/\lambda$, while the eigenvectors of the original can be calculated from those of the tri-diagonal matrix.

2. Transient analysis in FEM

In a mechanical system, a transient or natural response is the response of a system to disturb from equilibrium. Specifically, transient responses in the system are the portion of the response that approaches zero after a sufficiently long time.

The rotordynamic force equilibrium Eq. (9.2) can be rewritten in the following form as a set of N second order differential equations:

$$[\boldsymbol{M}]\{\ddot{\boldsymbol{u}}\} + [\boldsymbol{C}]\{\dot{\boldsymbol{u}}\} + [\boldsymbol{K}]\{\boldsymbol{u}\} = \sum_{j=1}^{J} \{\boldsymbol{f}_j g_j(t)\}. \tag{9.47}$$

All possible types of time-dependent loading can be represented by a sum of "J" space vector, where $\{\boldsymbol{f}_j\}$ are not a function of time, and $g_j(t)$ are time functions. The number of dynamic degrees-of-freedom is equal to the number of lumped masses in the system. In the mode superposition method, the separation of variables is used to solve Eq. (9.47). This approach presumes the solution can be expressed in the following form:

$$\{\boldsymbol{u}(t)\} = [\boldsymbol{\Phi}]\{\boldsymbol{Y}(t)\} \tag{9.48a}$$

where $[\boldsymbol{\Phi}]$ is an "$N \times L$" matrix containing L spatial vectors which are not a function of time, and $\{\boldsymbol{Y}(t)\}$ is the modal ordinate, a vector containing L functions of time. And let

$$[\Phi]^T[\boldsymbol{M}][\Phi] = [\boldsymbol{I}] \tag{9.48b}$$

and

$$[\Phi]^T[\boldsymbol{K}][\Phi] = \left[\Omega_h^2\right] \tag{9.48c}$$

where $[\boldsymbol{I}]$ is a diagonal unit matrix and $[\boldsymbol{\Omega}_h^2]$ is a diagonal matrix that may or may not contain free vibration frequencies.

After substitution of Eq. (9.48) into (9.47) and the pre-multiplication by $[\boldsymbol{\Phi}]^T$, the following matrix of L equations is produced:

$$[\boldsymbol{I}]\left\{\ddot{\boldsymbol{Y}}(t)\right\} + [\boldsymbol{d}]\left\{\dot{\boldsymbol{Y}}(t)\right\} + \left\{\Omega_h^2\right\} = \sum_{j=1}^{J}\left\{\boldsymbol{p}_j g_j(t)\right\} \tag{9.49}$$

where $\{\boldsymbol{\Omega}_h^2\} = [\boldsymbol{\Omega}_h^2]\ \{\boldsymbol{I}\}$ ($\{\boldsymbol{I}\}$ is unit vector), $\{\boldsymbol{p}_j\} = [\boldsymbol{\Phi}]^T\ \{\boldsymbol{f}_j\}$ and both are defined as the modal participation factors for time function j. The term p_{nj} is associated with the nth mode.

For all real structures, the ''$L \times L$'' matrix is not diagonal; however, in order to uncouple the modal equations it is necessary to assume that there is no coupling between the modes. Therefore, the matrix is thought to be diagonal with the modal damping terms defined by

$$d_{nn} = 2\varsigma_n\omega_n$$

where d_{nn} is the ratio of the damping in mode; ς_n to the critical damping of the mode; ω_n is the critical frequency of the mode. A typical uncoupled modal equation for linear shaft systems is in the form of

$$\ddot{y}_n(t) + 2\varsigma_n\omega_n\dot{y}_n(t) + \omega_n^2 y_n(t) = \sum_{j=1}^{J} p_{nj}g_j(t). \tag{9.50}$$

Based on the foregoing equations, the transient dynamic response of the shaft system due to the initial conditions and arbitrary loading could be solved with the mode superposition method.

The mode superposition method is a very powerful method applied to reduce the number of unknowns in a dynamic response analysis. All types of loading can be accurately approximated by piece-wise linear functions within a small time increment. An exact solution exists for this type of loading and this solution can be computed with a trivial amount of computer time for equal time increments. Consequently, there is no need to present other methods for the numerical evaluation of modal equations when a computer program is involved.

To solve for the linear dynamic response of a shaft system subjected to periodic loading it is only necessary to add a corrective solution to the transient solution for a typical time period of loading. Hence, only one numerical algorithm is required to solve a large number of different dynamic response problems in structural engineering (CSI 2009). Another method for the linear dynamic response of shaft system is the direct integrate method introduced in last section.

9.3.2 Element Analysis and Excitation in Establishing the FED Model

The selection and analysis of the elements in turbine shaft systems, and the hydraulic, mechanical and magnetic excitations acting on the systems are explained in this section for the rotordynamic FED analysis.

9.3.2.1 Selection of the Element Type

Selection of an element type is important for analysis of the shaft-system dynamics in FEM. The 3D solid element should be considered to simulate the shaft itself. In most cases, the beam element is selected for shaft because it has 6 degrees of freedom: 3 degrees are the displacement along 3 coordinate axes, and 3 are the rotating angles around those axes. The 3D solid disc element is usually to be chosen for rotor and runner, which have the lumped mass, the equatorial and axial moments of inertia around their section center and their three directions' diameters, respectively. Springs serve as their supports with an elastic stiffness to simulate the interaction between the rotor (runner) and stator.

Three guide bearings of the shaft system are modeled by special bearing elements, as shown in Fig. 9.11.

The stiffness matrix $[\boldsymbol{K}_c]$, the damping matrix $[\boldsymbol{C}_c]$ and the strain matrix $[\boldsymbol{S}_c]$ of the bearing element in the x-y plane are expressed as Eqs. (9.51)–(9.53). Elements in the shaft system are assembled into a global computation mesh for the system of a hydraulic turbine unit marked in Fig. 9.12, which has a total of 21 elements and 23 nodes.

$$[\boldsymbol{K}_c] = \begin{bmatrix} k_{11} & k_{12} & 0 & -k_{11} & -k_{12} & 0 \\ k_{21} & k_{22} & 0 & k_{21} & k_{22} & 0 \\ 0 & 0 & 0 & 0 & 0 & 0 \\ -k_{11} & -k_{12} & 0 & k_{11} & k_{12} & 0 \\ -k_{21} & -k_{22} & 0 & k_{21} & k_{22} & 0 \\ 0 & 0 & 0 & 0 & 0 & 0 \end{bmatrix} \tag{9.51}$$

$$[\boldsymbol{S}_c] = \begin{bmatrix} \frac{k_{11}\varepsilon_0^1}{l_1} & \frac{k_{12}\varepsilon_0^2}{l_2} & 0 & \frac{k_{11}\varepsilon_0^1}{l_1} & -\frac{k_{12}\varepsilon_0^2}{l_2} & 0 \\ \frac{k_{21}\varepsilon_0^1}{l_1} & \frac{k_{22}\varepsilon_0^2}{l_1} & 0 & -\frac{k_{21}\varepsilon_0^1}{l_1} & -\frac{k_{22}\varepsilon_0^2}{l_2} & 0 \\ 0 & 0 & 0 & 0 & 0 & 0 \\ -\frac{k_{11}\varepsilon_0^1}{l_1} & -\frac{k_{12}\varepsilon_0^2}{l_2} & 0 & \frac{k_{11}\varepsilon_0^1}{l_1} & \frac{k_{12}\varepsilon_0^2}{l_2} & 0 \\ -\frac{k_{21}\varepsilon_0^1}{l_1} & -\frac{k_{22}\varepsilon_0^2}{l_2} & 0 & \frac{k_{21}\varepsilon_0^1}{l_1} & \frac{k_{22}\varepsilon_0^2}{l_2} & 0 \\ 0 & 0 & 0 & 0 & 0 & 0 \end{bmatrix} \tag{9.52}$$

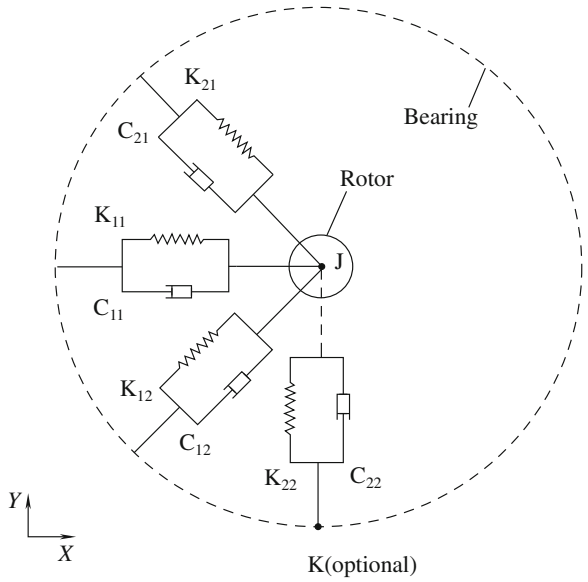

Fig. 9.11 Bearing element (Zhang 2008)

$$[\boldsymbol{C}_c] = \begin{bmatrix} c_{11} & c_{12} & 0 & -c_{11} & -c_{12} & 0 \\ c_{21} & c_{22} & 0 & c_{21} & c_{22} & 0 \\ 0 & 0 & 0 & 0 & 0 & 0 \\ -c_{11} & -c_{12} & 0 & c_{11} & c_{12} & 0 \\ -c_{21} & -c_{22} & 0 & c_{21} & c_{22} & 0 \\ 0 & 0 & 0 & 0 & 0 & 0 \end{bmatrix} \tag{9.53}$$

where k_{11}, k_{12}, k_{21}, k_{22} are the stiffness coefficients; c_{11}, c_{12}, c_{21}, c_{22} are the damping coefficients. And

$$\varepsilon_0^1 = u_j - u_i \text{ and } \varepsilon_0^2 = v_j - v_i$$

where u and v are the displacements along x and y directions, respectively; l_1 is the distance between nodes I and J; l_2 is the distance between nodes k.

Elements in the shaft system are assembled into a global computation mesh of the system of a hydraulic turbine unit marked in Fig. 9.12, which has a total of 21 elements and 23 nodes.

9.3.2.2 The Basic Consideration of Excitation and Element Parameters

Excitations from the hydraulic source, the mechanical source, as well as the magnetic source were introduced in Chaps. 5 and 6. For the excitations and parameters of each element type, the following problems should be considered in the shaft system of this unit (Wang et al. 2005):

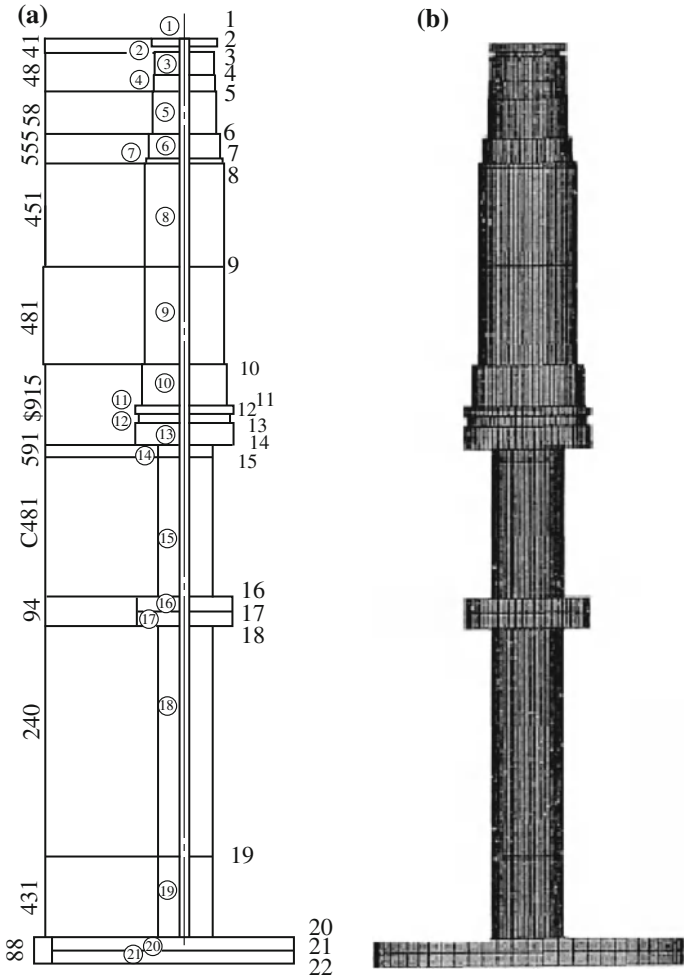

Fig. 9.12 Finite element model of shaft system. **a** Number of elements and nodes. **b** FEM mesh (Zhang 2008)

1. The bearing stiffness includes stiffness of oil film in the bearing, the bearing bracket, and its base. The stiffer the bearings are, the higher the critical velocity of the shaft system is. The stiffness of thrust on the shaft system has little effect to system critical speed, so in some established FEM models for some hydraulic turbine units the thrust stiffness is not considered.
2. The effect of the magnetic pull to the shaft works in the opposite direction of the oil film's supporting force. When the eccentric gap exists in the rotor, the generator stator will pull the rotor in an outward direction, and the pull magnitude is proportional to the eccentric clearance between rotor and stator. In computation, the eccentric gap between rotor and stator is treated as an elastic

support with negative stiffness as shown in Fig. 9.10. The magnet pull will reduce the critical speed noticeably.

3. The water mass in the runner should be added to the computation. It is convenient to add the water mass to the runner lumped mass node.
4. The imbalanced magnetic force F_1 from the stator acting on the rotor, which is a function with respect to the time and rotation frequency of shaft system Ω is

$$F_1 = A\cos\Omega t \tag{9.54}$$

where A is the amplitude of the imbalanced force, with the value 30 kN in this example computation.

5. An imbalanced water force acting on the rotor is caused by the out-of-round runner and the swing movement of the shaft. It is expressed as

$$F_2 = K\cos(\Omega_1 t + \phi) \tag{9.55}$$

where K is the magnitude of the force; Ω_1 is round frequency; and ϕ is the phase difference angle between F_1 and F_2. In computation, it is assumed that $\phi = \pi$ because it will create a maximum response. And also $K = 80$ kN, and Ω_1 is taken to be double the rotating frequency of the shaft in computation.

6. The damping of the shaft system comes from the oil film in the bearings and water movement in the sealing gap.

9.3.2.3 Torque Calculation of the Generator at Transient Process

Under stable conditions, the hydraulic torque acting on the runner is in balance with the magnetic torque of the generator of shaft system, and the resulting torque not induce any torsion vibration of the shaft. In the transient process of the hydraulic turbine unit, such as in the process of starting up, shutting down, increasing and decreasing unit load, the equivalence of total torque will be destroyed, resulting in system torsion vibration. But the hydraulic torque variation is slow, which will not able to induce the torsion vibration and will be treated as constant toque at the moment.

The magnetic torque in a stable condition can be obtained from the magnetic calculation of the generator.

Two basic methods are used in calculating the electromagnetic force between the stator and rotor in the generator. The two methods are based on Maxwell stress tensor and the principle of virtual work. For calculation of force and torque in generators the FEM is commonly used in addition to the analytical methods (Gustavsson and Aidanpää 2003, 2004, 2006).

The electromagnetic pull acting on the generator rotor depends on asymmetry in the air gap between the rotor and stator. In a perfectly symmetric machine the radial pull forces should add up to zero. However, all practical generators have

some asymmetry in the air gap. A common example of asymmetry is when the rotor centre and stator centre do not coincide with each other. The relative eccentricity is defined as

$$e = u_r/\Delta R \tag{9.56}$$

where u_r is the radial displacement of the rotor centre and the average air gap ΔR is the radial clearance between the inner radius of the stator R_s and the outer radius R_r of the rotor.

In a three-phase generator with an arbitrary number of poles the magnetic pull force is composed of a constant part and an alternating part. The alternating part of the force alternates twice the supply frequency for static eccentricity, and twice the supply frequency multiplied by the slip for dynamic eccentricity. The alternating force component decreases with an increasing number of poles in the generator. Hydropower generators usually have several poles and operate as synchronous machines. This implies that the alternating magnetic pull force is negligible in comparison to the constant magnetic pull force. The mean value of the magnetic pull force can be expressed as

$$F_1 = \frac{\mu_0 S_S^2 R_S^3 h\pi}{2p^2\Delta R^2} e \Big/ \sqrt{(1-e^2)^3} \tag{9.57}$$

where S_S is the stator linear current density, p is the number of poles, h is the length of the rotor, and μ_0 is the permeability of free space. The result of Eq. (9.57) is that the magnetic pull force is a non-linear function of the air gap eccentricity and the magnetic pull force will destabilize the rotor system with an increasing rotor eccentricity.

The air gap eccentricity can be divided into two categories: stator eccentricity and rotor eccentricity. In the case of stator eccentricity the rotor will be in a fixed position relative to the stator under a constant magnetic pull force, meaning that the smallest air gap will be in a same direction during the rotation of the shaft. Characteristic for rotor eccentricity is that the rotor will whirl around the centre line of the rotor in an orbit. However, the most common case of eccentricity is a combination of stator and rotor eccentricity and the rotor centre will whirl around a fixed position in the stator bore with the angular speed of rotation.

9.3.3 Dynamic Calculation of Shaft System of Hydraulic Turbine Unit

The dynamic calculation of the shaft system in a hydraulic turbine unit presented in this section includes the critical speed of lateral and torsional vibrations, and the lateral response of the system.

Table 9.4 Calculation results of critical speed for lateral and torsion vibrations (Wang et al. 2005)

Order	Lateral vibration		Torsion vibration
	Critical speed (rpm)	Natural frequency (Hz)	Natural frequency (Hz)
1	383.7	6.40	17.36
2	497.0	8.28	142.715

9.3.3.1 Critical Speed of Lateral and Torsional Vibrations

The shaft of a large scale hydraulic turbine unit is a rigid type of rotor system, where two orders of critical speeds are important for the stability of the shaft system. Table 9.4 lists the natural frequencies for both its lateral and torsion vibrations from the shaft system vibration modal computation in a hydraulic turbine unit by Wang et al. (2005). Data in this table indicates the first order critical speed is higher than 1.4 times of the runway speed of the unit (210 rpm). Figures 9.13, 9.14 show the lateral vibration mode shapes (dotted line) at first and second critical speeds of the shaft system. At the first critical speed, the mode shape curve is intersected with the central axis of the shaft system near the node of the water turbine guide bearing. For the second critical speed, the generator and the turbine shaft all have very small amplitude. The maximum amplitude appears at the end node of runner.

Figures 9.15, 9.16 plot the torsion mode shapes (dotted line) at first and second natural speeds of the shaft system torsion vibration. At the first order of torsion vibration, the maximum angle deforming also appears at the runner node.

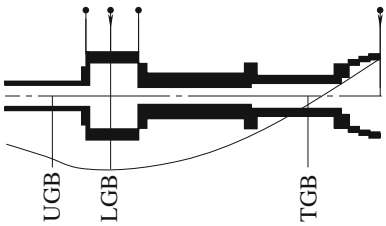

Fig. 9.13 First order mode of critical speed (Wang et al. 2005)

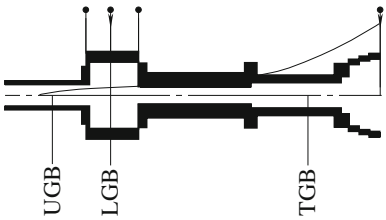

Fig. 9.14 Second order mode of critical speed (Wang et al. 2005)

Fig. 9.15 First order torsion mode (Wang et al. 2005)

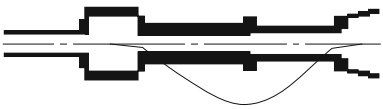

Fig. 9.16 Second order torsion mode (Wang et al. 2005)

Table 9.5 Calculation results of shaft swing at rated load case (Wang et al. 2005)

Survey points	Swing (mm)	
	Amplitude	Vector value
UGB	0.17	0.095
Rotor center	0.19	0.112
WGB	0.23	0.126
Runner center	0.60	0.332

9.3.3.2 Transient Lateral Vibration Response of the Shaft System

1. In the rated-load case

Table 9.5 indicates computational results of the transient lateral vibration response under excitation of the imbalanced hydraulic force and excitation of the emblazed magnetic pull at the water turbine's rated load case. The time waveform of the amplitude of lateral vibration at UGB, rotor center, WGB, and runner center positions at this case are shown in Figs. 9.17, 9.18, 9.19, 9.20, respectively. The orbits of the UGB and WGB center are shown in Figs. 9.21 and 9.22, respectively.

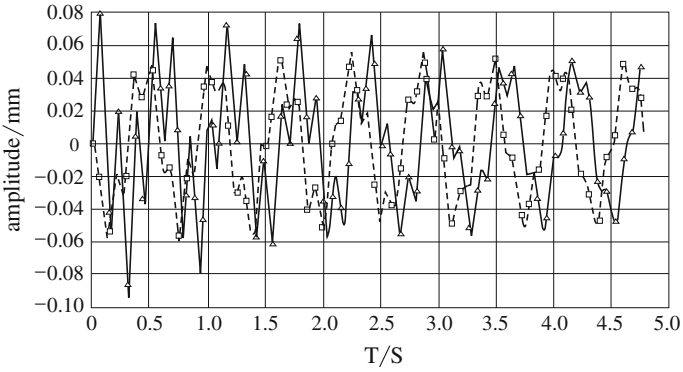

Fig. 9.17 Response of upper generator bearing under rated conditions. *Note abscissa* time (s), *ordinate* amplitude (mm), Δ amplitude along *x* direction; □ amplitude along *y* direction (Wang et al. 2005)

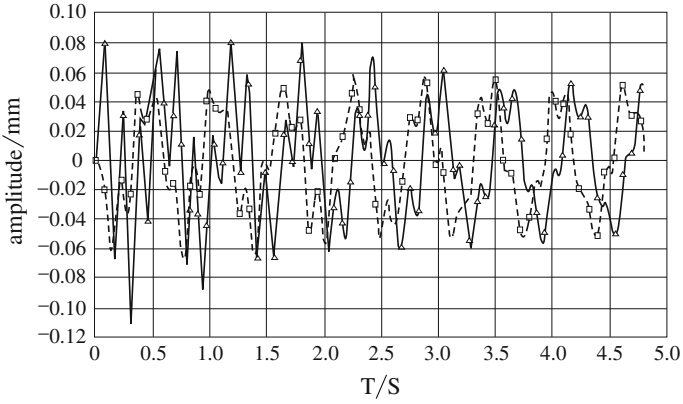

Fig. 9.18 Response of rotor center under rated conditions. *Note abscissa* time (s), *ordinate* amplitude (mm), Δ amplitude along *x* direction, □ amplitude along *y* direction (Wang et al. 2005)

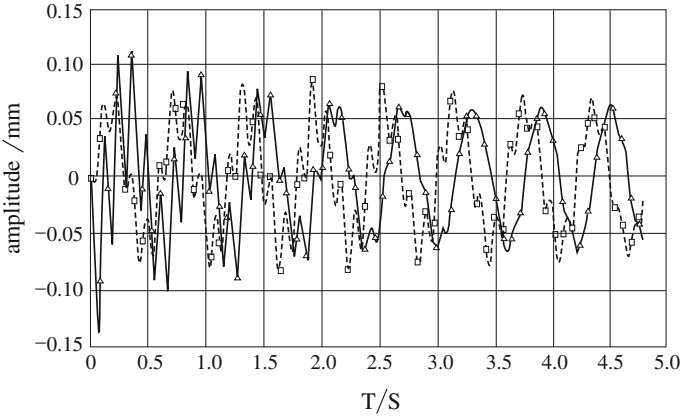

Fig. 9.19 Response of turbine bearing under rated conditions *Note abscissa* time (s), *ordinate* amplitude (mm), Δ amplitude along *x* direction, □ amplitude along *y* direction (Wang et al. 2005)

From the orbits one can see that the imbalanced force excitation starts from the x direction, then the response amplitudes along x and y direction tend to be equal.

Figure 9.23 shows measured results of shaft swing amplitudes of the unit at different load cases and at UGB and WGB survey points. Table 9.6 shows calculated results of shaft swing at rated load case. Comparison between test and calculated data implies that the tested amplitude is larger than that of the calculation at the UGB survey point. The imbalanced magnetic pull is smaller that the hydraulic imbalanced force. And at the WGB survey point the test and calculated results agree well with each other.

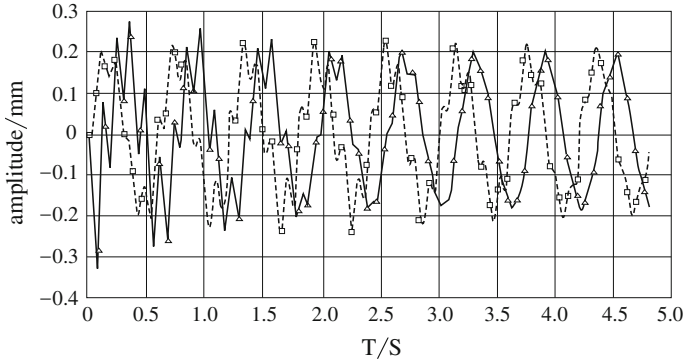

Fig. 9.20 Response of runner center under rated conditions. *Note abscissa* time (s), *ordinate* amplitude (mm), Δ amplitude along *x* direction, □ amplitude along *y* direction (Wang et al. 2005)

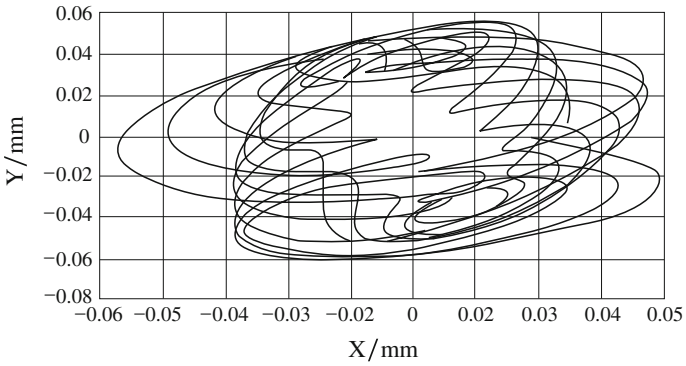

Fig. 9.21 Orbit of journal center of upper guide under rated conditions *Note abscissa* amplitude along *x* (mm); *ordinate* amplitude along *y* (mm) (Wang et al. 2005)

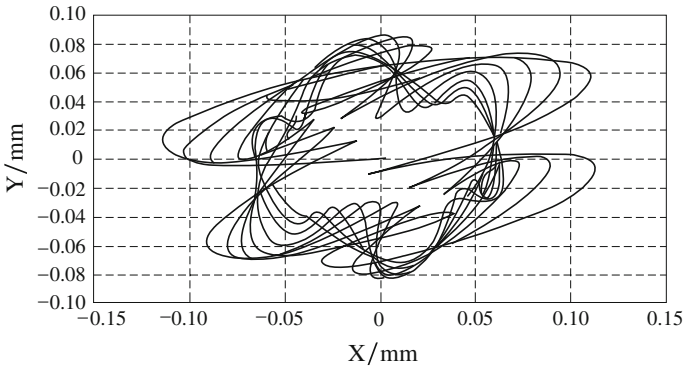

Fig. 9.22 Orbit of journal center of water guide under rated conditions *Note abscissa* amplitude along *x* (mm); *ordinate* amplitude along *y* (mm) (Wang et al. 2005)

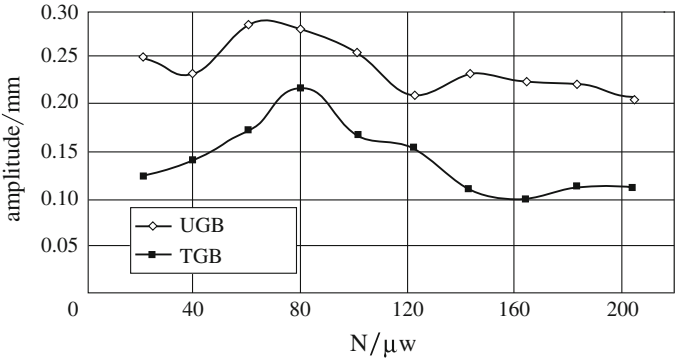

Fig. 9.23 Measured shaft swing of the unit (Wang et al. 2005)

Table 9.6 Calculation results of transient response of shaft system (Wang et al. 2005)

No	water force K(kN)	water force fre. ω_2	Mag. Pull A (kN)	Fre. ω_1	Shaft swing (mm)							
					UGB		Rotor		WGB		Runner	
					Am	Ve	Am	Ve	Am	Ve	Am	Ve
1	162.6	10.5	29.2	10.47	0.27	0.15	0.30	0.18	0.47	0.26	1.20	0.65
2	243.9	10.5	29.2	10.47	0.37	0.21	0.41	0.25	0.71	0.39	1.80	0.98
3	40	20.9	0	0	0.06	0.04	0.08	0.04	14	0.08	0.33	0.18
4	80	20.9	0	0	0.12	0.07	0.15	0.08	0.28	0.15	0.64	0.36
5	20	31.4	0	0	0.07	0.04	0.08	0.04	0.09	0.05	0.24	0.13
6	40	31.4	0	0	0.13	0.07	0.15	0.08	0.19	0.10	0.48	0.25

Note *Case* operation case of the turbine; *Water force* the imbalanced hydraulic force; *Mag. pull* the generator imbalanced pull to the rotor; *Fre.* frequency; *No.* Case number
Am. the amplitude of time wave form of the transient response of shaft lateral displacement; *Ve.* vector mode of the response

2. In the part-load case

In 6 operation part-load cases, the transient excitation responses caused by an imbalanced magnetic pull and hydraulic imbalanced force have been carried out for the same hydraulic turbine unit. The whole calculated data are listed in Table 9.6.

From the results, one can find that the imbalanced excitation force is proportional to the transient response amplitude. In case 2 in Table 9.6, the amplitude of WGB position reaches a maximum value of 0.71 mm.

3. Results remarks

(a) The response data of the shaft system satisfy the standard requirement, but in some cases, the amplitude reaches to 0.4 mm at the bearing point and 1.0 mm at the runner position.

(b) The response amplitude caused by imbalanced forces at WGB is two times of that at UGB. The imbalanced magnetic pull is much smaller.
(c) The response amplitude at runner center is 215 times of that at WGB. And it is also 115 times of that at rotor center.
(d) At the same excitation amplitude, the higher the doubling frequency of excitation, the greater the swing of shaft.

The forgoing results may benefit evaluations of stability in the shaft systems of hydraulic turbine units.

9.4 Pump Rotordynamic Parameters

The rotordynamics of pumps is more complicated due to a number of operating features mostly load dependent; i.e., related to the pressure and flow conditions.

The analysis of pump rotordynamic coefficients such as the prediction of seal reaction forces should be brought into scope at first.

Any movement of the rotational axis of the shaft on a pump relative to its casing induces fluid forces on the shaft and the casing, which in turn will increase or decrease the rotor deflection or vibration. Contributions to these rotor dynamic forces can arise from seals, the rotor side space, the flow through the impeller, leakage flows, or the flow in the bearings themselves (Guinzburg et al. 1994). The pump rotor's dynamic coefficients are required as input data for the prediction of rotor vibration. These parameters can be determined by experiments, bulk flow analysis, and CFD simulation, as shown in Fig. 9.24 (Staubli and Bissig 2002). Chapters 5 and 6 included the necessary coverage on determining these parameters in the field of engineering. This section will present the bulk flow analysis and CDF simulation for pumps.

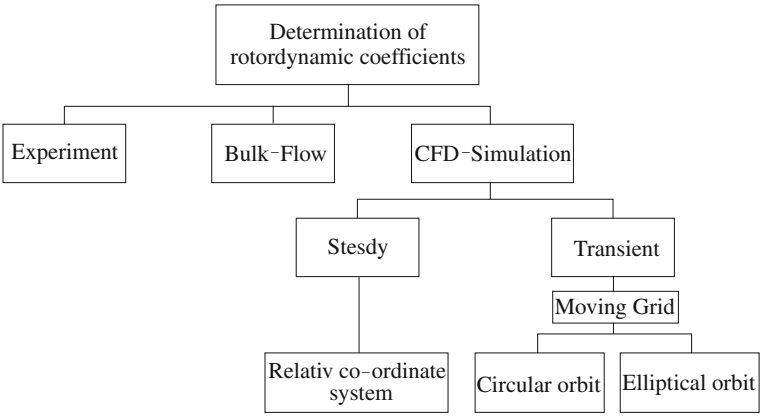

Fig. 9.24 Determination of rotordynamic parameters (Staubli and Bissig 2002)

Assuming a linear relationship of force and displacement, while neglecting the influences of high derivatives of the motion, one could describe this force–displacement model with the following rotor dynamic stiffness, damping, and mass matrices:

$$\begin{Bmatrix} -f_x(t) \\ -f_y(t) \end{Bmatrix} = \begin{bmatrix} K_{xx} & K_{yx} \\ -K_{xy} & K_{yy} \end{bmatrix} \begin{Bmatrix} x \\ y \end{Bmatrix} + \begin{bmatrix} C_{xx} & C_{yx} \\ -C_{xy} & C_{yy} \end{bmatrix} \begin{Bmatrix} \dot{x} \\ \dot{y} \end{Bmatrix} + \begin{bmatrix} M_{xx} & M_{yx} \\ -M_{xy} & M_{yy} \end{bmatrix} \begin{Bmatrix} \ddot{x} \\ \ddot{y} \end{Bmatrix} \tag{9.58}$$

For small motions and full rotational symmetry of the rotor and stator, the cross-coupled terms of damping and stiffness matrices become equal in magnitude. According to experimental findings the cross-coupled inertia terms of the mass matrix may be neglected and are set to zero ($M_C = 0$). However, the direct inertia term M cannot be neglected except in cases where the laminar seal flow dominates, e.g. for slide bearings. Thus, the coefficient matrices can be simplified in the case of small concentric perturbations:

$$\begin{Bmatrix} -f_x(t) \\ -f_y(t) \end{Bmatrix} = \begin{bmatrix} K & K_C \\ -K_C & K \end{bmatrix} \begin{Bmatrix} x \\ y \end{Bmatrix} + \begin{bmatrix} C & C_C \\ -C_C & C \end{bmatrix} \begin{Bmatrix} \dot{x} \\ \dot{y} \end{Bmatrix} + \begin{bmatrix} M & M_C \\ -M_C & M \end{bmatrix} \begin{Bmatrix} \ddot{x} \\ \ddot{y} \end{Bmatrix} \tag{9.59}$$

9.4.1 Bulk-Flow Model

The bulk-flow theory of Hirs (1973), e.g. described by Childs (1983, 1993), is a well-Gustavsson and validated tool to calculate rotor dynamic coefficients. To introduce this model, the following description will focus on the labyrinth seal (see Williams and Flack 1998).

9.4.1.1 Principal of Bulk-Flow Model

The solution technique consists of deriving the continuity and momentum equations for each labyrinth cavity representing a single control volume similar to that performed by Childs and Scharrer (1986). A leakage model is used to account for the axial leakage from one chamber to the next. The resulting set of partial differential equations is linear via a perturbation analysis for small motion about a centered position (Williams and Flack 1998).

Zero order equations are solved for the pressure and velocity in each cavity. The temporal and spatial derivatives in the first order equations are eliminated on the assumption of an elliptical shaft orbit and resulting responses for the pressure and velocity fluctuations. The resulting set of linear algebraic equations is worked out for the pressure and velocity perturbations about the circumference. The dynamic coefficients are determined by integrating the pressure perturbations around and

along the shaft. Details of the method can be found in Williams (1992). The three dimensional flow in a labyrinth seal is very complex. In order to create a set of tractable equations which describe the flow, simplifying assumptions must be made:

(1) The circumferential velocity and pressure within a labyrinth chamber are constant in the axial direction and are functions of the angular position only in a perturbed case. (2) The temperature within each seal cavity is constant. (3) The gas is assumed to be ideal. (4) Pressure variations within a cavity are negligible relative to the pressure difference across a seal tooth. (5) The eccentricity of the rotor is small relative to the radial seal clearance. (6) The acoustic resonance frequency of a cavity is much higher than that of the rotational frequency. (7) The axial component of velocity is negligible in determining the circumferential shear stress. (8) The shear stress contribution to the stiffness and damping coefficients is negligible.

A set of equations can be developed which approximately describes the flow within a labyrinth seal. Principles for conservation of mass and conservation of circumferential momentum are applied to each labyrinth chamber which serves as a control volume. In order to solve these equations, one should perform a perturbation analysis with the eccentricity ratio $\varepsilon = e/C_r$ (C_r is the nominal seal clearance radial, e is the eccentricity) serving as the perturbation parameter.

Perturbation variables consist of a static component (zero order) denoted by the superscript 0 and a varying component (first order) denoted by the superscript 1. For example, $P_i = P_i^0 + \varepsilon P_i^1$ and $V_i = V_i^0 + \varepsilon V_i^1$, these variables are used with the above equations and like orders of the perturbation parameter $\varepsilon(\varepsilon^0, \varepsilon^1)$ are grouped. The zero order equation ε^0 determines the circumferential velocity and pressure distribution for a centered position along the seal length. In the centered case, pressure and velocity are constant within a given chamber and vary only from chamber to chamber. The zero order equation also defines the mass flow leakage rate. The first order equation ε^1 determines the pressure and velocity perturbations resulting from the eccentricity of the rotor. In the eccentric case, the velocity and pressure perturbations are not constant within a given chamber but are functions of circumferential position and time. These pressure fluctuations are responsible for the forces applied to the rotor by the seal.

The spatial and temporal derivatives are eliminated with the assumption of a synchronous elliptical orbit for the rotor and similar pressure and velocity fluctuations. Substitution and grouping like terms of sines and cosines leads to a set of eight linear simultaneous equations for each cavity. The equations can be solved for pressure and velocity perturbations caused by the eccentricity of the rotor. Once the pressure fluctuations are known, the rotordynamic coefficients can be calculated.

9.4.1.2 Predictions of Force Coefficients in Off-Centered Grooved Seals

1. Short-length seal. Andrés and Delgado (2008) summarized the dynamic coefficients of short length seals (Fig. 9.25).

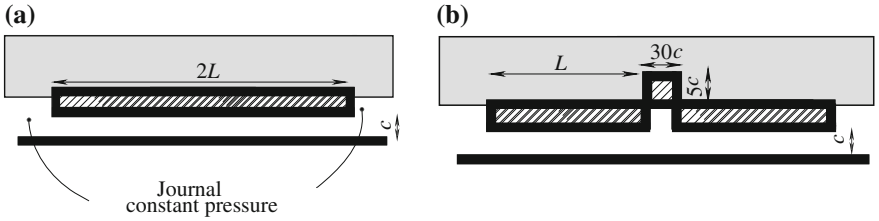

Fig. 9.25 Short-length seal. **a** Short-length smooth seal without groove. **b** *2-land seal* (deep groove divides lands) (Andrés and Delgado 2008)

Figure 9.25 shows the simple short-length seals. For the smooth seal without groove (a), the damping, cross-coupled stiffness and inertia mass may be expressed as

$$C_{XX} = 2\pi\mu DL^3/c^3,\ K_{XY} = 0.5\Omega C_{XX},\ M_{XX} = 0.4\pi\rho DL^3/c. \tag{9.60a}$$

For the 2-land seal: (deep groove divides lands) seal (b), they are

$$C_{XX} = 0.25\,\pi\,\mu\,D\,L^3/c^3,\ K_{XY} = 0.5\Omega\,C_{XX},\ M_{XX} = 0.05\pi\,\rho\,D\,L^3/c. \tag{9.60b}$$

For the ¼ of original seal:

$$C_{XX} = 0.5\pi\,\mu\,D\,L^3/c^3,\ K_{XY} = 0.5\Omega\,C_{XX},\ M_{XX} = 0.1\pi\,\rho\,D\,L^3/c \tag{9.60c}$$

where Ω is rotating speed of shaft.

2. Short-length seal leakage

Andrés and Delgado (2008) calculated results that predicted leakage correlates well with experiments for both smooth land and grooved seal at a condition of 10,000 rpm rotating speed and 70 bar pressure head of the turbomachine (see Fig. 9.26), and damping, stiffness as well as added mass-of-inertia by an improved bulk flow model. The results are for compressors, but they are useful for high speed pumps.

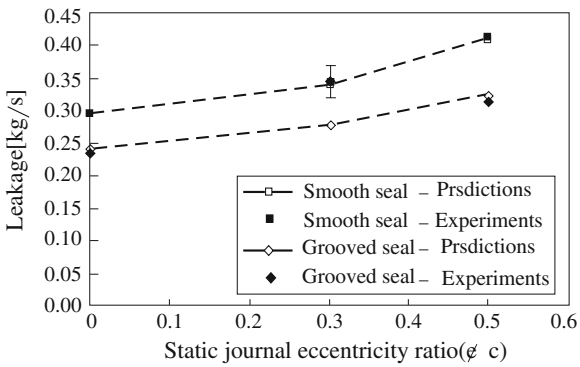

Fig. 9.26 Smooth and grooved seals by improved bulk fluid model. Leakage (at condition 10,000 rpm, 70 bar) (Andrés and Delgado 2008)

9.4.1.3 Identification of the Adding Moment of Inertia of a Disc in Water Using the Perturbation Analysis

The moment of inertia of water in a partly filled cylindrical container is mainly identified by the thickness of the boundary layer against the walls. The periodic boundary layer of swaying water perturbed by harmonic rotation in a circular cylinder has been studied by Reismann et al. They found that the equatorial moment of inertia and the damping coefficient are the functions of the boundary layer thickness. For a standard cylindrical container the equatorial moment of inertia is mainly determined by the boundary layers on the bottom and side walls of the cylinder.

The laminar flow on the rotating disc is described by the following simplified N–S equations:

$$\frac{\partial u}{\partial t} = \frac{\mu}{\rho}\frac{\partial u^2}{\partial^2 Z} \tag{9.61}$$

where the Z-axis is perpendicular to the disc. Under harmonic perturbation of rotating vibrations, $\varphi = \varphi_0 \sin(\Omega t)$ and with some boundary conditions the solution of Eq. (9.61) is

$$u = r\Omega e^{-\sqrt{\Omega/2\nu}Z}\left[\cos(\sqrt{\frac{\Omega}{2\nu}}Z)\cos(\Omega t) + \sin(\sqrt{\frac{\Omega}{2\nu}}Z)\sin(\Omega t)\right]\theta_0. \tag{9.62}$$

Then the shear stress $\tau_b = \mu(\partial u/\partial Z)$ can be obtained as

$$\tau_b = \mu\sqrt{\Omega/2\nu}Zu + \frac{\rho}{2\sqrt{\Omega/2\nu}Z}\frac{\partial u}{\partial t}. \tag{9.63}$$

One can get the shear moment of liquid around the central axis of the disc by integration in the form of

$$T_b = \int_0^{2\pi}\int_0^R (\tau_b)_{Z=0} r^2 dr d\theta = J_b\ddot{\varphi} + C_b\dot{\varphi} \tag{9.64}$$

where J_b and C_b are the effective equatorial moment of inertia and the damping of liquid on the disc respectively. Likewise, one can get these coefficients of water near the side walls of a circular cylinder as follows:

$$T_w = J_w\ddot{\varphi} + C_w\dot{\varphi}. \tag{9.65}$$

Then one can get the full coefficients of water in the cylindrical container:

$$T_0 = J_0\ddot{\varphi} + C_0\dot{\varphi}. \tag{9.66}$$

The equatorial moment of inertia of liquid in the container J_0 can be got through the solution of torsion moment T_0 by solving the following equation numerically:

$$T_0 = C_0\varphi_0\Omega\cos(\Omega t) - J_0\varphi_0\Omega^2\sin(\Omega t) = k\cos(\Omega t + \alpha) \tag{9.67}$$

where the factor $k = \varphi_0\Omega(C_0^2 + I_0^2\Omega^2)^{1/2}$; and the phase angle is satisfied with

$$\sin\alpha = \frac{I_0\Omega}{\sqrt{C_0^2 + I_0^2\Omega^2}}, \cos\alpha = \frac{C_0}{\sqrt{C_0^2 + I_0^2\Omega^2}}. \tag{9.68}$$

9.4.2 Identification of Dynamic Coefficients of Pumps by CFD Simulation

The use of computational fluid dynamics (CFD) for pump simulation has been established (see Chap. 7). Unsteady CFD-simulations are state-of-the-art and today, pressure fluctuations can be predicted with acceptable accuracy. Numerical simulations of entire pumps including rotor side spaces and seals have been completed. Thus, the interaction of leakage and main flow as well as inflow conditions into seal portions have been simulated, yet no assumptions have to be made. In this section the procedures to determine rotordynamic coefficients from CFD simulation and its results are presented.

9.4.2.1 Identification of Coefficients from CFD Simulation

The following procedures will be presented to determine rotordynamic coefficients from a numerical flow simulation (Staubli and Bissig 2001).

1. Steady State Simulation

For a circular rotor motion around a centered position, it is possible to find a relative coordinate system in which the flow becomes a steady state. This relative coordinate system must rotate backwards with the frequency of the orbit motion. Rotationally symmetric geometry and inflow conditions are necessary assumptions for steady state flow. Figure 9.27 shows this coordinate system with a relative rotor angular velocity of $\Omega_{Rrel} = \Omega_R - \Omega_E$, where Ω_R is the impeller rotating speed, Ω_E is the precession (orbit) angular speed of the rotor system. Accordingly, the stator must rotate backwards with a relative angular velocity of $\Omega_{Srel} = -\Omega_{Rrel}$. In the absolute coordinate system this corresponds to an orbit motion equivalent to Eq. (9.69):

$$x = \varepsilon S_0\cos(\Omega_E t),\ y = \varepsilon S_0\sin(\Omega_E t),\ \varphi = \Omega_E t \tag{9.69}$$

Integration of calculated pressure distributions on the rotor surface leads to the resulting fluid force on the rotor at a given operating condition and orbit frequency. The force acting on the rotor can be decomposed in a radial force component F_r

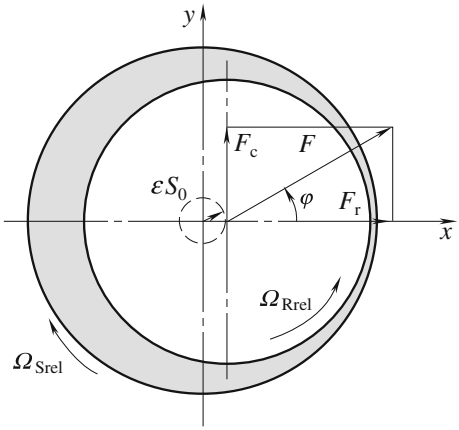

Fig. 9.27 Relative coordinate system (Staubli and Bissig 2001)

and circumferential force component F_c with respect to the orbit center. Rotordynamic coefficients can then be identified from the regression of calculated forces for various orbit frequencies.

These integrations were performed for constant leakage, rotor speed and preswirl at the inlet as a function of the orbit's angular frequency. Introducing these forces into Eq. (9.59) and setting the time to $t = 0$ in Eq. (9.69) leads to:

$$F_x(\Omega_E(t = 0))/(\varepsilon S_0) = F_r(\Omega_E)/\varepsilon S_0 = -K - C_C + M\Omega_E^2 \tag{9.70}$$

$$F_y(\Omega_E(t = 0))/(\varepsilon S_0) = F_C(\Omega_E)/(\varepsilon S_0) = -K_C - C\Omega_E \tag{9.71}$$

In order to determine the rotor's dynamic coefficients, one has to determine *Fc* and *Fr* as functions of the orbit's angular frequency from Eqs. (9.70) and (9.71). For numerical calculations this means that the angular velocities of the stator and rotor have to be varied in the relative coordinate system. Employing a second order regression on Eq. (9.70) will yield the coefficients of stiffness *K*, cross damping C_C, and inertia *M* from the calculated radial forces *Fr*. The damping coefficient *C* and the cross stiffness are determined from a linear regression of *Fc* in Eq. (9.71).

2. Transient simulation

In the absolute coordinate system the orbital motion generates an unsteady flow in the seal as indicated in Fig. 9.28. For simulation in the absolute system, the grid has to be adapted to the instantaneous position of the rotor. An unsteady flow and varying geometry increases the computational expense for CFD calculations considerably. Therefore, such simulations would only make sense if the inflow conditions or the geometry are not rotationally symmetric.

If more general boundary conditions prevail, one should simulate in the absolute frame of reference. To achieve that, the technique of a moving grid has to be applied and transient simulations have to be performed. Such moving grid simulations were performed for test-case geometry. Two different ways to

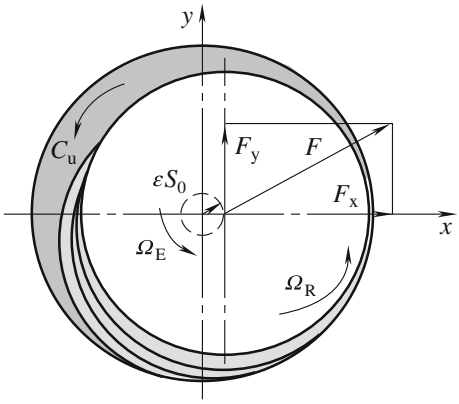

Fig. 9.28 Absolute coordinate system (Staubli and Bissig 2001)

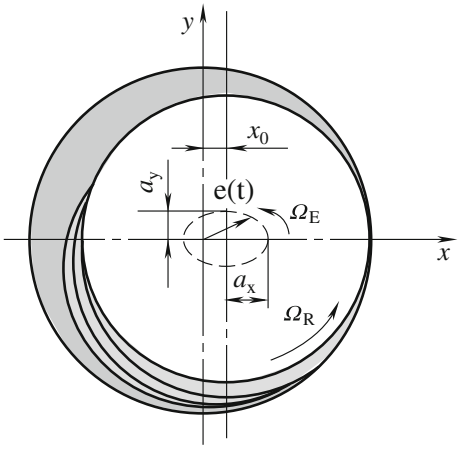

Fig. 9.29 Elliptical orbit (Staubli and Bissig 2001)

determine rotordynamic coefficients are applicable depending on the type of orbit motion prescribed.

(a) Circular orbit

If a circular orbit is prescribed, it is necessary to simulate at least three different orbit frequencies. In a next step the radial *Fr* and circumferential forces *Fc* have to be determined from a coordinate transformation of the forces *Fx* and *Fy*. Then the coefficients can be obtained in the same way as the relative co-ordinate system.

(b) Elliptical orbit

A very efficient and elegant method for determining rotordynamic coefficients becomes possible if the rotor center prescribes an elliptical orbit (Fig. 9.29). In this case, a single transient simulation is sufficient to determine all rotordynamic coefficients. A variation is not needed.

9.4.2.2 Calculated Results of Coefficients from CFD Simulation

From a series of calculations by Staubli and Bissig (2001, 2002), rotor dynamic coefficients can be identified for varying circumferential rotor speeds and three different leakage flow rates. The results of test case simulations are included in Fig. 9.30 and are compared with those from bulk-flow calculations as well as to experimental data (Graf 1991).

For clarification only, experimental data at $Cm = 8.3$ m/s are included in the graph. Obviously all data suffer from a scatter, but reproduce the same trends and order of magnitudes. The coefficients calculated from the elliptical orbit fit very

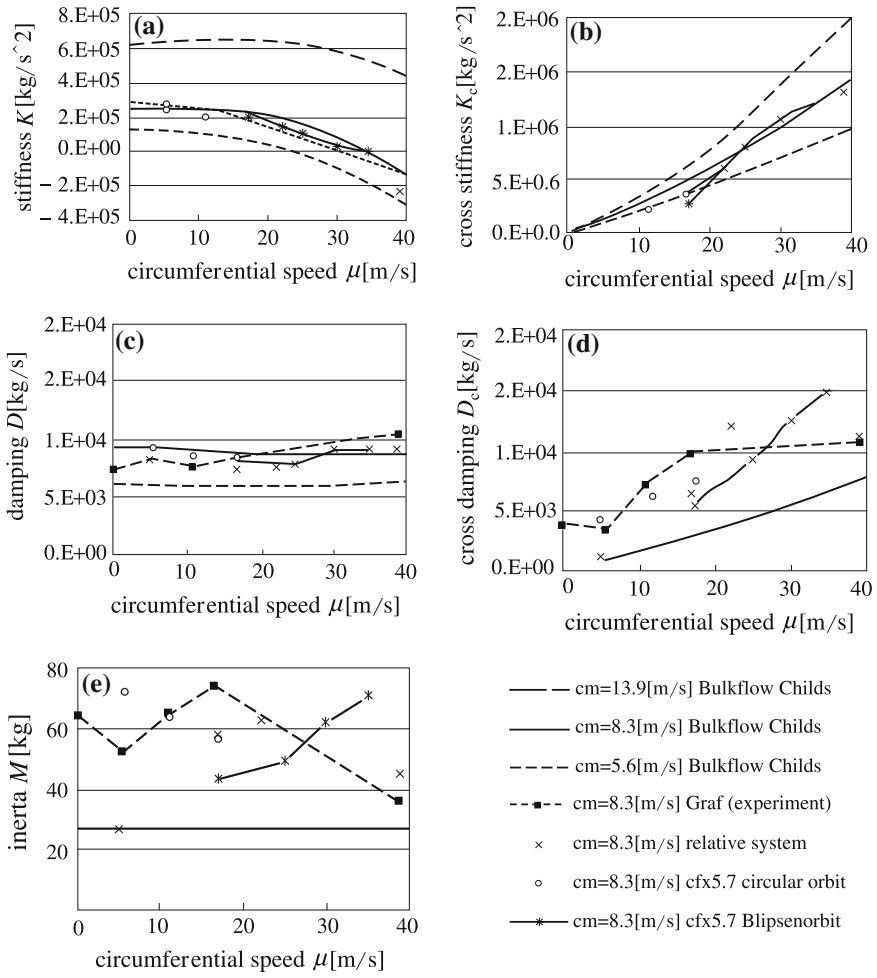

Fig. 9.30 Comparison of simulated rotordynamic coefficients with measurements and bulk-flow theory **a** stiffness. **b** cross stiffness. **c** damping. **d** cross damping. **e** inertia (Staubli and Bissig 2002)

well with the points determined from other methods. Largest deviations are observed for the mass coefficients, which are determined from the curvature of the parabolas (except for elliptical orbits). Generally, experiments and simulations show larger-than-expected-values from bulk-flow theory.

9.4.3 Static Radial Loads on Centrifugal Pumps

Two formulas are used for estimation of the static radial load acting on a centrifugal pump, one from the Hydraulic Institute (1994) and the other attributed to Stepanoff. Both formulas are derived from extensive measurements. The two methods predict a minimum radial load near the best efficiency point (BEP). The Stepanoff was introduced in Chap. 6. Radial loads increase as the flow increases or decreases from the BEP. The Hydraulic Institute (HI) method predicts radial loads increasing at a faster rate with deviations from the BEP % volumetric rate at higher specific speeds.

Figure 9.31 displays the load direction and its relative magnitude. From Andrés (2006), at 0 % flow capacity the radial load vector peaks and lies along a line from shaft center to the cutwater. As the flow increases, the load decreases and moves around the volute in a direction opposite to the shaft rotation. At the BEP, the load direction is opposite to the line joining the shaft center and the cutwater. This trend continues as the volumetric capacity increases to over 100 %.

The empirical formulae for estimation of a radial load in single volute pumps using the Hydraulic Institute method and Stepanoff method, as well as the load factor curve with respect to the percent-flow capacity for several specific speeds of pumps were presented by Andrés (2006). Nowadays, the radial load of any type of pumps at any operant condition can be predicted by 3D steady and unsteady turbulent flow simulation through the entire flow passage of the pumps, as explained in Chap. 7.

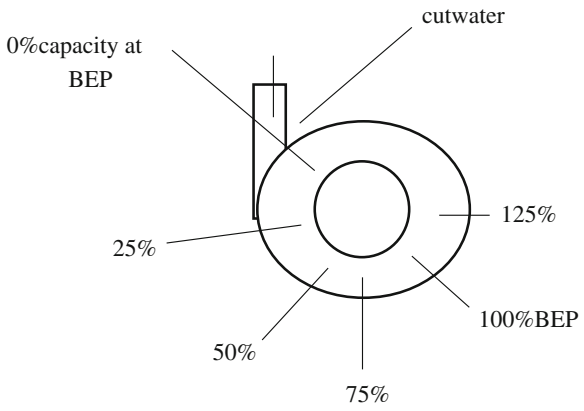

Fig. 9.31 Direction of radial load on single volute casing pump (Hydraulic Institute 1994)

9.4.3.1 The Hydraulic Imbalance Force on Centrifugal Pumps

Unsteady flow conditions within the pump also generate time-varying forces. The most apparent force is that induced by the rotating fluid, i.e., a centrifugal load, synchronous with shaft speed, and exacerbated by the surface condition of the flow path within the pump impeller. The predicted hydraulic dynamic load, F_{imb}, relies on empirical test data and follows the definition:

$$F_{imb} = K_{1X}\rho g H D_0 b \tag{9.72}$$

The dynamic hydraulic load is proportional to the fluid density, pressure discharge P, the impeller outlet diameter D_0, and impeller width b. The empirical dynamic load factor (K_{1X}) is a function of the flow condition (Q/Q_{BEP}), recommended for operation at BEP from published test data,

$$0.005 \leq K_{1X} \leq 0.015;\ 0.02 \leq K_{1X} \leq 0.12 \tag{9.73}$$

for precision-cast and sand-cast impellers, respectively.

The hydraulic imbalance load was simulated by CFD unsteady turbulent flow computation mentioned above.

9.4.3.2 Impeller-Rotor Interaction Forces in Centrifugal Pumps

As is indicated by Andrés (2006), dynamic forces are largely determined by the lateral motions of the pump rotor, i.e., they depend on the rotor (radial and angular) displacement, velocity, and acceleration and they are described with conventional stiffness, damping, and inertia matrices.

When the rotor vibrates, the impeller moves and opens/closes the secondary flow paths along the front shroud and back face of the impeller. The fluid flowing through these gaps is also displaced and a dynamic pressure field is generated creating the dynamic forces and torques acting on the rotor.

After extended periods of operation, all impellers will tend to degrade with mechanical imbalance (wear, tear, debris accumulation), which exacerbates the hydraulic imbalance force as surface flow conditions also degrade.

The impeller-rotor interaction force combines with dynamic forces from the front and back faces of the impeller as well as those from neck-ring seal and interstage seals. Impeller lateral forces are typically modeled as Eq. (9.59).

This reduced-force model assumes rotational symmetry and circular-centered orbital motions. Test results are typically presented in a dimensionless form:

$$\bar{K}, \bar{K}_C = \frac{K, K_C}{m_{ref}\Omega^2};\ \bar{C},\ \bar{C}_C = \frac{C, C_C}{m_{ref}\Omega};\ \bar{M},\ \bar{M}_C = \frac{\bar{M}, \bar{M}_C}{m_{ref}};\ m_{ref} = \frac{\pi\rho b_2 D_0^2}{4} \tag{9.74}$$

where Ω is the pump speed and m_{ref} is a reference fluid mass. The magnitude of the reference mass is large, since it is linked to the volume of a solid disk of diameter D_0 and thickness b_2. If $M_C \sim 0$, the whirl frequency ratio, $WFR = K_C/(C_D\Omega)$,

relates the whirl frequency of unstable motions to shaft speed. A $WFR = 0.5$ means that the pump cannot operate with stability at a speed above two times (=1/WFR) the system's first natural frequency. Table 8.4.1 presents the dimensionless force coefficients given in the literatures of Andrés (2006).

9.5 Rotordynamic Computation of Pumps

A turbopump is comprised of two main components: a rotordynamic pump and a driving turbine, both mounted on the same shaft. A turbopump can refer to either a centrifugal pump where the pumping is done by throwing fluid outward at a high speed, or an axial pump where alternating rotating and static blades progressively raise the pressure of a fluid. The rotordynamic analysis of a turbopump is conducted in this section.

9.5.1 Critical Speed and Excitation Computation of a Turbopump Rotor

Turbopumps in rockets are so important and problematic that launch vehicles bearing them have been caustically described as a "turbopump with a rocket attached"—up to 50 % of the total costs are ascribed to this area. Engineers have to know the critical speed of the pump rotor system in its design.

9.5.1.1 Turbopump at Critical Speed and Excitation Response

Figure 9.32a shows the structure of a turbopump rotor system, (b) shows the simplest model of a rotor system consisting of a shaft without mass, a single

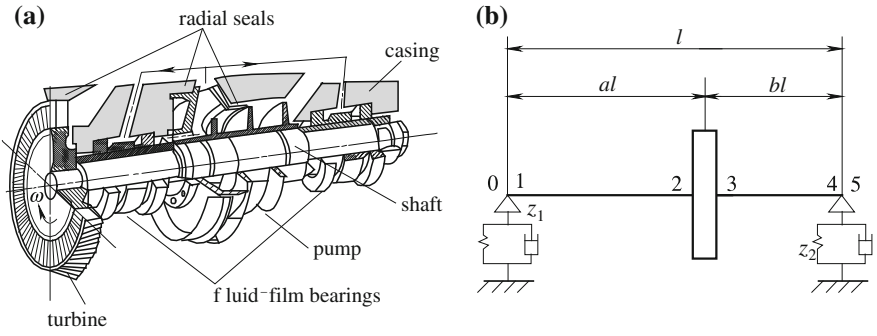

Fig. 9.32 **a** Rotor system of turbopump. **b** Structure of single disc rotor

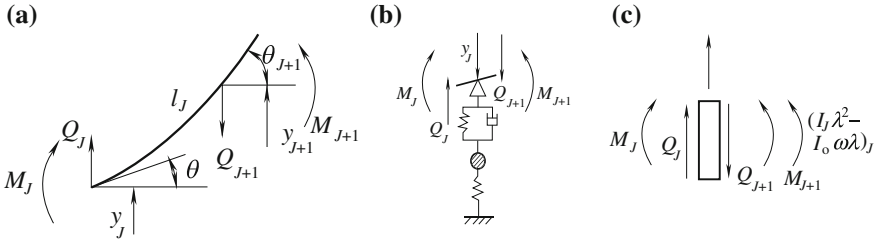

Fig. 9.33 Acted force and displacement of shaft, support and disc at natural vibration. **a** Shaft. **b** Support. **c** Disc

rotating disc with lumped mass and an angular speed, and the supports having circumferential homogeneous distribution of stiffness and damping. The acting shear forces Q, the bending torques M, the elastic deflection y, and the angle of deflection θ for the shaft, its support and disc are marked in Fig. 9.33 respectively (He et al. 1998).

Based on the conditions of the acting force and displacement, transfer matrices of the shaft, disc, and supports at natural vibrations can be derived. For example, the section of shaft in Fig. 9.33a can be expressed as

$$\begin{Bmatrix} Q_{j+1} \\ M_{j+1} \\ \theta_{j+1} \\ y_{j+1} \end{Bmatrix} = \begin{bmatrix} 1 & 0 & 0 & 0 \\ l_i & 1 & 0 & 0 \\ \beta_i & \nu_i & 1 & 0 \\ \gamma_i & \varepsilon_i & l_i & 1 \end{bmatrix} \begin{Bmatrix} Q_j \\ M_j \\ \theta_j \\ y_j \end{Bmatrix} \tag{9.75}$$

where $\nu_i = l_i/(EJ_i)$, $\beta_i = \varepsilon_i = l_i^2/(2EJ_i)$, $\gamma_i = l_i^3/(6EJ_i)$ [see Eq. (9.23)].

The different types of supports have a different compound variety of elastic components with stiffness K, dampers with damping coefficient C, and masses m_0, as well as their bases with stiffness K_0 and mass as shown in Table 9.7. The complex stiffness of different compound supports also is presented in the table [see Eq. (9.28)].

In a similar way, one can get the displacement and acting force equations at natural vibration for the section of rotating disc and shaft, respectively, like Eq. (9.75).

Table 9.7 Impeller force coefficients from test data by Andrés (2006)

Coefficient	$\bar{K}$	$\bar{K}_C$	$\bar{C}$	$\bar{C}_C$	$\bar{M}$	$\bar{M}_C$	WFR	Note
CT-volute	−2.5	1.10	3.14	7.91	6.51	−0.58	0.35	$\Phi = 0.092$
CT-diffuser	−2.65	1.04	3.80	8.96	6.60	−0.90	0.27	$\Phi = 0.092$
Radial impeller	−0.42	0.09	1.08	1.88	1.86	−0.27		BEP, vaneless diffuser
S-Diffuser (2)	−5.0	4.4	4.2	17.0	12.0	3.5	1.05	2 krpm
S-Diffuser (4)	−2.0	7.5	4.2	8.5	7.5	2.0	1.78	4 krpm
S-with swirl brake	−2.2	7.7	3.4	8.6	6.7	3.1	2.26	4 krpm, BEP, Type D
S-with face seal	−4.2	5.1	4.6	13.5	11.0	4.0	1.11	BEP, Type A

S: Sulzer test data (small clearance); *CT*: Cal Tech test data; $\boldsymbol{\phi = 2Q/(\pi\Omega D_0 b_2)}$ flow coefficient

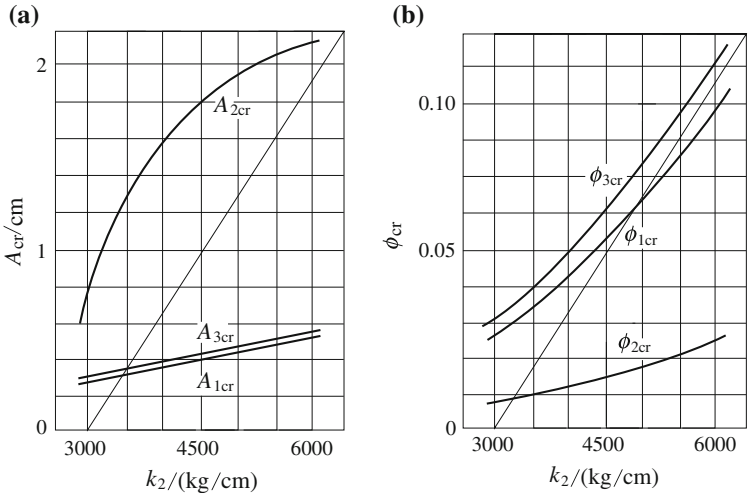

Fig. 9.34 Response of forced vibration at excitation (He et al. 1998). **a** Amplitude versus support stiffness, **b** Phase angle versus support stiffness

The transfer matrices of each section can be obtained. Equations of frequency and amplitude at natural vibration can be deduced based on overall arrangement of rotor structure. From this, the natural critical rotation speeds and amplitudes of shaft system for each order could be solved.

When the excitation is imposed on the rotor system, such as, the excitation force f and excitation moment m_f are expressed as

$$f_i = m_i \varepsilon_i \Omega^2 e^{i\varphi_i},\ m_{fi} = \left(J_{pi} - J_{di}\right)\delta_i \Omega^2 e^{i\varphi_i'} \tag{9.76}$$

where Ω is the angular speed of rotor; m is the mass of the rotor; J_p is its equatorial moment of inertia to rotor center; J_d is its axial of inertia to rotor diameter; ε is the eccentricity of rotor; δ is the eccentric angle of rotor; and φ and φ' are initial phase angles of $\varepsilon$and δ, respectively.

Figure 9.34 shows the variations of amplitude and the phase angler of forced vibration as the excitation response in Eq. (9.76) from computation results of He et al. (1998).

The rotor system model is the simplest model with one single disc and bearings that have homogeneous circumferential distributions of parallel stiffness and damping, presented in Table 9.8 ⑤. From the figures, notice that the amplitude of forced vibration is shrinking with the support stiffness decrease, yet the vibration phase angle is growing.

Table 9.8 Structure of variant compound support and their complex stiffness (He et al. 1999)

No	Type of complex support	Global complex stiffness	Figure
①	Elasticity support	$Z = K$	
②	Elasticity support regarding mass	$Z = -m_0\omega_n^2 + K$	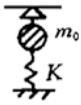
③	Support possessing viscosity damping	$Z = \mathrm{i}\omega_n C$	
④	In-line support of viscosity damping and elasticity unit	$Z = \frac{1}{1/K+1/(\mathrm{i}\omega_n C)}$	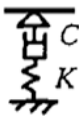
⑤	Parallel connection support of viscosity damping and elastic unit	$Z = K + \mathrm{i}\omega_n C$	
⑥	Parallel connection support of viscosity damping and elasticity unit, and regarding support mass	$Z = -m_0\omega_n^2 + K + \mathrm{i}\omega_n C$	
⑦	Parallel connection support of viscosity damping and elasticity unit and regarding support mass and shell stiffness	$Z = \frac{1}{\frac{1}{K+\mathrm{i}\omega_n C}+\frac{1}{k_0+m_0\omega_n^2}}$	

Note ω_n is natural circular frequency of rotor system considering damping: $\omega_n = \lambda + \mathrm{i}\alpha$, where λ is its natural frequency without damping and α is its coefficient

9.5.1.2 Turbopump Critical Speed Computation of Support Rotor

Turbopump critical speed of natural vibration computation was carried out on the same model in Fig. 9.32 but with the circumferential non-homogeneous supports (He et al. 1999).

In the computation, the complex stiffness of a support was non-homogeneous along the circle, and the stiffness could be resolved on two main planes perpendicular to each other. There is maximum or minimum stiffness in the main planes. Simultaneously, the acting forces and displacements at vibration were also resolved on the main planes.

The transfer matrices were respectively built for shaft, support, and plate elements. Then, the calculated equations of natural rotational speeds and amplitudes were deduced according to the overall arrangement of rotors.

Figure 9.35 plots the frequency spectrum (Campbell diagram) of rotor systems with non-homogeneous supports along the bearing circle (a), and with homogeneous supports along the circle (see last section).

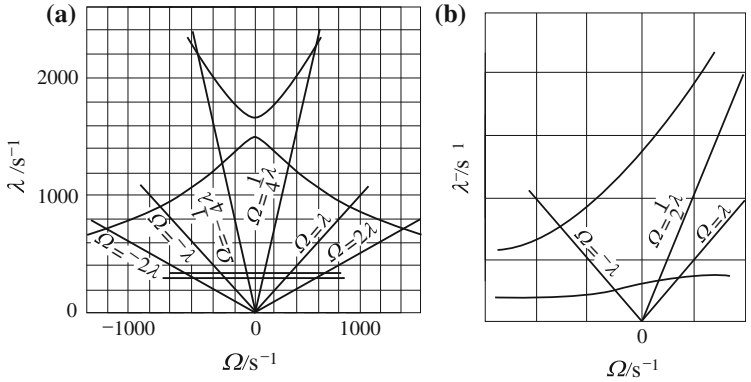

Fig. 9.35 The frequency spectrum (*Campbell diagram*) of rotor system (He et al. 1999). **a** With non-homogeneous supports. **b** With homogeneous support

By comparing Fig. 9.35a, b, one may find that the non-homogeneous rotor is essentially distinct from the homogenous one in frequency spectrum. The critical rotational speed of the former rotor will increase twice because its stiffness coefficients of support along two perpendicular directions are not equal to each other. For the rotor, there are two values for one order of critical speed. For example, the calculation results of two values of first order critical speed are 3,163 and 3380 rpm from Fig. 9.35a (section point on the curve $\Omega = 2\lambda$); the test results are 2,625 and 3,300 rpm by He et al. 1999. The vibration occurred in the direction of minimum stiffness first and the orbit of the rotor vibration was an ellipse.

9.5.1.3 Turbopump Critical Speed Computation Considering Fluid Acting Forces

When the pump eccentric impeller is filled with liquid, the fluid action on the impeller may be divided into several kinds of forces and moments (He et al. 1999):

1. Lift to impeller P_L:

$$P_L = \Gamma\omega^2 A \tag{9.77}$$

where A is its acted area on impeller; Γ is the lift coefficient:

$$\Gamma = \frac{\rho_L V\left\{\left[-1+(r_i/r_0)^2\right]+\left[1+3(r_i/r_0)^2\right]\Omega/\omega-2(r_i/r_0)^2\Omega^2/\omega^2\right\}}{\left[1-(r_i/r_0)^2\right]}$$

where r_i is the radius of the impeller; r_0 is the inner radius casing; ρ_I is liquid density; V is the impeller volume; Ω is the angular impeller speed; and ω is the natural rotating speed of rotor.

2. Draft to impeller P_D:

$$P_D = f\omega A \tag{9.78}$$

where $f = \mu_L \pi S(r_i/r_0)^2 (\eta_i - \eta_0 \Omega/\omega)$. And μ_L is liquid viscosity, S is the impeller width; and η_i and η_0 are factors which are functions of (Ω/ω).

3. Centrifugal force to impeller P_C:

$$P_C = m\omega^2 r \tag{9.79}$$

where m is liquid mass. The action of centrifugal force and lift may be treated as the addition of an equivalent mass to the impeller.

4. Draft moment to impeller M_f is balanced by the driving force of impeller.
5. Eccentric osculating to impeller M_D:

$$M_D = \bar{f}\alpha^{\circ} \tag{9.80}$$

where $\bar{f}$ is the damping coefficient; α° is the impeller deflection angle.

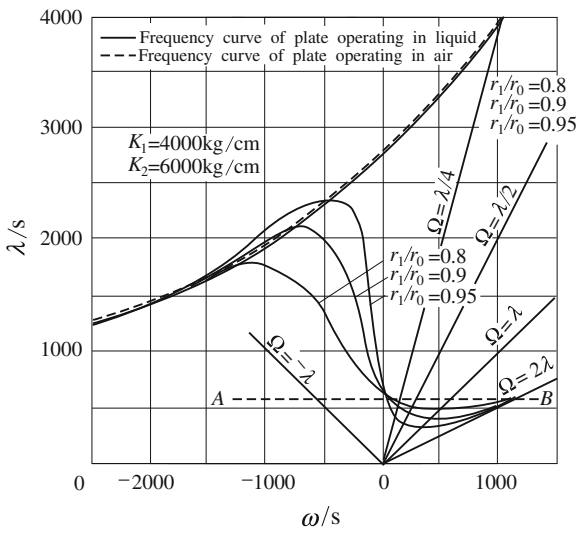

Fig. 9.36 Frequency spectrums (*Campbell diagram*) of rotor in liquid and air (He et al. 1999)

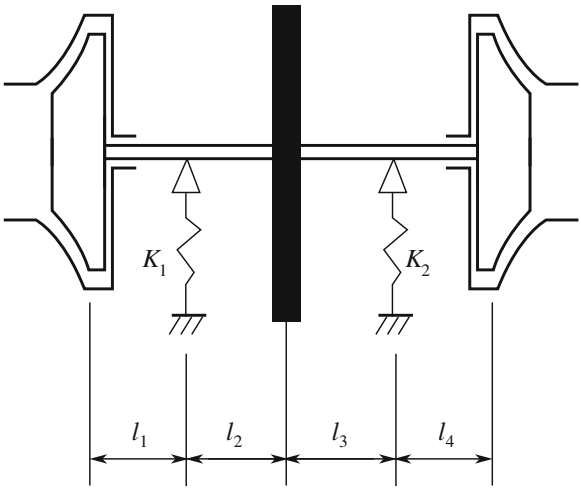

Fig. 9.37 Schematic of a turbopump structure with three rotors

Table 9.9 Critical rotating speed of three rotor pump in liquid and in air (He et al. 1999)

Term	1st order	2nd order	3rd order
Not considering liquid action (rpm)	11,173	18,392	29,641
Considering liquid action (rpm)	8,222	14,897	25,793

The forces and moment could be added into the transfer matrices, and then the natural frequency of the rotor system could be obtained as shown in Fig. 9.36 for the model in Fig. 9.32 but with consideration of the liquid flow actions to impeller.

Figure 9.36 shows a comparison of frequency spectrums between rotors in liquid and in air.

The two spectrums have obvious differences, but the critical frequencies are similar.

On the rotor's precession conditions, the liquid has significant influence on the natural frequencies. The first order of natural frequency will decrease at the positive direction precession, but increase at negative direction procession. With the positive precession, the added liquid mass increases the rotor mass.

Another sample calculation involves a turbopump with three rotors as shown in Fig. 9.37. The critical speed calculations of the rotor system both in liquid and air are listed in Table 9.9. The critical rotational speed of the turbopump rotor possessing three plates, two supports, and single shaft was calculated.

The results imply that there is an essential distinction between the frequency spectrums in two conditions. The liquid action on the pump wheel obviously influences the critical rotation speed of the rotor.

9.5.2 Critical Speed Computation for a Multi-Stage Centrifugal Pump

An ultrahigh-pressure multi-stage centrifugal pump works at high speeds with a long shaft, and is featured in complex structures. In order to improve the safety and reliability of such operations demanded in a high level, the ultrahigh-pressure multi-stage centrifugal pump develops in the direction of large equipment and the integration of pump and electromotor. The characteristics and the stability of the shafting system have a great impact on quality, lifespan, and reliability of ultra-high-pressure multi-stage centrifugal pumps.

Therefore, it is important to conduct dynamic analysis for the rotor shafts of ultrahigh-pressure centrifugal pumps. In this section, the problems of modeling a steady rotor system with sliding bearings and ring seal via FEM are discussed. Discussion has been conducted on the film force of sliding bearings and the method of its application in modeling, as well as the method of simulating film stiffness in Chap. 5.

Radial stiffness and damping of film are the important dynamic characteristics of the rotor system; the circumferential stiffness and damping are both small and generally not considered. In the dynamics mode of Chap. 5, incremental film force and the dynamic characteristic of film was calculated, by pulsing small disturbances to the film in the static equilibrium position. Aiming for the rotor-bearing system, the FEM mesh model of a 3,800 KW, multi-stage centrifugal pumps was built. In the simulation analysis, modal shapes and critical speeds of the rotor were calculated.

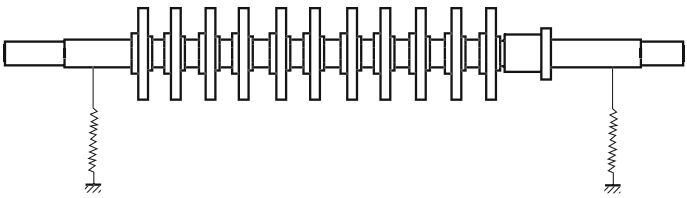

Fig. 9.38 Model of shaft operation in the air (Ping et al. 2008)

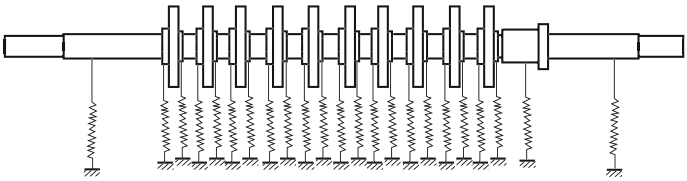

Fig. 9.39 Model of shaft operation in the water (Ping et al. 2008)

Table 9.10 The result of the calculation (Ping et al. 2008)

Type of critical speed	1st Order bending (rpm)	2nd Order bending (rpm)
"dry" critical speed	3,158	9,731
"wet" critical speed	6,342	12,956

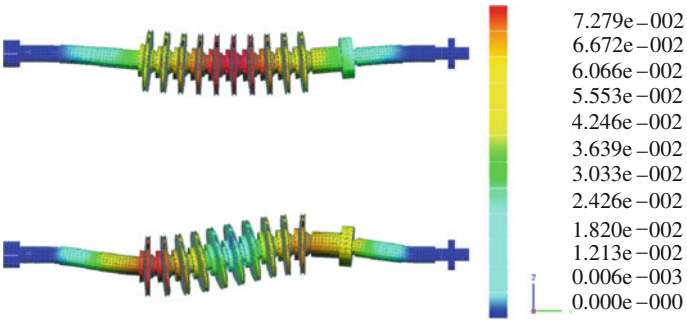

Fig. 9.40 The first and second order mode diagram (Ping et al. 2008)

In the analysis of the centrifugal pumps, the concepts of "dry" and "wet" critical speed are introduced. "Dry" denotes a critical speed that does not include the dynamic characteristic-effect of the seal; "wet" denotes a critical speed at which the pump is in the working station and therein, dynamic characteristics of the seal need to be considered (see Figs. 9.38, 9.39).

Table 9.10 shows the critical-speed calculation results of first and second order lateral rotating speeds in dry and in wet models. Figure 9.40 depicts the mode (Ping et al. 2008).

The "wet" critical speed is significantly higher than the "dry" one, which proves that the dynamic characteristics of seal have a great effect on the rotor's critical speeds in the centrifugal pump. Therefore, the characteristics of the seal should be considered in the design.

9.5.3 Dynamic Stability of the Pump's Rotor System

The liquid layer in slotted seals of centrifugal pumps exerts an effect on the nature of rotor motion. Transferred by pumps, the liquid has a comparatively high viscosity, and due to this fact, large hydrodynamic forces act on the eccentric annular slots of the seals. They change the values of the critical speeds, lower the amplitudes of resonance vibrations, and facilitate the onset of strong self-vibrations at high revolution rates (Tian and Zhu 2000).

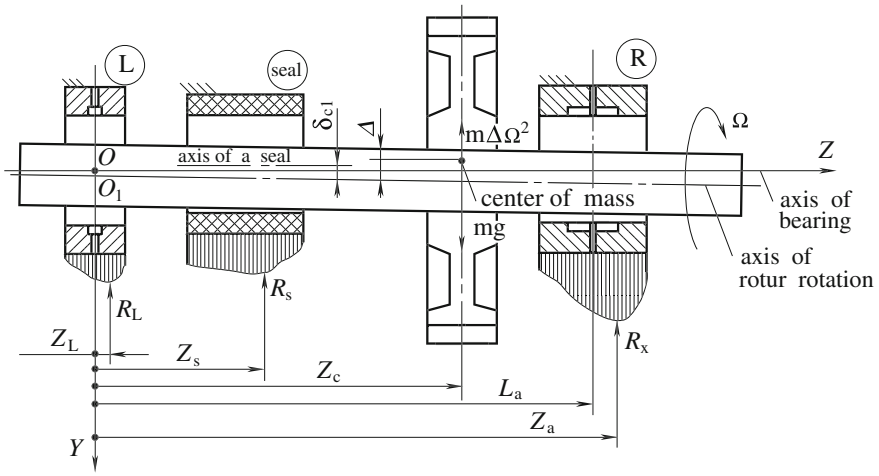

Fig. 9.41 Dynamic model of a rotor system (Savina and Solomin 2003)

9.5.3.1 Dynamics of a Rotor: Fluid-Film Bearings–Contactless Seals System

Consider the model of "rotor—fluid-film bearings—seals" with four degrees of freedom that consists of a rigid rotor supported by two fluid-film bearings and contactless seals (Fig. 9.41, Savin and Solomin 2003).

Lagrange's equations of motion for this rotor system with four degrees of freedom in the Cartesian coordinates can be written as

$$
\begin{aligned}
m\left[\frac{Z_D}{L_{LR}}\left(\ddot{X}_R-\ddot{X}_L\right)+\ddot{X}_L\right] &= R^B_{XR}+R^B_{XL}+R^S_X+F_X+m\Omega^2\Delta\sin\Omega t\\
m\left[\frac{Z_D}{L_{LR}}\left(\ddot{Y}_R-\ddot{Y}_L\right)+\ddot{Y}_L\right] &= R^B_{YR}+R^B_{YL}+R^S_Y+F_Y+m\Omega^2\Delta\cos\Omega t+mg\\
\frac{J_p\Omega}{L_{LR}}\left(\dot{X}_R-\dot{X}_L\right)+J_dT\Omega^2\sin[2(\Omega t-\Gamma)] &= R^B_{XL}Z_D-R^B_{XR}(L_{LR}-Z_D)-R^S_X(Z_S-Z_D)\\
\frac{J_p\Omega}{L_{LR}}\left(\dot{Y}_R-\dot{Y}_L\right)-J_dT\Omega^2\sin[2(\Omega t-\Gamma)] &= R^B_{YL}Z_D-R^B_{YR}(L_{LR}-Z_D)-R^S_Y(Z_S-Z_D)
\end{aligned}
\tag{9.81}
$$

where X, Y are coordinates of a shaft center; $\ddot{X}, \ddot{Y}$ are the acceleration of a shaft center; m is the mass of a rotor; Δ is the static unbalance of a rotor; R is the hydrodynamic forces of bearings and seals; F is the frictional force; Z_D and Z_S are the axial coordinates at the center of the rotor mass and the application point of seal forces; L_{LR} is the distance between supports; $T$and Γ are the angles describing unbalance of a rotor;

and J_d and J_p are axial and equatorial moments of inertia. Indexes: B is for bearing; S for seal; R and L are for right and left bearings accordingly.

Analysis on the AFC (amplitude-frequency characteristics) of a rotor system was based on the analysis of trajectories that allowed for the study of vibrations and stability of a rotor system in a nonlinear case. The trajectory of a rotor system motion over a certain period of time can be computed by means of a direct numerical integration of differential equations of rotor dynamics and equations that describe hydrodynamic forces in fluid-film bearings and seals. The AFC and stability thresholds of the rotor system can be determined by obtaining trajectories of rotor motion. Analysis of the results allow to estimate the influence of various types of seals–their geometric and working parameters on dynamic behavior of a high-speed rigid rotor (see Savin and Solomin 2003).

9.5.3.2 Dynamic Stability of a Pump Rotor

The dynamic stability of an engineered rotor-labyrinth seal system has been investigated. The Muszyńska (1986a) model and the FEM were adopted to evaluate the rotor system stability of a turbopump (Xia et al. 2006).

1. Dynamic equations of the rotor-labyrinth seal system

The rotor-labyrinth seal system proposed in Xia et al. (2006), Li et al. (2007) is shown in Fig. 9.42. It assumes that a single disk rotor is supported rigidly or with a sliding bearing and the seal forces act equivalently on the disk. In the following expressions, Ω is the rotation speed. m_d the is mass of the disk, k is the generalized (modal) stiffness coefficients of the rotor, and c is the generalized (modal) damping coefficients. c_{od} is the seal clearance. x_d and y_d are disk displacements. M_b is the mass of the journal. x_b and y_b are journal displacements. c_b is the journal clearance. f_x and f_y are bearing forces. r is the unbalance radius.

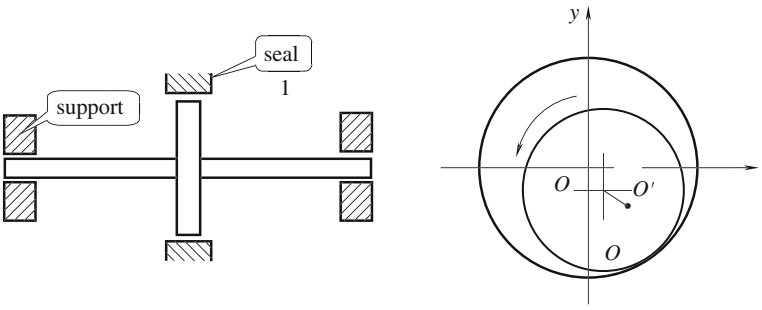

Fig. 9.42 The model of rotor/seal system (Xia et al. 2006)

(a) Dynamic equation of a rotor system rigidly supported

For the rotor system supported rigidly, the mathematical model is presented as below where the mass of journal is neglected:

$$\begin{cases} m_d\ddot{x}_d + c\dot{x}_d + kx_d = f_x + m_d r\Omega^2\cos\Omega t \\ m_d\ddot{y}_d + c\dot{y}_d + ky_d = f_y + m_d r\Omega^2\sin\Omega t - m_d g \end{cases}. \tag{9.82}$$

If the rotor is balanced, there are no $m_{\mathrm{d}} r\Omega^2\cos\Omega t$ and $m_{\mathrm{d}} r\Omega^2\sin\Omega t$ in the above equation.

(b) Dynamic equation of the rotor system supported with sliding bearing

In practice, many rotors are supported with sliding bearing, so it is more valuable to investigate the stability of this system. The mathematical model of this kind is presented as

$$\begin{cases} m_d\ddot{x}_d + c\,\dot{x}_d + k(x_d - x_b) = f_x + m_d r\Omega^2\cos\Omega t \\ m_d\ddot{y}_d + c\,\dot{y}_d + k(y_d - y_b) = f_y + m_d r\Omega^2\sin\Omega t - m_d g \\ m_b\ddot{x}_b - 0.5k(x_d - x_b) = f_x \\ m_b\ddot{y}_b - 0.5k(y_d - y_b) = f_y \end{cases} \tag{9.83}$$

(c) Model for seal fluid force

Based on Muszyńska (1986b) model, the labyrinth seal force, which reflects the fluid dynamic action, is

$$\begin{Bmatrix} f_x \\ f_y \end{Bmatrix} = -\begin{bmatrix} m_f & 0 \\ 0 & m_f \end{bmatrix}\begin{Bmatrix} \ddot{x} \\ \ddot{y} \end{Bmatrix} - \begin{bmatrix} C & 2\tau_f\Omega m_f \\ -2\tau_f\Omega m_f & C \end{bmatrix}\begin{Bmatrix} \dot{x} \\ \dot{y} \end{Bmatrix} - \begin{bmatrix} K - m_f\tau_f^2\Omega^2 & \tau_f\Omega C \\ -\tau_f\Omega C & K - m_f\tau_f^2\Omega^2 \end{bmatrix}\begin{Bmatrix} x \\ y \end{Bmatrix}. \tag{9.84}$$

The Muszyńska model assumes that the fluid force that stems from averaging the circumferential flow is rotating at angular velocity $\tau_f\,\Omega$, where Ω is the journal rotation speed and τ_f is the key variable of Muszyńska model–one that represents the fluid average circumferential velocity ratio. In Eq. (9.84), K, C, and m_f are fluid stiffness, damping, and inertia coefficients, respectively. K, C and τ_f vary with increasing journal eccentricity and can be expressed as

$$\begin{cases} K = K_0\left(1 - e^2\right)^{-n},\ C = C_0\left(1 - e^2\right)^{-n},\ (n = 0.5 \sim 3); \\ \tau_f = \tau_0\left(1 - e^2\right)^b,\ (0 < b < 1) \end{cases} \tag{9.85}$$

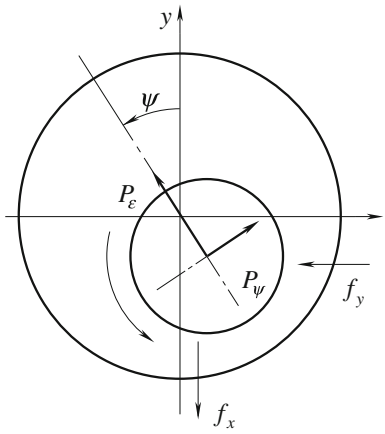

Fig. 9.43 The sliding bearing force. *Note* c_d is the radial clearance of seal; l is the length of seal; m_0, n_0 are experiential coefficient; R is the radius of seal; v_a is the axial fluid speed; z is the inlet loss coefficient; ΔP is the pressure margin of seal (Xia et al. 2006)

where the relative eccentricity $e = (x_d^2 + y_d^2)^{1/2}/c_d$; c_d is the seal clearance, and n, b, τ_0 are determined by material seal. Generally $\tau_0 < 0.5$. The Muszyńska model of seal fluid forces is applied to investigate stability of the rotor. The coefficients K_0, C_0, and m_f involved in seal length, seal clearance, pressure margin, and seal radius are calculated with Black-Childs Equations (Childs and Scharrer 1986):

$$K_0 = \mu_3\mu_0,\ C_0 = \mu_3\mu_1 T,\ m_f = \mu_2\mu_3 T^2 \tag{9.86}$$

where

$$\mu_0 = 2\sigma^2/(1+z+2\sigma)E(1-m_0),\ \mu_2 = \sigma(1/6+E)/(1+z+2\sigma)$$
$$\mu_1 = 2\sigma^2/(1+z+2\sigma)[E/\sigma + 0.5B(1/6+E)],\ \mu_3 = \pi R\Delta P/\lambda,\ T = l/v_a$$

where

$$R_v = Rc_d\Omega\boldsymbol{\rho}/\mu,\ R_a = 2v_a c_d\rho/\mu,$$
$$\lambda = n_0 R_a^{m_0}\left[1 + (R_v/R_a)^2\right]^{\frac{1+m_0}{2}},\ \sigma = \frac{\lambda l}{c_d},\ E = \frac{1+z}{1+z+2\sigma},\ B = 2 - \frac{(R_v/R_a)^2 - m_0}{1+(R_v/R_a)^2}.$$

(d) Short sliding bearing force

The model of short bearing is applied to the bearing force, which has an analytical solution. The bearing force can be expressed with radial force P_ε and tangent force P_ψ shown in Fig. 9.43 as

$$\begin{Bmatrix} f_x \\ f_y \end{Bmatrix} = \begin{Bmatrix} P_\varepsilon \sin\psi - P_\psi \cos\psi \\ -P_\varepsilon \cos\psi - P_\psi \sin\psi \end{Bmatrix} = \frac{1}{\sqrt{x_b^2 + y_b^2}} \begin{bmatrix} -P_\varepsilon & -P_\psi \\ P_\psi & -P_\varepsilon \end{bmatrix} \begin{Bmatrix} x_b \\ y_b \end{Bmatrix} \tag{9.87}$$

where polar angle $\psi = \text{arctg}\ [x_b/(-y_b)]$.

(e) Dimensionless equation of rotor system

Dimensionless quantities are defined as

$$\begin{gathered} x_1 = \frac{x_d}{c_d},\ y_1 = \frac{y_d}{c_d},\ x_2 = \frac{x_b}{c_b},\ y_2 = \frac{y_b}{c_b},\ \tau = \Omega t,\ M = m_d + m_f,\ \rho = \frac{m_d e}{M c_d} \\ \frac{\mathrm{d}}{\mathrm{d}t} = \Omega \frac{\mathrm{d}}{\mathrm{d}\tau},\ \frac{\mathrm{d}^2}{\mathrm{d}t^2} = \Omega^2 \frac{\mathrm{d}^2}{\mathrm{d}\tau^2},\ \varepsilon = \sqrt{x_2^2 + y_2^2} \end{gathered} \tag{9.88}$$

In dimensionless terms, L/R_b is the ratio of length to radius of bearing, and $S = \eta\Omega R_b/(\pi W)(R_b/c_b)^2$ is the Summerfield coefficient.

Let $x' = \frac{\mathrm{d}x}{\mathrm{d}\tau},\ x'' = \frac{\mathrm{d}^2 x}{\mathrm{d}\tau^2}$

Then the dimensionless translation of (9.82) may be rewritten as

$$\begin{Bmatrix} x_1'' \\ y_1'' \end{Bmatrix} + \begin{bmatrix} d_1 & d_2 \\ -d_2 & d_1 \end{bmatrix} \begin{Bmatrix} x_1' \\ y_1' \end{Bmatrix} + \begin{bmatrix} k_1 & k_2 \\ -k_2 & k_1 \end{bmatrix} \begin{Bmatrix} x_1 \\ y_1 \end{Bmatrix} = \begin{Bmatrix} 0 \\ G \end{Bmatrix} + \rho \begin{Bmatrix} \cos\tau \\ \sin\tau \end{Bmatrix}. \tag{9.89}$$

And Eq. (9.83) may be written as

$$\begin{aligned} &\begin{Bmatrix} x_1'' \\ y_1'' \end{Bmatrix} + \begin{bmatrix} d_1 & d_2 \\ -d_2 & d_1 \end{bmatrix} \begin{Bmatrix} x_1' \\ y_1' \end{Bmatrix} + \begin{bmatrix} k_1 & k_2 \\ -k_2 & k_1 \end{bmatrix} \begin{Bmatrix} x_1 \\ y_1 \end{Bmatrix} - \frac{k\beta}{M\Omega^2} \begin{Bmatrix} x_2 \\ y_2 \end{Bmatrix} = \begin{Bmatrix} 0 \\ G \end{Bmatrix} \\ &\quad + \rho \begin{Bmatrix} \cos\tau \\ \sin\tau \end{Bmatrix} \begin{Bmatrix} x_2'' \\ y_2'' \end{Bmatrix} + \left(\frac{k}{2m_b\Omega^2} + \frac{\pi W S_0}{2m_b c_b \Omega \sqrt{x_2^2 + y_2^2}} \left(\frac{L}{R_b} \right)^2 \begin{bmatrix} \bar{P}_\varepsilon & \bar{P}_\psi \\ -\bar{P}_\psi & \bar{P}_\varepsilon \end{bmatrix} \right) \begin{Bmatrix} x_2 \\ y_2 \end{Bmatrix} \\ &\quad - \frac{k}{2\beta m_b \Omega^2} \begin{Bmatrix} x_1 \\ y_1 \end{Bmatrix} = \begin{Bmatrix} 0 \\ -g/c_b\Omega^2 \end{Bmatrix} \end{aligned} \tag{9.90}$$

where

$$\begin{gathered} d_1 = \frac{c + C}{M\Omega},\ d_2 = \frac{2\tau_f m_f}{M},\ k_1 = \frac{k + K - \tau_f^2 m_f \Omega^2}{M\Omega^2},\ k_2 = \frac{\tau_f D}{M\Omega},\ \rho = \frac{m_d r}{M c_d} \\ G = -\frac{m_d g}{M c_d \Omega^2},\ \beta = \frac{c_b}{c_d},\ M = m_d + m_f,\ S_0 = \frac{S}{\Omega},\ W = m_b g + \frac{m_d g}{2} \end{gathered}$$

2. Analysis of stability

(a) Stability of a balanced rotor with rigid support

Equation (9.89) can be transformed into state equations in matrix form with four degrees of freedom:

$$\begin{Bmatrix} x_1' \\ y_1' \\ x_1 \\ y_1 \end{Bmatrix} = \begin{Bmatrix} \rho^2 \cos t \\ G + \rho^2 \sin t \\ 0 \\ 0 \end{Bmatrix} - \begin{bmatrix} d_1 & d_2 & k_1 & k_2 \\ -d_2 & d_1 & -k_2 & k_1 \\ -1 & 0 & 0 & 0 \\ 0 & -1 & 0 & 0 \end{bmatrix} \begin{Bmatrix} x_1' \\ y_1' \\ x_1 \\ y_1 \end{Bmatrix} = \begin{Bmatrix} f_1(x_1', y_1', x_1, y_1, \Omega, t) \\ f_2(x_1', y_1', x_1, y_1, \Omega, t) \\ f_3(x_1', y_1', x_1, y_1, \Omega, t) \\ f_4(x_1', y_1', x_1, y_1, \Omega, t) \end{Bmatrix}. \tag{9.91}$$

If the rigidly supported rotor is balanced, the solution of Eq. (9.89) is an equilibrium point that can be obtained by iterating the following equation:

$$\begin{bmatrix} k_1 & k_2 \\ -k_2 & k_{12} \end{bmatrix} \begin{Bmatrix} x_1 \\ y_1 \end{Bmatrix} = \begin{Bmatrix} 0 \\ G \end{Bmatrix}. \tag{9.92}$$

According to the first Liapunov theory, the stability of a nonlinear system is determined by the eigenvalues of its simple approximate system. If all real parts of the eigenvalues of the Jacobi matrix are negative, the system is stable at the equilibrium point. If a pair of eigenvalues have real part of zero and the others have real parts of negative values, the system is in the state of critical stability. If an eigenvalue of Jacobi matrix is positive, the system is unstable. If the equilibrium point is (x_0, y_0), the simple approximate expansion of Eq. (9.91) at (x_0, y_0) is

$$J = Df\big|_{(x_0,y_0)} = \begin{bmatrix} \frac{\partial f_1}{\partial x_1'} & \frac{\partial f_1}{\partial y_1'} & \frac{\partial f_1}{\partial x_1} & \frac{\partial f_1}{\partial y_1} \\ \frac{\partial f_2}{\partial y_1'} & \frac{\partial f_2}{\partial y_1'} & \frac{\partial f_2}{\partial x_1} & \frac{\partial f_2}{\partial y_1} \\ \frac{\partial f_3}{\partial y_1'} & \frac{\partial f_3}{\partial y_1'} & \frac{\partial f_3}{\partial x_1} & \frac{\partial f_3}{\partial y_1} \\ \frac{\partial f_4}{\partial y_1'} & \frac{\partial f_4}{\partial y_1'} & \frac{\partial f_4}{\partial x_1} & \frac{\partial f_4}{\partial y_1} \end{bmatrix}. \tag{9.93}$$

(b) Stability analysis results for a balanced rotor with rigid supports

Xia et al. (2006), Li & Xu (2003), Li et al. (2007) completed the analysis for stability of high speed turbopumps. They achieved the following similar results.

Table 9.11 Parameter list of rotor system (see Li et al. 2007)

Disk mass (kg)	Generalized dumping coefficient (N.s/m)	Generalized stiffness coefficient (N/m)	Journal mass (kg)
50	5000	8×10^6	10
L/R_b	Journal clearance (mm)	Seal clearance (mm)	Unbalance radius (mm)
1	0.04	1	0.05
Sommefeld coefficient	Parameter n	Parameter b	Parameter τ_0
0.001	2.5	0.045	0.2

The calculated results show that if the rotation speed is below critical speed, the balanced rotor is stable at an equilibrium position and all real parts of the eigenvalues of Jacobi matrix are negative. If the rotation approaches critical speed the rotor system evolves into periodic vibration and the Hopf bifurcation arises, where a pair of eigenvalues have a real part of zero. The amplitude of the vibration increases along with an increase of rotation speed until rotor impact seal. Using the parameters in Table 9.11 and the New mark method to calculate, one would have the critical speed to be 1,140 rad/s and the eigenvalues of Jacobi matrix (0.0000 ± 0.3658i, -0.3205 ± 0.0605i).

Figure 9.46 displays motions of the rotor at different speed. The structural and physical parameters of the seal will influence the critical instability speed, such as the larger seal radius, seal clearance, and seal length, the higher critical instability speed and the smaller seal clearance corresponds to the higher critical instability speed.

(c) Stability of an unbalanced rotor with rigid supports

If the rotor is unbalanced, the solution of Eq. (9.87) is a periodic solution. Under the periodic excitation of rotor unbalance, the whirling vibration of the rotor is synchronous if the rotation speed is below the critical instability speed. The rotor vibration becomes severe and asynchronous, which is defined unstable, if the rotation speed exceeds critical instability speed.

To calculate a periodic solution, a lot of numerical methods such as the shooting method, the finite difference approach, the harmonic balance method, and Poincare mapping may be used. Stability of the synchronous solution can be discussed according to the Floquet theory. Supposing the synchronous solution $x^*(t)$ has been found by means of the shooting method, one could solve the following initial value problem:

$$\left(\frac{\partial x}{\partial x(0)}\right)^{*} = \frac{\partial f}{\partial x}(t, x^{*})\frac{\partial x}{\partial x(0)}; \left(\frac{\partial x}{\partial x(0)}\right)_{t=0} = I. \tag{9.94}$$

The eigenvalues of $(\partial x/\partial x(0))_{t=T}$ are Floquet multipliers λ. If all modules of Floquet multipliers are less than 1, the periodic solution is stable; if one or more

Table 9.12 Parameter list of unbalanced rotor system (see Li et al. 2007)

Disk mass (kg)	Generalized dumping	Generalized stiffness coefficient (N/m)	Journal mass (kg)
50	10	0.5×10^6	0.075
L/R_b	Journal clearance (mm)	Seal clearance (mm)	Unbalance radius (mm)
0.05	5	2.5	0.35
Sommefeld coefficient	Parameter n	Parameter b	Parameter τ_0
0.1	2.5	0.45	0.2

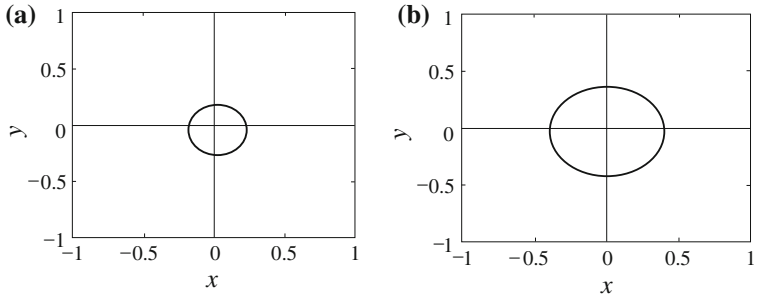

Fig. 9.44 The numerical simulation of a balanced rotor with rigid supports. **a** $\Omega = 1200$ rad/s, **b** $\Omega = 1500$ rad/s (Li et al. 2007)

modules of its multipliers are more than 1, it is unstable (Tam et al. 1988). The rotor-seal system makes synchronous vibration stable and all modules of Floquet multipliers are less than 1 when the rotation speed is below critical instability speed. The rotor vibration is unstable when the rotation speed exceeds critical instability speed, and in this case at least one module of Floquet multipliers is more than 1. When the rotor rotates at critical instability speed ω_c, at least one module of Floquet multipliers equals 1 and the others are less than 1. The calculated results reveal that the critical instability speed ω_c increases with growing unbalance, which has been proved in practice.

As the whirling amplitude climbs rapidly with increasing unbalance radius r, it is important for designers to determine a suitable r. To calculate with the parameters listed in Table 9.12, one would set the critical instability speed to be 1146.1 rad/s, whereas the Floquet multipliers are $(-0.6463 \pm 0.7631\text{i}, 0.1246 \pm 0.0479\text{i})$ and the ultimate module is 1. Figure 9.44 shows the unstable motion of this rotor system.

According to the bifurcation theory, a periodic solution may lose stability in three generic ways via Floquet multipliers, expressed by a unit circle in complex plane. The first way to lose stability is through a saddle-node or pitchfork

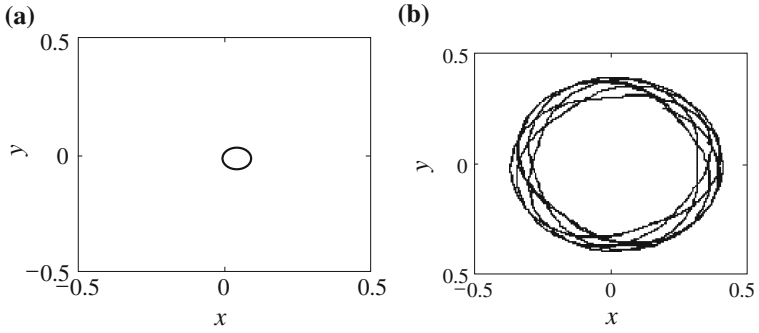

Fig. 9.45 The orbit of a rotor. **a** $\Omega = 900$ rad/s, **b** $\Omega = 1200$ rad/s (Li et al. 2007)

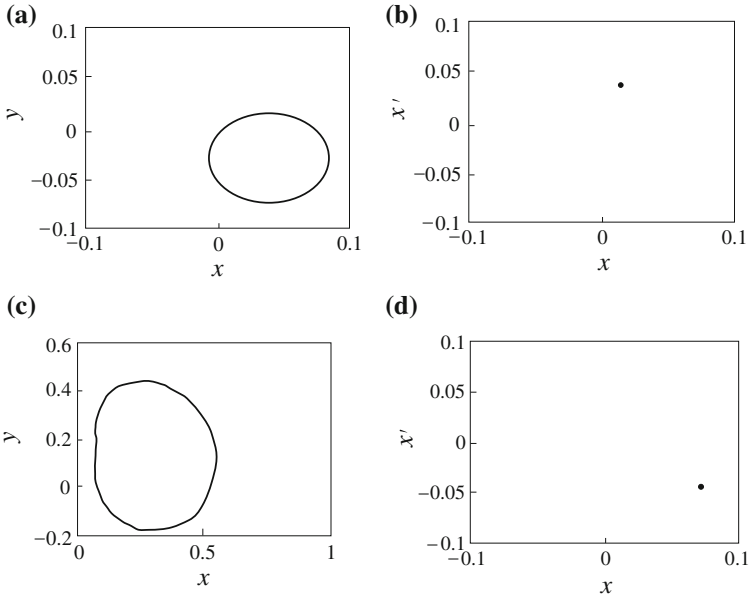

Fig. 9.46 The orbit and Poincare map of rotor at $\Omega = 500$ rad/s. **a** The orbit of disk, **b** Poincare map of disk, **c** The orbit of journal, **d** Poincare map of journal (Li et al. 2007)

bifurcation when a single real Floquet multiplier's largest module crosses the unit circle at +1. Another way is period-doubling bifurcation when a single real Floquet multiplier's largest module crosses the unit circle at −1. The third way is quasi-periodic bifurcation when a pair of complex conjugate eigenvalues whose largest module crosses the unit circle. The calculated results demonstrate that the unstable rotor-seal system with rigid support generates quasi-periodic bifurcation in most cases shown in Fig. 9.45b In some cases, the rotor will produce severe subharmonic vibration, which belongs to a typical nonlinear phenomenon. With the virtue of particular seal forces, the seal-rotor system yields periodic doubled bifurcation, and at this point imaginary parts of the Floquet multipliers are zero. To calculate with the parameters listed in Table 9.12, the periodic-doubled bifurcation takes place at $\Omega = 200\text{rad/s}$, where $\lambda_{1,2,3,4} = -1.0009, -0.9332, -0.6140, -0.5992$.

Based on the above results, one can see that the rotor vibration becomes severe when the system is losing stability and becomes quasi-periodic. The rotor may impact with seal as a result of high amplitude of bifurcation motion, which occurs with increasing rotor speed.

(d) Stability of a rotor with sliding bearing support

The dynamic stability of a rotor with sliding bearing support is different from a rotor with rigid support. To calculate with the parameters listed in Table 9.12, the critical instability speed is 770 rad/s. Simulating the movement of the rotor and the

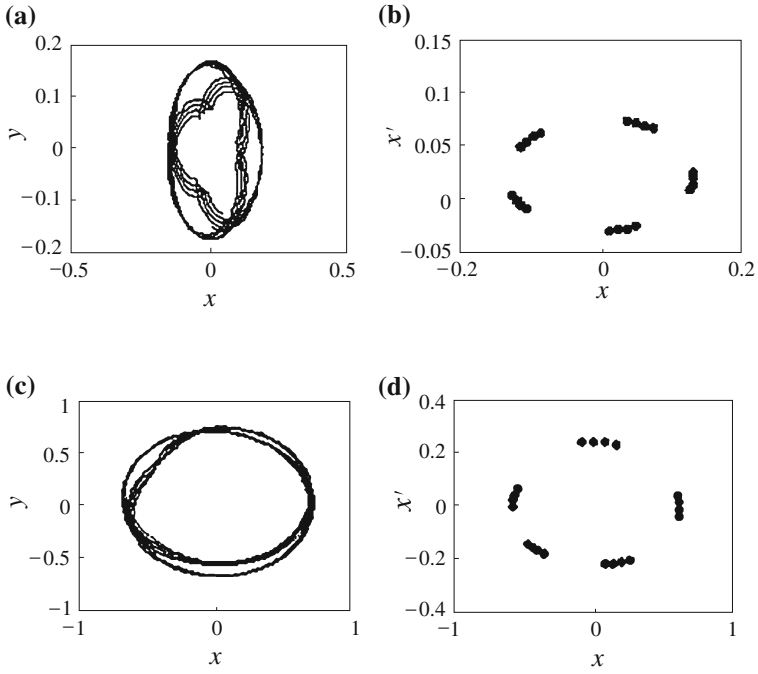

Fig. 9.47 The orbit and Poincare map of rotor at $\Omega = 1{,}000$ rad/s, **a** The orbit of disk, **b** Poincare map of disk, **c** The orbit of journal, **d** Poincare map of journal (Li et al. 2007)

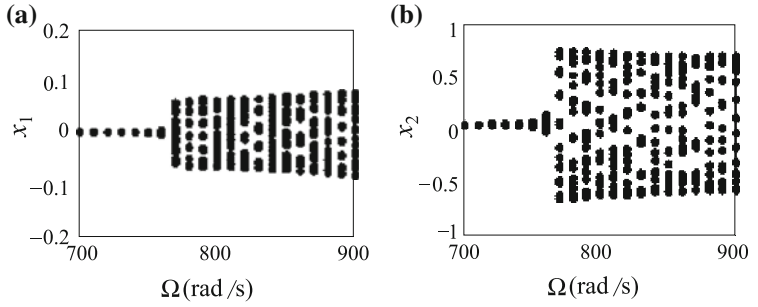

Fig. 9.48 The bifurcation diagram of a rotor. **a** Bifurcation diagram of disk. **b** Bifurcation diagram of journal (Li et al. 2007)

Poincare mapping yields a progression from Figs. 9.46, 9.47. Because the rotation speed is below critical instability speed, the rotor-seal system makes stable synchronous vibrations shown in Fig. 9.46. When it exceeds the critical speed, the vibration of rotor becomes severe and asynchronous (see in Fig. 9.47).

Figure 9.48 is the bifurcation map of disk and journal. The calculated results show that, like the rotor with rigid support, the periodic vibration of this rotor is stable when the rotation speed is below critical instability speed, whereas the periodic vibration becomes unstable when the rotation exceeds a critical speed.

As distinct from the rotor with rigid support, when the rotation exceeds a critical instability speed the vibration amplitude of the disk increases rapidly to a point, then increases slowly up to a given level and maintains this level. Whereas, when the speed arrives at critical instability, vibration amplitude of the journal goes up rapidly, then drops slowly,

Through calculation, it is found that in this rotor system the larger the seal radius, seal clearance, and seal length, and the higher the critical instability speed is, the smaller the seal clearance has of corresponding to higher critical instability speeds. Contrary to the case of rigid support, the critical instability speed ω_c decreases with increasing unbalance, so in practice the unbalance of a rotor with sliding bearing should be as small as possible.

The bearing parameter S_0 has inconspicuous influence on the critical instability speed. Compared with the case of rigid support, the critical instability speed is higher for the additional mass of journal. The calculated results prove that seal force is the main factor for rotor instability, but the bearing force has inconspicuous influence on critical instability speed and restrains amplitude of unstable vibration of rotor. As a result, the rotor-seal system may benefit from introduction of a sliding bearing.

References

Andrés, L.S. (2006). Introduction to pump rotordynamics, *Design and analysis of high speed pumps*, RTO EDUCATIONAL NOTES, RTO-EN-AVT-143.

Andrés, L.S., Delgado, A. (2008). A novel FE bulk-flow model for improved predictions of force coefficients in off-centered grooved oil seals, *Proceedings of the 28th TRC Annual Meeting*, paper No. TRC-SEAL-1-08.

Barp, B. (1976). Dynamic behavior of large pump turbine rotors. *Water Power and Dam Construct, 28*(11), 48–51.

Cervantes, M., Aidanpää, J-O., Glavatskikh, S., & Karlsson, T. (2005). Group dynamics (hydro power equipment). *International Water Power and Dam Construction*, *57*(12), 40-45. http://www.waterpowermagazine.com/story.asp?storyCode=2032590

Childs, D. W., & Scharrer, J. K. (1986). An Iwatsubo-based solution for labyrinth seals: comparison to experimental results. *Transactions of ASME Journal of Engineering for Gas Turbines and Power, 108*, 325–331.

Childs, D. W. (1983). Dynamic analysis of turbulent annular seals based on Hirs lubrication equation. *Transactions of ASME Journal of Lubrication Technology, 105*, 429–436.

Childs, D. W. (1993). *Turbomachinery rotor dynamics, phenomena, modeling and analysis*. New York: Wiley.

CSI. (2009). http://www.csiberkeley.com/Tech_Info/13.pdf.

Feng, F. Z., & Chu, F. L. (2001). Dynamic analysis of a hydraulic turbine unit. *Mechanics Based Design of Structures and Machines, 29*, 505–531.

Graf, K. (1991). *Spaltströmungsbedingte Kröfte an berü1hrungslosen Dichtungen von hydraulischen und thermischen Turbomaschinen*, PhD Thesis, ETH Zurich No 9319.

Guinzburg, A., Brennen, C.E., Acosta, A.J., and Caughey, T.K. (1994). Experimental results for therotordynamic characteristics of leakage flows in centrifugal pumps. *ASME J. Fluids Eng*, *116*, 110–115

Gustavsson, R. K., & Aidanpää, J. -O. (2003). Measurement of bearing load using strain gauges at hydropower unit, HRW. Vol 11. Nov 2003

Gustavsson, R. K., & Aidanpää, J. -O. (2004). The influence of magnetic pull on the stability of generator rotors. *Proceedings of the ISROMAC-10th International Symposium on Rotating Machinery*, Honolulu.

Gustavsson, R. K., & Aidanpää, J.-O. (2006). The influence off non-linear magnetic pull on hydropower generator rotors. *Journal of Sound and Vibration, 297*, 551–562.

He, H. Q., Shen, D. K., & Zhang, Z. W. (1998). Study on critical rotational speed of turbo pump rotors (I) The transfer matrix method for homogeneous support rotors. *Journal of Propulsion Technology in China, 19*(2), 83–87.

He, H. Q., Zhang, X. L., Shen, D. K., & Zhang, Z. W. (1999). Study on critical rotating speed of turbo pump rotors (II) (III), *Journal of Propulsion Technology in China*, *20*(1), 39–41 and *20*(2), 42–44.

Hirs, G. (1973). A bulk-flow theory for turbulence in lubricant films. *Journal of Lubrication Technology, 1973*, 137–146.

Hydraulic Institute. (1994). *Centrifugal pump design and application* (pp. 103–105). Published by Hydraulic Institute, Parsippany, NJ, USA.

Li, P., & Wang, Z. (1996). Dynamic characteristics of the rotor system for large pump turbine sets. *Journal of Tsinghua University (Science and Technology) in China, 36*(7), 52–57.

Li, S. T., & Xu, Q. Y. (2003). Nonlinear dynamic stability of labyrinth seal sliding bearing rotor system. *Acta Aeronautica et Astronautica Sinica in China, 124*(3), 226–229.

Li, S. T., Xu, Q. Y., & Zhang, X. L. (2007). Nonlinear dynamic behaviors of a rotor-labyrinth seal system. *Nonlinear Dynamics, 47*, 321–335.

Muszyńska, A. (1986a). Whirl and whip rotor/bearing stability problems. *Journal of Sound and Vibration, 110*(3), 443–462.

Muszyńska, A. (1986b). Model testing of Rotor/Bearing systems. *International Journal of Analytical and Experimental Model Analysis, 1*(3), 15–34.

Ping, S. L., Tan, S. G., Wu, D. Z., & Wang, L. Q. (2008). Analysis on modeling rotor system with sliding bearing and ring seal by using FEM. *Proceedings of the 4th International Symposium on Fluid Machinery and Fluid Engineering*, Paper No. Ch28.

Savin, L. A., & Solomin, O. V. (2003). Dynamics of high-speed multi-supporting rotor systems of cryogenic turbomachines with fluid-film bearings. *Proceedings of the 11th World Congress in Mechanism and Machine Science*, Tianjin.

Simon, F. (1982). On the computation of the dynamic behavior of shaft systems in hydro-electric power stations. *Voith Research Construct, 28*, paper 4.

Staubli, T., & Bissig, M. (2001). Numerically calculated rotor dynamic coefficients of a pump rotor side space. *International Symposium on Stability Control of Rotating Machinery (ISCORMA)*, South Lake Tahoe, August 2001.

Staubli, T., & Bissig, M. (2002). Numerical parameter study of rotor side spaces. *Proceedings of the Hydraulic Machinery and Systems 21st IAHR Symposium*, September 9–12, Lausanne.

Tam, L. T., et al. (1988). Numerical and analytical study of fluid dynamical forces in seals and bearings. *ASME Journal of Vibration, Acoustics, Stress and Reliability in Design, 110*(3), 315–325.

Tian, A. M., & Zhu, Z. G. (2000). Calculation for rotor stability in turbo pumps. *Journal of Propulsion Technology in China, 21*(3), 43–45.

Wang, Z. W., YU, J., Fang, Y., Wen, X. J., Cao, J. M., & Shi, Q. H. (2005). The characteristic analysis of rotor dynamics of large hydraulic generating unit. *Journal of Hydraoelectric Engneering in China, 24*(4), 62–66.

Williams, B.P. (1992). The calculation of rotordynamic coefficients for labyrinth seals, M.S. Thesis, University of Virginia

Williams, B. P., & Flack, R. D. (1998). Calculation of rotor dynamic coefficients for labyrinth seals. *International Journal of Rotating Machinery, 4*(4), 257–269.

Wu, Z. Y. (2002). *Computation and analysis of linear characteristics of vibration of the shaft of the hydroelectric machines.* Mater dissertation, Xi'an University of Technology, China.

Xia, F. Q., Li, S. T., & Xu, Q. Y. (2006). Nonlinear dynamic stability and bifurcation of turbo pump labyrinth seal rotor system. *Chinese Journal of Applied Mechanics in China, 23*(2), 16–21.

Zhang, W. (2008). *Research on dynamics of shaft system of hydro-electric generating set.* Mater dissertation, Dalian University of Technology, China.

Zhang, L. (2006). The dynamics characteristic analysis for the shaft hydraulic generator unit. Mater dissertation, Xi'an University of Technology, China.

Part V
System Instability and Monitoring

Chapter 10
Instability of System Caused by Hydraulic Machinery

This chapter mainly focuses on the instability of hydraulic turbine system. The stability of pumping system and the nonlinear models of hydraulic turbine system transient in hydro power plants are also introduced.

10.1 Introduction

Rheingans (1940) pointed out that extremely large power swings could be produced if pulsation of output power occurred at or near the natural frequency of the generator connected to power system. In addition, severe pressure pulsations could occur when discharge and head fluctuate at the natural frequency of the penstock. Even in situations where resonance is not a problem, the draft tube surging can cause excessive vibrations, noise, cavitation, and axial movement of the turbine runner and shaft (Dorfler 1985).

10.1.1 Hydroelectric Plant System

In a typical hydroelectric power plant shown in Fig. 10.1, hydroelectric energy is produced by falling water. The capacity to produce this energy depends on both the available flow rate and the height from which it falls. Stored behind a high dam, water accumulates potential energy. It is transformed into mechanical energy when the water rushes down the sluice and strikes the rotary blades of turbine. The turbine's rotation spins electromagnets which generate current in stationary coils of wire. Finally, the current is put through a transformer where the voltage is increased for long distance transmission over power lines. This constitutes a hydroelectric system.

During the exploitation of turbine power plants, installation is especially vulnerable to transient phenomena and resonance or instability. The prediction of these phenomena is crucial for the safety of the power plant. Numerical simulation of dynamic behavior of the whole installation enables these predictions. However, classical approaches feature two key drawbacks:

Y. Wu et al., *Vibration of Hydraulic Machinery*,
Mechanisms and Machine Science 11, DOI: 10.1007/978-94-007-6422-4_10,

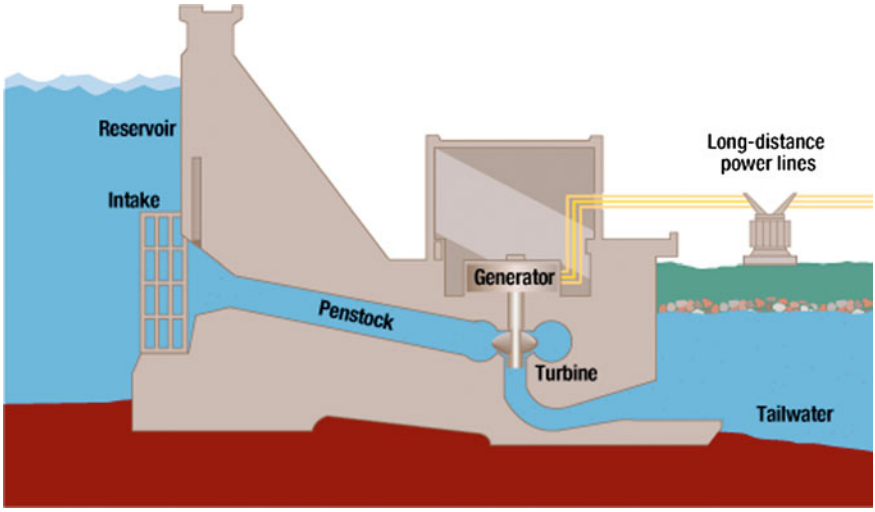

Fig. 10.1 Hydroelectric plant system (*Source*: US Geological Survey 2007) Tennessee Valley Authority, http://www.tva.gov/power/hydroart.htm

1. The focus of the modeling is usually concentrated on either the hydraulic side or the electrical side, with one side left oversimplified;
2. Most of the stability/resonance analysis is based on linearized models, but accurate prediction of amplitudes requires system non-linearities.

Strong interaction between the hydraulic and electrical parts of an installation exists in nature. The coupled investigations on the impact of hydraulic machinery to system instability are necessary for a complete quantification of the phenomena related to control optimization, resonance and instability risk assessment.

10.1.2 Linear System

The stability/resonance analysis of a hydroelectric plant system and of hydraulic machinery system has been conducted on both linear and nonlinear systems.

A linear system is a mathematical model of a system based on the use of a linear operator. Linear systems typically exhibit features and properties that are much simpler than those in a nonlinear case. A general deterministic system can be described in operator H that maps an input $x(t)$ as a function of t to an output $y(t)$. Linear systems satisfy the properties of superposition and scaling.

Given two valid inputs, $x_1(t)$ and $x_2(t)$, as well as their respective outputs, $y_1(t) = H(x_1(t))$ and $y_2(t) = H(x_2(t))$, a linear system must satisfy

$$\alpha y_1(t) + \beta y_1(t) = H(\alpha x_1(t) + \beta x_1(t))$$

for any scalar values α and β.

Subjected to a complex input, the behavior of the resulting system can be described as a sum of responses to simpler inputs.

For time-invariant systems this is the basis of impulse response or frequency response methods, which describe a general input function $x(t)$ in terms of unit impulses or frequency components.

Typical differential equations of linear time-invariant systems are well adapted to analysis with the Laplace transform in a continuous case, and the Z-transform in a discrete case.

Another perspective is that solutions to linear systems comprise a system of functions acting like vectors in the geometric sense.

A common application of linear models is to describe a nonlinear system by linearization.

10.1.2.1 Time-Varying Impulse Response

The time-varying impulse response $h(t_2, t_1)$ of a linear system is defined as the system response at time $t = t_2$ to a single impulse applied at time $t = t_1$. In other words, if the input $x(t)$ to a linear system is

$$x(t) = \delta(t - t_1)$$

where $\delta(t)$ represents the Dirac delta function, the corresponding response $y(t)$ of the system is

$$y(t)|_{t=t_2} = h(t_2, t_1)$$

where the function $h(t_2, t_1)$ is the time-varying impulse response of the system.

10.1.2.2 Time-Varying Convolution Integral

The output of any continuous linear time system is related to the input by the time-varying convolution integral:

$$y(t) = \int_{-\infty}^{\infty} h(t, s)x(s)\mathrm{d}s$$

or, equivalently,

$$y(t) = \int_{-\infty}^{\infty} h(t, t - \tau)x(t - \tau)\mathrm{d}\tau$$

where $\tau = t - s$ represents the lag time between the stimulus at time s and the response at time t.

10.1.2.3 Discrete Time

The output of any discrete linear time system is related to the input by the time-varying convolution sum:

$$y[n] = \sum_{k=-\infty}^{\infty} h[n,k]x[k]$$

or equivalently,

$$y[n] = \sum_{m=-\infty}^{\infty} h[n,n-m]x[n-m]$$

where $k = n - m$ represents the lag time between the stimulus at time m and the response at time n.

A linear system is causal if and only if the system's time varying impulse response is exactly zero whenever the time t of the response is earlier than the time s of the stimulus. In other words, for a causal system, the following condition must hold

$$h(t,s) = 0 \quad \text{for } t < s.$$

10.1.3 Nonlinear System

A nonlinear system is a system which does not satisfy the superposition principle. The variables of any problem in a nonlinear system to be solved cannot be written as a linear sum of independent components.

A nonhomogeneous system is nonlinear according to a strict definition. But such systems are usually studied alongside linear systems, because they can be transformed to a linear system as long as a particular solution is known.

Nonlinear problems are useful because most physical systems are inherently nonlinear in nature. Nonlinear equations are difficult to solve and give rise to interesting phenomena such as chaos. In mathematics, a linear function (or map) $f(x)$ is one which satisfies both of the following properties:

Additivity:

$$f(x+y) = f(x) + f(x).$$

Homogeneity:

$$f(\alpha x) = \alpha f(x).$$

An equation written as $f(x) = C$ is called linear if $f(x)$ is linear but nonlinear otherwise.

Note that x does not need to be a scalar (it can be a vector, function, etc.), and C must not depend on x. The equation is called homogeneous when $C = 0$.

Generally, nonlinear algebraic problems are often accurately solved. If not, they usually can be understood in qualitative and numeric analysis. A nonlinear recurrence relation defines successive terms of a sequence as a nonlinear function of preceding terms.

Problems involving nonlinear differential equations are extremely diverse, and methods of solution or analysis are very problem dependent.

One of the greatest difficulties of nonlinear problems is that it is not generally possible to combine known solutions into new solutions. In linear problems, for example, a family of linearly independent solutions can be used to construct general solutions through the superposition principle.

First order ODEs are often solvable by separation of variables, especially for autonomous equations. For example, the nonlinear equation

$$\frac{\mathrm{d}u}{\mathrm{d}x} = -u^2$$

will easily yield $u = (x + C)^{-1}$ as a general solution which happens to be simpler than the solution to the linear equation

$$\frac{\mathrm{d}u}{\mathrm{d}x} = -u.$$

The equation is nonlinear because it may be written as

$$\frac{\mathrm{d}u}{\mathrm{d}x} + u^2 = 0$$

and the left-hand side of the equation is not a linear function of u and its derivatives.

Second and higher order ODEs (more generally, systems of nonlinear equations) rarely yield closed form solutions, though implicit solutions and solutions involving nonelementary integrals are encountered.

Common methods for the qualitative analysis of nonlinear ODEs include: (1) Linearization via Taylor expansion, (2) Change of variables into something easier to study, and (3) Perturbation methods (can be applied to algebraic equations too).

The most common approach to study nonlinear PDEs is to change the variables and simplify the resulting problem. Sometimes, the equation may be transformed into one or more ODEs, as seen in the similarity transform or separation of variables, which is always useful whether or not the resulting ODE(s) is solvable.

The nonlinear Navier–Stokes equations can be simplified into one linear PDE in the case of a transient, laminar, one-dimensional flow in a circular pipe. The scale analysis provides conditions under which the flow is laminar and one-dimensional which yields the simplified equation.

10.2 The Hydroacoustic Model for Stability of Hydroelectric Systems

Nicolet (2007) proposed a one-dimensional modeling approach, the hydroacoustic modeling, which enabled the simulation, analysis, and optimization of the dynamic behavior of hydroelectric power plants. The capability of this approach has been proven to simulate both transient and periodic phenomena properly. It can predict the stability of a hydroelectric system caused by unsteadiness in hydraulic machines. This section briefly introduces this model, and the following two sections will focus on its application.

10.2.1 Fundamental Equations

A mathematical model based on mass and momentum conservations can properly describe the dynamic behavior of a pipe filled with water. Hydraulic installations have greater longitudinal dimensions along the main flow direction than along transversal dimensions, which justifies the one-dimensional approach on the following assumption:

1. The flow is normal to the cross-sections A;
2. The pressure p, the flow velocity C, and the density ρ are uniform in a cross-section A.

The momentum equation and continue equation are applied to the control volume (the dashed line in Fig. 10.2) of length dx, which leads to the following governing equations:

$$\begin{cases} \frac{1}{\rho}\frac{\partial p}{\partial x} + \frac{\partial C}{\partial t} + C\frac{\partial C}{\partial x} + g\sin\alpha + \frac{\lambda C|C|}{2D} = 0 \\ \rho a^2 \frac{\partial C}{\partial x} + \frac{\partial p}{\partial t} + C\frac{\partial p}{\partial x} = 0 \end{cases} \tag{10.1}$$

where D is the pipe diameter and λ is the friction coefficient according to Darcy-Weisbach, which has the following relation with the shear stress:

$$\tau_0 = \rho\lambda C^2/8.$$

And a is a wave speed:

$$a^2 = 1\Big/\left\{\rho\left(\frac{1}{E_{water}} + \frac{D}{eE_C}\right)\right\}$$

where E_C and E_{water} are the bulk modulus of pipe walls material and water respectively; and e is the pipe thickness.

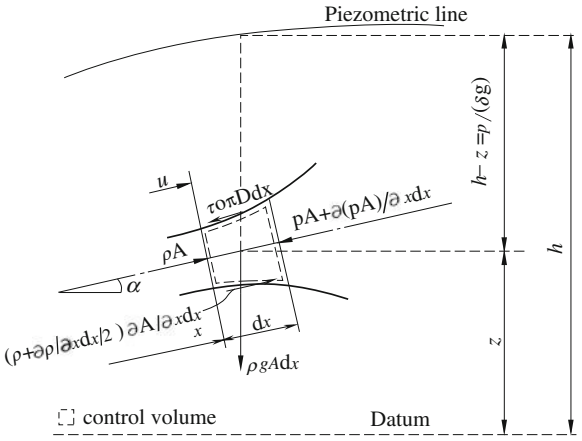

Fig. 10.2 Momentum equation applied to the control volume of length dx (Nicolet 2007)

In hydraulics, it is helpful to use the discharge Q and the piezometric head h as state variables instead of flow velocity C and pressure p. The discharge and the piezometric head are defined as

$$h = Z + \frac{p}{\rho g} \tag{10.2}$$

$$Q = CA \tag{10.3}$$

where Z is the elevation. The piezometric head is the pressure given in meters of water column (mWC) above a given datum. Based on the assumption that there are no vertical displacements in the pipe $\partial z/\partial t \cong 0$, one introduces Eqs. (10.2) and (10.3) into Eq. (10.1) and notices that $\partial z/\partial x = \sin\alpha$:

$$\begin{cases} \dfrac{\partial h}{\partial x} + \dfrac{1}{gA}\left[\dfrac{\partial Q}{\partial t} + C\dfrac{\partial Q}{\partial x}\right] + \dfrac{\lambda Q|Q|}{2gDA^2} = 0 \\ \left[\dfrac{\partial h}{\partial t} + C\dfrac{\partial h}{\partial x}\right] + \dfrac{a^2}{gA}\dfrac{\partial Q}{\partial x} = 0 \end{cases}. \tag{10.4}$$

Hydroacoustic phenomena are characterized by a high wave speed a (a = 1,430 m/s at 20 °C in water) and low flow velocities (C = 10 m/s), thus the convective terms $C(\partial/\partial x)$ related to transport phenomena can be neglected with respect to propagative terms $\partial/\partial t$. This simplification leads to the following set of partial derivative equations:

$$\begin{cases} \dfrac{\partial h}{\partial x} + \dfrac{1}{gA}\dfrac{\partial Q}{\partial t} + \dfrac{\lambda Q|Q|}{2gDA^2} = 0 \\ \dfrac{\partial h}{\partial t} + \dfrac{a^2}{gA}\dfrac{\partial Q}{\partial x} = 0 \end{cases}. \tag{10.5}$$

10.2.2 Electrical Analogy

The solution to a system of hyperbolic PDEs such as Eq. (10.5) could be analogous to the resolution of the propagation equations of electrical waves in conductors:

$$\begin{cases} \dfrac{\partial U}{\partial x} + L_e' \dfrac{\partial i}{\partial t} + R_e' i = 0 \\ \dfrac{\partial U}{\partial t} + \dfrac{1}{C_e'} \dfrac{\partial Q}{\partial x} = 0 \end{cases} \tag{10.6}$$

where i is the electrical current; U is the electrical potential; $R_e{}'$ is the electrical resistance of unit length of the conductor; $L_e{}'$ is the electrical inductance of unit length; and $C_e{}'$ is the electrical capacitance of unit length.

The analogy between Eq. (10.5) modeling pressure wave propagation in hydraulic systems and Eq. (10.6) modeling the propagation of voltage waves in conductors identifies the lineic hydraulic resistance R', a lineic hydraulic inductance L', and a lineic hydraulic capacitance C'. Equation (10.5) can be rewritten as

$$\begin{cases} \dfrac{\partial h}{\partial x} + L' \dfrac{\partial Q}{\partial t} + R'(Q)Q = 0 \\ \dfrac{\partial h}{\partial t} + \dfrac{1}{C'} \dfrac{\partial Q}{\partial x} = 0 \end{cases} \tag{10.7}$$

where the lineic hydroacoustic parameters are defined as

1. The lineic hydroacoustic capacitance $C' = gA/a^2$ [m];
2. The lineic hydroacoustic inductance $L' = 1/(gA)$ [s^2/m^3].;
3. The lineic hydroacoustic resistance $R' = \lambda/(2gDA^2)$ [s/m^3].

Hydraulic and electrical systems are both characterized by an extensive state variable (i.e. discharge Q and current i) and by a potential state variable (i.e. piezometric head h and voltage U). The electrical analogy enables the application of mathematical formalism that is developed initially for electrical purposes to hydroacoustic problems and the usage of powerful concepts, such as an equivalent scheme, impedance, or transfer matrix. Two modeling approaches of the hydraulic system are distinguished: (1) to consider the system as a system with distributed parameters or as a continuous system, or (2) to consider the system as a system with lumped parameters or as a discrete system.

10.2.3 Pipe Viscoelastic Model

The hydraulic circuits of hydroelectric power plants are made of several components whose dynamic behaviors have to be included in the model. The modeling of the following components have been presented: (1) elastic or viscoelastic pipe, (2)

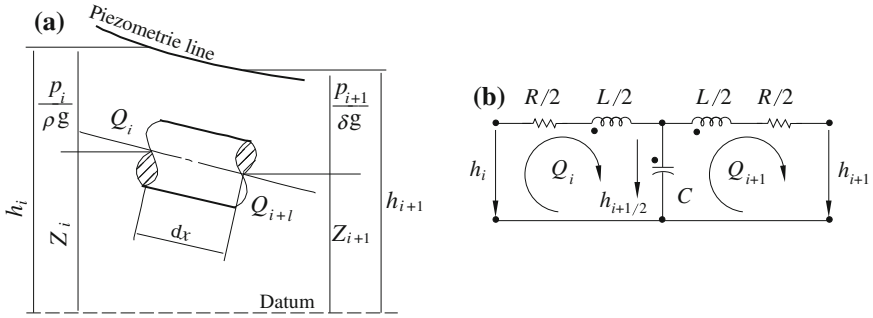

Fig. 10.3 Modeling of a pipe of length dx. **a** a pipe of length dx, **b** corresponding equivalent scheme (Nicolet 2007)

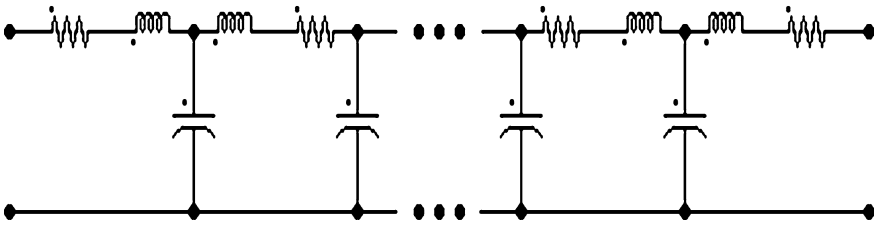

Fig. 10.4 Full length pipe model made by n element (Nicolet 2007)

valve, (3) surge tank, (4) surge shaft, (5) air vessel, (6) cavitating flow (Nicolet 2007). In this section the pipe model in viscoelastic modeling is described.

The model of the pipe derived from the momentum and mass equations leads to the representation of pipe length dx by an equivalent electrical circuit made of two resistances, two inductances, and one capacitance as presented in Fig. 10.3. This modeling approach can be extended to a full length pipe with consideration of n equivalents schemes in series as shown in Fig. 10.4.

Viscoelastic models present dynamic behavior as stress σ in the material is not only proportional to the rated deformation ε, but also a function of the rate of deformation $\mathrm{d}\varepsilon/\mathrm{d}t$.

The modeling of viscoelastic behavior can be achieved with rheological models made of springs and dashpots.

Maxwell's, Kelvin-Voigt's and Standard models are three common rheological models presented in Table 10.1 with their equivalent electrical schemes. These models are elementary models from which more advanced models can be derived.

Without loss of generality, a viscoelastic pipe accounting for both pipe material and water viscoelasticity can be simulated based on two Kelvin-Voigt models as presented in Fig. 10.5.

Therefore, considering first the viscoelastic behavior of the pipe wall material and assuming a pipe perimeter deflection $\varepsilon = \mathrm{d}D/D$ due to pressure increase, one would have

Table 10.1 Rheological models of viscoelastic materials and their equivalent scheme (Nicolet 2007)

Model	Rheological model	Equivalent scheme	Equations
Maxwell	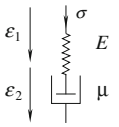	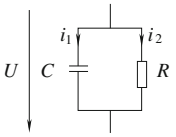	$\sigma = \varepsilon_1 E = \mu \frac{d\varepsilon_2}{dt}$ $U = \frac{1}{C}\int i_1 dt = R i_2$
Kelvin-voigt	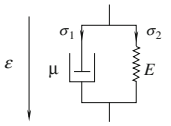	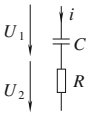	$\sigma = \sigma_1 + \sigma_2 = \varepsilon E + \mu \frac{d\varepsilon}{dt}$ $U = U_1 + U_2 = \frac{1}{C}\int i dt + Ri$
Standard	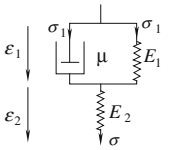	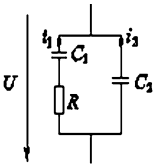	$\sigma = \varepsilon_2 E_2 = \varepsilon_1 E_1 + \mu \frac{d\varepsilon_1}{dt}$ $\varepsilon = \varepsilon_1 + \varepsilon_2 \quad i = i_1 + i_2$ $U = \frac{1}{C_2}\int i_2 dt,\ U = \frac{1}{C_1}\int i_1 dt + Ri_1$

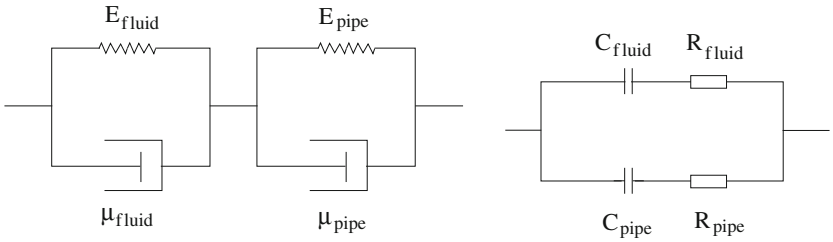

Fig. 10.5 Rheological (*left*) and equivalent (*right*) models of a viscoelastic pipe with contribution of water and pipe material viscoelastic behavior (Nicolet 2007)

$$\sigma = E_{pipe}\varepsilon + \mu_{pipe}\frac{d\varepsilon}{dt} = E_{pipe}\frac{dD}{D} + \mu_{pipe}\frac{1}{D}\frac{d(dD)}{dt} \tag{10.8}$$

where μ is dynamic viscosity.

The total derivative of the volume of a pipe V of length dx is given by

$$dV = 0.5\pi D dD. \tag{10.9}$$

Introducing the piezometric head, $h = p/(\rho g) + z$, and neglecting vertical displacement of the pipe $(dz/dt = 0)$, one yields

$$\frac{d\sigma}{dt} = \frac{D\rho g}{2e}\frac{dh}{dt}. \tag{10.10}$$

Combining Eqs. (10.8), (10.9) and (10.10) and introducing the stored discharge $Q_p = dV/dt$, one has

$$\frac{\mathrm{d}h}{\mathrm{d}t} = \frac{E_{pipe}e}{AD\rho g\mathrm{d}x} Q_p + \frac{\mu_{pipe}e}{AD\rho g\mathrm{d}x} \frac{\mathrm{d}Q_p}{\mathrm{d}t}. \tag{10.11}$$

By integrating Eq. (10.11), one gets Kelvin-Voigt's equation of the pipe wall material:

$$h = \frac{1}{C_{pipe}} \int Q_p \mathrm{d}t + R_{pipe} Q_p \tag{10.12}$$

where the viscoelastic resistance R_{pipe} and capacitance C_{pipe} of a pipe of length dx are given by

$$R_{pipe} = \frac{\mu_{pipe}e}{AD\rho g\mathrm{d}x}, \; C_{pipe} = \frac{AD\rho g\mathrm{d}x}{E_{pipe}e}. \tag{10.13}$$

Then, considering the fluid compressibility and the viscosity μ_{fluid} one gets

$$\frac{\mathrm{d}p}{\mathrm{d}t} = \frac{E_{fluid}}{\rho} \frac{\mathrm{d}\rho}{\mathrm{d}t} + \frac{\mu_{fluid}}{\rho} \frac{\mathrm{d}^2\rho}{\mathrm{d}t^2}. \tag{10.14}$$

Reintroducing the piezometric head $h = p/(\rho g) + z$ and the stored discharge due to fluid compressibility

$$Q_f = -\frac{V}{\rho} \frac{\mathrm{d}\rho}{\mathrm{d}t}$$

one obtains

$$\frac{\mathrm{d}h}{\mathrm{d}t} = \frac{E_{fluid}}{A\rho g\mathrm{d}x} Q_f + \frac{\mu_{fluid}}{A\rho g\mathrm{d}x} \frac{\mathrm{d}Q_f}{\mathrm{d}t} \tag{10.15}$$

$$h = \frac{1}{C_{fluid}} \int Q_f \mathrm{d}t + R_{fluid} Q_f \tag{10.16}$$

where the viscoelastic resistance R_{fluid} and capacitance C_{fluid} of a pipe of length dx are given by

$$R_{fluid} = \frac{\mu_{fluid}}{A\rho g\mathrm{d}x}; \; C_{fluid} = \frac{A\rho g\mathrm{d}x}{E_{fluid}}. \tag{10.17}$$

It can be also noticed that, if, in the pipe model of Fig. 10.5, the 2 viscoelastic resistances of the fluid and of the wall material are neglected, the two capacitances in parallel are equivalent to the capacitance of the elastic pipe:

$$C_{equ} = C_{pipe} + C_{fluid} = A\rho g \; \mathrm{d}x \left[\frac{D}{E_{pipe}e} + \frac{1}{E_{fluid}} \right] = \frac{A\rho g \; \mathrm{d}x}{a^2}. \tag{10.18}$$

In the same way, if compressibility effects are neglected, the two viscoelastic resistances in parallel can be expressed as

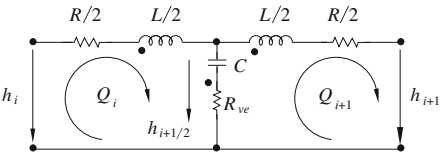

Fig. 10.6 Equivalent scheme of a viscoelastic pipe of length dx (Nicolet 2007)

$$R_{equ} = \frac{1}{\frac{1}{R_{pipe}} + \frac{1}{R_{fluid}}} = \frac{1}{A\rho g \mathrm{d}x} \frac{1}{\frac{D}{\mu_{pipe} e} + \frac{1}{\mu_{fluid}}} = \frac{\mu_{equ}}{A\rho g \ \mathrm{d}x} \tag{10.19}$$

From a strict modeling point of view, a viscoelastic pipe is modeled based on considering the equivalent scheme of Fig. 10.5 made of two Kelvin-Voigt models for both pipe material and fluid instead of a single capacitance of the elastic pipe model of Table 10.1 (right). From a practical point of view, determination of either the second viscosity of the fluid or the viscosity of pipe material is very difficult to perform with good accuracy. However, experiments described by Haban et al. (2002) have provided data for a pipe filled with water. In this case, the equivalent viscosity is determined rather than the fluid viscosity as in the experiment both viscosity contributions cannot be dissociated.

As a result, it is most convenient to use one Kelvin-Voigt model of the whole pipe that covers both the fluid and the pipe material. In this model the capacitance is calculated according to Eq. (10.18) and the viscoelastic resistance R_{equ} is calculated according to Eq. (10.19). The resulting model is presented in Fig. 10.6.

10.2.4 Analysis of Simplified Hydraulic Systems

The electrical equivalent modeling helps to establish the simplified models of hydraulic installation to study their global dynamic behavior. The simplified models are preferably of a low order to obtain the analytical solutions of the related differential equation set. Such solutions render the main dynamic quantities of the system in terms of eigen frequencies and damping.

10.2.4.1 Mass Oscillations Problems

In Nicolet (2007), the eigen frequency related to mass oscillation problems has been analyzed for various types of tanks, i.e. (1) a surge tank, (2) a surge shaft, and (3) an air vessel. In this section only the analysis on the topic of a hydraulic system with a surge tank is explained.

The dynamic behavior of the hydraulic circuit shown by Fig. 10.7 (left) comprising an upstream reservoir, a gallery, a surge tank and a penstock with a downstream valve is investigated. The compressibility of both pipes can be neglected because only low frequencies are paid attention to. Thus the equivalent

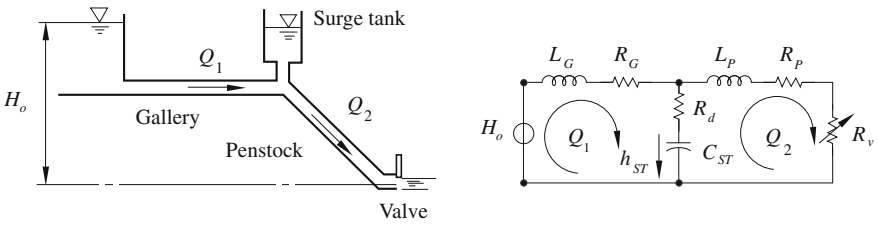

Fig. 10.7 Hydraulic circuit with surge tank (Nicolet 2007)

circuit of this system is made of a pressure source H_0, the gallery inductance L_G and resistance R_G, the surge tank capacitance C_{ST} and the diaphragm resistance R_d, the penstock inductance L_P and resistance R_P, and the valve resistance R_v as presented in Fig. 10.7 (right). The consequence of a sudden closure of the valve is analyzed under an initial steady state condition and constant valve opening. The differential equations written based on Kirchhoff's law applied to the left hand loop leads to

$$\begin{cases} H_0 = L_G \dfrac{\mathrm{d}Q_1}{\mathrm{d}t} + (R_d + R_G)Q_1 + h_{ST} \\ C_{ST} \dfrac{\mathrm{d}h_{ST}}{\mathrm{d}t} = Q_1 \end{cases}. \tag{10.20}$$

Combining the two above equations leads to the following characteristic equation:

$$\frac{\mathrm{d}^2 h_{ST}}{\mathrm{d}t^2} + 2\mu \frac{\mathrm{d}h_{ST}}{\mathrm{d}t} + \omega_0^2 h_{ST} = 0 \tag{10.21}$$

where $\mu = (R_d + R_G)/(2L_G)$, $\omega_0^2 = 1/(C_{ST}Lg)$.

The general solution of the above equation is given by

$$h_{ST}(t) = h_{ST0}\mathrm{e}^{-\mu t} \sin(\omega_1 t) \tag{10.22}$$

where

$$\omega_1 = \omega_0 \sqrt{1 - \varsigma^2}, \varsigma = \mu/\omega_0. \tag{10.23}$$

The natural frequency of the frictionless system is given by

$$\omega_0 = 1 \Big/ \sqrt{C_{ST} L_G}. \tag{10.24}$$

The related period is then given by $T_0 = 2\pi \left(A_{ST} L_G/(A_G g)\right)^{1/2}$ where L_G is the gallery length; A_{ST} the surge tank cross section; A_G the gallery cross section.

The period T_0 is usually very low as the cross section of the surge tank and the gallery length are large and the gallery cross section is small. This period is called the mass oscillation period, and is related to the oscillation of the discharge in the gallery between the reservoir and the surge tank. If the cross section of the surge tank is constant and the system is frictionless, amplitude of the water level oscillations in

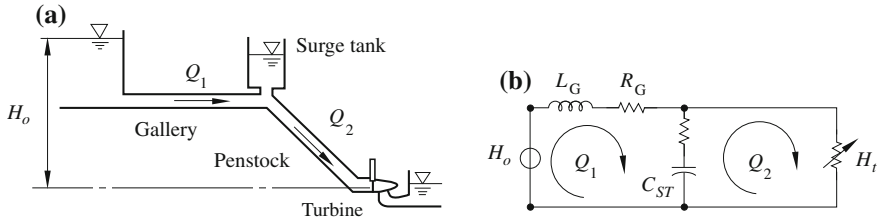

Fig. 10.8 Hydraulic system with surge tank and regulated turbine (Nicolet 2007)

surge tank can be obtained considering a solution of $h_{ST}(t) = h_{ST0}\sin(\omega_0 t + \varphi)$ whose first derivative introduced in Eq. (6.1) gives the oscillation amplitude:

$$h_{ST}(t) = \frac{Q_{10}}{C_{ST}\omega_0} = C_{10}\sqrt{\frac{A_G l_G}{A_{ST} g}} \tag{10.25}$$

where $C_{10} = Q_{10}/C_{ST}$ is the initial flow velocity in the gallery.

10.2.4.2 Stability of Hydraulic Circuit

In this section, stability criteria are determined for the power plant with a regulated turbine and surge tank.

1. Mass oscillation stability: Thoma cross section criteria. A hydraulic circuit comprising an upstream reservoir, a gallery, a surge tank, and a penstock connected to a turbine driven by a speed controller is subject to system instabilities. The system and the corresponding equivalent scheme are shown in Fig. 10.8. For the present study, the dynamic behavior of the penstock and the diaphragm losses are neglected and the perturbation is thought to be small so that the turbine efficiency can be viewed constant. The differential equation related to the loop of discharge Q_1 is given by

$$\begin{cases} H_0 = L_G \frac{\mathrm{d}Q_1}{\mathrm{d}t} + R_G Q_1 + h_{ST} \\ C_{ST} \frac{\mathrm{d}h_{ST}}{\mathrm{d}t} = Q_{ST} \end{cases}. \tag{10.26}$$

The continuity equation gives

$$Q_{ST} = Q_1 - Q_2. \tag{10.27}$$

From the second loop, it can be stated that the piezometric head of the surge tank corresponds to the turbine head H_t which is equal to the initial head H_{t0} plus a perturbation z and is therefore given by

$$h_{ST} = H_t = H_{t0} + z. \tag{10.28}$$

The similitude of the turbine efficiency gives

$$Q_2 H_t = Q_{20} H_{t0}. \tag{10.29}$$

Then the discharge of the turbine can be expressed with Eq. (10.28) and then expressed with the limited development ($1/(1+x) = 1 - x + x^2 - x^3 \ldots$), leading to

$$Q_2 = Q_{20} H_{t0}/(H_{t0} + z) \cong Q_{20}(1 - z/H_{t0}). \tag{10.30}$$

Combining Eqs. (10.28) and (10.30), yields

$$\frac{\mathrm{d}Q_2}{\mathrm{d}t} = -\frac{Q_{20}}{H_{t0}} \frac{\mathrm{d}h_{ST}}{\mathrm{d}t}. \tag{10.31}$$

Introducing Eqs. (10.27) and (10.31) into Eq. (10.26), one has

$$L_G \left[-\frac{Q_{20}}{H_{t0}} \frac{\mathrm{d}h_{ST}}{\mathrm{d}t} + C_{ST} \frac{\mathrm{d}^2 h_{ST}}{\mathrm{d}t^2} \right] + R_G Q_1 + h_{ST} = H_0. \tag{10.32}$$

The head loss in the gallery is a non-linear term that needs to be developed, and therefore the head losses are expressed as

$$R_G Q_1 = R'_G Q_1^2. \tag{10.33}$$

With Eqs. (10.27) and (10.30), the discharge in the gallery becomes

$$Q_1^2 = (Q_{ST} + Q_2)^2 = (Q_{ST} + Q_{20}(1 - h_{ST}/H_{t0}))^2. \tag{10.34}$$

Equation (10.34) above can be rearranged in the following form:

$$Q_1^2 = Q_{20}^2 \left[1 + \left(\frac{Q_{ST}}{Q_{20}} - \frac{h_{ST}}{H_{t0}} \right) \right]^2 \cong Q_{20}^2 \left[1 + 2 \left(\frac{Q_{ST}}{Q_{20}} - \frac{h_{ST}}{H_{t0}} \right) \right]. \tag{10.35}$$

Introducing Eqs. (10.26), (10.31) and (10.35) into Eq. (10.32) leads to the characteristic equation:

$$\frac{\mathrm{d}^2 h_{ST}}{\mathrm{d}t^2} + 2\mu \frac{\mathrm{d}^2 h_{ST}}{\mathrm{d}t^2} + \omega_0^2 h_{ST} = \frac{H_{t0} - R'_G Q_{20}^2}{L_G C_{ST}} \tag{10.36}$$

where

$$\mu = \frac{R'_G Q_{20}}{L_G} - \frac{Q_{20}}{2 H_{t0} C_{ST}}, \omega_0^2 = \left(1 - 2 \frac{R'_G Q_{20}^2}{H_{t0}} \right) \frac{1}{L_G C_{ST}}.$$

The system stability is ensured when $2\mu > 0$, which leads to the following stability criteria:

$$C_{ST} > \frac{Q_{20}}{H_{t0}} \frac{L_G}{2 R_G}. \tag{10.37}$$

Based on expressions of the inductance, resistance, and capacitances, the stability criteria give the Thoma cross section:

$$A_{ST} > \frac{Q_{20}^2}{2g} \frac{L_G}{H_{t0} H_{rG0} A_G} \tag{10.38}$$

where H_{rG0} is the head loss in the gallery calculated with the initial discharge Q_{20}. L_G and A_G are respectively the length and the area of the cross section of the gallery, and H_{t0} is the initial head of the turbine. This Thoma cross section is the one at the surge tank limit below which the system becomes unstable after a perturbation induced by the turbine.

10.3 Influence of the Hydraulic Turbine on System Stability at Full Load Condition

Alligné et al. (2008) identified the influence of a full-load excitation source location with respect to the eigenmodes shapes on system stability. A new eigenanalysis tool, based on eigenvalues and eigenvectors computation of a set of nonlinear differential equations, has been developed. First the modal analysis method and linearization of the set of the nonlinear differential equations are fully described. Then, nonlinear hydro-acoustic models of hydraulic components based on electrical equivalent schemes are presented and linearized. Finally, a hydro-acoustic SIMSEN model of a simple hydraulic power plant is used to perform the modal analysis and to show the influence of the turbine location on system stability.

10.3.1 Model Analysis

The dynamic behavior of a hydroelectric system is given by a set of n first order nonlinear ordinary differential equations of the following form:

$$[\boldsymbol{A}] \frac{\mathrm{d}}{\mathrm{d}t} \{\boldsymbol{X}\} + [\boldsymbol{B}(\boldsymbol{X})] \{\boldsymbol{X}\} = \{\boldsymbol{V}(\boldsymbol{X})\} \tag{10.39}$$

where $[\boldsymbol{A}]$ and $[\boldsymbol{B}(\boldsymbol{X})]$ are the state global matrices of dimension $[n \times n]$, $\{\boldsymbol{X}\}$ and $\{\boldsymbol{V}(\boldsymbol{X})\}$ are the state vector and the boundary condition vector with n components. This set of equations feature nonlinearity since the matrix $[\boldsymbol{B}(\boldsymbol{X})]$ and the boundary condition vector $\{\boldsymbol{V}(\boldsymbol{X})\}$ are functions of the state vector.

The system stability is deduced from the eigenvalues of the linearized set of differential equations.

Assume that

$$\{\boldsymbol{f}\} = [\boldsymbol{B}(\boldsymbol{X})]\{\boldsymbol{X}\} - \{\boldsymbol{V}(\boldsymbol{X})\}$$

a vector of n nonlinear functions and Eq. (10.39) becomes

$$[\boldsymbol{A}]\frac{\mathrm{d}}{dt}\{\boldsymbol{X}\} + \{\boldsymbol{f}\} = 0. \tag{10.40}$$

Considering a small perturbation from the equilibrium point $\{\boldsymbol{X}_0\}$ defined by

$$\{\boldsymbol{X}\} = \{\boldsymbol{X}_0\} + \delta\{\boldsymbol{X}\} \tag{10.41}$$

this new state vector must satisfy Eq. (10.39). And a first order Taylor development yields the linearized matrix form:

$$[\boldsymbol{A}]\frac{\mathrm{d}}{\mathrm{d}t}(\delta\{\boldsymbol{X}\}) + [\boldsymbol{B}_l](\delta\{\boldsymbol{X}\}) = 0 \tag{10.42}$$

where

$$B_{lij} = \left.\frac{\partial f_i}{\partial X_j}\right|_0$$

is the linearized state global matrix.

Hence, eigenvalues of the matrix $[\boldsymbol{M}] = -[\boldsymbol{A}]^{-}1\ [\boldsymbol{B}_1]$ define the system stability. They can be either real or complex numbers. A real eigenvalue is a non oscillatory eigenmode whereas a complex eigenvalue is an oscillatory one. In both cases damping and oscillation frequency of the eigenmode are given by the real and imaginary part of the eigenvalue. Therefore, if at least one of the eigenvalue has a positive real part, the system is unstable.

10.3.2 Modeling and Linearization of Hydraulic Components

The modal analysis is applied to a simple hydraulic power plant including viscoelastic pipes and a Francis turbine with a cavitation vortex rope. Nonlinear models of hydraulic elements involved in this case study are presented and linearized in this section.

10.3.2.1 Viscoelastic Pipe

Assuming uniform pressure and velocity distributions in the cross section without the convective terms, the one-dimensional momentum and continuity balances for an elementary pipe filled with water of length dx, cross section A and wave speed a, yields the well-known Allievi hyperbolic equations, (see Sect. 10.2).

Using the Finite Difference Method with a 1st order-centered scheme discretization in space and a scheme of Lax for the discharge variable, one arrives at a set of ODEs (10.39) which can be represented as a T-shaped equivalent electrical scheme shown in Fig. 10.3. The RLC parameters of this equivalent scheme are given by

$$R_i = \frac{\lambda |Q_i| \mathrm{d}x}{2A^2 Dg}, C = \frac{Ag\mathrm{d}x}{a^2}, L = \frac{\mathrm{d}x}{Ag} \tag{10.43}$$

where λ is the local loss coefficient. The hydraulic resistance R, the hydraulic inductance L, and the hydraulic capacitance C correspond respectively to energy losses, inertia, and storage effects due to wall deflection and fluid compressibility. Moreover, to accurately predict the amplitude of pressure fluctuation and system stability, it is necessary to take into account the viscoelastic behavior owing to energy dissipation during the wall deflection. This additional dissipation gives rise to a resistance in the series with the capacitance as shown in Fig. 10.10.

This viscoelastic resistance is responsible for both fluid and pipe material viscoelasticity and can be expressed as (Eq. 10.19)

$$R_{ve} = \frac{\mu_{equ}}{A\rho g \mathrm{d}x}$$

where μ_{equ} is the equivalent viscoelastic damping of both the fluid and the wall. The resulting set of nonlinear differential equations relative to equivalent electrical circuit is set up according to Kirchoff laws and can be written under matrix form:

$$\begin{aligned} &\begin{bmatrix} C & 0 & 0 \\ 0 & L/2 & 0 \\ 0 & 0 & L/2 \end{bmatrix} \left(\frac{\mathrm{d}}{\mathrm{d}t} \begin{Bmatrix} h_{i+1/2} \\ Q_i \\ Q_{i+1} \end{Bmatrix} \right) \\ &+ \begin{bmatrix} 0 & -1 & 1 \\ 1 & R_i/2 + R_{ve} & -R_{ve} \\ -1 & -R_{ve} & R_{i+1}/2 + R_{ve} \end{bmatrix} \begin{Bmatrix} h_{i+1/2} \\ Q_i \\ Q_{i+1} \end{Bmatrix} \\ &= \begin{Bmatrix} 0 \\ h_i \\ -h_{i+1} \end{Bmatrix} \end{aligned} \tag{10.44}$$

Resistance R_i proportional to the discharge Q_i induces nonlinearity proportional to the square exponent of the discharge. Applying the linearization, one obtains

$$\delta\left(R_i' Q_i^2\right) = 2R_i' Q_i \big|_0 \delta Q_i \tag{10.45}$$

where $Q_i|_0$ is the discharge at the equilibrium point and R'_i the reduced resistance defined by

$$R_i' = \lambda \mathrm{d}x / \left(2gDA^2\right). \tag{10.46}$$

Hence, the linearized state global matrix for the viscoelastic pipe is

$$\begin{bmatrix} C & 0 & 0 \\ 0 & L/2 & 0 \\ 0 & 0 & L/2 \end{bmatrix} [\boldsymbol{B}_l]_{\text{viscoelastic pipe}} = \begin{bmatrix} 0 & -1 & 1 \\ 1 & R_i' Q_i|_0 + R_{ve} & -R_{ve} \\ -1 & -R_{ve} & R_i' Q_i|_0 + R_{ve} \end{bmatrix}. \quad (10.47)$$

10.3.2.2 Francis Turbine

The Francis turbine can be modeled as a pressure source that converts hydraulic energy into mechanical work, an inductance related to the inertial effects of the water and a resistance which models the head losses through the turbine. The resulting nonlinear differential equation is

$$L_t \frac{\mathrm{d}Q_i}{\mathrm{d}t} + R_t Q_i = -H_t + H_I - H_T. \quad (10.48)$$

Moreover, momentum equation applied to the rotational inertias is taken into account and leads to

$$J_t \frac{\mathrm{d}\Omega}{\mathrm{d}t_i} = T_t - T_{elec} \quad (10.49)$$

where J_t, Ω, T_t, T_{elec} are respectively the turbine's moment of inertia, rotational speed, mechanical torque and electromagnetic torque. Combined with Eq. (10.48) the set of differential equations under matrix are

$$\begin{bmatrix} L_t & 0 \\ 0 & J_t \end{bmatrix} \frac{\mathrm{d}}{\mathrm{d}t} \begin{Bmatrix} Q_i \\ \Omega \end{Bmatrix} + \begin{bmatrix} R_t & 0 \\ 0 & 0 \end{bmatrix} \begin{Bmatrix} Q_i \\ \Omega \end{Bmatrix} = \begin{Bmatrix} -H_t + H_I - H_T \\ T_t - T_{elec} \end{Bmatrix}. \quad (10.50)$$

The pressure source $H_t(Q_i, \Omega, y)$ and the mechanical torque $T_t(Q_i, \Omega, y)$ depend on turbine characteristics which are nonlinear functions of discharge, rotational speed and guide vane opening. Similar to the viscoelastic pipe model, the resistance term of the Francis turbine model induces nonlinearity proportional to the square exponent of the discharge.

Therefore linearization of this term is identical. On the other part, the linearization of the pressure source and the mechanical torque is given by

$$\delta H_t = \frac{\partial H_t}{\partial Q_i} \delta Q_i|_0 + \frac{\partial H_t}{\partial \Omega} \delta \Omega|_0 + \frac{\partial H_t}{\partial y} \delta y|_0 \quad (10.51)$$

$$\delta T_t = \frac{\partial T_t}{\partial Q_i} \delta Q_i|_0 + \frac{\partial T_t}{\partial \Omega} \delta \Omega|_0 + \frac{\partial T_t}{\partial y} \delta y|_0 \quad (10.52)$$

where partial derivative terms are gradients of the characteristic curves at the equilibrium point. Hence, the linearized state global matrix is

$$[\boldsymbol{B}_l]_{\text{turbine}} = \begin{bmatrix} 2R_{t0} + \frac{\partial H_t}{\partial Q_i}\Big|_0 & \frac{\partial H_t}{\partial \Omega}\Big|_0 \\ \frac{\partial T_t}{\partial Q_i}\Big|_0 & \frac{\partial T_t}{\partial \Omega}\Big|_0 \end{bmatrix}. \tag{10.53}$$

10.3.2.3 Pipe with Vortex Rope Self-Excitation

The gaseous volume of a vortex rope at full load conditions can be modeled as a function of two state variables: the head and the discharge. The resulting state space continuity equation defining the discharge variation due to the occurrence of gaseous volume at the node $i + 1/2$ is

$$Q_i - Q_{i-1} = C_{rope}\frac{\mathrm{d}H_{i+1/2}}{\mathrm{d}t} + \chi\frac{\mathrm{d}Q_{i+1}}{\mathrm{d}t} \tag{10.54}$$

where rope C and χ are respectively the rope cavitation compliance and the mass flow gain factor defined by

$$C_{rope} = -\frac{\mathrm{d}V_{rope}}{\mathrm{d}H_{i+1/2}}; \chi = -\frac{\mathrm{d}V_{rope}}{\mathrm{d}Q_{i+1}}. \tag{10.55}$$

The resulting equivalent electrical scheme of a vortex rope at full load conditions is given in Fig. 10.9a.

Modeling a pipe of length L with a vortex rope self excitation leads to combining the equivalent electrical schemes of the vortex rope and the viscoelastic pipe. Moreover, only one pressure node is utilized to model the pipe of length L (Fig. 10.9b). It leads to an equivalent concentrated compliance C_{equ} defined by two capacitances in parallel:

$$C_{equ} = C_0 + C_{rope} \tag{10.56}$$

where C_0 is the compliance of the wall deformation. Hence, in modeling the vortex rope self excitation in pipe, two rope parameters are available: the rope cavitation compliance and the mass flow gain factor. For this investigation, cavitation rope

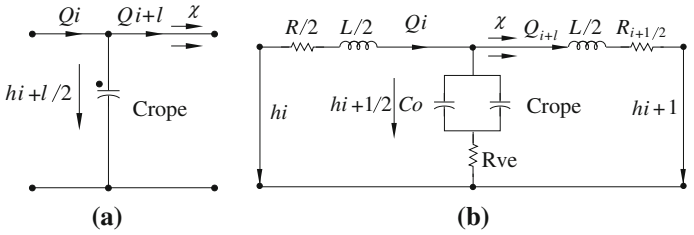

Fig. 10.9 **a** Vortex rope modeling. **b** Pipe of length L with vortex rope self excitation (Alligné, et al. 2008)

compliance and the mass flow gain factor are constant. Therefore nonlinearity and linearization are the same as the ones of the viscoelastic pipe model (Alligné et al. 2008).

10.3.3 Case Studies

The study by Alligné et al. (2008) is an highly effective work on the stability of vortex rope with respect to eigenmodes shapes of the hydraulic system.

10.3.3.1 Pipe with Cavitation Development

The object of the first case study is a pipe with a uniform cross section subdivided in three parts as illustrated in Fig. 10.10. The central part is where the cavitation is modeled with the vortex rope self excitation model, see Fig. 10.9b.

Both viscoelastic damping and excitation location influence the stability limits of the system. First of all, the equivalent viscoelastic damping parameter μ_{equ} of the pipe model is decisive in prediction of the stability limit and the amplitude of pressure fluctuations. To assess the effect of this parameter, compliance and mass flow gain factors are set to zero so that cavitation development in the system is not taken into account. System eigenvalues are computed for different modal dampings and plotted in Fig. 10.11a. Moreover, for the first ten eigenmodes, damping is plotted as a function of the equivalent viscoelastic damping in Fig. 10.11b.

If the viscoelastic damping equals zero, then damping of all the eigenmodes are equal. However, according to Fig. 10.11b, the more the viscoelastic damping is, the more the modal damping increases. Moreover, for a given viscoelastic damping, eigenmodes of high frequencies have a damping higher than those of low frequencies.

10.3.3.2 Hydraulic Power Plant

The simplified hydraulic power plant features two significant cross sections of pipe as illustrated in Fig. 10.12 and Table 10.2. Full load operating conditions defined in Table 10.2 are investigated with the modal analysis to show the influence of vortex rope self-excitation on system stability. L_i, D_i, and a_i are respectively the length, diameter and wave speed of the ith pipe. System stability is assessed via

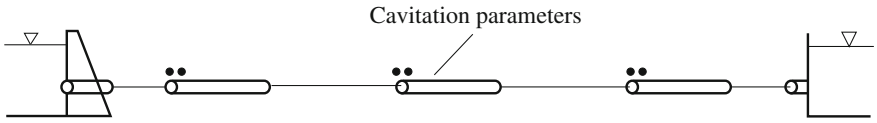

Fig. 10.10 Pipe with cavitation development (Alligné et al. 2008)

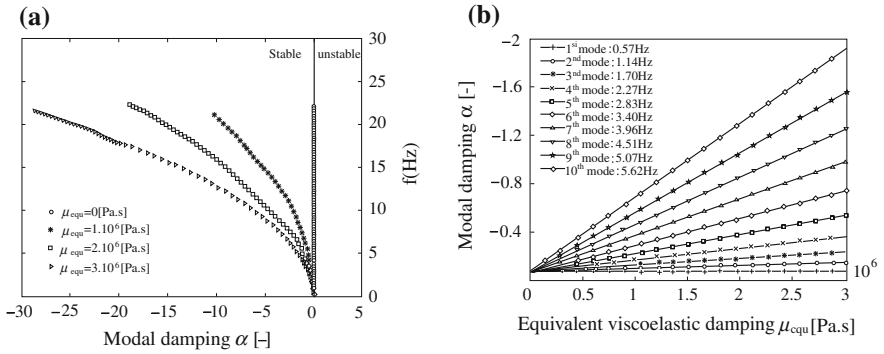

Fig. 10.11 Viscoelastic damping effect on eigenvalues. **a** System eigenvalues via modal damping. **b** Model damping via viscoelastic dampings (Alligné et al. 2008)

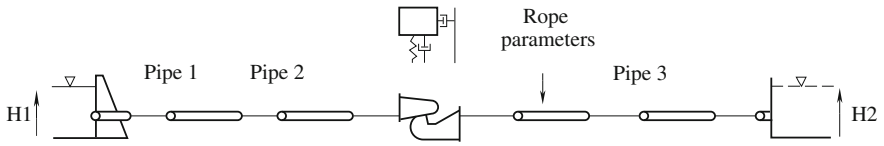

Fig. 10.12 Simplified layout (Alligné et al. 2008)

Table 10.2 Layout dimensions and turbine parameters (Alligné, et al. 2008)

Reservoirs	Pipe 1	Pipe 2	Pipe 3	Pump turbine
$H1$ 497 m	$L1$ 615 m	$L2$ 180 m	$L3$ 85 m	Specific speed 0.306
$H2$ 194 m	$D1$ 10 m	$D2$ 5 m	$D3$ 5 m	Rotational speed 300 rpm
	$a1$ = 1,000 m/s	$a2$ = 1,200 m/s	$a3$ = 1,200 m/s	Moment of inertia 2.77 106 kg.m2
				Thoma number 0.18

computation of eigenvalues as a function of the two rope parameters in Fig. 10.13a. Eigenvalues with positive real part are plotted which identify unstable couple parameters. For this investigation, the chosen rope parameters are: $C = 0.01$ m^2 and $\chi = -0.04$ s. According to the instability diagram of Fig. 10.13a, these parameters are identified as unstable ones, leading to eigenvalues plotted in Fig. 10.13b.

In Fig. 10.13, the third eigenmode with 1.8 Hz frequency is unstable. Conclusions established from the case study of the uniform pipe with cavitation development can be used to explain why the third eigenmode damping is positive.

The hydro-acoustic analysis of a pumped storage plant experiencing such pressure and power oscillation has been presented by Koutnik et al. (2006), to illustrate the self induced oscillation nature of the observed event.

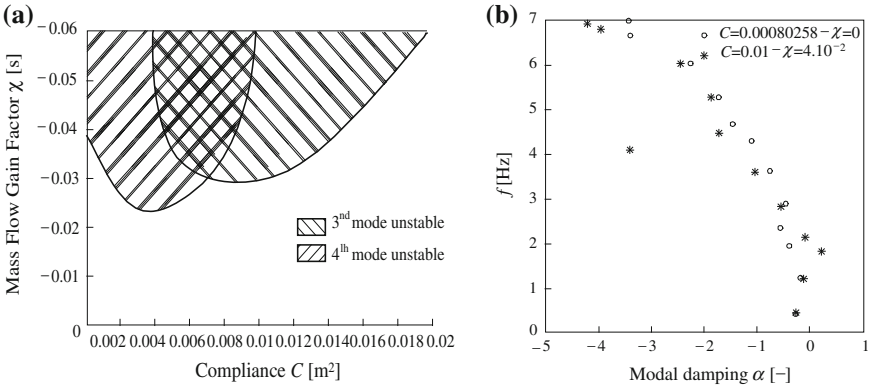

Fig. 10.13 Computing eigenvalues of pump-turbine system. **a** Instability diagram. **b** Eigenvalues for unstable rope parameters (Alligné et al. 2008)

10.4 Part Load Resonance Impact on System Stability of Francis Turbine Power Plants

At low flow rate, Francis turbines feature a cavitating vortex rope in draft tube that results from swirling flow of the runner outlet. The unsteady pressure field related to the precession of the vortex rope induces plane wave propagating in the entire hydraulic system. Because the frequency of the vortex rope precession is between 0.2 and 0.4 times the turbine rotational speed, there is a risk of resonance among the hydraulic circuit, the synchronous machine, and the turbine.

10.4.1 Introduction

In this section, a systematic methodology proposed by Nicolet et al. (2006) can be used in the assessment of resonance risk for a given Francis turbine power plant. The test case is a 1GW×4 Francis turbine power plant, as shown in Fig. 10.14. The methodology is based on a transient simulation of the dynamic behavior of the whole power plant considering a 1D model of the hydraulic installation, comprising gallery, surge chamber, penstock, Francis turbine, and mechanical masses, synchronous machines, transformer, grid model, speed and voltage regulators (Nicolet et al. 2006). A stochastic excitation with the energy uniformly distributed in the frequency range of interest is taken into account in the draft tube.

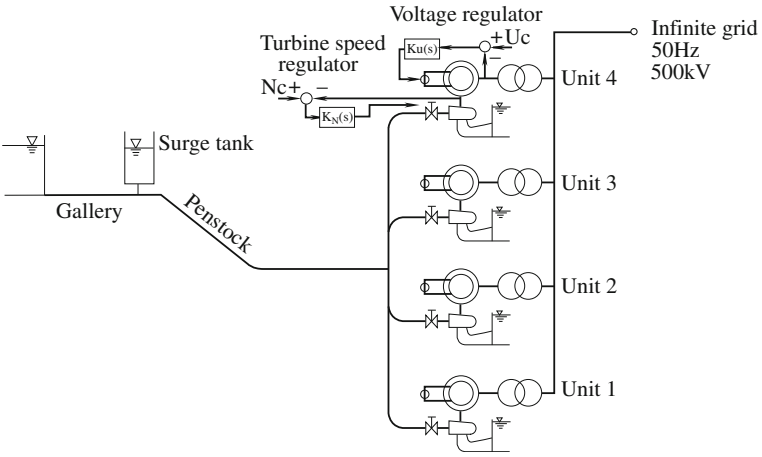

Fig. 10.14 Hydraulic power plant layout (Nicolet et al. 2006)

10.4.2 Modeling of the Hydroelectric Power Plant

The simulated hydroelectric power plant model in this section comprises a hydraulic system model, that is, an elementary viscoelastic pipe model, a Francis turbine draft tube model, and the local power plant model simulated in this study.

10.4.2.1 Hydraulic System Modeling

An elementary viscoelastic pipe model and the one-dimensional momentum and continuity balances for the pipe were explained in Eq. (10.5) and Fig. 10.3. The system is solved through the Finite Difference Method with a 1-order centered scheme discretization in space and a scheme of Lax for the discharge variable. This approach involves a system of ODEs that can be represented as a T-shaped equivalent scheme, presented in Fig. 10.3. The RLC parameters of this equivalent scheme are given by

$$R = \frac{\lambda |Q| \mathrm{d}x}{2A^2 Dg},\ C = \frac{Ag\mathrm{d}x}{a^2},\ L = \frac{\mathrm{d}x}{Ag} \tag{10.57}$$

where λ is the local loss coefficient. The hydraulic resistance R, the hydraulic inductance L, and the hydraulic capacitance C correspond respectively to energy losses, inertia, and storage. The model of a pipe of length L is made of a series of n_b elements based on the equivalent scheme of Fig. 10.3. The system of equations relative to this model is set up according to Kirchoff's laws. The model of the pipe, as well as the model of valve, surge tank, and Francis turbine, etc., can be completed (see Nicolet 2007). The time-domain integration of the full system is achieved by a Runge–Kutta 4th order procedure.

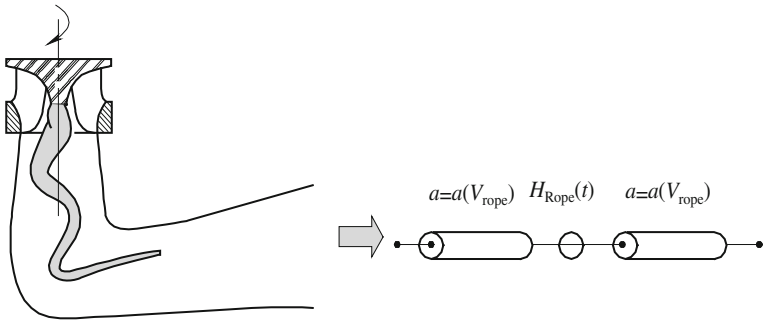

Fig. 10.15 Modeling of the draft tube (Nicolet 2007)

10.4.2.2 Draft Tube Model

For resonance risk assessment purposes, the draft tube of the Francis turbine can be properly modeled by a pressure source excitation in a series with 2 pipes, as presented in Fig. 10.15.

Assuming a cross section of draft tube with diameter D and with a rope diameter D_R, one can determine the gas volume fraction of the cross section as follows:

$$\alpha = \frac{A_{Rope}}{A_{tot}} = \left(\frac{D_R}{R}\right)^2 \tag{10.58}$$

where A_{Rope} is the cross section of the rope and A_{tot} is the total draft tube cross section for a given curvilinear abscissa. The wave speed in the liquid gas mixture is given as (Wallis 1969)

$$a_m^2 = 1 \Big/ \left[\rho_m \left(\alpha \Big/ \left(\rho_g a_g^2\right) + (1-\alpha)/\left(\rho_L a_L^2\right)\right)\right]. \tag{10.59}$$

The wave speed of the liquid gas mixture is represented as a function of the gas volume fraction, as shown in Fig. 10.16, and the function of the cavitation rope rated diameter through combination of Eqs. (10.58) and (10.59), shown in Fig. 10.17. Cavitating rope diameter up to $D_R/D = 0.1$ is common in a part-load operation of Francis turbine.

10.4.2.3 Hydraulic Power Plant Model

The simulated hydroelectric power plant is made of a gallery with 1,515 m in length, a surge tank with variable section, a penstock with 1,388 m in length and a manifold feeding 4 × 250 MW Francis turbines. The main parameters of the plant and the characteristics of the turbine should be known before the simulation as listed in Nicolet et al. (2006).

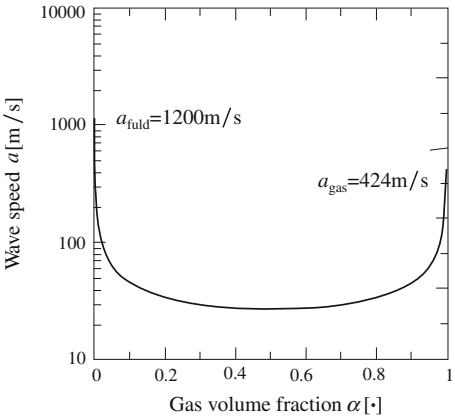

Fig. 10.16 Wave speed in vapor/water mixture

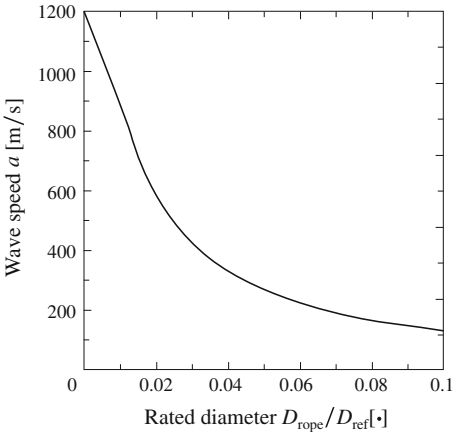

Fig. 10.17 Wave speed versus rated diameter (by Nicolet et al. 2006)

10.4.3 Resonance Risk Assessment

The natural frequencies of the piping system in a power plant can be estimated through analysis of the natural frequencies of an equivalent pipe in an adduction system. Due to longitudinal symmetry of the piping, a simplified piping model can be used. It is presented in Fig. 10.18 and Table 10.3, comprising 2 pipes: the adduction and the draft tube. Thus influence of wave speed variation of the draft tube with natural frequencies can be qualitatively investigated.

The equivalent wave speed of the piping system is given by

$$\bar{a} = (L_1 + L_2)/(L_1/a_1 + L_2/a_2). \tag{10.60}$$

Considering both upstream and downstream free surface boundary conditions of the piping, one could write the equivalent wave length of the *i*th natural mode of the piping as

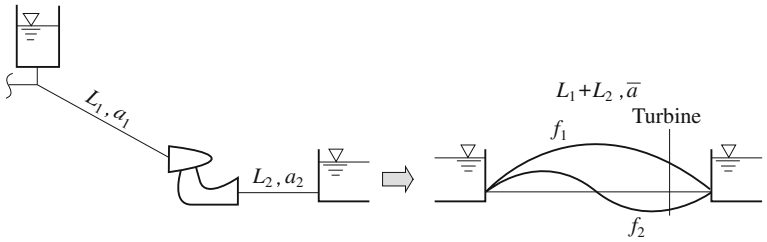

Fig. 10.18 Simplified piping model

Table 10.3 Main characteristics of the simplified model in Fig. 10.18

Description	Length L (m)	Wave speed a (m/s)
Adduction	1,478	1,146
Draft tube	30	1,200, 200, 100, 50

$$\lambda_i = 2/i(L_1 + L_2). \tag{10.61}$$

The corresponding natural frequency is therefore given by Wylie and Streeter (1993):

$$f_i = \bar{a}/\lambda_i = i/2(L_1/a_1 + L_2/a_2). \tag{10.62}$$

The first 10 natural frequencies of the simplified piping are computed for wave speed in a draft tube ranging from $a = 1{,}200$ m/s to $a = 50$ m/s. The length and wave speed of the simplified model are summarized in Table 10.3. Natural frequencies for different cavitating rope diameters can be obtained. As expected, the natural frequencies of the piping system decrease with respect to the wave speed. The natural frequency of the generator is $f_{gen} = 1.21$ Hz.

An intersection between the 4th piping's natural frequency and the generator's natural frequency locates at a draft tube wave speed of 77 m/s. This point is in the range where pressure pulsation induced by the cavitating vortex rope extends from 0.2 to 0.4 times the turbine rotating frequency, f_n.

10.5 One-Dimensional Analysis of a Hydraulic System

One-dimensional stability analysis of a hydraulic system composed of a penstock, a runner, and a draft tube was carried out to determine the cause of the fully-loaded draft tube surge presented by Tsujimoto et al. (2008). It was assumed that the cavity volume at the runner exit is a function of the pressure at the vortex core and an additional pressure decrease due to the centrifugal force on the swirling flow. It was found that the diffuser of the draft tube had a destabilizing effect over the

whole range of flow rate while the swirl effect stabilizes/destabilizes the system at larger/smaller flow rates than the swirl free flow rate. Explanations of the destabilizing mechanism were given for the diffuser and swirl flow effects.

10.5.1 Introduction

Securing stable operation is one of the most important issues in hydraulic power generation systems. At part load, a draft tube surge occurs when frequency of the vortex rope whirl agrees with resonant frequency of the hydraulic system (Jacob and Prenat 1996; Nishi 1984; Nishi et al. 1982, 1994; Angelico et al. 1986). It is also known that a surge can emerge even at full load (Prenat and Jacob 1986), but the cause is still not clear. Koutnik and Pulpitel (1996) simulated the full load surge by representing the effect of cavitation in draft tube using cavitation compliance and mass flow gain factor (see Sect. 10.4). It was shown that instability occurs when the absolute value of negative mass flow gain factor exceeds a certain value which depends on the value of cavitation compliance and system head losses. This model was combined with the numerical analysis software SIMSEN to analyze the full load surge observed in a real plant (Koutnik et al. 2006).

Although Koutnik et al. (2006) showed that full load surge could be successfully simulated with an appropriate value of mass flow gain factor, the flow mechanism determining the value of mass flow gain factor was not clear yet. Tsujimoto et al. (2008) intended to clarify the diffuser effect of the draft tube and the downstream swirl effect of the runner on the hydraulic instabilities in power generation plants (Chen et al. 2008a, b). The effect of finite sound velocity in the penstock was discussed.

10.5.2 Analytical Model

As shown in Fig. 10.19, one should consider a system composed of an inlet pipe of length L_i and area A_i, a turbine runner, and a draft tube with the inlet and exit areas A_c and A_e. A cavity of volume V_c is assumed downstream of the turbine and

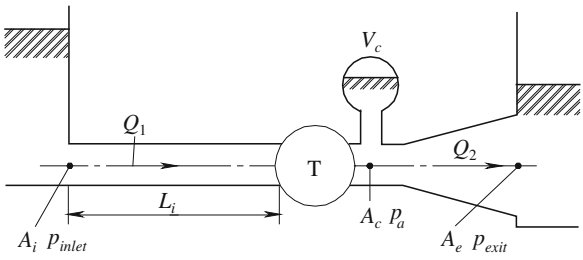

Fig. 10.19 Hydraulic system

upstream of the draft tube. Then, the continuity equation between upstream and downstream flow rates Q_1 and Q_2 is

$$Q_2 - Q_1 = \mathrm{d}V_c/\mathrm{d}t. \tag{10.63}$$

By applying Bernoulli's equation to the draft tube, one obtains

$$p_a = p_{exit} + \rho \frac{L_e}{A_e}\frac{\mathrm{d}Q_2}{\mathrm{d}t} + \rho \frac{\zeta_2 - D}{2A_e^2} Q \tag{10.64}$$

where

$$L_e = \int (A_e/A(s))\mathrm{d}s$$

is the effective length of draft tube, ζ_2 is the loss coefficient of draft tube, and $D = (A_e/A_c)^2 - 1$ is the diffuser factor. Equation (10.64) ignores the flow compressibility in draft tube.

At the off-design operating point, the discharge flow from the runner swirls and then a vortex is formed. If the pressure p_c at the vortex center is lower than the vapor pressure, a cavity would appear. The volume of the cavity can be considered to be a function of the core pressure p_c:

$$V_c = V_c(p_c) \tag{10.65}$$

Due to the centrifugal force of the swirling flow, the core pressure p_c is lower than the ambient pressure p_a and can be expressed as

$$p_c = p_a - \rho \alpha c_{\theta 2}^2. \tag{10.66}$$

Here, $c_{\theta 2}$ is a representative swirl velocity and α is a pressure coefficient for the swirl effects. If one assumes a Rankine's combined vortex with the core radius r and the outer radius R, α is determined to be $\alpha = (R/r)^2 - 1/2$, with $c_{\theta 2}$ evaluated at the outer radius R (Susan-Resiga et al. 2006).

From the velocity triangle at the runner exit as shown in Fig. 10.20, one obtains

$$c_{\theta 2} = c_{m2} cot\beta_2 - U_2 = \frac{Q_1}{S} cot\beta_2 - U_2 \tag{10.67}$$

where β_2 is the vane angle at runner exit, S is the area at runner exit, and U_2 is the peripheral speed at runner exit.

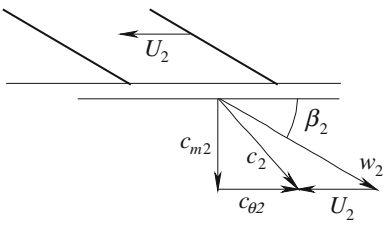

Fig. 10.20 Velocity triangle at the runner exit

By combining Eqs. (10.64) and (10.67) with Eq. (10.66), one gets

$$p_c = p_{exit} + \rho \frac{L_e}{A_e}\frac{dQ_2}{dt} + \rho \frac{\zeta_2 - D}{2A_e^2} Q_2^2 - \rho\alpha\left(\frac{\cot\beta_2}{S} Q_1 - U_2\right)^2. \tag{10.68}$$

The cavitation compliance C is defined as

$$C = -dV_c/dp. \tag{10.69}$$

Then, the continuity Eq. (10.63) can be expressed as

$$\begin{aligned} Q_2 - Q_1 &= \frac{\mathrm{d}V_c}{\mathrm{d}t} = \frac{\mathrm{d}V_c}{\mathrm{d}p_c}\frac{\mathrm{d}p_c}{\mathrm{d}t} = -C\frac{\mathrm{d}p_c}{\mathrm{d}t} = -\rho C \frac{L_e}{A_e}\frac{\mathrm{d}^2 Q_2}{\mathrm{d}t^2} \\ &+ \rho C \frac{D-\zeta_2}{A_e^2} Q_2 \frac{\mathrm{d}Q_2}{\mathrm{d}t} + 2\rho C\alpha \frac{\cot\beta_2}{S}\left(\frac{\cot\beta_2}{S} Q_1 - U_2\right)\frac{\mathrm{d}Q_1}{\mathrm{d}t}. \end{aligned} \tag{10.70}$$

The second term with $\mathrm{d}Q_2/\mathrm{d}t$ represents the diffuser effect corresponding to the mass flow gain factor. If the discharge Q_2 is increased, the ambient pressure p_a is decreased; if the diffuser effect D is larger than the loss ζ_2, the result is an increase in cavity volume, which would promote further increase of Q_2. The third term with $\mathrm{d}Q_1/\mathrm{d}t$ represents the effect of swirl. This term is also called "mass flow gain factor" but associated with the upstream flow Q_1. At the flow rate lower than the design condition ($Q_1 < Q_{sf} = U_2 S \tan\beta_2$), the tangential velocity $c_{\theta 2}$ and the cavity volume decrease as the upstream flow rate Q_1 is increased. This would promote an increase in Q_1.

Considering the compressibility of the fluid and the elasticity of pipe wall, the momentum and continuity equations applied to the flow in upstream penstock are

$$\frac{\partial u}{\partial t} + \frac{1}{\rho}\frac{\partial p}{\partial x} = 0 \tag{10.71}$$

$$\frac{\partial p}{\partial t} + \rho a^2 \frac{\partial u}{\partial x} = 0 \tag{10.72}$$

where a is the wave speed and can be evaluated from the speed of sound and the geometry of penstock section. The convective term is ignored as being small with respect to other terms.

By taking the partial derivative of Eq. (10.72) with respect to t and Eq. (10.71) with respect to x, one may eliminate u, which yields

$$\frac{\partial^2 p}{\partial t^2} - a^2 \frac{\partial^2 p}{\partial x^2} = 0. \tag{10.73}$$

In a similar manner, p may be eliminated, giving

$$\frac{\partial^2 u}{\partial t^2} - a^2 \frac{\partial^2 u}{\partial x^2} = 0. \tag{10.74}$$

The general solutions of Eqs. (10.71–10.74) can be expressed as

$$p = R(t - x/a) + L(t + x/a),\ \rho a u = R(t - x/a) - L(t + x/a).$$

The function $R(t - x/a)$ describes a wave propagating towards positive x while $L(t + x/a)$ is another wave propagating towards negative x. During the stability analysis, one separates each quantity into steady and unsteady components: $Q = \bar{Q} + \tilde{Q}(t)$, $p = \bar{p} + \tilde{p}(t)$ and $u = \bar{u} + \tilde{u}(t)$. The absolute value of the steady part is assumed to be much larger than unsteady part. If it is a sinusoidal fluctuation, one can express the unsteady part as follows, using an imaginary unit i:

$$\tilde{p} = p_R \cdot e^{\mathrm{i}\omega\left(t - \frac{x}{a}\right)} + p_L \cdot e^{\mathrm{i}\omega\left(t + \frac{x}{a}\right)} \tag{10.75}$$

$$\rho a \tilde{u} = p_R \cdot e^{\mathrm{i}\omega\left(t - \frac{x}{a}\right)} - p_L \cdot e^{\mathrm{i}\omega\left(t + \frac{x}{a}\right)}. \tag{10.76}$$

Solutions (10.75) and (10.76) satisfy Eqs. (10.73) and (10.74) generally, even with a complex value of ω. Assuming no pressure fluctuation ($\tilde{p} = 0$) at the entrance of the inlet pipe ($x = 0$), one can obtain $p_R + p_L = 0$ from Eq. (10.75). By introducing this result back into Eqs. (10.75) and (10.76), one acquires the pressure and velocity fluctuations along the inlet pipe:

$$\tilde{p} = p_R e^{\mathrm{i}\omega t}\left(e^{-\mathrm{i}\omega\frac{x}{a}} - e^{\mathrm{i}\omega\frac{x}{a}}\right) = -2j \cdot p_R e^{\mathrm{i}\omega t} \sin\left(\omega\frac{x}{a}\right) \tag{10.77}$$

$$\rho a \tilde{u} = p_R e^{\mathrm{i}\omega t}\left(e^{-\mathrm{i}\omega\frac{x}{a}} + e^{\mathrm{i}\omega\frac{x}{a}}\right) = 2 \cdot p_R e^{\mathrm{i}\omega t} \cos\left(\omega\frac{x}{a}\right). \tag{10.78}$$

Combined with each other, the pressure fluctuation of Eqs. (10.77) and (10.78) can be correlated with the velocity fluctuation. The pressure fluctuation $\tilde{p}_{inlet}$ at the inlet of the runner $x = L_i$ can be correlated with the velocity fluctuation $\tilde{u}_{inlet}$ there:

$$\tilde{p}_{inlet} = -\mathrm{i}\rho a \tan(\omega L_i/a) \cdot \tilde{u}_{inlet}. \tag{10.79}$$

Assume that the pressure difference between the inlet and exit of runner can be present by

$$p_{inlet} - p_a = 0.5\rho\zeta_T u_{inlet}^2 = 0.5\rho\zeta_T\left(\bar{u}_{inlet}^2 + 2\bar{u}_{inlet}\tilde{u}_{inlet} + \tilde{u}_{inlet}^2\right)$$

where p_a is the pressure at the runner exit and ζ_T is a coefficient which represents the effect of runner. The unsteady part is

$$\tilde{p}_{inlet} - \tilde{p}_a = \rho\zeta_T \bar{u}_{inlet}\tilde{u}_{inlet} = \frac{\rho\zeta_T}{A_i^2}\bar{Q}_1\tilde{Q}_1. \tag{10.80}$$

The unsteady part of Bernoulli's Eq. (10.64) applied to the draft tube is

$$\tilde{p}_a = \tilde{p}_{exit} + \frac{\rho L_e}{A_e}\mathrm{i}\omega\tilde{Q}_2 + \frac{\rho(\zeta_2 - D)}{A_e^2}\bar{Q}_2\tilde{Q}_2. \tag{10.81}$$

By applying Eqs. (10.80) and (10.81) to (10.79), one obtains

$$-\mathrm{i}\rho a\tan\left(\omega\frac{L_i}{a}\right)\cdot\frac{\tilde{Q}_1}{A_i}-\left(\frac{\rho L_e}{A_e}\mathrm{i}\omega\tilde{Q}_2+\frac{\rho(\zeta_2-D)}{A_e^2}\bar{Q}_2\tilde{Q}_2\right)=\frac{\rho\zeta_T}{A_i^2}\bar{Q}_1\tilde{Q}_1$$

which can be reduced to

$$\tilde{Q}_1=-\frac{\frac{\rho L_e}{A_e}\mathrm{i}\omega+\frac{\rho(\zeta_2-D)}{A_e^2}\bar{Q}_2}{\frac{\rho\zeta_T}{A_i^2}\bar{Q}_1+\mathrm{i}\frac{\rho a}{A_i}\tan\left(\omega\frac{L_i}{a}\right)}\tilde{Q}_2. \tag{10.82}$$

The unsteady part of the continuity Eq. (10.70) between upstream and downstream flow rates Q_1 and Q_2 is

$$\begin{aligned}\tilde{Q}_2-\tilde{Q}_1=&-\frac{\rho L_e C}{A_e}\frac{\mathrm{d}^2\tilde{Q}_2}{\mathrm{d}t^2}+\frac{\rho C}{A_e^2}(D-\zeta_2)\bar{Q}_2\frac{\mathrm{d}\tilde{Q}_2}{\mathrm{d}t}\\&+\frac{2\rho C\alpha\cot\beta_2}{S}\left(\frac{\cot\beta_2}{S}\bar{Q}_1-u_2\right)\frac{\mathrm{d}\tilde{Q}_1}{\mathrm{d}t}.\end{aligned} \tag{10.83}$$

Substitute Eq. (10.82) into (10.83) and use $\tilde{Q}_1=A_i\tilde{u}_l$, the system characteristic equation including the effect of a sound velocity in the penstock is

$$\begin{aligned}&\left(\frac{\rho a}{A_i}\frac{\rho^C L_e}{A_e}jC\right)\omega^2\tan\left(\omega\tfrac{L_i}{a}\right)-\left[\frac{\rho a}{A_i}\frac{\rho C}{A_e^2}(D-\zeta_2)\bar{Q}_2\right]\omega\tan\left(\omega\tfrac{L_i}{a}\right)\\&+\left[\frac{\rho\zeta_T}{A_i^2}\bar{Q}_1\cdot\frac{\rho L_e C}{A_e}+\frac{2\rho C\alpha\cot\beta_2}{S}\left(\frac{\cot\beta_2}{S}\bar{Q}_1-u_2\right)\cdot\frac{\rho L_e}{A_e}\right]\omega^2\\&+\left[\frac{\rho\zeta_T}{A_i^2}\bar{Q}_1\cdot\frac{\rho C}{A_e^2}(D-\zeta_2)\bar{Q}_2\mathrm{i}-\frac{2\rho C\alpha\cot\beta_2}{S}\left(\frac{\cot\beta_2}{S}\bar{Q}_1-u_2\right)\cdot\frac{\rho(\zeta_2-D)}{A_e^2}\bar{Q}_2\right.\\&\left.-\frac{\rho L_e}{A_e}\mathrm{i}\right]\mathrm{i}\omega-\mathrm{i}\frac{\rho a}{A_i}\tan\left(\omega\tfrac{L_i}{a}\right)+\left[-\frac{\rho(\zeta_2-D)}{A_e^2}\bar{Q}_2-\frac{\rho\zeta_T}{A_i^2}\bar{Q}_1\right]=0\end{aligned} \tag{10.84}$$

Equation (10.84) is a transcendental equation in terms of ω. From the characteristic Eq. (10.84), the complex frequency $\omega=\omega_R+\mathrm{i}\omega_I$ can be determined. The expression $e^{\mathrm{i}\omega t}=e^{\mathrm{i}\omega_R t}\cdot e^{-\omega_I t}$ shows that the real part ω_R gives the frequency and the imaginary part ω_I the damping rate.

10.5.3 Discussions on Instabilities with a Large Sound Velocity

When the sound velocity a is large, one can approximate

$$\tan\left(\omega\frac{L_i}{a}\right)\approx\omega\frac{L_i}{a}\ \text{and}\ \mathrm{i}\frac{\rho a}{A_i}\tan\left(\omega\frac{L_i}{a}\right)\approx\frac{\rho L_i}{A_i}\mathrm{i}\omega$$

In this case, the characteristic equation is reduced to a third order equation, which has been obtained for the case of incompressible flow in the penstock (Chen et al. 2008a, b).

$$
\begin{aligned}
&-\left(\frac{\rho L_i}{A_i}\frac{\rho L_e}{A_e}C\right)(\mathrm{i}\omega)^3-\left[\frac{\rho\zeta_T}{A_i^2}\bar{Q}\frac{\rho L_e C}{A_e}-\frac{\rho L_i}{A_i}\frac{\rho C}{A_e^2}(D-\zeta_2)\bar{Q}\right.\\
&+2\rho C\alpha\frac{\cot\beta_2}{S}\left(\frac{\cot\beta_2}{S}\bar{Q}-U_2\right)\frac{\rho L_e}{A_e}\Big](\mathrm{i}\omega)^2+\left[-\frac{\rho L_e}{A_e}-\frac{\rho L_i}{A_i}\right.\\
&+\frac{\rho\zeta_T}{A_i^2}\frac{\rho C}{A_e^2}(D-\zeta_2)\bar{Q}^2-2\rho C\alpha\frac{\cot\beta_2}{S}\left(\frac{\cot\beta_2}{S}\bar{Q}-U_2\right)\frac{\rho(\zeta_2-D)}{A_e^2}\bar{Q}\Big](\mathrm{i}\omega)\\
&+\left(-\frac{\rho(\zeta_2-D)}{A_e^2}\bar{Q}-\frac{\rho\zeta_T}{A_i^2}\bar{Q}\right)=0.
\end{aligned}
\tag{10.85}
$$

By taking the complex conjugate of Eq. (10.85), one can show that, if $\omega_1=\omega_{1R}+\mathrm{i}\omega_{1I}$ is a solution of Eq. (10.85), $\omega_2=-\omega_{1R}+\mathrm{i}\omega_{1I}$ is another solution. The solutions ω_1 and ω_2 are similar with the same frequency ω_{1I} and common damping ω_{1I}. This also requires that the real part of the third solution equals zero ($\omega_{3I}=0$). So, the solutions can be expressed as $\omega_1=\omega_{1R}+\mathrm{i}\omega_{1I}$, $\omega_2=-\omega_{1R}+\mathrm{i}\omega_{1I}$, and $\omega_3=\mathrm{i}\omega_{3I}$

Since Eq. (10.85) is a 3rd order equation in terms of $\mathrm{i}\omega$ with real coefficients, Hurwitz' criterion can be applied to obtain the stability condition:

$$
\begin{aligned}
&\left[\frac{\zeta_T}{A_i^2}\bar{Q}\frac{L_e}{A_e}-\frac{L_i}{A_i}\frac{D-\zeta_2}{A_e^2}\bar{Q}+2\alpha\frac{\cot\beta_2}{S}\left(\frac{\cot\beta_2}{S}\bar{Q}-U_2\right)\frac{L_e}{A_e}\right]\\
&\times\left[\frac{L_e}{A_e}+\frac{L_i}{A_i}-\frac{\zeta_T}{A_i^2}\frac{\rho C}{A_e^2}(D-\zeta_2)\bar{Q}^2-2\rho C\alpha\frac{\cot\beta_2}{S}\left(\frac{\cot\beta_2}{S}\bar{Q}-U_2\right)\frac{(D-\zeta_2)}{A_e^2}\bar{Q}\right]\\
&>\frac{L_i}{A_i}\frac{L_e}{A_e}\left(\frac{\zeta_2-D}{A_e^2}+\frac{\zeta_T}{A_i^2}\right)\bar{Q}.
\end{aligned}
\tag{10.86}
$$

Equation (10.86) can be utilized to determine the stable/unstable flow rate regions. However, the equation is rather complicated and thus the stability will be discussed in terms of the direct solution of the characteristic Eq. (10.85).

10.5.3.1 Diffuser Effect of the Draft Tube

Equation (10.83) can be written as

$$
\rho C\frac{L_e}{A_e}\frac{\mathrm{d}^2\tilde{Q}_2}{\mathrm{d}t^2}+\rho C\frac{\zeta_2-D}{A_e^2}\bar{Q}\frac{\mathrm{d}\tilde{Q}_2}{\mathrm{d}t}+\tilde{Q}_2=\tilde{Q}_1+2\rho C\alpha\frac{\cot\beta_2}{S}\left(\frac{\cot\beta_2}{S}\bar{Q}-U_2\right)\frac{\mathrm{d}\tilde{Q}_1}{\mathrm{d}t}.
\tag{10.87}
$$

If one considers the case of $\tilde{Q}_1=0$, negative damping occurs when

$$
D>\varsigma_2.
\tag{10.88}
$$

This is caused by the diffuser effect of the draft tube. The frequency is given by

$$
\omega_e=\sqrt{A_e/(\rho L_e C)}.
\tag{10.89}
$$

This mechanism can be explained as follows. Consider the case when Q_2 is increased. From Eq. (10.64), p_a will decrease if $D>\zeta_2$, due to the diffuser effect and the cavity volume V_c is increased. Then Eq. (10.63) implies that Q_2 is

increased further if Q_1 is kept constant. This positive feedback is the cause of the instability from the diffuser effect.

10.5.3.2 Swirl Effect

From Eq. (10.70), one obtains the following equation

$$\rho C\frac{L_i}{A_i}\frac{\mathrm{d}^2\tilde{Q}_1}{\mathrm{d}t^2}+\left[\rho C\frac{\zeta_T}{A_i^2}\bar{Q}+2\rho C\alpha\frac{\cot\beta_2}{S}\left(\frac{\cot\beta_2}{S}\bar{Q}-U_2\right)\right]\frac{\mathrm{d}\tilde{Q}_1}{\mathrm{d}t}+\tilde{Q}_1=\tilde{Q}_2. \tag{10.90}$$

Here, consider the case with $\tilde{Q}_2=0$. The first term of the multiplier on $d\tilde{Q}_1/dt$ denotes the damping caused by the resistance of the runner. The second term represents the negative or positive effect of swirl depending on the value of tangential velocity $c_{\theta 2}=c_{m2}\cot\beta_2-U_2=(\bar{Q}/S)\cot\beta_2-U_2$. The tangential velocity becomes zero at the flow rate $Q_{sf}=SU_2\tan\beta_2$ which is called the swirl free flow rate. With a flow rate smaller than the swirl free flow rate Q_{sf}, the swirl contributes to instability by reducing the damping coefficient. When the flow rate is larger than the swirl free flow rate, the swirl has an effect to enhance damping. These effects can be explained below.

The velocity triangle at the runner exit is shown in Fig. 10.21, for three flow rates Q_a, Q_{sf}, and Q_b. At smaller flow rate Q_a, the absolute value of the tangential velocity will decrease if the flow rate Q_a is increased. Then, the pressure in the vortex core will go up and the cavity volume shrinks. The continuity Eq. (10.63) shows that the inlet flow rate Q_a is increased further. This positive feedback is the cause of the instability. With a larger flow rate Q_b, the tangential velocity increases if the flow rate is increased. Then the core pressure drops and the cavity volume grows. This results in the decrease of the upstream flow rate Q_b. This negative feedback is the cause of the stabilizing effect at higher flow rate.

10.5.3.3 Energy Balance

Consider the displacement work of the cavitation region:

$$E=\int p_a(Q_2-Q_1)\mathrm{d}t=\int p_aQ_2\mathrm{d}t-\int p_aQ_1\mathrm{d}t=E_2-E_1. \tag{10.91}$$

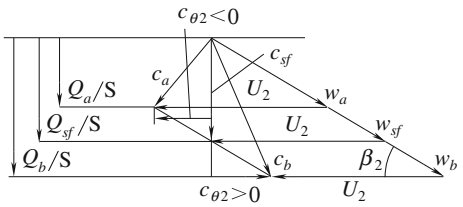

Fig. 10.21 Velocity triangle at the runner exit for three flow rates

Under a steady oscillation condition, the pressure p_a near the cavitation region can be evaluated from Eq. (10.64). Separate p_a into steady $\bar{p}_a$ and unsteady $p'_{a0}e^{i\omega t}$ components at the two cases and assume $p'_{a0} \leq \bar{p}_a$. From Eqs. (10.79) and (10.80) one obtains

$$\bar{p}_a = p_{inlet} - \rho \frac{\zeta_T}{2A_i^2} \bar{Q}^2 \tag{10.92}$$

$$\tilde{p}_a = -\rho \frac{L_i}{A_i} i\omega \tilde{Q}_1 - \rho \frac{\zeta_T}{A_i^2} \bar{Q}_1 \tilde{Q}_1. \tag{10.93}$$

And Eq. (10.64) leads to

$$\bar{p}_a = p_{exit} + \rho \frac{\zeta_2 - D}{2A_e^2} \bar{Q}_2^2 \tag{10.94}$$

$$\tilde{p}_a = \rho \frac{L_e}{A_e} i\omega \tilde{Q}_2 + \rho \frac{\zeta_2 - D}{A_e^2} \bar{Q}_2 \tilde{Q}_2. \tag{10.95}$$

First, the upstream energy transfer is considered within a period T:

$$\begin{aligned} E_1 &= \int_0^T p_a Q_1 \mathrm{d}t = \int_0^T (\bar{p}_a + \tilde{p}_a)(\bar{Q}_1 + \tilde{Q}_1)\mathrm{d}t = \bar{p}_a \bar{Q}_1 T + \int_0^T \tilde{p}_a \tilde{Q}_1 \mathrm{d}t \\ &= \bar{E}_1 + \tilde{E}_1. \end{aligned} \tag{10.96}$$

In the same way,

$$E_2 = \int_0^T p_a Q_2 dt = \bar{p}_a \bar{Q}_2 T + \int_0^T \tilde{p}_a \tilde{Q}_2 dt = \bar{E}_2 + \tilde{E}_2. \tag{10.97}$$

As for the unsteady displacement work $\tilde{E}_1$ and $\tilde{E}_2$, one can obtain the upstream work $\tilde{E}_1$ using expression (10.93):

$$\begin{aligned} \tilde{E}_1 &= \int_0^T \tilde{p}_a \tilde{Q}_1 \mathrm{d}t = -\rho \frac{L_i}{A_i} \int_0^T (j\omega \tilde{Q}_1) \tilde{Q}_1 \mathrm{d}t - \rho \frac{\zeta_T}{A_i^2} \bar{Q}_1 \int_0^T \tilde{Q}_1 \tilde{Q}_1 \mathrm{d}t \\ &= -\rho \frac{\zeta_T}{A_i^2} \bar{Q}_1 \left|\tilde{Q}_{10}\right|^2 \frac{\pi}{\omega}. \end{aligned} \tag{10.98}$$

By using Eq. (10.95), one gets

$$\tilde{E}_2 = \rho \frac{\zeta_2 - D}{A_e^2} \bar{Q}_2 \left|\tilde{Q}_{20}\right|^2 \frac{\pi}{\omega}. \tag{10.99}$$

Thus,

$$\tilde{E} = \tilde{E}_2 - \tilde{E}_1 = \rho \bar{Q} \frac{\pi}{\omega} \left(\frac{\zeta_2 - D}{A_e^2} \left|\tilde{Q}_{20}\right|^2 + \frac{\zeta_T}{A_i^2} \left|\tilde{Q}_{10}\right|^2 \right). \tag{10.100}$$

This illustrates that the displacement work is dissipated because of upstream and downstream resistances.

The above discussion is based on dynamics of the upstream and downstream flow channel, Eqs. (10.93) and (10.95) do not include the dynamics of cavitation. To clarify the contribution of cavitation, the continuity equation under cavitation Eq. (10.83) is used.

$$\tilde{Q}_2 - \tilde{Q}_1 = -\rho C \frac{L_e}{A_e} \frac{\mathrm{d}^2 \tilde{Q}_2}{\mathrm{d}t^2} + \rho C \frac{D - \zeta_2}{A_e^2} \bar{Q} \frac{\mathrm{d}\tilde{Q}_2}{\mathrm{d}t} + 2\rho C \alpha \frac{\cot \beta_2}{S} \left(\frac{\cot \beta_2}{S} \bar{Q} - U_2 \right) \frac{\mathrm{d}\tilde{Q}_1}{\mathrm{d}t}. \tag{10.101}$$

By using Eqs. (10.93) and (10.95), one obtains

$$\tilde{E} = \int_0^T \tilde{p}_a (\tilde{Q}_2 - \tilde{Q}_1) \mathrm{d}t = -\rho \frac{L_i}{A_i} \cdot 2\rho C \alpha \frac{\cot \beta_2}{S} \left(\frac{\cot \beta_2}{S} \bar{Q}_1 - U_2 \right) \cdot \omega^2 \frac{\pi}{\omega} \left| \tilde{Q}_{10} \right|^2 \tag{10.102}$$

By equating (10.100) and (10.103), one obtains

$$\rho \bar{Q} \frac{\pi}{\omega} \left(\frac{\zeta_2 - D}{A_e^2} \left| \tilde{Q}_{20} \right|^2 + \frac{\zeta_T}{A_i^2} \left| \tilde{Q}_{10} \right|^2 \right) = - \rho \frac{L_i}{A_i} \cdot 2\rho C \alpha \frac{\cot \beta_2}{S} \left(\frac{\cot \beta_2}{S} \bar{Q} - U_2 \right) \cdot \omega^2 \frac{\pi}{\omega} \left| \tilde{Q}_{10} \right|^2 \tag{10.103}$$

Equation (10.103) shows the following properties.

1. The displacement work by the cavity due to swirl shown by the right hand side should be dissipated due to the resistance in the upstream and downstream.
2. With $D = \zeta_2$, steady oscillation is possible for

$$\bar{Q}_1 < S U_2 \tan \beta_2.$$

3. With $\alpha = 0$, steady oscillation occurs for

$$D = \zeta_2 + \left(\frac{A_e}{A_i} \right)^2 \left(\frac{\tilde{Q}_{10}}{\tilde{Q}_{20}} \right)^2 \zeta_T.$$

4. The cavity provides energy only through the swirl-flow effects. With the diffuser effects, the energy is provided by the diffuser and the cavity does not contribute to the energy supply. The cavity is needed only to constitute a vibration system.

10.6 Three-Dimensional Flow Simulation at Load Reject Transient

Based on RANS method (see Chap. 7) in a variation rotational frame of reference fixed, the 3D unsteady flow simulation through the complete flow passage of a Francis turbine with its penstock has been carried out at the load rejection transient. Simulation and experimental results show that good agreement is obtained regarding the pressure fluctuation during the transient process in the turbine. Further, it indicates that variations of all the parameters of the hydraulic turbine can be predicted during the process. Impact of turbine transient character to penstock flow will be considered in this simulation.

10.6.1 Introduction

Hydraulic turbines exhibits transient features during startup, load change, and shutdown, as well as under abnormal conditions, such as load rejection and runaway emergencies. During the transient processes, direction and magnitude of all the working parameters are functions of time, and there is at least one parameter which changes its direction (positive, negative, zero) at the end of the process. This kind of process is also called the large fluctuant unsteady process. The runaway transient and the load rejection of the Francis turbine in operation belong to this kind of process. The runaway transient happens when the hydropower unit suddenly rejects a load. For example, speed controller breaks down, and the guide vanes can't close. In these cases, the rotational speed of its runner increases to maximum rapidly owing to the hydraulic moment effect. The load rejection process takes place when the hydropower unit suddenly rejects a load, although the speed controller operates normally and the guide vanes can close down rightly as the scheduled regulation process. But heavy pressure fluctuation happens in the turbine and in the penstock, and hance the unit's rotating speed increases.

There are a series of unsteady phenomena caused by additional inertial forces during the transient process. Oversized dynamic loads can cause breakdown of the unit, inducing penstock and surge-chamber, even catastrophic accidents of the whole hydropower station. Therefore, simulation of the transients is necessary for each hydropower station, and the result is used to evaluate the feasibility of the project as one of fundamental standards.

In traditional numerical simulations of the transients, the whole characteristic curve of hydraulic machinery was used as the boundary condition for solving the one-dimension inviscid unsteady flow problem. Obviously, it is difficult to carry out simulations without this kind of curve. In the early eighties, a new method called internal characteristic analysis was brought forth by Chang (2005). As a result, the whole characteristic curve of hydraulic machinery is no longer needed, and one can now deduce the governing equations based on geometric dimensions

and the one-dimension inviscid hypothesis. The previous methods focused on simulation of the whole hydraulic system especially inducing penstock, while research mentioned in the work of Li (2008) and Li et al. (2007) focused on the whole flow passage of the Francis turbine. Unsteady 3D turbulent simulation is done based on Reynolds-averaged continuity and Navier–Stokes equations to show the impacts of the turbine unsteadiness in the transient process to the penstock.

10.6.2 Governing Equations

During the runaway and load rejection transient of the hydraulic turbine, the external load is either null or getting smaller, and speed of the rotational system increases till runaway status, with effect of hydraulic moment. During the processes, the moment equation of the rotational system is depicted as

$$\{\boldsymbol{M}\} = J\frac{\mathrm{d}\{\boldsymbol{\omega}\}}{\mathrm{d}t} \tag{10.104}$$

where $\{\boldsymbol{M}\}$ is the moment vector of the rotational system, $\{J\}$ is the rotational inertia of the shaft system, and $\{\boldsymbol{\omega}\}$ is the angular velocity vector.

As for water in the runner, the governing equations are still Reynolds-averaged continuity and Navier–Stokes equations in the relative rotating reference frame. While there is still something different, the frame reference is in accelerated status. Through deduction, the governing equations are

$$\nabla \cdot \{\boldsymbol{W}\} = 0 \tag{10.105}$$

$$\frac{D\{\boldsymbol{W}\}}{\mathrm{D}t} = \{\boldsymbol{f}\} + \omega^2\{\boldsymbol{r}\} - 2\{\boldsymbol{\omega}\} \times \{\boldsymbol{W}\} - \left\{\frac{\nabla p}{\rho}\right\} + \frac{\mu}{\rho}\Delta\{\boldsymbol{W}\} - \frac{\mathrm{d}\{\boldsymbol{\omega}\}}{dt} \times \{\boldsymbol{R}\} \tag{10.106}$$

where $\{\boldsymbol{W}\}$ is the relative velocity in the accelerated relative rotating reference frame; $\{\boldsymbol{f}\}$ is the body force vector; μ is the dynamic viscosity of water; $\{\boldsymbol{r}\}$ is the radius vector from the rotational axis to the mass particle; and $\{\boldsymbol{R}\}$ is the vector from the grid origin to the mass particle.

From Eq. (10.106), it is known that there is an additional source force

$$-\frac{\mathrm{d}\{\boldsymbol{\omega}\}}{dt} \times \{\boldsymbol{R}\}.$$

It is decomposed into three components in the direction of x, y, z in the Cartesian coordinates, namely

$$y\frac{\mathrm{d}\{\boldsymbol{\omega}\}}{\mathrm{d}t}, \; -x\frac{\mathrm{d}\{\boldsymbol{\omega}\}}{\mathrm{d}t}$$

and zero respectively.

The governing equations of other passages are still Reynolds-averaged continuity and momentum equations in the Cartesian coordinates, which are depicted as

$$\frac{\partial \overline{v_i}}{\partial x_i} = 0 \tag{10.107}$$

$$\rho \frac{\partial \overline{v_i}}{\partial t} + \rho \frac{\partial \overline{v_l v_i}}{\partial x_j} = \rho \overline{S_i} - \frac{\partial \overline{p}}{\partial x_i} + \frac{\partial}{\partial x_j}\left[\mu\left(\frac{\partial \bar{v}_i}{\partial x_j} + \frac{\partial \bar{v}_j}{\partial x_i}\right)\right] - \rho \frac{\partial \overline{v_i' v_j'}}{\partial x_j} \tag{10.108}$$

where, $\bar{v}_i$, $\bar{p}$ are mean absolute velocity component and mean pressure respectively; v_i', v_j' are turbulent velocity fluctuating components; and $\overline{v_i' v_j'}$ is the Reynolds stress in turbulence.

At the rotating reference frame, the source of force in the equation is

$$\overline{S_i} = \overline{f_i} - \left[\varepsilon_{ijk} \frac{\mathrm{d}\omega_j}{\mathrm{d}t} r_k + 2\varepsilon_{ijk} \omega_j \overline{W_k} + \omega_j \omega_i r_j - \omega_j \omega_i r_i\right]. \tag{10.109}$$

10.6.3 Simulation Domain of the Francis Turbine and Penstock

The research object in the study is a Francis prototype turbine with the penstock in a hydropower plant, whose schematic diagram with description of each components and penstock is depicted in Fig. 10.22.

It is known that the following two aspects are to be realized to understand the simulation result of the transient. Rotational speed of the runner increases with

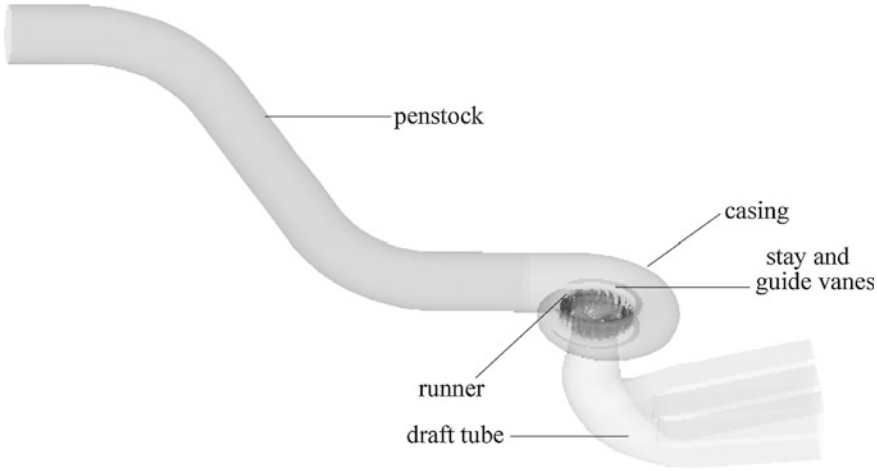

Fig. 10.22 A Francis prototype turbine with the penstock (Li et al 2007)

respect to time based on Eq. (10.104). Additional source force must be considered during the simulation. According to the above considerations, the UDF (User Defined Function) procedure is made and the steady simulation results at the unit rotational speed (71.4 rpm) are the initial condition for the simulation. During an unsteady turbulent simulation process, the time step is set as 0.001 s, and the rotational speed adjustment function and additional source force function is added to water in the runner region as shown in Eq. (10.109).

The governing equations are discretized with the finite volume method, and a second-order implicit format for the time item, a second-order central difference format for the diffusion item, a second-order upwind format for the convection item are employed. The SIMPLEC iteration procedure is choosed for the velocity–pressure coupling solution.

10.6.4 Calculating Results of Unsteady Flow at the Load Rejecting Transient

The unsteady turbulent flow computation is carried out through a Francis prototype turbine with its penstock in a hydropower plant at its load rejecting transient process. Table 10.4 lists the parameters of the Francis turbine.

The operation condition of the Francis turbine before the load rejection is the same in computation and experiment where it is also the initial condition. Under the operation condition the runner rotating speed is 71.4 r/min, the effective water head of the turbine is 67 m, the total travel of the hydraulic servomotor is 1019.5 mm,that is, the opening of guide vanes is 550 mm, and the turbine power is 580 MW.

Table 10.4 Parameters of the Francis turbine (Li et al 2007)

Term		Parameters
Head	Maximum	113.0 m
	Rated	85.5 m
	Minimum	71.0 m
Rated power		767 MW
Rated floe rate		1,000.6774 m^3/s
Rated speed		71.4 r/min
Specific speed		239.1 m·kW
Inlet diameter of spiral casing		12.21 m
Number of stay vanes		$Z_S = 23$
Number of guide vanes		$Z_0 = 24$
Number of runner vanes		$Z_B = 15$
Height of guide vanes		$B_0 = 0.3\ D_1$
Diameter of runner		$D_1 = 9.8$ m
Height of draft tube		$H_0 = 2.64\ D_1$
Length of draft tube		$L = 5.62\ D_1$

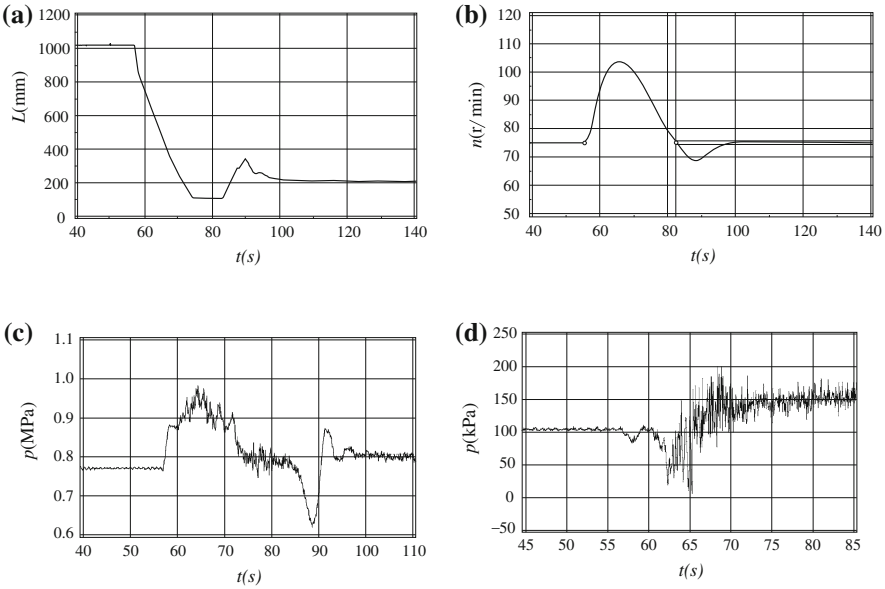

Fig. 10.23 Test results of prototype Francis turbine at load rejection from load 580 MW. **a** Time history of servomotor travel. **b** Time history of runner rotating speed. **c** Time history of pressure at S.C. entrance. **d** Time history of pressure at D.T. entrance (Li et al. 2007)

10.6.4.1 Experimental Results

Figure 10.23 shows the test results of the prototype Francis turbine at the load rejection from load 580 MW at the effective head 67 m, including the records of time histories of servomotor travel (a), runner rotating speed (b), pressure pulsation at entrance of spiral casing (c), and pressure pulsation at entrance of draft tube (d). After 100 s, the guide vanes will be at no-load condition.

10.6.4.2 Computational Results

Figures 10.24 and 10.25 present the calculated time history of pressure pulsations at the entrances of draft tube and spiral casing respectively, as well as comparisons between the calculation and test results. The cuver of Cal.1 in those figures is obtained through calculation of unsteady flow at this load rejecting process in the computation domain of the flow passage of the Francis turbine. The cuver of Cal.2 from the same calculation in the domain of the turbine and the penstock is shown in Fig. 10.22.

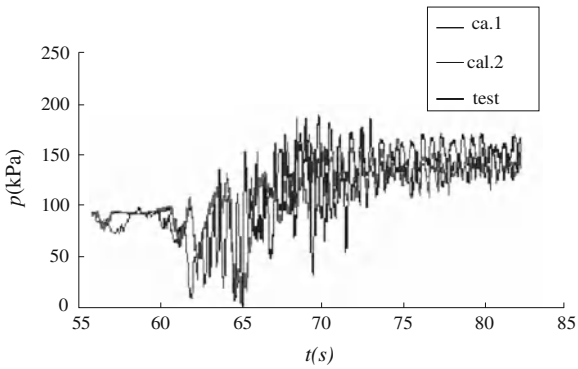

Fig. 10.24 Calculating time history of pressure pulsation at entrance of draft tube

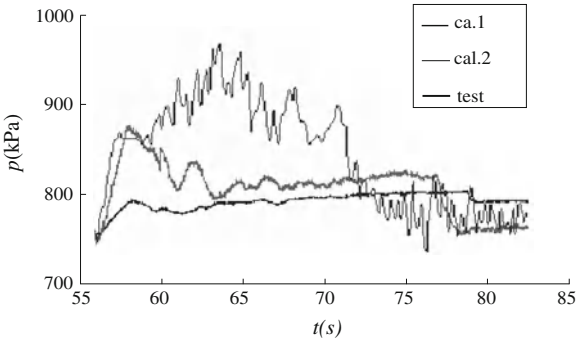

Fig. 10.25 Calculating time history of pressure pulsation at entrance of spiral casing (Li et al. 2007)

Tables 10.5, 10.6, and 10.7 are comparisons between the experimental and computational data of Cal. 1 and Cal. 2 of rotating speeds (Table 10.5), pressure pulsation at entrance of draft tube (Table 10.6) and pressure pulsation at the entrance of spiral casing (Table 10.7). It is seen that the calculation data of whole turbine with its penstock is close to the experimental data.

Further computation containing density variation and the effect of the tail water channel should be carried out to show the effect of the turbine transient to the whole hydraulic system of the turbine.

10.7 Stability of Pumping System

This section is devoted to a description of the methods to analysis the stability in pumps and their associated hydraulic systems.

Table 10.5 Rotating speed of runner (Li et al. 2007)

Case	Maximum (rpm)	Increasing rate (%)	Time at maximum (s)
Test	103.6	38.04	9.6
Cal.1	103.99	38.65	9.51
Cal.2	104.68	39.58	9.5

Table 10.6 Pressure pulsation at entrance of draft tube (Li et al. 2007)

Case	Max pressure (kPa)	Min pressure (kPa)	Increase rate (%)	Decrease rate (%)	Max time (s)	Min time (s)	Relative amplitude (%)
Test	200	14.72	90.73	85.96	13.09	9.24	28.09
Cal.1	187.3	17.43	80.49	83.22	13.55	9.2	25.92
Cal.2	200.9	17.92	93.6	82.73	13.85	9.12	27.92

Table 10.7 Pressure pulsation at entrance of spiral casing (Li et al. 2007)

Case	Max pressure (kPa)	Min pressure (kPa)	Increasing rate (%)	Decreasing rate (%)
Test	951.6	745.19	24.5	34.82
Cal.1	811.8	761.7	6.58	7.64
Cal.2	884.5	751.77	17.35	20.25

10.7.1 Basic Concepts of Static and Dynamic Stability of Pump Characteristics

A pump characteristic is regarded as stable if dH/dQ is negative, i.e. if the head drops when the flow rate is increased. If the system curve has a positive gradient dH_A/dQ, the pump operation may still be stable if the pump run back to its original operation point whenever there is a minor deviation of $\pm dQ$. The mechanism can be visualized with reference to Fig. 10.26. In order to assess the static stability it is

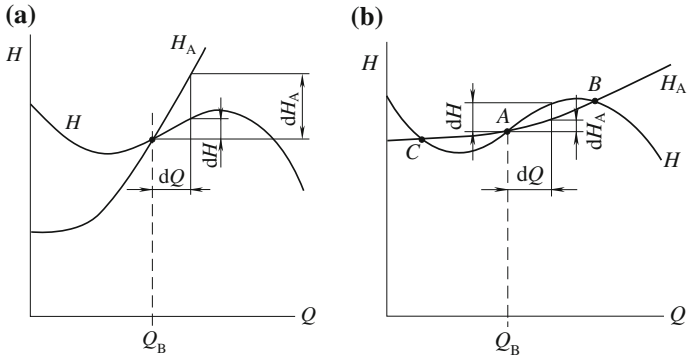

Fig. 10.26 Static stability (see Gülic 2007). **a** Stable operation. **b** Unstable operation

therefore necessary to know about the characteristics of the pump and system (see Gülic 2007).

The criterion of static stability may be still satisfied even when dH/dQ is positive (and consequently the characteristic is "unstable"). This situation is encountered if the system characteristic is steeper than the pump characteristic so that both characteristics intersect at only one point, as is shown in Fig. 10.26a. Given a momentary deviation of dQ, the system then requires dH_A whereas the pump only delivers dH.

Conditions are quite different in Fig. 10.26b where the system characteristic exhibits a smaller gradient than the pump. The pump reacts to a momentary deviation of dQ with a higher head rise than required by the system. The system can absorb additional flow, hence the deviation increases and the operation point shifts from point A to a higher flow rate at point B. With a momentary deficit of $-dQ$, the operation point would shift from point A to point C. The operation points B and C are stable (they meet the stability criterion). Point A is unstable if the system characteristic is sufficiently flat, i.e. when pumping against a high static pressure with low head losses in the system.

A dynamic instability is a self-excited vibration where periodic fluctuations of flow rate and pressure occur around a given operation point. There are two requirements for excitation of such vibrations: (1) the pump characteristic has to be unstable (hence, it must exhibit a positive gradient dH/dQ); and (2) the system must have sufficient compressibility for storing energy during the vibration cycle. Compressible volumes in this sense are vapor-filled spaces such as those found in deaerators or boilers, gas volumes in a tank for suction pressure control, cavitation zones or the elasticity, and compressibility of hot water in large-volume piping systems.

The mechanism of a dynamic instability can be explained with reference to Fig. 10.27. Consider the operation in the unstable range of the characteristic represented in the left graph and in the stable range (right graph) where flow rate and pressure are plotted against the time. In the unstable range dH/dQ is positive which indicates that H oscillates in phase with Q. The energy fed into the system per cycle is $dE = \rho g dH dQ$. The energy dE put into the system is positive, and it enhances the original perturbation and the oscillation increases.

In contrast, dH/dQ is negative on the stable branch of the characteristic. Fluctuations of pressure and flow rate are in opposite phase, dE becomes negative. Consequently, the energy added during the perturbation is dissipated and the amplitude decays (the role of damping is higher than that of excitation).

The stability analysis is performed using the method in control engineering. In addition to the pump and system characteristics, the oscillating fluid mass and the compressibility of the system must be known. The risk of self-excited vibrations increases with growing instability of the pump characteristic. Together with inadequate system damping, even slight instabilities of the characteristic (which normally would be barely detectable) can cause self-excited vibrations. The occurrence of vibration actually depends on the degree of instability of the Q–H-curve and on the system property (particularly damping). Dynamic instability can

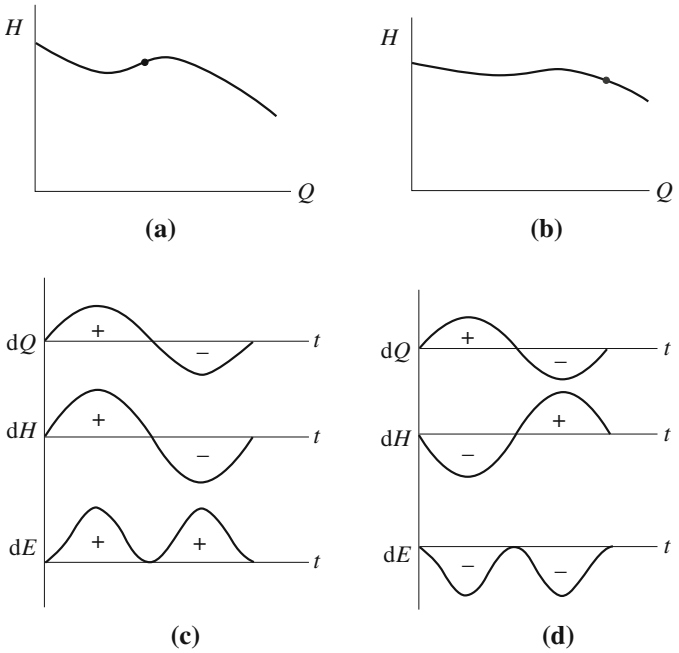

Fig. 10.27 Dynamic instability (see Gülic 2007) **a** unstable operation point. **b** stable operation point. **c** variation of flow rate, head and energy with time at unstable point. **d** variation of flow rate, head and energy with time at stable point.

occur even with a pump in single operation. It is manifested as low-frequency fluctuations of pressure and flow rate that can cause pipe vibrations and disturb the functioning of the control system.

10.7.2 Pump System Analysis

Pumping systems comprised of air vessel may feature instabilities as reported. Such a system can be simplified into a system comprised of a downstream reservoir, a pump with a fixed rotational speed, a pipe, a valve, an air vessel, and an upstream reservoir. The equivalent scheme of this system is made of the pump pressure source $Hp(Q)$, the pipe model with the pipe inductance Lp and resistance Rp, while the air vessel is modeled as its capacitance C_{AV}, and the valve as its resistance Rv (see Fig. 10.28). The compliance of the pipe is neglected with respect to the air vessel compliance (see Nicolet 2007).

The corresponding set of differential equations is given by:

$$\begin{cases} L_P \mathrm{d}Q_2/\mathrm{d}t + R_p Q_2 + R_v Q_2 + H_p(Q_2) = h_{AV} \\ C_{AV} \mathrm{d}h_{AV}/\mathrm{d}t = Q_1 - Q_2 \end{cases}. \tag{10.110}$$

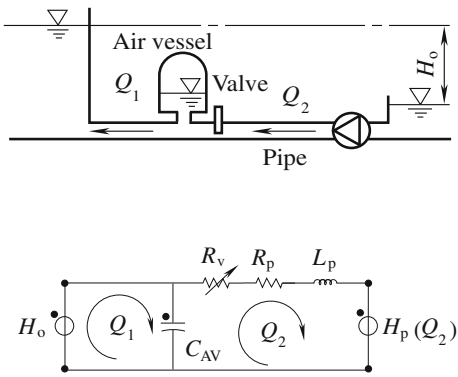

Fig. 10.28 Hydraulic circuit with pump

The head of the pump can be linearized around the operating point Q_{2*} of interest as follows:

$$H_p(Q_2) = H_{p*} + R_{Q2*}(Q_2 - Q_{2*}) \tag{10.111}$$

where $R_{Q2*} = (\mathrm{d}H/\mathrm{d}Q_2)_{Q2*}$.

Assuming the upstream discharge fluctuations being negligible, combining the above two equations leads to the following characteristic equation:

$$\frac{\mathrm{d}^2Q_2}{\mathrm{d}t^2} + 2\mu\frac{\mathrm{d}Q_2}{\mathrm{d}t} - \omega_0^2 Q_2 = 0 \tag{10.112}$$

where $2\mu = \left(R_v + R_p + R_{Q_{2*}}\right)/L_p$, $\omega_0^2 = 1/(C_{AV}L_P)$.

In this case, the system remains stable for $2\mu > 0$, leading to the following stability criteria:

$$R_v + R_p > -\frac{\mathrm{d}H}{\mathrm{d}Q_2}. \tag{10.113}$$

The above stability criteria shows that a negative slope of the characteristic curve of the pump $H_p = H_p\,(Q)$ with a negative discharge in pump mode may lead to system instability. A system is stable when the slope of energetic losses in the pipe and valve are higher than the slope of the pump characteristic, as illustrated in Fig. 10.29a. But if the former is below the latter, as illustrated in Fig. 10.29b, the system is unstable.

The layer of liquid in the slotted seals of centrifugal pumps exerts an effect on the nature of the rotor motion. The liquid transferred by pumps is of a comparatively high viscosity, and due to this fact, large hydrodynamic force acts in the eccentric annular slots of the seals. This effect may change the values of the critical speeds, lower the amplitudes of resonance oscillations, and facilitate the onset of strong self-oscillations at high revolution rates. For the dynamic stability of the pump rotor system, see the Sect. 9.5.3.

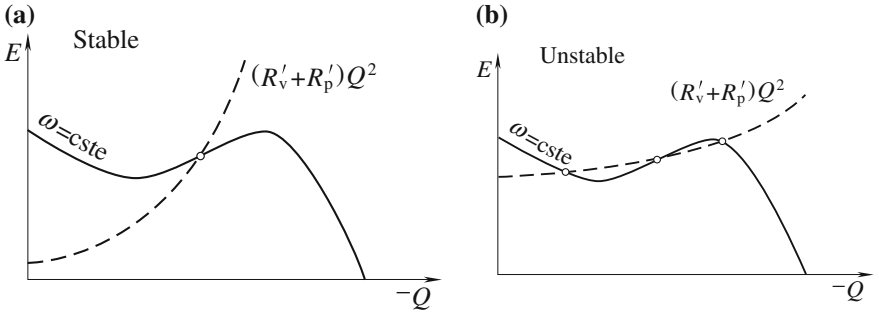

Fig. 10.29 Condition of stability of a pumping system. **a** Stable condition. **b** Unstable condition (Gülic 2007)

10.8 Introduction on Nonlinear Models of Hydro Turbine for Transient Process in Hydro Power Plant

Ng et al. (2004) presented a nonlinear mathematical model of the Francis turbine for a single-machine hydroelectric power plant to simulate the transient operations, as shown in Fig. 10.30.

The linearized equations for analyzing the stability of the hydro power system are still widely used in the control system of power industry. They are suitable only for the investigation of small power system perturbations or in first swing stability studies. Nonlinear simulations have been increasingly utilized from the early 1990s with the availability of greater computing capacity and the demands of more complex power system distribution grids.

Although a nonlinear IEEE (the Institute of Electrical & Electronics Engineers) model as shown in Fig. 10.31 (see WG 2007) has been introduced in the time domain simulations, it has oversimplified some important features of the hydraulic system.

The model, presented by Ng et al. (2004), focused on the operation of a simple power plant with a single Francis turbine and a short penstock (see Fig. 10.30). This eliminated the need to consider traveling pressure wave phenomena in a long waterway conduit and the problem of hydraulic interactions that frequently occur

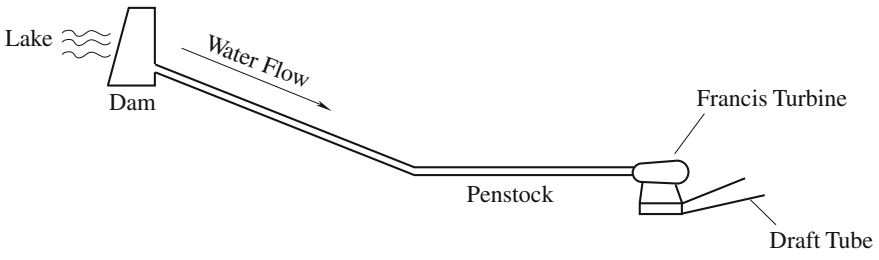

Fig. 10.30 Scheme of a hydro power plant in this study (Ng et al. 2004)

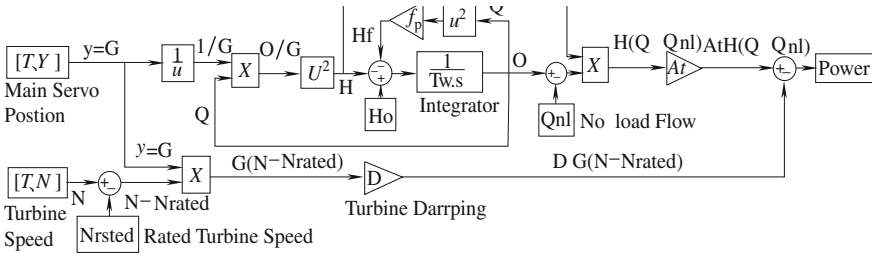

Fig. 10.31 Block diagram for 1992 nonlinear IEEE turbine model

in multiple turbine stations. Significant elements of the model developed by Ng et al. (2004) were

1. Nonlinear modeling of Francis turbine characteristics;
2. Allowance for water column inertia and unsteady flow effects in the turbine and draft tube;
3. Nonlinear guide vane (GV) function for the inlet guide vane (IGV) operation;
4. Correct allowance for effects of changing turbine speed and supply head.

10.8.1 The Power Plant Model-Conventional IEEE Model

For a short-penstock, single-machine station where traveling pressure wave (water hammer) effects are relatively insignificant, the inelastic water column theory using the linear momentum equation for incompressible flow is usually applied in the waterway conduit:

$$\bar{Q} = \frac{1}{T_w} \int \left(\bar{H}_0 - \bar{H} - \bar{H}_f\right) \mathrm{d}t \tag{10.114}$$

where $\bar{Q}$ is the per-unit turbine flow rate; $\bar{H}_0$ is the per-unit static head between reservoir and tailrace; $\bar{H}$ is the per-unit static head at the turbine admission; $\bar{H}_f$ is the per-unit conduit head losses; and TW is the water time constant, as follows:

$$TW = \sum Q_{\text{rate}} L_i / (g A_i h_{\text{rate}})$$

where L_i is the length of the conduit section I; A_i is the area of the conduit section I; g is the gravitational acceleration; Q_{rate} is the rated flow rate; and h_{rate} is the rated head.

No provision is made in the inelastic model to include unsteady flow effects in the turbine and draft tube caused by changing the GV position. Although these

effects may be insignificant in a station with a relatively long penstock, they would be more important for a station where the water column inertia is small.

In this generic model, the Francis turbine is depicted as an orifice with a constant discharge coefficient for a particular guide vane setting. The flow rate through the turbine is modeled in term of a simple orifice flow relation:

$$\bar{Q} = \bar{G}\sqrt{\bar{H}} \tag{10.115}$$

The guide vane (GV) function $\bar{G}$ in the existing model is assumed to vary linearly with the guide vane opening only. In reality, the slope of this function varies with flow coefficient, and the Reynolds number over the full range of turbine operations should be properly modeled as a nonlinear function. The turbine power output for the IEEE model is evaluated from:

$$\bar{P}_m = A_t\bar{H}(\bar{Q} - \bar{Q}_{nl}) - D\bar{G}(\bar{N} - \bar{N}_{\text{rate}}) \tag{10.116}$$

where $\bar{P}_m$ is the per-unit turbine power output; A_t is the turbine gain factor; $\bar{Q}_{nl}$ is the per-unit no-load flow; D is the speed-damping factor; $\bar{N}$ is the per-unit turbine rotational speed; and $\bar{N}_{rate}$ is the per-unit rated turbine rotational speed. The no-load flow $\bar{Q}_{nl}$ is used to correct the bearing friction and the windage losses in both turbine and generator. The turbine gain factor A_t allows for other internal flow losses. However, the resulting linearized model is not very accurate. The damping factor D in the IEEE model is introduced to allow for efficiency variations resulting from varied operating conditions; a constant value of $D = 0.5$ has been used for Francis turbine modeling.

In the current IEEE model, there is no dimensionless turbine characteristic. Equation (10.116) is inappropriate and could lead to significant error when the change in turbine operating conditions is large. In particular, the speed-damping factor D used in the model is unrealistic for the Francis turbine operation. The power (and the efficiency) change with speed may be positive or negative depending on the GV position, and their rates of change also vary with the GV position.

Damping effects due to head changes are also neglected in the existing model. In fact, changing the turbine net head, H will also change the flow rate of the machine, Q. At a constant turbine speed, N, this also changes the flow coefficient $C_Q \propto Q/N$ and moves to a different turbine operating point and efficiency. The magnitude is similar to the speed damping effect and must be taken into account in the simulation. Hence, dimensionless turbine performance curves should be employed to correctly represent the hydraulic turbine operation. For incompressible flow, the turbine operation is accurately described in the dimensionless relation:

$$C_{QM} = f(C_Q, Re) \tag{10.117}$$

where the flow coefficient is $C_Q = Q/Nd^3$; the head coefficient is $C_H = gH/N^2d^2$; the Reynolds number is $Re = 4\rho Q/\pi\mu d$; and d is the turbine characteristic diameter.

The net turbine head may vary due to transients or changes in the supply head. Similar operating conditions (C_Q, C_H constant) with varying speed require that $H \propto N^2$, $Q \propto N$ and $Q \propto H^{0.5}$, as assumed in Eq. (10.115). This is not suitable for a power plant that has been governed to maintain a constant runner speed in order to keep the AC frequency constant within the grid where case C_Q must vary with H for guide vanes fixed.

10.8.2 Nonlinear Models for Hydraulic Turbines

The nonlinear model for hydraulic turbines with or without surge tanks may take into account the effects of water inertia, water compressibility and pipe wall elasticity in the penstock (Quiroga 2000). The model of a hydraulic turbine with surge tank contains non-elastic water columns (penstock and tunnel). The model of a hydraulic turbine without a surge tank can also consider non-elastic water column in penstock.

The dynamics of the model of a hydraulic turbine are given by:

1. Dynamics of the penstock:

$$\bar{H}_t = f_p \bar{U}_t^2 \tag{10.118}$$

$$\frac{\mathrm{d}\bar{U}_t}{\mathrm{d}t} = \frac{\bar{H}_r - \bar{H}_t - \bar{H}_l}{T_{Wp}} \tag{10.119}$$

$$\bar{U}_t = \bar{G}\sqrt{\bar{H}_t} \tag{10.120}$$

where $\bar{U}_t$ is the per-unit water velocity in the turbine or turbine flow; $\bar{G}$ is the per-unit guide vane opening; $\bar{H}_r$ is the per-unit surge tank head; $\bar{H}_t$ is the per-unit turbine head; $\bar{H}_l$ is the per unit head loss in the penstock; f_n is the per unit head loss coefficient; and T_{Wp} is the water starting time of penstock.

2. Mechanical power:

$$\bar{P}_{\text{mechanical}} = A_t \bar{H}_t (\bar{U}_t - \bar{U}_{NL}) \tag{10.121}$$

where $\bar{P}_{\text{mechanical}}$ is the per unit turbine mechanical power; A_t is the per unit turbine gain factor; and $\bar{U}_{NL}$ is the per unit no-load flow.

3. Dynamics of the gate servomotor:

$$T_g \frac{\mathrm{d}\bar{G}}{\mathrm{d}t} + \bar{G} = u \tag{10.122}$$

where Tg is the main servomotor time constant; u is the per unit control effort.

4. Equation of motion in the turbine:

$$\bar{P}_{\text{mechanical}} - \bar{P}_{\text{load}} = 2H \frac{\mathrm{d}\bar{\Omega}_r}{\mathrm{d}t} + D\bar{\Omega}_r \tag{10.123}$$

where $\bar{P}_{\text{load}}$ is the per unit non-frequency-sensitive load; $\bar{\Omega}_r$ is the per unit runner speed; D is the per unit load damping constant; and H is the inertia constant of the shaft.

5. Dynamics of the tunnel:

$$\bar{H}_{12} = f_{p2}\bar{U}_c|\bar{U}_c| \tag{10.124}$$

$$\frac{\mathrm{d}\bar{U}_c}{\mathrm{d}t} = \frac{\bar{H}_0 - \bar{H}_r - \bar{H}_{12}}{T_{WC}} \tag{10.125}$$

where $\bar{H}_{12}$ is the per unit head loss in the tunnel; $\bar{U}_c$ is the per unit velocity or flow rate in tunnel; f_{n2} is the per unit tunnel head loss coefficient; $\bar{H}_0$ is the per unit total head.

6. Dynamics of the surge tank:

$$\frac{\mathrm{d}\bar{H}_r}{\mathrm{d}t} = \frac{\bar{U}_C - \bar{U}_t}{C_S} \tag{10.126}$$

The equations of the nonlinear model of a hydraulic turbine presented above, show strong nonlinearities of the system and the dependence of its behavior on the operating point.

10.8.3 New Features of the Proposed Model

The earlier IEEE model illustrated in Fig. 10.31, with its simplified turbine and guide vane characteristics, could not adequately represent all the transient behavior observed in the field tests. Such simplifications are no longer necessary with modern computing power. Thus, additional nonlinear features have been included to improve the accuracy of the turbine model by Ng et al. (2004).

1. A lookup table is included in the model to implement a nonlinear GV function. The table combines two nonlinear relationships: (1) The GV angle varies

nonlinearly with the main servo movement; and (2) The GV function varies nonlinearly with the GV movement. A quadratic term is introduced to provide a simple non-linear relation between flow and gate opening. It can be tuned to match the observed steady state power output.

2. A lookup table for the efficiency versus flow coefficient is used to replace the turbine gain and damping factors. This procedure incorporates damping effects due to both speed and head changes as well as losses in the turbine. The lookup table is constructed using a combination of data from full-scale steady-state tests, simulations and model test results. No further correction for variation from rated head is required.
3. A first order filter block (gate time delay) can be included to model the unsteady effects associated with gate movement. It has not been used in the present work, but will be implemented later when adequate data becomes available from computational studies, field tests or laboratory model tests.

Their model was evaluated by full-scale field tests involving both steady and transient operations (for details see Ng et al. 2004).

References

Alligné, S., Nicolet, C., Allenbach, P., Kawkabani, B., Simond, J. -J., & Avellan, F. (2008). Influence of the vortex rope location of a Francis turbine on the hydraulic system stability. *Proceedings of IAHR 24th Symposium on Hydraulic Machinery and Systems*, Foz do Iguassu, paper 82.

Angelico, F. M. G., Muciaccia, F. F., & Rossi, G. (1986). Part load behavior of a turbine: a study on a complete model of a hydraulic power plant, *Proceedings of the IAHR Symposium*, Montreal, paper 17.

Chang, J. S. (2005). *Transient of hydraulic machine installation*. China: Higher Education Press.

Chen, C., Nicolet, C., Yonezawa, K., Farhat, M., Avellan, F., & Tsujimoto, Y. (2008a). One-dimensional analysis of full load draft tube surge. *ASME Transactions on Journal of Fluids Engineering, 130*, 041106.

Chen, C., Nicolet, C., Yonezawa, K., Farhat, M., Avellan, F., & Tsujimoto, Y. (2008b). One-dimensional analysis of full load draft tube surge considering the finite sound velocity in the penstock. *Proceedings of 24th IAHR Symposium*, Foz do Iguassu, Paper 106.

Dorfler, P. K. (1985). Francis turbine surge prediction and prevention. *Proceedings of Waterpower' 85*, pp. 952–961.

Gülic, J. F. (2007). *Centrifugal pumps, chapter 11 operation of centrifugal pumps*. Berlin: Springer.

Haban, V., Koutnik, J., & Pochyly, F. (2002). One-d mathematical model of high frequency pressure oscillations induced by RSI including an influence of fluid second viscosity. *Proceedings of the 21st IAHR Symposium on Hydraulic Machinery and Systems* (*Lausanne*), pp. 735–740.

Imai, T., Akiyama, Y., Ikeya, T., Kudo, K., & Tsuzuki, S. (1987). Wave focusing by a submerged crescent plate. *Proceedings of Coastal Engineering in Japan*, pp. 487–491.

Jacob, T., & Prenat, J.-E. (1996). Francis turbine surge: discussion and data base. *Proceedings of 18th IAHR Symposium*, Valencia, Spain.

Koutnik, J., & Pulpitel, L. (1996). Modeling of the Francis turbine full-load surge. *Modeling, Testing and Monitoring for Hydro Power Plants*, Lausanne.

Koutnik, J., Nicolet, C., Schohl, G. A., & Avellan, F. (2006). Overload surge event in a pumped storage power plant. *Proceedings of 23rd IAHR Symposium,* Yokohama, paper 135.

Li, J. W., Wu, Y. L., Liu, S. H., & Zhu, Y. L. (2007). 3D unsteady turbulent simulation of the runaway transient of the Francis turbine. *Proceedings of the 5th Joint ASME/JSME Fluids Engineering Summer Conference*, FEDSM2007-37451.

Li, J. W.(2008). 3D unsteady turbulent simulation of the transient of the Francis turbine. *Dissertation of Ph Doctor Degree*. Tsinghua University in China.

Ng, T. B., Walker, G. J., & Sargison, J. E. (2004). Nonlinear model of transient behavior in a hydro-power plant. *Proceedings of 15th Australasian Fluid Mechanics Conference*, The University of Sydney, Sydney.

Nicolet, C. (2007). Hydroacoustic modeling and numerical simulation of unsteady operation of hydroelectric system. *Doctor dissertation*. Ecole Polytechnique Federale de Lausanne, http://library.epfl.ch/en/theses/?nr=3751&fmt=full.

Nicolet, C., Greiveldinger, B., Herou, J.-J., Kawakabani, B., Allenbach, P., Simond, J.-J., et al. (2006). High order modeling of hydraulic power plant in Islanded power network. *IEEE Transactions on Power Systems, 22*, 1870–1881.

Nishi, M. (1984). Surging characteristics of conical and elbow type draft tubes. *Proceedings of 12th IAHR Symposium on Hydraulic Machinery and System*, Stirling, pp. 272–283.

Nishi, M., Matsunaga, S., Kubota, T., & Senoo, Y. (1982). Flow regimes in an elbow-type draft tube. *Proceedings of 11th IAHR Symposium on Hydraulic Machinery and System*, Amsterdam, pp. 1–13, paper 38.

Nishi, M., Wang, X., Okamoto, M., & Matsunaga, S. (1994). Further investigation on the pressure fluctuations caused by cavitated vortex rope in an elbow draft tube. *Cavitation and Gas Fluid Flow Machinery and Devices*, *ASME*, pp. 63–70.

Prenat, J. -E., & Jacob, T. (1986). Investigating the behavior at high load of a Francis turbine model. *Proceedings of 13th IAHR Symposium*, Montreal.

Quiroga, O. D. (2000). Modeling and nonlinear control of voltage frequency of hydroelectric power plants. *Doctor dissertation*. Universidad Politécnica de Cataluna.

Rheingans, W. J. (1940). Power swing in hydroelectric power plants. *Transaction of ASME, 62*, 171–184.

Susan-Resiga, R., Ciocan, G. D., Anton, I., & Avellan, F. (2006). Analysis of the swirling flow downstream a Francis turbine runner. *Journal of Fluid Engineering, 128*, 177–189.

Tsujimoto, Y., Yonezawa, K., & Chen, C. (2008). One-dimensional analysis of a hydraulic system. *Fluid Machinery and Fluid Mechanics*, Springer, pp. 44–56.

US Geological Survey (2007) River science at the U.S. Geological Survey, committee on river science at the U.S. Geological Survey, National Research Council.

Wallis, G. B. (1969). *One-dimensional two-phase flow*. New York: Mc Graw-Hill.

WG. (2007). Working group on prime mover and energy supply models for system dynamic performance studies, Hydraulic turbine and turbine control models for system dynamic performance studies. *IEEE Transactions on Power Systems, 7*, 167–179.

Wylie, E. B., & Streeter, V. L. (1993). *Fluid transients in systems*. Englewood Cliffs: Prentice Hall.

Chapter 11
Vibration-Based Condition Monitoring

Condition monitoring is the process of monitoring a condition parameter in machinery, so that a significant change is indicative of a developing failure. The use of conditional monitoring allows maintenance to be scheduled, or other actions taken to avoid the consequences of failure before it actually occurs.

The most commonly used method for rotating machines is called vibration analysis. Measurements can be taken on machine bearing casings with seismic or piezo-electric transducers to test casing vibrations, and on the vast majority of critical machines, with eddy-current transducers that directly observe the rotating shafts to measure radial (and axial) vibration of the shaft. The level of vibration can be compared with historical baseline values such as former start-ups and shutdowns.

The ongoing trends are to operate hydraulic machinery units without personnel, to increase reliability, and reduce maintenance costs. In this situation an effective condition for monitoring machinery is necessary. A progressive change from time-based (preventive) to condition-based (predictive) maintenance is intended. An increase of the time intervals between overhauls and the avoidance of unpredicted stops is possible (Egusquiza et al. 2006; Egusquiza 2007).

11.1 Principle of Condition Monitoring of Rotating Machines

Condition monitoring of plant equipment consists of mechanical health monitoring and performance monitoring. The former includes techniques such as vibration analysis, oil and wear particle analysis, thermography, ultrasonics, and others. Performance monitoring on the other hand involves thermodynamic and hydraulic evaluation of the equipment.

Turbine and pump performance degrades over time due to irreversible mechanical wear and recoverable loss from fouling and changes in operating conditions. A typical plant may lose up to 10 % efficiency over several years of operation, most of which could be recovered through maintenance and fine tuning of the process.

Y. Wu et al., *Vibration of Hydraulic Machinery*,
Mechanisms and Machine Science 11, DOI: 10.1007/978-94-007-6422-4_11,

The performance monitoring system gives operators the necessary information to accurately assess machine performance, and schedule maintenance activities to optimize plant production.

11.1.1 Vibration Monitoring

Basic vibration measuring systems consist of a transducer, signal conditioning element and a display or recording unit. Accelerometers measure absolute vibration of the object to which they are attached. The maximum frequency up to which they can measure is approximately one-third their natural frequency. Tandon and Parey (2006) introduced some sensors used for measuring vibration signals as follows.

Conventional accelerometers have high output impedance and cannot be directly connected to measuring or analyzing instruments. To handle this problem, one could feed the accelerometer output through an impedance conversion pre-amplifier called a "charge amplifier".

Integrated Circuit-Piezoelectric (ICP) accelerometers convert the high impedance charge output of a piezoelectric crystal into a low impedance voltage output using an internal amplifier circuit.

Another type of accelerometers called transducer electronic data sheet (TEDS) uses smart sensors that apply mixed mode analogue and digital operations to communicate with condition monitoring instruments. These sensors send digital information stored in their electronic data sheet once a triggering protocol has been received.

Vibration can also be monitored from a distance through laser Doppler vibrometers (LDV), one that measures the vibration velocity of objects based on Doppler effect. The scattering Doppler frequency shift is given by

$$\Delta f = (2v/\lambda)\cos\theta \tag{11.1}$$

where v is the velocity of the object, λ is the wavelength and θ is a small angle between source and observer. The wave source is a laser and the observer is a photodetector, which measures the target surface velocity related to the Doppler shift.

Eddy-current-based, non-contact "proximity probes" are used to measure vibration displacement. These probes are commonly utilized to monitor shaft vibration in journal bearings. Two such probes can be used to obtain an "orbit plot" of "Lissajous figures" of shaft motion in journal bearings. A circle is obtained when one feeds horizontal and vertical vibration signals to horizontal and vertical amplifiers of an oscilloscope. The orbit plot shows the motion of the shaft centre. The shape of the orbit provides information about faults such as misalignment, rubbing etc. (Fig. 11.1).

A rotor system without rub yields a circular orbit shape orbit, whereas presence of rub creates additional loops in the orbit shape. The number of additional loops increases with advancement of rub. For full rub the orbit rotates in the opposite

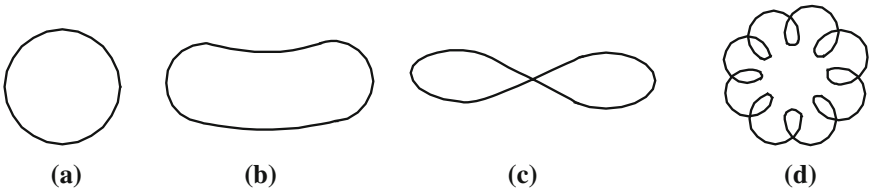

Fig. 11.1 Typical orbit plots from two proximity probes (Tandon and Parey 2006). **a** Normal, **b** misalignment, **c** severe misalignment, **d** rubbing

direction to the rotation of the shaft without any additional loop. Orbit analysis is basically suited to simple harmonic motion. For the analysis of multifrequency components, it becomes difficult to analyze the orbit diagram. A purified orbit diagram consists of only the specific frequency and other frequencies do not affect it. Another technique to minimize disturbances due to other frequencies is filtered orbit analysis.

The vibration signal from the accelerometer or proximity probe can be displayed on a vibration meter or on a computer using analogue to digital converters. Fast Fourier transform (FFT) analyzers are performed to obtain spectrum frequency of the vibration signal. In FFT analyzers, the input signal is considered over a finite time called the "frame" or "time window" and is digitized. Discrete Fourier transformation (DFT) of this signal gives the vibration frequency spectrum.

One has to choose an appropriate sampling rate for digitizing the vibration signal to avoid spurious frequency components due to "aliasing". According to the Nyquis theorem, the sampling frequency (the inverse of the sampling rate) should be at least twice the maximum frequency present in the signal.

Development of a fault or deterioration in the condition of machines is indicated by an increase in overall vibration levels. Unacceptable overall levels can be established by past experience on a particular machine. In its absence, the measured levels can be compared with vibration severity criteria such as the international standard ISO 10816 (1995–2001) series "Mechanical vibration-Evaluation of machine vibration measurements on non-rotating parts".

ISO 10816-3 separates the machines into four different groups and takes into account whether or not the machine installation is rigid or flexible in each group. Vibration levels for each group of machines are divided in four zones:

A (Green)	Vibration values from machines just put into operation.
B (Yellow)	Machines can run in continuous operation.
C (Orange)	Machine condition is acceptable only for a limited period of time.
D (Red)	Dangerous vibration values—damage could occur.

The maximum starting Root Mean Square (RMS) velocity level for zone D is from 11 mm/s. Frequency ranges are now broadened, and not limited to 10–1,000 Hz.

11.1.2 Introduction of a Vibration Monitoring Program

A monitoring program can be classified as more than one type according to its level of sophistication. This is reflected in the speed at which they can detect and locate faults (Gupta 1997). For diagnosing the source or trouble, some instruments are required to perform the time-based analysis to obtain the parameters and the frequency based vibration analysis as follows (Tranter 1989).

Overall level (RMS) measurements are common vibrations and the most simple and inexpensive type of measurement. Their greatest limitation is a lack of sensitivity and information available in the data. Unless a problem is severe, RMS may not change significantly.

Peak level detection is particularly useful for monitoring change in the amount of impulsiveness, possibly owing to increased beating damage. This method is not 100 % reliable, as other effects can also increase the peak level of a signal.

The crest factor (sometimes called the impact index) is the ratio of peak level to RMS level. This method also has limitations.

Shock pulse and spike energy are basically measuring factors of vibration level at the bearing resonance, usually above 30 kHz. Widely used, concern has been expressed over the fact that readings can decrease in later stages due to a reduction in impulsiveness and other conditions, such as turbulence and cavitation in pumps, which leads to false readings.

Kurtosis is a statistical parameter, derived from statistical moments of probability density function of the vibration signal. The main advantage of the kurtosis technique is that the calculated value is independent of load or speed variations.

Demodulation (envelope detection): Often the bearing signals are swamped by more dominant low frequency signals. This method, which can be implemented as a Hilbert transform, filters out low frequency signals, leaving a clean signal dominated by the bearing frequencies.

Phase indicates the relative timing between two points. It is used in balancing and is useful when one diagnoses imbalance, misalignment, looseness and other cases.

Time waveform: With an oscilloscope, it is possible to view the waveform of the vibration. Difficult to use in isolation, it can be a very helpful tool in combination with others.

Orbits: Uses a two-channel oscilloscope connected to proximity probes. More recently, they have been derived from a pair of frequency spectra. The major benefit is that they show relative motion of the dominant shaft vibration.

Fault detection at an earlier stage together with diagnosis is also possible when a system enables frequency analysis. Full frequency analysis and spectrum-frequency based vibration analysis is as follows (Tranter 1989).

Given that the running speed of the machine is directly proportional to the frequency measured, Fourier transform (FFT) may relate peaks in the spectrum to the machine components.

The waterfall plot (also known as spectral map and cascade plot) is a three-dimensional representation of spectra, usually with time as the third dimension.

A cestrum is the result of Fourier transform of the decibel spectrum as if it were a signal. Used to high-fight periodicities in the spectrum, it is useful in beating and gear-box analysis by mathematically subtracting two spectra or changes in level. Difference spectra are easily identified.

Fault frequency analysis is performed to relate frequencies to the machine components.

The RMS of difference between current spectrum and the baseline, and current spectrum and previous spectrum, have both been found to be helpful trending parameters.

Another method of trending the difference between vibrations is the matched filter spectra. The differences between spectra are quantified via summation of the squares of the corresponding amplitude ratios in the spectra and the logarithm of the result.

11.1.3 Vibration Signal Processing

Vibration signals acquired from machines for diagnostics purposes may be either deterministic or random. Deterministic signals can be further classified as periodic and non-periodic, whereas random signals can be classified as stationary and non-stationary. Useful information can be extracted from these signals by appropriate signal processing techniques. However, vibration signals often contain a lot of noise and if the noises are too great, the block useful information in signal processing and wrong conclusions may be drawn. In such cases techniques that enhance signal to noise ratio (SNR) are essential. Adaptive noise cancellation (ANC) is one such technique that enhances SNR (Khemili and Chouchane 2005).

11.1.3.1 Statistical Analysis

The vibration signal acquired from the machine using transducers is basically in the time domain. In order to obtain useful information for diagnostic purposes, various statistical operations can be performed. Crest factor is the ratio of maximum absolute value to the RMS value of the vibration signal, and sheds light on any impacts present in the signal. An increased value of crest factor over a period of time could stem from the presence of wear or pitting. Kurtosis measures the degree of peskiness of a distribution compared to a normal distribution. It is based on the size of the distribution's tail: the longer the tail, the higher the kurtosis value. In general, even statistical moments give information about spread. Kurtosis is defined as

$$\text{kurtosis} = M_4/M_2^2 = \frac{1}{N}\sum_{i=1}^{N}(x(n)-\bar{x})^4 \Bigg/ \left[\frac{1}{N}\sum_{i=1}^{N}(x(n)-\bar{x})^2\right]^2 \tag{11.2}$$

where M_4 is the fourth-order statistics moment; M_2 is the second-order statistics moment; $x(n)$ is the amplitude of the signal at the nth sample; $\bar{x}$ is the mean value of the amplitudes, and N is the number of samples taken in the signal.

The kurtosis value of a normal distribution is 3 and for a random signal it is close to $3(\pm 8\ \%)$. The presence of any impulse increases the kurtosis value from 3, depending upon the severity of the fault. Kurtosis is a better fault indicator than crest factor, because it can detect impulses with minimum repetition period. One of the limitations of the kurtosis method is that the kurtosis value falls to 3 when the damage is well advanced (Tandon and Parey 2006).

11.1.3.2 Time Domain Analysis and Frequency Domain Analysis

There are a large number of signal processing techniques that can be used to extract interesting information from a measured vibration signal. In the following, the basics of these techniques are outlined by Ingegneria (2008).

Simple statistical parameters evaluated over the measured time domain signal, can give some interesting information about potential defects. For example, the peak and root-mean-square values are referred to the overall vibration level. These statistical parameters are simple to implement, yet they are rather insensitive tools for defect detection. A useful technique in defect detection is the synchronous signal averaging technique (SSAT), the result of which is the signal average, which is the ensemble average of the angle domain signal, synchronously sampled with respect to rotation of one particular shaft. In the resulting signal average (SA), random noise as well as non-synchronous components are attenuated. The main advantage of the SSAT is the chance to extract a complex gearbox vibration signal, a simpler signal related to the gear of interest. However, this technique has a pivotal drawback related to the complexity of the measurement equipment. As a matter of fact an additional sensor is needed to measure the rotational shaft speed.

Furthermore, the SA can be bandpass filtered at the dominant meshing harmonic, and the application of the Hilbert transform provides both amplitude and phase modulation functions. This technique is termed as the narrow-band demodulation technique.

The time domain signal consists of different frequencies, stemming from various rotating components of a mechanical system. To diagnose a particular element, if the frequency of the element can be extracted from the signal, any changes in signal can easily be detected. Through time domain averaging, a periodic waveform can be extracted from the noisy signal. One can achieve this by repeating three steps: sampling, storing and ensemble averaging. First, sampling length is found, dependent on frequency of the signal to be extracted. To start sampling, a trigger pulse is required at the same frequency as the one of interest. This first sample is stored, before the next sample is obtained and that sample is stored after performing ensemble averaging.

The next sample is taken and ensemble averaged with the previously averaged signal. After repeating this process several times, the frequency of interest can be extracted.

Potential defects can be analyzed with a frequency domain spectrum of the vibration signal. In order to calculate the frequency spectrum of a sampled time signal, one should carry out the FFT algorithm as a numerically efficient method. It is important to notice that all digital FT methods assume stationary signals, periodic in the time window.

11.1.3.3 High Frequency Resonance Technique

The high frequency resonance method identifies the bearing defects by extracting characteristic defect frequencies which may be buried in noise and not identifiable in the direct spectrum. Each time a defect in bearings makes contact with another bearing surface, an impulse vibration is generated. The impact excites resonance of the bearing element, housing, or bearing structure. These resonances are excited periodically at the defect frequency. A signal indicative of bearing condition can be recovered by demodulating the resonance. The signal is first bandpass filtered around the resonance frequency. The frequency generated by misalignment, imbalance, gears, etc. are thus eliminated, leaving a narrow band carrier resonant frequency, amplitude modulated at the resonance frequency (Tandon and Parey 2006).

11.1.3.4 Cepstrum Analysis

Cepstrum analysis is a technique applied to enhance understanding of a spectrum. A cepstrum is the result of a Fourier transform (FT) of the decibel spectrum. There is a complex cepstrum, a real cepstrum, a power cepstrum, and a phase cepstrum.

The power cepstrum is defined as the inverse transform of the logarithm of the power spectrum. The complex cepstrum is defined as the inverse FT of the logarithm of the spectrum.

11.1.4 The Time–Frequency Analysis

There are three methods of time–frequency analysis of nonstationary signals: Windowed Fourier Transform (WFT), Winger-Ville Distribution (WVD) and Wavelet Analysis. Their traits and limitations will be illuminated below.

11.1.4.1 The Time–Frequency Analysis Methods

Wigner distribution (WD) is a common time–frequency representation. For multi-component signals, Wigner distribution is well energy-concentrated but holds cross-terms. The spectrogram, the magnitude-squared STFT, has no cross-terms but bad energy-concentration. Thus a time–frequency representation based on the geometric mean of WD and spectrogram (GMWS), which is simple and easy to realized, was introduced to integrate both advantages.

Until now, the Fourier transform (FT) has been used in vibration analysis of rotating machines. FT represents signal energy over frequency, and is useful for analysis of a stationary signal. It is well known that the time frequency representation (TFR) is more useful for analysis of time variance and transient signals.

The WD belongs to the TFR methods, and is interpreted as a function of the simultaneous energy distribution of a signal over time and frequency (Koo and Kim 2000).

The WD has high time and frequency resolution and precise location of patterns in the plane, but its drawback lies in the cross-interference term between the different components of a signal caused by an overlap in calculations (Wahl and Bolton 1993). To get rid of this interference term, an over-sampling technique is generally used or an analytic signal that is known as the Wigner–Ville distribution (WVD) (Boashash 1998).

The mathematical representation of WD can be described as follows. Let $x(t)$ be a complex continuous time analytic signal and $X(f)$ be its FT. The WD of $x(t)$ in the time and frequency domains is defined as (Cohen 1987)

$$W_x(t, f) = \int_{-\infty}^{\infty} x(t + \tau/2)x^*(t - \tau/2)\mathrm{e}^{-\mathrm{i}2\pi\tau}\mathrm{d}\tau \tag{11.3}$$

where $x(t)$ is a history signal, f represents frequency, and $x*(t)$ is a complex conjugate of $x(t)$.

For calculation of Eq. (11.3) with an on-line method, a signal $x(t)$ is band-limited to a specific time t_a as follows:

$$x_w(t, t_a) = x(t)w(t - t_a) \tag{11.4}$$

where, $w(t) = 0$, for $|t| > \tau w/2$.

The WD from the windowed signal of Eq. (11.4) can be calculated with Eq. (11.5), which is a pseudo Wigner distribution (PWD):

$$W_{xw}(t,f) = \int_{-\tau_w}^{\tau_w} x(t + \tau/2)x^*(t - \tau/2)w(-\tau/2)\mathrm{e}^{-\mathrm{i}2\pi f\tau}\mathrm{d}\tau. \tag{11.5}$$

The window function in the time domain operates as a smoothing in the frequency domain. The discrete Fourier transform (DFT) of Eq. (11.3) can be computed employing the fast Fourier transform (FFT) and is given as

$$W_{xd}(m,\ n) = 2\Delta t DFT\{x[(m+k)\Delta t]x^*[(m-k)\Delta t]\}. \tag{11.6}$$

Therefore, the discrete smoothed WD W'_{xd} given in Eq. (11.7) can be approximated via convolution of the discrete WD (*wxd*) in Eq. (11.6) and the discrete window function (*wd*).

$$W'_{xd}(m,\ n) = \Delta t \Delta w \sum_{k=m-M}^{m+M} \sum_{L=n-N}^{n+N} w_{xd}(k,\ l) w_d(m-k,\ n-l) \tag{11.7}$$

where, *k, l, m, n* are integers, *M, N* are the number of sample points, $\Delta w = \pi/k\Delta t$ is the sample interval (=$1/f_s$), and f_s is the sampling frequency.

11.1.4.2 Frequency Analysis and Faults

A vibration signals may be a combination of various harmonics, obtained by recessing the signal through a frequency analyzer. Each part of the frequency is a potential indicator of the machine condition. Spectrum analysis is the most powerful technique for diagnostic study.

The underlying principle is that each operating component of the machine generates identifiable frequencies. Thus, changes in vibration level at a given frequency can be related directly to the concerned machine components. Based on basic knowledge associated with the nature of machine operation, one should be able to calculate the frequencies consequent to the impending faults as shown in Table 11.1.

11.2 Vibration Monitoring of Hydro Turbine Units

The actual vibration behavior of hydro turbine units are quite complex. Vibration signatures measured in power plants change a lot depending on the type of turbine, measuring locations, shaft and bearing layout, foundation characteristics, and operating conditions. Of course when damage appears, signatures change as well (Egusquiza 2007).

11.2.1 Recommendations and International Standards

Two different techniques exist to monitor vibrations in rotating machines; both are applicable to hydro turbine units based on certain criteria. The first of these two techniques is vibration measurement performed on non-rotating elements, for example bearings: ISO 10816-1 and 10816-5 (these standards replace ISO 2372). The second of the techniques is vibration measurement performed on rotating shafts, for example the relative vibration between the shaft and its bearing: ISO

Table 11.1 Common faults and frequencies (Tranter 1989)

Frequency	Cause	Comments
1 × rpm	Imbalance	Steady phase that follows transducer, caused by load variation, material build-up, or pump cavitation
	Misalignment or bent shaft strain	High axial levels, 180 × axial phase relation at the shaft ends. Usually characterized by high 2 × rpm
		Caused by casing or foundation distortion, or from attached structures (e.g., piping)
	Looseness	Directional changes with transducer location. Usually high harmonic content and random phase
	Resonance	Drops off sharply with change in speed
	Electrical	Broken rotor bar in induction motor. 2 × slip frequency sidebands often produced
2 × rpm	Misalignment or bent shaft	High levels of axial vibration
Harmonics	Looseness	Impulsive or truncated waveform; large number of harmonics
	Rubs	Shaft contact with machine housing
Sub-rpm	Oil whirl	Typically 0.43–0.48 of rpm; unstable phase
	Bearing cage	Fundamental train = 0.5 × rps [1−(ball dia)/(pitch dial) × COS (contact angle)]
N × rpm	Rolling element bearings	Inner race = 0.5 × No. balls × rps [1 + (ball dia)/(Pitch dia) × COS (contact angle)]
		Ball defect = 0.5 × (pitch dia)/(ball dia) × rps [1−(ball dia)/(pitch dia) × COS (contact angle) 2]
	Gears	Gearmesh (No. teeth × rpm)
	Belts	Belt × running speed and 2 × running speed
	Blades/vanes	No. blades/vanes × rpm
N × power line	Electrical	Shorted stator; broken or eccentric rotor
Resonance		Several sources, including shaft, casing, foundation and attached structures. Frequency is proportional to stiffness and inversely proportional to mass

7919/1 and 7919/5. These standards will be replaced by ISO 10817-1 and 10817-5. Both methods are governed by the above-mentioned standards.

As a general rule, measurement of relative shaft vibration should be adopted for machines with journal bearings, independent of whether they are horizontal-axis or vertical-axis. Hydro turbine units fall into this category. However, because of the mechanical configuration and large dimensions of these machines, makes access to the bearing difficult, or the bearings are not sufficiently rigid to allow relative shaft vibration measurements, the only possibility is to measure the absolute vibration on the bearing or other machine structure. The use of accelerometers is limited to this type of machine if the frequency of interest is less than 3 Hz (180 rpm). In this situation other types of transducers such as velocimeters or piezo-resistive accelerometers must be used.

11.2.1.1 Measurements on Non-Rotating Parts

The CA201 is a very robust industrial accelerometer with a sensitivity of 100 pC/g. The device requires a separate charge amplifier (IPC 620) whose integral cable is protected by a flexible leakproof stainless steel tube. Its robustness and high sensitivity make it suitable for large machines operating at a frequency of $f > 3$ Hz. The CV210 velocimeter is equipped with its associated IVC 632 conditioner. This combination is the solution recommended for slow machines as it may be used for frequency measurement from $f = 1$ Hz. Besides, it has the advantage of providing a signal that represents the vibration velocity, thereby avoiding the need to integrate the acceleration signal. The SE120 is adopted for monitoring hydraulic machines.

11.2.1.2 Measurements on Rotating Shafts

This sort of measurement is affected by one of TQ400 series of eddy-current contactless displacement transducers with a matching IQS450 series signal conditioner. These transducers are available in various sizes and versions, optimizing the choice of one as a function of the environmental conditions at the mounting place.

11.2.1.3 Monitoring Equipment

The electronic equipment used for monitoring and/or protection of the machine can be a compact, single-channel, programmable unit or a modular, multi-channel system containing level detector and display modules (MMS system). These electronic systems contain relays which can activate alarms or shut down the machine when programmable thresholds are exceeded. Common or individual relay outputs can be used. In addition, these electronic systems produce available AC signals that may be utilized for frequency analysis or sent to data acquisition and processing systems for condition monitoring applications and/or to act as an aid for fault diagnosis.

11.2.2 Vibration Monitoring of a Hydro Turbine Unit

For hydro-electric machines as well as very high power machines, the vibration monitoring must be considered on a case-by-case basis depending on their configuration.

Propeller, Kaplan, and bubble turbines cover a large power range and are characterized by their relatively low rotational speed. They can work with vertical-axis machines for medium and large-scale power generation and also with bulb type horizontal-axis machines for small and medium-scale generation.

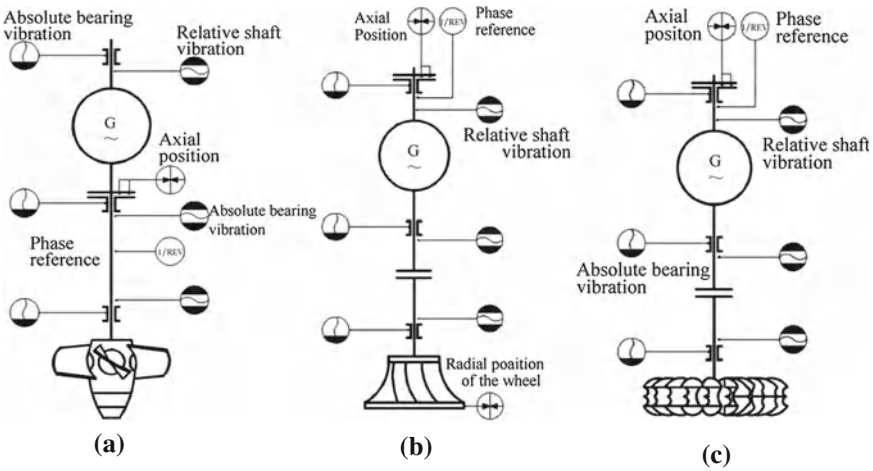

Fig. 11.2 Vibration monitoring systems of turbine generating units. **a** Kaplan turbine unit. **b** Francis turbine unit. **c** Pelton turbine unit

Francis turbines are applied on the widest field. This is not only due to the pressure head and the power but also to the rotational speed.

Pelton turbines cover a very large power range and are characterized by their relatively high rotational speed.

Vibration monitoring systems in the three types of hydraulic turbine units are shown in Fig. 11.2a, b, c respectively. There are two categories of vibration measurements: (1) absolute vibration measurement at bearing brackets and (2) relative vibration measurement at the shaft neck located near the upper guide bearing (UGB) above the generator, near the lower guide bearing (LGB) below the generator, and near the turbine guide bearing (TGB) above the turbine runner. The two sensors of axial position measurement are put at two locations of the thrust bearing, one on the disc bearing, another on the tilting-pad bearing. In Fig. 11.2a, the thrust bearing is below the generator for the Kaplan unit, and in both (11.2b) and (11.2c), it is above the generator. Only in the Francis turbine is there a radial position measurement, and the two sensors are put at the runner shroud rim and at the relative position of the runner chamber. In order to determine the axial center locus, the measurement of the shaft phase is necessary.

11.3 Vibration Monitoring System of Large Francis Turbine Unit

By increasing the specific speed of the Francis turbine, more and more stability problems were recently observed in the large turbine. Therefore, research on the stability of large Francis turbines is becoming very important. Based on condition

monitoring principles, system designs of the vibration monitoring for a large Francis turbine unit in China was conducted. The design is introduced in this section as an engineering example of hydraulic turbine unit monitoring (Zhu 2006).

11.3.1 Vibration Monitoring System of Large Francis Turbine Unit

The selection and arrangement of measuring points is significant for vibration signal acquisition. The reasonableness and accuracy of selection, as well as number of measuring points in the monitoring system are influenced by the hydro power unit's operation performance and the hydroelectric equipment's structural characteristics, which directly affect the authenticity of the signal acquisition and the whole system of diagnosis and analysis.

11.3.1.1 Selection and Arrangement of Monitoring Points

The most important issue of vibration in the Francis turbine unit (Francis unit) is the vortex-induced vibration in its draft tube. For Francis units, the monitoring of structural vibration, pressure pulsation and shaft swing is essential. Based on characteristics of Francis units, monitoring points for their vibration are arranged as follows:

Two points along *X*- and *Y*-directions at three bearings, those are, upper guide bearings (UGB), lower guide bearing (LGB), and turbine guide bearing (TGB) for shaft swings;

Three points along *X*-, *Y*- and *Z*-directions at the upper rack, the lower rack, and head cover of the turbine for vibration (Vib), respectively.

Considering that the upper rack will be subject to the weight of rotation components in the hydraulic thrust at the unit's run-time, two points are arranged along *X*- and *Y*-directions perpendicular to the vertical direction for vibration monitoring.

To monitor the stator core vibration, two measuring points in the horizontal direction are arranged at stator core shell at 90° angles to each other; in the vertical direction, one measuring point is arranged at the stator tooth plate. In order to measure the hydraulic characteristics of units, the monitoring and analysis of pressure fluctuations is needed at each turbine flow section.

These main measuring points of pressure should be arranged at the spiral case inlet, at the draft tube inlet, and on inner surface of head cover. For a Francis turbine, the draft tube inlet pressure pulse measuring points are located at the section below its inlet of (0.4–0.5) D_5 (D_5 is the draft tube inlet diameter) to the downstream side. Those monitoring points are shown in Table 11.2 and Fig. 11.3.

In order to analyze and monitor unit status, one has to introduce the relevant parameters (see in Table 11.3) to the monitoring system.

Table 11.2 Monitoring points in a large hydraulic turbine unit

No.	Item	Number	Sensor
1–1	Horizontal-Vib. Upper rack	1	Velocity
1–2	Vertical-Vib. Upper rack	1	Velocity
2–1	Horizontal-Vib. Stator core	1	Acceleration
2–2	Vertical -Vib. Stator core	1	Acceleration
3–1	Horizontal-Vib. Low rack	1	Velocity
3–2	Vertical-Vib. Low rack	1	Velocity
4–1	Horizontal-Vib. Head cover	1	Velocity
4–2	Vertical-Vib. Head cover	1	Velocity
5	X, Y-swings, UGB	2	Eddy current
6	X, Y-swings, LGB	2	Eddy current
7	X, Y-swings, TGB	2	Eddy current
8	Phase reference	1	Eddy current
9	Servomotor displacement	1	Displacement
10	Flow rate of turbine	1	Pressure dif. tran.
11	Pressure Pulse under head cover	2	Pressure tran.
12	Pressure Pulse at draft tube	2	Pressure tran.
13	Pressure Pulse at spiral case inlet	1	Pressure tran.
	Total	**23**	

Pressure Tran. Pressure transmitter, *Pressure dif. Tran.* Pressure difference transmitter

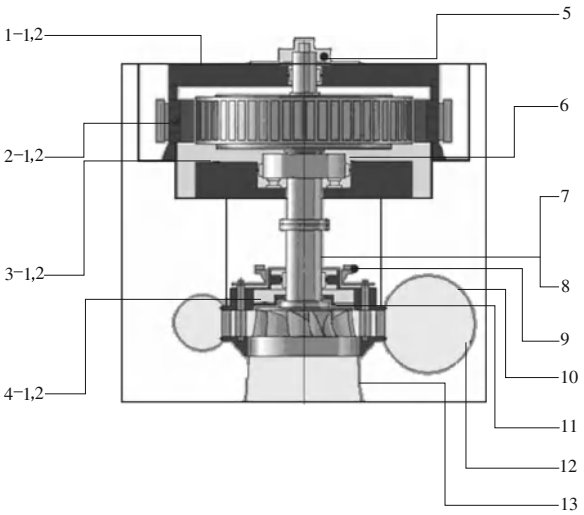

Fig. 11.3 Measuring points of Francis turbine unit (No. in Table 11.2) (Zhu 2006)

11.3.1.2 Alarm Value

Alarm values of the monitoring system are set according to National standards GB/T 11348.5-2002 "Radial vibration measurement and evaluation for rotating machinery shaft" in China, the power industry standard DL/T 507-2002 "Start test for hydro

Table 11.3 Parameters from controlling system (CS) (Zhu 2006)

No.	Signal item	Source
1	Water level at reservoir	Communicate from CS
2	Water level at tailrace	ditto
3	Active power	ditto
4	Reactive power	ditto
5	Stator three-phase current	ditto
6	Stator three-phase voltage	ditto
7	Excitation current	ditto
8	Excitation voltage	ditto
9	Power Factor	ditto
10	Bearing tiles' temperature	ditto
11	Bearing water temperature	ditto
12	Bearing lubricant temperature	ditto
13	Oil level signal	ditto
14	Signal of oil troubled waters	ditto

turbine-generating unit" in China, as well as the ensuring performances data of the main equipments provided from the contract with suppliers, listed in Table 11.4.

11.3.2 Selection and Installation of Sensors

Sensors are installed in or on the hydraulic machines to make appropriate measurements such as vibration, position, speed, pressure, power, and others. In this section, selection and installation of some sensors, such as the shaft phase sensor, the eddy current sensors for shaft swing, and the vibration sensors in hydraulic machines are introduced.

11.3.2.1 Shaft Phase Sensor

The eddy current sensor is installed to measure the shaft phase signal, (same as that used in key measurement of swing signals). At its installation, a piece of metal should be welded or bonded to the shaft surface, and the corresponding sensor can measure the displacement mutation position of the small metal. Taking advantage of this shift mutation, the analysis system can determine a fault in rotating parts or in fixed parts. If a rotating part is the source of the problem, the system can also determine where it is. With a shaft phase signal, the data acquisition system can be precise in sampling the entire cycle to avoid the phenomenon of aliasing and leakage in the spectral analysis by implementing the genuine and accurate analysis.

Table 11.4 Alarm values of the monitoring system (Zhu 2006)

No.	Monitoring item	1st alarm	2nd alarm
1	X, Y-swing, UGB(μm)	300	500
2	X, Y-swing, LGB (μm)	500	600
4	X, Y -swing, TGB(μm)	500	600
5	Horizontal vib. of upper rack (μm)	110	150
6	Vertical vib. of upper rack (μm)	80	120
7	Horizontal vib. of low rack (μm)	110	150
8	Horizontal vib. low rack (μm)	110	150
9	Vertical vib. of the rack (μm)	80	120
10	Horizontal vib. of head cover (μm)	120	200
11	Vertical vib. of head cover (μm)	120	200
12	Horizontal vib. of stator core (μm)	30	50
13	Vertical vib. of stator core (μm)	30	50
14	Pressure pulse under head cove1 (kPa)	200	400
15	Pressure pulse under head cover 2 (kPa)	200	400
16	Pressure pulse on inlet of draft tube at downstream side (kPa)	200	400
17	Pressure pulse on inlet of draft tube at upperstream side (kPa)	200	400
18	Pressure pulse at Spiral case inlet pressure fluctuation (kPa)	200	400

Note vib. vibration

11.3.2.2 Swing Sensors

Swing signals signify the stability characteristics of hydro turbine units, and they are direct signals of the stability criterion. Strong vibration will affect operation of a unit and reduce its service life, and even seriously threaten the security and stability of power grids. Vibration of the units is caused by three main factors, mechanical, hydraulic, electrical faults. No matter the cause of the vibration, it could lead to the further vibration of structural components of the unit and the swing of shaft. As a result, in-line monitoring and analysis to vibration and swing of the units is of great significance.

For the sensors to measure either swings or phase signals of the shaft, the eddy current sensors are adapted to complete the non-contact measurement. The main technical parameters of the eddy current sensor typed of IN-081 integration used in the system are as follows:

Measuring principle: eddy current; Frequency Response: 0–10 kHz (−3 dB); Measurement Range: 2 mm; Average location (the distance between the probe surface and the measured surface): About 2 mm; Sensitivity: −8 mV/μm (−200 mV/mil); Error: to meet the requirements of API670; Operating Temperature: −10 to +125 °C; Storage temperature: −30 to +125 °C; Cable length: Maximum 1,000 m; Supply Voltage: −18 V to −30 VDC, @ 5 mA.

11.3.2.3 Vibration Sensors

1. Velocity sensor. For hydraulic turbine units, low-frequency vibration is the inherent characteristic. For example, the pressure pulsation of the draft tube vortex has a frequency with its ratio of 1/4 to 1/3 to the unit rotating frequency in general. Therefore, measurement of low-frequency vibration in static components of the unit has been a difficult technique. In particular, for a speed of 75 r/min in large turbine units, rotating frequency of 1.25 Hz, and frequency of vortex tube of 0.3–0.4 Hz, low-frequency vibration measurements requires a special attention. Surveying of water vortex-induced vibration needs a sensor with a suitable range. Applied to measure vibrations of static turbine static, the velocity sensors are generally chosen. Their main technical parameters are as follows:

Sensitivity	8 V/mm ± 5 %;
Working frequency range	0.3–150 Hz (−3 dB);
Range	±1,000 μm;
Amplitude linearity	<5 %;
Operating Temperature	−30 to +60 °C

2. Acceleration sensor. Two acceleration sensors that measure the electromagnetic stator core vibration (100 Hz-based) are arranged near the central outer edge of stator iron core at the stator base. One is along the horizontal direction, another is along the vertical direction. Due to electromagnetic interference, magnetic-electric sensors cannot be applied, so the AS-030-type acceleration sensors are selected. Their technical indicators are as follows:

Sensitivity	100 mV/g;
Amplitude non-linear error	≦0.1 %;
Frequency	1.5–15,000 Hz;
Electricity supply	18–30 VDC;
Operating Temperature	−50 to 125 °C;
Weight	70 g

11.3.2.4 Pressure Transmitter

To a large extent, the hydraulic turbine stability problem is invoked by hydraulic excitation. Pressure fluctuation is the most common instability phenomenon of the turbine, so monitoring and analyzing the pressure fluctuation on the every flow section of the turbine can completely control the hydraulic characteristics of the hydro turbine and can guide the unit to run.

Each unit adopts 5 pressure transmitters, among them two are arranged under the turbine head cover to measure pressure pulsation, two in draft tube, and one at spiral case inlet. The ROSEMOUNT 3051 series transmitter is selected, in which

the pressure transmitter model is 3051 CG. Its main technical parameters are as follows:

Accuracy	±0.075 % range;
Dynamic performance: the delay time (Td)	45 ms;
Refresh rate	22 times/s;
Zero and range	zero with the range value can be set arbitrarily within the range limit;
Output	4–20 mA;
Damping	User settings;
Measuring range	2.0 MPa (optional);
Temperature limit	−40 to 121 °C;
Humidity limits	0–100 % of relative value.

11.3.3 Analysis Methods System Components

The condition monitoring system consists of sensors, data acquisition modules, servers and related network equipment, software and other components. The entire system adopts distributed hierarchical structure (as shown in Fig. 11.4).

The data servers of whole factory conditions, the Web servers, the engineer's workstations and network equipment (modems, fiber optic transceivers, switches, network security isolation equipment, etc.), and other control equipment all installed in the computer room of the central control station. They communicate with the plant MIS system through the communications server.

Its signal flow is as follows: Sensors at the site collect signals of the unit through the multi-core shielded cable to connect to the input terminal in the data acquisition unit, which then transmits to the acquisition modules through the dedicated cables. After the pre-processing module acquires and collects all the data, it is transformed into a digital signal, and run through the bus to the system board. Then online signals are treated and processed. Various characteristic parameters reflecting the operational status of the unit with some original data are obtained. These data are transmitted to the state data processing server and preserved. There, the real-time data and historical data may be analyzed.

11.3.4 Signal Analysis Methods

General vibration signal analysis methods have been introduced in the section of introduction of this chapter such as the vibration signal processing and analysis. In this section, we shall introduce some methods for time-domain analyzing and for spectrum analyzing in hydraulic machinery monitoring.

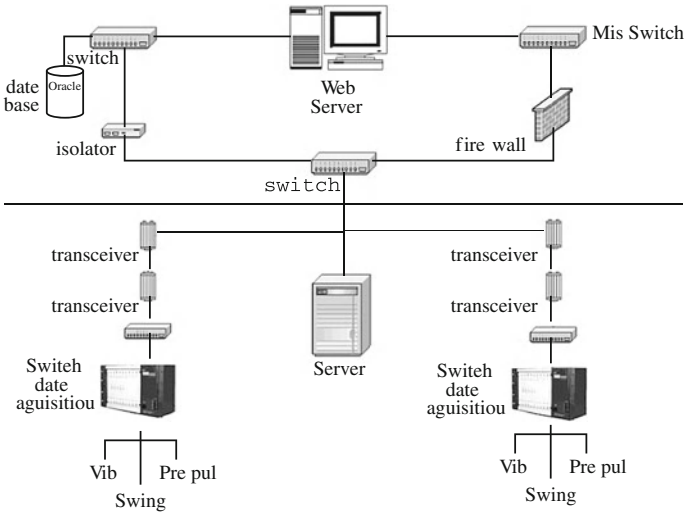

Fig. 11.4 Monitoring system network (*Notes Vib* Vibration, *Pre pul* Pressure pulsation) (Zhu 2006)

11.3.4.1 Time-Domain Analysis

1. Waveform analysis. Waveform is a time-history curve of the rotor response with respect to time. The abscissa of diagram is time. Usually it is expressed as the number of periods. Its ordinate is the real-time value of vibration, usually a positive wave approximation. It is the most original signal, and it has contains a large amount of information with intuitive, easy-to-understand features, but it can be difficult to see that the information is linked with unit fault. The fundamental frequency showing the vibration wave can be derived from the waveform diagram. With the relative phase signal, the time-based line signal can be treated as a direct reflection of the phase angle.
2. Orbit analysis. The shaft orbit is the trajectory of one point in the shaft relative to the bearing support. It is very important information for the fault diagnosis of rotating machinery. This orbit is on a plane perpendicular to the shaft axis-line. As a result, two sensors perpendicular to each other are required to be set in the plane. The complete testing device is shown in Fig. 11.5.

   (a) The direction of the shaft orbit. Orbit has its own direction that is not necessarily the same as the rotation direction of the shaft. It may be the same direction as the shaft spin direction, or it may be the contrary; it may be a clockwise direction, or it may be counter-clockwise direction. The change of shaft orbit direction is caused by different phases along the vertical and horizontal vibrations. The vibration signals, from two-channels along the vertical and horizontal axes, synthesize with the shaft movement

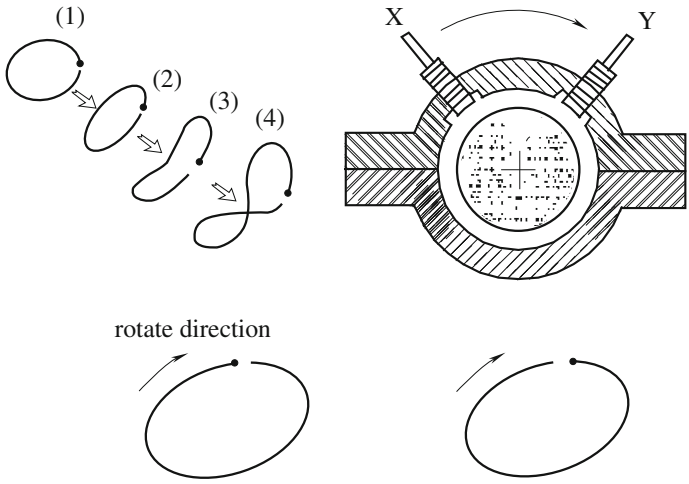

Fig. 11.5 The complete testing device of shaft orbit (Zhu 2006)

when coupled with shaft phase signal, then the shaft orbits with the phase signal can be obtained, shown in Fig. 11.5 (map between the black spots and the white spots is the phase signal).

The shaft phase signal can be used to judge the direction of the shaft center's movement. The orbit direction is shown by the black spots along the track direction toward the gap, which indicates that there is a key groove on the shaft surface. And if the gibbose part is used on the surface, the orbit direction is on the opposite, from a blank section to this black spot. The shaft center movement often is referred to as "eddy" or "precession". When the shaft center's movement direction and the rotation direction are the same, the movement is referred to as "positive precession". When its direction is opposite the rotation direction, it is called an "anti-precession". Both the shape of the orbit and its direction are very important to the rotating machinery fault diagnosis.

(b) The shape of shaft orbit. In different conditions, there are different orbit shapes (as shown in Fig. 11.6), if the dynamic stiffness of the unit contains a variety of binding forces (inertial force, elastic force, damping force). It is assumed that in a radial direction, if all forces are homogeneous and there is only one shaft interference of imbalance (such as the unbalanced mass) acting on the shaft, the axis orbit will be a round.

When other forces are not equal, the orbit shapes will differ. When the radial stiffness of the shafts are different, or preloads on the shaft have changed (for example, the shaft is eccentric, which results in load change on its each point), the shaft orbit is elliptical.

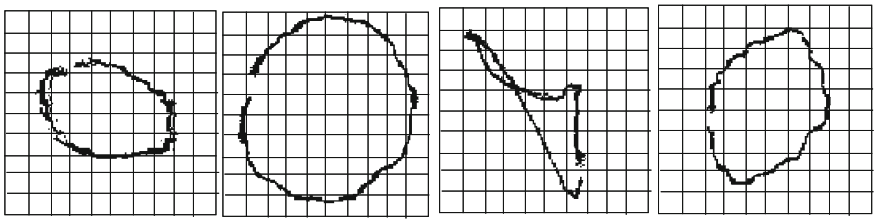

Fig. 11.6 Orbits of shaft (Zhu 2006)

For mass imbalance caused by the shaft center's movement, and assuming the same bending stiffness along different axes (including the supporting rigidity), shaft movement is the synchronous positive movement. The shaft center orbit is round. The harmonic vibration reflects the fundamental frequency in X and Y directions with equal amplitudes in two directions, which have a phase angle of 90° between them. In this case, the bending of shaft is unchanged for its different parts. But for many of the actual rotors, the shaft's bending rigidities vary in different directions as do the support stiffness, so the shaft orbit caused by mass imbalance is no longer a circle but an oval.

At this time, the vibration amplitudes are not the same in the X and Y directions, but the phase difference between the two direction vibrations is not 90°. In this case, the axis of the shaft's bending position is not fixed at a location, but will swing around a line from one side to another. This is because the curved surface of shaft does not rotate with equiangular speed, although its averaged value is still equal to the angular velocity Ω.

Under normal circumstances, and in addition to the above synchronous precession caused by the imbalance, there are non-synchronous positive precessions and anti-precession for shaft movement. The shaft has a more complicated trajectory.

11.3.4.2 Spectrum Analyzer

A general signal is measured directly in the form of the time domain. But the occurrence of failure often gives rise to changes in the structure of the signal frequency. In order to observe the dynamic behavior of objects through the measured signal, one should take advantage of the frequency domain signal. To transform the time-domain signal to a frequency domain is known as the spectral analysis. In this analysis, complex waveforms measured in the time course are decomposed into single harmonic components through the Fourier transform, in order to acquire a frequency structure of the signal, the harmonic amplitudes, and their phase information.

Spectrum analysis is the most widely used signal processing method for machine fault diagnosis. The frequency spectrum diagram of a signal usually

includes the amplitude spectrum and phase spectrum of the signal. If a diagram is derived with the frequency f as its abscissa and the amplitude as its ordinate, it is referred to as the amplitude spectrum. If it is with the frequency f as its abscissa and the phase as its ordinate, it is referred to as the phase spectrum. There are two types of graphic spectrum: the discrete spectrum (line graph) and the continuum spectrum. The former corresponds to periodic and quasi-periodic signals, while the latter corresponds to non-periodic signal and random signals.

The source of vibration in most a hydro turbine generating units is related to the speed of the unit, irregardless of whether it is a forced vibration or a self-excited vibration. The frequency of excitation is either several integral times or fractional times of the rotation speed. The corresponding response of the exciting force of vibration in the unit's support components, bearings, etc. is bound to include the generated frequency components. Therefore, when the sensor detects vibration signals, it may also pick up non-linear vibrations generated by other components and random noise.

Spectral analysis of complex periodic signals is separated into harmonic components with different frequencies. In the vibration analysis and fault diagnosis, an extraction of features and data compression play an important role, which is useful because some failures can be caused by a specific frequency of vibration.

Vibration signals in frequency domain analysis are simulated to the analog circuits with a band-pass filter or by the digital discrete Fourier transform (DFT) or a Fast Fourier Transform (FFT). In a modern computer or vibration analyzer, the digital Fourier transform is mainly applied to vibration monitoring and diagnostics.

11.3.4.3 Amplitude, Frequency Spectrum Analysis, and Time Analysis

A single signal only tells the vibration characteristics of a single moment of the machine at a specific speed and specific load conditions. However, records of the frequency data with amplitude at different speeds are also significant. For example, during the staring process of a machine, the resonance frequency or critical speed information under various forces with different frequencies should be obtained. Moreover, in the process, temperature or other changes at varying operating conditions are also necessary to assess the characteristics of amplitude and frequency.

The waterfall chart presents sizes of the various frequency components in trends over time for a hydro turbine generator unit within a certain period. It is a three-dimensional spectrum diagram composed of a group of the frequency spectrums obtained by continuous measurements at different time periods, in which X is expressed as the various frequency components, Y as the amplitude, Z as the time. Under normal circumstances, it is used to analyze the changes in vibration under rated speed conditions.

11.4 Monitoring Results and Stability Analysis of a Turbine Unit

A condition monitoring system of hydraulic turbine units in a large hydro power station has been established. The results of one large turbine generating unit have been recorded and its stability analysis has been carried out (Zhu 2006).

11.4.1 The Basic Parameters of the Large Hydro Turbine Unit

The large hydro turbine unit consists of a vertical shaft Francis turbine and generators with the semi-umbrella type structure. Its basic parameters are shown in Table 11.5.

11.4.2 The Variable Speed Test

Variable speed test of rotating machinery diagnoses whether there is a fault of mass imbalance. In the test course, measurement of vibration amplitudes and swings were carried out at the typical parts, such as the upper rack (UR), the lower rack (LR), the upper guide bearing (UGB), the low guide bearing (LGB), turbine guide bearing (TGB), etc. The test data are shown in Table 11.6 and, for example, the swing amplitude in guide bearings in Fig. 11.7.

As can be seen from the results, in the variation speed test the vibration amplitude at each measuring points increases with increasing speed, and is proportional to the square of speed, and the frequency of each vibration is proportional to unit rotating speed. So the mass imbalance of the shaft system generates the vibration of rotating parts. Dynamic balance test are necessary to eliminate this fault.

Table 11.5 The unit basic parameters (Zhu 2006)

Francis turbine		Generator	
Rated power (MW)	710	Power (MW)	700
Rated head (m)	80.6	Rated capacity (MVA)	777.8
Maximum head (m)	94	Max. capacity (MVA)	840
Minimum head (m)	61	Rated speed (rpm)	75
Blades No.	15	Bush No. of UGB	10
Vane No. of guide vanes	24	Bush No. of LGB	16
Vane No. of stay vanes	24	Bush No. of thrust B	24
Bush No. of TGB	12		

Table 11.6 Variable speed test data (Rotating speed: r/min, Amplitude: μm) (Zhu 2006)

Speed/Position	18.1	26.9	32.3	39.3	47.8	57.9	74.6	75.1
UGB X-dir.	71	70	67	73	111	120	127	133
UGB Y-dir.	73	70	67	69	90	99	106	127
LGB X-dir.	135	144	155	168	225	246	275	288
LGB Y-dir.	80	91	102	116	174	195	210	230
TGB X-dir.	67	72	80	95	157	178	166	195
TGB Y-dir.	66	73	76	96	144	151	159	188
UR X-dir.	8	20	29	39	84	104	114	123
UR Z-dir.	12	12	16	27	43	50	79	84
LR X-dir.	4	4	4	6	13	15	12	12
LR Z-dir.	5	8	10	22	35	37	39	40

Note dir. direction

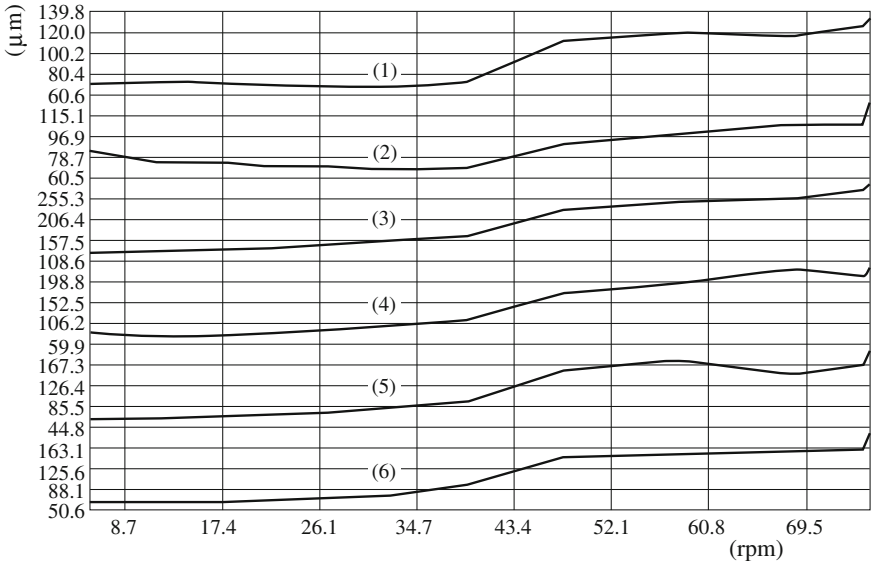

Fig. 11.7 Variations of swing of guide bearings with speed (*1* UGB X-direction, *2* UGB Y-direction, *3* LGB X-direction, *4* LGB Y-direction, *5* TGB X-direction, *6* TGB Y-direction) (Zhu 2006)

11.4.3 The Monitoring Results at Stable Operation

Monitoring data of a large Francis turbine unit at stable operation with different heads is reported in this section. Some information of the unit operation is discussed.

11.4.3.1 The Monitoring Data at Stable Operation

Monitoring data of the large Francis turbine unit at stable operation with 67 m head, including the data of vibration, swings and pressure pulsation at the measuring point are shown in Table 11.7.

The monitoring stations include the swings at the upper guide bearing along the *X* direction (UGB *X*-dir.), the upper guide bearing along the *Y* direction (UGB *Y*-dir.), the lower guide bearing along the *X* direction (LGB *X*-dir.), the lower guide bearing along the *Y* direction (LGB *Y*-dir.), the turbine guide bearing along the *X* direction (TGB *X*-dir.), the turbine guide bearing along the *Y* direction (TGB *Y*-dir.); the vibration at the upper rack of the unit along the horizontal direction (UR-Hori.), the upper rack of the unit along the vertical direction (UR-Vert.), the lower rack of the unit along the horizontal direction (LR-Hori.), the lower rack of the unit along the vertical direction (UR-Vert.), at the head cover of the unit along the horizontal direction (HC-Hori.) and along vertical direction (HC-vert.), and at the spiral casing of the unit along the horizontal direction (SC-Hori.) and along vertical direction (SC-vert.); pressure pulsations (pres) at the spiral casing of the unit (SC-Pres.), at two points under the head cover (HC-Pres. 1, HC-Pres. 2), and at the inlet section of draft tube on the upstream side and on the downstream side respectively (DT-In at US, DT-In at DS). The pressure pulsation is expressed in relative amplitude, the ratio of pressure pulsation over the rated head.

Similar monitoring results at 71 m water head condition are included in Table 11.8.

Table 11.7 The monitoring data at the measuring points at 67 m head

Power (MW)	437	476	496	516	525	541	556	580	596
UGB X-dir (μm)	70	73	79	71	77	104	71	80	77
UGB Y-dir (μm)	70	75	78	69	77	103	73	76	77
LGB X-dir (μm)	177	175	181	171	171	240	174	174	178
LGB Y-dir (μm)	119	114	104	111	102	142	111	110	108
TGB X-dir (μm)	74	74	73	72	74	119	80	81	83
TGB Y-dir (μm)	77	73	75	72	75	136	79	79	81
UR-Hori. (μm)	39	38	35	34	42	53	40	40	41
UR-Vert. (μm)	34	24	29	24	27	16	25	72	42
LR-Hori. (μm)	9	8	8	6	8	16	7	9	8
LR-Vert. (μm)	24	23	21	17	21	37	16	28	22
HC-Hori. (μm)	31	26	28	26	29	48	36	34	34
HC-Vert. (μm)	47	39	48	41	50	148	57	78	62
SC-Hori. (μm)	8	6	7	7	10	3	9	6	7
SC-Vert. (μm)	6	4	4	4	8	2	8	5	4
HC-Pres. 1 (%)	1.0	1.0	1.0	0.9	1.0	1.5	1.0	0.9	1.0
HC-Pres. 2 (%)	1.2	1.0	1.0	0.9	1.0	1.5	1.0	0.9	1.0
DT-In at US (%)	0.8	0.8	0.8	0.5	0.8	3.4	0.9	0.3	0.8
DT-In at DS (%)	3.7	3.4	3.6	3.2	3.4	3.4	3.7	3.3	3.6
SC-Pres. (%)	1.6	1.5	2.0	1.9	2.0	2.2	2.0	2.7	2.2

From Tables 11.7 and 11.8 it can be seen that this unit in stable operation process, in addition to 1st class alarm value of head cover vertical direction vibration under the power of 541 MW at 67 m head, as well as to the same value under the power of 580 MW at 71 m head, the other values of swing and vibration are allowed no more than the first class values of alarm settings.

11.4.3.2 The Reasons for the Vibration Alarm

At 67 m head: Fig. 11.8 indicates the vibration waveform and spectrum at the monitoring point on head cover at the power 541 MW condition. From the figure it can be found that the vibration amplitude along the vertical direction at the point is 158 μm, more than the second alarm setting value. From the vibration spectrum analysis (Fig. 11.8b), one can see that the maximum frequency and amplitude are 5.71 Hz and 58 μm, respectively. The second maximum frequency and amplitude are 5.63 Hz and 55 μm.

Figure 11.9 shows the pressure pulsation in draft tune, that is, the maximum frequency and amplitude of the pulsation are 5.71 Hz and 9 kPa respectively, the second maximum frequency and amplitude are 63 Hz and 8 kPa (Fig. 11.9b). So the high vibration on the head cover is caused by pressure pulsation in draft tube with 5.71 Hz.

Figure 11.10 indicates the vibration waveform and spectrum at the monitoring point on head cover at normal vibration condition. The horizontal vibration maximum frequency and amplitude are 1.25 Hz and 16 μm, the second maximum frequency and amplitude are 2.50 Hz and 6 μm and the vertical vibration maximum frequency and amplitude 1.25 Hz and 28 μm, the second maximum

Table 11.8 The monitoring data at the measuring points at 71 m head (Zhu 2006)

Power (MW)	490	510	520	531	540	550	561	580	590
UGB X-dir (μm)	81	82	78	80	85	89	77	89	83
UGB Y-dir (μm)	73	78	81	77	80	86	81	81	79
LGB X-dir (μm)	222	211	213	193	210	213	217	226	218
LGB Y-dir (μm)	128	120	121	131	123	119	132	131	123
TGB X-dir (μm)	89	86	90	103	82	93	88	96	99
TGB Y-dir (μm)	86	84	93	92	86	83	106	91	109
UR-Hori. (μm)	46	37	44	36	41	41	40	47	43
UR-Vert. (μm)	12	10	13	10	11	11	12	14	15
LR-Hori. (μm)	7	7	7	7	8	6	7	17	8
LR-Vert. (μm)	12	16	13	15	17	14	13	21	17
HC-Hori. (μm)	31	31	27	37	32	33	37	38	42
HC-Vert. (μm)	43	54	34	72	55	51	59	121	74
SC-Hori. (μm)	3	4	3	4	3	3	3	2	3
SC-Vert. (μm)	2	2	3	2	2	2	2	3	3
HC-Pres. (kPa)	7	8	8	8	8	8	8	9	8
SC-Pres. (kPa)	11	13	13	13	12	13	14	18	18

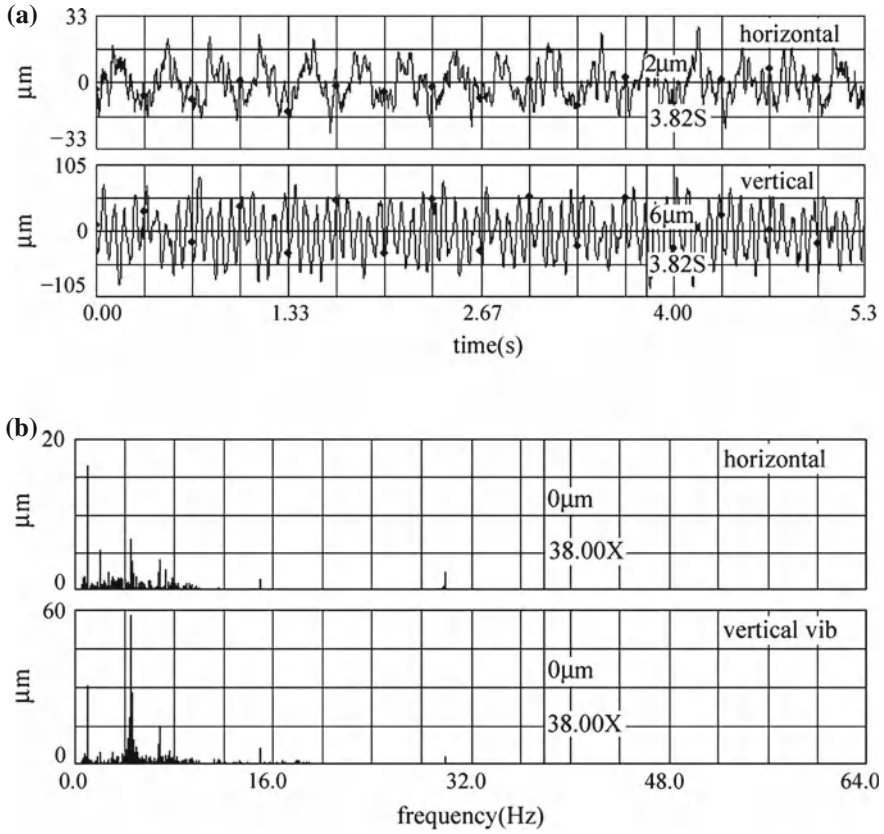

Fig. 11.8 Vibration data of head cover at 67 m head condition. **a** Waveform. **b** Frequency spectrum

frequency and amplitude 10.16 Hz and 9 μm. At the normal condition, there is no main frequency of 5.71 Hz. The reason for high vibration at the head cover at 541 MW power condition is the pressure fluctuation induced by a vortex rope in draft tube.

At 71 m head: At 71 m water head condition, the head cover vibration is large at the unit power 566 MW, compared with the situation for the 67 m head, and it can be seen that with an increase of the water head, the head cover vibration amplitude appears at within the high load region of the unit.

Figure 11.11 indicates the waveform and frequency spectrum of the head cover vibration for the unit power in 566 MW at 71 m water head.

From the figure it is evident that this large amplitude vibration may be caused by the vibration component with the main frequency 5.86 Hz. In the aforementioned situation at the head of 67 m with a power of 541 MW, this vibration main frequency is 5.71 Hz. Consequently with the increase of head, the vibration main

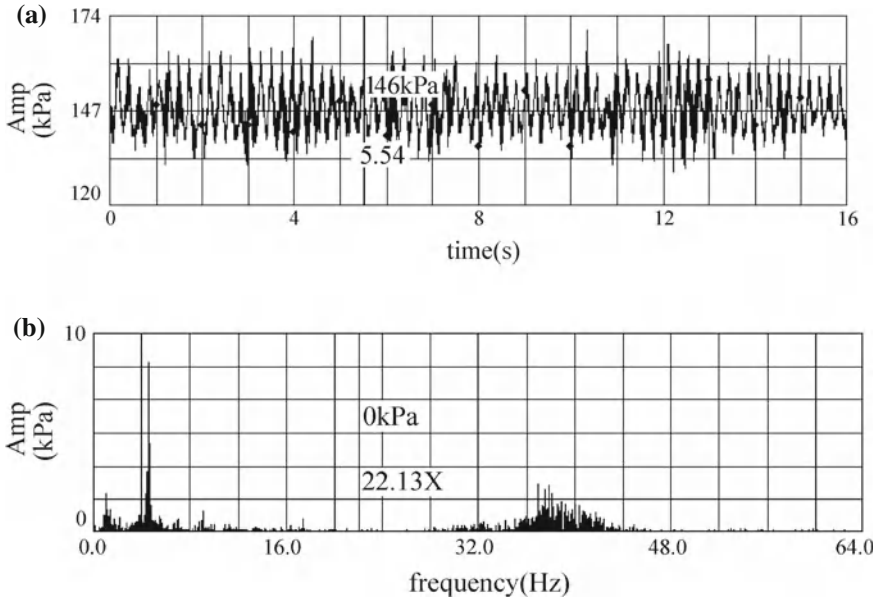

Fig. 11.9 Draft tube pressure pulse on inlet section at downstream side. **a** Waveform. **b** Frequency spectrum

frequency of the head cover will increase. From the above analysis it can be drawn that this unit should avoid operation at a load between 534 and 550 MW under the head 67 m, and at the load of 566 MW larger under the head 71 m because of the large vibration amplitude of the head cover of the turbine.

11.4.4 Instability Operation Condition of the Unit

For this hydro turbine generating unit in accordance with changes in working conditions, the running data implies that at the current running head, in a certain area of load, the vibration and the swing have a noticeable low-frequency signal, among which the swing signal is particularly evident. At the same time the pressure pulsation in the draft tube has also shown an obvious increase.

By analyzing swings of the unit's guide bearings with power changes in waterfall chart, one can see that a great amount of swing amplitude with very low-frequency components exists when the active power in the unit is between 280 and 410 MW. See an example of the upper guide bearing in Fig. 11.12. In the meantime, this situation also can be observed in Fig. 11.13, a waterfall chart of pressure pulsation in a draft tube in the same power region.

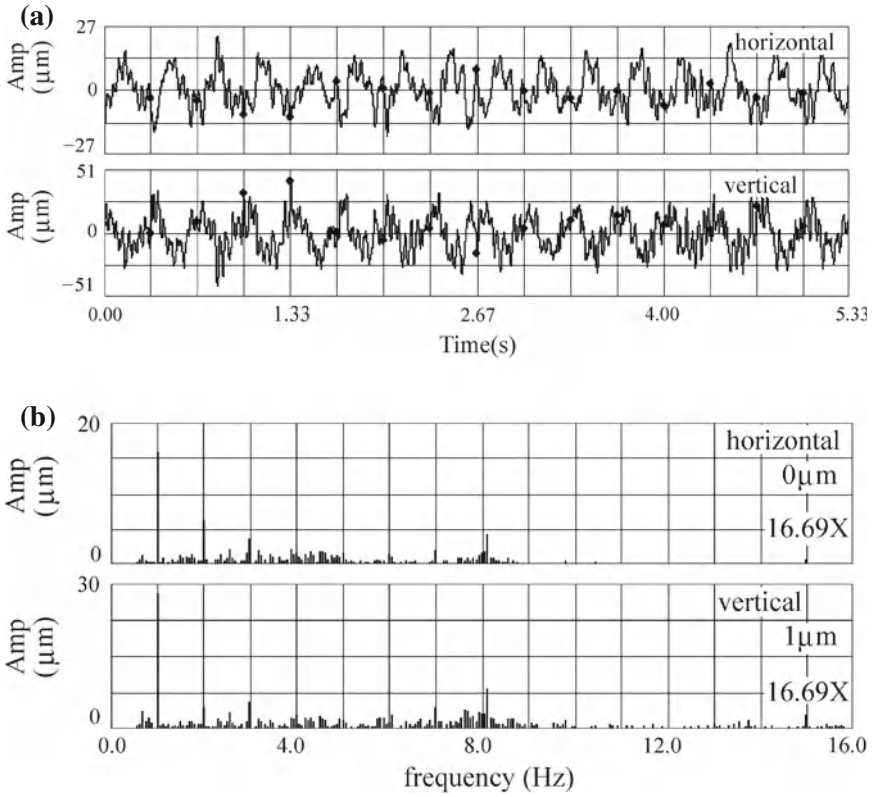

Fig. 11.10 Head cover vibration values at normal operation condition. **a** Waveform. **b** Frequency spectrum

At a select working condition with 68 m head and 315 MW power within the operation scope, further analysis of the conditions of the guide bearing swing (Fig. 11.14 for UGB) and of the draft tube pressure pulsation (Fig. 11.15) illustrates that the signals of the swing and pulsation have the main frequency 0.31 Hz, one-fourth of rotating frequency. This is the frequency of a vortex type in the draft tube with an amplitude 45 kPa and relative value of 6.72 %. This is the high draft tube pressure pulsation region in the operation range. The unit therefore should avoid running in the active power range between 280 and 410 MW.

11.4.5 Regional Division of the Unit Safe Operation

With the accumulation of data, analyses of the characteristics of each condition will result in the unit operation regional division, as shown in Fig. 11.16. In this picture,

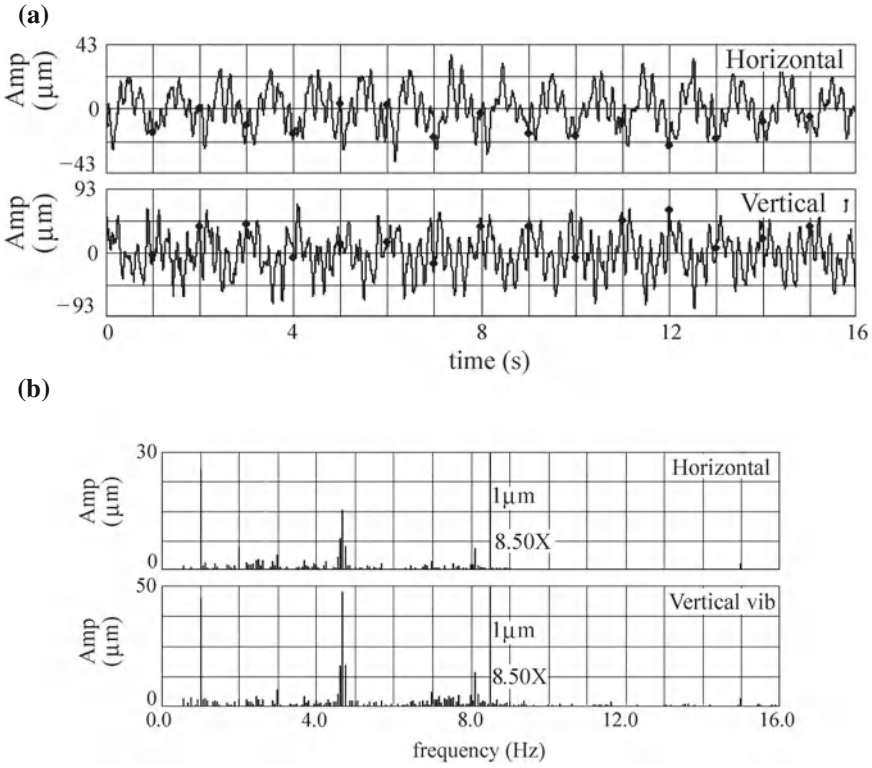

Fig. 11.11 Head cover vibration alarm value at 71 m water head. **a** Waveform. **b** Frequency spectrum. The horizontal vibration maximum frequency and amplitude: 1.25 Hz and 26 μm, the second maximum frequency and amplitude: 5.06 Hz and 15 μm; and the vertical vibration maximum frequency and amplitude: 5.06 Hz and 48 μm, the second maximum frequency and amplitude 1.25 Hz and 45 μm

the unit can be running in the green region for safe operation, and in the yellow region during the transitional operation, but avoid operation in the orange region.

11.5 Condition Monitoring System of Pumps

Vibration monitoring can identify a number of potential pump problems, including misalignment or coupling issues, mechanical looseness inside the pump or from the baseplate, cavitation issues and erosion of rotors identified as imbalanced. Pumping of heavy, viscous fluids can inflict damage to the rotors, which in turn could result in the pump going out of balance. Wear of gear teeth on gear pumps can also be monitored effectively by vibration analysis systems (Hartigan 2008).

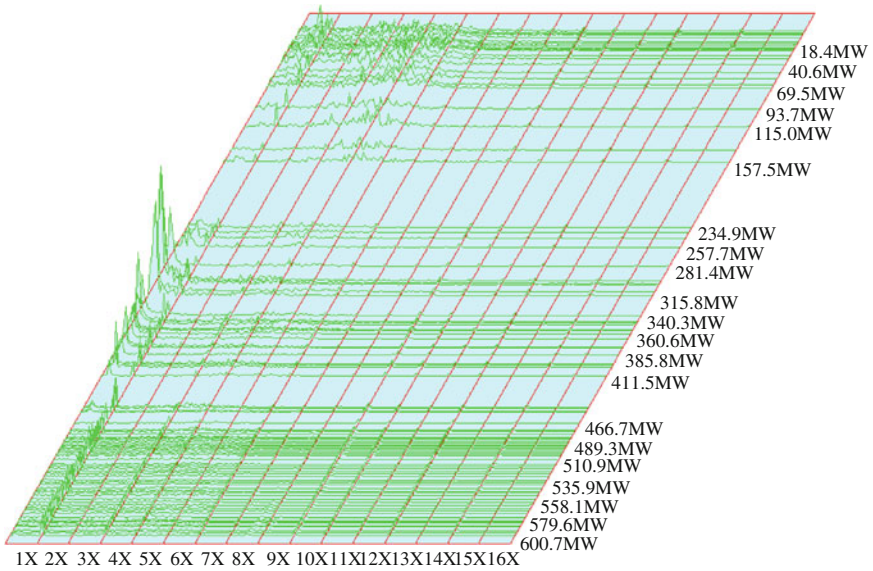

Fig. 11.12 Swing waterfall chats at upper guide bearing (UGB)

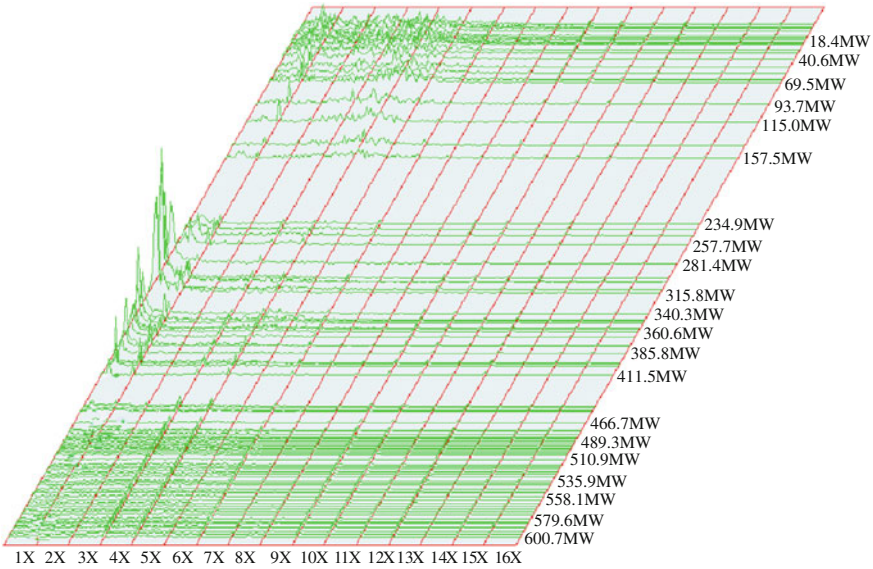

Fig. 11.13 Waterfall chart of draft tube pressure pulsation

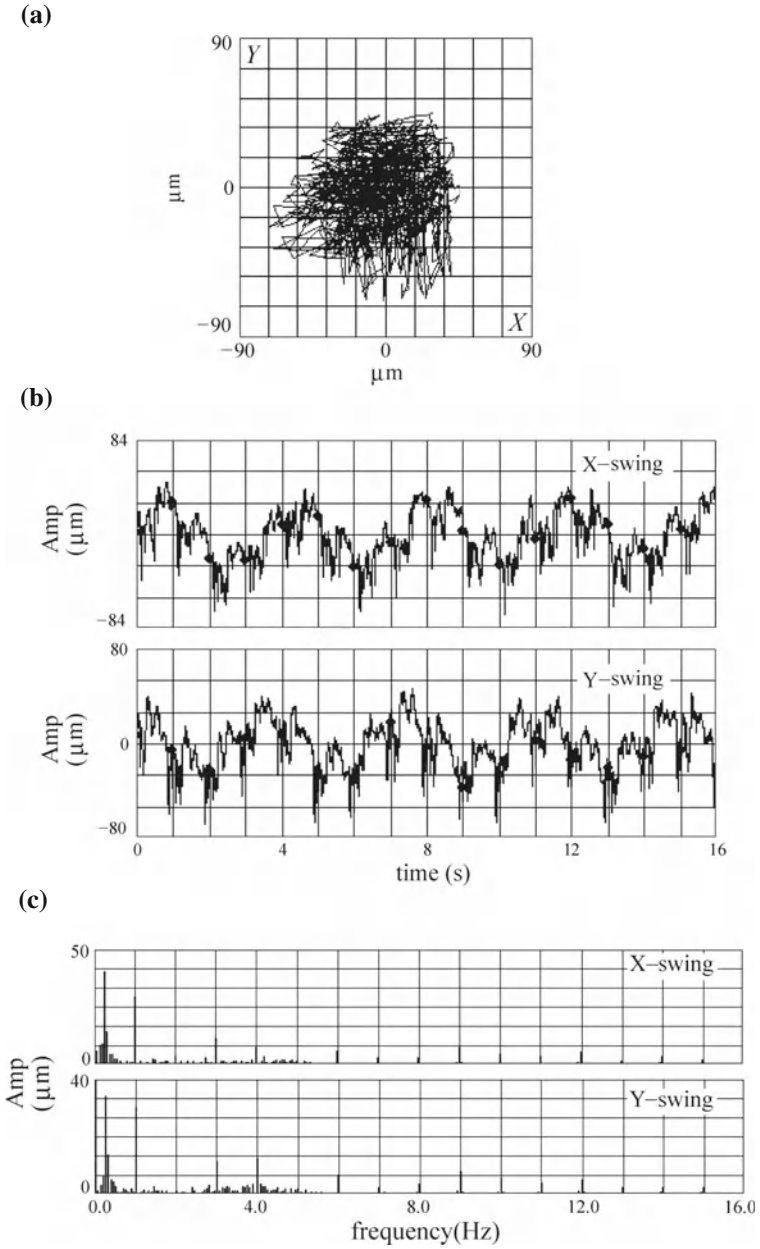

Fig. 11.14 Waveform and spectrum of swings at UGB. X-swings: Maximum frequency and amplitude: 0.31 Hz and 41 µm, Second maximum frequency and amplitude: 1.25 Hz and 30 µm; and Y-swings: Maximum frequency and amplitude: 0.31 Hz and 35 µm, Second frequency and amplitude 1.25 Hz and 30 µm **a** swing trajectory. **b** swing displacements **c** swing frequency spectrum

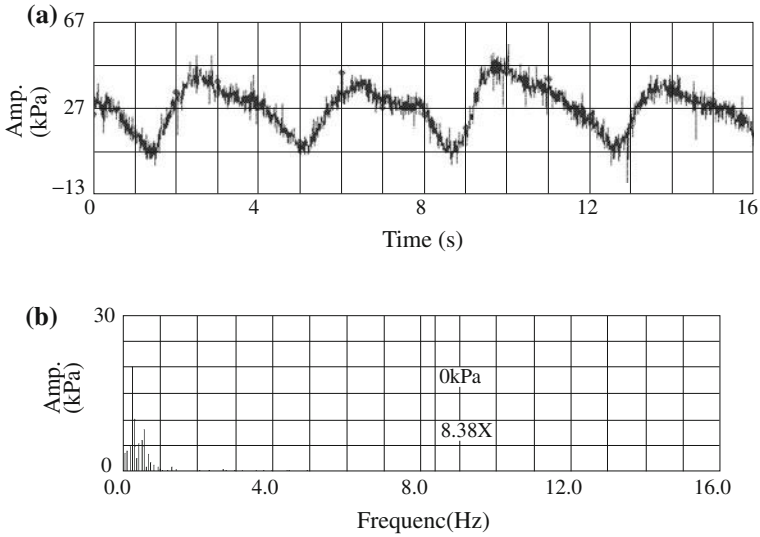

Fig. 11.15 Draft tube pressure pulse waveform and spectrum (Maximum frequency and amplitude: 0.31 Hz and 20 kPa, Second maximum frequency and amplitude 0.39 Hz and 10 kPa). **a** Waveform. **b** Frequency spectrum

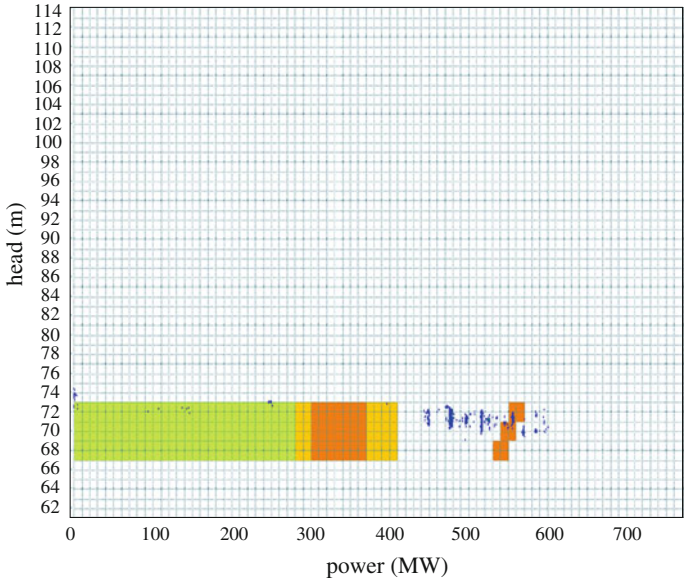

Fig. 11.16 Unit operation regional division and operating conditions

11.5.1 Vibration Monitoring System of Oil Pumps

In order to avoid invalidation troubles of an oil pump, the most valid measure was taken for its vibration monitoring and malfunction diagnosis. Liang et al. (2008) introduced the development of the oil pump vibration monitoring system (Fig. 11.17). The pump was used in first stop of a long-distance pipeline for refined oil with the following rated parameters: power $P = 1{,}000$ kW, speed $n = 2{,}980$ rpm, pump head $H = 320$ m, the flow $Q = 1{,}025$ m^3/h, impeller series 2.

11.5.1.1 Vibration Monitoring Equipment Selection and Installation

A schematic diagram of the monitoring system is shown in Fig. 11.17. In each bearing seat as close as possible, the HG-3518 vibrometer-based data acquisition system is installed to measure the parameters of acceleration, speed, displacement, temperature and so on. Taking into account the high pressure of the pump, the thrust will become a considerable asset if the internal gap in the thrust bearing vanishes, so it is needed to install the vibrometer, a temperature indicator, and an alarm in the thrust bearing.

Measuring points are shown in Fig. 11.18. The vibrometer is installed on major equipment and axial bearing end point. For the horizontal-type pump, the vibration monitors are installed on the four bearing sets to pick up data of vibrations along the vertical, horizontal and radial directions. Application of the eight confirmed groups of the peak/carpet values of vibration velocity and acceleration integrated together can easily find a major fault.

According to international standard ISO 2372, in the speed range of 600–1,200 r/min of a rotating machine, the vibration frequency should be 10–1,000 Hz. In normal operation of pump units with power 75 kW or more, the vibration velocity detected should be 4.5–11.2 mm/s. If the value surpasses 7.1 mm/s, then the machine should be considered in overhaul. In addition to machine power, other factors such as continuous heavy operation and the need for high security and reliability should also be taken into account for this value determination.

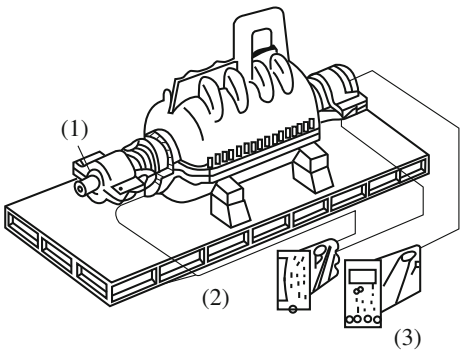

Fig. 11.17 Centrifugal pump vibration monitoring system. *1* Seniors on bearing shell, *2* one or two channels vibration monitor, *3* temperature and displacement sensors on thrust bearings

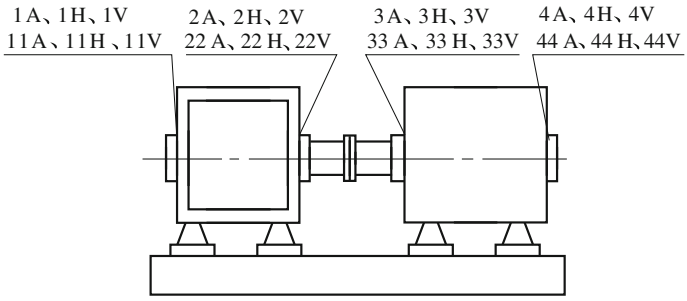

Fig. 11.18 Layout of measuring points

11.5.1.2 FFT Spectrum Analysis

In the data analysis, the Fast Fourier Transform (FFT) is used to get the amplitude spectrum. Amplitude spectrum can provide diagnostic information in the following aspects: (1) which frequency components and harmonic components compose the vibration signal; (2) which component has the highest amplitude.

In this vibrometer system, on each shaft support section, the vibration signals along vertical and horizontal directions are picked up and at the same time a comparison of these data with the frequency spectra at the normal condition is performed. Finally the fault position of the pump unit can be diagnosed.

11.5.2 Vibration Monitoring and Fault Diagnosis on Boiler Feed Pump

The boiler feed pump (BFP) in a fossil fuel station is one of the most important equipment in the unit set; its failure may result in disastrous consequences. It is of great importance to study the vibration monitoring technique of the BFP and improve the reliability of BFP operation. Based on the vibration characteristics of BFP system, (Chen et al. 1995) took the BFP of a 200 MW generator set as the research target and studied the predictive maintenance system of vibration monitoring.

11.5.2.1 Boiler Feed Pump Monitoring System and Data Analysis

The studied pump is a multistage barrel casing centrifugal type with speed regulation. In the monitoring system, accelerometer-typed sensors are installed at the survey points in each bearing pedestal to record vibration along three directions, the axial, horizontal, and vertical directions, shown in Fig. 11.17. Boiler feed pump failure usually appears at amplitude's obvious peak for a vibration

Table 11.9 Boiler feed pump vibration bands and corresponding fault

Item of band	Scope of band	Corresponding fault
Subharmonic band	2 Hz–0.9 rpm	Low-frequency hydrodynamic, lubricating film oscillation
1st order band	0.9–1.1 rpm	Dynamic imbalance, shaft thermal bending
2nd order band	1.1–2.1 rpm	Shaft misalignment, shaft crack
High-order harmonic (>2 rpm) including blade passing frequency	2.1–10.1 rpm Blade No. × rpm	Mechanical loosening, larger hydrodynamic shock pulse at exit
High-frequency band	1–20 kHz	Cavitation

Table 11.10 Recommended values of early warning and alarm (cm/s)

Band	Feed pump		Hydraulic coupling	
	Warning	Alarm	Warning	Alarm
Subharmonic band	0.127	0.138	0.381	0.635
1st order band	0.508	0.889	0.635	1.016
2nd order band	0.381	0.635	0.508	0.889
High-order harmonic band	0.254	0.508	0.635	1.270
Wide-band	0.508	0.889	0.763	1.270

component with frequency 0–10 times the rotating speed in rpm (expressed as 0–10 rpm). Detection of boiler feed water pump mechanical problem lies in dividing vibration bands of the pump into several bands with each band corresponding to a single or a class of faults. The pump monitoring band and its corresponding fault type are shown in Table 11.9.

It is difficult for the full-level vibration analysis method to detect the early stages of mechanical failure. Usually only when the machine is at the condition with very serious problem, the vibration level would exceed the warning value. Through frequency spectrum analysis of the vibration signals, the spectral band vibration alarm level was introduced for diagnosis of boiler feed pumps, as shown in Table 11.10.

11.5.2.2 Data Processing

The vibration band spectrum formula for the level of amplitude is

$$OA = \frac{\sqrt{\sum_{i=1}^{n} F_i^2}}{\sqrt{N_{BF}}} \tag{11.8}$$

where OA is the band vibration level; n is the number of frequency bands within the spectrum; F_i is the spectrum value; and N_{BF} is the noise bandwidth of a selected window function. Select Hanning window function, that is, $N_{BF} = 1.5$ so that

$$OA = 0.8165\sqrt{\sum_{i=1}^{n} F_i^2} \ (i = 1, 2, \cdots n) \tag{11.9}$$

According to the calculated vibration spectrum band level, further spectral analysis of the suspicious vibration band will lead possible causes of pump system faults.

11.5.2.3 Vibration Analysis of Boiler Feed Pump System

As the boiler feed pump vibration is mainly in the range of 0–10 rpm, after integration and high-frequency components flitting of the acceleration the band spectral analysis is computed, the vibration levels of velocity amplitude will be obtained to diagnose the pump faults.

In calculating the velocity spectrum, the anti-alias filter cut-off frequency is $f_c = 10 \times$ rpm/60; sampling frequency is $f_s = 2.5bf_c$ for the amplitude spectra obtained. Figures 11.19, 11.20, and 11.21 are the axial velocity spectrums on the pump bearing at the speed of 2,200, 1,500, and 1,100 rpm conditions.

11.5.2.4 Band Analysis of Subharmonic Frequency

From the three velocity amplitude spectra, among the sub-harmonic frequency bands 2 Hz–0.9 rpm, the low frequency vibration is large. Through test simulation, the larger low-frequency component is not due to the integrator, nor is it due to smaller sampling number. From the order analysis of synchronous sampling, it is not caused by lubricate film oscillation. Based on field experience, the

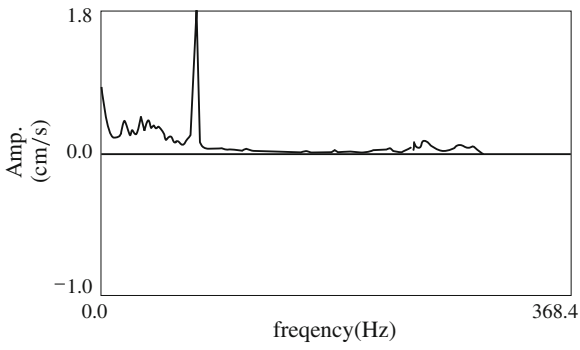

Fig. 11.19 Velocity spectrum along axial direction at 2,200 rpm case

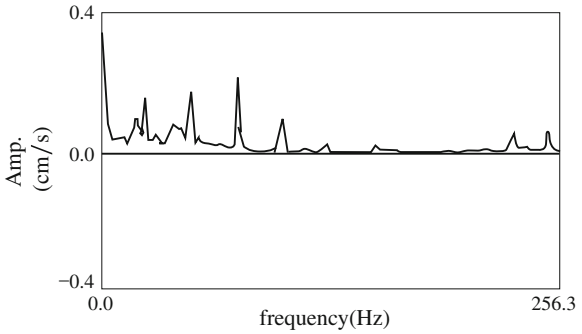

Fig. 11.20 Velocity spectrum along axial direction at 1,500 rpm case

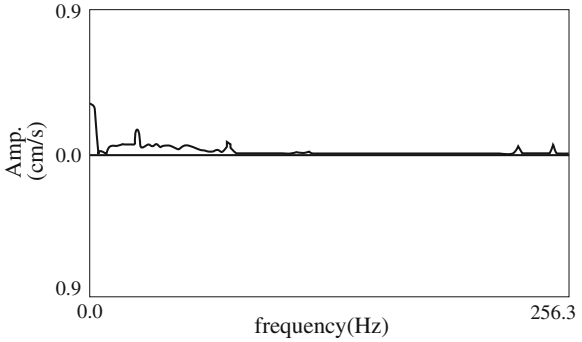

Fig. 11.21 Velocity spectrum along axial direction at 1,100 rpm case

low-frequency vibration is induced by hydraulic forces. Firstly due to improper assembly of the machine in site, it then results in an excessive eddy current and low frequency recirculation of internal flow in the pump. The second is because of the lower pressure at the pump entrance, while each impeller action results in an unequal pressure head at each stage of pump, creating the axial directions vibration with low frequency. The third one is from the high-pressure water flow from pump impeller out to casing and exit tube to form the low frequency interfering flow.

It can be concluded from the above analysis, that the spectral analysis of band-level vibration is very effective, and significantly better than the RMS level analysis.

11.5.3 Monitoring Abnormality in the Reactor Coolant Pump

An improved method to detect the reactor coolant pump (RCP) is suggested by Jung and Seong (2006), in which the Wigner–Ville Distribution (WVD) is used to diagnose abnormality of the pump.

11.5.3.1 RCP Abnormality Monitoring System Using WVD

The overall scheme of the RCP abnormality monitoring method was presented by Jung and Seong (2006). The motor torque was estimated by a three-phase voltage and current. The harmonic components of line frequency were modulated in the frequency spectrum of a single phase current. Torque is a function of current and voltage, so the modulation effect due to harmonic components of line frequency can be eliminated. The WVD of motor torque is beneficial in discerning weak characteristic harmonic components from the line and its harmonic frequencies.

11.5.3.2 Validation of the Proposed Method

For validation of the proposed method, the cross-comparison of test results between RCP vibration monitoring system (RCPVMS) and the power line signal analysis method was performed, and the polar plot of RCPVMS was measured during the cool-down phase. This plot is useful to confirm the weight balance of the shaft, resonance of the RCP structure, looseness, or cracks within the internal components. It indicates the phase and amplitude of the shaft vibration when the pump speed increase.

Figure 11.22 shows the impeller looseness phenomena. The increase of vibration amplitude along with shaft 1 × phase shifted to the opposite direction (180°) as time passed. As a result, the RCP internal components were replaced: pump seal, shaft, and impeller during an overhaul outage.

The power line signal was acquired from the switchgear room inside the turbine building. The three-phase voltage was acquired from a secondary tap of the potential transformer (PT) and the three-phase current was obtained from a current transformer (CT) output to a protection relay. This hook-up permits non-intrusive measurement and assures continuation of plant operation.

Figure 11.23 exhibits the three-dimensional plot of RCP condition before and after its components were replaced. Amplitude of the harmonic frequencies after

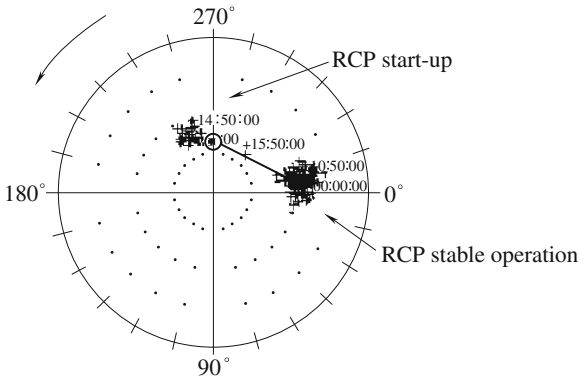

Fig. 11.22 Polar plot of VMS (before RCP replacement; Jung and Seong 2006)

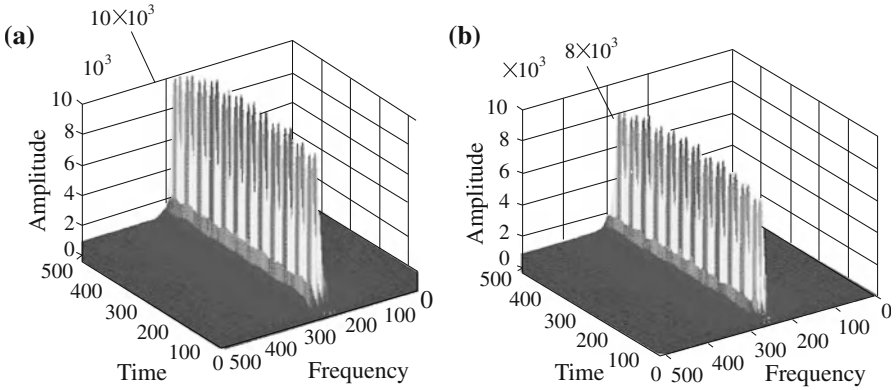

Fig. 11.23 Three-dimensional plot of WVD analysis result (Jung and Seong 2006). **a** Before maintenance. **b** After maintenance

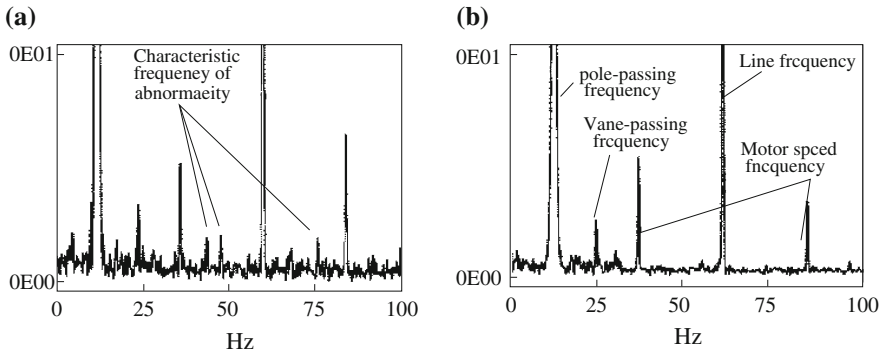

Fig. 11.24 Spectrum of RCP motor current (Jung and Seong 2006) **a** before maintenance. **b** aftermaintenance

replacement was reduced by more than 20 %. This illuminates that the pump condition is improved after maintenance.

The feature vector is 512 × 512 (frequency time) so the data generated in one measurement period is 262, 144. By conditional branching logic (if-then rule), (7450) samples (i_{read}) are extracted.

After RCP maintenance, the average feature area is decreased. The difference between the average feature areas before and after RCP maintenance is greater than 27 %. It is obvious that the RCP is in the healthy state due to components replacement and corrective action during overhaul-outage. For verification of this result, FFT spectrum from 0 to 100 Hz is investigated.

The frequency spectrum in Fig. 11.24 shows the characteristic harmonic components and also indicates that the abnormality is eliminated after the RCP maintenance (see Fig. 11.24b). The feature frequency that represents the shaft

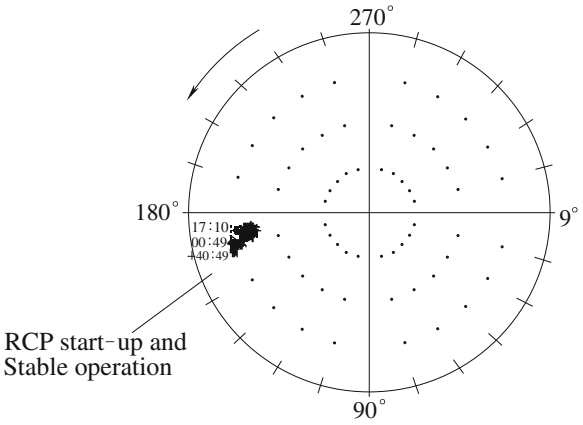

Fig. 11.25 Polar plot after VMS maintenance (Jung and Seong 2006)

speed is also reduced. Weak characteristics of harmonic frequencies appear in the frequency spectrum before RCP components were replaced (see Fig. 11.24a). These harmonic frequencies are due to the RCP impeller movement.

The polar plot that was captured after the pump's internal replacement does not show any symptom of abnormality as shown in Fig. 11.25 (Jung and Seong 2006).

Koo and Kim (2000) set a similar system of abnormality monitoring on RCP. They introduced a Wigner distribution (WD) to a vibration monitoring for analyzing signals, and developed an on-line diagnostic method using the neural network.

11.6 Orbit and Vibration of Hydro Unit Shaft at Transient Process

According to the rules of the rotate-speed change of hydraulic turbines during transient process, the method of intercepting data should be put forward, because data collection is not included in the process of signal. Combining spectral analysis with analysis of the shaft orbit, Li (2006) conducted a study on vibration and pressure pulsation at the start-up process of one hydro turbine generating unit at the Xiaolangdi Hydropower Station based on the monitoring data of the unit.

11.6.1 Measuring Points in the Unit Monitoring System

The test was carried in a unit of Xiaolangdi Hydropower Station, at 87 m head during the start-up transient process condition and the stable condition with 107.14 rpm (1.785 Hz), based on monitoring system of the unit. It measured the noise, vibration (vib.), and water pressure on generators' upper rack (UR) and

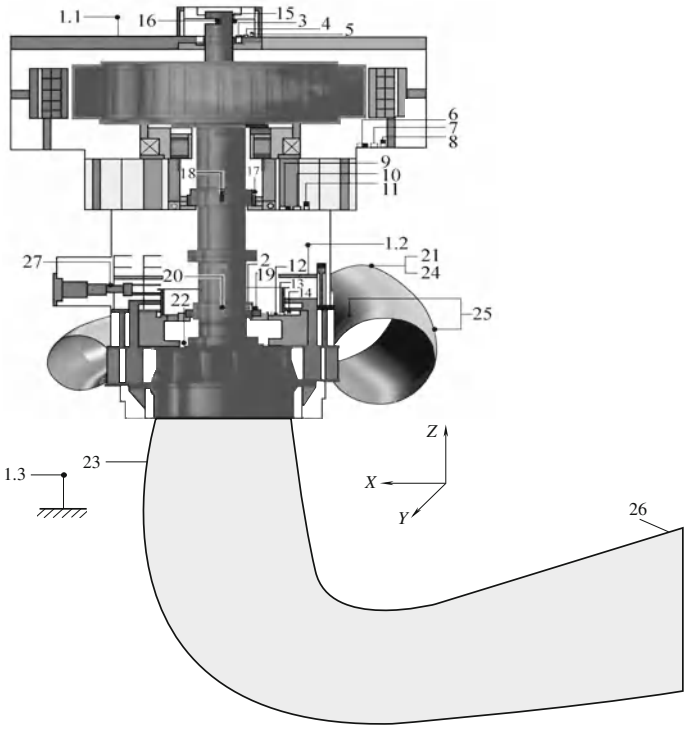

Fig. 11.26 Measuring points of hydro unit at Xiaoliangdi power station

lower rack (LR), on the head cover (HC), stator core (SC), draft tube (DT) and spiral casing (SC), as well as the swings on the upper guide bearing (UGB) and LGB and TGB and so on. In the start-up transient process, the unit speed variation was also measured. The measuring points of the unit are shown in Fig. 11.26, where the following positions are included: (1.1) generator noise, (1.2) HC noise, (1.3) DT noise, (2) speed (phase reference), (3) UR horizontal *X*-vib. (4) UR horizontal *Y*-vib. (5) UR vertical *Z*-vib. (6) SC horizontal *X*-vib. (7) SC horizontal *Y*-vib. (8) SC vertical *Z*-vib. (9) LR horizontal *X*-vib. (10) LR horizontal *Y*-vib. (11) LR vertical *Z*-vib. (12) HC horizontal *X*-vib. (13) HC horizontal *Y*-vib. (14) HC vertical *Z*-vib. (15) UGB horizontal *X*-swing. (16) UGB horizontal *Y*-swing. (17) LGB horizontal *X*-swing. (18) LGB horizontal *Y*-swing. (19) TGB horizontal *X*-swing. (20) TGB horizontal *Y*-swing. (21) Pressure pulsation at SC inlet. (22) Pressure pulsation in HC. (23) Pressure pulsation in DT. (24) Pressure at SC inlet. (25) Pressure difference in SC. (26) Pressure at DT exit. (27) Servomotor position.

Table 11.11 Amplitudes at the transient starting-up process

	X-dir.	Y-dir.	Z-dir.
UR vib. (mm)	0.257	0.240	0.0243
LR vib. (mm)	0.0231	0.0448	0.0287
HC vib. (mm)	0.0944	0.242	0.289
SC vib. (mm)	0.0108	0.102	0.0094
UGB swing (mm)	0.233	0.280	
LGB swing (mm)	0.498	0.401	
TGB swing (mm)	0.254	0.0704	
SC pressure pul. (m)	14.0		
HC pressure pul. (m)	26.4		

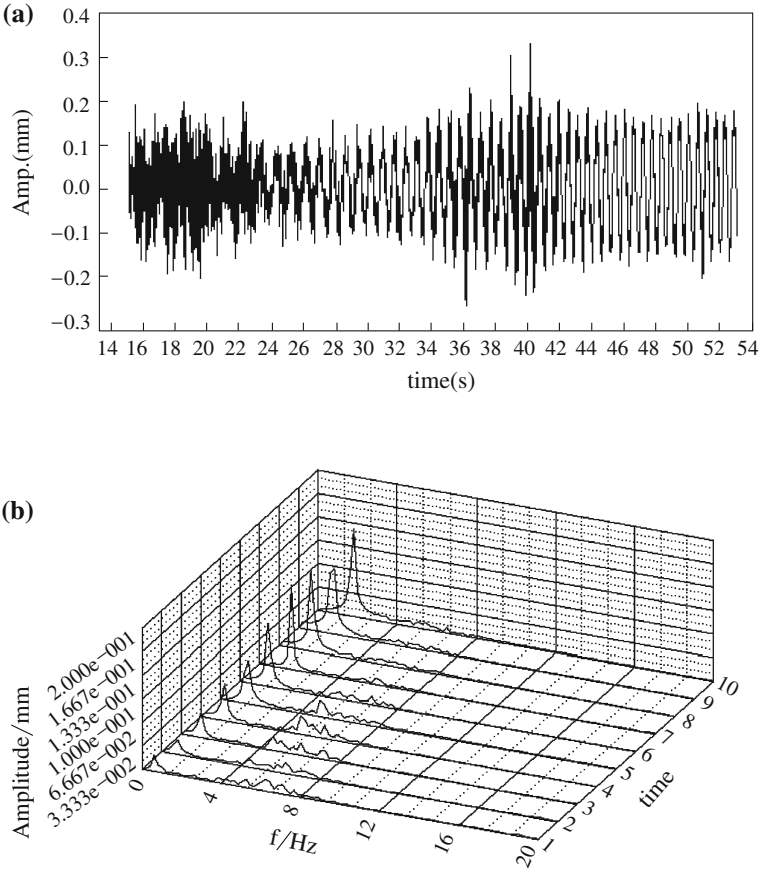

Fig. 11.27 Swing amplitude along *y* direction at LGB during starting-up. **a** Time history. **b** Waterfall chart

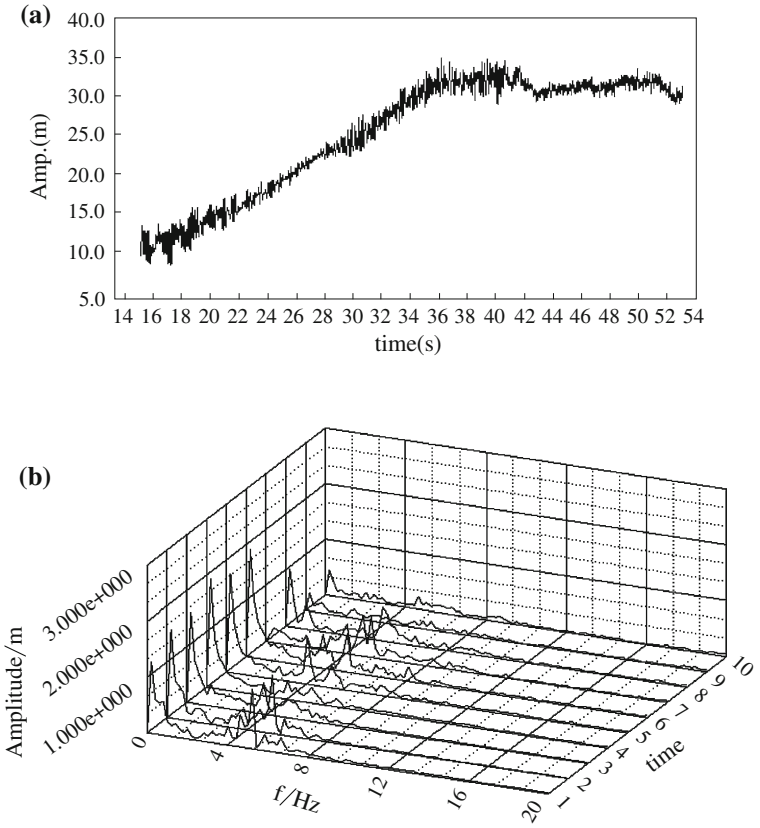

Fig. 11.28 Pressure pulsation in HC during starting-up. **a** Time history. **b** Waterfall chart

11.6.2 Analysis of Signal Amplitude at the Start-Up Process

According to the confidence probability of 0.97, the signal amplitudes at measuring points were recorded in the transient starting-up process of the unit in Table 11.11.

11.6.3 Signal Spectrum Analysis at Measuring Points During the Starting-Up Process

Figure 11.27 is the time history and waterfall chart of the swing amplitude along *Y*-direction at the LGB position during 15–53 s of starting-up process. With an increase of operating time, the amplitude corresponding to rotating frequency will climb gradually. During this period, the swing amplitude corresponding to

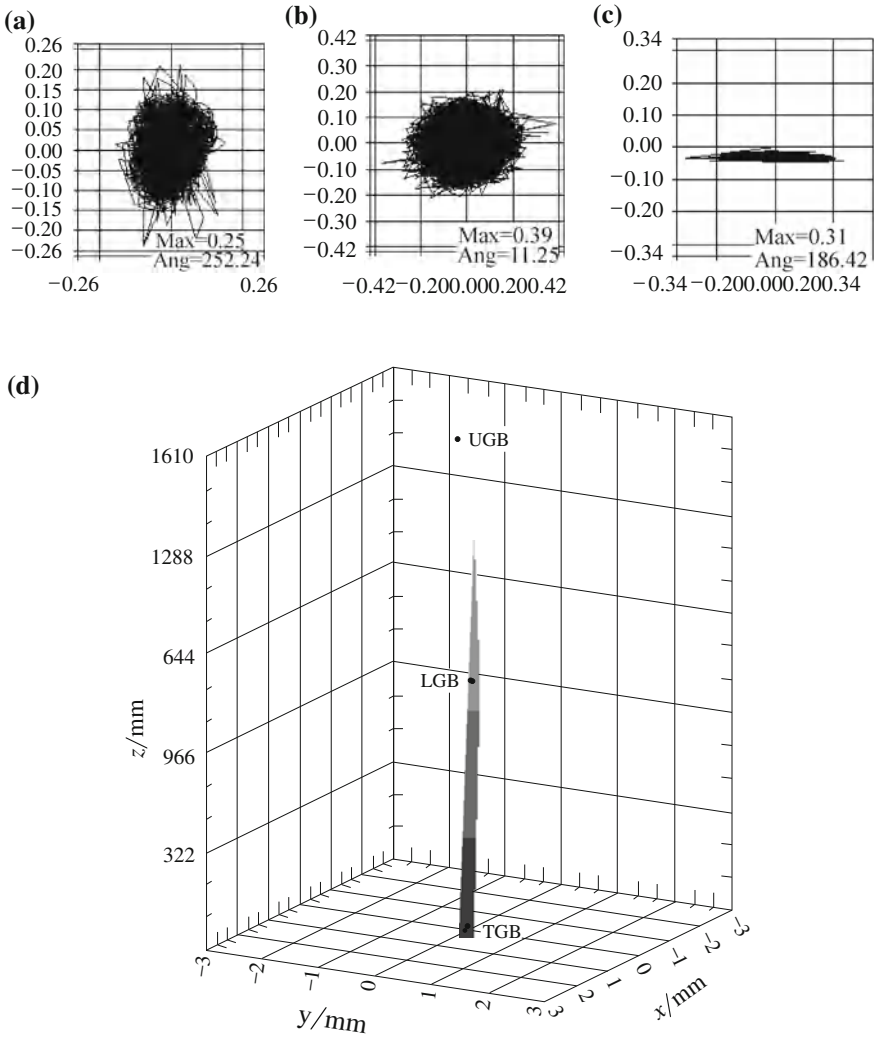

Fig. 11.29 Shaft bearing orbits and axis trajectory at 15–53 s of starting-up. **a** UGB. **b** LGB. **c** TGB. **d** Shaft axis trajectory in space

component with 4–8 Hz frequency is very large, and close to that of component with rotating frequency. It is clear that there is an imbalance mass in the unit shaft system.

Figure 11.28 is the time history and waterfall chart of pressure pulsation in the HC during 15–53 s of starting-up process. The water pressure rapidly increases during this period and finally stabilizes at around 30 m. After 53 s, the pressure pulsation amplitude of each component will gradually decrease.

11.6.4 Shaft Trajectory Analysis During the Start-Up Process

Figure 11.29 shows the shaft bearing orbits and its axis trajectory within 15–53 s in the unit start-up process. After that time, the turbine rotates at a rated frequency of 1.785 Hz. In the start-up transient process within 15–53 s, the maximum eccentric distance (MED) of the UGB is about 0.25 mm, the MED of the LGB about 0.39 mm, and the MED of the TGB is about 0.31 mm. After that time, the MED of bearings are 0.17, 0.29 and 0.16 mm, respectively.

The waterfall picture of swing data collected during the start-up process indicates that the rotor is with mass-unbalance. The orbit analysis of the start-up process demonstrates that the swings of the shaft at the upper guide bearing, lower guide bearing, and turbine guide bearing reach peak value at 22 % rated speed.

References

Boashash, B. (1998). Note on the use of the Wigner distribution for time-frequency signal analysis. *IEEE Transactions on Acoustics, Speech and Signal Processing*, *36*(9).

Chen, X. L., Yan, P. Q., & Wei, W. L. (1995). The vibration monitoring and fault diagnosis on boiler feed pump in fossil power station. *Vibration and impulsion in China, 3*, 7–11.

Cohen, L. (1987). On a fundamental property of the Wigner distribution, *IEEE Transactions on Acoustics, Speech and Signal Processing*, ASSP-*35*(4).

Egusquiza, E. (2007). Vibration behavior of hydraulic turbines, Application to condition monitoring, *Proceedings of 2nd IAHR International Meeting of the WG on Cavitation and Dynamic Problems in Hydraulic Machinery and Systems*, Timisoara.

Egusquiza, E., Liang, Q.W., Escaller, X. And Valero, C. (2006). Condition monitoring strategies in hydro powerplants, *Proceedings of The 1st International Conference on Hydropower Technology and Key Equipment*, Beijing.

Gupta, K. N. (1997). Vibration—A tool for machine diagnostics and condition monitoring. *Sadhana, 22*(3), 393–410.

Hartigan, K. (2008). Inside monitoring to extend pump life. *World Pumps, 502*, 28–30.

Ingegneria, F. D. (2008). Fault detection in rotating machines by vibration signal processing techniques, *Dissertation for Ph. Doctor degree*, Università degli Studi di Bologna, Italy.

Jung, J. C., & Seong, P. H. (2006). An improved method for reactor coolant pump abnormality monitoring using power line signal analysis. *Nuclear Engineering and Design, 236*(1), 57–62.

Khemili, I., & Chouchane, M. (2005). Detection of rolling element bearing defects by adaptive filtering. *European Journal of Mechanics A/Solids, 24*, 293–303.

Koo, I. S., & Kim, W. W. (2000). The development of reactor coolant pump vibration monitoring and a diagnostic system in the nuclear power plant. *ISA Transactions, 39*(3), 309–316.

Li, J. (2006). Analysis of orbit and vibration along shaft at low flow rate case of hydropower unit. *Dissertation of Master Degree on Engineering*, Tsinghua University in China.

Liang, F. H., Huang, Y. X., & Deng, Y. (2008). The vibration monitoring and malfunction diagnosis of the oil—pumps in the oil—pipeline. *Journal of Maoming University in China, 18*(4), 36–39.

Tranter, J. (1989). The fundamentals and the application of computers to condition monitoring and predictive maintenance, *Proceedings of International Congress on Condition Monitoring and Diagnostic Engineering* (COMADEM 1989). pp. 372–377.

Tandon, N., & Parey, A. (2006). *Condition monitoring of rotary machines, Condition monitoring and control for intelligent manufacturing* (pp. 109–136). London: Springer.

Wahl, T. J., & Bolton, J. S. (1993). The application of the Wigner distribution to the identification of structure borne noise components. *Journal of Sound and Vibration, 163*(1), 101–122.

Wikipedia, http://en.wikipedia.org/wiki/Cepstrum.

Zhu, Y. (2006). Study on Stability of Large Francis Turbine, Master degree thesis, Tsinghua University in China.

Appendix I
Nomenclature

1. Latin Letters

A	Amplitude, area, section area of draft tube
A_r	Turbine gain factor
$\bar{A}$	Relative amplitude
$[\boldsymbol{A}]$	"Stiffness" matrix in FEM
$[\boldsymbol{A}]$, $[\boldsymbol{B}(\boldsymbol{X})]$	State global matrices
$[\widetilde{A}]$	Dynamic matrix
a	Complex amplitude, sound speed in water, distance between upper bearing and disc mass centre (Fig. 4.2.1) opening of guide vanes
$a_i(t)$	Generalized coordinates
$\{\boldsymbol{a}\}$	Unit direction vector, amplitude vector, vector containing generalized coordinates
B	Relative frequency of $f_{k,}$ amplitude, Greitzer's factor
$\hat{B}$	Average magnetic flux density
$\{\boldsymbol{B}\}$	Right vector in FEM
$[\boldsymbol{B}]$	Compliance matrix
$[B(x,y,z)]$, $[B]$	Matrix with derivatives of shape functions
$[\tilde{B}]$	Input gain matrix
b	Mean sealing gap width
b_2	Pump impeller exit width
C	Constant, capacitance, cavitation compliance,
C	Mean velocity in a section
C_H	Head coefficient $C_H = gH/N^2d^2$
C_h	Hydraulic capacitance
C_Q	Flow coefficient $C_Q = Q/N\mathrm{d}^3$
C_{QM}	Operation dimensionless relation of turbine
$C_{M\alpha}$	Damping of oil film created by thrust disc swing
C_{xy}, C_{yx}	Cross-damping coefficient reflecting oil film

Y. Wu et al., *Vibration of Hydraulic Machinery*,
Mechanisms and Machine Science 11, DOI: 10.1007/978-94-007-6422-4,

C'	Lineic hydroacoustic capacitance $C' = gA/a^2$
C'_e	Electrical capacitance of unit length
$[\boldsymbol{C}]$	Damping matrix
$[\tilde{\boldsymbol{C}}]$	Output gain matrix
$\{\boldsymbol{C}_i\}$	Constraint force
c	Damping coefficient, wave speed in fluid
c_i	Constants defining $w(\boldsymbol{x})$
c_n	Non-rotating damping coefficient
c_r	Rotating damping coefficient
c_{xxi}, c_{xyi}, c_{yxi}, c_{yyi}	Damping factors of the ith pad
$c_{\theta 2}$	Swirl velocity
D	Damping coefficient, per unit load damping constant, character diameter of runner
D_1	Runner exit diameter at band
D_e	Draft tube inlet diameter
$[\boldsymbol{D}]$	Transfer matrix
$[\tilde{\boldsymbol{D}}]$	Matrix describing influence of inputs on outputs
d	Radius of long circular cylinder, turbine characteristic diameter
E	Young's modulus, output of turbine
E_c	Young's modulus for cable
E_r	Relative internal energy
E_{nD}	Unit energy coefficient
E_{pipe}	Pipe wall material viscoelastic behavior
E'	Transient electric potential of generator
$[\boldsymbol{E}]$	Stiffness matrix of material, Green-Lagrangian strain tensor
e	Base of exponential function
$\boldsymbol{e}_x$, $\boldsymbol{e}_y$	Unit vectors along x and y axes
e	Constant, eccentric distance of vortex rope
$\{\boldsymbol{e}\}=\{\theta_y, \theta_x, y\}^{\mathrm{T}}$	Displacement vector
F	Force
F_0	Radial force
F_D	Damping force
F_{ex}	External force
F_i	Spectrum value
F_k	Restoring force
F_{sm}	Amplitude of stator magnetic potential
F_{jm}	Amplitude of rotor magnetic potential
F_x F_y	Forces of oil film on xoz and yoz planes
F'_{sx} F'_{sy}	Unbalanced force
$F(w)$	Energy functional
$\{\boldsymbol{F}_{dn}\}$	Force due to non-rotating damping
$\{\boldsymbol{F}_{dr}\}$	Force due to rotating damping

$\{\boldsymbol{F}_e\}$	Elastic force
$\{\boldsymbol{F}_i\}$	Applied forces
$\{\boldsymbol{F}_n\}$	Force due to no-rotating damping, static load
$\{\boldsymbol{F}_{rxy}\}$	Force due to rotating damping in xy-plane
$\{\boldsymbol{F}_{r\xi\eta}\}$	Force due to rotating damping in $\xi\eta$-plane
$\{\boldsymbol{F}\sigma\}$	Loading vector caused by initial stresses at nodes
$[\boldsymbol{F}]$	Deformation gradient tensor
f	Unit external force, giving force in domain electric net frequency, cross-sectional area
f_0	Natural vibration frequency in draft tube
f_i	Generalized forces
f_b	Blade passing frequency
f_g	Guide vane passing frequency
f_k	Karman vortex street frequency
f_{oil}	Self-excitation frequency of oil film in bearing
f_{p2}	Per unit tunnel head loss coefficient
f_S	Stay vane passing frequency
f_n	Precession frequency of vortex rope, per unit head loss coefficient
f_r	Ratio of precession frequency
f_{rope}	Frequency of vortex rope
f_v	Frequency of pressure pulsation by vortex rope
f_{wh}	Hydraulic vibration frequency in penstock
f_x	Component along x axis of force
f_y	Component along y axis of force
$f(x, t)$	Function at Eulerian coordinates
$f^*(x, t)$	Function at reference coordinates
$f^{**}(x, t)$	Function at Lagrangian coordinates
$\{\boldsymbol{f}(x, y, z, t)\}$	Giving force vector
$\{\boldsymbol{f}\}$	Unit external force vector, body force
$\{\boldsymbol{f}^s\}$	External force of structure
$\{\boldsymbol{f}_g\}$	Body force in global frame in FEM
$\{\boldsymbol{f}(t)\}$	Forcing function
$\{\boldsymbol{f}(\sigma_f)\}$	Surface deformation due to fluid loads
$\{\boldsymbol{G}\}$, $\boldsymbol{G}$	Gravity force vector
G	Gravity force magnitude, shear modulus
G_x, G_y, Gx, Gy	Turbulent factor of oil
G^{ij}	Components of contravariant metric tensor
$\bar{G}$	Per-unit guide vane opening
$[\boldsymbol{G}]$	Skew-symmetric gyroscopic matrix
g	Gravity acceleration, giving condition on Neumann boundary
$\{\boldsymbol{g}\}$	Given function in flow on Dirichlet boundary
$\{\boldsymbol{g}(\boldsymbol{x}_s)\}$	Change of fluid stress from surface deformation

$\{\boldsymbol{H}\}$	Moment vector
$[\boldsymbol{H}]$	Skew-symmetric circulatory matrix with rotating, damping
H	Water head, chamber height of turbine, inertia constant of shaft
H_r	Relative total enthalpy (rothalpy)
H_n	Normalization helicity
$\bar{H}_0$	Per unit total head
$\bar{H}_{12}$	Per unit head loss in the tunnel
$\bar{H}_l$	Per unit head loss in the penstock
$\bar{H}_r$	Per-unit surge tank head
$\bar{H}_t$	Per-unit turbine head
ΔH	Pressure fluctuation amplitude
h	Thickness of oil film, piezometric head, distance between two rows of vortices, gap clearance
$h(t_1, t_2)$	Impulse response of a linear system
h_n	Oil film thickness at pad pivot
$\{\boldsymbol{h}\}$	Given function in flow on Neumann boundary
I	Phase current of generator
$\{\boldsymbol{I}\}$	Unit vector
$[\boldsymbol{I}]$	Identity tensor (diagonal unit matrix)
Im	Imaginary part
i	Imaginary number
i	Electrical current
J	Second moment of area, rotational inertia of shaft syste
J_t	Time-dependent Jacobian transversal moment of inertia around axis
$J(t)$	Jacobin in time t
Jp	Torsional moment of inertia polar moment of inertia around rotation axis
$J_{\beta j}$, $J_{\gamma j}$	Pad moment of inertia around pivot in circumferential and axial direction
$J_{di\text{-}1}$, J_{di}, $J_{pi\text{-}1}$, J_{pi}	Moment of inertia per unit length
$k = n - m$	Lag time between stimulus at time m and response at time n
K	Cavitation compliance
K, K'	Factors
$K_{x\beta}$, $K_{y\alpha}$, $K_{M\alpha}$, $K_{M\beta}$	Stiffness of oil film created by thrust disc swing
K_{xy}, K_{yx}	Cross-stiffness reflecting oil film force
$[\boldsymbol{K}]$	Stiffness matrix
$[\boldsymbol{K}_g]$	Stiffness matrix in global frame in FEM
$[\boldsymbol{K}_r]$	Diagonal matrix of stiffness
$[\boldsymbol{K}_{12}]$	Stiffness matrix of air gap magnetic field
$[\boldsymbol{K}_{ss}]$	Matrix of stiffness of structure to structure (FSI)
$[\boldsymbol{K}_{sf}]$	Matrix of stiffness of structure to fluid (FSI)
$[\boldsymbol{K}_{fs}]$	Matrix of stiffness of fluid to structure (FSI)

$[\boldsymbol{K}_{ff}]$	Matrix of stiffness of fluid to structure (FSI)
k	Stiffness, thermal conductivity, fluid volumetric modulus
k, l, m, n	Integers
k_i	Generalized stiffness in FEM
k_0	Efficient of unbalanced magnetic forces
$k_{xxi}, k_{xyi}, k_{yxi}, k_{yyi},$	Damping factors of the ith pad
k^*	Non-dimensional frequency, $k^* = k^*_R + \mathrm{i}\, k^*_I$
$\{\bar{\mathbf{k}}\}$	Rotor vibration eccentric vector
L	Moment, length of bearing, axial length of radial magnetic loop
L_h	Hydraulic inductance
L_u	Impeller loss coefficient
L_x, L_y	Moments of oil film on xoz and yoz planes
L'	Lineic hydroacoustic inductance $L' = 1/(gA)$
L'_e	Electrical inductance of unit length
l	Length of axis (in Fig. 4.2.1), length of penstock
l_i	Direction cosine of the axes x in global frame
l_s	Sealing passage length
$\{\boldsymbol{l}\}$	Torque vector
δL	Virtual work δL
M	Mass, bending moment, mass flow gain factor
M	Mole number of molecular weight
M_2, M_4	Second and fourth-order statistics moment
M, N	Number of sample points
M_x, M_y	Pressure moment on pad around x and y axises
M_{bx}, M_{by}	Bearing bracket equivalent masses along x and y
M_A	Normalized amplitude of pump driving torque
$\{\boldsymbol{M}\}$	Moment vector
$\{\boldsymbol{M}_g\}$	Moment of inertia force
$[\boldsymbol{M}]$	Mass matrix damping, and stiffness matrices
$[\boldsymbol{M}_g]$	Geometric stiffness matrix, mass matrix in global frame in FEM
$[\boldsymbol{M}_y]$	Diagonal matrix of mass
m	Mass, unbalanced mass number of resonance order of water
m_D	Magnetic torque of generator damping winding
m_e	Electro-magnetic torque of generator
m_g	Generator load torque (whole damping torque)
m_i	Direction cosine of the axes y in global frame
N	Number of degrees of freedom
N_{12}	Potential energy in the air gap of generator
N_D	Specific speed
N_{BF}	Noise bandwidth
$NPSH$	Net positive suction head

n	Constant defining $w(\boldsymbol{x})$, frequency of surge, order number of Taylor series, rotating speed of runner, number of frequency bands within the spectrum F_i spectrum value
n_{11}	Unit speed
n_i	Direction cosine of the axes x in global frame
n_{QE}	Unit rotating speed coefficient
$\{\boldsymbol{n}\}$	Unit normal vector
QA	Band vibration level
$O\xi\eta z$	Rotating reference frame
P	Dimension, pressure pair number of generator poles
P	Force acting on the bluff body, turbine output force acting on blade from Karman vortex
P_{11}	Unit power
$P_{r,}\ P_{\varphi}$	Nonlinear active force of bearing pad
$P_N(z,t)$	Pressure excitation
$\bar{P}_{\text{mechanical}}$	Per unit turbine mechanical power
$\bar{P}_{\text{load}}$	Per unit non-frequency-sensitive load
$\tilde{P}_{\text{Erms}}$	Dimensionless pulsation amplitude
Δp	Flow pressure drop
Q	Shearing, flow rate of turbine
Q_{11}	Unit flow rate
Q_{nD}	Unit flow rate coefficient
$\{\boldsymbol{Q}_i\}$	ith generalized force
$\{\boldsymbol{Q}(t)\}$	Generalized forces
q	Amplitude of excitation, modal participation factor
q_i	Generalized displacement in FEM
$q(s_i)$	Cavity region
$\{\boldsymbol{q}\}$	Transformed displacement vector, vectors of coordinates $\{\boldsymbol{q}\} = \{z,\ \boldsymbol{\phi}\}^{\mathrm{T}}$ real coordinates, solution of rotor dynamic equation, for example $\{\boldsymbol{q}\} = \{\boldsymbol{r}_1\}\mathrm{e}^{\mathrm{i}} + \{\boldsymbol{r}_2\}\mathrm{e}^{\mathrm{i}(2\Omega-\omega)t}$
$\{\boldsymbol{q}_i\}$	Displacement vector in FEM
$\{\boldsymbol{q}_g\}$	Displacement vector in global frame in FEM
$\{\boldsymbol{q}_i(x,\ y,\ z)\}$,	Assumed modes
q_i	Eigenvectors component
R	Restoring force magnitude, parameter in disc rotor $2R^2 = J_p/m$, inner radian of the pad, vortex rope radius, viscoelastic resistance
R_a	Resistance of generator armature
R_1	Inner radius of the stator
R_0	Outlet radius of generator rotor
$\mathbb{R}^3$	3 dimensional space
$\{\boldsymbol{R}\}$	Restoring force vector, vector from grid origin to mass particle, concentrated force vector

$[\boldsymbol{R}]$	Rotating matrix (FEM)
$[\mathbf{R}']$	Assembled rotating matrix (FEM)
$[\boldsymbol{R}pq(\mathrm{i}\omega)]$	Vector of transfer functions
Re	Real part
Re	Reynolds number (Fluid Mechanics)
Re_x	Reynolds number based on blade length
R_h	Hydraulic resistance
$R_h = Uh\rho/\mu$	Reynolds number in oil film
R^*	Measure of draft tube core size
R'	Lineic hydroacoustic resistance $R' = \lambda/\left(2gDA^2\right)$
R'_e	Electrical resistance of unit length of conductor
r	Radius, coefficient
r_p	Radial coordinate of pivot in inertial coordinates
$\boldsymbol{r}_1$	Mean inflected shape
$\boldsymbol{r}_2$	Component of deflected shape
$\{\boldsymbol{r}\}$	Vector from grid origin to mass particle, radial vector, position vector, sum vector of internal and external forces/fluxes, set of complex coordinates $\{\boldsymbol{r}\} = \{\boldsymbol{q}\}\mathrm{e}^{\mathrm{i}\Omega t}$
S	Finite dimensional subspace, boundary surface, runner exit area
Sh	Strouhal number
S_n	Constant
S_ϕ	Source term of ϕ
S_{ij}	Mean strain rate tensor
$\bar{S}_{ij}$	Rate-of-strain tensor for resolved scale
$\{\boldsymbol{S}_0\}$	First station vector
$\{\boldsymbol{S}_n\}$	Last station vector
$\{\boldsymbol{S}_{\mathrm{R}i}\}$, $\{\boldsymbol{S}_{\mathrm{L}i}\}$	State vectors at left and right ends of field
$[\boldsymbol{S}]$	2nd Piola–Kirchoff stress tensor
s	Circumferential wavelength, time of stimulus
T	Period, modal responses, torque on a section, torque of the fluid acting on the component, rotating period
T_0	Period
$T(\mathrm{t})$	Torsional torque around the disc center
$\hat{\boldsymbol{T}}_{ij}$	First order of Piola-Kirchhoff stress tensor
$[\boldsymbol{T}]$, $[\boldsymbol{T}_{ft}]$	Transfer matrix
$[\boldsymbol{T}_G]$	Overall transfer matrix
$\{\boldsymbol{T}\}$	External surface forces
T_g	Main servomotor time constant
T_{Wp}	Water starting time of penstock
$\tilde{T}$	Kinetic energy
t	Time, time of response
t_f	The end of time step of CFD
t_s	The end of time step of CSD

t_r	Rise time
Δt	Time Increment
U	Numerical solution voltage, linear velocity, circumferential velocity
U_2	Runner exit peripheral speed
U_a	Steady uniform velocity
$\tilde{U}$	Potential energy
$\bar{U}_c$	Per unit velocity or flow rate in tunnel
$\bar{U}_{NL}$	Per unit no-load flow
$\bar{U}_t$	Per-unit water velocity in turbine or turbine flow
u	Per unit control effort deflection of structure, true solution
u_s, v_s	Steady disturbance
$\tilde{u}$, $\tilde{v}$	Unsteady disturbance
U_j	Curvilinear coordinate
$\boldsymbol{u}$	
$\{\boldsymbol{u}\}$	Deflection of structure real coordinates $\{\boldsymbol{u}\}=\{\mathrm{Re}\{\boldsymbol{q}\}^{\mathrm{T}}, \mathrm{Im}\{\boldsymbol{q}\}^{\mathrm{T}}\}^{\mathrm{T}}$
$\{\boldsymbol{u}\}(x, y, z, t)\}$	Displacement field
$\{\boldsymbol{u}(t)\}$	Inputs vector affecting behavior of system
$\{\boldsymbol{u}_1\}$	General coordinate vector of generator
$\{\boldsymbol{u}_r\}$	"Whirl" velocity
$\{\boldsymbol{u}^*\}$	Generalized coordinates, $\{X, \varphi_{X'}, Y, \varphi_y\}^{\mathrm{T}}$
$\bar{u}$	Vibration mode shape
u_D	Giving condition on Dirichlet boundary
V	Shearing force, solution domain, velocity of main stream outside of wake, absolute velocity
V_0	Influent velocity at runner brim gap
V_c	Cavity volume
V_r	Voltage at generator output ends
V_{vap}	Elastic volume
V_u	Absolute velocity circumferential component
∂V	Boundary of control volume V
$\{\boldsymbol{V}_0\}$, $\{\boldsymbol{V}_{N+1}\}$	Vectors of dimension p
v	Relative velocity of vortex row to stream speed, velocity magnitude
v_θ	Absolute tangential velocity
$-\rho\overline{v_i' v_j'}$	Reynolds stresses
$\{\boldsymbol{v}\}$	Velocity vector, absolute velocity
$\{\boldsymbol{v}_r\}$	Relative velocity
$\{\boldsymbol{v}_\sigma\}$	Grid velocity of moving mesh, velocity of reference system
$\hat{v}$	Velocity of reference coordinates relative to space coordinates
$\{\boldsymbol{V}(\boldsymbol{X})\}$	Boundary conditions vector

W	Numerical basis function in FEM, mean velocity, relative velocity in runner complex potential
W_z	Pressure force on pad along z direction
W^*_∞	Free-stream axial velocity in draft tube
W^*_c	Centre line axial velocity in draft tube
ΔW^*	Velocity difference $\Delta W^* = W^*_c - W^*_\infty$
$W_x(t, f)$	Wigner distribution of $x(t)$
W_x	Window function
$[\boldsymbol{W}_k]$	$p \times p$ matrix
w_m	Meridian component of relative velocity
$w_i(x)$	Basis functions
Δw	Sample interval
X	Displacement material coordinates (Lagrangian description coordinates)
$\{\boldsymbol{X}\}$	Displacement amplitude vector, eigenvectors exact solution in FEM state vector
x	Ordinate, displacement, blade length space coordinates (Eulerian coordinates)
x_p	Excitation point
x_q	Generator shaft reactance
x'_d	Generator shaft reactance at transient process
$x(t)$	System input function
x_i, y_i	Journal displacements
x_f, y_f	Bearing bracket displacements
$x(t)$	History signal
$x^*(t)$	Complex conjugate of $x(t)$
$\mathrm{d}x$	Length
$\Delta x, \Delta y$	Small disturbances
δx	Virtual displacement
$\{\boldsymbol{x}\}$	Displacement vector, generalized coordinates
$\{\boldsymbol{x}^c\}$	Response displacement vector
$\{\boldsymbol{x}_s\}$	Surface position of structure wetted by fluid (FSI)
$\dot{x}$	Velocity
$\{\dot{\boldsymbol{x}}\}$	Velocity vector
$\ddot{x}$	Acceleration
$\{\ddot{\boldsymbol{x}}\}$	Acceleration vector
X_q	Reactance of generator armature
Y	Amplitude along y direction discretized solution, vibration amplitude
$\{\boldsymbol{Y}(t)\}$	Modal ordinates
y	Homogeneous solution, eccentricity, ordinate
$y_{\min}$	The shortest distance to wall from station
$y(t)$	System output function
$\{\boldsymbol{y}(t)\}$	Output vector

Z	Partition function, blade number
Z_1, Z_2	Complex constants
Z_g	Guide vane number
z	Axis ordinate
$z = x + \mathrm{i}y$	Complex number
z_0	Value of amplitude of z
$\boldsymbol{z}$	Complex coordinate $\boldsymbol{z} = x + \mathrm{i}y$
$\bar{\boldsymbol{z}}$	Complex conjugate $\bar{\boldsymbol{z}} = x - \mathrm{i}y$
$\{\boldsymbol{z}\}$	State vector

2. Greek Letters

∇	Gradient
Λ_0	Mean magnetic conductance
α	Phase angle, angle deformation, pressure coefficient, angle between velocity vector and radius R, vortex type factor, normalized cavity volume
$\alpha*$	Stiffness ratio $\alpha* = k_\eta / k_\xi$
α, β	Torsional angle displacement a of thrust disc on xoz and yoz planes, scalar values of a system
α, q	AI/CI characters
β	Phase, characteristic factor, relative flow angle, dimensionless parameter, factor to consider deleting high order terms
β_0	Runner exit vane angle
β_j	Tilting angle of pad in radial direction
β_n	Non-rotating damping factor with nonlinear
β_r	Rotating damping factor with nonlinear effect
$\Delta\beta$	Attack angle
χ	Angle between symmetrical and rotating axises, reference coordinates, mass flow gain factor
$\{\boldsymbol{\chi}\}$	Deforming reference system
Δ	Laplace operator, Δ-criterion, the largest dimension of the grid cell, mesh scale, difference of momentum
δ	Dirac delta function, operation angle expressed as difference between torsion angle of shaft and its initial value, mean radius gap, added mass effect ratio
δ_0	Mean gap
δ_2	Blade thickness
δ_{Fe}	Equivalent gap coefficient of ferromagnet
δ_v	Virtual boundary layer thickness
ε	Turbulent dissipation rate, eccentricity, over time of end time of CSD (FSI), pipe perimeter deflection $\varepsilon = \mathrm{d}D/D$
ε_0, φ_0	Equilibrium position ordinates of journal

$\hat{\varepsilon} = \varepsilon/\delta$	Relative eccentricity
$\{\varepsilon\}$	Strain
$\{\varepsilon^*\}$	Consistent strains
$\boldsymbol{\varepsilon}(\boldsymbol{v})]$	Strain-rate tensor
ϕ	complex angular coordinate $\phi = \varphi y - \mathrm{i}\varphi_{X'}$ flow potential, flow coefficient of pump generator inner power coefficient general scalar
$[\phi]$	Matrix of equation character vectors
$\boldsymbol{\Phi}$	Amplitude of angular vibration phase of state unbalance vector response
$[\boldsymbol{\Phi}]$	"$N \times L$" Solution matrix containing L spatial vectors without time
φ	Phase angle, angular position circumferential ordinate angular coordinate of any point on pad
φ_{T1}, $\varphi_{T2}, \ldots,$	Pad swing angle
$\{\boldsymbol{\varphi}(\{\boldsymbol{\chi}\}, \boldsymbol{t})\}$	Deformation with unique mapping
Γ	Modal participation factor, closed bounder velocity circulation, diffusion coefficient
Γ_D	Dirichlet boundary
Γ_N	Neumann boundary
Γ_t	Time dependent boundary
γ	Surface tension coefficient effect coefficient considering the shear stress
γ_i	Tilting angle of pad in circumferential direction
$\gamma_1(s_1), \gamma_2(s_2)$	Vortex distributions on blades
$\gamma_1(\xi)$	Free vortex distribution downstream of blades
η	Mass-proportional damping coefficient
η_h	Hydraulic efficiency
η_s	Dynamic viscosity
$(\eta_1, \cdots, \eta_N)$	Shape functions of elements
$[\Lambda]$	Character values diagonal matrix
λ	Coefficient, friction loss coefficient fluid circumferential average velocity ratio, wavelength
λ_m	Lam'e constant
μ	Dynamic viscosity coefficient of nonlinear term of stiffness coefficient of vortex rope
μ_0	Magnetic conductivity in the air space
μ_m	Lam'e constant
$\mu_{i\text{-}1}$, μ_i	Mass per unit length
μ_t	Turbulent viscosity subgrid-scale turbulent viscosity
v	Kinematic viscosity
σ	Tomas coefficient, small unsteady change of pressure eigenvalues of velocity gradient tensor
σ_{kj}	Cauchy stress tensor at Eulerian system
$\{\boldsymbol{\sigma}\}$	Internal stresses

$\{\boldsymbol{\sigma}_f\}$	Stresses exerted by fluid on structure
$[\boldsymbol{\sigma}^S]$	Cauchy stress tensor of structure
θ	Torsional angle, inner power angle of generator, angular coordinate, small angle between source and observe
θ_p	Angular coordinate of pivot in inertial coordinate
θ_{yj}, θ_{xj}	Components of tilting angle of thrust block
θy, θ_x	Projected on pivot coordinate
ρ	Density
ρ^s	Material density of structure
ζ	Complex coordinates defined in $\xi\eta$-plane, local loss coefficient, damping factor or damping ratio
ζ_n, ζ_r	Damping ratios with the linearized system frame
τ	Torque, lag time between stimulus at time s and response at time t, τ=t-s
$[\boldsymbol{\tau}]$, $[\boldsymbol{\tau}_r]$	Viscous stress tensor
τ_{ij}	Reynolds stress tensor
$\Omega\{\boldsymbol{\Omega}\}$	Angular velocity, angular velocity of rotor rotor,
Ω	Unit angular speed Ω=$\pi D_1 n/(60(2gh)^{1/2})$
$\Omega_{cr\mathrm{I}}$	First order critical velocity
$\Omega_{cr\mathrm{II}}$	Second order critical velocity
Ω_t	Spatial domain
$\bar{\Omega}_r$	Per unit runner speed
Ω^*	Relative spin speed $\Omega^* = \Omega/\Omega_{cr\mathrm{I}}$
$\bar{\Omega}_r$	Angular momentum
Ω_c^*	Angular velocity at the axis in draft tube
$[\boldsymbol{\Omega}_h^2]$	Diagonal matrix
ω	Frequency, precession angular speed (whirl speed), system vibration frequency,complex frequency, specific dissipation
ω^*	Relative whirl speed in xy-plane $\omega^* = \omega/\Omega_{cr\mathrm{I}}$
ω_R	Real part of complex frequency
ω_I	Imaginary part of complex frequency damping rate
ω_N	Gyroscopic speed of water in gap
ω_n	Natural frequency
$\{\boldsymbol{\omega}\}$	Eddy of fluid flow
$\{\boldsymbol{\omega}_n\}$	Angular speed vector of precession rotation
Ω'	Complex whirl speed in $\xi\eta$-plane
Ω'^*	Relative complex whirl speed
ξ	Friction coefficient
$[\boldsymbol{\Psi}]$	Transfer matrix
$\boldsymbol{\Psi}$	Head coefficient, pressure coefficient
ς_{T}	Coefficient represented effect of runner
ς_2	Loss coefficient of draft tube
ς	Stiffness-proportional damping coefficient

3. Superscripts

-1	Inverse
$*$	Relative value, dimensionless, scale value
k	Addend
n, $n+1$	At current and next time level
s	Structure
T	Transpose
$\wedge$	At AEL reference coordinates
$[^-]$	Matrix in modal ordinates
‘	Smooth discrete Fourier transform

4. Subscripts

0	Initial condition, constant one, mean value
1	Nonlinear, at inlet upstream of the runner
2	Quadratic, at outlet at downstream side of runner
A	Angule
a	Air
av	Air vessel
B	Bearing bracket
C	Cos function
Cor	Coriols effect
c	Centre
ca	Cavitation
cr	Critical
comp	Complete
D	Design point, diaphragm
d	Under damped vibration, discrete Fourier transform
e	Exit, element
elec	Electromagnetic
eq, *equ*	Equivalent
f, fluid	Fluid
G	Gallery
gen	Generator
s	Sample
ST	Surge tank
T	Turbine runner
i	Inlet, ith elementary pipe
inlet	Inlet
I	Imaginary part
L	Left
M	Material coordinates

mag	Magnetic
max	Maximum
m, n	Order number
o	Optimum case
P	Penstock
p	Pump
pipe	Pipe
R	Real part, reference coordinates, vortex rope, right
r	Risel, rated, radius component, rotating
rad	Radial direction
ref	Reference
rop	Cavitation vertex rope
S	Sin function, space coordinates
s	Static, stationary
sk	Skew-symmetric
spin	Rotating effect
static	Static
sym	Symmetric
t	Turbine
tan	Tangential direction
throat	Throat in draft tube
tot	Total
u	Non-dissolved gas
v	Vapor, valve
ve	Viscoelastic
w	Water
x	Component along x axis
y	Component along y axis
z	Component along z axis
φ	Circumferential component
ξ	Component along ξaxis
η	Component along η axis
ζ	Component along ζ axis

Appendix II
Abbreviation

3-D	Three dimensional
ANC	Adaptive noise cancellation
AI	Absolute instability
AEL	Arbitrary Eulerian-Lagrangian method
BOP	Best operation point
CFD	Computational fluid dynamics
CI	Convective instability
CRS	Critical speed
CS	Controlling system
CSD	Computational solid dynamics
CTD	Computational thermal dynamics
DAF	Dynamic amplification factor
DFT	Discrete Fourier transformation
DGCL	Discrete geometric conservation laws
DES	Detatched eddy simulations
DNS	Direct numerical simulation
DSM	Differential stress models
D.T.	Draft tube
EVM	Eddy-viscosity models
FEM	Finite element method
FFT	Fast Fourier transform
FT	Fourier transform
FSI	Fluid solid interaction
GMWS	Geometric mean of WD and spectrogram
G.V.	Guide vanes
ISO	International Organization for Standardization
IEC	The International Electrotechnical Commission
LDV	Laser Doppler vibrometers
LES	Large-eddy simulation
LGB	Lower guide bearing of turbine unit
MED	Maximum eccentric distance

Y. Wu et al., *Vibration of Hydraulic Machinery*,
Mechanisms and Machine Science 11, DOI: 10.1007/978-94-007-6422-4,

MSM	Modal synthesis method
ND	Nodal diameters
NPSH	Net positive suction head
NLEVM	Non-linear eddy-viscosity models
Pre pul	Pressure pulsation
PWD	Pseudo Wigner distribution
RANS	Reynolds averaging Navier-Stokes equations
RCP	Reactor coolant pump
RLC	Resistance, inductance and capacitance
RMS	Root mean square
RNG	Renormalization group
RSI	Rotor stator interaction
RSMM	Riccati transfer matrix method
RSTM	Reynolds-stress transport models
SA	Averaged signal
S.C.	Spiral casing
SDTF	Sole draft tube flow
SNR	Signal to noise ratio
SOC	Second-order closure models
S.V.	Stay vanes
TFR	Time frequency representation
TGB	Turbine guide bearing
TMM	Transfer matrix method
TRTMM	Transfer Riccati transfer matrix method
UGB	Upper guide bearing of turbine unit
Vib	Vibration
VMS	Vibration monitoring system
WA	Wavelet analysis
WD	Wigner distribution
WFT	Windowed Fourier transform
WTF	Whole turbine flow
WVD	Winger-Ville distribution

Index

Y. Wu et al., *Vibration of Hydraulic Machinery*,
Mechanisms and Machine Science 11, DOI: 10.1007/978-94-007-6422-4,